Preface

This report contains the 2004 annual progress reports of the Research Fellows and students of the Center for Turbulence Research in its eighteenth year of operation. A separate report documenting the findings from the tenth biennial CTR Summer Program which included fifty participants from fourteen countries was published earlier this year. CTR publications, including this report and the Summer proceedings are available on the world wide web (http://ctr.stanford.edu).

Since its inception in 1987, the objective of the CTR has been to advance the physical understanding of turbulent flows and development of physics based predictive tools for engineering analysis and turbulence control. Turbulence is ubiquitous in nature and in engineering devices. The studies at CTR have been motivated by applications where turbulence effects are significant; these include a broad range of technical areas such as planetary boundary layers, formation of planets, solar convection, magnetohydrodynamics, environmental and eco systems, aerodynamic noise, propulsion systems and high speed transportation. Numerical simulation has been the predominant research tool at CTR which has required a critical mass of researchers in numerical analysis and computer science in addition to core disciplines such as applied mathematics, chemical kinetics and fluid mechanics. Maintaining and promoting this interdisciplinary culture has been a hallmark of CTR and has been responsible for the realization of the results of its basic research in applications. Continued demonstration of the utility of research results in applications has, in turn, led to a strong and mutually beneficial relationship with industry through Stanford's Thermal and Fluid Sciences Industrial Affiliate Program.

Last year CTR hosted thirteen resident Postdoctoral Fellows, eleven Research Associates, and ten Senior Fellows. The support for the Research Associates and Senior Fellows were largely provided by the Department of Energy's ASC program at Stanford. The major portion of Stanford's graduate student research in turbulence which is carried out at CTR is sponsored by the United States Air Force Office of Scientific Research, the Office of Naval Research and the Department of Energy.

The first group of reports in this volume are directed towards development, analysis and application of novel numerical methods for flow simulations. Development of methods for large eddy simulation of complex flows has been a central theme in this group. The second group is concerned with turbulent combustion, scalar transport and multi-phase flows. The final group is devoted to geophysical turbulence where the problem of solar convection has been a new focus of considerable attention recently at CTR.

The CTR roster for 2004 is provided in the Appendix. Also listed are the members of the CTR Steering Committee which has met quarterly to act on fellowship applications. We have also included, with a deep sense of gratitude, a list of all members of the Advisory Committee who have served the Center for Turbulence Research since its inception in 1987. Without their invaluable insights, and the intellectual and infrastructure support of NASA, CTR would not have been able to serve the international turbulence research community in the comprehensive fashion it has become known for.

It is a great pleasure to thank Millie Chethik for her day to day management of the Center and together with Dr. Xiaohua Wu for their skillful compilation of this report.

Parviz Moin
Nagi N. Mansour

Energy conservation in collocated discretization schemes on unstructured meshes

By F. Ham AND G. Iaccarino

1. Motivation and Objectives

Recently, Mahesh *et al.* (2004) proposed a control-volume-based collocated fractional step method for the incompressible Navier-Stokes equations suitable for large-eddy simulation (LES) and direct numerical simulation (DNS) on hybrid unstructured grids. Their approach emphasizes kinetic energy conservation for the convection and pressure terms. A significant contribution of their work is a novel least-squares pressure gradient reconstruction, which attempts to minimize the non-conservation of the pressure term in the context of a collocated discretization. They report that this least squares reconstruction was found imperative to obtain robust, accurate solutions in the presence of highly skewed elements; unstable solutions were obtained in its absence.

The present report describes our efforts to develop an alternative reconstruction for pressure by considering consistency in the presence of mesh skewness as an additional constraint to that of the minimization of any non-conservation of kinetic energy.

2. Algorithm

Figure 1 illustrates the location of variables used in the present formulation, with the full velocity vector u_i and pressure p stored at the control volume centroid, and the normal component of velocity U_f stored at each face. Based on this arrangement of variables, a fractional-step semi-discretization of the incompressible Navier-Stokes equations with good kinetic energy conservation properties is as follows (Kim & Moin 1985; Zang *et al* 1994; Kim & Choi 2000; Mahesh *et al.* 2004):

$$V_p \frac{\widehat{u}_{i,p} - u^n_{i,p}}{\Delta t} + \sum_f U^{n+1/2}_f \left(\frac{u^{n+1/2}_{i,p} + u^{n+1/2}_{i,nbr}}{2} \right) A_f = -V_p \frac{\partial p}{\partial x_i}^{n-1/2} \tag{2.1}$$

$$\frac{u^*_{i,p} - \widehat{u}_{i,p}}{\Delta t} = + \frac{\partial p}{\partial x_i}^{n-1/2} \tag{2.2}$$

$$\frac{u^{n+1}_{i,p} - u^*_{i,p}}{\Delta t} = - \frac{\partial p}{\partial x_i}^{n+1/2} \tag{2.3}$$

In the above notation, the subscript p indicates a value associated with the control volume, and nbr indicates a neighbor control volume sharing a common face f. Superscripts are used to indicate time level. We have of course not included the viscous terms.

On staggered grids, one can immediately take the divergence of the last equation (2.3) and get a Poisson system for pressure, using continuity to eliminate the dependence on the unknown velocity $u^{n+1}_{i,c}$. With a collocated formulation, however, this will lead to the well-known velocity/pressure decoupling, and it is necessary to introduce some smoothing

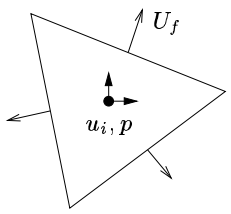

FIGURE 1. Spatial location of variables for collocated discretization.

to the pressure. In the present approach, we introduce the necessary smoothing implicitly by interpolation. Writing equation 2.3 at the face in the face-normal direction:

$$\frac{U_f^{n+1} - U_f^*}{\Delta t} = -\frac{\partial p}{\partial n}^{n+1/2} \tag{2.4}$$

Taking the discrete divergence of of eqn 2.4, and using the continuity equation $\sum_f U_f^{n+1} A_f = 0$ yields a Poisson system for pressure which can be solved and used to correct the face normal velocity components to be divergence-free.

$$\sum_f \frac{\partial p}{\partial n}^{n+1/2} A_f = \frac{1}{\Delta t} \sum_f U_f^* A_f \tag{2.5}$$

In the previous equations, the required pressure gradients have been left in differential form. Their precise discrete form is the focus of this work.

3. Conservative Properties

In their differential form, the incompressible Navier-Stokes equations conserve mass, momentum, and kinetic energy (in the inviscid limit). The kinetic energy equation can be derived by contracting the momentum equation with the velocity vector, u_i. In the absence of viscosity, all terms can be rearranged to yield either a divergence form or the continuity equation (i.e. zero), and thus kinetic energy conservation is a property of the underlying equations. For example:

$$u_i \left(\frac{\partial u_i}{\partial t} + \frac{\partial u_j u_i}{\partial x_j} = -\frac{\partial p}{\partial x_i} \right) \tag{3.1}$$

Expanding each of the 3 resulting terms yields:

$$\begin{aligned} (Time) &= u_i \frac{\partial u_i}{\partial t} \\ &= \frac{\partial u_i u_i / 2}{\partial t} \equiv \frac{\partial K}{\partial t} \end{aligned} \tag{3.2}$$

$$\begin{aligned} (Conv.) &= u_i \frac{\partial u_j u_i}{\partial x_j} \\ &= \frac{\partial u_j u_i u_i / 2}{\partial x_j} - \frac{1}{2} u_i u_i \frac{\partial u_j}{\partial x_j} \end{aligned} \tag{3.3}$$

$$
\begin{aligned}
(Pres.) &= -u_i \frac{\partial p}{\partial x_i} \\
&= -\frac{\partial u_i p}{\partial x_i} + p\frac{\partial u_i}{\partial x_i}
\end{aligned} \tag{3.4}
$$

We can apply the same procedure to our discrete system to investigate its conservation properties. Here we operate on the sum of equations (2.1), (2.2) and (2.3). For the unsteady term:

$$
\begin{aligned}
\int (Time)\, dV &\approx u_{i,p}^{n+1/2} \left(\frac{u_{i,p}^{n+1} - u_{i,p}^{n}}{\Delta t} \right) V_p \\
&= \frac{u_{i,p}^{n} + u_{i,p}^{n+1}}{2} \left(\frac{u_{i,p}^{n+1} - u_{i,p}^{n}}{\Delta t} \right) V_p \\
&= \left(\frac{(u_{i,p}u_{i,p}/2)^{n+1} - (u_{i,p}u_{i,p}/2)^{n}}{\Delta t} \right) V_p \\
&= \left(\frac{K^{n+1} - K^{n}}{\Delta t} \right) V_p
\end{aligned} \tag{3.5}
$$

For the convective term:

$$
\begin{aligned}
\int (Conv.)\, dV &\approx u_{i,p}^{n+1/2} \sum_f U_f^{n+1/2} \left(\frac{u_{i,p}^{n+1/2} + u_{i,nbr}^{n+1/2}}{2} \right) A_f \\
&= \sum_f U_f \left(\frac{u_{i,nbr}u_{i,p}}{2} \right) A_f - \frac{u_{i,p}u_{i,p}}{2} \sum_f U_f A_f
\end{aligned} \tag{3.6}
$$

where the superscripts that indicate the mid-point in time (a simple average) are dropped in the second line. The first term on the RHS of equation (3.6) is in discrete divergence form and, therefore, is discretely conservative. The second term includes the discrete continuity equation as a factor, and is zero locally and globally.

For the pressure term, we initially use a Green-Gauss reconstruction with equal-weighted interpolations to the faces as follows:

$$
\begin{aligned}
&\int (Pres.)\, dV \\
&\quad \approx -u_{i,p}^{n+1/2} \sum_f \frac{\left(p_{nbr}^{n+1/2} + p_p^{n+1/2} \right)}{2} n_{i,f} A_f \\
&\quad = -\sum_f \left(\frac{u_{i,p}p_{nbr} + u_{i,nbr}p_p}{2} \right) n_{i,f} A_f + p_p \sum_f \left(\frac{u_{i,p} + u_{i,nbr}}{2} \right) n_{i,f} A_f
\end{aligned} \tag{3.7}
$$

Once again we have dropped the superscripts that indicate the midpoint in time. The first term on the RHS of equation (3.7) is in discrete divergence form and thus is discretely conservative. Although the second term looks like a discrete divergence of the velocity field, it will not (necessarily) be zero when continuity is satisfied because $(u_{i,p} + u_{i,nbr})n_{i,f}/2 \neq U_f$. As pointed out by Mahesh *et al.*, minimizing the non-

conservation of kinetic energy associated with the pressure term is analogous to minimizing the magnitude of this discrete divergence.

Using equations (2.2) and (2.4), the continuity-like portion of the pressure term can be rearranged as follows:

$$\begin{aligned}
&\sum_f \left(\frac{u_{i,p}+u_{i,nbr}}{2}\right) n_{i,f} A_f \\
&\quad = \sum_f \left(\frac{u^*_{i,p}+u^*_{i,nbr}}{2}\right) n_{i,f} A_f - \Delta t \sum_f \frac{1}{2}\left(\left.\frac{\partial p}{\partial x_i}\right|_p + \left.\frac{\partial p}{\partial x_i}\right|_{nbr}\right) n_{i,f} A_f \\
&\quad = \sum_f U^*_f A_f - \Delta t \sum_f \frac{1}{2}\left(\left.\frac{\partial p}{\partial x_i}\right|_p + \left.\frac{\partial p}{\partial x_i}\right|_{nbr}\right) n_{i,f} A_f \\
&\quad = \sum_f U_f A_f + \Delta t \sum_f \left[\frac{\partial p}{\partial n} - \frac{1}{2}\left(\left.\frac{\partial p}{\partial x_i}\right|_p + \left.\frac{\partial p}{\partial x_i}\right|_{nbr}\right) n_{i,f}\right] A_f \\
&\quad = \Delta t \sum_f \left[\frac{\partial p}{\partial n} - \frac{1}{2}\left(\left.\frac{\partial p}{\partial x_i}\right|_p + \left.\frac{\partial p}{\partial x_i}\right|_{nbr}\right) n_{i,f}\right] A_f
\end{aligned} \tag{3.8}$$

In arriving at this expression, we have employed a definition of U^*_f that affords the simplification to terms involving pressure only, namely:

$$U^*_f = \left(\frac{u^*_{i,p}+u^*_{i,nbr}}{2}\right) n_{i,f} \tag{3.9}$$

It is straightforward to show that the non-conservative term is a discrete approximation to a term involving the 4th derivative of pressure. Using a Taylor-series expansion of $\partial p/\partial n$ at each control volume associated with a face and assuming a control volume spacing of Δn:

$$\begin{aligned}
&\Delta t \sum_f \left[\left.\frac{\partial p}{\partial n}\right|_f - \frac{1}{2}\left(\left.\frac{\partial p}{\partial x_i}\right|_p + \left.\frac{\partial p}{\partial x_i}\right|_{nbr}\right) n_{i,f}\right] A_f \\
&\qquad \approx \Delta t \sum_f \left[-\frac{1}{2}\left(-\frac{\Delta n}{2}\left.\frac{\partial^2 p}{\partial n^2}\right|_p + \frac{\Delta n}{2}\left.\frac{\partial^2 p}{\partial n^2}\right|_{nbr}\right)\right] A_f \\
&\qquad \approx \Delta t \sum_f \left[-\frac{\Delta n^2}{4}\left.\frac{\partial^3 p}{\partial n^3}\right|_f\right] A_f \\
&\qquad \approx -\frac{\Delta t \Delta x_i^2}{4}\left.\frac{\partial^4 p}{\partial x_i^4}\right|_p V_p
\end{aligned} \tag{3.10}$$

In the kinetic energy equation, it is also straightforward to show that the effect of this non-conservative term is dissipative:

$$\frac{\partial K}{\partial t} + \frac{\partial}{\partial x_i}(...) = -\left(\frac{\Delta t \Delta x_i^2}{4}\right) p \frac{\partial^4 p}{\partial x_i^4}$$

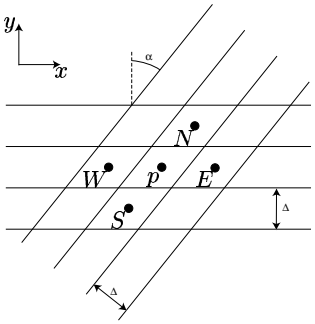

FIGURE 2. Skewed two-dimensional mesh with mesh spacing Δ and skewness angle α.

$$= -\left(\frac{\Delta t \Delta x_i^2}{4}\right)\left(\frac{\partial}{\partial x_i}\left(p\frac{\partial^3 p}{\partial x_i^3}\right) - \frac{\partial p}{\partial x_i}\frac{\partial^3 p}{\partial x_i^3}\right)$$
$$= -\left(\frac{\Delta t \Delta x_i^2}{4}\right)\left(\frac{\partial}{\partial x_i}\left(p\frac{\partial^3 p}{\partial x_i^3} - \frac{\partial p}{\partial x_i}\frac{\partial^2 p}{\partial x_i^2}\right) + \left(\frac{\partial^2 p}{\partial x_i^2}\right)^2\right) \quad (3.11)$$

The first term is in divergence form, and thus will not add or remove to the kinetic energy, but just redistribute it between adjacent control volumes (assuming constant Δt and Δx_i). The right-most term is a square and thus the net effect on K is guaranteed dissipative. Note that the summation convention does not apply to the individual terms involving pressure in equation (3.11).

4. Discussion

The algorithm thus far has been developed using equally-weighted interpolations. On meshes with skewness and non-uniform spacing, these approximations can introduce significant errors that manifest in a lack of robustness.

To address this problem, Mahesh *et al.* developed a face-area-weighted least-squares minimization to reconstruct the pressure. Their choice of weighting is motivated by the form of the non-conservative term in equation (3.8). For example, at control volume p the following error expression is minimized with respect to the three unknown components of the gradient at point p:

$$\varepsilon_p = \sum_f A_f \left(\left.\frac{\partial p}{\partial x_i}\right|_p n_{i,f} - \left.\frac{\partial p}{\partial n}\right|_f\right)^2 \quad (4.1)$$

where the normal component of the pressure gradient at each face is approximated as:

$$\left.\frac{\partial p}{\partial n}\right|_f = \frac{p_{nbr} - p_p}{(x_{i,nbr} - x_{i,p})\, n_{i,f}} \quad (4.2)$$

Consider the two-dimensional skewed mesh shown in figure 2. This mesh has been skewed by angle α such that the face areas remain the same in all directions. Applying this least-squares reconstruction yields the following expressions for the components of the pressure gradient at point p:

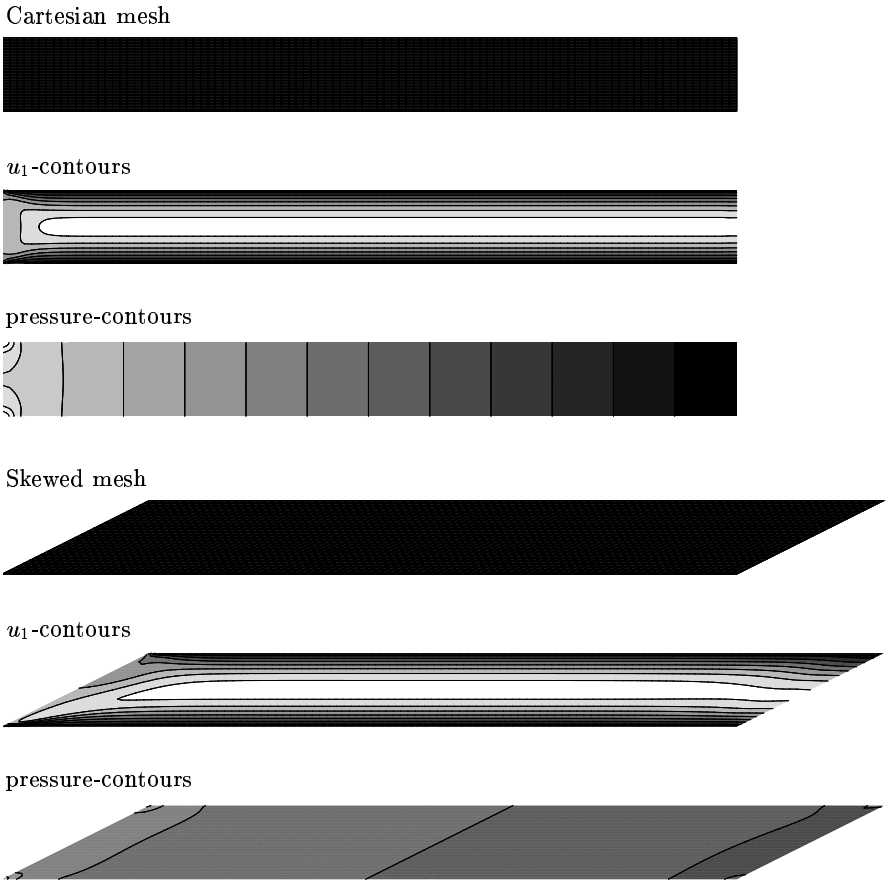

FIGURE 3. Laminar channel flow at $Re = Uh/\nu = 10$ at steady-state for both a Cartesian grid and a skewed grid using the least-squares pressure gradient reconstruction. Contour spacing is the same for both pressure plots.

$$\left.\frac{\partial p}{\partial x}\right|_p = \frac{p_E - p_W + (p_N - p_S)\ sin(\alpha)}{2\ \Delta\ cos(\alpha)} \tag{4.3}$$

$$\left.\frac{\partial p}{\partial y}\right|_p = \frac{p_N - p_S}{2\ \Delta} \tag{4.4}$$

Note the counterintuitive result that the y-component of the gradient is unaffected by the skew angle. To illustrate how this can significantly affect the accuracy of a computation on skewed grids, consider the problem of a laminar channel with a specified uniform velocity at the inlet. At Reynolds number $Re = Uh/\nu = 10$, where h is the channel height, the flow can be integrated to steady-state, yielding the expected laminar parabolic profile with uniform pressure drop, as illustrated in the computation shown in figure 3. For the Cartesian case, the predicted pressure gradient exactly matches the theoretical result required to balance the viscous drag in the downstream region.

When significant skewness is introduced to the mesh, however, the contours of pressure

become skewed as well, and the pressure drop is significantly under-predicted (also figure 3. For calculations involving more complex geometries, such as a swirl nozzle in a jet engine combustor, it is very difficult to avoid mesh skewness in the many small passages involved, and an alternative pressure reconstruction is considered necessary to improve the accuracy of the predictions.

5. An alternative reconstruction

Using the Green-Gauss reconstruction, the expressions for the gradient components on the two-dimensional skewed mesh shown in figure 2 would be:

$$\left.\frac{\partial p}{\partial x}\right|_p = \frac{(p_E - p_W)\ cos(\alpha)}{2\ \Delta} \tag{5.1}$$

$$\left.\frac{\partial p}{\partial y}\right|_p = \frac{p_N - p_S - (p_E - p_W)\ sin(\alpha)}{2\ \Delta} \tag{5.2}$$

The solution to the problem of skewness sensitivity of the results, however, is not quite as simple as replacing the least-squares reconstruction with Green-Gauss. The approximation to the normal derivative used in formulating the Poisson system must also properly account for any skewness. Following Zwart (Zwart 1999), we write the normal pressure gradient at the face in terms of a component along the unit vector formed by joining the two control volume centroids $s_{i,f}$:

$$\begin{aligned}\left.\frac{\partial p}{\partial n}\right|_f &= \left.\frac{\partial p}{\partial x_i}\right|_f n_{i,f} \\ &= \left.\frac{\partial p}{\partial x_i}\right|_f \alpha_f s_{i,f} + \left.\frac{\partial p}{\partial x_i}\right|_f (n_{i,f} - \alpha_f s_{i,f})\end{aligned} \tag{5.3}$$

where we have introduced the face-based scalar α_f. The first term on the RHS of equation (5.3) can be approximated to second order using:

$$\left.\frac{\partial p}{\partial x_i}\right|_f \alpha_f s_{i,f} = \alpha_f \frac{\partial p}{\partial s} \approx \alpha_f \frac{p_{nbr} - p_p}{|x_{i,nbr} - x_{i,p}|} \tag{5.4}$$

For the second term, we can use the simple average of the Green-Gauss gradients at the adjacent control volume centroids p and nbr, yielding the following expression for the full normal component:

$$\frac{\partial p}{\partial n} \approx \alpha_f \frac{\partial p}{\partial s} + \frac{1}{2}\left(\left.\frac{\partial p}{\partial x_i}\right|_p + \left.\frac{\partial p}{\partial x_i}\right|_{nbr}\right)(n_{i,f} - \alpha_f s_{i,f}) \tag{5.5}$$

where it remains to define the most suitable value of α_f. At this point it is instructive to substitute this expression for the normal gradient into the non-conservative term derived earlier in equation (3.8).

$$\Delta t \sum_f \left[\frac{\partial p}{\partial n} - \frac{1}{2}\left(\left.\frac{\partial p}{\partial x_i}\right|_p + \left.\frac{\partial p}{\partial x_i}\right|_{nbr}\right) n_{i,f}\right] A_f$$

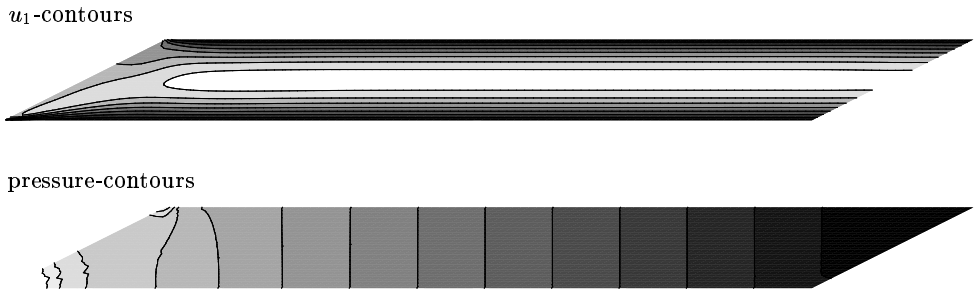

FIGURE 4. Laminar channel flow at $Re = Uh/\nu = 10$ using a skewed grid and the Green-Gauss pressure reconstruction with skew corrections.

$$= \alpha_f \Delta t \sum_f \left[\frac{\partial p}{\partial s} - \frac{1}{2} \left(\left. \frac{\partial p}{\partial x_i} \right|_p + \left. \frac{\partial p}{\partial x_i} \right|_{nbr} \right) s_{i,f} \right] A_f \tag{5.6}$$

So minimization of the non-conservation of kinetic energy due to the pressure term is equivalent to minimizing the above expression, or specifically minimizing α_f. The choice $\alpha_f = 0$ would actually result in a formulation that discretely conserves kinetic energy, but would of course also lead to the decoupling of velocity and pressure in the collocated formulation. In the present work, we choose the dot product $\alpha_f = s_{i,f} n_{i,f}$, which yields $\alpha = 1$ when the mesh is locally orthogonal, and always less than one when skewed. This is the same choice as ultimately made by Zwart, although in our case the justification is based on reducing the non-conservation of kinetic energy in the presence of skewness.

6. Results

6.1. *Skewed channel*

Figure 4 shows the results of the skewed laminar channel flow calculated using the Green-Gauss pressure reconstructions with face normal pressure gradient components approximated as described in the previous section. The correct mean pressure gradient in the fully developed part of the channel is recovered.

6.2. *Skewed Taylor vorticies*

The Taylor vortex problem is a second example that can be used to illustrate the sensitivity of the two reconstructions to skewness. The flow field consists of an array of decaying vortices with the following analytic expressions for velocity and pressure:

$$u = -cos(\pi x) sin(\pi y) e^{-\frac{2\pi^2 t}{Re}} \tag{6.1}$$

$$v = sin(\pi x) cos(\pi y) e^{-\frac{2\pi^2 t}{Re}} \tag{6.2}$$

$$p = -\frac{1}{4}(cos(2\pi x) + cos(2\pi y)) e^{-\frac{4\pi^2 t}{Re}} \tag{6.3}$$

where Re is the Reynolds number based on unit length and velocity scales. It is possible to integrate the kinetic energy over the periodic domain as well, yielding:

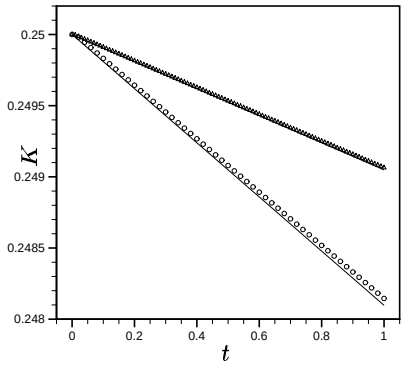

FIGURE 5. Kinetic energy for inviscid simulations of taylor problem on 32×32 Cartesian grid: $\triangle$ calculation with $\Delta x = 2/32$, $\Delta t = 0.01$; $\circ$ calculation with $\Delta x = 2/32$, $\Delta t = 0.02$; ——— equation (6.7). Both the least-squares and Green-Gauss reconstructions are identical for this case.

$$K_{taylor} = \frac{1}{V}\int_{-1}^{1}\int_{-1}^{1}\frac{u^2+v^2}{2}\,dx\,dy \tag{6.4}$$

$$= \frac{1}{4}e^{-\frac{4\pi^2 t}{Re}} \tag{6.5}$$

Solving the Taylor problem in the limit of infinite Reynolds number should result in a steady solution of non-decaying vortices with constant kinetic energy, $K = 1/4$. To perform this numerical experiment, a square domain was used with dimensions $-1 \leq x \leq 1$, and $-1 \leq y \leq 1$ and periodic boundary conditions. We note that other authors have typically used Dirichlet boundary conditions by applying the analytic velocity at the boundary. The use of periodic boundary conditions allows us to confirm numerically the non-conservation present in the scheme without the need to account for energy transfers at the boundaries. Using the analytic expression for pressure in the inviscid limit, the integration of the non-conservative term in the kinetic energy equation (3.11) over the periodic domain yields (per unit volume):

$$\frac{\partial K}{\partial t} = \frac{1}{V}\int_{-1}^{1}\int_{-1}^{1}\left(-p\frac{\Delta t \Delta x_i^2}{4}\frac{\partial^4 p}{\partial x_i^4}\right)dx\,dy \tag{6.6}$$

$$= -\frac{\pi^4}{4}\Delta t \Delta x^2 \tag{6.7}$$

where we have assumed a uniform cartesian grid with $\Delta x = \Delta y$.

Skewness can be introduced in the Cartesian mesh used for the Taylor problem by the following transformation:

$$x' = x + \beta sin(\pi y) \tag{6.8}$$

$$y' = y + \beta sin(\pi x) \tag{6.9}$$

where the parameter β controls the amount of skewness. Figure 6 compares a 32×32 Cartesian grid with one that has been *skewed* using $\beta = 0.2$.

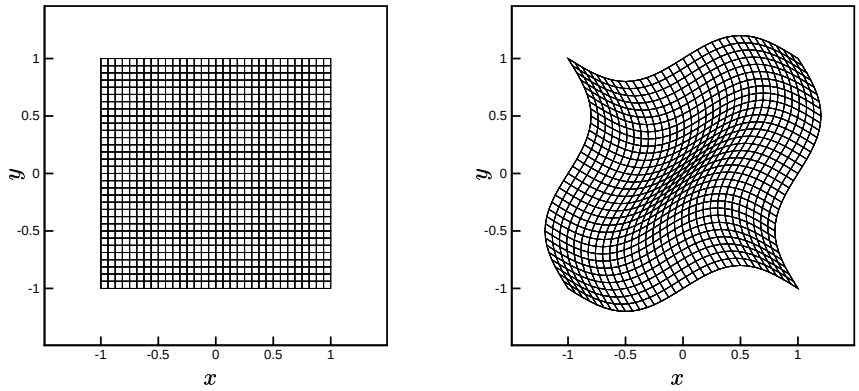

FIGURE 6. Comparison of Cartesian and Skewed meshes used for Taylor problem. Skew transformation is equation (6.9) with the $\beta = 0.2$.

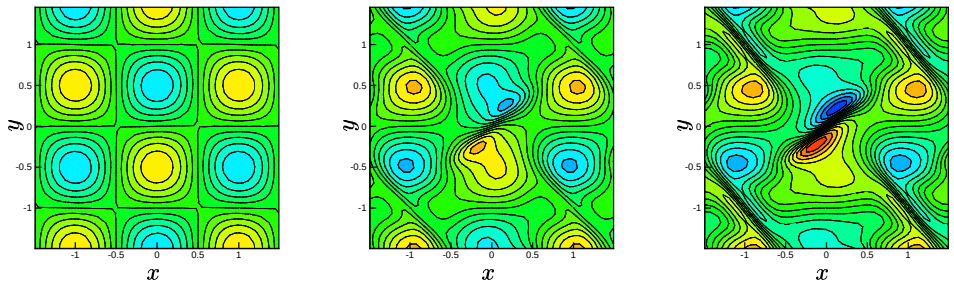

(a) Least-squares reconstruction at $t = 0, 0.25, 0.5$

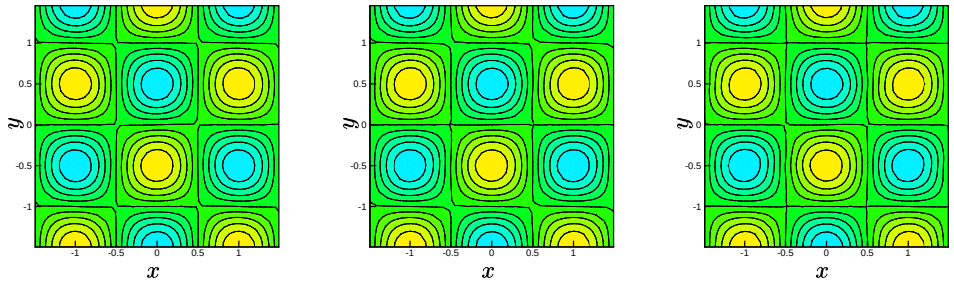

(b) Green-Gauss reconstruction at $t = 0, 0.25, 0.5$

FIGURE 7. Contours of u-velocity from the inviscid Taylor problem on the skewed mesh shown in figure 6 comparing results for different pressure reconstructions.Contour spacing is 0.2. Results have been copied in periodic directions for clarity.

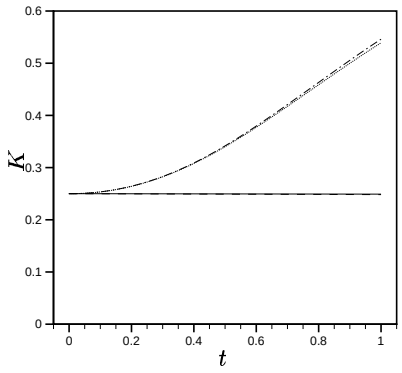

FIGURE 8. Kinetic energy for inviscid simulations of taylor problem on 32×32 skewed grid: ——— , – – – – present reconstruction for $\Delta t = 0.01, 0.02$ respectively; — – —, ····· mahesh *et al.* for $\Delta t = 0.01, 0.02$ respectively.

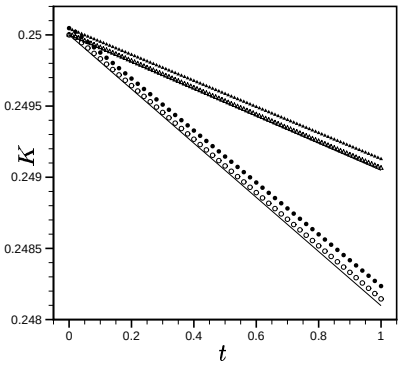

FIGURE 9. Kinetic energy for inviscid simulations of taylor problem on 32×32 Cartesian and skewed grid: $\triangle$ Cartesian grid with $\Delta x = 2/32$, $\Delta t = 0.01$; $\circ$ Cartesian grid with $\Delta x = 2/32$, $\Delta t = 0.02$; Solid symbols are the skewed grid results for the same grid size and time step; ——— equation (6.7) for both cases.

Computations were carried out on the skewed grid using the least-squares pressure reconstruction and the Green-Gauss reconstruction. Figure 7 compares contour plots of the instantaneous u-velocity field at three equally spaced times. The least-squares reconstruction significantly alters the velocity field, and actually increases the total kinetic energy. Figure 9 compares the time history of the integrated kinetic energy for both reconstructions for 2 different computational time steps. For this problem, the least-squares reconstruction resulted in the eventual divergence of the solution.

The reconstruction of Zwart, however, remains very well behaved, accurately retaining the vortex pattern even on the highly skewed grid. A slight reduction in kinetic energy was observed over the course of the simulation. Figure 9 compares the time history of the kinetic energy to the Cartesian results reported earlier, along with the analytic result. Apart from the slight discrepency in the initial condition, which does not yield exactly $K = 0.25$ when summed on the grid, the behavior is nearly identical.

7. Conclusions

Modifications to the pressure gradient reconstruction for both the normal component at the face and the full gradient at the control volume centroid have been proposed and analyzed analytically in terms of their impact on kinetic energy conservation. The analytic results have been confirmed numerically using inviscid simulations of Taylor vortices. The modified reconstruction has been shown to substantially improve the accuracy and conservation properties of the algorithm in the presence of mesh skewness. The only apparent drawback of this modified approach is the increase in stencil size of the resulting Poisson system, which must now include immediate neighbors, and neighbors of neighbors. Work is ongoing to analyze the accuracy and robustness of the reconstruction in the presence of non-uniform grid spacing, where the equal weightings used in the Green-Gauss gradient reconstruction (and required for kinetic energy conservation) can introduce substantial errors.

8. Acknowledgement

Support for this work was provided by the United States Department of Energy under the Advanced Simulation and Computing (ASC) program.

REFERENCES

Kim, D. & Choi, H. 2000 A second-order time-accurate finite volume method for unsteady incompressible flow on hybrid unstructured grids. *J. Comput. Phys.* **162**:411–428.

Kim, J. & Moin, P. 1985 Application of a fractional-step method to incompressible Navier-Stokes equations. *J. Comput. Phys.* **59**:308.

Mahesh, K., Constantinescu, G. & Moin, P. 2004 A numerical method for large-eddy simulation in complex geometries. *J. Comput. Phys.* **197**:215–240.

Verzicco, R. & Orlandi, P. 1996 A finite-difference scheme for three-dimensional incompressible flows in cylindrical coordinates. *J. Comput. Phys.* **123**:420–414.

Zang, Y., Street, R. L. & Koseff, J. R. 1994 A non-staggered grid, fractional step method for time-dependent incompressible Navier-Stokes equations in curvilinear coordinates. *J. Comput. Phys.* **114**:18–33.

Zwart, P. J. 2000 The integrated space-time finite volume method. *Ph.D. Thesis, University of Waterloo, Waterloo, Ontario, Canada.*

On mass conservation and desingularization of the Level Set/Vortex Sheet method

By M. Herrmann

1. Motivation and objectives

The Level Set/Vortex Sheet (LSVS) method has been introduced by Herrmann (2002, 2003*b*, 2004*a*,*b*). Its objective is to provide a framework for the derivation of the so called Large Surface Structure (LSS) model (Herrmann 2003*b*) that describes the primary breakup of turbulent liquid jets and sheets. The advantage of the LSVS method as compared to other, more traditional approaches is the fact that it contains explicit local source terms for each individual physical process that occurs at the phase interface, thus making these directly accessible to modeling attempts of the LSS subgrid terms.

As has been argued by Yecko *et al.* (2002) and Li *et al.* (2004), viscous effects might play an important role during primary breakup. The LSVS method, on the other hand, has been derived theoretically for the limit of inviscid fluids. However, its numerical implementation necessitates the introduction of a desingularization of the governing equations by introducing shear layers of finite width (Herrmann 2004*a*), thus imitating some effects of viscous fluids to a certain extend. This effect shall be analyzed in this paper.

Furthermore, as with any level set based method, the problem of mass conservation has to be addressed. To this end, different level set correction methods have already been proposed (Bourlioux 1995; Sussman & Fatemi 1999; Enright *et al.* 2002). Unfortunately, within the scope of the LSVS method, these correction methods lead to unacceptable fluctuations in the surface tension term due to the fact that all corrections are performed locally (Herrmann 2004*a*). On this account, a method to de-localize the correction methods has been proposed by Coyajee *et al.* (2004), resulting in significant, but unfortunately insufficient improvements with respect to the LSVS method. Hence, an alternative and rather simple and straightforward approach is proposed here, named refined level set grid (RLSG) method.

This paper is divided into three parts. First, the governing equations of the LSVS method for three-dimensional two-phase interface dynamics are summarized. Also, the numerical methods employed to solve the LSVS equations and the RLSG method and its implications within the LSVS method are presented. Second, numerical results are presented addressing both the performance of the RLSG method and the effect of desingularization inherent in the LSVS method. Finally, conclusions are drawn and an outlook to future work is given.

2. The Level Set/Vortex Sheet method

The LSVS method describes the dynamics of the phase interface Γ between two inviscid, incompressible fluids 1 and 2, as shown in Fig. 1. Defining the iso-surface of a level set scalar $G = 0$ to be the location of the phase interface, the motion of Γ can be tracked

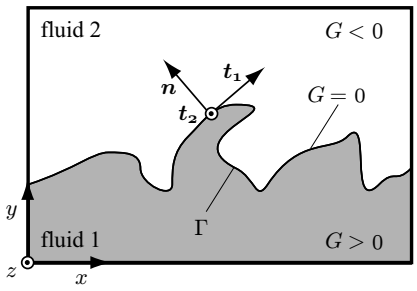

FIGURE 1. Phase interface definition.

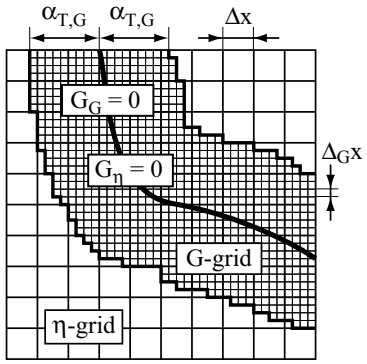

FIGURE 2. Refined level set grid definition.

by the so called level set equation (Osher & Sethian 1988),

$$\frac{\partial G}{\partial t} + \boldsymbol{u} \cdot \nabla G = 0\,, \tag{2.1}$$

where $\boldsymbol{u}$ is the velocity vector.

The velocity field generated by the phase interface can be described by a vortex sheet strength $\boldsymbol{\eta}$, which is equal to the jump in tangential velocity at the phase interface. The transport equation for $\boldsymbol{\eta}$ (Pozrikidis 2000; Herrmann 2003*b*) is given by

$$\begin{aligned}\frac{\partial \boldsymbol{\eta}}{\partial t} + \boldsymbol{u} \cdot \nabla \boldsymbol{\eta} = &-\boldsymbol{n} \times [(\boldsymbol{\eta} \times \boldsymbol{n}) \cdot \nabla \boldsymbol{u}] + \boldsymbol{n}\,[(\nabla \boldsymbol{u} \cdot \boldsymbol{n}) \cdot \boldsymbol{\eta}] \\ &+ \frac{2(A+1)}{\mathrm{We}}\,(\boldsymbol{n} \times \nabla \kappa) + 2A\boldsymbol{n} \times \boldsymbol{a}\,.\end{aligned} \tag{2.2}$$

Here, $\boldsymbol{n}$ is the interface normal vector, A the Atwood number, We the Weber number, κ the interface curvature, and $\boldsymbol{a}$ is the average acceleration of fluid 1 and fluid 2 at the interface. Note that Eq. (2.2) contains on the right hand side individual, local source terms describing the physical processes at the phase interface explicitly, namely, from left to right, two stretching terms, a surface tension term, and a density difference term.

Strictly speaking, Eqs. (2.1) and (2.2) are valid only at the location of the interface itself. However, to facilitate the numerical solution of both equations throughout the whole computational domain, $\boldsymbol{\eta}$ is set constant in the interface normal direction,

$$\nabla \boldsymbol{\eta} \cdot \nabla G = \boldsymbol{0}\,, \tag{2.3}$$

and G is chosen to be a distance function away from the interface,

$$|\nabla G|\Big|_{G \neq G_0} = 1\,. \tag{2.4}$$

Equations (2.1) and (2.2) are coupled by the self-induced velocity $\boldsymbol{u}$ of the vortex sheet. To calculate $\boldsymbol{u}$, the vector potential $\boldsymbol{\psi}$ is introduced,

$$\Delta \boldsymbol{\psi} = \boldsymbol{\omega}\,. \tag{2.5}$$

Here, the vorticity vector $\boldsymbol{\omega}$ is calculated following a vortex-in-cell type approach (Christiansen 1973; Cottet & Koumoutsakos 2000) by either

$$\boldsymbol{\omega}(\boldsymbol{x}) = \int_\Gamma \boldsymbol{\eta}(\boldsymbol{x}_\Gamma)\delta(\boldsymbol{x} - \boldsymbol{x}_\Gamma)d\boldsymbol{x}_\Gamma\,, \tag{2.6}$$

named method $\mathcal{M}_2$ in the following, or

$$\boldsymbol{\omega}(\boldsymbol{x}) = \int_V \boldsymbol{\eta}(\boldsymbol{x}')\delta(\boldsymbol{x}-\boldsymbol{x}')\delta\left(G(\boldsymbol{x}')-G_0\right)|\nabla G(\boldsymbol{x}')|d\boldsymbol{x}'\,, \tag{2.7}$$

named method $\mathcal{M}_3$. In general, method $\mathcal{M}_2$ is preferable, because Eq. (2.6) ensures vorticity conservation (Herrmann 2004*a*). However, $\mathcal{M}_2$ necessitates the geometric reconstruction of the interface location and is thus very tedious in three dimensions. Therefore, method $\mathcal{M}_2$ is used in two-dimensions, whereas $\mathcal{M}_3$ is the method of choice in three-dimensions.

In Eqs. (2.6) and (2.7), δ is the delta-function that is approximated by the following smoothed version (Peskin 1977),

$$\delta_\varepsilon(x) = \begin{cases} \dfrac{1}{2\varepsilon}\left[1+\cos\left(\dfrac{\pi x}{\varepsilon}\right)\right] & : \quad |x| \le \varepsilon \\ 0 & : \quad |x| > \varepsilon \end{cases}\,. \tag{2.8}$$

Note that this in fact changes the tangential velocity boundary condition at the phase interface from a jump, as appropriate for inviscid fluids, to a smoothed, constant shear layer thickness type boundary condition, reminiscent of viscous fluids. It is in principle possible to recapture the shear layer thickness and profile of viscous fluids by modifying ε and the functional form of Eq. (2.8), however, in the present work, Eq. (2.8) is used as shown and only the effect of varying the shear layer thickness is analyzed.

Finally, $\boldsymbol{u}$ can be calculated from

$$\boldsymbol{u}(\boldsymbol{x}) = \int_V \delta(\boldsymbol{x}-\boldsymbol{x}')\left(\nabla\times\boldsymbol{\psi}\right)d\boldsymbol{x}'\,. \tag{2.9}$$

In summary, Eqs. (2.1), (2.2), and (2.5) - (2.9) constitute the LSVS method and describe the three-dimensional two-phase interface dynamics.

2.1. *Numerical methods*

Numerically, Eqs. (2.1) and (2.2) are solved in a narrow band (Peng *et al.* 1999) by a 5^{th}-order WENO scheme (Jiang & Peng 2000) using a 3^{rd}-order TVD Runge-Kutta time discretization (Shu & Osher 1989). The reinitialization of G (2.4) is solved by the iterative procedure outlined in Sussman *et al.* (1994) and Peng *et al.* (1999). The redistribution of $\boldsymbol{\eta}$, Eq. (2.3), is solved by a Fast Marching Method (Sethian 1996; Adalsteinsson & Sethian 1999; Herrmann 2003*a*). The interested reader is referred to Herrmann (2002, 2003*a*, 2004*a*) for a detailed description of the numerical methods employed in the level set/vortex sheet method and a summary of the domain decomposition parallelization approach used.

2.1.1. *Refined Level Set Grid (RLSG) method*

Tracking interfaces by a standard level set approach (Osher & Sethian 1988) unavoidably introduces volume, respectively mass errors that are proportional in size to the employed numerical grid size. To avoid these errors, two different approaches can be followed in principle. One can correct the level set solution using an interface tracking method that either inherently preserves the volume, as for example the volume of fluid method (Noh & Woodward 1976; Kothe & Rider 1995; Gueyffier *et al.* 1999), or at least preserves the volume with higher accuracy than the level set method alone, like for example marker particles (Brackbill *et al.* 1988; Rider & Kothe 1995; Unverdi & Tryggvason 1992). Correction methods along these lines have been proposed by Bourlioux (1995),

Sussman & Fatemi (1999), Enright *et al.* (2002), and van der Pijl *et al.* (2004). Alternatively, one can reduce the mass error by refining the underlying numerical grid. This can be done adaptively (Ham & Young 2003). However, this introduces an additional level of complexity that is not necessary in certain cases. Since the goal of the LSVS method is to perform three-dimensional DNS of the primary breakup process, it can be assumed that a refined grid is necessary in large portions of the phase interface. The grid on which the level set equation is solved shall thus be refined as a whole. Note that due to the narrow band implementation, this does not constitute a prohibitive numerical cost, since the G-grid needs only be stored in a small neighborhood of the $G = 0$ iso-surface, see Fig. 2. This refined level set grid (RLSG) method is described in more detail in the following.

Let Δx be the cell size of the equidistant Cartesian grid on which the $\boldsymbol{\eta}$-equation, Eq. (2.2), is solved. This grid is termed the $\boldsymbol{\eta}$-grid in the following. The level set equation, Eq. (2.1), is then solved on a narrow band consisting of equidistant Cartesian grid cells of size $\Delta_G x$ width

$$\Delta_G x = \Delta x / n_G \,, \tag{2.10}$$

where n_G is the grid refinement factor. The width of the narrow band $\alpha_{T,G}$ is chosen in such a way that enough cells are present to allow for the evaluation of the 5^{th}-order WENO stencil during a single CFL-limited time step on the $\boldsymbol{\eta}$-grid. To fulfill the CFL-criterion on the G-grid, subcyling typically has to be employed. This results in a width of the narrow band of

$$\alpha_{T,G} = \begin{cases} 9\Delta_G x & : \quad n_G \leq 4 \\ (1.5 n_G + 3)\Delta_G x & : \quad n_G > 4 \end{cases} , \tag{2.11}$$

see Fig. 2. All other narrow band widths described in Herrmann (2003*a*, 2004*a*) are defined accordingly.

The coupling of the $\boldsymbol{\eta}$-grid and the G-grid is two-fold: for one, the level set scalar field solved on the finer G-grid has to be transferred to the $\boldsymbol{\eta}$-grid. Let G_G be the level set scalar defined on the G-grid and $G_{\boldsymbol{\eta}}$ be the level set scalar defined on the $\boldsymbol{\eta}$-grid. Then, remembering that any G is defined as the distance function away from the interface, the embedded interface $G_G = 0$ can be viewed as a higher order approximation of the interface as defined by $G_{\boldsymbol{\eta}} = 0$. This implies that at the same node location, the value of $G_{\boldsymbol{\eta}}$ should be exactly equal to the value of G_G, since both values describe the distance to the same interface geometry. It is important to note that this coupling does not constitute a filtering operation of G_G to $G_{\boldsymbol{\eta}}$. To do this, a more complex marker particle based scheme would have to be employed (Oberlack *et al.* 2001; Pitsch 2002). Here, the goal is rather to make use of a higher order approximation of the interface to eliminate numerical errors on the coarser grid.

In practice, $G_{\boldsymbol{\eta}}$ is determined from G_G on all $\boldsymbol{\eta}$-grid nodes that are directly adjacent to the $G_{\boldsymbol{\eta}} = 0$ interface. All other $G_{\boldsymbol{\eta}}$ values up to a certain distance away from the interface are then reconstructed using the Fast Marching Method.

Secondly, the velocity $\boldsymbol{u}$ is initially only defined on the $\boldsymbol{\eta}$-grid. To solve Eq. (2.1), $\boldsymbol{u}$ has to be transferred to the G-grid. This is done by simple trilinear interpolation.

Additionally, by solving the level set equation separate from the $\boldsymbol{\eta}$-equation on a refined grid, the RLSG method allows for a different approach in calculating the source terms in Eq. (2.2). These can still be evaluated using $G_{\boldsymbol{\eta}}$ (Herrmann 2004*a*). However, to make full use of the available geometry information on the G-grid, these source terms $\boldsymbol{S}(\boldsymbol{x}_{\boldsymbol{\eta}})$ defined on the $\boldsymbol{\eta}$-grid can now also be evaluated using G_G on the G-grid and then surface averaged onto the $\boldsymbol{\eta}$-grid. This process is a three-step procedure: first, all source

terms on the right-hand side of Eq. (2.2) are evaluated on the G-grid. Then, these terms are redistributed in the interface normal direction by solving Eq. (2.3) using the Fast Marching Method. Finally, the surface integration is performed by evaluating

$$\boldsymbol{S}(\boldsymbol{x}_{\boldsymbol{\eta}}) = \frac{\int_{\Delta\Gamma_{\boldsymbol{\eta}}} \boldsymbol{S}(\boldsymbol{x}_{\Gamma_G}) d\boldsymbol{x}_{\Gamma_G}}{\int_{\Delta\Gamma_{\boldsymbol{\eta}}} d\boldsymbol{x}_{\Gamma_G}} = \frac{\int_{\Delta V_{\boldsymbol{\eta}}} \boldsymbol{S}(\boldsymbol{x}_G)\delta(G_G(\boldsymbol{x}_G))|\nabla G_G(\boldsymbol{x}_G)| d\boldsymbol{x}_G}{\int_{\Delta V_{\boldsymbol{\eta}}} \delta(G_G(\boldsymbol{x}_G))|\nabla G_G(\boldsymbol{x}_G)| d\boldsymbol{x}_G}\,, \tag{2.12}$$

where $\Delta\Gamma_{\boldsymbol{\eta}}$ is the part of the $G_G = 0$ interface that lies within the $\boldsymbol{\eta}$-cell located at $\boldsymbol{x}_{\boldsymbol{\eta}}$ and $\Delta V_{\boldsymbol{\eta}}$ is the volume of that $\boldsymbol{\eta}$-grid cell. The integration above is performed on the G-grid.

Using this procedure also avoids one potential pitfall when evaluating the surface tension term. Using finite differences, this term involves a stencil that extends at least three cells in the front normal direction. Thus, as soon as two fronts approach each other closer than six grid cells, the results for the surface tension term will be incorrectly influenced due to the single valued nature of G. Ideally the surface tension term should depend only on the position of the interface, requiring a geometric reconstruction of the interface location which is tedious in three dimensions.

To alleviate the stencil problem, the calculation of the surface tension term is split into three steps. First, the curvature κ is calculated on the G-grid using a standard 3x3x3 stencil. Then, κ is redistributed on the G-grid using the Fast Marching Method. Finally, $\nabla \times \kappa$ is evaluated using central differences. The intermediate FMM step effectively limits the stencil size of the surface tension term to just two cells in the interface normal direction, thereby improving the results considerably.

Note that using a G-grid of $n_G \geq 4$, interfaces can now approach each other up to Δx, before the stencil problem occurs. Modifying the surface averaging step in such a way, that G-nodes with two fronts closer than $4\Delta_G x$ are rejected in the averaging procedure, will then avoid the stencil problem alltogether. The derivation of such an averaging procedure will be addressed in future work.

3. Results

3.1. *Zalesak's disk*

The solid body rotation of a notched circle, also known as Zalesak's disk (Zalesak 1979), is one of the standard test problems for evaluating the accuracy of level set methods. A disk of radius 0.15, notch width 0.05, and notch height 0.25 is placed in a 1×1 box at $(0.5, 0.75)$. The velocity field is given by

$$\boldsymbol{u}(\boldsymbol{x}, t) = (0.5 - y, x - 0.5)\,. \tag{3.1}$$

Figure 3 shows the shape of the interface at $t = 2\pi$ after one full rotation of the disk using no correction scheme, the particle correction method, and the RLSG method with varying n_G. Obviously, using no correction method at all causes the notch height to decrease substantially and the lower sharp corners to become significantly rounded. This in turn increases the area A/A_0 of the disk and decreases the length of the interface s/s_0 considerably, as shown in Fig. 4.

Using the particle correction method improves the results significantly. However a slight asymmetry occurs. The area of the disk decreases slightly, see Tab. 1, while showing noticeable fluctuations over time, Fig. 4. These are due to the local, non-continuous correction step of the particle correction method.

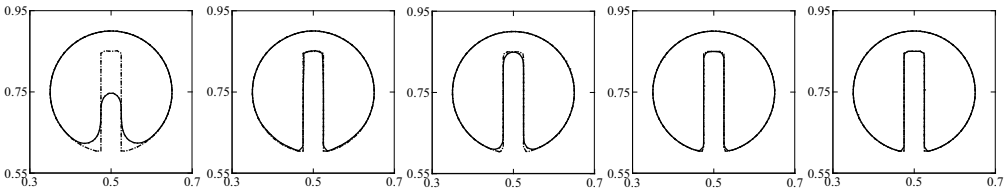

FIGURE 3. Interface shape after one full rotation of Zalesak's disk. Solid line denotes numerical solution and dash-dotted line is exact solution. From left to right: no correction method, particle correction method, RLSG method $n_G = 2$, $n_G = 4$, and $n_G = 8$.

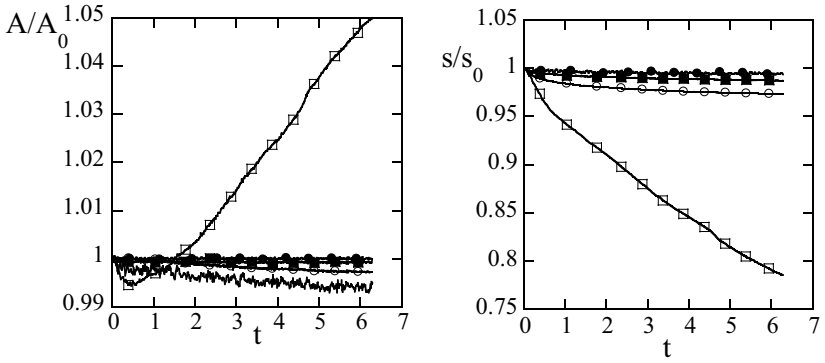

FIGURE 4. Normalized area A/A_0 (left) and interface length s/s_0 (right) during one full rotation of Zalesak's disk. Particle correction method (solid line), no correction method (open box), RLSG method $n_G = 2$ (open circle), $n_G = 4$ (full box).

	PC	none	RLSG $n_G = 2$	RLSG $n_G = 4$	RLSG $n_G = 8$
A/A_0	0.99502	1.05004	0.99723	0.99987	0.99990
s/s_0	-	0.78519	0.97316	0.98694	0.99368

TABLE 1. Normalize disk area A/A_0 and interface length s/s_0 after one full rotation of Zalesak's disk

Employing the RLSG method with $n_G = 2$ results in markedly improved results as compared to using no correction method at all. The area of the disk is preserved better than in the case of the particle correction method. However, this is due to two errors canceling each other: one at the sharp corners leading to an area decrease and the other at the top of the notch leading to an area increase, see Fig. 3. This cancelation of errors results in an area decrease of only 0.28%. The total length of the interface, on the other hand decreases by about 2.7 %.

Successively refining the G-grid continues to improve these results. The interface shape obtained with $n_G = 4$ is already superior to that of the particle correction method. For $n_G = 8$ almost no difference between the exact solution and the numerical result can be

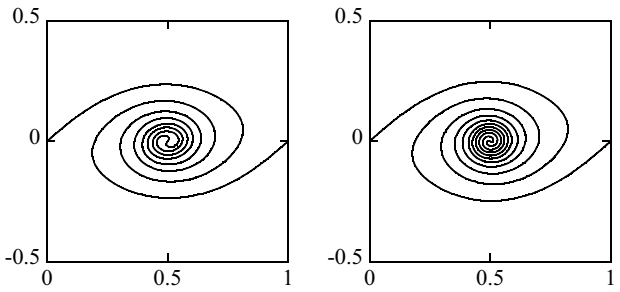

FIGURE 5. Vortex sheet roll-up interface shape at $t = 3$, no correction method (left) and RLSG method $n_G = 8$.

discerned, see Fig. 3, and 99.99% of the disk's area and 99.4 % of the interface length is preserved, see Tab. 1.

The results of this test case indicate, that the RLSG method with $n_G \geq 4$ performs comparable, if not superior, to the particle correction method with respect to area preservation, while maintaining symmetry and avoiding any fluctuations introduced by the correction step of the particle correction method.

3.2. *Vortex sheet roll-up*

Pure vortex sheets represent a special class of phase interfaces in that no surface tension forces exist. Thus, they constitute an ill posed problem, since linear theory predicts that the growth rate of a sinusoidal disturbance of wave number k is proportional to k. Consequently, as pointed out by Moore (1979), a vortex sheet develops a singularity at some critical time t_c, typically a discontinuity in curvature. In order to calculate the behavior of the vortex sheet beyond t_c, some form of desingularization has to be introduced, either by replacing the exact equations by desingularized versions, see for example the vortex blob method (Krasny 1986), or by adding physical effects like surface tension forces (Pullin 1982) or viscosity (Tryggvason *et al.* 1991).

In the case of the LSVS method, desingularization is two-fold. For one, all transport equations are solved by a finite difference scheme on an underlying numerical grid. Thus, all derivatives of finite quantities are inherently limited by the employed grid spacing. Secondly, the delta functions in Eqs. (2.6) and (2.7) are approximated by the numerical delta function δ_ε of finite width ε, Eq. (2.8). Thus, vorticity is not solely located at the interface, but spread out to neighboring grid nodes. To some extent, this crudely mimics the effect of viscosity (Tryggvason *et al.* 1991), since the shear layer is not of zero thickness as in the inviscid case, but rather has a finite, constant thickness proportional to ε. However, if the extend of the desingularization is reduced, i.e. the grid is refined and ε reduced, the LSVS method should be able to reproduce the Moore singularity at t_c.

Furthermore, after the critical time, the vortex sheet rolls up in the inner core region in such a way, that adjacent interfaces are tightly packed, see Fig. 5, requiring high fidelity level set solution algorithms, i.e. level set correction methods.

In the following, first, the performance of the different level set correction methods beyond the critical time is analyzed. Then, the LSVS method in the non-desingularized limit is verified. Finally, the influence of varying the shear layer thickness is ascertained.

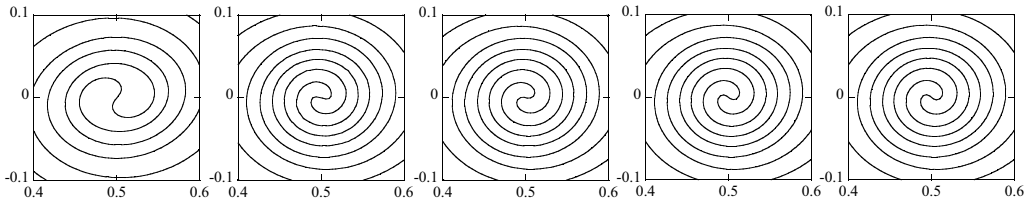

FIGURE 6. Inner core region of the vortex sheet roll-up at $t = 3$. From left to right: no correction method, particle correction method, RLSG method with $n_G = 2$, $n_G = 4$, and $n_G = 8$.

3.2.1. *Influence of level set correction methods*

The vortex sheet roll-up is initiated by placing a sinusoidal interface

$$G(\boldsymbol{x}, t = 0) = y - A_0 \sin\left(\frac{2\pi}{B}\left[x - A_0 \sin\frac{2\pi}{B}x\right]\right), \tag{3.2}$$

with amplitude $A_0 = 0.01$, $B = 1$, and vortex sheet strength

$$\eta_{\mathrm{VS}}(\boldsymbol{x}, t = 0) = \frac{\eta^*}{\sqrt{1 + \dfrac{4\pi A_0}{B}\cos\dfrac{2\pi}{B}x + 2\left[\dfrac{2\pi A_0}{B}\cos\dfrac{2\pi}{B}x\right]^2}}, \tag{3.3}$$

with $\eta^* = -1$, into a box of size $B \times B$, resolved by an $\boldsymbol{\eta}$-grid of 256×256 equidistant Cartesian grid cells. Periodic boundary conditions are employed at the left and right boundaries, and no-slip walls are used at the bottom and top boundaries, with the tangential wall velocity set to $u_w = \mp 0.5$. In all cases, $\varepsilon = 16/256$. Simulations were performed using no correction method at all, the particle correction method, and the RLSG method with $n_G = 2$, 4, and 8.

Figure 5 shows the interface shape at $t = 3$ obtained by using no correction method and the RLSG method with $n_G = 8$. As discussed in Herrmann (2004*a*), numerical diffusion and the incorrect merging of characteristics leads to significantly less turns in the inner core region where these errors are dominant, when using no correction method as compared to both the results by Krasny (1986) and those obtained using a correction method.

To evaluate the performance of the RLSG method as compared to the particle correction method, Fig. 6 shows a zoom of the inner core region of the vortex sheet at $t = 3$. Figure 7 depicts the interface curvature κ along the normalized interface arc length s/L, and Fig. 8 shows the tangential derivative of the interface curvature, $\partial_s \kappa$ i.e. the term proportional to the surface tension term in Eq. (2.2). Looking first at the interface shape, using any of the two correction methods yields very similar good results as compared to using no correction method at all. On close inspection, however, it can be seen that the RLSG method with $n_G = 2$ and $n_G = 4$ generates slightly less respectively more turns than the particle correction method. Using the RLSG method with $n_G = 8$ leads to results that are virtually undistinguishable from those obtained with $n_G = 4$, demonstrating grid convergence with respect to the G-grid.

The analysis of the interface curvature distribution reveals the drawbacks of the particle correction method. As discussed in Herrmann (2004*a*) and Coyajee *et al.* (2004), a correction method that corrects the level set scalar locally, like the particle correction method, will introduce fluctuations in the higher derivatives of G. As can be seen in Fig.

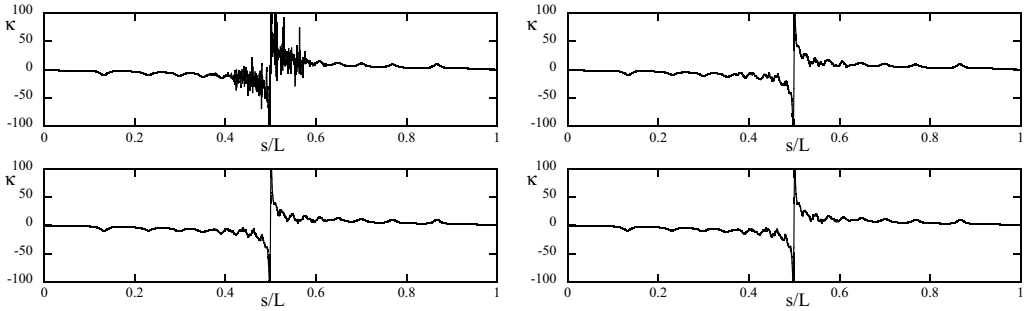

FIGURE 7. Interface curvature κ for vortex sheet roll-up at $t = 3$, particle correction method (top left) (Herrmann 2004*a*), RLSG method with $n_G = 2$ (top right), $n_G = 4$ (bottom left), and $n_G = 8$ (bottom right).

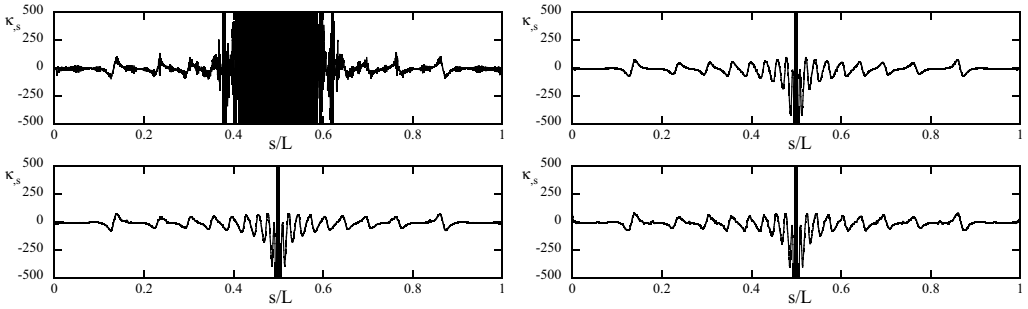

FIGURE 8. Tangential curvature derivative $\partial_s \kappa$ for vortex sheet roll-up at $t = 3$, particle correction method (top left), RLSG method with $n_G = 2$ (top right), $n_G = 4$ (bottom left), and $n_G = 8$ (bottom right).

8 this would lead to unacceptable fluctuations in the surface tension term, making any local correction method unapplicable within the context of the LSVS method. The delocalization method developed in Coyajee *et al.* (2004) could help alleviate this problem and will thus be further analyzed in the future. The RLSG method, on the other hand, delivers smooth, virtually non-fluctuating distributions of both the curvature, and more importantly, the tangential curvature derivative, making it ideal within the context of the LSVS method. The variations in both κ and $\partial_s \kappa$ are due to the fact that the vortex sheet is slightly elongated, see Fig. 5, resulting in the shown distributions. Also, the results for $n_G = 4$ and $n_G = 8$ show virtually identical distributions of both κ and $\partial_s \kappa$ demonstrating again, grid convergence, even for these higher derivatives of G.

3.2.2. *Moore singularity*

The initial conditions used to recover the Moore singularity are those proposed by Meiron *et al.* (1982). Initially, the vortex sheet is flat and located at $y = 0$ inside a box of size $[0, 2\pi] \times [-\pi, \pi]$ with a sinusoidal disturbance of the vortex sheet strength, $\eta = 1 + a \cos x$ and $a = 0.125$. With these initial conditions, the predicted critical time is $t_c \approx 2.84$ (Shelley 1992). Three calculations were performed, successively reducing the desingularization, i.e. the grid spacing and the spreading parameter, from $\Delta x = 2\pi/256$ with $\varepsilon = 16/256$, to $\Delta x = 2\pi/512$ with $\varepsilon = 8/256$, and to $\Delta x = 2\pi/1536$ with $\varepsilon = 6/256$. Since the amplitude of the disturbance throughout the simulations remains relatively small, no level set correction method has been used.

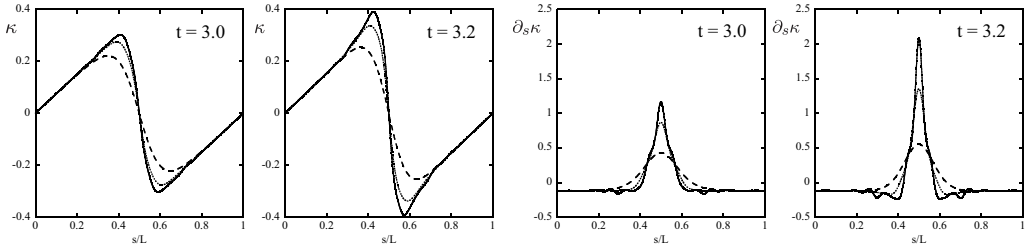

FIGURE 9. Vortex sheet curvature (left) and curvature derivative (right) at times close to the critical time, $t = 3.0$ (left) and $t = 3.2$ (right) for $\varepsilon = 16/256$ (dashed), $\varepsilon = 8/256$ (dotted), and $\varepsilon = 6/256$ (solid).

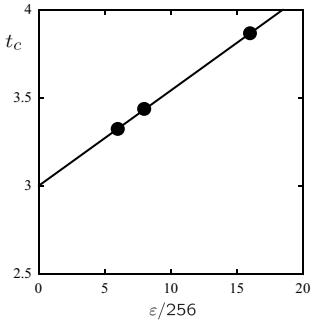

FIGURE 10. Estimation of the critical time t_c.

Figure 9 shows the distribution of curvature and curvature derivative, $\partial_s \kappa$, along the normalized interface arc length s/L at two different times close to the critical time t_c. Both the curvature and the curvature derivative distributions clearly show the onset of the Moore singularity at $s/L = 0.5$. Decreasing the desingularization obviously increases the curvature derivative at any given time. However, the $\varepsilon = 6/256$ case shows some small fluctuations of $\partial_s \kappa$ not present in the other two cases. This is due to the fact that a decrease of ε increases the growth rate of higher wave number fluctuations (Krasny 1986). The initial amplitudes of these higher wave number disturbances are due to the numerical error associated with the employed numerical grid. Obviously, the 1536×1536 grid is barely sufficient to delay the growth of these higher wave number disturbances. A further reduction of ε would thus require a substantially finer grid. Furthermore, at $t = 3.2$ the $\partial_s \kappa$ distribution for both $\varepsilon = 8/256$ and $\varepsilon = 6/256$ exhibits two local minima directly adjacent to the central maximum. This behavior is consistent with that reported by Shelley (1992).

To determine t_c in the non-desingularized limit, the critical time for each of the three calculations is estimated using a procedure proposed by Shelley (1992). The values of $1/\partial_s \kappa$ at $s/L = 0.5$ between $t = 1.0$ and $t = 3.2$ are extrapolated to zero using a third order polynomial that provides an excellent fit to the data points. The resulting critical times are shown in Fig. 10 as a function of the spreading parameter ε. A linear extrapolation is then used to estimate t_c for $\varepsilon \to 0$ and $\Delta x \to 0$, yielding a critical time of $t_c = 3.001$. Although this time is slightly larger than the critical time predicted by theory, it is in excellent agreement with the results of Shelley (Shelley 1992), who estimates $t_c = 3.015$ using a high accuracy point-vortex method.

3.3. *Kelvin-Helmholtz instability in the linear regime*

A velocity shear between two fluids can give rise to the so-called Kelvin-Helmholtz instability, if the velocity profile between the two fluids exhibits an inflection point (Rayleigh 1880). This phenomenon was first studied by Helmholtz (1868) and Kelvin (1871) in the inviscid limit for a shear layer of zero thickness, i.e. a velocity discontinuity. For fluids of equal density, the growth rate w in the linear regime for the unbounded case is

$$w(\mathrm{We}) = \frac{k}{2}\sqrt{1 - \frac{2k}{\mathrm{We}}}. \tag{3.4}$$

The case of a shear layer of finite size and constant shear was subsequently analyzed by Rayleigh (1880). In the inviscid and $\mathrm{We} = \infty$ limit, the growth rate w in the linear regime becomes

$$w(d) = \frac{k}{2}\sqrt{\frac{e^{-2kd} + 2kd - 1}{(kd)^2} - 1}\,, \tag{3.5}$$

with d the shear layer thickness defined as

$$d = \frac{\eta}{(\partial u/\partial y)_{\max}}\,. \tag{3.6}$$

Although numerical solutions are possible for arbitrary shear layer velocity profiles (Michalke 1964; Yecko *et al.* 2002), comparisons will be limited to the above analytical solutions for validation purposes.

The initial conditions for the level set scalar G are given by Eq. (3.2) with $A_0 = 1 \cdot 10^{-5}$ and $B = 1$. The initial vortex sheet strength distribution is calculated from

$$\eta(\boldsymbol{x}, t = 0) = \frac{w(\mathrm{We})}{w(\mathrm{We} = \infty)}\left(\eta_{\mathrm{VS}}(\boldsymbol{x}, t = 0) - \eta^*\right) + \eta^*\,, \tag{3.7}$$

with $\eta^* = -1$ and η_{VS} given by Eq. (3.3). Periodic boundary conditions are employed at the left and right domain boundary, whereas slip conditions are used at the lower and upper boundary. This in theory constitutes a bounded shear layer flow. However, the upper and lower boundaries are placed sufficiently far away from the interface, as to have no further influence on the presented results, thus allowing comparisons with the theoretical results of the unbounded case. All simulations are performed in a $B \times 2B$ box employing an $\boldsymbol{\eta}$-grid of 256×512 equidistant Cartesian grid cells. Due to the small amplitude of the disturbance, no level set correction method is required.

Figure 11 compares the growth rates w,

$$w = \frac{1}{t_1}\int_0^{t_1} w(t)dt\,, \quad t_1 = 0.5\,, \tag{3.8}$$

to the results obtained by linear theory for varying We, Eq. (3.4). Table 2 lists the respective numerical values. For the lowest value of the spreading parameter, $\varepsilon = 4/256$, method $\mathcal{M}_2$, Eq. (2.6), slightly under-predicts the linear growth rate by about 3%. This is due to the introduction of the numerical spreading function in Eq. (2.6) and the consequently theoretically reduced linear growth rate, cp. Eq. (3.5). Method $\mathcal{M}_3$, Eq. (2.7), on the other hand marginally over-predicts the linear growth rate for $\varepsilon = 4/256$, but gives slightly lower w than $\mathcal{M}_2$ for larger ε. The reason for this behavior is not directly apparent, but it is most likely due to the lack of a consistent level set based interpolation step to calculate the vortex sheet induced velocity $\boldsymbol{u}$, Eq. (2.9), (Herrmann 2004*a*).

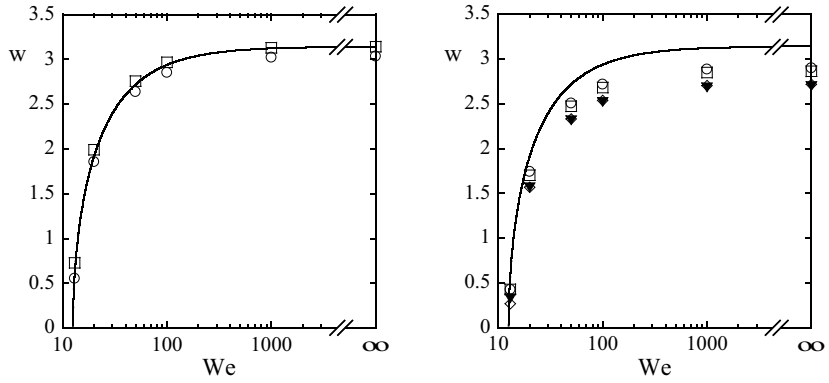

FIGURE 11. Growth rate w of the Kelvin-Helmholtz instability in the linear regime, method $\mathcal{M}_2$ $\varepsilon = 4/256$ (circle, left), $\mathcal{M}_3$ $\varepsilon = 4/256$ (box, left), $\mathcal{M}_2$ $\varepsilon = 8/256$ (circle, right), $\mathcal{M}_3$ $\varepsilon = 8/256$ (box, right), $\mathcal{M}_2$ $\varepsilon = 16/256$ (full triangle, right), $\mathcal{M}_3$ $\varepsilon = 16/256$ (open triangle,right), and linear theory (lines).

Method / We	13	20	50	100	1000	∞
Theory	0.574	1.915	2.718	2.938	3.122	3.142
$\mathcal{M}_2$, $\varepsilon = 4/256$	0.552	1.856	2.638	2.852	3.021	3.034
$\mathcal{M}_3$, $\varepsilon = 4/256$	0.726	1.991	2.756	2.965	3.129	3.140
$\mathcal{M}_2$, $\varepsilon = 8/256$	0.426	1.744	2.505	2.717	2.886	2.899
$\mathcal{M}_3$, $\varepsilon = 8/256$	0.429	1.703	2.472	2.682	2.849	2.863
$\mathcal{M}_2$, $\varepsilon = 16/256$	0.329	1.568	2.316	2.521	2.685	2.698
$\mathcal{M}_3$, $\varepsilon = 16/256$	0.267	1.569	2.332	2.539	2.703	2.717

TABLE 2. Linear growth rates w of the Kelvin-Helmholtz instability for varying ε and We, 256×512 grid, methods $\mathcal{M}_2$ and $\mathcal{M}_3$.

Altogether, increasing ε results in a consistent reduction of the growth rate for both $\mathcal{M}_2$ and $\mathcal{M}_3$.

In order to further analyze this behavior, Fig. 12 depicts the growth rate w as a function of the shear layer thickness $d = \varepsilon$ in the limit of $\mathrm{We} = \infty$ as compared to the analytical solutions, Eqs. (3.4) and (3.5). The corresponding numerical values are shown in Tab. 3. While the qualitative behavior of the simulations and the theory for a linear velocity profile is similar, both $\mathcal{M}_2$ and $\mathcal{M}_3$ exhibit overall larger growth rates and hence reach their neutrally stable solution at a larger shear layer thickness of $d = \varepsilon \approx 0.8$. This quantitative deviation is due to the different velocity profile of Eq. (3.5) and the LSVS method. The former assumes a linear profile, whereas the latter employs a rather complex profile due to the schemes outlined in section 2. In principle, it seems possible to change the velocity profile used in the LSVS method by modifying the numerical delta function δ_ε, Eq. (2.8). A detailed comparison with the viscous linear theory by Yecko *et al.* (2002) and Li *et al.* (2004) will reveal the necessary modifications to Eq. (2.8).

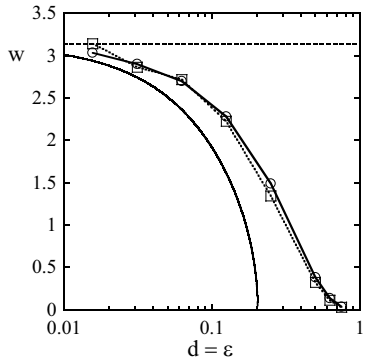

FIGURE 12. Growth rate w of the Kelvin-Helmholtz instability in the linear regime as function of the shear layer thickness $d = \varepsilon$. Theory for linear velocity profile (——), theory for velocity discontinuity (– – –), methods $\mathcal{M}_2$ (circle) and $\mathcal{M}_3$ (box).

Method / $d = \varepsilon$	4/256	8/256	16/256	32/256	64/256	128/256	160/256	192/256
Theory Eq. (3.4)	3.142	3.142	3.142	3.142	3.142	3.142	3.142	3.142
Theory Eq. (3.5)	2.939	2.742	2.361	1.609	stable	stable	stable	stable
$\mathcal{M}_2$	3.034	2.899	2.698	2.281	1.489	0.380	0.133	0.032
$\mathcal{M}_3$	3.140	2.863	2.717	2.224	1.342	0.320	0.110	0.026

TABLE 3. Linear growth rates w of the Kelvin-Helmholtz instability for varying ε and $\mathrm{We} = \infty$.

4. Conclusions and future work

A method has been presented that addresses the problem of mass conservation inherent in the level set approach. This so-called Refined Level Set Grid (RLSG) method achieves mass conservation results comparable to other level set correction methods, like for example the particle correction method, but demonstrates clearly superior performance with respect to the convergence of higher derivatives of the level set scalar. In particular the convergence of the interface curvature derivative is crucial within the context of the LSVS method and has been demonstrated in the case of vortex sheet roll-up.

Although the LSVS method has been derived for the limit of inviscid fluids, the numerical implementation necessitates the introduction of a finite shear layer thickness, representing an additional level of desingularization. The non-desingularized, inviscid limit of the Moore singularity can however be recovered, if the the extend of the desingularization is successively reduced.

The influence of the desingularization introduced by the finite shear layer thickness has been further analyzed in the case of the Kelvin-Helmholtz instability in the linear regime. It was found that the finite, constant shear layer thickness qualitatively mimicks certain features of viscous fluids. However, only a detailed comparison to the fully viscous theory by Yecko *et al.* (2002) and Li *et al.* (2004), planned for the future, will help quantify this effect and point to possible enhancements of the LSVS method.

Acknowledgments

The support of the German Research Foundation (DFG) is gratefully acknowledged.

REFERENCES

ADALSTEINSSON, D. & SETHIAN, J. A. 1999 The fast construction of extension velocities in level set methods. *J. Comput. Phys.* **148**, 2–22.

BOURLIOUX, A. 1995 A coupled level-set volume-of-fluid algorithm for tracking material interfaces. In *Sixth International Symposium on Computational Fluid Dynamics*, , vol. IV, pp. 15–22. Lake Tahoe, NV.

BRACKBILL, J. U., KOTHE, D. B. & RUPPEL, H. M. 1988 FLIP: A low dissipation, particle-in-cell method for fluid flow. *Comput. Phys. Commun.* **48**, 25–38.

CHRISTIANSEN, J. P. 1973 Numerical simulation of hydrodynamics by the method of point vortices. *J. Comput. Phys.* **13**, 363–379.

COTTET, G.-H. & KOUMOUTSAKOS, P. D. 2000 *Vortex Methods*. Cambridge: Cambridge University Press.

COYAJEE, E., BOERSMA, J. B. & HERRMANN, M. 2004 Effects of inertia on trajectories of drops in liquid flows. In *Proceedings of the 2004 Summer Program*. Stanford, CA: Center for Turbulence Research.

ENRIGHT, D., FEDKIW, R., FERZIGER, J. & MITCHELL, I. 2002 A hybrid particle level set method for improved interface capturing. *J. Comput. Phys.* **183**, 83–116.

GUEYFFIER, D., LI, J., NADIM, A., SCARDOVELLI, S. & ZALESKI, S. 1999 Volume of Fluid interface tracking with smoothed surface stress methods for three-dimensional flows. *J. Comput. Phys.* **152**, 423–456.

HAM, F. & YOUNG, Y.-N. 2003 A cartesian adaptive level set method for two-phase flows. In *Annual Research Briefs-2003*, pp. 227–237. Stanford, CA: Center for Turbulence Research.

HELMHOLTZ, H. V. 1868 On discontinuous movements of fluids. *Philos. Mag.* **36**, 337–346.

HERRMANN, M. 2002 An Eulerian level-Set/Vortex-sheet method for two-phase interface dynamics. In *Annual Research Briefs-2002* (ed. P. Bradshaw), pp. 103–114. Stanford, CA: Center for Turbulence Research.

HERRMANN, M. 2003*a* A domain decomposition parallelization of the Fast Marching Method. In *Annual Research Briefs-2003*, pp. 213–226. Stanford, CA: Center for Turbulence Research.

HERRMANN, M. 2003*b* Modeling primary brekaup: A three-dimensional Eulerian level set / vortex sheet method for two-phase interface dynamics. In *Annual Research Briefs-2003*, pp. 185–196. Stanford, CA: Center for Turbulence Research.

HERRMANN, M. 2004*a* A Eulerian level set/vortex sheet method for two-phase interface dynamics. Accepted for publication in J. Comput. Phys.

HERRMANN, M. 2004*b* A level set/vortex sheet method for modeling phase interface dynamics during primary breakup. In *ILASS Americas 2004, 17th Annual Conference on Liquid Atomization and Spray Systems, NIST Special Publication 1016* (ed. C. Presser & B. Helenbrook).

JIANG, G.-S. & PENG, D. 2000 Weighted ENO schemes for Hamilton-Jacobi equations. *SIAM J. Sci. Comput.* **21** (6), 2126–2143.

KELVIN, L. 1871 Hydrokinetic solutions and observations. *Philos. Mag.* **42**, 362–377.

KOTHE, D. B. & RIDER, W. J. 1995 Comments on modelling interfacial flows with Volume-of-Fluid methods. *Tech. Rep.* LA-UR-3384. Los Alamos National Laboratory.

KRASNY, R. 1986 Desingularization of periodic vortex sheet roll-up. *J. Comput. Phys.* **65**, 292–313.

LI, J., LOPEZ-PAGES, E., YECKO, P. & ZALESKI, S. 2004 Droplet formation in sheared liquid-gas layers. Submitted to Theor. Comput. Fluid Dyn.

MEIRON, D. I., BAKER, G. R. & ORSZAG, S. A. 1982 Analytic structure of vortex sheet dynamics. Part 1. Kelvin-Helmholtz instability. *J. Fluid Mech.* **114**, 283–298.

MICHALKE, A. 1964 On the inviscid instability of the hyperbolic-tangent velocity profile. *J. Fluid Mech.* **19**, 543–556.

MOORE, D. W. 1979 The spontaneous appearance of a singularity in the shape of an evolving vortex sheet. *Proc. R. Soc. Lond. A* **365**, 105–119.

NOH, W. F. & WOODWARD, P. 1976 SLIC (Simple Line Interface Calculation). In *Lecture Notes in Physics, Vol. 59, Proceedings of the Fifth International Conference on Numerical Methods in Fluid Dynamics* (ed. A. I. V. D. Vooren & P. J. Zandenbergen), pp. 330–340. Berlin: Springer.

OBERLACK, M., WENZEL, H. & PETERS, N. 2001 On symmetries and averaging of the G-equation for premixed combustion. *Combust. Theory Modelling* **5**, 363–383.

OSHER, S. & SETHIAN, J. A. 1988 Fronts propagating with curvature-dependent speed: Algorithms based on Hamilton-Jacobi formulations. *J. Comput. Phys.* **79**, 12–49.

PENG, D., MERRIMAN, B., OSHER, S., ZHAO, H. & KANG, M. 1999 A PDE-based fast local level set method. *J. Comput. Phys.* **155**, 410–438.

PESKIN, C. S. 1977 Numerical analysis of blood flow in the heart. *J. Comput. Phys.* **25**, 220–252.

VAN DER PIJL, S. P., SEGAL, A., VUIK, C. & WESSELING, P. 2004 A mass-conserving level-set method for modeling multi-phase flows. Submitted to Int. J. Numer. Meth. Fluids.

PITSCH, H. 2002 A G-equation formulation for large-eddy simulation of premixed turbulent combustion. In *Annual Research Briefs-2002* (ed. P. Bradshaw), pp. 3–14. Stanford, CA: Center for Turbulence Research.

POZRIKIDIS, C. 2000 Theoretical and computational aspects of the self-induced motion of three-dimensional vortex sheets. *J. Fluid Mech.* **425**, 335–366.

PULLIN, D. I. 1982 Numerical studies of surface-tension effects in nonlinear Kelvin-Helmholtz and Rayleigh-Taylor instability. *J. Fluid Mech.* **119**, 507–532.

RAYLEIGH, L. 1880 On the stability, or instability, of certain fluid motions. *Proc. London Math. Soc.* **11**, 57–70.

RIDER, W. J. & KOTHE, D. B. 1995 Stretching and tearing interface tracking methods. *Tech. Rep.*. Los Alamos National Laboratory, AIAA Paper 95-1717.

SETHIAN, J. A. 1996 A fast marching level set method for monotonically advancing fronts. *Proc. Natl. Acad. Sci. USA* **93**, 1591–1595.

SHELLEY, M. J. 1992 A study of singularity formation in vortex-sheet motion by a spectrally accurate vortex method. *J. Fluid Mech.* **244**, 493–526.

SHU, C.-W. & OSHER, S. 1989 Efficient implementation of essentially non-oscillatory shock-capturing schemes. *J. Comput. Phys.* **77**, 439–471.

SUSSMAN, M. & FATEMI, E. 1999 An efficient, interface-preserving level set redistancing

algorithm and its application to interfacial incompressible fluid flow. *SIAM J. Sci. Comput.* **20** (4), 1165–1191.

SUSSMAN, M., SMEREKA, P. & OSHER, S. 1994 A level set method for computing solutions to incompressible two-phase flow. *J. Comput. Phys.* **119**, 146.

TRYGGVASON, G., DAHM, W. J. A. & SBEIH, K. 1991 Fine structure of vortex sheet rollup by viscous and inviscid simulation. *J. Fluids Eng.* **113**, 31–36.

UNVERDI, S. O. & TRYGGVASON, G. 1992 A front-tracking method for viscous, incompressible, multi-fluid flows. *J. Comput. Phys.* **100**, 25–37.

YECKO, P., ZALESKI, S. & FULLANA, J.-M. 2002 Viscous modes in two-phase mixing layers. *Phys. Fluids* **14** (12), 4115–4122.

ZALESAK, S. T. 1979 Fully multidimensional flux-corrected transport algorithms for fluids. *J. Comput. Phys.* **31**, 335–362.

Accurate and efficient immersed-boundary interpolations for viscous flows

By S. Kang, G. Iaccarino AND P. Moin

1. Motivation and background

The Immersed Boundary (IB) method is a technique for solving flow problems with irregular boundaries using a simple Cartesian grid solver. Specifically, the computational grid does not conform to all the boundaries of the domain and the numerical algorithm in the vicinity of these *immersed* surfaces is modified to enforce the desired boundary conditions. This greatly reduces the difficulties of generating meshes for complex boundaries. In addition, the IB method has the potential of high efficiency as the computational cost per grid cell is generally lower than that of general-purpose unstructured (body fitted) grid solvers.

There are numerous variants of the IB method, mainly in relation to the specific treatment of the computational cells crossing the immersed surfaces. Two major family of approaches can be distinguished: *(i)* based on strict finite volume discretization based on the cells cut by the IB (cut-cell approach) and *(ii)* based on forcing terms or solution interpolation in the vicinity of the IB.

The objective of the present study is to further develop an IB method based on forcing which has sufficient accuracy for Large Eddy Simulations (LES) at high Reynolds numbers with minimal increase in computational cost with respect to the simple, underlying Cartesian grid solver. The starting point for the present IB method is the interpolation method described in Fadlun *et al.* (2000). In addition to its simplicity, it has several advantages. The velocity boundary condition is enforced with implicit forcing, there is no severe limit on the time step, and the velocity components from the regions across the immersed boundary are decoupled. In the present study, revisions to this approach are introduced with the objective of increasing the accuracy and consistency of this method. In addition we analyze the practical importance of strict mass conservation.

In the next section, a general description of the numerical method used is given. The analysis of a various interpolation methods for the velocity field near the IB are presented in section 3. In addition, the issues of mass conservation and pressure accuracy are addressed. Results from numerical tests for laminar and turbulent flows are shown in section 4.

2. Numerical Method

The Navier-Stokes equations for an incompressible fluid are solved on a Cartesian grid using a staggered arrangement of the variables. A variant of the fractional step method (Kim & Moin 1985) is employed. The Crank-Nicholson scheme and the third-order Runge-Kutta scheme for the discretization of the diffusive and convective terms are used, respectively. An approximate ADI scheme is used to solve the momentum equation; to solve the Poisson equation for the pseudo-pressure either a direct method using the fast Fourier transform (FFT) or a multigrid method is used. In general, algorithms are

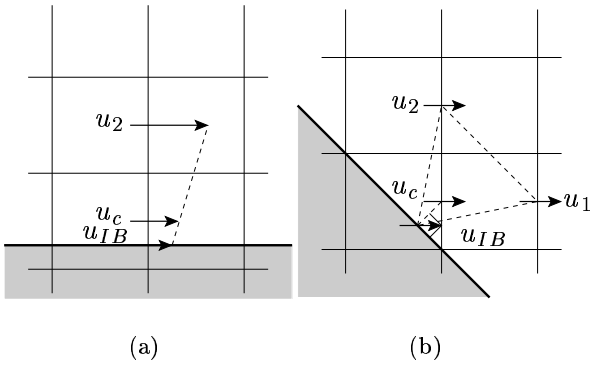

FIGURE 1. Configuration of the immersed boundary, grid and nodes in the linear interpolation method: ▬▬, immersed boundary; ———, grid; ⟶, velocity node.

parallelized using MPI, and the parallel tridiagonal matrix solver developed by Mattor *et al.* (1995) is used.

3. Interpolation methods at the immersed surfaces

In the original approach of Fadlun *et al.* (2000) the velocity components at the first grid point off the IB are determined using a linear interpolation formula rather than the discretized Navier-Stokes equation. The method is equivalent to assuming a one-dimensional linear velocity profile near the boundary. As consequence of the interpolation the velocity components are independent of each other and each component is determined by a separate interpolation. In the present study, four different interpolation methods have been considered:

- Linear interpolation method (LIM)
- Revised linear interpolation method (RLIM)
- Quadratic interpolation method (QIM)
- Quadratic+momentum interpolation method(QMIM)

3.1. *Linear interpolation method*

Fig. 1 shows two IB configurations commonly found in practical problems. In Fig. 1 (a), since the IB is approximately parallel to grid lines, a linear interpolation with u_{IB}, u_c and u_2 is easily formed along the x_2 coordinate. In Fig. 1 (b), there are two velocity components (u_1 and u_2) nearest in the horizontal and vertical directions to u_c. Then, a triangle is constructed by using two adjacent velocity nodes and a point on the IB (u_{IB}) surrounding u_c. Then, a linear interpolation stencil is built using the information available at the vertices of the triangle. The resulting interpolation formula has the following form:

$$u^k_{i,c} = w_{i,1}u^k_{i,1} + w_{i,2}u^k_{i,2} + w_{i,IB}u^k_{i,IB}, \tag{3.1}$$

where subscripts 1 and 2 denote adjacent velocity nodes in the x_1 and x_2 directions, and subscript IB denotes the point on the IB which is the boundary-normal projection of the velocity node c. Superscript k denotes the next time step, and w_i is an interpolation coefficient determined by the geometric configuration. Extending this method to a three-

dimensional geometry is straightforward. In the framework of the fractional step method the linear interpolation can be applied to either $\hat{u}_{i,c}$ or $\Delta u_{i,c} = \hat{u}^k_{i,c} - u^{k-1}_{i,c}$.

Assuming a local coordinate system whose center is located at the velocity node c, we can restate the linear interpolation method as:

$$\begin{aligned} u^k_i(x_1, x_2) = &\quad a^k_{i,1} x_1 + a^k_{i,2} x_2 + u^k_{i,c} \\ u^k_i = &\quad u^k_{i,IB} \text{ at immersed boundary,} \end{aligned} \tag{3.2}$$

where $a_{i,1}$ and $a_{i,2}$ are coefficients determined by the geometry of the local IB and velocity components.

When comparing Eq. (3.1) with the discretized momentum equation it can be shown that the linear interpolation method does not explicitly account for effects of the some of the terms, i.e. the pressure forcing, the temporal variation, etc. It can be argued that through the use of the two velocity components, $u_{i,1}$ and $u_{i,2}$ (determined by the discretized momentum equation), the effects of these terms are *indirectly* included.

A notable feature of the linear interpolation method (Eq. (3.1)) is that there is no explicit contribution from the velocity field at the previous time step. Numerical errors, once generated, are accumulated and/or transfered to other regions by advection and diffusion. A problem we encountered in numerical experiments is the occurrence of abnormal pressure fluctuations around the volume cells crossed by the IB. This effect is equivalent to the so-called "checker-board effect" observed in a non-staggered grid system where the solution of the momentum equation does not reflect the local pressure gradient.

3.2. *Revised linear interpolation method*

It is possible to derive an interpolation formula based on both $\hat{u}^k$ and Δu. After some manipulations and introducing a blending factor η we obtain:

$$\begin{aligned} \hat{u}^k_{i,c} = &\; w_{i,1}\hat{u}^k_{i,1} + w_{i,2}\hat{u}^k_{i,2} + w_{i,IB}\hat{u}^k_{i,IB} \\ &+ \eta \left(u^{k-1}_i - w_{i,1}u^{k-1}_{i,1} - w_{i,2}u^{k-1}_{i,2} - w_{i,IB}u^{k-1}_{i,IB} \right), \end{aligned} \tag{3.3}$$

The effect of the local pressure gradient can be accounted for by using:

$$\begin{aligned} \hat{u}^k_{i,c} = &\; w_{i,1}\hat{u}^k_{i,1} + w_{i,2}\hat{u}^k_{i,2} + w_{i,IB}\hat{u}^k_{i,IB} \\ &+ \eta \left(u^{k-1}_i - w_{i,1}u^{k-1}_{i,1} - w_{i,2}u^{k-1}_{i,2} - w_{i,IB}u^{k-1}_{i,IB} \right) \\ &- (\gamma_k + \rho_k)\Delta t \left(\left.\frac{\partial p^{k-1}}{\partial x_i}\right|_c - w_{i,1} \left.\frac{\partial p^{k-1}}{\partial x_i}\right|_1 - w_{i,2} \left.\frac{\partial p^{k-1}}{\partial x_i}\right|_2 - w_{i,IB} \left.\frac{\partial p^{k-1}}{\partial x_i}\right|_{IB} \right). \end{aligned} \tag{3.4}$$

where the coefficient γ_k and ρ_k are related to the time integration scheme. It is easy to prove that the numerical accuracy of Eq. (3.4) is the same as the original linear interpolation formula - second order in space. Also, note that what is interpolated is $\hat{u}^k_i - u^{k-1}_i + (\gamma_k + \rho_k)\Delta t \partial p^{k-1}/\partial x_i$ when $\eta = 1$. Coupling between neighboring pressure points is then considered with this "simulated" momentum equation. This approach is referred to in the following as Revised Linear Interpolation Method (RLIM).

In practice, computing $\partial p^{k-1}/\partial x_i$ at 1, 2 and c locations is straightforward since these points are existing velocity nodes at the cell faces, but interpolation is necessary to

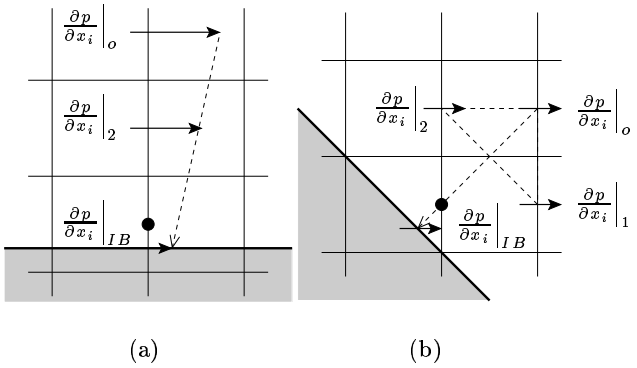

FIGURE 2. Points participating in interpolation of the pressure gradient on the IB.

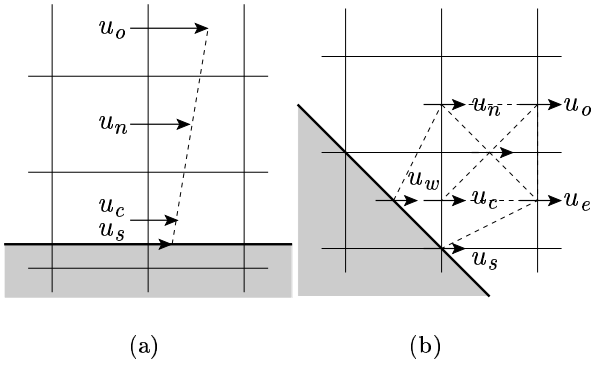

FIGURE 3. Configuration of the immersed boundary, grid and nodes in the quadratic interpolation method: ——, immersed boundary; ——, grid; ⟶, velocity node.

compute $\partial p^{k-1}/\partial x_i$ at the IB location. Applying linear interpolation using $\partial p^{k-1}/\partial x_i$ at 1, 2 and c is not appropriate in this case. So, an additional point near c is used in interpolation.

Fig. 2 shows a schematic representation of the stencil used for the pressure interpolation. This form of extrapolation has second order accuracy but becomes unstable when the c and IB points are close to each other. It is used only when η is larger than user-defined η_{crit}. Other alternatives to $\partial p^{k-1}/\partial x_i$ at IB are $\partial p^{k-1}/\partial x_i$ at c location and $\partial p^{k-1}/\partial x_i = 0$. The former produces a smaller error in the present numerical experiments and it is used when η is smaller than η_{crit}. This approximation produces a first order error term which is found not to affect the accuracy as shown in § 4.1. For the problems tested in the present study, η_{crit}=0.4 is used.

3.3. *Quadratic interpolation method*

The quadratic interpolation formula considered in the present study is:

$$\hat{u}_i^k(x_1, x_2) = a_{i,1}^k x_1^2 + b_{i,1}^k x_1 + a_{i,2}^k x_2^2 + b_{i,2}^k x_2 + \hat{u}_{i,c}^k, \tag{3.5}$$

where the origin of the local coordinate system is located at the position of $\hat{u}_{i,c}$ which is determined by the interpolation formula.

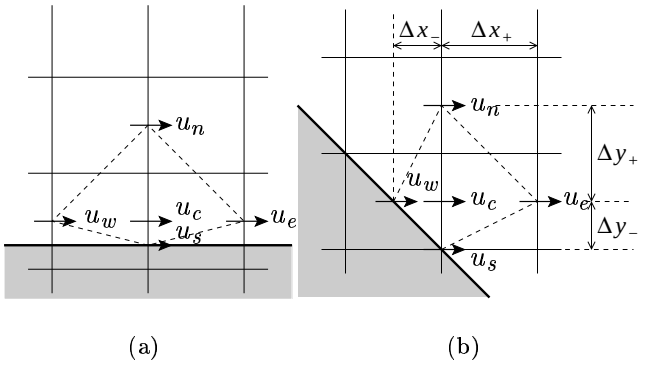

FIGURE 4. Configuration of the immersed boundary, grid and nodes in the quadratic+momentum interpolation method: ▬▬, immersed boundary; ———, grid; ⟶, velocity node.

Fig. 3 shows two IB configurations of interest. The number of velocity points needed to construct the quadratic formula is six (including $\hat{u}_{i,c}$). We can select $\hat{u}_{i,c}$ and the four surrounding velocity points. In addition, another point (subscript o) is necessary to define the interpolation stencil. In Fig. 3 (a), we choose the additional point to be the third velocity point away from the IB. Then, the points to the the left and right of $\hat{u}_{i,c}$ are ignored and a quadratic formula is generated using the four points along the coordinate normal to the IB line. In Fig. 3 (b), we choose the additional point as the center of four additional velocity nodes near the IB line.

With this quadratic interpolation formula, it is possible for the local velocity to have a non-linear profile. Also, only the spatial accuracy is increased and temporal behavior remains the same of the LIM.

3.4. *Quadratic+momentum interpolation method*

In the quadratic interpolation formula described above, there are five unknowns (including $\hat{u}^k_{i,c}$) all determined using velocities at fluid points computed through the solution of the governing equations. It is possible to follow another approach which reduces the stencil required to *close* the interpolation formula. In Fig. 4 the four adjacent velocity points are used to define four equations to determine the coefficients. The fifth relation is obtained from enforcing the momentum equations with a second order finite difference. The pressure gradient at a velocity node can be easily computed in the present staggered grid system although if some of the pressure points used may be in the boundary region (shaded region in Fig. 4). Interpolation coefficients are determined dynamically depending on the spatial and temporal flow field rather than having fixed values depending on geometry. The quadratic+momentum interpolation method (QMIM) has similarity to the cut-cell approach as a formal discretization of the momentum equation that accounts for the physical location of the IB is used.

The QMIM is computationally more complex than the LIM due to explicit evaluation of the convective and viscous terms. The overhead is about 10∼15% of the original computation time for the two-dimensional test cases presented afterward.

3.5. *Enforcing mass conservation*

The interpolation methods considered focus on the velocity and the momentum equation. There is another issue that plays a crucial role in practical calculations: mass conservation.

In IB approaches, the computational domain is divided into fluid regions where solutions to the Navier-Stokes equations are desired, and solid regions (e.g. shaded area in Fig. 1) where no solution is needed. The immersed surface separates these two regions. In Fadlun *et al.* (2000), the interpolation method determines the velocity components near the IB in the flow region. These components are not directly related to the velocity field in the boundary region. But, the flow field in the fluid region is affected by the velocity field in the solid region, since conservation of mass is satisfied for all the computational cells regardless of the presence of the IB. Mass conservation is not satisfied for the virtual cells obtained from cutting the fluid cells with the IB, and the subsequent errors may not be negligible.

To address mass conservation, the basic idea is to build new computational cells formed by the IB and existing cell faces, and to completely decouple the solid region from the fluid region. that the velocity. This is closely related to the finite volume method for an unstructured polyhedral mesh, and it is similar to the mass forcing concept by Kim *et al.* (2001) and cut-cell approaches (Ye *et al.* (1999); Kirkpatrick *et al.* (2003), among others. The present IB method, therefore, uses an efficient interpolation method for the velocity components and a modified finite volume operator for mass conservation at the immersed surfaces.

The finite volume discretization for the cut-cells introduces substantial complexity and, moreover, the computational stencil requires the modification of the linear system solver with potential negative impact on the efficiency of the code. An alternative approach is to consider strict flux conservation only for the explicit terms in the discretization stencil, leaving the implicit matrix unchanged (*lagged* correction). We refer to the former approach as a *strict* conservation and the latter as *approximate* conservation.

3.6. *Recovering the pressure field*

The final aspect of the IB algorithm that we investigated is the compatibility between the pressure field and the velocity field after any of the interpolation operators is used.

The basic idea is to perform an additional correction step (solving an extra Poisson equation) after the standard pressure correction equation. This equation is obtained by inserting the interpolated field at IB (obtained using any of the previously described interpolation formula) in the momentum equation and taking its divergence.

The amount of correction is clearly different depending on the specific interpolation method used. Our numerical experiments show that the QMIM interpolation requires the least correction.

4. Numerical experiments: decaying vortex problem

The problem of decaying vortices in a periodic has been widely used as a benchmark case to test the accuracy of numerical schemes, since it is an unsteady problem with an analytic solution. The velocity and pressure fields are given as:

$$u(x,y,t) = -\cos\pi x \sin\pi y \, e^{-2\pi^2 t/Re}, \tag{4.1}$$

$$v(x,y,t) = \sin\pi x \cos\pi y \, e^{-2\pi^2 t/Re}, \tag{4.2}$$

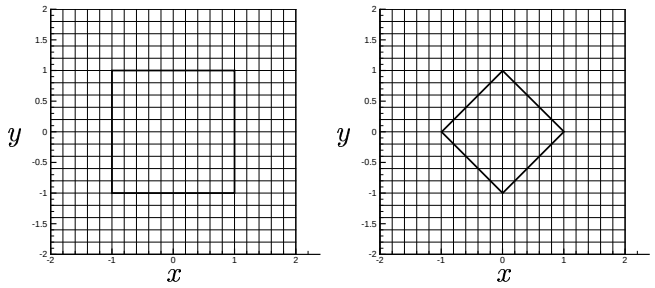

(a) Square (b) Rotated

FIGURE 5. Grid and IB configuration for a decaying vortex problem: (a) IB lines aligned on the grid lines; (b) IB lines inclined by 45° with respect to the grid lines.

$$p(x,y,t) = -0.25\,(\cos 2\pi x + \cos 2\pi y)\,e^{-4\pi^2 t/Re}. \tag{4.3}$$

In the present study, the exact flow field at $t = 0$ is integrated in time. The Reynolds number is set to 10. The computed flow field at $t = 0.2$ is compared with the analytic solution. The order of accuracy is investigated by computing the maximum (L_∞) error of the u_1 velocity and pressure fields with different grid sizes and time steps. A set of grid sizes (Δx=0.2, 0.1, 0.05 and 0.025) is chosen with a set of time steps (Δt=0.02, 0.01, 0.005 and 0.0025) as parameters. Both grid size and time step are halved to test the order accuracy of the numerical scheme in space and time at once.

4.1. *Linear interpolation methods*

In this section, results with the linear interpolation methods introduced in § 3.1-3.2 are shown. The list of the tested cases are:

A. LIM for $\hat{u}^k$, Eq. (3.1)
B. LIM for Δu, the delta form of Eq. (3.1)
C. Mixed LIM of A and B, Eq. (3.3)
D. RLIM, Eq. (3.4)

Tested IB geometries are the same as those used by Kim *et al.* (2001). In these geometries, grid lines in both directions and the IB lines meet at the edge points of the grid cells, which maintains a constant configuration between the grid and the IB lines independent of the number of grid points used. This problem setup allows for an effective investigation on the accuracy of IB methods. Fig. 5 shows the test geometries with the grid. Unless specified otherwise, the velocity field inside the IB geometry is solved and the velocity field outside of the IB is set to zero.

Fig. 6 shows the maximum error in u_1 and p with different numbers of grid points. When the IB line coincides with a grid line (square IB in Fig. 5 (a)), every interpolation method produces an acceptable result. In this case, the maximum absolute value of $\nabla \cdot u$ is $10^{-3} \sim 10^{-4}$ without any special treatment for mass conservation. But, when the IB line is inclined by 45° with respect to grid lines (rotated IB in Fig. 5 (b)), a large error ($\sim 10^2$) in the pressure is found for the LIM and mixed LIM cases (not shown in the figure). This indicates the occurrence of the local pressure build-up mentioned earlier. Interestingly, the accuracy of the velocity field is still acceptable. The LIM for Δu and the RLIM (Eq. (3.4)) show relatively reasonable pressure error. Between the LIM for Δu and Eq. (3.4), the accuracy of the pressure is shown to be better for the latter,

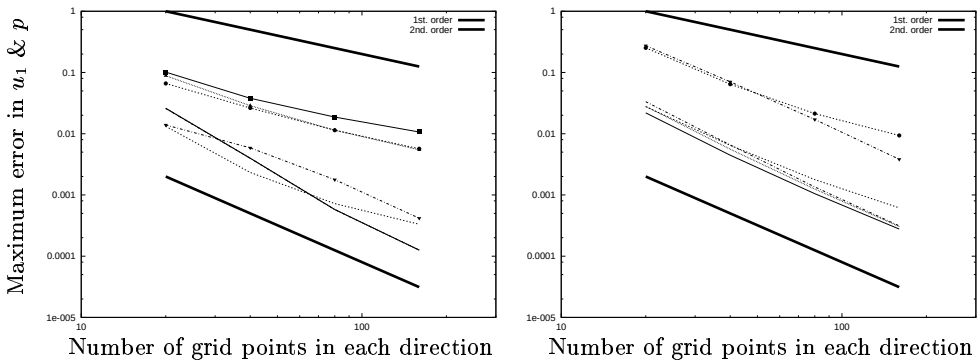

(a) Square (b) Rotated

FIGURE 6. Maximum error in u_1 and p at t=0.2 with the linear interpolation schemes: ——— , LIM for $\hat{u}^k$; – – – –, LIM for Δu; · · · ·, mixed LIM; —·—, RLIM. The symbol denotes the pressure.

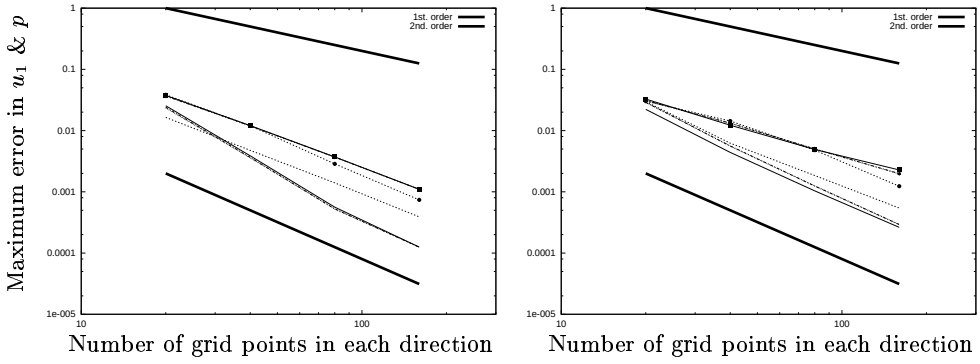

(a) Square (b) Rotated

FIGURE 7. Maximum error in u_1 and p at t=0.2 with the linear interpolation schemes and the pressure recovery scheme: ———, LIM for $\hat{u}^k$; – – – –, LIM for Δu; · · · ·, mixed LIM; —·—, RLIM. The symbol denotes the pressure.

which justifies the revision made by accounting for the local pressure gradient. Notably, with the LIM for Δu, the accuracy of the flow field is shown to decrease as the mesh becomes finer. For these cases, $\partial\phi/\partial\mathbf{n}$ is not zero at the IB since the approximation to the discretized Poisson equation is used. Thus, every velocity component is modified by the velocity projection step including the boundary conditions. If Δu at the IB is used as the boundary condition at the next time step, pre-existing error will not be reduced and will accumulate. The order of accuracy of the velocity field with the other interpolation methods is shown to be second order in Fig. 6.

Fig. 7 shows the maximum error with the pressure recovery scheme introduced in § 3.6. For the square IB, all error curves of the pressure collapse except for the LIM for Δu.

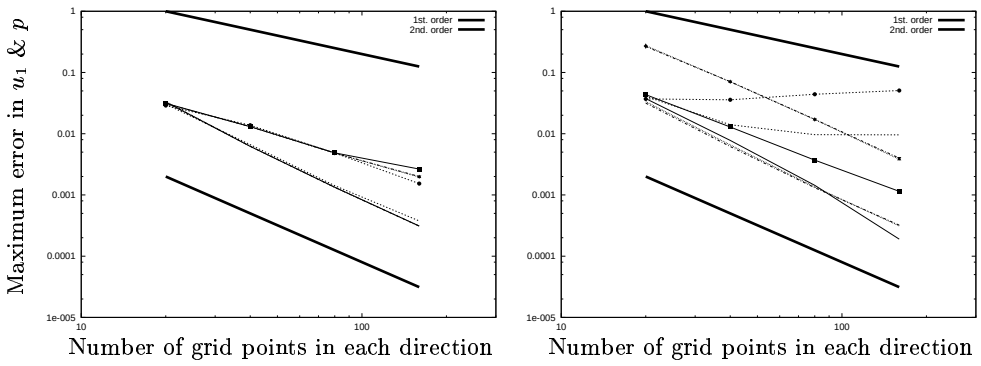

(a) (b)

FIGURE 8. Maximum error in u_1 and p at t=0.2 for the rotated IB case: (a) with the LIMs, the pressure recovery scheme, and strict mass conservation: ——— , LIM for $\hat{u}^k$; - - - - , LIM for Δu; · · · · , mixed LIM; —·— , RLIM (b) with the different settings for mass conservation with the RLIM : ——— , with the analytic initial and boundary conditions outside of the IB; - - - - , with the analytic initial condition only; · · · · , with the approximate mass conservation; —·— , with strict mass conservation. The symbol denotes the pressure.

For all cases, the pressure accuracy is increased. There is no noticeable change in the accuracy of the velocity.

Fig. 8 (a) shows the maximum error with the pressure recovery scheme and strict mass conservation introduced in § 3.5 for the rotated IB case. The maximum value of $|\nabla \cdot u|$ is kept less than 10^{-5} at every time step. The accuracy of the velocity is not increased except when the LIM for Δu is used. For this method, however, the deterioration of the accuracy on finer meshes disappeared. With strict mass conservation, $\partial\phi/\partial\mathbf{n} = 0$ is satisfied at the IB, and there is no accumulation of error. The pressure accuracy is slightly different for the different interpolation methods.

In order to further investigate the importance of mass conservation for the accuracy of the present IB method, two additional simulations without the mass conservation corrections of § 3.5 are tested. In this case the flow fields on both sides of the IB are coupled. The first set of results corresponds to the specification of the velocity and pressure outside the computational domain based on the exact solution. In the second calculation, on the other hand, the initial exact field (corresponding to $t = 0$) is used at all late times. Fig. 8 (b) shows the maximum error with the RLIM and the different option for mass conservation described above. The results indicates that the flow field in the flow region is affected to a large extent by the flow field in the boundary region if mass conservation for the IB cells is not properly satisfied. Also, the difference between the approximate and strict mass conservation cases is shown to be small.

To summarize, the IB method based on the LIM shows second order accuracy in time and space. Among the linear interpolation variants, the RLIM (Eq. (3.4)) is found to be most viable in the different IB geometries, even without strict mass conservation. In order to reduce the error in the pressure, the pressure recovery scheme is found to be more effective than strict mass conservation for the IB cells.

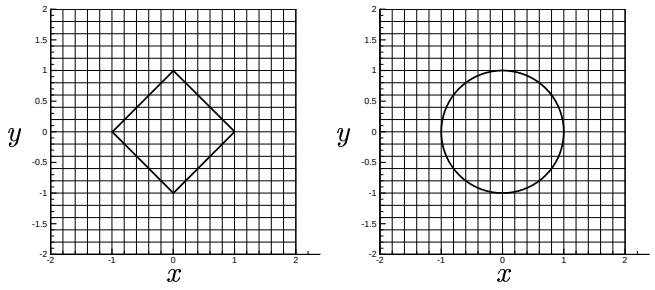

(a) Rotated (b) Circle

FIGURE 9. Grid and IB configuration for a decaying vortex problem: (a) IB lines inclined by 45° with respect to the grid lines; (b) IB line of a circular shape.

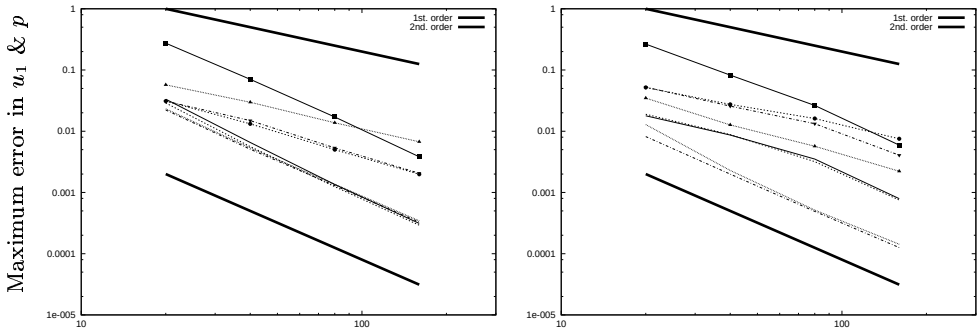

(a) Rotated (b) Circle

FIGURE 10. Maximum error in u_1 and p at t=0.2 with the different interpolation methods: ——— , RLIM; – – – –, RLIM with the pressure recovery scheme; · · · ·, QMIM; —·—, QMIM with the pressure recovery scheme. The symbol denotes the pressure.

4.2. *Quadratic interpolation method*

Quadratic interpolation method is here compared with the most accurate linear scheme presented in the previous section: the RLIM. These interpolation methods are tested with two IB geometries shown in Fig. 9. Fig. 9 (a) shows the rotated IB geometry identical to that in Fig. 5 (b). Fig. 9 (b) shows a circular IB geometry. This last configuration is more realistic as the intersection between the grid and the IB lines changes with the number of grid points. Considering that the error of an IB method is a function of distance between the fluid points and the IB, this configuration may cause some fluctuations in the observed accuracy. Fig. 10 shows the maximum error in u_1 and p with and without the pressure recovery scheme. In the rotated IB geometry, all cases show second order accuracy for the velocity. In the circular IB geometry, the QMIM (in § 3.4) shows second order accuracy for the velocity, while the RLIM (Eq. (3.4)) shows second order accuracy only when the grid spacing Δx is less than 0.05. The accuracy of the pressure is close to first order for the QMIM. The RLIM produces a higher order of accuracy for the

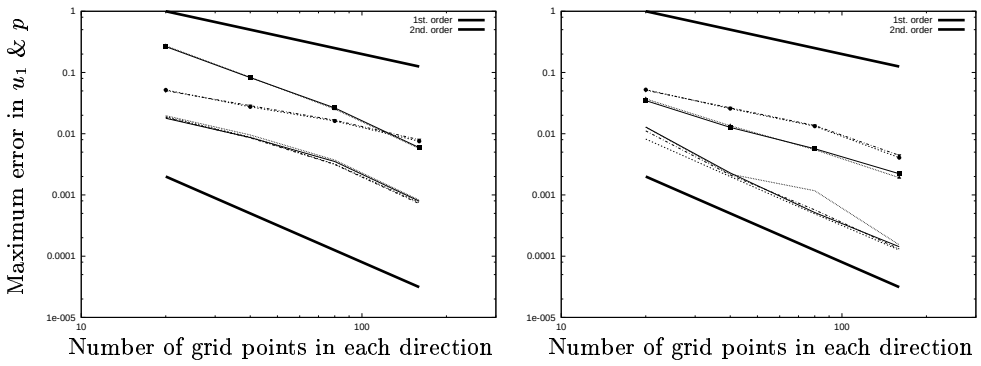

(a) RLIM (b) QMIM

FIGURE 11. Maximum error in u_1 and p at t=0.2 with the different interpolation methods and additional treatments in the circular IB: ——— , no additional treatment; – – – – , pressure recovery scheme; · · · · · , strict mass conservation; —·— , both treatments. The symbol denotes the pressure.

pressure, but the magnitude of the pressure error is larger than the QMIM for the grid spacings used.

With the pressure recovery scheme, velocity and pressure error is reduced in most cases. Also, the result confirms that the pressure recovery scheme is effective in reducing pressure error in a coarse mesh. It is noteworthy that the pressure recovery scheme seems to be less helpful in combination with the QMIM than with the RLIM.

Fig. 11 shows the maximum error in u_1 and p with the different additional corrections indicated before to investigate the combinations that are effective. A noticeable enhancement is observed when using strict mass conservation, but its effect is much smaller than that of using the pressure recovery scheme or different interpolation method. Considering the large amount of computational time used for strict mass conservation, it does not seem to be cost-effective for the cases tested.

In summary, the QMIM scheme is observed to be more viable than the other interpolation methods in a practical IB configuration. One weakness it showed is the lower order of accuracy in the pressure than the RLIM.

4.3. *Comparison of instantaneous flow fields*

As shown in the previous sections, all the interpolation methods considered in the present study show acceptable accuracy of the velocity and pressure, but some methods may result in spurious local pressure oscillations. Fig. 12 shows the instantaneous pressure contours obtained when using the LIM for $\hat{u}^k$ (Eq. (3.1)), revised LIM (Eq. (3.4)), and QMIM scheme (§ 3.4) for the circular IB geometry. The pressure recovery scheme is not used for these cases. A grid spacing of Δx=0.1 is used and the grid lines are shown in the figures. Large pressure oscillations and build-up at the cells crossed by the IB are clearly visible in the case of the LIM for $\hat{u}^k$. Much smaller errors are found in the pressure contours from the RLIM case; the results obtained with the QMIM are clean with no distortions.

Fig. 13 shows the instantaneous pressure contours from the different interpolation methods with the pressure recovery scheme. The pressure contours for all cases are now

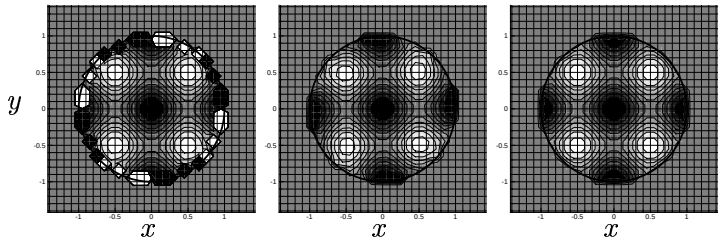

FIGURE 12. Instantaneous pressure contours computed using the different interpolation methods without the pressure recovery scheme: (a) LIM for $\hat{u}^k$; (b) RLIM; (c) QMIM.

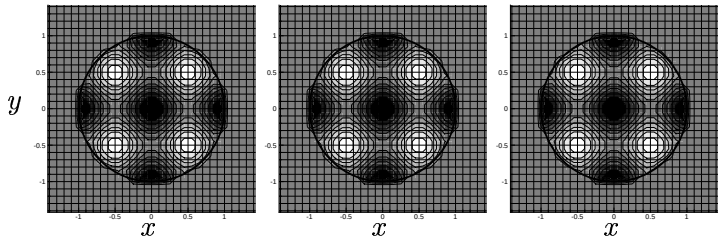

FIGURE 13. Instantaneous pressure contours computed using the pressure recovery scheme: (a) LIM for $\hat{u}^k$; (b) RLIM; (c) QMIM.

clean and look very similar. It must be pointed out that clean pressure contours are obtained for the LIM for $\hat{u}^k$ and RLIM as the grid resolution becomes very fine, even if the pressure recovery scheme is not used. This result confirms that a fine mesh resolution or the special treatment is necessary to get an acceptable pressure field when the LIM is used.

5. Conclusions

The immersed boundary method is a promising numerical method for flow problems with complex boundaries as it relaxes the difficulties associated with mesh generation. The major issues to be addressed are sufficient accuracy for LES or DNS and numerical efficiency. To this end, several revisions to the method of Fadlun *et al.* (2000) were considered in the present study.

In spite of second order accuracy shown theoretically as well as numerically, the simple linear interpolation method (LIM) was found to have incompatibilities with the time-marching scheme. This incompatibility is expressed as local error accumulated in the pressure field. In order to mitigate this problem, a revised version of the LIM was proposed. A few additional corrections were added by handling the contributions from some of the terms in the decoupled momentum equation explicitly. The decaying vortex test problem indicated that the RLIM is effective in reducing error in the pressure field while maintaining the accuracy of the original LIM. Another interpolation method was devised

by combining a quadratic interpolation formula and the momentum equation. The resulting scheme, QMIM, simulates the discretized Navier-Stokes equation more directly than the LIM, and is similar to the cut-cell approach in that a formal discretization of the momentum equation is used. In the numerical tests, the QMIM scheme produces smaller errors especially when for coarse grid resolutions. Second order accuracy for the velocity and higher than first order accuracy for the pressure were observed for both interpolation methods. Computational overhead was found to be less than 15% of the original computation time for the test case considered.

Another approach for addressing the incompatibility between the interpolation method and the time-marching scheme was introduced. A condition for the intermediate velocity field was enforced to obtain proper accuracy for the pressure. In order to satisfy this condition, a correction to the intermediate velocity field was considered. This additional correction, referred to as a pressure recovery scheme, reduced the velocity and pressure error in most cases. The pressure recovery scheme is especially effective for coarse meshes. The practical importance of mass conservation for the IB method was another issue addressed. The additional treatments for mass conservation are closely related to the finite volume method for an unstructured mesh. The different levels of mass conservation for new volume cells formed by the IB and existing cell faces were considered. This revision is very useful when the velocity boundary condition is not zero. In the numerical test, we observed that the flow field can be affected to a large extent by the boundary region if mass conservation for the IB cells is not carefully considered. Various approaches have been considered to solve this problem.

REFERENCES

FADLUN, E.A., VERZICCO, R., ORLANDI, P., AND MOHD-YUSOF, J. 2000 Combined immersed-boundary/finite-difference methods for three-dimensional complex flow simulations, *J. Comput. Phys.* **161**, 35.

KIM, J., KIM, D. AND CHOI, H. 2001 An immersed-boundary finite-volume method for simulations of flow in complex geometries, *J. Comput. Phys.* **171**, 132.

KIM, J. AND MOIN, P. 1985 Application of a fractional-step method to incompressible Navier-Stokes equations, *J. Comput. Phys.* **59**, 308.

KIRKPATRICK, M.P., ARMFIELD, S.W. AND KENT, J.H. 2003 A representation of curved boundaries for the solution of the Navier-Stokes equations on a staggered three-dimensional Cartesian grid, *J. Comput. Phys.* **184**, 1.

MATTOR, N., WILLIAMS, T.J. AND HEWETT, D.W. 1995 Algorithm for solving tridiagonal matrix problems in parallel, *Parallel Computing* **21**, 1769.

YE, T., R. MITTAL, R., UDAYKUMAR, H.S. AND SHYY, W. 1999 An accurate Cartesian grid method for viscous incompressible flows with complex immersed boundaries, *J. Comput. Phys.* **156**, 209.

A computational and experimental investigation of flow inside branched coral colony

By S. Chang †, G. Iaccarino, C. Elkins ‡, J. Eaton ‡ AND S. Monismith †

1. Motivation and objective

Coral reefs have the highest biodiversity of any marine ecosystem. Though they cover only 15 percent of the ocean surface between the depth of 0 to 30 meters (Smith, 1978), coral reefs shelter nearly a quarter of all marine life. The host of organisms that thrive in the reef system, of which only about 10 percent have been described, bears tremendous potential for modern medicine (Serageldin 1998). Furthermore, coral reefs are important economic resources, serving as fisheries and breakwaters for coastal communities. In spite of their ecological and economic significance, 30 percent of the world's coral reefs are severely damaged, and 60 percent are projected to be lost by 2030 (Wilkinson 2002). Overfishing, agricultural pollution, and coastal development alter the species and nutrient balance in the water, making corals less competitive against fleshy seaweed (Hughes 1994; McClanahan *et al.* 2002). Warming of the seawater caused by global climate change overheats the coral, which is extremely temperature sensitive. The coral, in response, expels its symbiotic algae, zooxanthellae, such that the coral itself becomes white, or bleached. Prolonged bleaching episodes, which have been observed to increase in frequency and magnitude in the last 30 years (Hughes *et al.* 2003), cause coral death throughout reef systems.

Given both the importance and the fragile state of coral reefs, understanding the mechanisms for coral growth is crucial to the survival and possible recovery of the remaining reef systems around the world. Corals are able to flourish in low-nutrient, oligotrophic waters because of their ability to efficiently use their limited resources for growth. In this work we hope to explore the role of hydrodynamics in coral growth through innovative computational and experimental methods.

Hydrodynamics directly affect coral growth, energetics, and health. Sessile organisms such as corals rely on water flow to deliver their nutrients, and consequently the nature of the flow plays an important role in determining nutrient availability. Coral has two metabolic roles that have functional dependence on flow: one as a zooplankton-ingesting heterotroph, another as a benefactor of symbiotic autotrophs. As heterotrophs, the coral polyps capture zooplankton that is carried by the flow for sustenance. As autotrophs, the symbiotic algae zooxanthellae depend on the concentration gradient of inorganic nutrients established by the diffusive boundary layer. Additionally, the structural integrity of the coral is susceptible to the amount of force the moving fluid imposes on the geometry. Clearly, hydrodynamics plays a crucial role in coral subsistence.

Corals live in a variety of hydrodynamic conditions, with flow velocities ranging from 5 cm/s in the fore reef up to 100 cm/s in the surf zone (Sebens 1997). Consequently, corals have adapted structurally, resulting in morphologies that vary in branch-spacing

† Environmental Fluid Mechanics Laboratory, Civil and Environmental Engineering Department, Stanford University
‡ Mechanical Engineering Department, Stanford University

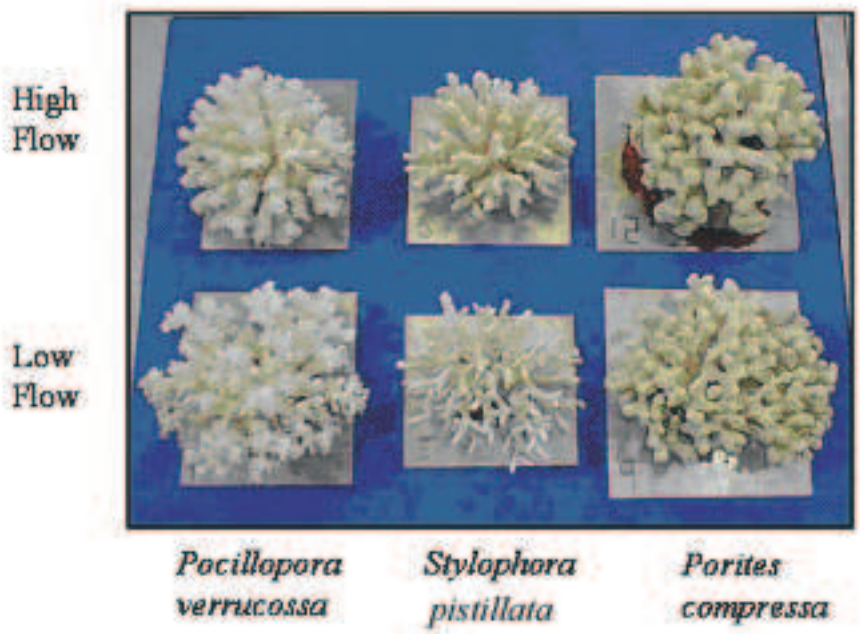

FIGURE 1. Low and high flow morphologies of several corals from Eilat, Israel.

and width (Fig. 1), from plate-like to massive. For instance, coral geometries with denser branching tend to divert more flow to the exterior, establishing a larger stagnant region in the core of the geometry and greater shear above the colony due to a higher exterior velocity. For the same flow condition, coral geometries with sparser branching will allow more flow through the interior, resulting in greater force imposed upon the interior branches by the flow. Quantifying the functional dependence of the resulting flow field on coral morphology and hydrodynamic environment will significantly contribute to understanding nutrient transport.

Hydrodynamics also directly affect the corals' requirements for structural stability. As the large-scale physical damages to coral reefs by hurricane-driven waves attest, the structural integrity of the coral structure is susceptible to damage due to the amount of force the moving fluid places on it (Sebens 1997). Corals that live in wavy, high-energy environments need more robust branches and lower surface area to volume ratios in order to prevent breakage. In slower flows, corals can afford structurally weaker morphologies to optimize for nutrient and feeding priorities. Conversely, some species take advantage of periodic storm events by having thin branches that break off, and then recolonize elsewhere on the seafloor (Sebens 1997). No matter what the adaptive behavior is, the force that the flow imparts on the coral structure deems particular morphologies more suitable for one versus another hydrodynamic environment.

Additional complexity arises from the fact that the hydrodynamics throughout the colony, defined as one skeletal unit, e.g. one head, are locally variable and therefore cannot be adequately modeled with bulk flow and roughness parameters at the scale important for these processes. The coral geometry acts as a bluff body that perturbs the flow, resulting in recirculation zones and regions of localized acceleration, deceleration, and stagnation (Chamberlain & Graus 1975). Such spatially and temporally variable flow

in turn leads to differential local nutrient concentrations and boundary layer thicknesses throughout a coral colony, which, after a long enough time, may induce localized calcification for a single coral head resulting in a specific preferential growth form (Oliver *et al.* 1983; Lesser *et al.* 1994; Bruno and Edmunds 1997). The resulting new geometry then interacts with the flow in a slightly different way, which once again has direct consequences on local nutrient availability and coral growth (Kaandorp & Kűbler 2001).

To better address this complex interaction, we believe that it is possible to create a comprehensive model of corals based on first principles, *i.e.* a virtual coral. This model would simulate numerically the flow and mass transfer in and around a coral colony, given the specific geometry of the coral. Since the geometry of the coral itself depends on local calcification rates, the rates would be calculated using model representations of the chemistry of calcification and of photosynthesis by the zooxanthellae. This comprehensive approach would require models of the light field incident on the coral surfaces, including among other physics the focusing effects of surface waves. When complete, this model should be capable of testing hypotheses relating changes in flow, morphology, nutrient, light level, and temperature to the coral's physiological response, *e.g.* calcification rates and pattern, photosynthesis rates, or bleaching. As the first step in the development of the virtual coral model, we will perform detailed calculations of flow through a single coral head, allowing for the explicit computation of local stresses, forces, and mass transfer rates at every point on the surface of a coral head. Specifically, we propose to:

- Compute and validate through comparisons with experiments the variability of stress and velocity fields throughout a single colony, including the interstitial area between the branches.
- Assess the effect of the flow conditions (*e.g.* variable velocities, unidirectional versus oscillatory flow) on mass transport.
- Assess the effect of roughness on mass transport, considering both
  - large-scale geometric roughness as characterized by morphologies from different species and flow regimes;
  - small-scale surface roughness as characterized by the mucus membrane and polyps attached to the large-scale geometry.

To achieve these goals, we will use a numerical simulation technique based on the Immersed Boundary (IB) method to calculate the flow and mass transfer around a single coral colony. The IB technique has proven to be effective and efficient for computing flows around complex geometries (Iaccarino *et al.* 2003; Iaccarino & Verzicco 2003; Grigoriadis *et al* 2004). The coral morphology and flow conditions can be varied in the simulations to determine the effects on the flow field and on nutrient transport. The results will be validated using a combination of Magnetic Resonance Velocimetry (MRV) for the interstitial flow and Particle Image Velocimetry (PIV) for the wake region of the coral.

2. Experimental setup

2.1. *Coral geometry acquisition*

In order to mimic the flow around corals in the field conditions, we need to incorporate realistic geometries in our experiments. For this purpose we have selected *Stylophora pistillata*, a Red Sea coral found more commonly in slower, unidirectional flow regimes, for this purpose.

The coral need to be digitally represented so that the geometry can be built using rapid prototyping manufacturing and imported into the computational flow domain.

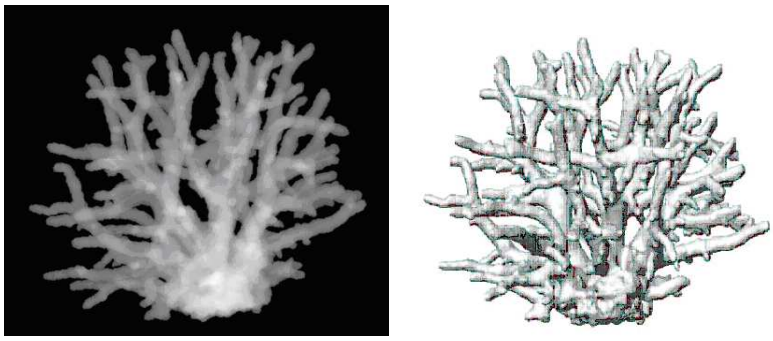

FIGURE 2. *Stylophora pistillata*, low flow morphology. (a) CT scan: This image is a compilation of 245 images taken at every 0.7 mm (in the direction out of the page). The pixel size is 0.35 mm x 0.35 mm with an 18 cm by 18 cm field of view, resulting in a 512 x 512 matrix of intensity values for each image. (b) Postprocess with MIMICS to create a three-dimensional representation in stl format.

The digital format is obtained by scanning the coral skeletons using x-ray computed tomography (CT). This medical technology is ideal for our purpose; the method is able to effectively image calcium carbonate, the basis for both bones and coral skeletons, and render occlusions in the contorted coral geometries. Two-dimensional images (Fig. 2a) are constructed from linear projections of x-rays taken at many different angles along a single plane, which then are shifted by a small distance (thickness) perpendicular to the image plane to acquire the next set of projections (Bushberg *et al.* 1994). Each image then has an associated thickness.

2.2. *Coral model and setup*

The size of the experimental facility is limited by the MRV system. In order to accommodate the restriction, a 75% model of the coral colony was built by Dr. Ryan Wicker at University of Texas at El Paso (UTEP) using a fused deposition manufacturing system (Figure 8 shows the 100% model, Figure 9 shows the 75% model in the channel). MRV-compatible resin manufactured by DSM Somos was layered with water-soluble supports for the overhanging branches. The supports were then dissolved to create the final model. To house the model, a unidirectional flow laboratory setup (3) has been designed and constructed to create an inlet flow condition that is as uniform as possible (see *e.g.* Vogel, 1983). To fit inside the 26 cm diameter head coil, the channel is confined to the maximum size of 19 cm wide by 17 cm tall. Attached to the front of the channel is a diffuser with three differential pressure drops (50% void ratio in the center region, 75% around the perimeter) to prevent the flow from stalling. The inlet contains two additional screens and a baffle for the same purpose. The outflow releases into a reservoir, which is connected to a pump and then recirculates to the inflow. The velocity in the channel with the current set up is approximately 5 cm/s.

3. Computational study

The Immersed Boundary (IB) technique enables numerical simulations of the flow around very complex geometries to be performed on simple Cartesian grids with local grid refinement. In the present application the coral is not physically present in the computational domain when the mesh is generated and its presence is accounted for via modifications to the governing equations. These modifications take the form of a forcing

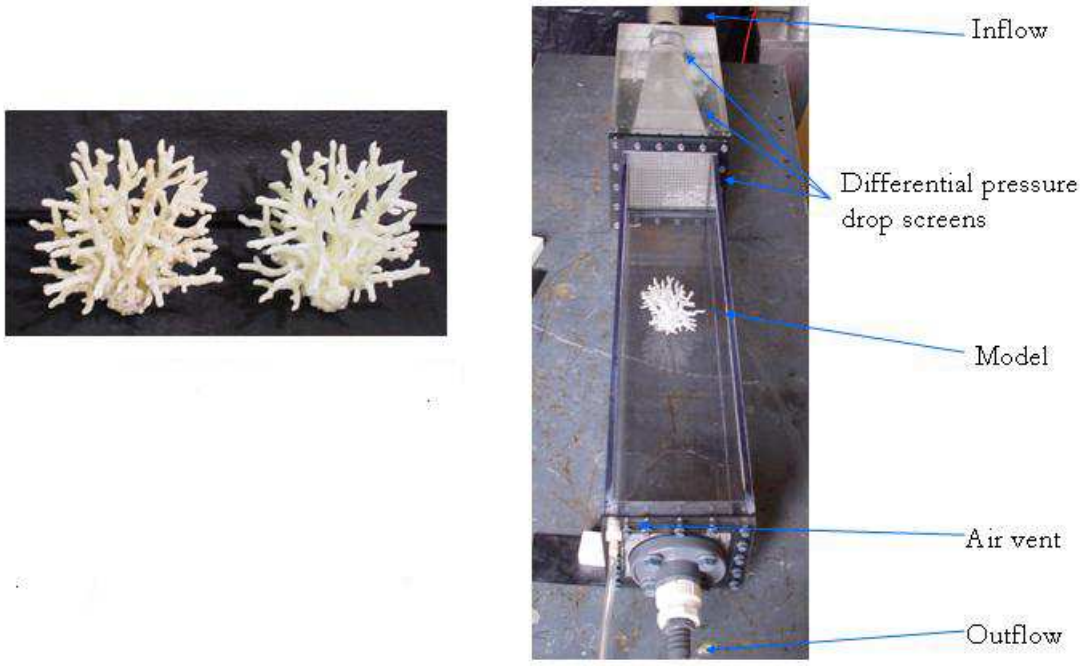

FIGURE 3. *Stylophora pistillata* skeleton (left) and rapid-prototyped model (center). Channel set-up for MRV and PIV (right)

term which mimics the effect of the physical boundary conditions enforced on the coral surface. In the present implementation of the IB approach the solution in the vicinity of the coral is reconstructed on the basis of the computed flow away from the body and the no-slip condition on the surface. Inverse distance interpolation is used (Iaccarino & Verzicco 2003). Although the objective is to ultimately perform Large Eddy Simulation with the IB technique, we have carried out some preliminary simulations with a Reynolds Averaged Navier-Stokes (RANS) model to gather initial solutions to be compared to experiments and to investigate the grid resolution requirements for capturing the details of the flow. The computation code used, namely IBRANS, is based on the solution of the three-dimensional, steady-state RANS equations using a finite volume, collocated discretization where all the flow variables (*e.g.* pressure and velocity) are defined at the center of each grid cell (see Iaccarino *et al.* 2003 and Iaccarino & Verzicco 2003 for details). The SIMPLE (Semi-Implicit Method for Pressure-Linked Equations) pressure-correction algorithm is used. The continuity equation is converted into a discrete Poisson equation which subsequently is used to correct the momentum equations. A second-order accurate discretization is used to solve the governing equations; the solution is computed iteratively using a fully implicitly scheme. The boundary conditions are treated explicitly, where no slip is assumed along the immersed boundary of the solid surface.

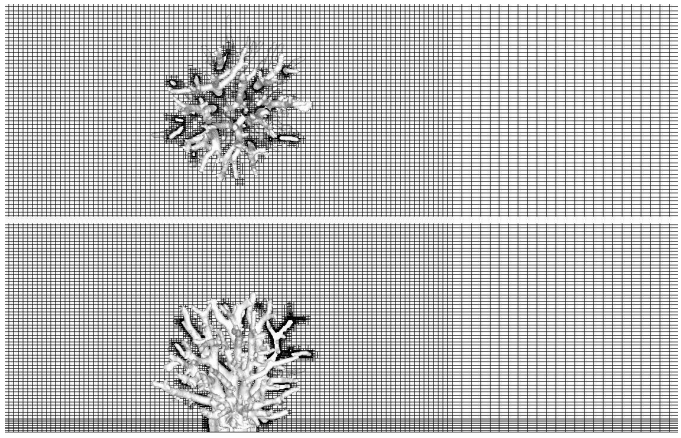

FIGURE 4. Computational grids generated for the RANS simulations. Horizontal plane at 1/3 the coral height (top) and vertical plane at midspan of the duct (bottom). The mesh contains $\approx$ 2 million cells

Computational grids are generated automatically starting from the CAD definition of the coral geometry (in stereo-lithography format); the duct described previously is modeled without the inlet diffuser; the flow is assumed to be uniform at the inlet and no-slip boundary conditions are specified on the duct walls. The mesh size is specified on the coral surface and grid resolution is achieved through local grid refinement. Three grids have been generated and their cross-sections (corresponding to a longitudinal plane halfway through the duct) are reported in Fig. 4.

4. Experimental study

MRV is a non-invasive experimental technique which allows the acquisition of the entire three-component mean velocity field in a three-dimensional flow domain a medical Magnetic Resonance Imaging (MRI) scanner. MRI is a medical technology that uses magnetic field and sequences of radio frequency pulses to extract images inside an object. The method relies on the atomic structure of the object being imaged. In the absence of a magnetic field, the spin and charge distribution of the individual atoms result in magnetic dipoles that is randomly oriented due to thermal energy. The MRI coil imposes an external gradient magnetic field such that the net magnetic moment of the atoms in the sampled object aligns itself with the field, while each individual dipole precesses around the orientation of the magnetic field such that at any given time its position can be described by a phase. When motion is present, the location of fluid parcels are marked based on their phase, which then can be reconstructed with Fourier transform. This method has been used to measure turbulent flow in a highly complex internal flow geometry modeling the internal cooling passage of a gas turbine engine blade (Elkins *et al.* 2003). The data have been validated against PIV measurements on selected planes and have also been used to validate a numerical simulation of the same geometry using the IB technique (Iaccarino *et al.* 2003).

The setup shown in Fig. 3 was placed in the MRI chamber and preliminary measurement were collected. The flow-meter indicated the flowrate as 81 L/min, which is equivalent to 5.2 cm/s for the channel. The resolution is approximately 1.25 mm by 1.25 mm in the xy plane, with 1 mm thick slices along the z axes. Total scan time was 9.35

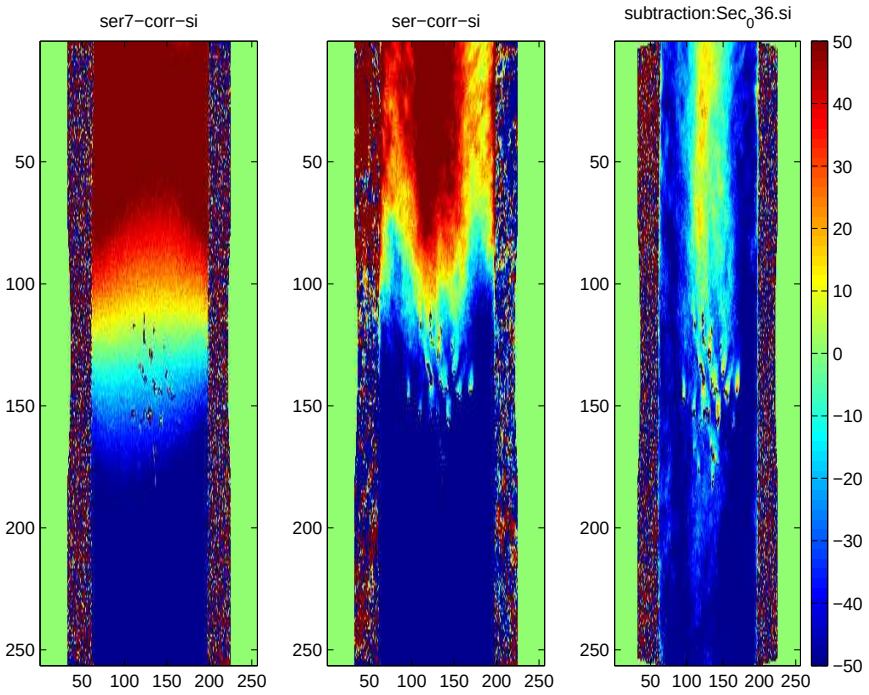

FIGURE 5. MRV velocity result at approximately 1/3 of the height of the coral. The images are scans flow off, flow on, and flow off subtracted from flow on, respectively. Flow is going from bottom to top. The color gradation is an indication of streamwise velocity in mm/s. The velocities are inverted; negative velocity indicate upward direction, and conversely, positive velocity indicate downward or reverse direction.

minutes. A 0.5% by volume gadolinium solution was used to enhance the signal. An example of the results is shown in Fig. 5. The MR signal of the setup with the pump on and off were recorded, such that the flow off condition can be subtracted from the flow on condition such that the signal would only be from the flow.

The preliminary result clearly show a wake behind the coral geometry as a whole, as well as effects of the coral branches itself. Because of the size of the channel, which in effect occupy the entire space in the magnet coil, the edges of our domain, where the magnetic field lines curve, require more refined reconstruction.

5. Preliminary analysis of the flow field

Preliminary calculations and measurements are compared in a vertical plane corresponding to the duct mid-span and in an horizontal plane at 1/3 of the coral height (in Fig. 6 and Fig. 7, respectively). The Reynolds number, based on the coral height and the inflow bulk velocity, is $Re = 4,700$. The (steady-state) calculations indicate the presence of a rather large wake with maximum negative velocities twice v_{inflow}. The structure of the wake is highly three-dimensional and the branch distribution is clearly visible through the presence of high velocity spots. The comparison between MRV and IB data is, at this point, not satisfactory. It must be noted that from visual observation during the measurements, the flow has a strong unsteady nature. This is neglected by the current steady-state calculations and can lead to substantial overpredictions of the wake

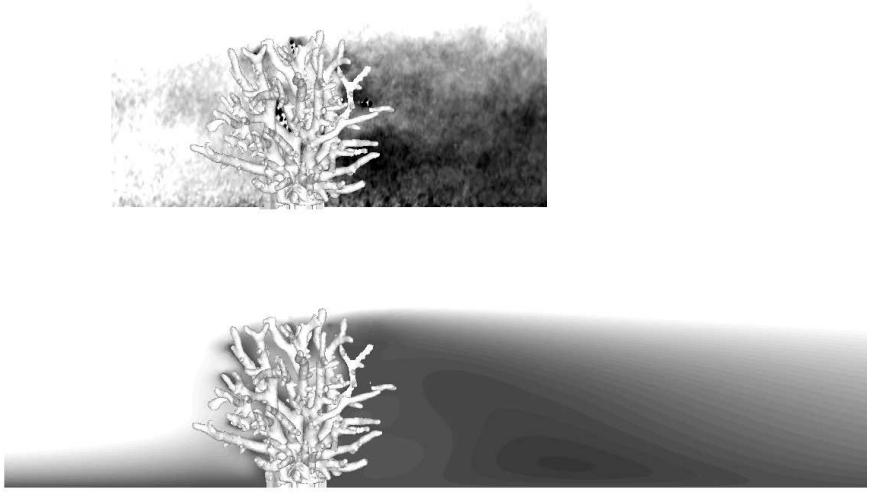

FIGURE 6. Comparison of experimental (MRV, top) and numerical (IB, bottom) results for a vertical plane at the duct mid-span section. Streamwise velocity shown.

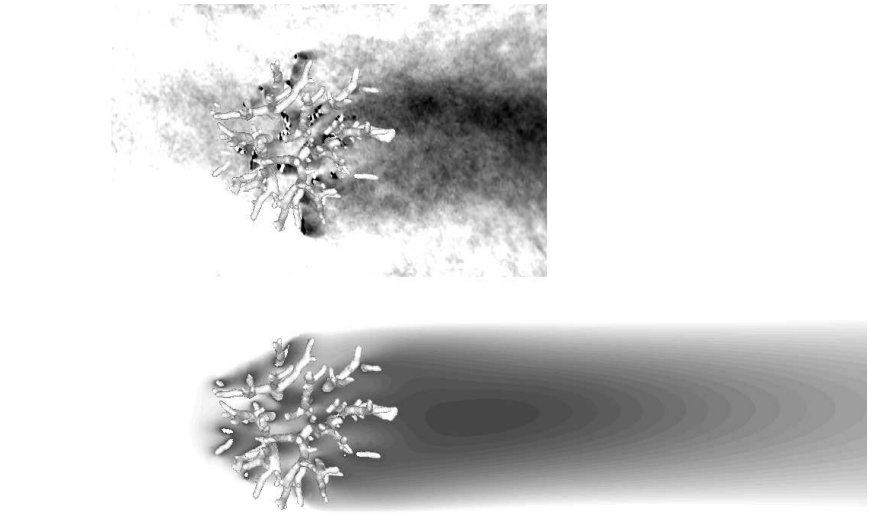

FIGURE 7. Comparison of experimental (MRV, top) and numerical (IB, bottom) results for a horizontal plane at 1/3 height of the coral. Streamwise velocity shown.

strength and size (Durbin, 1995). In addition, the MRV data are collected in frequency space over ≈ 10 minutes. For this reason, the collected data might not represent correctly neither the time-averaged or the instantaneous flow field. Moreover, flow rate measurements show large discrepancies during the testing. These difficulties in the acquisition of satisfactory experimental and simulation data are currently being addressed.

6. Conclusion

Coral reefs are clearly of great ecological significance, and as is often the case with ecosystems of importance, the health and survival of coral reefs are threatened. In order to diminish the degree of degradation and even possibly facilitate the recovery of coral reefs, a better understanding of coral biology must be developed, within context of the environment that so greatly influences its fate. As shown repeatedly in the literature, basic aspects of coral ecology, growth, and health, can strongly depend on flow.

In order to examine this dependence, this work has spanned a wide array of techniques. The acquisition of a real coral geometry in digital format required scanning the coral skeleton using CT; the same model is then used for both the computations and the measurements as a physical model of the coral (not the actual skeleton) must be used. For the construction of this model, a complex rapid-prototyping technique (Iyengar *et al.* 2004) was utilized due to the very complex geometry with many occlusions and overhangs. The model was placed in a channel built for this experiment and the velocities were extracted using MRV. The numerical technique IB was used for its efficiency with complex geometries, resulting in some preliminary computational results to compare with the experimental results.

These innovative computational and experimental methods will elucidate previously unresolved dynamics on the scales important to mass transfer. As hydrodynamics continue to change due to increased storm events resulting from climate change and continued human manipulation of the coastline by dredging and building infrastructures such as breakwaters, understanding the interactions between hydrodynamics and coral will be crucial for preserving the remaining coral reefs.

Acknowledgments

The authors would like to thank Professor Jeff Koseff for his involvement and guidance on the project. Gratitude also to Professor Amatzia Genin of Steinitz Laboratory in Eilat, Israel, for providing the coral skeleton. The CT scan is coordinated by Mary Draney at Stanford medical facilities and rapid prototype model built by Professor Ryan Wicker at UTEP and Frank Medina. Many thanks also to Professor Lars Saetran for guidance. The scanning was performed by Dr. Marc Alley. Also gratitude to Georgi Kalitzin and Frank Ham on use of the IB method. This work has been supported by NSF grant OCE-0117859 and is currently supported by NSF grant OCE-0425312.

REFERENCES

Bruno, J. & Edmunds, P. 1997 Clonal variation for phenotypic plasticity in the coral Madracis mirabilis. *Ecology*, **78**, 2177-2190.

Bushberg, J., Seibert, J., E.M. Leidholdt, J. & Boone, J. 1994 *The Essential Physics of Medical Imaging*, Williams and Wilkins.

Chamberlain, J. & Graus, R. 1975 Water flow and hydromechanical adaptations of branched reef corals. *Bulletin of Marine Science*, **25**, 112-125.

Durbin, P. A. 1995 Separated Flow Computations with the k-e-v2 Model. *AIAA J.*, **33**, 659-664.

Elkins, C., Eaton, J., Markl, M. & Pelc, N. 2003 4d magnetic resonance velocimetry for mean velocity measurements in complex turbulent flows. *Exp. in Fluids*, **34**, 494-503.

GRIGORIADIS, D., BARTZIS, J. & GOULAS, A. 2004 Efficient treatment of complex geometries for large eddy simulations of turbulent flows. *Computers and Fluids*, **33**, 201-222.

HUGHES, T. 1994 Catastrophes, phase shifts, and large-scale degradation of a Caribbean coral reef. *Science*, **265**, 1547-1551.

HUGHES, T., BAIRD, A., BELLWOOD, D., CARD, M., CONNOLLY, S., FOLKE, C., GROSBERG, R., HOEGH-GULDBERG, O., JACKSON, J., KLEYPAS, J., LOUGH, J., MARSHALL, P., NYSTROM, M., PALUMBI, S., PANDOLFI, J., ROSEN, B. & ROUGHGARDEN, J. 2003 Climate change, human impacts and the resilience of coral reefs. *Science*, **301**, 929-933.

IACCARINO, G., KALITZIN, G. & KHALIGHI, B. 2003 Towards an immersed boundary RANS flow solver. *AIAA 41st Aerospace Sciences Meeting and Exhibit*, Reno, Nevada.

IACCARINO, G. & VERZICCO, R. 2003 Immersed boundary technique for turbulent flow simulations. *Appl. Mech. Rev.*, **56**, 331-347.

IYENGAR A., ELKINS C., ALLEY M., MEDINA F. & WICKER R.B. 2004 PIV and MRV Measurements in Human Thoracic Aorta Phantoms. American Physical Society, Seattle, WA, November 21-23.

KAANDORP, J. & KUBLER, J. 2001 *The Algorithmic Beauty of Seaweeds, Sponges, and Corals*, Springer.

LESSER, M., WEIS, V., PATTERSON, M. & JOKIEL, P. 1994 Effects of morphology and water motion on carbon delivery and productivity in the reef coral, Pocillopora damicornis Linnaeus: Diffusion barriers, inorganic carbon limitation, and biochemical plasticity. *J. Exp. Mar. Biol. Ecol.*, **178**, 153-179.

MCCLANAHAN, T., POLUNIN, N. & DONE, T. 2002 Resilience of coral reefs. In *Resilience and Behavior of Large-Scale Systems*, Island Press.

OLIVER, J., CHALKER, B. & DUNLAP, W. 1983 Bathymetric adaptations of reef-building corals at Davis Reef, Great Barrier Reef, Australia. I. Long-term growth responses of Acropora vormosa Dana 1846. *J. Exp. Mar. Biol. Ecol.*, **73**, 11-35.

SEBENS, K. 1997 Adaptive responses to water flow, morphology, energetics, and distribution of reef corals. *Proc. 8th Int. Coral Reef Sym.*, **2**, 1053-1058.

SERAGELDIN, I. 1998 Coral reef conservation: Science, economics, and law. In *Coral Reefs: Challenges and Opportunities for Sustainable Management* (ed. M. Hatziolos, A. Hooten & M. Fodor), 3-7. The World Bank.

SMITH, S. 1978 Coral-reef area and the contributions of reefs to processes and resources of the world's oceans, *Nature*, **273**, 225-226.

VOGEL, S. 1983 *Life in moving fluids*, Princeton Press.

WILKINSON, C. 2002 *Status of Coral Reefs of the World*, Australian Institute of Marine Science.

Numerical issues and freestream behavior of the v^2-f model.

By G. Kalitzin

1. Motivation and objectives

The numerical method used to solve the equations of a turbulence model is of comparable importance to the concerns about the representation of the flow physics, as its efficiency and robustness determines the overall performance of the flow solver. The v^2-f model by Durbin (1995) has shown to reproduce mean flow and turbulence quantities accurately for a large number of turbulent flows (Durbin 1995; Parneix & Durbin 1997; Kalitzin 1999). However, the stiffness of the equations and, in particular, of the wall boundary condition that results from the strong near-wall coupling of the $\overline{v^2}$ transport equation and the elliptic relaxation equation for f, hindered its application to large scale industrial flow applications.

Lien & Durbin (1996) proposed a 'code-friendly' version of the v^2-f model. In this version, source terms have been introduced in the $\overline{v^2}$ and f equations and $f = 0$ is imposed at the wall. This model allowed a segregated solution of the turbulence field equations and it has found wide spread use in many commercial CFD codes. Although this version of the model was constructed to reproduce the results obtained with the 1995 version of the model, it has been found, that the introduced modifications lead to larger deviations in certain flow regimes. In general, the modified model predicts a delayed laminar-turbulent transition. For low-Reynolds number flows this may actually improve flow field predictions. However, the model prediction mechanism of transition is not fully understood and it is undesirable as it also affects flow predictions at high-Reynolds numbers.

In the search for robustness, Laurence *et al.* (2004) proposed another 'code-friendly' version of the v^2-f model. This model is based on the substitution of the ratio $\overline{v^2}/k$ with a variable ϕ and the alteration of the governing equation by neglecting source terms in the f-equation. The developers of this model have tested the model on channel, diffuser flow and flow over periodic hills. Results reported reproduce the results of the 1995 version of v^2-f, while retaining the easier convergence properties of this 'code-friendly' version.

Kalitzin (2002) presents a numerical scheme for the solution of the 1995 version of the v^2-f model. That scheme solves the implicit, pairwise coupled discretized equations of the model using a Diagonally Dominant Alternating Direction Implicit (DDADI) solver. For steady state computations, local time stepping is utilized for the advancement of the turbulence equations.

The present paper proposes a modification to that scheme. It is argued that the robustness of the DDADI algorithm applied to the v^2-f model can greatly be improved when local time stepping is substituted with explicit under-relaxation. The resulting scheme has some very desirable properties and shows a very efficient and robust behavior.

In addition, the paper also conducts an analysis of the freestream behavior of the v^2-f model. It is shown, that under certain flow conditions the model provides a negative solution for the turbulent kinetic energy in the freestream. This may lead to numerical

instabilities if not prevented by minimum limiters for the turbulence variables. A modification of the model is proposed that eliminates this problem and no such limiters are required.

The new DDADI scheme with explicit under-relaxation is applied to the prediction of flow over a wing that generates a large wing-tip vortex. For this case, the turbulence field is strongly coupled with the mean flow. Comparisons with the model by Spalart & Allmaras (1994) reveal significant differences in the prediction of the wing-tip vortex.

2. Improvement of the solution algorithm for the v^2-f model

The v^2-f turbulence model by Durbin (1995) consists of, in addition to the usual transport equation for the turbulent kinetic energy k and dissipation ε, a transport equation for the scalar $\overline{v^2}$ and an elliptic relaxation equation for f:

$$\left.\begin{aligned}
\partial_t k + u\cdot\nabla k &= \frac{1}{\rho}\nabla\cdot[(\mu+\mu_t)\nabla k] + P_k - \varepsilon \\
\partial_t \varepsilon + u\cdot\nabla \varepsilon &= \frac{1}{\rho}\nabla\cdot[(\mu+\frac{\mu_t}{\sigma_\varepsilon})\nabla\varepsilon] + \frac{C_{\varepsilon 1}P_k - C_{\varepsilon 2}\varepsilon}{T} \\
\partial_t \overline{v^2} + u\cdot\nabla \overline{v^2} &= \frac{1}{\rho}\nabla\cdot\left[(\mu+\mu_t)\nabla\overline{v^2}\right] + kf - \frac{\varepsilon}{k}\overline{v^2} \\
f &= L^2\nabla^2 f + \frac{C_1}{T}\left[\frac{2}{3} - \frac{\overline{v^2}}{k}\right] + C_2\frac{P_k}{k}
\end{aligned}\right\} \qquad (2.1)$$

where the eddy-viscosity is defined as:

$$\nu_t = C_\mu T \overline{v^2} \qquad (2.2)$$

The stiffness of the model results mainly from the f wall boundary condition:

$$f_w = -20\nu^2\overline{v_1^2}/(\varepsilon_w y_1^4) \qquad (2.3)$$

Kalitzin (2002) describes the implementation of this model in the compressible, structured multiblock code TFLO. The model is solved in a separate set of subroutines, segregated from the mean flow. In each block, multigrid is used for the mean flow and at each multigrid cycle the model's subroutines are called on the finest grid. They return an updated value of the eddy-viscosity and turbulent kinetic energy. These two quantities are passed to the mean flow solver for the determination of the Reynolds stresses.

The model equations are solved in an implicit, pairwise coupled manner, with a cell centered finite difference scheme. The pairwise coupled solution of the field equations allows an implicit treatment of the wall boundary conditions. The implicit matrices are factorized with a DDADI scheme. The treatment of the boundary conditions as source terms prior to factorization allows an implicit treatment of the boundary conditions in each sweeping direction of the scheme, decreasing the sensitivity of the factorization scheme to the order of the sweeping directions. The diffusion terms are discretized with second order central differences. First order upwind differences are used for the discretization of the convective terms.

In Kalitzin (2002) steady state solutions are achieved by marching in time from an initial guess. The time step was determined by scaling the local time step obtained from the mean flow with a constant factor. This factor was obtained by numerical experimentation. Another way of advancing the turbulence equations is by means of implicit under-relaxation. Implicit under-relaxation is equivalent of local time stepping with the

time step:

$$\Delta t = \frac{\alpha}{(1-\alpha)B} \tag{2.4}$$

where α is the relaxation parameter ($0 < \alpha < 1$). B is the diagonal element of the implicit matrix that depends on the solution and grid. The advantage of implicit under-relaxation is that the time step for the turbulence equations is determined by the numerical properties of the discretized turbulence equations rather than through mean flow criteria and numerical experimentation for the scaling factor.

However, there are some disadvantages when implicit under-relaxation is applied to the v^2-f equations. When implicit under-relaxation is employed it introduces automatically an unsteady term in the f-equation changing its elliptic nature. Following equation (2.4) it also introduces local time stepping when a constant under-relaxation parameter is used. Local time stepping has been found to worsen the convergence of the v^2-f model for certain flows with strong shock-boundary layer interaction.

A way to avoid the introduction of an unsteady term in the f-equation is to use explicit under-relaxation. Here, the solution of the discretized model (2.1) in delta-form is weighted and added to the previous iterate:

$$\phi^{n+1} = \phi^n + \alpha \Delta\phi \tag{2.5}$$

where α is again the relaxation parameter with $0 < \alpha < 1$.

Computations show that explicit under-relaxation works well when a DDADI factorization scheme is used. The factorization error, that is usually scaled by the time step, seems to have no significant impact. Further work needs to be done to assess this error.

3. Freestream solutions

In the freestream the velocity is $u = u_\infty$. By neglecting diffusion and production the equations of the model (2.1) simplify for the steady state as:

$$u_\infty \frac{\partial k}{\partial x} = -\varepsilon \tag{3.1}$$

$$u_\infty \frac{\partial \varepsilon}{\partial x} = -\frac{C_{\varepsilon 2}}{T}\varepsilon \tag{3.2}$$

$$u_\infty \frac{\partial \overline{v^2}}{\partial x} = kf - \frac{\varepsilon}{k}\overline{v^2} \tag{3.3}$$

$$f = \frac{C_1}{T}\left[\frac{2}{3} - \frac{\overline{v^2}}{k}\right] \tag{3.4}$$

The turbulence time scale is bounded at the lower end with the Kolmogorov scale as:

$$T = max\left[\frac{k}{\varepsilon}, 6\sqrt{\frac{\nu}{\varepsilon}}\right] \tag{3.5}$$

For $T = k/\varepsilon$ the analytical solutions of the differential equations (3.1)-(3.3) are:

$$k = k_0 \hat{z}^{\frac{-1}{C_{\varepsilon 2}-1}} \tag{3.6}$$

$$\varepsilon = \varepsilon_0 \hat{z}^{\frac{-C_{\varepsilon 2}}{C_{\varepsilon 2}-1}} \tag{3.7}$$

$$\overline{v^2} = k\left[\frac{2}{3} - (\frac{2}{3} - \frac{\overline{v^2}_0}{k_0})\hat{z}^{\frac{-C_1}{C_{\varepsilon 2}-1}}\right] \tag{3.8}$$

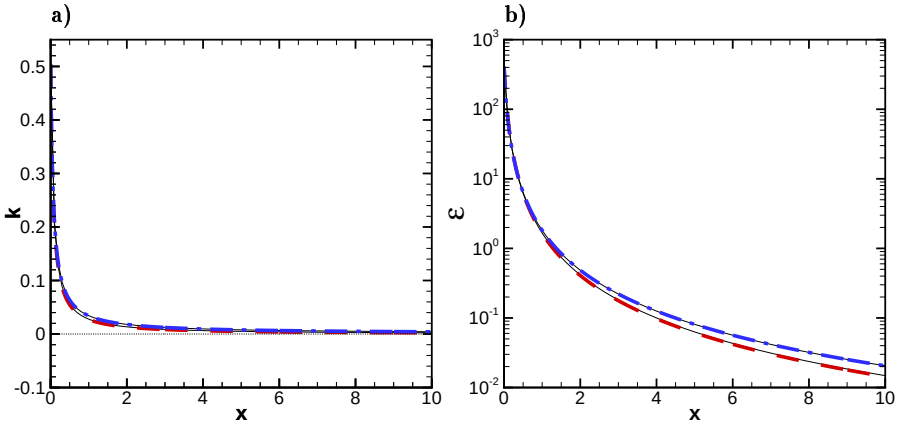

FIGURE 1. Turbulent kinetic energy (a) and dissipation (b) of convecting freestream turbulence with $T_{u,0} = 0.01$, $\nu_{t,0}/\nu = 3.6$. ---- : $T = k/\varepsilon$; —·— : $T = 6\sqrt{\nu/\varepsilon}$; ——— : analytical solution.

with $\hat{z} = \frac{C_{\varepsilon 2}-1}{u_\infty}\frac{\varepsilon_0}{k_0}(x - x_0) + 1$.

For $T = 6\sqrt{\nu/\varepsilon}$ the equations (3.1)-(3.2) decouple and the analytical solutions are:

$$k = k_0 - \frac{12\sqrt{\varepsilon_0 \nu}}{C_{\varepsilon 2}}(1 - \frac{1}{\tilde{z}}) \tag{3.9}$$

$$\varepsilon = \frac{\varepsilon_0}{\tilde{z}^2} \tag{3.10}$$

$$\overline{v^2} = k\left[\frac{2}{3} - (\frac{2}{3} - \frac{\overline{v^2}_0}{k_0})\tilde{z}^{\frac{-2C_1}{C_{\varepsilon 2}}}\right] \tag{3.11}$$

with $\tilde{z} = \frac{C_{\varepsilon 2}\sqrt{\varepsilon_0}}{12 u_\infty \sqrt{\nu}}(x - x_0) + 1$. In contrast to equation (3.6), the equation (3.9) gives negative values for k for certain values of ε_0 and a computational domain that exceed a critical length.

Turbulence at the inflow boundary of the computational domain can be specified through the turbulence intensity, T_u, and the ratio of eddy to molecular viscosity, ν_{t0}/ν:

$$k_0 = \frac{3}{2}(T_u\, u_\infty)^2\ , \quad \varepsilon_0 = 0.09\beta\frac{k_0^2}{\nu_{t0}} \tag{3.12}$$

The dissipation is here specified using the standard eddy-viscosity definition and equation (2.2). The coefficient is $\beta = C_\mu \overline{v^2}_0 T_0/(0.09 k_0^2/\varepsilon_0)$. In the freestream the factor β is about $\beta \approx 1.4$ assuming that $T_0 = k_0/\varepsilon_0$ and $\overline{v^2}_0 = 2k_0/3$. The coefficient C_μ is 0.19.

In equation (3.9), $\tilde{z} = 1$ for $x = x_0$. At this location, k has its maximum. The minimum of k is located at $z \to \infty$ which corresponds to $x \to \infty$. For it to be positive the initial value k_0 has to be:

$$k_0 > \frac{12\sqrt{\varepsilon_0 \nu}}{C_{\varepsilon 2}} \tag{3.13}$$

Substituting ε_0 with the relation (3.12) a minimum bound for the ratio of eddy to molecular viscosity can be derived as:

$$\frac{\nu_{t0}}{\nu} > \left(\frac{3.6}{C_{\varepsilon 2}}\right)^2 \beta \approx 3.61\beta \tag{3.14}$$

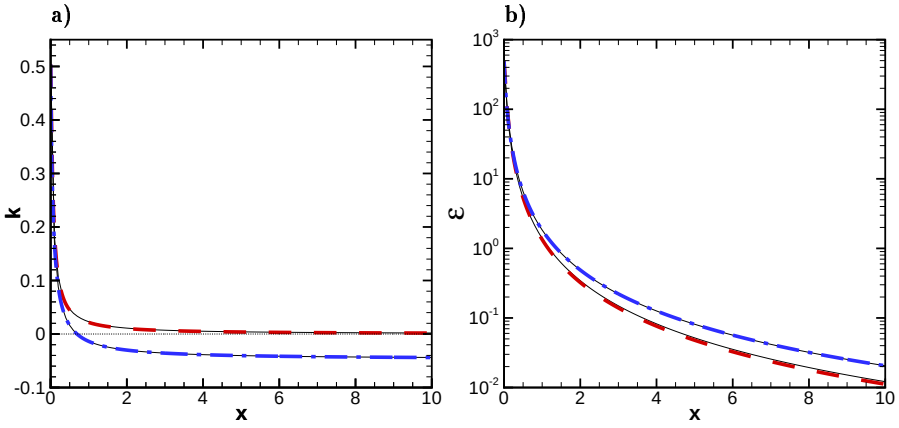

FIGURE 2. Turbulent kinetic energy (a) and dissipation (b) of convecting freestream turbulence with $T_{u,0} = 0.01$, $\nu_{t,0}/\nu = 3.0$. - - - - : $T = k/\varepsilon$; —·— : $T = 6\sqrt{\nu/\varepsilon}$; ——— : analytical solution.

This bound guarantees $k > 0$ for any x.

The solution of equations (3.6) and (3.9) are plotted in Figure 1a. The figure includes the analytical and the numerical solutions obtained by solving the full v^2-f model (2.1) for uniform flow. The chosen flow conditions are: $u_\infty = 58m/s, \nu = 1.55\,10^{-5}m^2/s, T_u = 0.01$ and $\nu_{t,0}/\nu = 3.6$. The computational domain is $10m$ long. The coefficient $C_{\varepsilon 2}$ is equal 1.9. It can be seen that the solutions for k are very similar and positive for both cases with $T = k/\varepsilon$ and $T = 6\sqrt{\nu/\varepsilon}$.

Figure 2 shows the solution for $\nu_{t,0}/\nu = 3.0$. Equation (3.9) gives now negative values for k. Comparing Figures 1b and 2b it is interesting to note the large change in k while the ε distribution (3.10) hardly changed.

It can be shown that the turbulence time scale (3.5) is eventually bounded with the Kolmogorov scale independently of the values of k_0 and ε_0 at the inflow. When $T = k/\varepsilon$, the turbulent kinetic energy is related to the dissipation following equations (3.6) and (3.7) as:

$$k = k_0 \left(\frac{\varepsilon}{\varepsilon_0}\right)^{1/C_{\varepsilon 2}} \tag{3.15}$$

The turbulence time scale, defined by equation (3.5), hits the lower bound when

$$k = 6\sqrt{\nu\varepsilon} \tag{3.16}$$

The two functions (3.15) and (3.16) intersect for

$$\varepsilon_1 = \left(\frac{\varepsilon_0^{2/C_{\varepsilon 2}} 36\nu}{k_0^2}\right)^{\frac{C_{\varepsilon 2}}{2-C_{\varepsilon 2}}} \tag{3.17}$$

The corresponding location is according equation (3.7):

$$x_1 = x_0 + \left(\left(\frac{\varepsilon_1}{\varepsilon_0}\right)^{\frac{1-C_{\varepsilon 2}}{C_{\varepsilon 2}}} - 1\right) \frac{u_\infty k_0}{(C_{\varepsilon 2} - 1)\varepsilon_0} \tag{3.18}$$

Once the bound is reached, the turbulence variables are given by equations (3.9)-(3.11) whereby the values at x_1 are used as initial values.

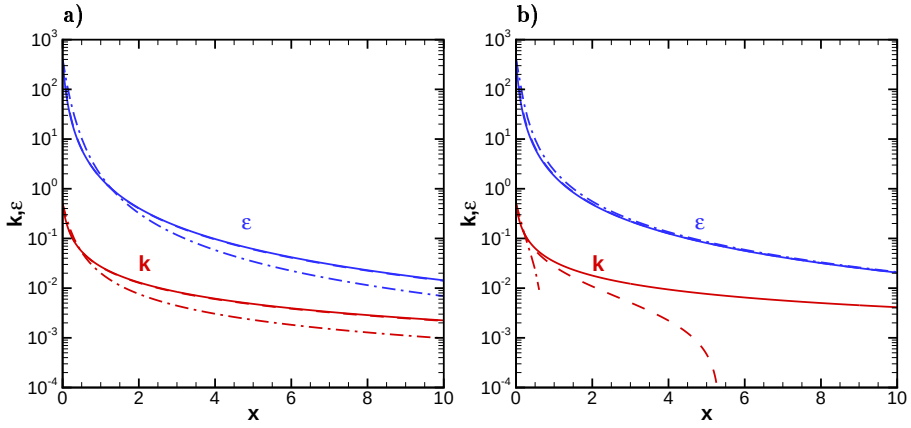

FIGURE 3. Turbulent kinetic energy and dissipation of convecting freestream turbulence with $T_{u,0} = 0.01$ and $\nu_{t,0}/\nu = 3.6$. The turbulence time scale is: a) $T = k/\varepsilon$ and b) $T = 6\sqrt{\nu/\varepsilon}$. ——— : $\Delta x = 0.0025$, 2^{nd} order; - - - - : $\Delta x = 0.025$, 1^{st} order; —·— : $\Delta x = 0.1$, 1^{st} order.

The behavior of $\overline{v^2}$ in the freestream is given by equations (3.8) and (3.11) for the unbounded and bounded case, respectively. Note that the variable $\overline{v^2}$ behaves like k when $\overline{v^2}_0/k_0 = 2/3$. In this case f in the freestream is identical zero.

3.1. *Discretization error*

For robustness, the convection terms are usually discretized with an upwind scheme. It can be shown that the numerical dissipation resulting from the upwind treatment of the convection terms aggravates the problem of negative turbulent kinetic energy in the freestream. For this, we analyze the transport equation for the turbulence kinetic energy in the freestream discretized for cell i with first order upwind. For $u_\infty > 0$ the discretized equation (3.1) becomes:

$$u_\infty \frac{k_i - k_{i-1}}{\Delta x} = -\varepsilon_i \tag{3.19}$$

A Taylor series expansion gives

$$k_{i-1} = k_i - \left(\frac{\partial k}{\partial x}\right)_i \Delta x - \left(\frac{\partial^2 k}{\partial x^2}\right)_i \frac{\Delta x^2}{2} \tag{3.20}$$

which leads to:

$$u_\infty \left(\frac{\partial k}{\partial x}\right)_i = -\varepsilon_i - u_\infty \left(\frac{\partial^2 k}{\partial x^2}\right)_i \frac{\Delta x}{2} \tag{3.21}$$

The second derivative of k is positive according to equation (3.9). The second term on the right hand side of equations (3.21) acts as negative source term. Results for different grids and discretizations are shown in Figure 3 for the same flow conditions as used for Figure 1. Clearly, for both time scale definitions the numerical error deteriorates the solution. However, the lack of coupling between the k and ε equation for $T = 6\sqrt{\nu/\varepsilon}$ prevents ε to decrease for lower values of k as shown for the case $T = k/\varepsilon$ in Figure 3a.

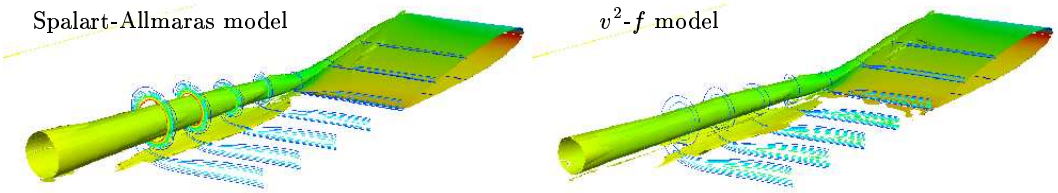

FIGURE 4. Wing-tip vortex visualized with λ_2-surface colored with pressure contours and eddy-viscosity contour-lines in selected planes

4. Model modification

The lower bound for the turbulence time scale has been designed by Durbin (1995) to enforce the correct asymptotic behavior of the k-ε equations near the wall. Thus it should be applied only in the near wall region. There are several ways to eliminate the lower bound in the freestream. The simplest way is to define a large value for the eddy-viscosity at the inflow. One can also define a distance from the wall which specifies the near wall region and thus the region where the limiter (3.5) is active. More sophisticated solutions include the use of an interpolation function similar to that used by Durbin (1995) for the coefficient $C_{\varepsilon 1}$ or the one used by Menter (1993) for the switch between the k-ω and k-ε models. The latter two possibilities require testing to avoid the situation that the bound is not active when it is needed. At the current stage we utilize a larger ratio of ν_{t_0}/ν at the inflow.

5. Wing-tip vortex

The goal of this test case is the accurate prediction of a wing tip vortex generated by a low aspect ratio wing. The flow conditions are: $Re_c = 4.6\,10^6$, $M = 0.15$ and $\alpha = 10^o$ for which extensive experimental data is available by Dacles-Mariani *et al.* (1995). To reduce the influence of the inflow and outflow boundaries, the computational domain has been extended both upstream and downstream by one cord length. The wall normal grid spacing is such that $y^+ < 0.5$. The wind tunnel walls are treated as inviscid walls to reduce the grid size. The computations were carried out with TFLO with a low dissipative Roe's approximate Riemann solver in combination with a second order reconstruction scheme and several turbulence models.

Preliminary results obtained with the Spalart-Allmaras and v^2-f turbulence models are shown in Figure 4. The wing-tip vortex is visualized with a $\lambda_2 \approx 0$ surface as described by Jeong & Hussain (1995). The λ_2 surface is colored with pressure contours. Eddy-viscosity contours are plotted in selected planes.

The eddy-viscosity contours show that the level of turbulence in the vortex is much less for v^2-f than for Spalart-Allmaras. The lower levels of eddy-viscosity mean that there is less diffusion in the vortex and therefore it is preserved over a longer distance. As demonstrated in Figure 4, the diameter of the vortex core grows much slower when v^2-f is used.

6. Conclusion and future work

The first part of the paper describes a modification to the DDADI scheme developed earlier by Kalitzin (2002) for the solution of the v^2-f turbulence model. A significant improvement in robustness can be achieved when explicit under-relaxation is used instead of (local) time stepping when solving the turbulence equations. The described solution algorithm makes computation with the 1995 version of Durbin's v^2-f model comparable efficient and robust as with other RANS turbulence models like the Spalart-Allmaras or Menters SST model.

The second part of the paper describes the freestream behavior of the v^2-f model. It concludes that a modification of the lower bound for the turbulence time scale is needed to prevent its use in the freestream where it may cause negative values for the turbulent kinetic energy. These may also be prevented when large values for the eddy-viscosity are specified at the inflow.

7. Acknowledgments

The flow computation of the wing-tip vortex were performed with TFLO by Edwin van der Weide. The used grid was generated by Sang Ho Kim. Gratitude is extended to Gianluca Iaccarino and Paul Durbin for their comments on the freestream analysis. The support by the US Department of Energy under the ASCI program is gratefully acknowledged.

REFERENCES

Dacles-Mariani J., Zilliac G.G., Chow J.S. and Bradshaw P 1995 Numerical/experimental study of a wingtip vortex in the near field. *AIAA J.*, **33(9)**, 1561-1570.

Durbin, P. A. 1995 Separated flow computations with the k-ε-$\overline{v^2}$ model. *AIAA J.*, **33**, 659-664.

Jeong J. and Hussain F. 1995 On the identification of a vortex. *JFM*, **285**, 6994.

Kalitzin G. 1999 Application of v^2-f turbulence model to transonic flows, *AIAA*, **99-3780**.

Kalitzin, G. 2002 An efficient and robust algorithm for the solution of the v^2-f turbulence model with application to turbomachinery flow. *WEHSFF2002*.

Laurence D., R., Uribe J., C. and Utyuzhnikov S., V. 2004 A robust formulation of the v^2-f model, *APPL*.

Lien, F. S. & Durbin, P. A. 1996 Non-linear k-ε-v^2 modeling with application to high-lift. *CTR summer proceedings*.

Menter F. R., 1993, Zonal two-equation k-ω turbulence model predictions. *AIAA*, **93-2906**.

Parneix S. & Durbin, P. A. 1997 Numerical simulation of 3D turbulent boundary layers using the V2F model, CTR-Annual Research Briefs. 135-148.

Spalart P. R. & Allmaras S. R. 1994 A one-equation turbulence model for aerodynamic flows. *La Recherche Aerospatiale*, **1**, 1-23.

A turbulence model for polymer flows

By Y. Dubief, G. Iaccarino AND S. K. Lele

1. Motivation and background

Recent advancements in the modeling of polymer drag reduction in the context of RANS simulation are discussed. The present model is derived from the current understanding of the mechanism of near-wall turbulence in drag reduced polymer flows described in Dubief *et al.* (2004) and adapted to the $v^2 - f$ turbulence model introduced by Durbin (1995) for Newtonian flows. Results for channel flows with homogeneous polymer concentrations prove to be very satisfactory. The model captures accurately the behavior of the mean velocity profiles for the two main regimes, called LDR and HDR, Low and High Drag Reduction, respectively.

1.1. *LDR and HDR*

For drag-reduced flows with polymers, turbulent statistics have been extensively characterized by experiments. Warholic *et al.* (1999) established the existence of two distinct statistical regimes. For a given polymer molecule, the mean velocity profile experiences an upward shift of its log-law region for the smallest concentration, up to a drag reduction (DR) of the order of 40%. This regime is referred to as the Low-Drag Reduction (LDR) regime. A further increase in concentration leads to a change in the slope of the log-law which defines the High-Drag Reduction (HDR) regime. As more polymers are added, the flow tends toward an asymptotic state, called the Maximum Drag Reduction (MDR) regime, for which drag is slightly higher than the laminar state Virk & Mickley (1970). The components of the Reynolds stress tensor $\overline{u_i u_j}$ decrease in magnitude when scaled with outer variables (here, the centerline mean velocity of the Poiseuille flow U_c and the channel half-width h) as DR increases. Yet the diminution of the rms u' of the streamwise velocity fluctuations is small compared to v', w' or $\overline{uv}$ and it results in an increase of the maximum of u'^+ in the wall region ($^+$ denotes the scaling by inner variables based on the skin-friction velocity u_τ and the viscosity ν). LDR produces the largest maximum values of u'^+ whereas the peak seems to reduce back to the $DR = 0\%$ case at HDR and MDR. The latter regime is still not completely understood from a physical point of view and will not be further discussed here.

1.2. *Conceptual model for the mechanism of polymer drag reduction*

Using Brownian dynamics simulation, Terrapon *et al.* (2004) showed that polymers experience significant stretching in upwash and downwash flows generated by vortices. Dubief *et al.* (2004) completed Terrapon's work by studying how polymers interact with coherent structures. The viscoelastic simulations performed in this latter article confirmed that polymers extract energy from vortices causing them to weaken. In the meantime, a significant part of the energy stored by polymers that are caught in downwash flows is released in high-speed streaks where viscous forces dominate. The damping of streamwise velocity fluctuations by Newtonian forces is therefore countered by viscoelastic forces. Dubief *et al.* (2004) then proceeded to incorporate polymers in the regeneration cycle of near-wall turbulence as proposed by Jiménez & Pinelli (1999), as sketched in Fig. 1. For

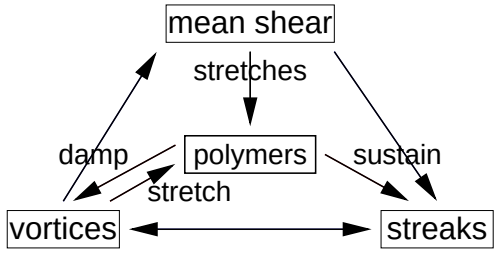

FIGURE 1. Model of the mechanism of polymer drag reduction in near-wall turbulence.

a Newtonian flow, the mean shear gives birth to streaks through instabilities. Perturbations and instabilities then produce vortices which transfer momentum vertically and sustains the mean shear. According to the dynamics introduced earlier, polymers sits at the center of this regeneration cycle as shown in Fig. 1.

2. Governing equations and numerical method

2.1. *Polymer model*

The evolution of polymers is represented on the basis of bead-spring (dumbbell) models. Each dumbbell is subject to the hydrodynamic forces exerted by the flow on the beads, the spring force and Brownian forces. The balance of forces gives an evolution equation for the end to end dumbbell vector $\mathbf{q}$, known as the FENE model (Finitely Extensible Nonlinear Elastic). A constitutive approach is obtained by taking into account the Brownian motion using a phase average of the product of the $\mathbf{q}$-components, which defines the conformation tensor $c_{ij} = \langle q_i q_j \rangle$. The hydrodynamic and relaxation (spring) forces are explicitly simulated; the latter force can be estimated with various models. The model used here is the FENE-P model, where P stands for the Peterlin function, f, defining the following set of equations

$$\partial_t c_{ij} + u_k \partial_k c_{ij} = c_{kj}\partial_k u_i + c_{ik}\partial_k u_j - \frac{1}{\lambda}(f c_{ij} - \delta_{ij}) \ , \tag{2.1}$$

$$f = \frac{1}{1 - c_{kk}/L^2} \, . \tag{2.2}$$

The parameter L is the maximum polymer extension and λ is the relaxation time of the polymers. The relevant non-dimensional quantity to describe a polymer solution is the Weissenberg number, We, the ratio of the polymer to the flow time scales which can be the outer or inner scales:

$$We = \frac{\lambda U_c}{h} \text{ or } We_\tau = \frac{\lambda u_\tau^2}{\nu} \ , \tag{2.3}$$

where u_τ is the skin-friction velocity of the Newtonian flow, unless specified otherwise. U_c and h are the integral scales for a channel flow, namely the centerline velocity and the channel half-width. Finally the contribution of polymers to the flow is brought in the momentum equations via the divergence of the polymeric stress tensor τ_{ij},

$$\tau_{ij} = \frac{1}{\lambda}(f c_{ij} - \delta_{ij}) \ , \tag{2.4}$$

run	$We_{\tau 0}$	β	b
1	36	0.9	10000
2	60	0.9	3600
3	120	0.9	10000
4	36	0.9	19600
5	36	0.9	3600
6	60	0.9	19600
7	40	0.4	25600

TABLE 1. Polymer parameters for the channel flow DNS database used for the validation of $v^2 - f - p$. The Reynolds number

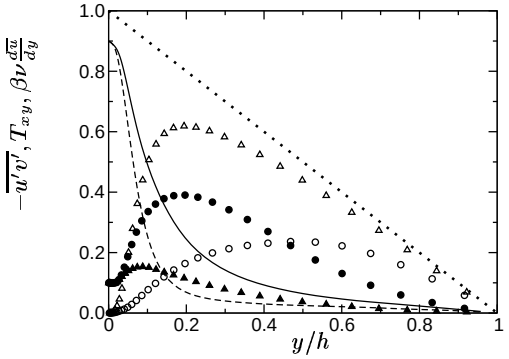

FIGURE 2. Contributions of the Reynolds shear, polymer and viscous stresses to the balance Eq. (2.6. For LDR: ——— , $\beta\nu\frac{d\overline{u}}{dy}$; ∘ , $-\overline{u'v'}$; • , T_{xy}. FOR HDR: – – – – , $\beta\nu\frac{d\overline{u}}{dy}$; △ , $-\overline{u'v'}$; ▲ , T_{xy}. ····· , $1 - \frac{y}{h}$. The stresses are normalized by u_τ and ν.

yielding the viscoelastic momentum equations,

$$\partial_t u_i + u_j \partial_j u_i = -\partial_i p + \beta\nu\partial_j\partial_j u_i + (1-\beta)\nu\partial_j \tau_{ij} \ , \tag{2.5}$$

where β is the ratio of the solvent viscosity ν_s to the total viscosity ν. The last term in the rhs of Eq. (2.5) is the contribution of the viscoelastic stress to the flow.

2.2. *Reference DNS solutions*

The model development and validation is performed using a series of DNS solutions in a channel flow. The numerical method for the DNS calculations is described in Dubief *et al.* (2005).

The Reynolds number based on the bulk velocity is $Re_M = 5000$, $Re_\tau = 300$ based on the skin-friction velocity. The flow is driven by conservation of the mass flow. The runs used for the present study are summarized in Table 1.

2.3. *Statistical properties of LDR and HDR*

A RANS model is based on statistical equations derived from the momentum equations (Eq. 2.5). In the case of interest here, the balance of stresses is:

$$-\overline{u'v'} + \beta\nu\frac{d\overline{u}}{dy} + T_{xy} = \left[-\frac{d\overline{p}}{dx}\right]\left(1 - \frac{y}{h}\right) \ , \tag{2.6}$$

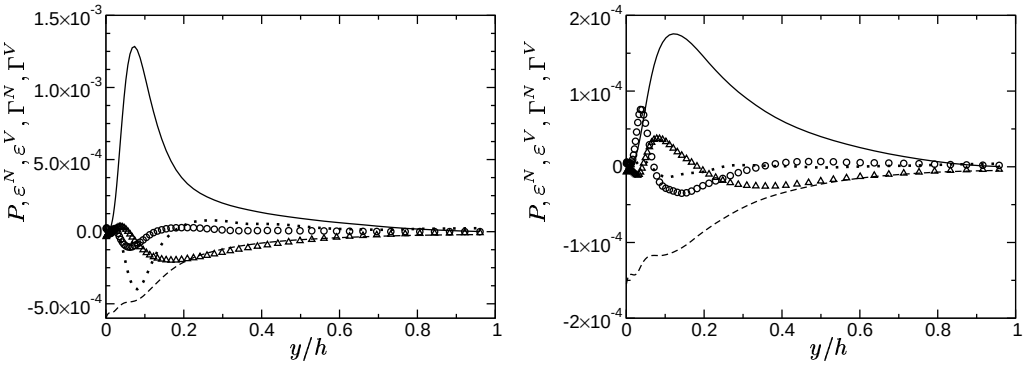

FIGURE 3. Production, Newtonian and viscoelastic dissipation, Newtonian and viscoelastic transport terms for LDR (*left*) and HDR (*right*). (runs 1 and 3 of Tab. 1, respectively). ——— , P; ····· , Γ^N; – – – – , ε^N; □ , ε^V; ○ , Γ^V;

where T_{xy} is the polymer stress

$$T_{xy} = (1-\beta)\nu\frac{d\overline{\tau}_{xy}}{dy} \tag{2.7}$$

Hereafter, the instantaneous quantities are decomposed in a mean and fluctuating part, $u = \overline{u} + u'$. The Reynolds shear stress, viscous stress and polymer stress are plotted in Fig. 2 for LDR (DR=30%, run 1) and HDR (DR=60%, run 3). The polymer stress increases with increasing DR to become comparable to (or larger than) the Reynolds shear stress at HDR.

The second equation to be modeled is usually the turbulent kinetic energy budget,

$$\begin{aligned}\partial_t\overline{u_i'u_j'} + \overline{u}_k\partial_k\overline{u_i'u_j'} = &\underbrace{-\overline{u_i'u_k'}\partial_k\overline{u}_j - \overline{u_j'u_k'}\partial_k\overline{u}_i}_{P}\underbrace{-\partial_k\overline{u_i'u_j'u_k'}}_{\Gamma^N}\\ &-\left(\overline{u_i'\partial_j p' + u_j'\partial_i p'}\right) + \beta\nu\partial_k\partial_k\overline{u_i'u_j'} - \underbrace{2\beta\nu\overline{\partial_k u_i'\partial_k u_j'}}_{\varepsilon^N}\\ &\underbrace{+(1-\beta)\nu\partial_k\left(\overline{u_i'\tau_{jk}' + u_j'\tau_{ik}'}\right)}_{\Gamma^V} - \underbrace{(1-\beta)\nu\overline{\tau_{ik}\partial_k u_j' + \tau_{jk}'\partial_k u_i'}}_{\varepsilon^V}\end{aligned} \tag{2.8}$$

Even though, the v^2-f model incorporates closures for all the Newtonian terms, it is of interest to get an indication of the behavior of production (P), dissipation (ε) and turbulent transport (Γ), relative to the additional viscoelastic terms as shown in Fig. 3. The superscripts N and V denote Newtonian and viscoelastic dissipation and transport, respectively. For clarity, the velocity pressure gradient term and the diffusion term are not plotted. The role of polymers is observed to increase relatively to the production and Newtonian dissipation as DR increases. The near-wall behavior is further discussed in the modeling section.

2.4. v^2-f model

The model used for polymer drag reduction is the v^2-f model developed by Durbin (1995). This model is an extension of the classical $k-\varepsilon$ model to correctly represent the near-wall behavior (and viscous damping) of the turbulent quantities. This is realized by a modification of the eddy-viscosity formulation and by solving two additional partial

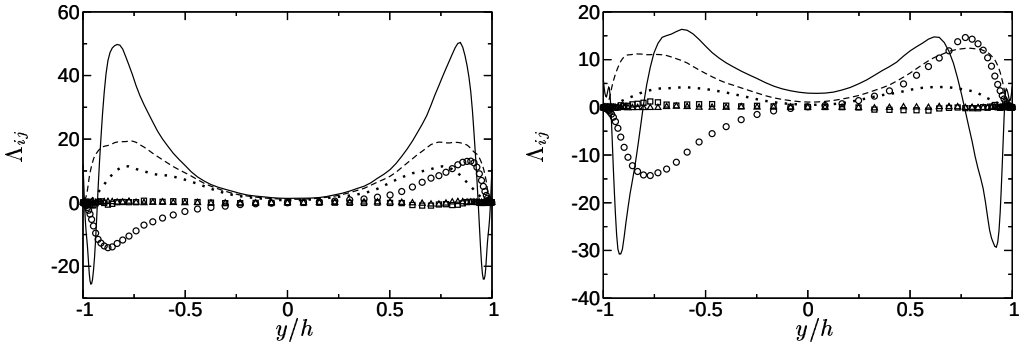

FIGURE 4. Components of the stretching tensor Λ_{ij} for LDR (*left*) and HDR (*right*). (runs 1 and 3 of Tab. 1, respectively). ——— , Λ_{11}; ····· , Λ_{22}; – – – – , Λ_{33}; ∘ , Λ_{12}; □ , Λ_{13}; △ , Λ_{23}.

differential equations: a transport equation for the turbulent intensity of the velocity fluctuations $\overline{v'^2}$ normal to the streamlines and an elliptic relaxation equation for f. The latter represents the effect of the turbulence redistribution. The major advantage of $v^2 - f$ over $k - \varepsilon$ is the absence of wall-damping function. The model solves the following equations:

- turbulent viscosity

$$\nu_t = 0.22\overline{v'^2}T_t \tag{2.9}$$

- kinetic energy transport equation

$$\partial_t k_t + \overline{u}_i \partial_i k_t = P_t - \varepsilon + \partial_j \left[(\nu + \nu_t)\, \partial_j k_t \right] \tag{2.10}$$

- dissipation transport equation

$$\partial_t \varepsilon + \overline{u}_j \partial_j \varepsilon = \partial_j \left(\frac{\nu_t}{1.3} \partial_j \varepsilon \right) + \frac{1}{T_t} \left(-1.4 \sqrt{1 + 0.045 k / \overline{v'^2}}\, P_t - 1.9\varepsilon \right) \tag{2.11}$$

- v^2 transport equation

$$\partial_t \overline{v'^2} + \overline{u}_j \partial_j \overline{v'^2} = k_t f - 6\overline{v'^2} \frac{\varepsilon}{k} + \partial_j \left[(\nu + \nu_t)\, \partial_j \overline{v'^2} \right] \tag{2.12}$$

- elliptic relaxation equation for f

$$f - L_t^2 \partial_j \partial_j f = 1.4 \frac{2/3 - \overline{v'^2}/k_t}{T_t} + 0.3 \frac{P_t}{k_t} + \frac{5\overline{v'^2}/k}{T_t} \tag{2.13}$$

- turbulent production (S is the mean strain rate tensor, $S_{ij} = (\partial_j \overline{u}_i + \partial_i \overline{u}_j)$)

$$P_t = \nu_t S^2 \tag{2.14}$$

- turbulent length and time scales

$$T_t = \max \left[\frac{k_t}{\varepsilon}, 6 \left(\frac{\nu}{\varepsilon} \right)^{1/2} \right] \ , \ L_t = 0.3 \max \left[\frac{k_t^{3/2}}{\varepsilon}, 70 \left(\frac{\nu^3}{\varepsilon} \right)^{1/4} \right] \tag{2.15}$$

3. $v^2 - f - p$ model

3.1. *Modeling the polymer dynamics in turbulent flows*

The tensorial nature of the FENE-P model makes it complex and unattractive in the context of a simple eddy-viscosity based closure. The modeling of the stretching term is non-trivial as shown by Fig. 4 where the individual components of the tensor

$$\Lambda_{ij} = \overline{c'_{ik}\partial_k u'_j} + \overline{c'_{kj}\partial_k u'_i} \,. \tag{3.1}$$

Of particular importance is the modeling of the near-wall behavior of Λ_{xx}. The negative peak marks the region where polymers inject energy into turbulence, which explains why this phenomenon is more pronounced at HDR. Note that Λ_{kk} and the viscoelastic dissipation (3) have similar behavior, yet opposite in sign. Using the quantities available from v^2-f, k_t, $\overline{u}_i$, $\overline{u'_i u'_j}$ and S_{ij}, did not yield satisfactory models. This approach required individual constants per components and failed to reproduce the near-wall behavior so important to the transfer of energy from the polymers to turbulence.

The difficulty of modeling Λ_{ij} has motivated the development of an algrebaic model capable of capturing the energy transfer between polymers and turbulence. Instead of focusing on the stretching term alone, a simpler measure of this energy exchange is considered: the polymer elongation, c_{ii}. When turbulence stretches polymers, turbulent energy is stored by the polymers. When polymers coil, elastic energy is released in turbulence. Fig. 5 outlines the difference between LDR and HDR in terms of the distribution of c_{ii} in the near wall region where local extrema can be interpreted as relative stretching (local maximum) or recoil (local minimum). The dip close to the wall defines therefore the region where elastic energy goes to streaks (see the model of polymer drag reduction, Fig. 1). Further away from the wall, the local maximum located in the buffer region denotes the vortex damping action of the polymers.

The evolution equation for polymer elongation can be recast as

$$D_t c_{ii} = \underbrace{2c_{ij}\partial_j u_i}_{\text{production}} - \underbrace{\frac{1}{\lambda}\left(f c_{ii} - 3\right)}_{\text{destruction}} , \tag{3.2}$$

where $D_t = \partial_t + u_j\partial_j$. The stretching term is analogous to a production term, while the relaxation term effectively destroys elongation. In this framework familiar to RANS modeling, we can develop models based on our physical understanding of the phenomenon. Note that Eq. (3.2) is unclosed due to the cross terms present in the production term. The modeling is developed here only for steady-state channel flow with homogeneous concentration of polymers for which the transport terms in $\overline{D_t c_{ii}}$ vanish. In the destruction term, the first order approximation $\overline{f c_{ii}} = \overline{f}\,\overline{c}_{ii}$ is reasonable as shown in Fig. 5 and will be used in the following. Using our conceptual model of the mechanism of polymer drag reduction (Fig. 1), we decompose the production into two contributions: contribution from the mean shear and contribution from turbulence, which, in our schematic representation in Fig. 1, would be the vortices.

If the polymers were subject to the mean shear only, the FENE-P model would reduce to:

$$\overline{c}_{ik}\partial_k\overline{u}_j + \overline{c}_{kj}\partial_k\overline{u}_i - \frac{1}{\lambda}\left(\overline{f}\,\overline{c}_{ij} - \delta_{ij}\right) = 0 \,. \tag{3.3}$$

For the steady-state channel flow, the system reduces to a single equation, third-order

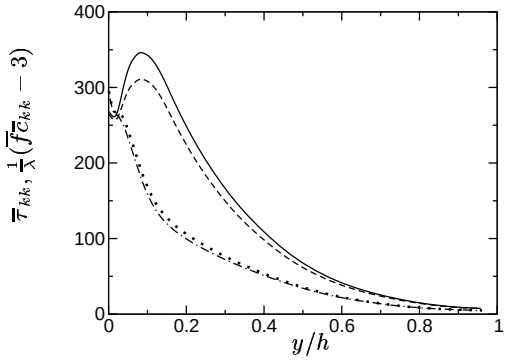

FIGURE 5. Approximation of $\overline{\tau}_{kk}$ by $\frac{1}{\lambda}(\overline{f}\overline{c}_{kk}-3)$of for LDR and HDR . (runs 1 and 3 of Tab. 1, respectively). ——— : exact, HDR; ····· : exact, LDR; - - - - : approximation, HDR; —·— : approximation, LDR.

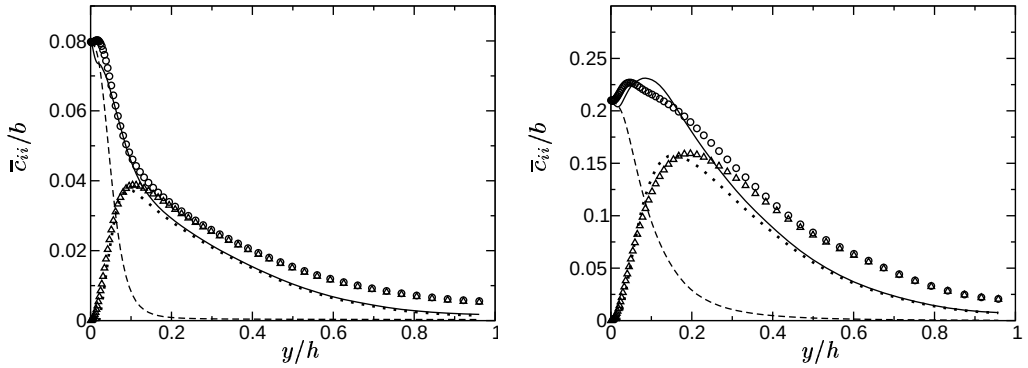

FIGURE 6. Modeling of the mean polymer extension $\overline{c}_{ii}$ for LDR (*left*) and HDR (*right*). (runs 1 and 3 of Tab. 1, respectively). ——— , exact $\overline{c}_{ii}$; - - - - , $\overline{c}_{ii}^M$ obtained from the mean shear only (Eq. 3.4); ····· , $\overline{c}_{ii}-\overline{c}_{ii}^M$; $\triangle$, model for $\overline{c}_{ii}-\overline{c}_{ii}^M$; $\circ$, model for $\overline{c}_{ii}-\overline{c}_{ii}^M$.

polynomial in $\overline{f}$:

$$0 = 2\frac{\lambda S^2}{\overline{f}^2} - \frac{1}{\lambda}\left(\overline{f}\,\overline{c}_{kk} - 3\right) \ , \tag{3.4}$$

where S^2 reduces to $(\partial_y \overline{u})^2$. The solution of this polynomial is shown in Fig. 6 for LDR and MDR regimes. The wall value of $\overline{c}_{kk}$ is accurately predicted by Eq. (3.4) since turbulent velocity fluctuations vanish at the wall, leaving the mean shear as the only stretching source for the polymers.

The turbulent contribution to stretching, difference between the total elongation and the solution to Eq. (3.4), is very similar to the profile of kinetic energy across the channel flow, as shown in Fig. 6. This resemblance has prompted a model based around $k_t\lambda$ which can be interpreted as a *turbulent viscoelastic viscosity*, ν_{tp}. The effect of turbulence on polymers is so far described as a linear function of the polymer length b. The proper scaling of this model imposes the introduction of a turbulent length scale h. The choice for this length scale is still not clear and in the following, h is chosen as the channel half-width. Polymers can only be stretched by turbulent eddies only if the time scales of the eddies is larger than the relaxation time scale. Therefore, under the approximations considered for the present study, the trace of the conformation tensor is governed by the

following equation:

$$0 = 2\frac{\lambda S^2}{\overline{f}^2} + \gamma_1 b \frac{k_t \lambda}{h^2} - \frac{1}{\lambda}\left(\overline{f}\overline{c}_{kk} - 3\right) \ . \tag{3.5}$$

3.2. *Modeling the effect of polymers on turbulent structures*

In the recent extensive statistical studies performed using viscoelastic DNS, it was observed that most turbulent quantities decrease with increasing drag reduction (see Dimitropoulos *et al.* 2001, for instance). From a RANS viewpoint, the pressure-strain term decrease needs to be accurately modeled since it determines the level of anisotropy of the flow and has a direct effect on the behavior the mean velocity, especially in the log-region. Our first attempt was to add a term in the elliptic equation (2.13) which is the effective pressure redistribution mechanism in the $v^2 - f$ model. This addition was inspired by Leighton *et al.* (2003) who developed a Reynolds-stress model for LDR flows. We found the term to be able to reproduce the upward shift in the log-law but the solution is extremely sensitive to the user-defined constant related to this term. By increasing the constant, the flow becomes laminar without ever showing any HDR characteristics.

It was then suggested to us (P. Durbin, private communication) that Eq. (2.13) is controlled by the turbulent length scale $L_t = C_L k_t^{3/2}/\varepsilon$. We can then argue that the drop in pressure-strain is a mere consequence of the increase of the typical length scale of turbulent structures (vortices and streaks), which translates into an augmentation of L_t. This increase must be a function of the polymer concentration, β in the case of the FENE-P model, the relaxation time λ or We and the local polymer stretching. We propose a linear dependence on these quantities as a first approximation yielding

$$L_t = C_L \left(1 + \gamma_L (1-\beta)\frac{c_{ii}}{b} We\right) \frac{k_t^{3/2}}{\varepsilon} \tag{3.6}$$

where We is used instead of λ to satisfy the non-dimensionality of the viscoelastic function.

The modeling of the interaction between polymers and turbulence uses an approach similar to the one developed for the polymer dynamics. In the balance of stresses, the viscoelastic stress $\overline{T}_{xy} = (1-\beta)\overline{\tau}_{xy}$ is decomposed in its solution for the mean shear and a model for the contribution of turbulence. The viscoelastic stress can then be written in a Boussinesq-like form:

$$\overline{T}_{ij} = (1-\beta)\left(\frac{\nu}{\overline{f}} + \underbrace{\gamma_\nu k_t \lambda}_{\nu_{tp}}\right) S_{ij} \tag{3.7}$$

The viscoelastic contribution to the kinetic energy equation is then modeled using the turbulent viscoelastic viscosity in the form of a production term:

$$\partial_t k_t + \overline{u}_i \partial_i k_t = P_t + P_{tp} - \varepsilon + \partial_j \left[\left(\nu + \nu_t\right)\partial_j k_t\right] \tag{3.8}$$

with

$$P_{tp} = \nu_{tp} S^2 \ . \tag{3.9}$$

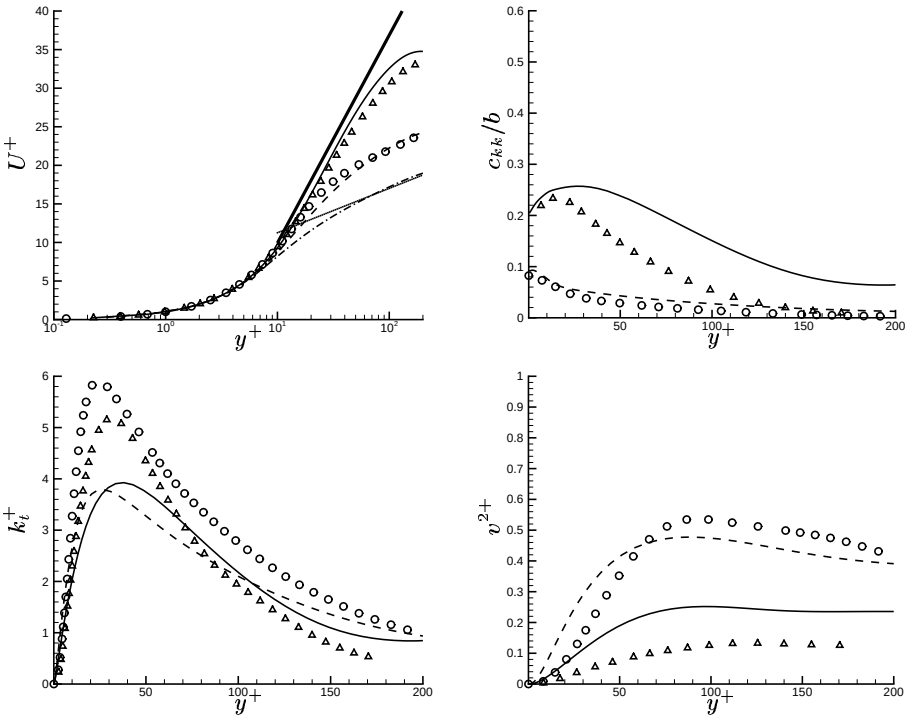

FIGURE 7. Comparison between $v^2 - f - p$ and DNS for $Re_M = 5000$, $b = 10000$ at LDR ($We_\tau = 36$: $\circ$, DNS; - - - - , $v^2 - f - p$) and HDR ($We_\tau = 120$: $\triangle$, DNS; ——— , $v^2 - f - p$) 0*Upper left*: mean velocity profiles. —·— , $v^2 - f - p$ (Newtonian flow); ····· , Newtonian log-law ($U^+ = 2.5\ln(y^+) + 4.1$); ——— , Virk's asymptote ($U^+ = 11.7\ln(y^+) - 17$). *Upper right*: Polymer elongation . *Lower left*: Turbulent kinetic energy. *Lower right* Wall-normal velocity fluctuations.

4. Channel flow predictions

The calibration and validation of our model is based on our database of viscoelastic DNS runs performed in a channel flow at $Re_M = 5000$, described in Table 1. These runs cover most of the physical parameters for realistic polymer simulations. The three constants entering the model $v^2 - f - p$ are adjusted using run 1 (LDR, DR=35%) and 3 (HDR, DR=60%) only. The mean velocity profiles for these two runs (Fig. 7) are found to exhibit the expected behavior, namely a shift of the log-law for LDR and the right change of slope for HDR. The mean polymer elongation is overestimated, however, $v^2 - f - p$ captures the maximum away from the wall, critical feature of HDR. The kinetic energy and wall-normal velocity fluctuations are also overpredicted, nevertheless they are shown to decrease with increasing DR. Finally the comparison for the calibration runs and the remaining runs is depicted in Fig. 8. The agreement is very good with DR (%) predicted with a $\pm 5\%$ accuracy.

5. Conclusion and future work

The prediction of drag-reduced turbulent polymer flows has been shown to be within reach using the $v^2 - f$ model. The current model $v^2 - f - p$ is simple and robust:

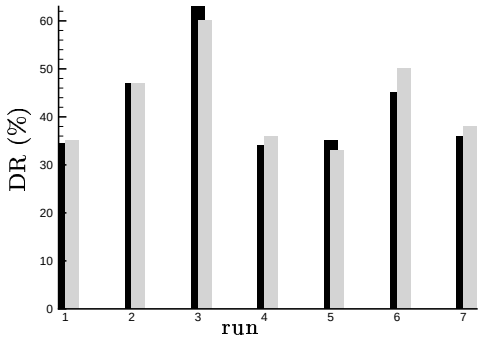

FIGURE 8. Comparison between $v^2 - f - p$ (dark bars) and DNS for $Re_M = 5000$ for various relaxtion time and polymer length described in Tab. 1

only three additional constants and no ad-hoc wall functions are introduced. It proves to accurately reproduce drag reductions computed from channel flow direct numerical simulations. More importantly, the model predicts the right change of slope of the mean velocity profile in the log-law region, for the first time without any direct assumption on the slope change in the tuning of the coefficients.

The model is nevertheless at its very early stage. Although the results are extermely encouraging, the closure for the production term of the polymer elongation transport equation (Eq. 3.5) is not satisfactory, since it involves one arbitrary length scale and there is no dependence on a turbulent time scale. The linearity in the closure for the turbulent length scale also needs to to be investigated especially toward MDR. The future work will include the development of a closure for the transport term for $\overline{c}_{ii}$ and the addition of the transport equation for the polymer concentration in order to simulate turbulent boundary layers subject to injection of polymers from a slot.

The support of DARPA and its project manager, Dr. Lisa Porter, are gratefully acknowledged. This work is sponsored by Defense Advanced Research Projects Agency, Advanced Technology Office, Friction Drag Reduction Program, DARPA order No.: K042/31, K042/13,N115/00. Issued by DARPA/CMO, Contract No.: MDA972-01-C-0041.

REFERENCES

DIMITROPOULOS, C. D., SURESHKUMAR, R., BERIS, A. N. & HANDLER, R. A. 2001 Budget of reynolds stress, kinetic energy and streamwise enstrohpy in viscoelastic turbulent channel flow. *Phys. Fluids* **13** (4), 1016–1027.

DUBIEF, Y., TERRAPON, V. E., WHITE, C. M., SHAQFEH, E. S. G., MOIN, P. & LELE, S. K. 2005 New answers on the interaction between polymers and vortices in in turbulent flows. *Flow, Turbulence and Combustion* To appear.

DUBIEF, Y., WHITE, C. M., TERRAPON, V. E., SHAQFEH, E. S. G., MOIN, P. & LELE, S. K. 2004 On the coherent drag-reducing and turbulence-enhancing behavior of polymers in wall flows. *J. Fluid Mech.* **514**, 271–280.

DURBIN, P. A. 1995 Separated flow computations with the $k - \varepsilon - v^2$ model. *AIAA J.* **33**, 659–664.

JIMÉNEZ, J. & PINELLI, A. 1999 The autonomous cycle of near-wall turbulence. *J. Fluid Mech.* **389**, 335–359.

LEIGHTON, R. I., WALKER, D. T., STEPHENS, T. R. & GARWOOD, G. C. 2003 Reynolds-stress modeling for drag-reducing viscoelastic flow. In *2003 Joint ASME/JSME Fluids Engineeing Symposium on Friction Drag Reduction*. Honolulu, Hawaii, USA.

MIN, T., YOO, J. Y. & CHOI, H. 2001 Effect of spatial discretization schemes on numerical solutions of viscoelastic fluid flows. *J. Non-Newtonian Fluid Mech.* **100**, 27–47.

TERRAPON, V. E., DUBIEF, Y., MOIN, P., SHAQFEH, E. S. G. & LELE, S. K. 2004 Simulated polymer stretch in a turbulent flow using brownian dynamics. *J. Fluid Mech.* **504**, 61–71.

VIRK, P. S. & MICKLEY, H. S. 1970 The ultimate asymptote and mean flow structures in Tom's phenomenon. *Trans. ASME E: J. Appl. Mech.* **37**, 488–493.

WARHOLIC, M. D., MASSAH, H. & HANRATTY, T. J. 1999 Influence of drag-reducing polymers on turbulence: effects of Reynolds number, concentration and mixing. *Exp. Fluids* **27**, 461–472.

Flux corrected finite-volume scheme for preserving scalar boundedness in large-eddy simulations

By M. Herrmann, G. Blanquart, and V. Raman

1. Motivation and objectives

Large-Eddy Simulation (LES) has emerged as the next generation simulation tool for handling industrially relevant turbulent reacting flows. Of particular interest is the use of LES for modeling complex combustors used both in power-production and aircraft engines (Ham *et al.* 2003; di Mare *et al.* 2004). Similarly, the chemical processing industry deals with a variety of turbulent flows that involve interaction of mixing and reaction with the final aim of controlling product selectivity and optimizing yield. As LES technique moves from being an academic tool to a practical simulation strategy, robustness of the LES solvers is a key issue to be answered. In low-mach number combustion, the staggered representation of the primary variables combined with an energy conserving scheme for the momentum equations has been shown to be a stable methodology for a wide variety of flows (Morinishi *et al.* 1998). In spite of the vast advancement in solving the momentum equations, the scalar transport equations that represent the species distribution inside the geometry and is thus key to predicting combustor performance, have not been studied in detail.

Numerical schemes for scalar transport equations are challenging from the viewpoint of stability. The advection equation solved using central difference based schemes can lead to oscillations and instabilities (Pierce 2001). To counter this problem, all known explicit schemes use an upwind bias that reduces numerical oscillations. As can be expected, this upwind bias reduces the numerical accuracy of the scheme and leads to artificial diffusion. In spite of this drawback, such schemes are widely used to their robust numerical stability. Many of these schemes suffer from one another drawback in that the species values are not bounded. In principle, a scalar transport equation solved using bounded initial and boundary conditions should preserve the boundedness (Pope 2000). In the present study, we consider the simulation of a conserved scalar, namely mixture fraction. Common combustion models use mixture-fraction to parameterize all species composition and is thus relevant to reactive flows. By definition, the solution to the mixture-fraction transport equation should always be in the set $[0, 1]$. The source of error in low-mach number formulations come from the staggering of the velocity and scalar variable locations. Usually, the velocity is defined at the cell-faces while the scalar is defined at the cell center. To compute the face based fluxes, an interpolative scheme is used based on a fixed stencil to obtain scalar values at the cell faces. Such interpolations do not impose a constraint on the scalar bounds which lead to oscillations around the local maximum and minimum values of the scalar.

Recently, a new class of schemes called Weighted Essentially Non-Oscillatory (WENO) schemes have been introduced that devise a total variation bounded (TVB) non-oscillatory scheme for advection type equations (Jiang & Peng 2000). Though these methods can be

extended to higher-order accuracy, the interpolative coefficients need to be reconstructed at each iterative loop. Again, extensions to complex unstructured grids are not straightforward and could be computationally expensive. In this work, a well-tested numerical scheme for scalars, namely the Quadratic-Upwind biased Interpolative Convective scheme (QUICK) (Leonard 1979) will be used. By switching between two interpolative functions, it will be shown that scalar boundedness as well as reduced oscillatory nature can be ensured. In addition, through detailed analysis of the numerical errors, it will be illustrated that the numerical accuracy is equivalent to the QUICK scheme.

2. Bounded QUICK scheme

It is known that a first-order upwind based interpolation is unconditionally bounded (within CFL restrictions) but can lead to large dissipative errors. In this work, we utilize the boundedness property of the first-order upwind scheme to formulate a dual valued stencil for the scalar. Each time-step is split into two sub-steps that can be constructed as a predictor-corrector algorithm. The predictor step moves the solution from the previous time-step to a predicted step. Locally, in cells where the predicted scalar solution is outside physical or acceptable boundaries, the interpolative scheme is switched to the full first-order upwind scheme while the rest of the domain uses the original QUICK stencil. Using this new stencil and the initial scalar field before the predictor step, the corrector step advances the scalar field to the next time level. This modified method is termed Bounded QUICK (BQUICK) scheme. In spite of the added local dissipation it is observed that the overall accuracy is not degraded and that the the boundedness is ensured to within velocity field divergence errors.

3. Numerical implementation

For clarity, the discussion in the following is limited to the one-dimensional case. Extension to two and three dimensions is straightforward.

The underlying numerical scheme of BQUICK is the original QUICK method (Leonard 1979) which has been implemented in both uniform and stretched grids. The advection time-stepping consists of two sub-steps termed predictor and corrector steps. In the predictor step the solution is advanced to the next time step using,

$$\phi^0(t) \overset{\text{QUICK}}{\longrightarrow} \phi^p(t+\Delta t)\,, \tag{3.1}$$

using cell face values $\phi^0_{i-1/2}$ calculated with the original QUICK scheme. Then, in the corrector step, all cells whose predicted values ϕ^p are outside their acceptable bounds $\phi_{\min}$ and $\phi_{\max}$ are discarded and recalculated using a first order approximation for the cell face values $\phi^1_{i-1/2}$ and $\phi^1_{i+1/2}$. All other cell faces retain their values from the predictor step. Figure 1 summarizes the algorithm of the BQUICK corrector step.

In practical LES computations, several sub-iterations are carried out in each time-step iteration to ensure numerical stability. In such cases, the above predictor-corrector step is executed in each sub-iteration with the initial scalar values determined by the field at the previous sub-iteration. The next section describes numerical tests to illustrate the performance and accuracy of the new scheme.

for all control volumes V_i **do**
  $\phi^1_{i-1/2} = \phi^0_{i-1/2}$
end for
for all control volumes V_i **do**
  if $\phi^p_i > \phi_{\max}$ or $\phi^p_i < \phi_{\min}$ **then** {revert cell update to first order}
    if $u_{i-1/2} \geq 0$ **then**
      $\phi^1_{i-1/2} = \phi^0_{i-1}$
    else
      $\phi^1_{i-1/2} = \phi^0_i$
    end if
    if $u_{i+1/2} \geq 0$ **then**
      $\phi^1_{i+1/2} = \phi^0_i$
    else
      $\phi^1_{i+1/2} = \phi^0_{i+1}$
    end if
  end if
end for

FIGURE 1. BQUICK corrector step.

4. Numerical tests

A series of tests are used to compare the new scheme with the original QUICK scheme and, in order to make a comparison with TVB based schemes, a 3rd order WENO scheme.

4.1. *1D tests*

To determine the order of accuracy, a sine wave function extending over a domain of $[0, 2\pi]$ is convected using a constant velocity and imposing periodic boundary conditions. Since the sine wave is a smooth function, numerical dispersion errors are minimized. Two different functions are used to test the effect of sharper curves. The first test uses as initial condition

$$Z(x) = \frac{1}{2}\left(\sin(\pi x) + 1\right). \tag{4.1}$$

The simulations are carried out on increasing resolution up to a grid of 1024 points. Using the exact solution, L_1, L_2 and L_∞ errors in the predictions are computed. Table 1 shows the errors in each simulation for the three different numerical schemes. It is seen from the L_2 error that the BQUICK and QUICK scheme both show slightly more than second order accuracy while the WENO scheme shows more than 4th order accuracy. The second function uses a sharper profile for the initial conditions.

$$Z(x) = \sin^4(\pi x). \tag{4.2}$$

Table 2 shows the errors as well as the accuracy estimates for the different numerical schemes. The QUICK and BQUICK scheme have retained second order accuracy for this profile. In fact, the BQUICK scheme shows almost identical results as for the previous test case. However, the WENO scheme shows a dramatic reduction in accuracy. The order of the scheme has dropped from over 4 in the previous case to between 2.5-3.5. As explained in the previous section, the WENO scheme uses an arbitrary smoothness factor that determines the extent of influence of the upwind biased correction. The weighting factor is determined by the gradients at the location which increases the lower order flux correction leading to reduction of the overall accuracy of the scheme.

Though the above test reveals the truncation error, scalar profiles in turbulent flow are rarely smooth and involve strong gradients. To test such a scenario a canonical 1-D

TABLE 1. Accuracy for $Z(x) = \frac{1}{2}(\sin(\pi x) + 1)$

Method	N	L_∞ error	L_∞ order	L_1 error	L_1 order	L_2 error	L_2 order
Quick	128	1.07E-04		6.81E-05		6.69E-06	
	256	2.56E-05	2.06	1.63E-05	2.06	1.13E-06	2.56
	512	6.33E-06	2.02	4.03E-06	2.02	1.98E-07	2.52
	1024	1.58E-06	2.00	1.00E-06	2.00	3.49E-08	2.50
Bquick	128	1.15E-04		7.27E-05		6.97E-06	
	256	2.85E-05	2.01	1.75E-05	2.06	1.18E-06	2.57
	512	7.24E-06	1.98	4.27E-06	2.03	2.04E-07	2.53
	1024	1.92E-06	1.92	1.05E-06	2.03	3.56E-08	2.52
WENO-3	128	7.00E-03		1.40E-03		2.10E-04	
	256	1.28E-03	2.45	1.61E-04	3.12	2.01E-05	3.39
	512	8.94E-05	3.84	1.16E-05	3.80	8.84E-07	4.51
	1024	3.11E-06	4.85	1.27E-06	3.19	4.45E-08	4.31

TABLE 2. Accuracy for $Z(x) = \sin^4(\pi x)$

Method	N	L_∞ error	L_∞ order	L_1 error	L_1 order	L_2 error	L_2 order
Quick	128	3.55E-03		1.81E-03		1.83E-04	
	256	6.54E-04	2.44	3.29E-04	2.46	2.38E-05	2.95
	512	1.45E-04	2.18	7.20E-05	2.19	3.71E-06	2.68
	1024	3.49E-05	2.05	1.73E-05	2.06	6.32E-07	2.55
BQuick	128	3.59E-03		1.77E-03		1.86E-04	
	256	6.51E-04	2.47	3.27E-04	2.43	2.42E-05	2.94
	512	1.45E-04	2.17	7.22E-05	2.18	3.74E-06	2.70
	1024	3.49E-05	2.05	1.74E-05	2.05	6.34E-07	2.56
WENO-3	128	6.70E-02		1.49E-02		2.02E-03	
	256	2.41E-02	1.48	3.27E-03	2.19	4.06E-04	2.32
	512	6.35E-03	1.92	5.15E-04	2.67	5.73E-05	2.83
	1024	9.03E-04	2.81	5.35E-05	3.27	4.26E-06	3.75

convection Jiang & Shu (1996) problem is used. As initial conditions, a profile consisting of several shapes with sharp gradients are distributed across the domain. A uniform velocity field is imposed with periodic boundaries. A fourth-order Runge-Kutta based time-integration is used to minimize temporal errors. The simulation is carried out for

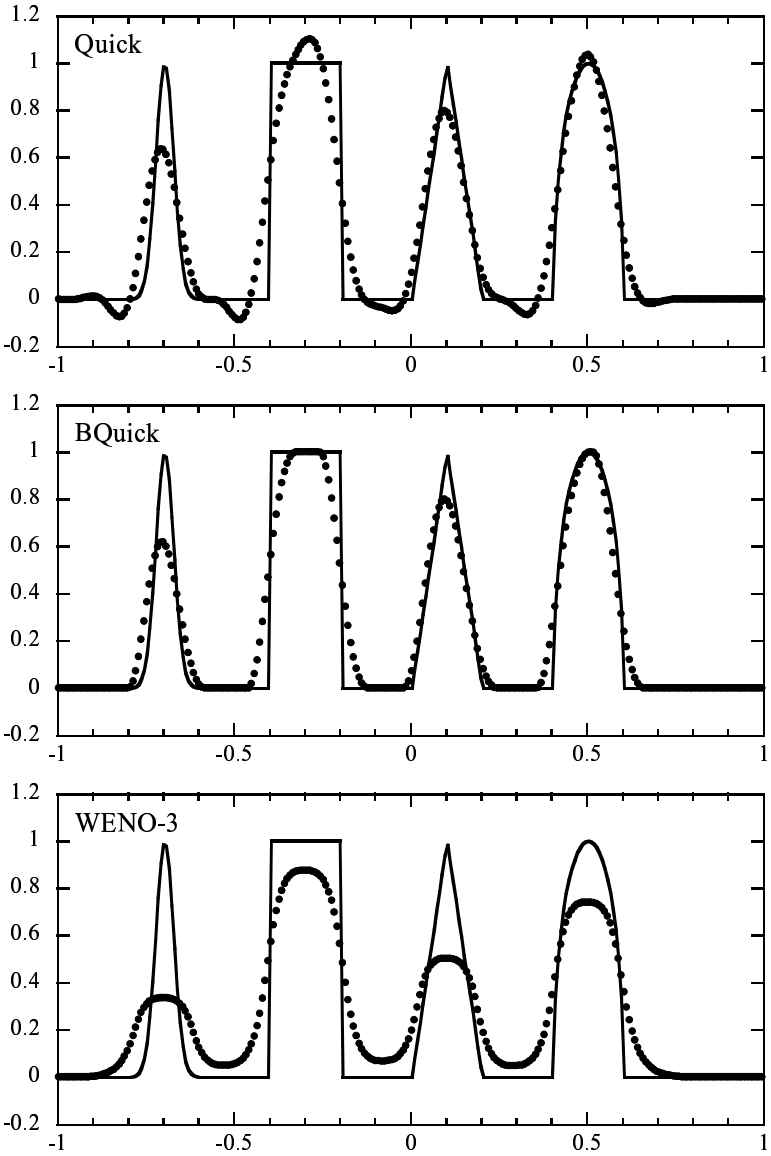

FIGURE 2. 1-D convection test case. Comparison of numerical schemes after 4 rotations. Lines indicate exact result while symbols denote numerical computation.

4 rotations where each rotation is defined as the time taken for the initial profile to be convected back to its initial location. Figure 2 compares the results from the QUICK, BQUICK and WENO schemes. It can be seen that the QUICK scheme locally exceeds the initial bounds of the scalar. In addition, it exhibits oscillations near regions of sharp gradients. The BQUICK scheme on the other hand maintains the boundedness accurately while also reducing the unphysical oscillations. Interestingly, the BQUICK scheme performs better at capturing the peaks as compared to the WENO scheme. This clearly illustrates the negative effects of TVB type damping of scalar fluctuations that are crucial in LES simulations.

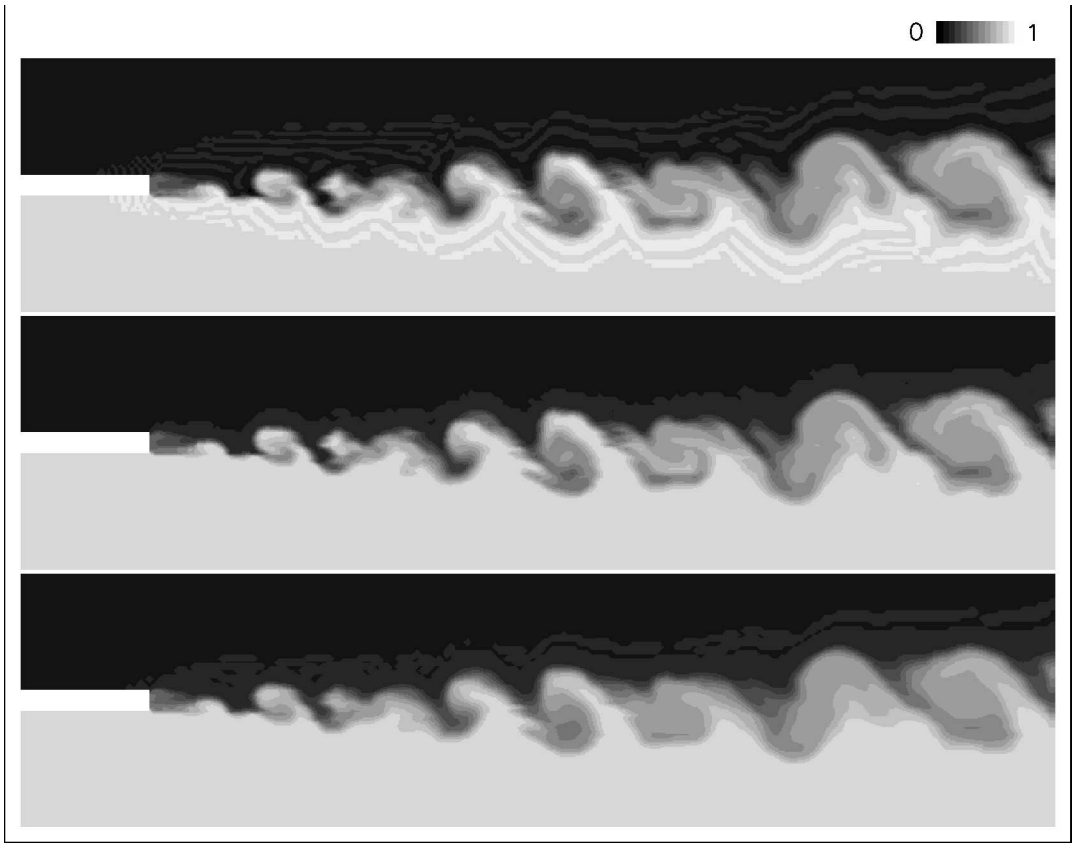

FIGURE 3. Two-dimensional profile of the instantaneous mixture-fraction in a mixing-layer. The top figure shows the QUICK results clipped between 0 and 1. The middle figure shows the BQUICK results. The bottom figure shows the WENO results.

4.2. *Mixing layer tests*

The second set of tests consists of an actual multi-dimensional implementation of the three schemes (QUICK, BQUICK and WENO). Two configurations are investigated: a spatially evolving mixing layer using LES and a temporal mixing layer using DNS. The equations for both of these simulations are solved in non-dimensional units using a domain decomposition based parallel solver. Further details of the code as well as the sub-filter models used (in the case of LES) can be found in Pierce (2001).

4.2.1. *Spatial mixing layer*

The inflow bulk velocities of the two streams are set to a ratio of 1:2.5 with laminar profiles. A splitter plate initially divides the streams and the mixing layer starts at X=0. The domain, including the splitter plate stretches for 80 units while the width is set at 20 units. Figure 3 shows the instantaneous scalar concentration using the three schemes. The QUICK scalar field has been clipped between 0 and 1 while the BQUICK and the WENO scalar field maintain the bounds. Visually the differences between the QUICK and BQUICK schemes are not noticeable. On the other hand the WENO scalar field is smoother than the two other schemes. To better understand the effect of the BQUICK scheme, crosswise scalar profiles are plotted (Fig. 4). It is seen that the BQUICK main-

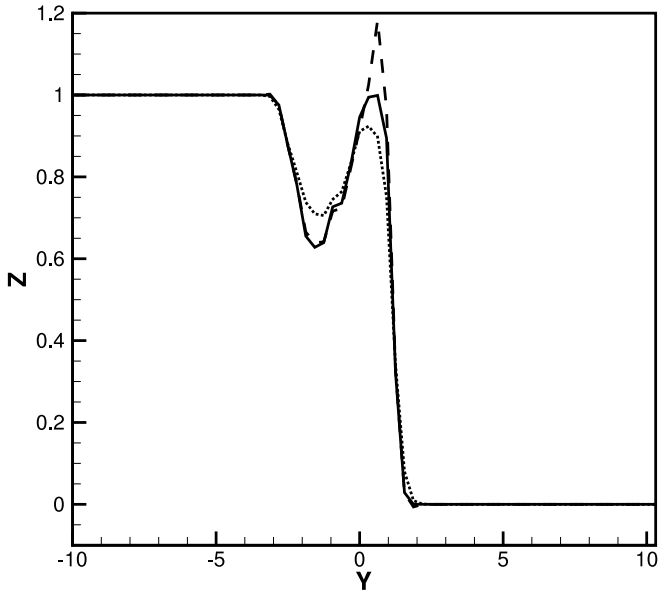

FIGURE 4. Cross-stream profile of mixture fraction obtained in the mixing layer at an arbitrary downstream location. Dashed lines show the QUICK profile, solid lines show the BQUICK profile and, dotted lines show the WENO profile.

tains the same profile as the QUICK scheme away from the bounds of the scalar while closer to 0 and 1, the BQUICK adjusts itself to maintain the bounds. The WENO profile is also bounded but it is much smoother than the BQUICK profile and does not show the same scalar gradient. The lower-order correction for the BQUICK at the bounds in composition space has limited impact on the physical transport. To further substantiate this argument, time-averaged profiles of both the scalar as well as the scalar RMS value are plotted in Fig. 5. Increased numerical diffusion will reduce the RMS fluctuations. However, the profiles indicate that the BQUICK correction has no substantial effect on the accuracy of the scheme. The upwind correction does not lead to substantial numerical diffusion that is characteristic of the first-order upwind scheme. As such, the corrections are applied in a very small fraction of the computational domain and hence the RMS fluctuations are not damped by dispersion errors. On the other hand the time-averaged WENO profile of scalar RMS shows much more dissipation than the BQUICK scheme: the RMS fluctuations of the scalar are damped by about 20% compared to the QUICK/BQUICK RMS fluctuations.

4.2.2. *Temporal mixing layer*

The computational domain used for the simulation of the temporal mixing layer was initially divided into two streams separated by an interface located at $Y = 0$. The initial mean velocity distribution is given by a hyperbolic tangent velocity profile. Three dimensional perturbations with wavelength of up to a quarter of the domain length were superimposed on the mean velocity profile. The different variables were non-dimensionalized

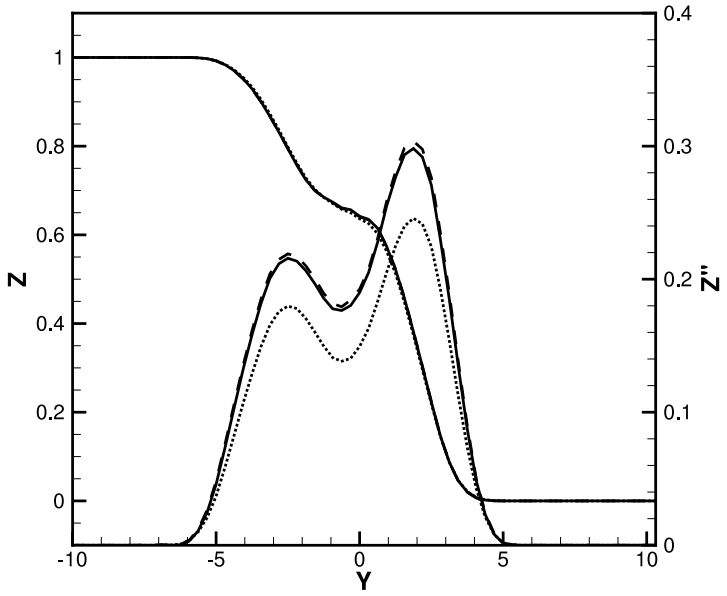

FIGURE 5. Time-averaged cross-stream profile of mixture-fraction obtained in the mixing layer at an arbitrary downstream location. Dashed lines show QUICK profiles, solid lines show BQUICK profiles and, dotted lines show WENO profiles.

using the initial vorticity thickness (δ_ω) and the mean velocity difference between the two streams. Based on these definitions, the initial Reynolds number was $Re_{\omega,0} = 435$. The simulation was performed on a grid with $256 \times 256 \times 256$ control volumes. Figure 6 shows the one-dimensional streamwise energy spectrum of the streamwise velocity component at $t = 92$. For reference, the slope of the inertial range is indicated. The energy spectrum is in good agreement with previous work (Vreman 1995).

To better isolate the effect of numerical dissipation by the different schemes, the scalar transport equation was solved without molecular diffusion. In such a configuration the energy cascade still occurs but the energy should not be dissipated at the lowest length scales. However numerical dissipation introduced by the schemes will prevent the energy from piling up at the smallest length scales. Figure 7 shows the one-dimensional energy spectra of the scalars. The inertial range is accurately captured by the three schemes. However numerical dissipation damps out the energy at the highest wave numbers. As is can be observed, the WENO scheme introduces more numerical dissipation than the QUICK and BQUICK schemes. This result can be further ascertained by considering the RMS fluctuations of the scalar (Fig. 8). The upwind correction of the BQUICK scheme has little effect on the RMS fluctuations. Once again the fraction of computational domain where the correction is applied is very small. On the other hand the WENO profile shows lower RMS value (of about 15%) compared to QUICK/BQUICK profiles. The additional numerical dissipation introduced by the the WENO scheme also affects the shape of the material interface. The WENO scheme does not only dissipate more than the BQUICK scheme it also reduces the total surface area of the interface. Figure 9 show the iso-surface

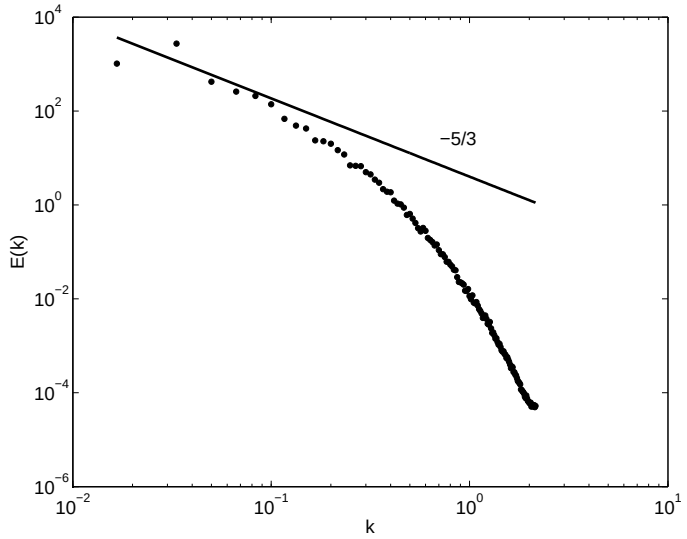

FIGURE 6. One-dimensional (planar averaged) streamwise energy spectrum of the streamwise velocity component at $Y = 0$ ($t = 92$).

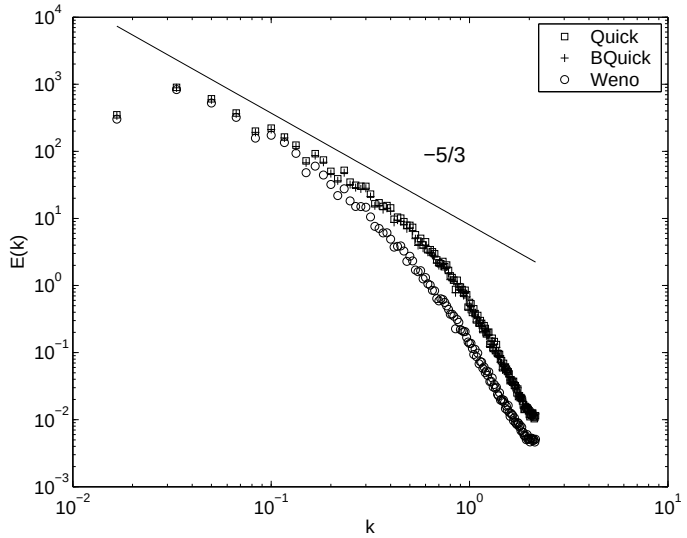

FIGURE 7. One-dimensional (planar averaged) streamwise energy spectrum at $Y = 0$ and $t = 92$ of the QUICK scalar (squares), the BQUICK scalar (crosses) and WENO scalar (circles).

$Z = 0.5$ for the BQUICK and WENO schemes. It is seen that the WENO does not show the small structures as the BQUICK scheme does. As a consequence this scheme is not able to capture small packets of low mixture fraction surrounded by high mixture fraction and vice versa. Consistent resolution of these situations will have a significant impact in increasing the predictive capability of LES.

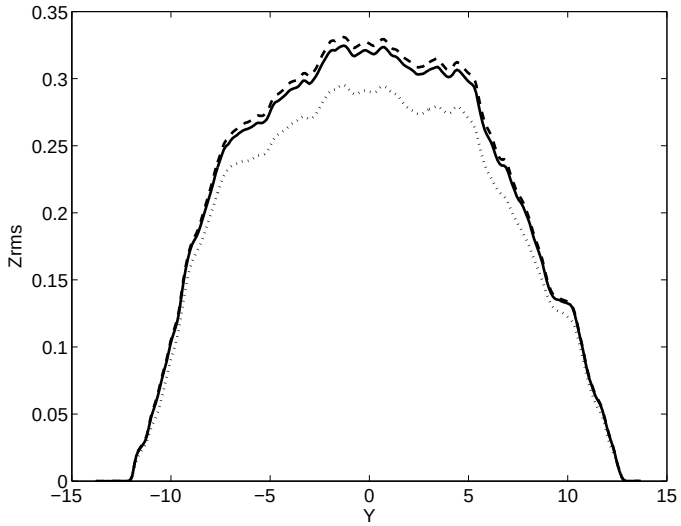

FIGURE 8. Plane averaged cross-stream profiles of mixture fraction obtained in the mixing layer at $Y = 0$ and $t = 92$. Dashed lines show QUICK profile, solid lines show BQUICK profile and, dotted lines show WENO profile.

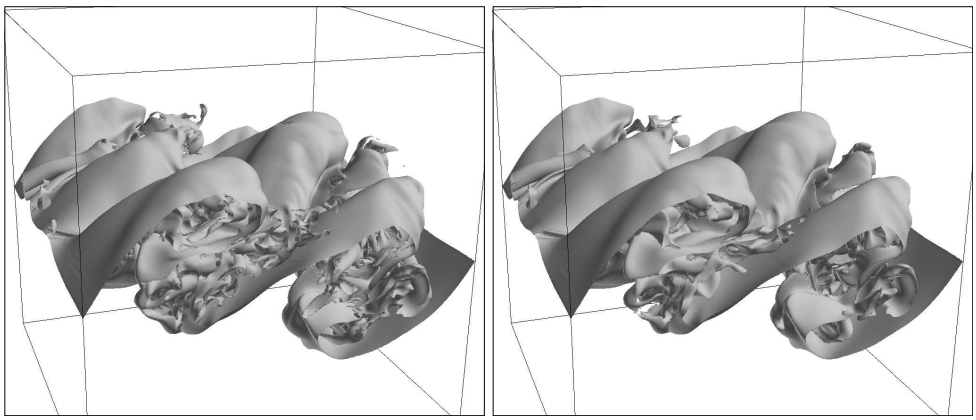

FIGURE 9. Iso-surface $Z = 0.5$ at $t = 46$ for the BQUICK scalar field (left) and the WENO scalar field (right).

5. Conclusion

In conclusion, these tests have clearly shown that the flux-corrected third-order scheme, BQUICK, is clearly superior to TVB based formulations or the original QUICK scheme without scalar bounds. This new scheme will be especially useful in combustion simulations with lean fuel mixture. The low stoichiometric mixture fraction associated with such fuel mixtures leads to very strong density gradients in the mixture-fraction space close to mixture-fraction value of 0. The QUICK scheme leads to extended excursions below 0 that can cause large and unphysical temporal change of density. This feeds itself into the continuity equation thereby leading to algorithmic instability. The BQUICK scheme has been successfully implemented in constant and variable density flows for both structured and unstructured grid based LES solvers. Preliminary calculations follow the

same trend as the simulations shown here. Results from this work will be communicated in the near future.

Acknowledgements

The authors would like to thank Frank Ham and Heinz Pitsch for fruitful discussions concerning WENO schemes.

REFERENCES

Ham, F., Apte, S., Iaccarino, G., Wu, X., Herrmann, M., Constantinescu, G., Mahesh, K. & Moin, P. 2003 Unstructured LES of reacting multiphase flows in realistic gas turbine combustors. In *Annual Research Briefs-2003*, pp. 139–160. Stanford, CA: Center for Turbulence Research.

Jiang, G.-S. & Peng, D. 2000 Weighted ENO schemes for Hamilton-Jacobi equations. *SIAM J. Sci. Comput.* **21** (6), 2126–2143.

Jiang, G. S. & Shu, C. W. 1996 Efficient implementation of weighted ENO schemes. *J. Comput. Phys.* **126**, 202–228.

Leonard, B. P. 1979 A stable and accurate convective modelling procedure basedon quadratic upstream interpolation. *Comput. Methods Appl. Mech. Engrg.* **19**, 59–98.

di Mare, F., Jones, W. P. & Menzies, K. R. 2004 Large eddy simulation of a model gas turbine combustor. *Comb. Flame* **137** (3), 278–294.

Morinishi, Y., Lund, T. S., Vasilyev, O. V. & Moin, P. 1998 Fully conservative higher order finite difference schemes for incompressible flow. *J. Comput. Phys* **143** (1), 90–124.

Pierce, C. D. 2001 Progress-variable approach for large-eddy simulation of turbulence combustion. PhD thesis, Stanford University.

Pope, S. B. 2000 *Turbulent Flows*. Cambridge University Press.

Vreman, B., Geurts, B., Kuerten, H. 1995 A priori tests of large eddy simulation of the compressible plane mixing layer. *J. Eng. Math* **29** (4), 299–327.

Zalesak, S. T. 1979 Fully multidimensional flux-corrected transport algorithms for fluids. *J. Comput. Phys.* **31**, 335–362.

Stability for the Wall-Pierce-Moin implicit scheme

By B. Gustafsson †

1. Motivation and Objectives

Explicit schemes are not well suited for simulation of low Mach number flow, due to the severe restriction on the time-step. Implicit schemes on the other hand, give rise to large non-linear systems coupling all dependent variables. Iterative methods have to be used for solving these systems, but iteration to full convergence in each time-step may be time-consuming. One way to reduce the work, is to limit the number of iterations, such that the system is not fully solved, but still has a reasonable accuracy. Sometimes such a method is called semi-implicit.

In Wall *et al.* (2002) a new method for the Navier-Stokes equations was introduced. It uses a staggered grid as suggested in Pierce (2001), and it is semi-implicit in the sense mentioned above. There is a stability analysis in Wall *et al.* (2002) for the simplified case where the system has been reduced to the acoustic wave equation with constant speed of sound and periodic solutions on a uniform staggered grid. In this analysis, it is assumed that the system of equations is solved exactly in each step, i.e., the fully implicit scheme is analyzed. It is shown that the scheme is not only unconditionally stable, but also energy conserving in the sense that the Fourier modes are propagated without any change in magnitude.

The purpose with this paper is to generalize the stability analysis for the fully implicit scheme in two ways. The first generalization is that we allow for nonzero advective velocity. The second one is that we start from the full non-linear difference scheme, and linearize from there. We will assume constant coefficients, and use Fourier analysis to prove unconditional stability and energy conservation even in this case.

2. The model equation and the linearization

The simplified model problem is obtained by disregarding the viscous terms, and substitute the enthalpy equation by an equation of state $p = p(\rho)$ connecting the density ρ and the pressure p. With u denoting the advective velocity, the system of differential equations is

$$\begin{aligned} g_t + (\rho u^2)_x + p_x &= 0\,, \\ \rho_t + g_x &= 0\,, \end{aligned}$$

where $g = \rho u$ and $p = p(\rho)$. The speed of sound a is defined by $a^2 = dp/d\rho$. The system can be expressed in terms of the two variables g and ρ. With

$$U = \begin{bmatrix} g \\ \rho \end{bmatrix}\,, \qquad F(U) = \begin{bmatrix} g^2/\rho + p(\rho) \\ g \end{bmatrix}\,,$$

we have

$$U_t + (F(U))_x = 0\,.$$

† Department of Scientific Computing, Uppsala University, Sweden

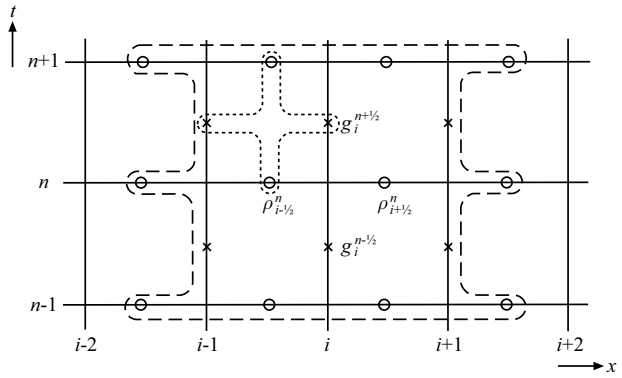

FIGURE 1. The staggered grid and the computational stencil

Let $U' = (g', \rho')^T$ be a perturbation around the state $U = [g, \rho]^T$. The linearized system is obtained as

$$U'_t + \frac{\partial F}{\partial U} U'_x = 0\,, \tag{2.1}$$

where the Jacobian matrix is given by

$$\frac{\partial F}{\partial U} = \begin{bmatrix} 2g/\rho & -g^2/\rho^2 + a^2 \\ 1 & 0 \end{bmatrix} = \begin{bmatrix} 2u & a^2 - u^2 \\ 1 & 0 \end{bmatrix}.$$

The eigenvalues of $\partial F/\partial U$ are $u \pm a$.

For the discretization on the staggered grid, we use here a slightly different notation compared to Wall *et al.* (2002), such that subscripts and superscripts denote the location of the variables, see Fig 1. The notation is

$$\begin{aligned} g_i^{n+1/2} &= g(x_i,\, t_{n+1/2}) = g(i\Delta x,\, (n+1/2)\Delta t)\,, \\ \rho_{i+1/2}^{n} &= \rho(x_{i+1/2},\, t_n) = \rho((i+1/2)\Delta x,\, n\Delta t)\,. \end{aligned}$$

For averages, the sub/super-scripts denote the location where the average is centered. For example,

$$\overline{\rho}_i^{n+1/2} = \frac{1}{4}(\rho_{i+1/2}^{n+1} + \rho_{i-1/2}^{n+1} + \rho_{i+1/2}^{n} + \rho_{i-1/2}^{n})$$

denotes the average centered at $(x_i,\, t_{n+1/2})$, see Fig 2.

With $\lambda = \Delta t/\Delta x$, the scheme is

$$\begin{aligned} &g_i^{n+1/2} - g_i^{n-1/2} + \lambda(\overline{g}_{i+1/2}^{n}\overline{u}_{i+1/2}^{n} - \overline{g}_{i-1/2}^{n}\overline{u}_{i-1/2}^{n}) \\ &\qquad + \frac{\lambda}{4}(p_{i+1/2}^{n+1} + 2p_{i+1/2}^{n} + p_{i+1/2}^{n-1} - p_{i-1/2}^{n+1} - 2p_{i-1/2}^{n} - p_{i-1/2}^{n-1}) = 0\,, \\ &\rho_{i-1/2}^{n} - \rho_{i-1/2}^{n-1} + \lambda(g_i^{n-1/2} - g_{i-1}^{n-1/2}) = 0\,. \end{aligned} \tag{2.2}$$

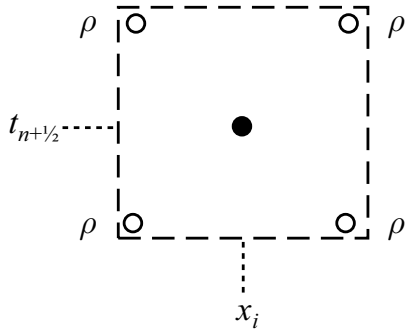

FIGURE 2. The average for ρ

Here

$$\overline{u}^n_{i+1/2} = \frac{g^{n+1/2}_{i+1}}{\rho^{n+1}_{i+3/2}+\rho^{n+1}_{i+1/2}+\rho^{n}_{i+3/2}+\rho^{n}_{i+1/2}} + \frac{g^{n+1/2}_{i}}{\rho^{n+1}_{i+1/2}+\rho^{n+1}_{i-1/2}+\rho^{n}_{i+1/2}+\rho^{n}_{i-1/2}}$$
$$+ \frac{g^{n-1/2}_{i+1}}{\rho^{n}_{i+3/2}+\rho^{n}_{i+1/2}+\rho^{n-1}_{i+3/2}+\rho^{n-1}_{i+1/2}} + \frac{g^{n-1/2}_{i}}{\rho^{n}_{i+1/2}+\rho^{n}_{i-1/2}+\rho^{n-1}_{i+1/2}+\rho^{n-1}_{i-1/2}},$$
$$\overline{g}^n_{i+1/2} = \frac{1}{4}(g^{n+1/2}_{i+1} + g^{n+1/2}_{i} + g^{n-1/2}_{i+1} + g^{n-1/2}_{i}),$$

and $p^k_j = p(\rho^k_j)$ for all j, k.

We make a few remarks concerning the method (2.2).

We first note that the second equation by itself is explicit. However, the first equation involves not only the $g^{n+1/2}$-values, but also the ρ^{n+1}-values via the p^{n+1}- and $\overline{u}^n$-expressions. This means that the scheme is fully implicit in the sense that the solution $\{g^{n+1/2}, \rho^{n+1}\}$ at the highest time level is coupled across several points in space, and depends on all the values behind.

Secondly we note that (2.2) is effectively a one-step scheme, even if the first equation couples three time levels for ρ. It is easily seen by the fact that only one level for each of the variables ρ and g are required to start the scheme. Assume that ρ^0 and $g^{1/2}$ are known. The second equation is first advanced one step providing the ρ^1-values. After that we let $n = 2$ in the second equation and couple it to the first equation with $n = 1$. This provides the ρ^2- and $g^{3/2}$-values, and the scheme is then advanced by stepping up n and repeating the last part of the algorithm.

We next turn to the linearization. As seen in Fig 1, there are 18 different variables occuring in the discrete equations, and by lining them up in a vector V, the scheme can be written in the form $G(V) = 0$. Then the linearized equations are

$$\frac{\partial G}{\partial V}(V)V' = 0\,.$$

In the evaluation of the Jacobian $\partial G/\partial V$, it is assumed that all values are independent of x and t, such that

$$g^n_i = g\ , \quad u^n_i = u\ , \quad dp/d\rho|_{i,n} = a^2$$

for all i, n. As an example, we get

$$\frac{\partial}{\partial g_{i+1}^{n+1/2}}(\overline{g}_{i+1/2}^n \overline{u}_{i+1/2}^n) = \frac{\partial \overline{g}_{i+1/2}^n}{\partial g_{i+1}^{n+1/2}} \overline{u}_{i+1/2}^n + \overline{g}_{i+1/2}^n \frac{\partial \overline{u}_{i+1/2}^n}{\partial g_{i+1}^{n+1/2}} = \frac{1}{4}u + g\frac{1}{4\rho} = \frac{u}{2}\,.$$

For completeness we list all the derivatives for the convection term, the other ones are simpler.

	$\overline{g}_{i+1/2}^n \overline{u}_{i+1/2}^n$	$\overline{g}_{i-1/2}^n \overline{u}_{i-1/2}^n$
$\partial/\partial g_{i+1}^{n+1/2}$	$u/2$	0
$\partial/\partial g_{i}^{n+1/2}$	$u/2$	$u/2$
$\partial/\partial g_{i-1}^{n+1/2}$	0	$u/2$
$\partial/\partial g_{i+1}^{n-1/2}$	$u/2$	0
$\partial/\partial g_{i}^{n-1/2}$	$u/2$	$u/2$
$\partial/\partial g_{i-1}^{n-1/2}$	0	$u/2$
$\partial/\partial \rho_{i+3/2}^{n+1}$	$-u^2/16$	0
$\partial/\partial \rho_{i+1/2}^{n+1}$	$-u^2/8$	$-u^2/16$
$\partial/\partial \rho_{i-1/2}^{n+1}$	$-u^2/16$	$-u^2/8$
$\partial/\partial \rho_{i-3/2}^{n+1}$	0	$-u^2/16$
$\partial/\partial \rho_{i+3/2}^{n}$	$-u^2/8$	0
$\partial/\partial \rho_{i+1/2}^{n}$	$-u^2/4$	$-u^2/8$
$\partial/\partial \rho_{i-1/2}^{n}$	$-u^2/8$	$-u^2/4$
$\partial/\partial \rho_{i-3/2}^{n}$	0	$-u^2/8$
$\partial/\partial \rho_{i+3/2}^{n-1}$	$-u^2/16$	0
$\partial/\partial \rho_{i+1/2}^{n-1}$	$-u^2/8$	$-u^2/16$
$\partial/\partial \rho_{i-1/2}^{n-1}$	$-u^2/16$	$-u^2/8$
$\partial/\partial \rho_{i-3/2}^{n-1}$	0	$-u^2/16$

We drop the $'$ notation for the new variables, and arrive at the complete linearized

system

$$
\begin{aligned}
& g_i^{n+1/2} + \frac{\lambda u}{2}(g_{i+1}^{n+1/2} - g_{i-1}^{n+1/2}) \\
& \qquad - \frac{\lambda u^2}{16}(\rho_{i+3/2}^{n+1} + \rho_{i+1/2}^{n+1} - \rho_{i-1/2}^{n+1} - \rho_{i-3/2}^{n+1}) + \frac{\lambda a^2}{4}(\rho_{i+1/2}^{n+1} - \rho_{i-1/2}^{n+1}) \\
& -g_i^{n-1/2} + \frac{\lambda u}{2}(g_{i+1}^{n-1/2} - g_{i-1}^{n-1/2}) \\
& \qquad - \frac{\lambda u^2}{8}(\rho_{i+3/2}^{n} + \rho_{i+1/2}^{n} - \rho_{i-1/2}^{n} - \rho_{i-3/2}^{n}) + \frac{\lambda a^2}{2}(\rho_{i+1/2}^{n} - \rho_{i-1/2}^{n}) \\
& \qquad - \frac{\lambda u^2}{16}(\rho_{i+3/2}^{n-1} + \rho_{i+1/2}^{n-1} - \rho_{i-1/2}^{n-1} - \rho_{i-3/2}^{n-1}) + \frac{\lambda a^2}{4}(\rho_{i+1/2}^{n-1} - \rho_{i-1/2}^{n-1}) = 0\,, \\
& \lambda(g_i^{n-1/2} - g_{i-1}^{n-1/2}) + \rho_{i-1/2}^{n} - \rho_{i-1/2}^{n-1} = 0\,.
\end{aligned}
$$

Here λ, u, a are all constants. Note that the system is consistent with the linear system (2.1).

3. Stability analysis

For the stability analysis, we Fourier transform the system by substituting $g_j^{n+1/2} = \hat{g}^{n+1/2} e^{i\omega x_j}$ etc.. With $\xi = \omega \Delta x$, we get

$$
\begin{aligned}
& (1 + \lambda u i \sin\xi)\hat{g}^{n+1/2} - \frac{\lambda u^2}{8} i(\sin\frac{\xi}{2} + \sin\frac{3\xi}{2})\hat{\rho}^{n+1} + \frac{\lambda}{2} a^2 i \sin\frac{\xi}{2}\hat{\rho}^{n+1} \\
& \quad + (-1 + \lambda u i \sin\xi)\hat{g}^{n-1/2} - \frac{\lambda u^2}{4} i(\sin\frac{\xi}{2} + \sin\frac{3\xi}{2})\hat{\rho}^{n} + \lambda a^2 i \sin\frac{\xi}{2}\hat{\rho}^{n} \\
& \quad - \frac{\lambda u^2}{8} i(\sin\frac{\xi}{2} + \sin\frac{3\xi}{2})\hat{\rho}^{n-1} + \frac{\lambda}{2} a^2 i \sin\frac{\xi}{2}\hat{\rho}^{n-1} = 0\,, \\
& 2\lambda i \sin\frac{\xi}{2}\hat{g}^{n-1/2} + \hat{\rho}^{n} - \hat{\rho}^{n-1} = 0\,.
\end{aligned}
\tag{3.1}
$$

Let

$$
\hat{V}^n = \begin{bmatrix} \hat{g}^{n-1/2} \\ \hat{\rho}^n \end{bmatrix}.
$$

With the notation

$$
s_1 = \sin\frac{\xi}{2}\,, \quad s_2 = \sin\xi\,, \quad s_3 = \sin\frac{3\xi}{2}\,,
$$

the system can be written in two-step form

$$
Q_2\hat{V}^{n+1} + Q_1\hat{V}^n + Q_0\hat{V}^{n-1} = 0\,, \tag{3.2}
$$

where

$$
\begin{aligned}
Q_2 &= \begin{bmatrix} 1 + \lambda u i s_2 & -\frac{\lambda}{8} i[(s_1+s_3)u^2 - 4s_1a^2] \\ 0 & 0 \end{bmatrix}, \\
Q_1 &= \begin{bmatrix} -1 + \lambda u i s_2 & -\frac{\lambda}{4} i[(s_1+s_3)u^2 - 4s_1a^2] \\ 2\lambda i s_1 & 1 \end{bmatrix}, \\
Q_0 &= \begin{bmatrix} 0 & -\frac{\lambda}{8} i[(s_1+s_3)u^2 - 4s_1a^2] \\ 0 & -1 \end{bmatrix}.
\end{aligned}
$$

Looking for the amplification factor z of this two-step scheme, we substitute $\hat{V}^n = z^n \hat{V}$, and put the determinant equal to zero. We get

$$\begin{aligned}
&\mathrm{Det}(Q_2 z^2 + Q_1 z + Q_0) \\
&\quad = \mathrm{Det} \begin{bmatrix} (1+\lambda u i s_2) z^2 + (-1+\lambda u i s_2) z & -\frac{\lambda}{8} i [(s_1+s_3)u^2 - 4 s_1 a^2](z^2+2z+1) \\ 2\lambda i s_1 z & z-1 \end{bmatrix} \\
&\quad = [z^2 - z + (z^2+z)\lambda u i s_2](z-1) - \frac{\lambda^2}{4} s_1 z [(s_1+s_3)u^2 - 4 s_1 a^2](z+1)^2 = 0 \,.
\end{aligned}$$

One root is zero. The reason for this is that for convenience we have included $\hat{g}^{n-3/2}$ in the two-step form (3.2), but it is not present in the equations (3.1). (If $\hat{g}^{-3/2}$ would be given a non-zero value at the start, it would never show up in the computation.) Furthermore, since we have a one-step scheme for two variables ρ and g as explained above, there are only two remaining roots z.

In order to find these remaining roots, we substitute

$$\alpha = \lambda u s_2 \,, \quad \beta = \frac{\lambda^2}{4} s_1 [(s_1+s_3)u^2 - 4 s_1 a^2] \,,$$

and obtain

$$z^2 - 2\frac{1+\beta}{1+i\alpha-\beta} z + \frac{1-i\alpha-\beta}{1+i\alpha-\beta} = 0 \,,$$

with the solutions

$$z = \frac{1+\beta \pm \sqrt{4\beta - \alpha^2}}{1+i\alpha-\beta} \,,$$

where

$$4\beta - \alpha^2 = \lambda^2 [(s_1^2 + s_1 s_3 - s_2^2)u^2 - 4 s_1^2 a^2] \,.$$

The coefficient multiplying u^2 is identically zero, which is seen by introducing the notation $\theta = \xi/2$ and expanding:

$$\begin{aligned}
s_1^2 + s_1 s_3 - s_2^2 &= -\frac{1}{4}[(e^{i\theta} - e^{-i\theta})^2 + (e^{i\theta} - e^{-i\theta})(e^{3i\theta} - e^{-3i\theta}) - (e^{2i\theta} - e^{-2i\theta})^2] \\
&= -\frac{1}{4}(e^{2i\theta} - 2 + e^{-2i\theta} + e^{4i\theta} - e^{-2i\theta} - e^{2i\theta} + e^{-4i\theta} - e^{4i\theta} + 2 - e^{-4i\theta}) = 0 \,.
\end{aligned}$$

Hence, $4\beta - \alpha^2 = -4\lambda^2 s_1^2 a^2 \le 0$, and

$$|z|^2 = \left|\frac{1+\beta \pm i\sqrt{\alpha^2 - 4\beta}}{1-\beta+i\alpha}\right|^2 = \frac{1+2\beta+\beta^2+\alpha^2-4\beta}{1-2\beta+\beta^2+\alpha^2} = 1 \,.$$

The only possibility for a multiple root z is $4\beta - \alpha^2 = 0$, i.e., $\xi = 0$, but this is the trivial case with a constant solution being forwarded without any change. Hence, we have shown unconditional stability. Furthermore, we note that both roots of the characteristic equation have modulus one, which means that there is energy conservation for the periodic case.

4. Future plans

The analysis above is done for a quite simplified case, and for generalization there are several directions to go:

- Analyze the effect of not solving the equations to full convergence in each time-step (making the scheme "semi-implicit").
- Introduce non-periodic boundary conditions.
- Include also the enthalpy equation in the analysis.
- Treat the multidimensional case.

The first item is important, but very difficult if applied to the full system. An analysis of a simpler model problem could give some indications.

Regarding the non-periodic boundary conditions, there is first of all a question of how to impose the boundary conditions for the full system of differential equations. For solid walls, the conditions are given on physical grounds, but for open boundaries there are still many difficulties to overcome. Furthermore, the method analyzed here has a quite wide computational stencil as illustrated by Fig 1. Therefore, extra numerical boundary conditions must be constructed in order to get the algebraic system well defined at each time level. Stability has to be secured, but in addition, a special challenge here would be to keep energy conservation in the case this holds for the system of differential equations.

Acknowledgment

The work described here was done while the author was visiting CTR in January 2004.

REFERENCES

C. Pierce, *Progress-variable approach for large-eddy simulation of turbulent combustion*, PhD thesis, Stanford University (2001).

C. Wall, C. Pierce, and P. Moin 2002 *A semi-implicit method for resolution of acoustic waves in low mach number flows*, *J. Comput. Phys.* **181**, 545-563.

A formulation of incompressible Navier-Stokes equations in a quasi-generalized coordinate system

By D. You AND M. Wang

1. Motivation and objectives

In large-eddy simulation (LES) of flows in complex geometries, the generation of a high quality mesh and the large memory requirement for the metric quantities of coordinate transformation are often major obstacles, when a three-dimensional structured, body-fitted mesh is employed. The problem is particularly severe for flow solvers employing the staggered mesh arrangement, which is strongly preferred in non-dissipative LES codes for stability and discrete energy conservation (e.g. Mittal & Moin 1997; Nagarajan, Lele & Ferziger 2003). For instance, at least 80 (8 positions with 10 variables (metric coefficients plus Jacobian) per mesh element) three-dimensional arrays are required, compared to 10 three-dimensional arrays for collocated meshes. This makes LES impractical on large grids. In addition, the increase of partial derivative terms in the transformed governing equations cause a significant increase in computational cost.

On the other hand, many geometries in engineering and scientific applications can be handled using a two-dimensional curvilinear mesh with mild variations along the remaining third direction. Frequently observed variations are shift, rotation, magnification/contraction, and skewing of the curvilinear plane along a perpendicular direction to that plane. The airplane wing is an example of the shift and contraction of the airfoil section, and the axial compressor or turbine blades are observed to be twisted along the radial direction maintaining the blade section profile.

The objective of this study is to exploit these geometric simplification in the design of a numerical method, which is applicable to a wide class of problems while minimizing the memory requirement and computational cost. To this end, a formulation of incompressible Navier-Stokes equations based on a quasi-generalized coordinate system which consists of two-dimensional generalized curvilinear coordinates and a reasonably smooth variation along the perpendicular remaining direction is proposed. Using such an approach, one can efficiently treat geometric difficulties, and, at the same time, alleviate problems associated with a fully generalized coordinate transformation.

The incompressible Navier-Stokes equations are transformed to present a quasi-generalized coordinate system in Section 2. Then, in Section 3, formulae for some example geometric variations and the corresponding metric coefficients and Jacobians are given. In Section 4, an implementation of the present formulation is evaluated by considering the flow over a tapered circular cylinder, and this is followed by a brief summary in Section 5.

2. Transformation of governing equations

The incompressible Navier-Stokes equations based on Cartesian coordinates are as follows:

$$\frac{\partial u_i}{\partial t} + \frac{\partial}{\partial x_j} u_i u_j = -\frac{\partial p}{\partial x_i} + \frac{1}{\mathrm{Re}} \frac{\partial}{\partial x_j} \frac{\partial u_i}{\partial x_j}, \tag{2.1}$$

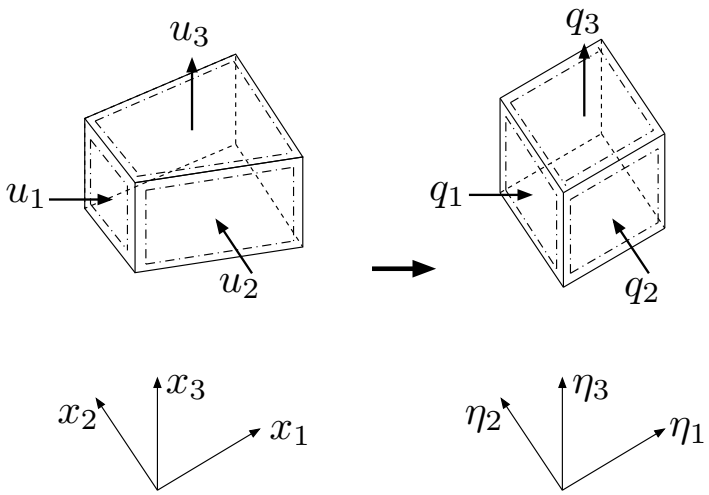

FIGURE 1. Schematic diagram of coordinate transformation from Cartesian coordinates to curvilinear coordinates. Note that planes perpendicular to the third direction (η^3) are required to be parallel.

$$\frac{\partial u_i}{\partial x_i} = 0, \tag{2.2}$$

All the coordinate variables, velocity components, and pressure are nondimensionalized by the length scale L, the reference velocity U_{ref}, and ρU_{ref}^2, respectively. The time is normalized by L/U_{ref}.

Equations (2.1) and (2.2) can be rewritten in the conservative form in a generalized coordinate system as

$$\frac{\partial q^i}{\partial t} = -N^i(\mathbf{q}) - G^i(p) + L^i(\mathbf{q}), \tag{2.3}$$

$$D^i q^i = 0, \tag{2.4}$$

where $\mathbf{q} = (q^1, q^2, q^3)$, N^i is the nonlinear convection term, $G^i(p)$ is the pressure gradient term, and L^i represents the diffusion term, respectively. D^i denotes the divergence operator. Generalized coordinates are introduced in figure 1 as

$$(x_1, x_2, x_3; u_1, u_2, u_3) \rightarrow (\eta^1, \eta^2, \eta^3; q^1, q^2, q^3). \tag{2.5}$$

The variable q^i is the volume flux across the faces of the cells, which is equivalent to the contravariant velocity components on a staggered grid multiplied by the Jacobian of the coordinate transformation. Then, the terms in (2.3) are expressed in generalized coordinates as

$$N^i(\mathbf{q}) = \frac{1}{J}\gamma_m^i \frac{\partial}{\partial \eta^j}\frac{1}{J}c_k^m q^k q^j, \tag{2.6}$$

$$G^i(p) = \alpha^{ij}\frac{\partial p}{\partial \eta^j}, \tag{2.7}$$

$$L^i(\mathbf{q}) = \frac{1}{J}\gamma_m^i \frac{\partial}{\partial \eta^k}\alpha^{kj}\frac{1}{\mathrm{Re}}\frac{\partial}{\partial \eta^j}\frac{1}{J}c_l^m q^l, \tag{2.8}$$

where

$$q^j = \gamma_k^j u_k, \quad c_k^j = \partial x_j/\partial \eta^k, \quad \gamma_k^j = J(c_j^k)^{-1}, \quad \alpha^{jk} = J(c_j^m c_k^m)^{-1},$$

$$\text{and} \quad J = \left(\|c_j^m c_k^m\|\right)^{\frac{1}{2}} \quad \text{for} \;\; j,k,l,m,n = 1,2,3.$$

When the fully three-dimensional curvilinear coordinate system is used, the number of partial derivative terms in the transformed governing equations and the required memory for three-dimensional metric coefficients and Jacobians severely limit the applicability of this approach to a relatively small number of mesh points. Here, we propose an approach which drastically reduces the memory requirement and computational cost by imposing a constraint which requires the planes to be parallel along a perpendicular direction (η^3 direction in the present formulation). This results in $c_1^3 = c_2^3 = \gamma_1^3 = \gamma_2^3 = 0$. With these vanishing metric quantities, a significant reduction of derivative terms in the transformed Navier-Stokes equations, compared to the equations in a fully three-dimensional generalized curvilinear coordinate system, is obtained:

$$\begin{aligned}
\frac{\partial q^i}{\partial t} = &-\frac{1}{J}\gamma_1^i \frac{\partial}{\partial \eta^j}\frac{1}{J}c_k^1 q^k q^j - \frac{1}{J}\gamma_2^i \frac{\partial}{\partial \eta^j}\frac{1}{J}c_k^2 q^k q^j - \frac{1}{J}\gamma_3^i \frac{\partial}{\partial \eta^j}\frac{1}{J}(\underbrace{c_1^3 q^1 + c_2^3 q^2}_{=0} + c_3^3 q^3) q^j \\
&+\alpha^{ij}\frac{\partial p}{\partial \eta^j} \\
&+\frac{1}{J}\gamma_1^i \frac{\partial}{\partial \eta^k}\alpha^{kj}\nu\frac{\partial}{\partial \eta^j}\frac{1}{J}c_l^1 q^l + \frac{1}{J}\gamma_2^i \frac{\partial}{\partial \eta^k}\alpha^{kj}\nu\frac{\partial}{\partial \eta^j}\frac{1}{J}c_l^2 q^l \\
&+\frac{1}{J}\gamma_3^i \frac{\partial}{\partial \eta^k}\alpha^{kj}\nu\frac{\partial}{\partial \eta^j}\frac{1}{J}(\underbrace{c_1^3 q^1 + c_2^3 q^2}_{=0} + c_3^3 q^3),
\end{aligned} \tag{2.9}$$

for $i = 1,2,$ and $j,k,l = 1,2,3$, and

$$\begin{aligned}
\frac{\partial q^3}{\partial t} = &-\underbrace{\frac{1}{J}\gamma_1^3 \frac{\partial}{\partial \eta^j}\frac{1}{J}c_k^1 q^k q^j}_{=0} - \underbrace{\frac{1}{J}\gamma_2^3 \frac{\partial}{\partial \eta^j}\frac{1}{J}c_k^2 q^k q^j}_{=0} - \frac{1}{J}\gamma_3^3 \frac{\partial}{\partial \eta^j}\frac{1}{J}(\underbrace{c_1^3 q^1 + c_2^3 q^2}_{=0} + c_3^3 q^3) q^j \\
&+\alpha^{3j}\frac{\partial p}{\partial \eta^j} \\
&+\underbrace{\frac{1}{J}\gamma_1^3 \frac{\partial}{\partial \eta^k}\alpha^{kj}\nu\frac{\partial}{\partial \eta^j}\frac{1}{J}c_l^1 q^l}_{=0} + \underbrace{\frac{1}{J}\gamma_2^3 \frac{\partial}{\partial \eta^k}\alpha^{kj}\nu\frac{\partial}{\partial \eta^j}\frac{1}{J}c_l^2 q^l}_{=0} \\
&+\frac{1}{J}\gamma_3^3 \frac{\partial}{\partial \eta^k}\alpha^{kj}\nu\frac{\partial}{\partial \eta^j}\frac{1}{J}(\underbrace{c_1^3 q^1 + c_2^3 q^2}_{=0} + c_3^3 q^3), \;\; \text{for } j,k,l = 1,2,3.
\end{aligned} \tag{2.10}$$

The total number of derivative terms is only about one half of that in the fully generalized curvilinear coordinate system.

Compared to the formulation with two-dimensional generalized curvilinear coordinates and a nonuniform Cartesian third direction (e.g. You *et al.* 2004), the above formulation which allows the third coordinate to be mildly curvilinear does not change the computational cost significantly, since the computations needed for both approaches are based on a fractional-step method. The computational cost is dominated by the inversions of factored matrices and multigrid operations for solving the pressure Poisson equation, which are not much altered by this change.

The three-dimensional metric coefficients in the present coordinates can be expressed as products of metric coefficients in a two-dimensional plane and one-dimensional functions along its perpendicular direction, with decoupled Jacobians $J = (c_1^1 c_2^2 - c_2^1 c_1^2)^{\frac{1}{2}} c_3^3$. These decoupled metric coefficients and Jacobians, with smooth variations of the plane mesh

along the perpendicular third direction, as exemplified in the following section, result in a significant reduction of required memory.

3. Plane variations and metric coefficients

In this section, we present several examples of grid topology in which variations along one direction is given by an algebraic relationship. Note that non-algebraic but smooth variations are also allowed in the present formulation, as long as the mesh planes perpendicular to that direction are parallel to one another. In addition, more flexibility in the geometry can be achieved by combining some of the variations.

(a) Shift (Fig. 2(a))

$$\begin{cases} x_{1_{i,j,k}} = x_{1_{i,j,1}} + x^s_{1_k} \\ x_{2_{i,j,k}} = x_{2_{i,j,1}} + x^s_{2_k}, \end{cases}$$

(b) Magnification/Contraction (Fig. 2(b))

$$\begin{cases} x_{1_{i,j,k}} = a_k(x_{1_{i,j,1}} - x_{1_{im,jm,1}}) + x_{1_{im,jm,1}} \\ x_{2_{i,j,k}} = b_k(x_{2_{i,j,1}} - x_{2_{im,jm,1}}) + x_{2_{im,jm,1}}, \end{cases}$$

(c) Rotation (Fig. 2(c))

$$\begin{cases} x_{1_{i,j,k}} = \cos\phi_k(x_{1_{i,j,1}} - x_{1_{ir,jr,1}}) - \sin\phi_k(x_{2_{i,j,1}} - x_{2_{ir,jr,1}}) + x_{1_{ir,jr,1}} \\ x_{2_{i,j,k}} = \sin\phi_k(x_{1_{i,j,1}} - x_{1_{ir,jr,1}}) + \cos\phi_k(x_{2_{i,j,1}} - x_{2_{ir,jr,1}}) + x_{2_{ir,jr,1}}, \end{cases}$$

(d) Skewing to x_1 direction (Fig. 2(d))

$$\begin{cases} x_{1_{i,j,k}} = (x_{2_{i,j,1}} - x_{2_{i,js,1}})\tan^2\varphi_{x_k} + x_{1_{i,j,1}} \\ x_{2_{i,j,k}} = (x_{2_{i,j,1}} - x_{2_{i,js,1}})(1 + \tan^2\varphi_{x_k}) + x_{2_{i,js,1}}, \end{cases}$$

(e) Skewing to x_2 direction (Fig. 2(e))

$$\begin{cases} x_{1_{i,j,k}} = x_{1_{i,j,1}} \\ x_{2_{i,j,k}} = (x_{1_{i,j,1}} - x_{1_{is,j,1}})\tan\varphi_{y_k} + x_{2_{i,j,1}}. \end{cases}$$

In the formulae (a)-(e), $x^s_{1(2)_k}$ is the amount of shift in $x_1(x_2)$ direction. $x_{1(2)_{im,jm,1}}$, $x_{1(2)_{ir,jr,1}}$, $x_{2_{i,js,1}}$, and $x_{1_{is,j,1}}$ denote reference points for magnification, rotation, and skewing variations in x_1 and x_2 directions, respectively. a_k and b_k are the magnification/contraction factors in x_1 and x_2 directions, while ϕ_k, φ_{x_k}, and φ_{y_k} are the rotation and skewing angles. Other needed formulae can also be derived to meet any geometric need.

These algebraic variations, as well as combinations of the variations, result in not only geometric flexibility but also decoupled metric coefficients, which allow a great reduction of memory. For example, the magnification and rotation operations can be combined using formulae (b) and (c) to give

$$\begin{cases} x_{1_{i,j,k}} = p^1_k x_{1_{i,j,1}} + p^2_k x_{1_{ir,jr,1}} + p^3_k x_{1_{im,jm,1}} + p^4_k x_{2_{i,j,1}} + p^5_k x_{2_{ir,jr,1}} \\ x_{2_{i,j,k}} = p^6_k x_{1_{i,j,1}} + p^7_k x_{1_{ir,jr,1}} + p^8_k x_{2_{i,j,1}} + p^9_k x_{2_{ir,jr,1}} + p^{10}_k x_{2_{im,jm,1}}, \end{cases}$$

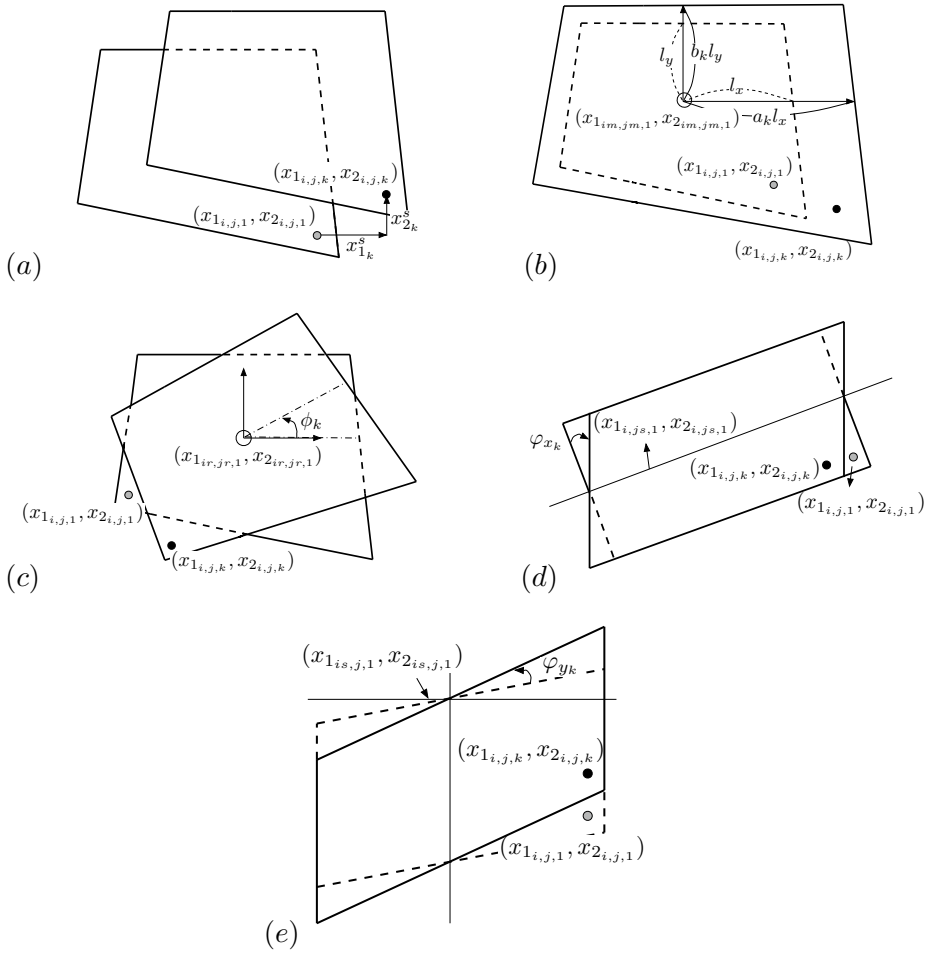

FIGURE 2. Examples of algebraic functions applicable in the proposed formulation: (*a*) shift; (*b*) magnification/contraction; (*c*) rotation; (*d*) skewing to x_1 direction; (*e*) skewing to x_2 direction.

where

$$\begin{cases} p_k^1 = a_k(1+\cos\phi_k) \\ p_k^2 = -a_k\cos\phi_k \\ p_k^3 = 1-a_k \\ p_k^4 = -b_k\sin\phi_k \\ p_k^5 = b_k\sin\phi_k \end{cases} \qquad \begin{cases} p_k^6 = a_k\sin\phi_k \\ p_k^7 = -a_k\sin\phi_k \\ p_k^8 = b_k(1+\cos\phi_k) \\ p_k^9 = -b_k\cos\phi_k \\ p_k^{10} = 1-b_k. \end{cases}$$

In this example, the metric coefficients for the coordinate transformation become

$$\begin{cases} \frac{\partial x_1}{\partial \eta^1}|_{i,j,k} = p_k^1 \frac{\partial x_1}{\partial \eta^1}|_{i,j,1} + p_k^4 \frac{\partial x_2}{\partial \eta^1}|_{i,j,1} \\ \frac{\partial x_1}{\partial \eta^2}|_{i,j,k} = p_k^1 \frac{\partial x_1}{\partial \eta^2}|_{i,j,1} + p_k^4 \frac{\partial x_2}{\partial \eta^2}|_{i,j,1} \\ \frac{\partial x_1}{\partial \eta^3}|_{i,j,k} = \frac{\partial p_k^1}{\partial \eta^3} x_{1_{i,j,1}} + \frac{\partial p_k^2}{\partial \eta^3} x_{1_{ir,jr,1}} + \frac{\partial p_k^3}{\partial \eta^3} x_{1_{im,jm,1}} + \frac{\partial p_k^4}{\partial \eta^3} x_{2_{i,j,1}} + \frac{\partial p_k^5}{\partial \eta^3} x_{2_{ir,jr,1}}, \end{cases}$$

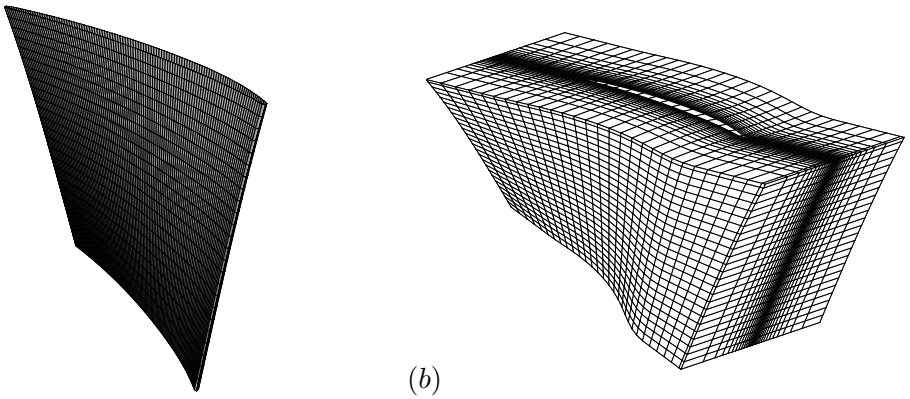

(a) (b)

FIGURE 3. A twisted compressor blade generated by mesh rotation and skewing: (a) compressor blade; (b) mesh around the blade.

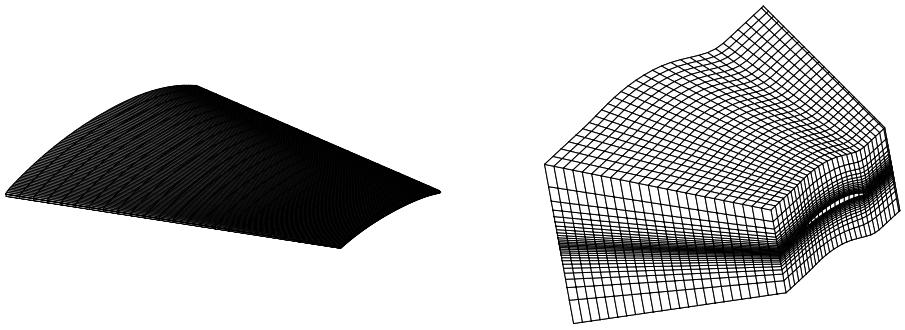

(a) (b)

FIGURE 4. An airplane wing generated by contraction and shift: (a) airplane wing; (b) mesh around the wing.

$$\begin{cases} \frac{\partial x_2}{\partial \eta^1}|_{i,j,k} = p_k^6 \frac{\partial x_1}{\partial \eta^1}|_{i,j,1} + p_k^8 \frac{\partial x_2}{\partial \eta^1}|_{i,j,1} \\ \frac{\partial x_2}{\partial \eta^2}|_{i,j,k} = p_k^6 \frac{\partial x_1}{\partial \eta^2}|_{i,j,1} + p_k^8 \frac{\partial x_2}{\partial \eta^2}|_{i,j,1} \\ \frac{\partial x_2}{\partial \eta^3}|_{i,j,k} = \frac{\partial p_k^6}{\partial \eta^3} x1_{i,j,1} + \frac{\partial p_k^7}{\partial \eta^3} x1_{ir,jr,1} + \frac{\partial p_k^8}{\partial \eta^3} x2_{i,j,1} + \frac{\partial p_k^9}{\partial \eta^3} x2_{ir,jr,1} + \frac{\partial p_k^{10}}{\partial \eta^3} x2_{im,jm,1}, \end{cases}$$

$$\begin{cases} \frac{\partial x_3}{\partial \eta^1}|_{i,j,k} = 0 \\ \frac{\partial x_3}{\partial \eta^2}|_{i,j,k} = 0 \\ \frac{\partial x_3}{\partial \eta^3}|_{i,j,k} = \frac{\partial x3_k}{\partial \eta^3}. \end{cases}$$

Any metric coefficients and Jacobians can be expressed as multiples of those in the base grid at $k = 1$ and variational functions along the k-direction. This results in a great reduction of computational memory requirements with a small increase in computational operations.

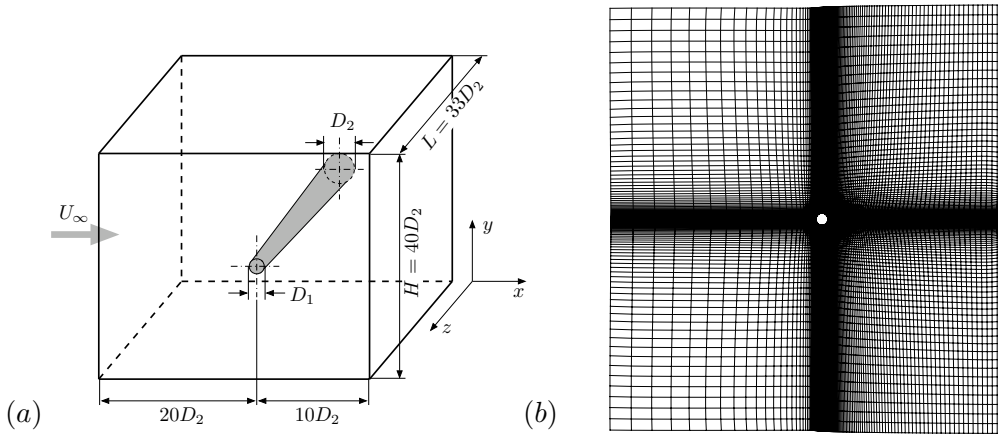

FIGURE 5. (a) Flow configuration and (b) computational grid in a base $x - y$ plane for numerical simulation of flow over a tapered circular cylinder.

Figures 3 and 4 are examples of the geometries which can be represented using the present formulation. Figure 3 shows a compressor blade which is twisted along the blade span while the blade cross-section profile is maintained. For this geometry, the base mesh is rotated and skewed along the blade wall normal direction with angles of up to 30°, and the skewing allows a periodic boundary condition to be applied in that direction in a simulation of flow in a blade passage. An airplane wing can be meshed by contraction and shift operations of the base grid, as shown in Fig. 4.

Enhanced geometric flexibility can be achieved by combining partially or approximately body-fitted meshes with an immersed boundary method. This method has been successfully applied to the rotor tip-clearance flow found in axial turbomachines (You *et al.* 2004).

4. Implementation and evaluation

Numerical simulation of vortex shedding behind a linearly tapered cylinder is performed to evaluate the present methodology and implementation. The configuration, shown in Fig 5(a), is the same as that studied experimentally by Piccirillo & Van Atta (1993). The taper ratio, $R_T = L/(D_2 - D_1)$, is set to 50, where L is the cylinder length, and D_1 and D_2 are the diameters of the small and large ends of the cylinder, respectively. The Reynolds numbers based on the diameters and freestream velocity are 60 and 180 at the small and large ends, respectively.

The base grid of 257×257 mesh points is shown in Fig. 5(b), and parallel mesh planes are generated along the perpendicular spanwise direction by contraction and expansion operations. 33 points are allocated uniformly along the span. A uniform laminar inflow is used and convective and no-stress boundary conditions are employed at the exit and each side wall, respectively. About 110 seconds on 4 CPUs of SGI Origin 300 are used per time step, and this is only about 10% more than that measured by the solver based on the two-dimensional generalized curvilinear coordinate coupled with a straight third direction and with the same number of mesh points.

Figure 6 shows snap-shots of instantaneous vortical structures behind the tapered cylinder observed in both experiments (Piccirillo & Van Atta 1993) and the present

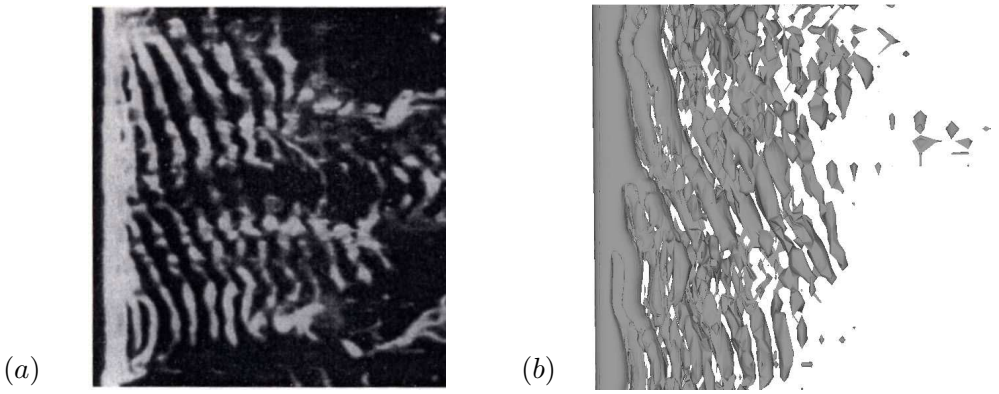

(a) (b)

FIGURE 6. Instantaneous vortical structures behind a tapered circular cylinder: (a) water tunnel flow visualization (Piccirillo & Van Atta 1993); (b) λ_2 vortex identification from computational results.

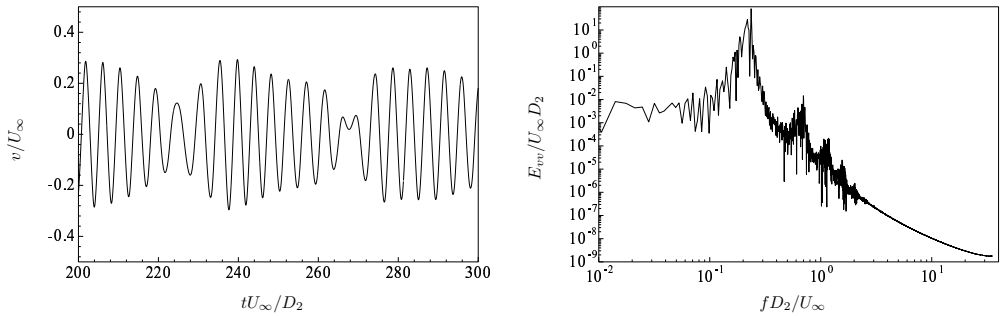

(a) (b)

FIGURE 7. (a) Time-history and (b) frequency energy-spectrum of the vertical velocity at $x/D_2 = 1, y/D_2 = 0, z/D_2 = 13.5$.

numerical simulation. The oblique vortex shedding is a hallmark of this flow observed experimentally, and the present numerical approach is shown to capture this phenomenon. In contrast to the laminar vortex shedding observed behind a straight cylinder, phase differences of the vortex shedding along the spanwise direction is clearly observed, and this complicates the downstream vortical structures. This phase difference accelerates the decay of downstream vortices due to enhanced mixing.

Figure 7 shows a typical velocity time-history and its auto-spectrum as a function of nondimensional frequency. The main Strouhal number is 0.203, which in good agreement with the experimental result ($fD_2/U_\infty = 0.204$) of Piccirillo & Van Atta (1993).

5. Summary

The incompressible Navier-Stokes equations have been formulated in a two-dimensional, generalized curvilinear coordinate system complemented by a third coordinate which varies smoothly. By requiring all the two-dimensional planes to be parallel in the perpendicular direction, the proposed approach significantly improves the geometric capability needed for treating complex flows. In particular, it alleviates the huge memory

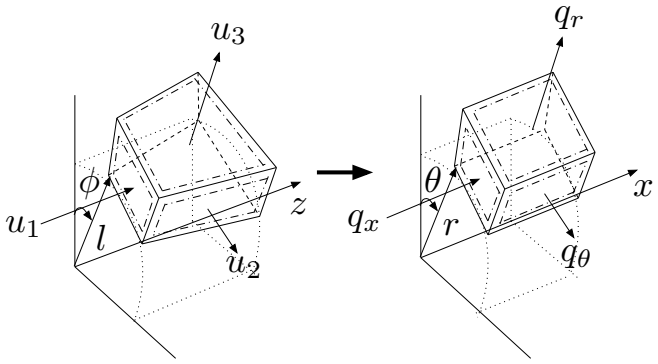

FIGURE 8. Schematic diagram of coordinate transformation from Cylindrical coordinates to curvilinear coordinates. Note that planes along the third directions (r) are aligned in parallel.

requirement for metric coefficients and Jacobians in the use of structured meshes for fully three-dimensional geometries. The formulation can be easily adapted to an existing solver based on a two-dimensional generalized coordinate system coupled with a Cartesian third direction, with only a small increase in computational cost.

Acknowledgments

The authors acknowledge the support of the Office of Naval Research under grant number N00014-99-1-0389, with Ki-Han Kim as program manager. Computer time was provided by the Challenge Project Grant C82 from the US Department of Defense High-Performance Computing Modernization Program (HPCMP) through Army Research Laboratory (ARL) Major Shared Resource Center.

Appendix. Quasi-generalized cylindrical transformation

The proposed *quasi-generalized coordinate formulation* can be extended to a cylindrical base coordinate system which can be particularly effective for treating rotating blades in turbomachines. Using the following transformation (see Fig. 8)

$$(x_1, x_2, x_3; \eta^1, \eta^2, \eta^3) = (z, l\cos\phi, l\sin\phi; x, \theta, r)$$

with the geometric constraint of $z = z(x, \theta, r), l = l(r)$, and $\phi = \phi(x, \theta, r)$, we can calculate the metric quantities as:

$$\begin{aligned} c_j^i &= \begin{pmatrix} c_1^1 & c_2^1 & c_3^1 \\ c_1^2 & c_2^2 & c_3^2 \\ c_1^3 & c_2^3 & c_3^3 \end{pmatrix} \\ &= \begin{pmatrix} z_x & z_\theta & z_r \\ -(l\sin\phi)\phi_x & -(l\sin\phi)\phi_\theta & (\cos\phi)l_r - (l\sin\phi)\phi_r \\ (l\cos\phi)\phi_x & (l\cos\phi)\phi_\theta & (\sin\phi)l_r + (l\cos\phi)\phi_r \end{pmatrix}, \end{aligned} \tag{5.1}$$

and

$$\gamma_i^j = \begin{pmatrix} \gamma_1^1 & \gamma_2^1 & \gamma_3^1 \\ \gamma_1^2 & \gamma_2^2 & \gamma_3^2 \\ \gamma_1^3 & \gamma_2^3 & \gamma_3^3 \end{pmatrix}$$

$$= \begin{pmatrix} d_1^1 & d_2^1\cos\phi - d_3^1\sin\phi & d_2^1\sin\phi + d_3^1\cos\phi \\ d_1^2 & d_2^2\cos\phi + d_3^2\sin\phi & d_2^2\sin\phi - d_3^2\cos\phi \\ 0 & d_2^3\cos\phi & d_3^3\sin\phi \end{pmatrix}, \tag{5.2}$$

where

$$\begin{pmatrix} d_1^1 & d_2^1 & d_3^1 \\ d_1^2 & d_2^2 & d_3^2 \\ d_1^3 & d_2^3 & d_3^3 \end{pmatrix} = \begin{pmatrix} -l\phi_\theta l_r & (\phi_\theta z_r - \phi_r z_\theta)l & z_\theta l_r \\ l\phi_x l_r & (\phi_r z_x - \phi_x z_r)l & z_x l_r \\ 0 & (\phi_x z_\theta - \phi_\theta z_x)l & (\phi_x z_\theta - \phi_\theta z_x)l \end{pmatrix}. \tag{5.3}$$

The constant Δr or constant l between each $x-\theta$ or $z-\phi$ planes results in the decoupled Jacobian (such that $J = \text{function}(r) \times \text{function}(x,\theta)$):

$$J = ll_r(z_\theta\phi_x - z_x\phi_\theta). \tag{5.4}$$

Geometric variation along the radial (r) direction can be implemented as considered in Section 3 so that the memory requirement is kept small.

In addition, similarly to the *quasi-generalized coordinates* based on a Cartesian coordinate system, the vanishing γ_1^3 and trigonometric relations significantly reduce the number of partial derivative terms in the transformed governing equations. Here we consider the equation for $i = 3$ to illustrate how the geometric constraint reduces computational cost compared to the fully generalized coordinate system.

$$\begin{aligned} \frac{\partial q^3}{\partial t} = &- \underbrace{\frac{1}{J}\gamma_1^3\frac{\partial}{\partial\eta^j}\frac{1}{J}c_k^1 q^k q^j}_{=0} \underbrace{- \frac{1}{J}\gamma_2^3\frac{\partial}{\partial\eta^j}\frac{1}{J}c_k^2 q^k q^j - \frac{1}{J}\gamma_3^3\frac{\partial}{\partial\eta^j}\frac{1}{J}c_k^3 q^k q^j}_{=A} \\ &+\alpha^{3j}\frac{\partial p}{\partial\eta^j} \\ &+ \underbrace{\frac{1}{J}\gamma_1^3\frac{\partial}{\partial\eta^k}\alpha^{kj}\nu\frac{\partial}{\partial\eta^j}\frac{1}{J}c_l^1 q^l}_{=0} \\ &+\frac{1}{J}\gamma_2^3\frac{\partial}{\partial\eta^k}\alpha^{kj}\nu\frac{\partial}{\partial\eta^j}\frac{1}{J}c_l^2 q^l + \frac{1}{J}\gamma_3^3\frac{\partial}{\partial\eta^k}\alpha^{kj}\nu\frac{\partial}{\partial\eta^j}\frac{1}{J}c_1^3 q^l, \end{aligned} \tag{5.5}$$

where the numbers of partial derivative terms in A can be significantly reduced by the cancellation:

$$\begin{aligned} A &= -\frac{1}{J}d_2^3\left\{\frac{\partial}{\partial\eta^j}\left[\left(\cos\phi\cdot c_k^2 + \sin\phi\cdot c_k^3\right)q^k\frac{1}{J}q^j\right] - \frac{1}{J}\phi_{\eta^j}q^j q^k\left(-\sin\phi\cdot c_k^2 + \cos\phi\cdot c_k^3\right)\right\} \\ &= -\frac{1}{J}d_2^3\left\{\frac{\partial}{\partial\eta^j}\left(l_r\frac{1}{J}q^3 q^j\right) - \frac{1}{J}\phi_{\eta^j}q^j l\left(\phi_x q^1 + \phi_\theta q^2 + \phi_r q^3\right)\right\}, \end{aligned} \tag{5.6}$$

where $j,k = 1,2,3$.

Similar cancellations can be achievable in the equations for q^1 and q^2. Therefore, the present *quasi-generalized coordinate* transformation also provides significantly reduced number of partial derivative terms as well as lower memory requirement in the cylindrical-base coordinates. However, it is worth to note that this reduction makes it difficult to keep the governing equations in the (weak) conservative form (*c.f.* the Navier-Stokes equations in cylindrical, non-curvilinear coordinates are expressed as non-conservative forms).

REFERENCES

Mittal, R. & Moin, P. 1997 Suitability of upwind-biased schemes for large-eddy simulation of turbulent flows. *AIAA J.* **36**, 1415–1417.

Nagarajan, S., Lele, S. K. & Ferziger, J. H. 2003 A robust high-order compact method for large-eddy simulation. *J. Comp. Phys.* **191**, 392–419.

Piccirillo, P. S. & Van Atta, C. W. 1993 An experimental study of vortex shedding behind linearly tapered cylinders at low Reynolds number. *J. Fluid Mech.* **246**, 163–195.

You, D., Mittal, R., Wang, M. & Moin, P. 2004 Computational methodology for large-eddy simulation of tip-clearance flows. *AIAA J.* **42** (2), 271–279.

On LES outflow conditions for integrated LES-RANS computations

By J. U. Schlüter AND X. Wu

1. Motivation and objectives

For the numerical prediction of turbulent flows of industrial relevance two approaches are currently in use. One is based on the Reynolds-Averaged Navier Stokes (RANS) approach, which computes essentially an ensemble-average of the flow and uses a turbulence model to approximate all scales of turbulence. The other approach is that of Large-Eddy Simulations (LES), where the large scales of motion are resolved in time and space and only the smallest scales are modeled. Although LES is considered the more accurate approach, its application to a number of flow applications is prohibited by the increased computational costs. One way to combine both methods is the integrated LES-RANS approach, where two separate flow solvers, one RANS flow solver and one LES flow solver, are executed simultaneously, each computing a portion of a given domain (Schlüter *et al.* 2003; Schlüter *et al.* 2004a). This approach has been used for the computation of flows in gas turbines (Schlüter *et al.* 2004b; Schlüter *et al.* 2004c; Schlüter *et al.* 2004d). In these previous studies of flows in complex geometries, the RANS domain is upstream of the LES domain, and hence the LES has to use the RANS data to define its inflow.

For the following study we want to concentrate on the reverse case, where the LES domain is upstream of the RANS domain. The RANS solver receives flow data from the LES solver to define its inflow boundary conditions. In return, the upstream LES solver has to receive flow information from the downstream RANS flow solver. This last step is necessary in order to take into account the influence of the downstream flow development onto the flow in the LES domain. In previous years, we have developed LES outflow boundary conditions for integrated LES-RANS computations and tested these using a structured LES flow solver (Schlüter *et al.* 2002; Schlüter *et al.* 2004e). It has been demonstrated that the downstream flow can have a significant effect on the upstream flow features, and we have shown that the previously developed method of body forces can transfer the necessary flow information to the LES domain.

Here, we first recapitulate the method of body forces for integrated LES-RANS computations. We will then elaborate on the determination of the body force constant. Finally, we will report the implementation and validation of this method for unstructured flow solvers.

2. Body force method

In integrated LES-RANS computations we consider overlapping grids between the upstream LES and the downstream RANS. In the LES portion of the overlap region we can use virtual body forces to drive the LES solution to a RANS solution delivered by the downstream flow solver. This body force is employed on the right hand side of the momentum equations.

$$F_i(\mathbf{x}) = \sigma \left(\overline{u}_{i,\mathrm{RANS}}(\mathbf{x}) - \overline{u}_{i,\mathrm{LES}}(\mathbf{x}) \right) . \tag{2.1}$$

In Eq.(2.1) $\overline{u}_{i,\mathrm{RANS}}$ is the vector of target velocities obtained from the RANS computation, $\overline{u}_{i,\mathrm{LES}}$ is the vector of time-averaged velocities from the LES computation, and σ is a the body force constant.

This body force term is defined using a temporal mean velocity of the LES solution. This temporal mean can be determined by a trailing time-window over which the LES solution is time-averaged. This allows to correct the mean velocity of the LES solution while allowing for temporal fluctuations due to fine scale turbulence. This preserves the resolved turbulence in the body force volume.

The choice of σ controls the characteristic response time of the LES solution to a change in the outlet boundary condition. If σ tends to zero, the body force becomes essentially ineffective resulting in a drift of the outflow mean velocity profile towards the unforced solution. High values of σ lead to faster change to the desired velocity field, but may lead to numerical instabilities.

3. Estimation of body force constant σ

Previously, we gave a crude estimate for σ from the bulk velocity and the length of the forcing region (Schlüter *et al.* 2002). We now want to provide a more accurate estimate for the choice of σ. This is carried out using a 1D analysis of the stationary Euler equations:

$$\frac{\partial u}{\partial t} + u\frac{\partial u}{\partial x} = -\frac{\partial p}{\partial x} + \sigma(\langle \bar{u} \rangle_{\mathrm{RANS}} - \langle \bar{u} \rangle_{\mathrm{LES}}) . \tag{3.1}$$

To simplify the equation, we assume a zero pressure gradient and a constant convection velocity u_B. Furthermore, we assume that the flow is stationary, which makes $\langle \bar{u} \rangle_{\mathrm{LES}} = u$. With $\langle \bar{u} \rangle_{\mathrm{RANS}} = u_t$, the target velocity Eq. 3.1 becomes:

$$u_B \frac{\partial u}{\partial x} = \sigma(u_t - u) . \tag{3.2}$$

This ordinary differential equation can be solved analytically and leads to the following expression for u:

$$u(x) = u_t + (u_0 - u_t) \exp\left(-\frac{\sigma}{u_B} x\right) \tag{3.3}$$

with u_0 being the velocity at the beginning of the forcing region.

We now want to determine σ so that at the end of the forcing region ($x = l_F$) the velocity difference is smaller than the relative error

$$\epsilon = \frac{|u(l_F) - u_t|}{u_t} . \tag{3.4}$$

Then, Eq. 3.3 leads to

$$\sigma_{\min} = \frac{u_B}{l_F} \ln\left(\frac{|u_0 - u_t|}{\epsilon u_t} \right) . \tag{3.5}$$

Although this estimate for σ ensures the accuracy of the approach for steady flows, in truly unsteady coupled computations a higher value for σ should be used in order to decrease the time-lag in which the flow solution adjusts to the target velocity obtained from an unsteady downstream computation.

On the upper end, σ is limited by numerical stability considerations. Here, it is useful

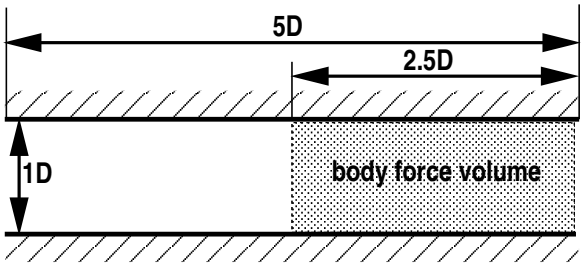

FIGURE 1. Geometry of the pipe test-case

to write σ as an inverse time-scale τ_F. The upper limit is then defined corresponding to the CFL-condition:

$$\sigma_{\max} = \left(\frac{1}{\tau_{\mathrm{F}}}\right)_{\max} = \frac{u_{\mathrm{c}}}{\Delta x_{\mathrm{F}}} \tag{3.6}$$

with Δx_{F} being the size of the smallest cell in the forcing region and u_{c} is the local convection velocity in this cell.

4. Assessment of body force constant

In the following section we want to assess the influence of this constant. For this purpose we consider a pipe flow with diameter D, and length $5D$. The virtual body force is applied in a volume of length $2.5\,D$ at the end of the pipe flow and is used to force the flow to a solution which would not naturally occur in this flow. This setup corresponds to the original investigation of the body force method (Schlüter *et al.* 2001).

For this investigation we use a structured LES flow solver (Pierce & Moin 1998). The flow solver solves the filtered momentum equations with a low-Mach number assumption on an axisymmetric structured mesh. A second-order finite-volume scheme on a staggered grid is used (Akselvoll & Moin 1996). The subgrid stresses are approximated with an eddy-viscosity approach. The eddy viscosity is determined by a dynamic procedure (Germano *et al.* 1991; Moin *et al* 1991). For numerical purposes a convective boundary condition is applied at the outlet plane of the LES domain.

The mesh for the pipe flow consists of $128\times32\times64$ cells. We consider a laminar flow at Reynolds-number $Re = 1000$.

Fig. 2 shows the results for a series of computations. The solid-crossed line shows the parabolic inlet profile corresponding to the solution of a fully-developed pipe flow. Without forcing, this would be the solution at any downstream location in the pipe. The circles denote an arbitrarily-chosen velocity profile, with the same mass flow rate as the inlet profile, which is to be matched at the outlet. Considering these two velocity profiles as the initial and the target velocity. For a desired accuracy of 1% ($\epsilon = 0.01$) this leads to:

$$\sigma_{\min} = \frac{1.0}{2.5} \cdot \ln\left(\frac{|2.0 - 0.75|}{0.01 \cdot 0.75}\right) = 2.05 \tag{4.1}$$

and

$$\sigma_{\max} = \frac{1.0}{\frac{5.0}{128}} = 25.6 \tag{4.2}$$

In order to show the robustness of the method to the choice of σ, several computations were performed with varying σ. Fig. 2 shows that with increasing σ the accordance of

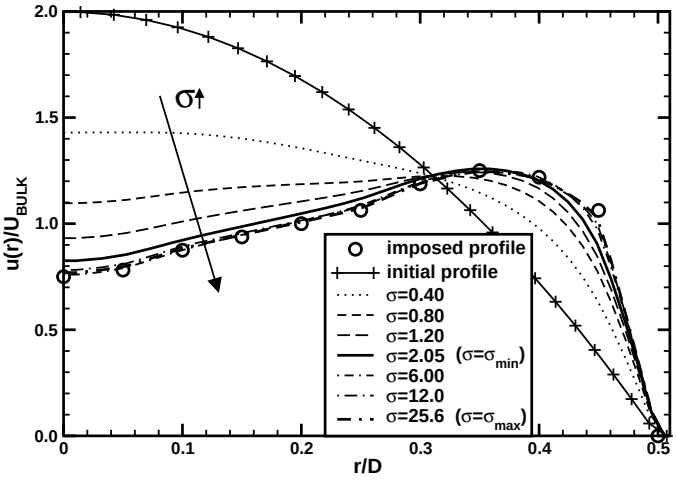

FIGURE 2. Laminar pipe flow: profiles of axial velocity at the outlet ($x/D = 5.0$) in dependance of body force constant σ. Solid lines with crosses: inlet profile. Symbols: imposed profiles. All other lines: LES solution at the outlet plane using different values of σ.

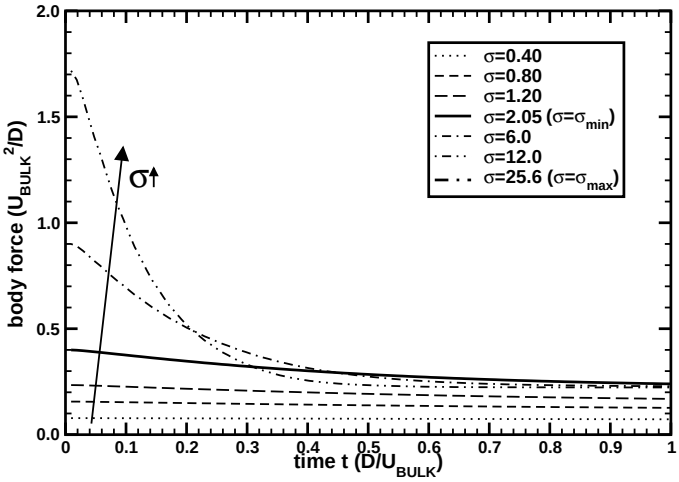

FIGURE 3. Laminar pipe flow: temporal development of body force in the outlet plane in dependance of body force constant σ.

the LES solution with the imposed profile improves. The solutions using $\sigma \geq \sigma_{\min}$ show satisfactory results. Computations using a $\sigma = 35.0 > \sigma_{\max}$ resulted in a diverging solution.

The temporal development of the body force dependent on the σ is shown in Fig. 3. Here, the spatial average of the body force in the outlet plane is computed and normalized with the bulk velocity and the diameter. Above the minimum σ the body force converges to the same residual body force that is needed to uphold the enforced velocity distribution. A higher body force allows the solution to converge in a shorter period of time.

5. Body force method for unstructured flow solvers

In order to prepare for integrated LES-RANS simulations of complex geometries, we implemented and validated the body force method in the unstructured LES flow solver CDP. Even though the underlying organization of an unstructured LES solver is more complex than a structured LES code, the local nature of the definition of the boundary treatment requires little additional work in for the porting process to unstructured solvers.

The LES flow solver used for this study is the CDP code (Ham *et al.* 2003; Moin & Apte 2004). The filtered momentum equations are solved on a cell-centered unstructured mesh and are second-order accurate. An implicit time-advancement is applied. The subgrid stresses are modeled with a dynamic procedure.

We want to validate the flow solver and the body force method on a swirl flow. Swirl is an important feature in combustor fluid dynamics, since it determines the mixing behavior as well as the evolving pressure field in the combustor. Its complexity and sensitivity to small changes makes it a challenging test-case.

The considered test-case corresponds to that of the experimental investigation of Dellenback *et al.* (Dellenback 1986; Dellenback *et al.* 1988). The geometry is a pipe with a sudden axisymmetric expansion with a ratio in diameters of 1:2 leading to a area ratio of 1:4. The Reynolds-number is $Re = 30,000$ and the swirl number $S = 0.6$ with S defined as:

$$S = \frac{1}{R} \frac{\int_0^R r^2 \langle \bar{u} \rangle_x \langle \bar{u} \rangle_\phi \, dr}{\int_0^R r \langle \bar{u} \rangle_x^2 \, dr}, \tag{5.1}$$

where u_x is the axial velocity component, u_ϕ the azimuthal velocity component, and R the radius of the nozzle. The LES inflow in the simulation was generated by using a swirling pipe flow database (Pierce & Moin 1998).

First, we will compute a reference LES solution using a computational domain sufficiently large to simulate this flow. This geometry will reach from $x/D = -0.5$ to $x/D = 10$ with the origin of the coordinate system at the center of the expansion. The comparison with experimental data will demonstrate the accuracy of the LES solver.

Then, we will compute a smaller domain by truncating the flow domain behind the expansion at $x/D = 1.5$. We will show that this domain is not sufficiently large to simulate this flow, since the influence of the outlet will disturb the flow solution.

Next, we will use a body force volume from $x/D = 1.1$ to $x/D = 1.5$ to drive the LES solution to the mean flow field as determined by the reference solution. We will show that the body force method is able to simulate the effect of the downstream domain.

Two different methods are used to determine the time-averaged LES solution $\overline{u}_{i,\mathrm{LES}}$ for Eq. 2.1. The first method uses an overall time-average using all available time-steps. This is the most accurate description for $\overline{u}_{i,\mathrm{LES}}$ for a statistically steady flow. However, we want to apply the integrated LES-RANS approach also to statistically unsteady flows. Hence, we will also use an average over a trailing time-window to determine $\overline{u}_{i,\mathrm{LES}}$, which allows for unsteadiness in the target solution.

Figure 4 shows the results of the reference solution. The LES solution (solid lines) matches well with the experimental data (symbols).

Figure 5 shows the axial velocity component for the simulations with the truncated domain. We can see that the simulations using a truncated domain without the body force (dashed lines) is disturbed by the proximity of the outflow and deviates from the reference solution. Using a body force (dotted lines and dashed dotted lines) corrects this

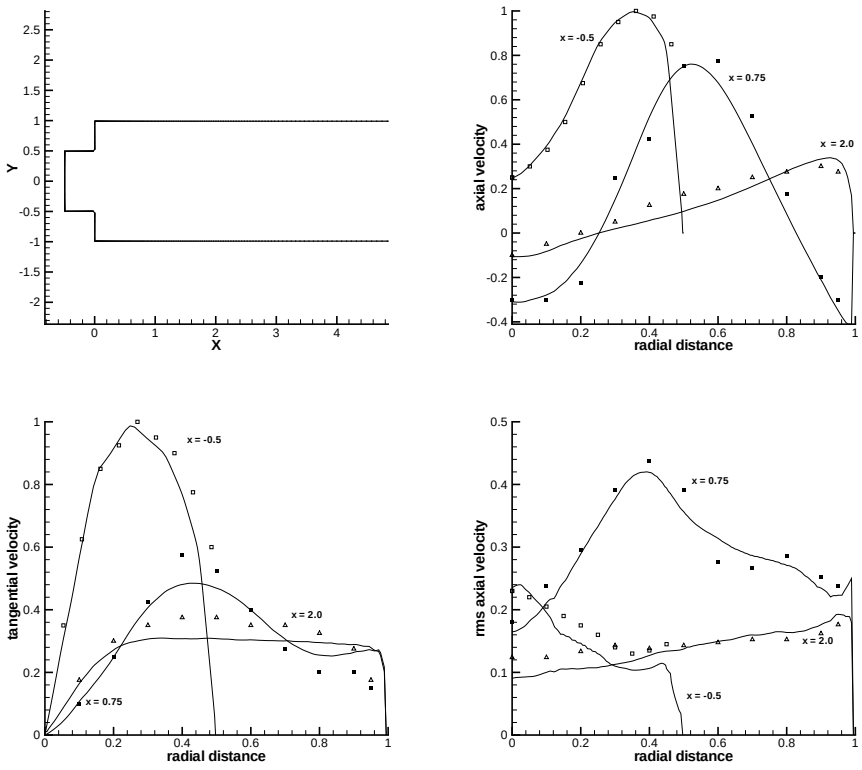

FIGURE 4. Geometry and velocities of a swirling flow through an sudden 1:2 axisymmetric expansion. Reference test case using sufficiently large computational domain. Symbols: experimental data. Solid lines: LES.

behavior and the solution tends towards the reference solution. We can also determine that the use of a trailing time-window for the determination of $\overline{u}_{i,\mathrm{LES}}$ is as accurate as the use of the overall mean.

Figure 6 shows the tangential velocity component for these simulations. The effect of the domain truncation and the correction using a body force are even more apparent.

The results demonstrate that the influence of the downstream flow development on the upstream flow can be simulated using the body force method.

6. Conclusions

For integrated LES-RANS simulations the body force method has been previously developed in order to modify the LES outflow to take the flow development downstream of the LES domain into account.

Here, we gave an estimate for the body force constant σ based on a 1D Euler analysis. We tested the influence of the body force constant on a simple test-case. Furthermore, we implemented the body force method into an unstructured LES solver. The implementation allows to move towards the computation of complex geometries with the integrated LES-RANS approach.

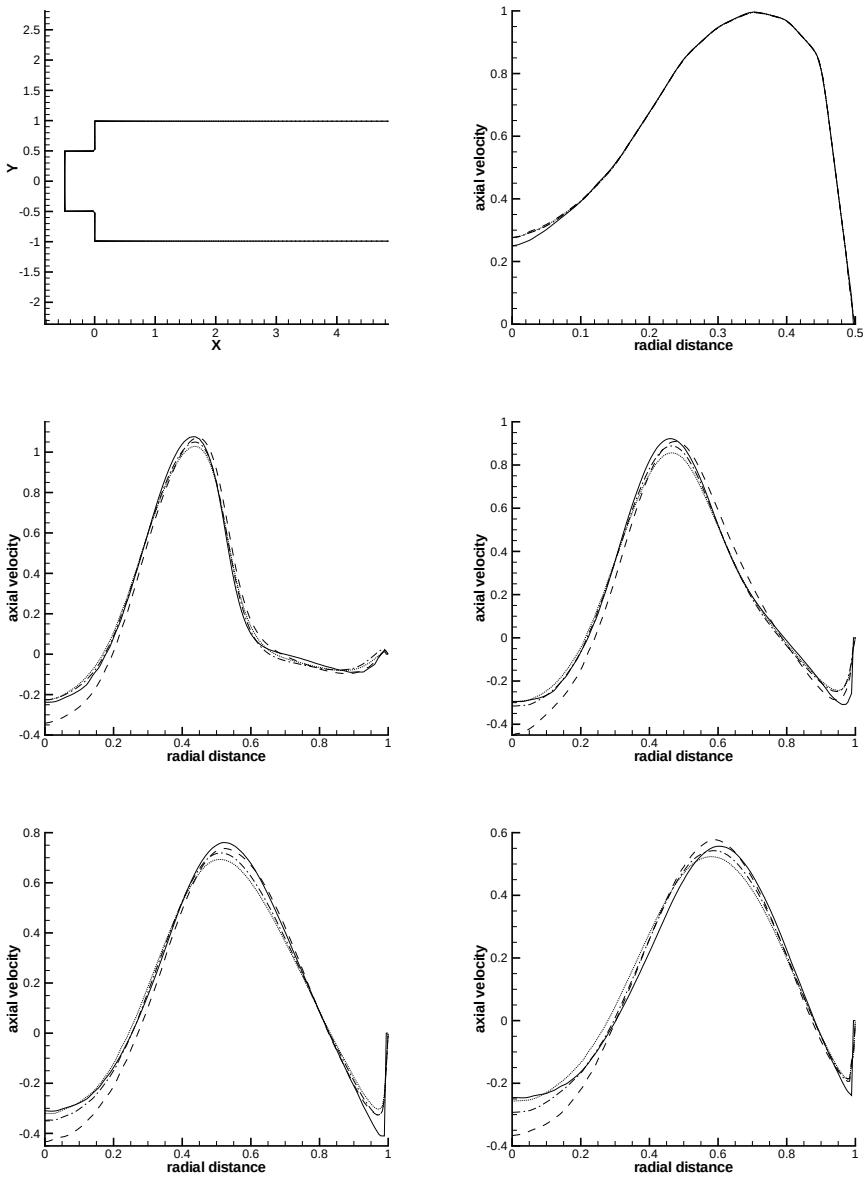

FIGURE 5. Influence of body force on flow development: axial velocity component Solid lines: reference solution using full geometry. Dashed lines: geometry truncated at x=1.5, no body force used. Dotted lines: geometry truncated at x=1.5 using body force scheme with trailing time window. Dash-dotted lines: geometry truncated at x=1.5 using body force scheme without trailing time window. Results are for x=-0.49, 0.25, 0.5,0.75 and 1.0, respectively (row major).

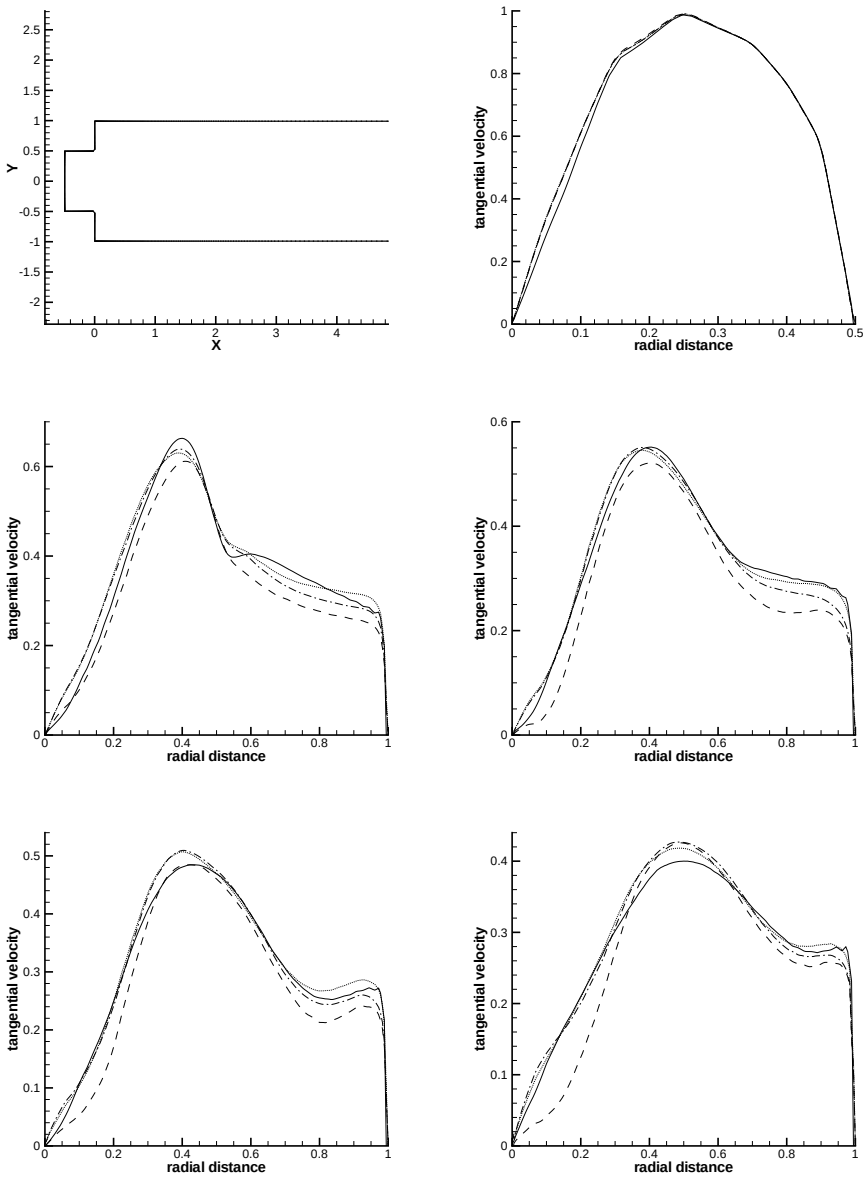

FIGURE 6. Influence of body force on flow development: azimuthal velocity component Solid lines: reference solution using full geometry. Dashed lines: geometry truncated at x=1.5, no body force used. Dotted lines: geometry truncated at x=1.5 using body force scheme with trailing time window. Dash-dotted lines: geometry truncated at x=1.5 using body force scheme without trailing time window. Results are for x=-0.49, 0.25, 0.5,0.75 and 1.0, respectively (row major).

These are important steps toward the use of integrated LES-RANS to applications of industrial relevance.

7. Acknowledgments

We wish to thank the US Department of Energy for the support under the ASC program.

We want to thank Dr. Frank Ham for the support using the LES flow solver CDP.

REFERENCES

AKSELVOLL, K., & MOIN, P. 1996 Large-eddy simulation of turbulent confined coannular jets. *J. of Fluid Mech.*, **315**, 387–411.

DELLENBACK, P. A., METZGER, D. E. & NEITZEL, G. P 1988 Measurements in turbulent swirling flow through an abrupt axisymmetric expansion. *AIAA J.*, **26**, 669-681.

DELLENBACK, P. A. 1986 *Heat transfer and velocity measurements in turbulent swirling flows through an abrupt axisymmetric expansion.* PhD thesis, Arizona State University.

GERMANO, M., PIOMELLI, U., MOIN, P. & CABOT, W., 1991 A dynamic subgrid-scale eddy viscosity model. *Phys. Fluids* A **(3)**, 1760-1765.

HAM, F., APTE, S., IACCARINO, G., WU, X., HERRMANN, M., CONSTANTINESCU, G., MAHESH, K., MOIN, P. 2003 Unstructured LES of reacting multiphase flows in realistic gas turbine combustors. *CTR Annual Research Briefs*, pages 139–160, 2004. Center for Turbulence Research, Stanford.

MOIN, P., SQUIRES, K., CABOT, W. & LEE, S. 1991 A dynamic subgrid-scale model for compressible turbulence and scalar transport. *Phys. Fluids*, A **(3)**, 2746-2757.

MOIN, P., APTE, S. 2004 Large-eddy simulation of realistic gas turbine combustors. *AIAA Paper*, (AIAA 2004-0330), January 2004.

SCHLÜTER, J. U., PITSCH, H. 2001 Consistent boundary conditions for integrated LES/RANS simulations: LES outflow conditions. *CTR Annual Research Briefs*, pages 19–30, 2001. Center for Turbulence Research, Stanford.

SCHLÜTER, J. U., PITSCH, H., MOIN, P., 2002 Consistent boundary conditions for integrated LES/RANS simulations: LES outflow conditions. *AIAA paper* 2002-3121

SCHLÜTER, J., SHANKARAN, S., KIM, S., PITSCH, H., ALONSO, J. J., 2003 Towards multi-component analysis of gas turbines by CFD: integration of RANS and LES flow solvers. *ASME paper*, (ASME GT2003-38350), 2003. ASME Turbo Expo 2003, June 16-19, 2003, Atlanta, GA.

SCHLÜTER, J. U., WU, X., KIM, S., ALONSO, J. J., PITSCH, H. 2004A A framework for coupling Reynolds-averaged with large eddy simulations for gas turbine applications. *Journal of Fluids Engineering*, submitted, 2004.

SCHLÜTER, J. U., WU, X., KIM, S., ALONSO, J. J., PITSCH, H. 2004B Integrated RANS-LES computations of gas turbines: Compressor-diffuser. *AIAA Paper*, (AIAA 2004-0369), January 2004.

SCHLÜTER, J. U., WU, X., KIM, S., ALONSO, J. J., PITSCH, H. 2004C Coupled RANS-LES Computation of a Compressor and Combustor in a Gas Turbine Engine. *AIAA Paper*, (AIAA 2004-3417), July 2004.

SCHLÜTER, J. U., WU, X., KIM, S., ALONSO, J. J., PITSCH, H. 2004D Integrated RANS-LES of a realistic compressor and combustor in a gas turbine engine *CTR Annual Research Briefs*, 2004. Center for Turbulence Research, Stanford.

SCHLÜTER, J. U., PITSCH, H., MOIN, P., 2004E Outflow conditions for integrated Large-Eddy simulation/Reynolds-averaged Navier-Stokes simulations. *AIAA J.* accepted, to appear 2004.

PIERCE, C. D. & MOIN, P. 1998 Method for generating equilibrium swirling inflow conditions. *AIAA J.*, **36**, 1325-1327.

Integrated RANS-LES of a realistic gas turbine compressor/combustor assembly

By J. U. Schlüter, X. Wu, S. Kim, J. J. Alonso AND H. Pitsch

1. Motivation and objectives

In the development of a gas turbine, computational fluid dynamics (CFD) is usually used to predict the flow in single components of the engine, such as the compressor, the combustor, or the turbine. The simulation of the *entire* flow path of a gas turbine engine using today's flow solvers is prohibited by the enormous computational costs. However, the increasing computational resources and the improved efficiency of future flow solvers puts the simulation of an entire engine within reach. In order for such a simulation to be useful in the design process, it has to deliver accurate results within a reasonable turnover time.

The goal of the Advanced Simulation and Computing (ASC) program of the Department of Energy (DoE) at Stanford is to develop high-performance flow solvers which are able to use highly parallel super-computers for the simulation of the entire flow path in an aircraft engine. However, considering the wide variety of the flow phenomena, which have to be simulated in the flow path of the engine, it is obvious that only the use of multiple specialized flow solvers, one for the turbo-machinery parts and one for the combustor, can guarantee appropriate efficiency and accuracy of a simulation. The reason for this is that the flow regimes and the turbulent scales vary dramatically in these two components. Most flow solvers used nowadays in the engine design process are specialized for one of the two tasks.

The flow field in the turbomachinery portions of the domain is characterized by both high Reynolds-numbers and high Mach-numbers. The accurate prediction of the flow requires the precise description of the turbulent boundary layers around the rotor and stator blades, including tip gaps and leakage flows. A number of flow solvers that have been developed to deal with this kind of problems have been in use in industry for many years. These flow solvers are typically based on the Reynolds-Averaged Navier-Stokes (RANS) approach. Due to the complexity of the flows in turbo-machinery, various parameters in the required turbulence models have to be adapted in order to provide accurate solutions. For turbomachinery flows, these parameters are usually well known, and hence, the flow solvers deliver reasonably good results.

The flow in the combustor, on the other hand, is characterized by detached flows, chemical reactions and heat release. The prediction of detached flows and free turbulence is greatly improved using flow solvers based on Large-Eddy Simulations (LES). While the use of LES increases the computational cost, LES has been the only predictive tool able to simulate these complex flows consistently. LES resolves the large scale turbulent motions in time and space and only the influence of the smallest scales, which are usually more universal and hence, easier to represent, has to be modeled (Ferziger 1996; Sagaut 2002). Since the energy containing part of the turbulent scales is resolved, a more accurate description of scalar mixing is achieved, leading to improved predictions of the combustion process (Veynante & Poinsot 1996). LES flow solvers have been shown in the past to be

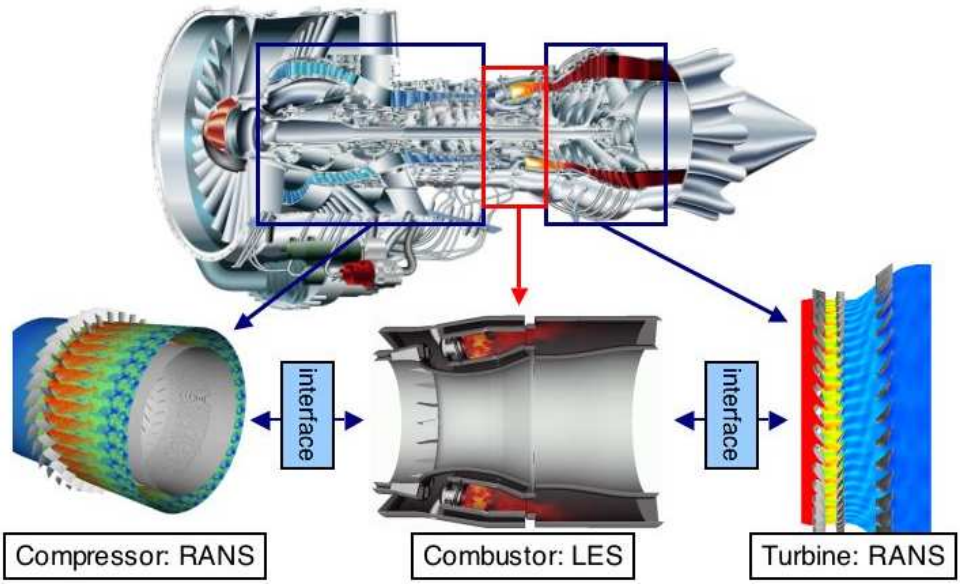

FIGURE 1. Decomposition of the engine for flow simulations. Compressor (Schlüter *et al.* 2004c) and turbine (Davis *et al.* 2002) with RANS; Combustor with (LESMoin & Apte 2004).

able to model simple flames and are currently adapted for use in gas turbine combustors (Poinsot *et al.* 2001; Constantinescu *et al.* 2003).

Here, we want to predict multi-component effects, such as compressor-combustor instabilities, combustor-turbine hot-streak migration and combustion instabilities. The flow solvers describing the different components in the gas turbine have to run simultaneously, each computing a part of the domain, and periodically exchanging flow information at the interface (Fig. 1). The simultaneous execution of multiple parallel flow solvers requires the definition of an interface which allows for the exchange of flow information and a framework for well-posed boundary conditions in order to process the exchanged data.

The approach to couple multiple simulation codes has already been applied in different fields, most notably in global climate simulations (Trenberth 1992), and found recently more attention in other areas of mechanical engineering (Adamis *et al.* 1998). However, coupling RANS and LES flow solvers is a very recent approach and a unique method to construct an LES-RANS hybrid. While other LES-RANS hybrid approaches, such as Detached-Eddy Simulations (DES) (Spalart 2000) and Limited-Numerical Scales (LNS) (Batten *et al.* 2002) combine LES and RANS in a single flow solver, the approach to couple two existing flow solvers has the distinct advantage to build upon the experience and validation that has been put into the individual codes during their development, and also to run simulations in different domains at different time-steps.

In the current study we are presenting the coupling approach and apply it to a compressor-prediffuser geometry of a real Pratt & Whitney aircraft gas turbine engine. The interface between compressor and combustor constitutes the upstream interface of a full engine simulation (Fig. 1). The flow leaving the compressor enters first into the prediffuser of the combustor. The function of the prediffuser is to decelerate the flow with a maximum of pressure gain (Klein 1995). For this reason, prediffusers are operated close to the point of flow separation. The flow conditions in the prediffuser ultimately

influence the flow split in the combustor and determine the amount of air entering the combustion chamber through the fuel injector. Although the performance of the diffuser is influenced by the flow field leaving the compressor (Barker & Carrotte 2001a; Barker & Carrotte 2001b), little is known about the exact flow features at this location during the design phase of an engine. The reason for this is that the two components are usually developed in isolation and combined tests are done only in the final prototype assembly.

Here, we will apply the approach of multiple flow solvers to study the flow interactions between these two components. A RANS flow solver computing the final stage of the compressor is coupled with an LES flow solver computing the combustor. The flow in the turbomachinery parts is compressible and governed by the flow around the blades. Hence, a RANS flow solver is an appropriate tool to assess the flow in this section. On the other hand, the prediction of flow separation is facilitated in the LES approach. And while the flow in the current design is not separated, predictions of design modifications have to be able to assess these flow features accurately.

The present paper is organized in the following way:

(*a*) Firs, we describe the RANS and LES flow solvers as well as the interface and the boundary conditions.

(*b*) Then, the application of this approach to a generic compressor/diffuser geometry is shown.

(*c*) Finally, the approach is applied to a real Pratt & Whitney gas turbine engine geometry.

2. Flow Solvers and Interface

In the following we briefly present the computational framework of this study consisting of the flow solvers and the interface. A more comprehensive description of the interface can be found in Schlüter *et al.* (2003b) and Schlüter *et al.* (2004d).

2.1. *RANS Flow Solver*

The RANS flow solver used for this investigation is the TFLO code developed at the Aerospace Computing Lab (ACL) at Stanford. The flow solver computes the unsteady Reynolds Averaged Navier-Stokes equations using a cell-centered discretization on arbitrary multi-block meshes (Yao *et al.* 2000). The solution procedure is based on efficient explicit modified Runge-Kutta methods with several convergence acceleration techniques such as multi-grid, residual averaging, and local time-stepping. These techniques, multigrid in particular, provide excellent numerical convergence and fast solution turnaround. Turbulent viscosity is computed from a $k-\omega$ two-equation turbulence model. The dual-time stepping technique (Jameson 1991; Alonso *et al.* 1995; Belov *et al.* 1996) is used for time-accurate simulations that account for the relative motion of moving parts as well as other sources of flow unsteadiness.

2.2. *LES Flow Solver*

The LES flow solver used for the current study is the CDP code developed at the Center for Turbulence Research (CTR) at Stanford. The filtered momentum equations are solved on a cell-centered unstructured mesh and are second-order accurate. An implicit time-advancement is applied. The subgrid stresses are modeled with a dynamic procedure.

2.3. *Interface*

Part of the efforts to integrate these flow solvers is the definition of the interface. The optimization of the communication and the processing of the exchanged data to meaningful boundary conditions are some of the challenges encountered. In previous work interface routines have been established and validated with simple geometries (Shankaran *et al.* 2001; Schlüter *et al.* 2003c; Schlüter *et al.* 2004d).

The interface used for establishing a connection between the flow solvers consists of routines following an identical algorithm in all flow solvers. The message passing interface MPI is used to create communicators, which are used to communicate data directly between the individual processors of the different flow solvers. This means that each processor of one flow solver can communicate directly with all of the processors of the other flow solvers. This requires the interface routines to be part of the source code of all flow solvers. A detailed description of the common algorithms can be found in Schlüter *et al.* (2003a) and Schlüter *et al.* (2004d).

In a handshake routine, each processor determines whether its domain contains points on the interface. The location of these points are sent to all processors of the other peer flow solvers. The processors of the peer flow solvers then determine and communicate back, whether the received points are within their own domain. During the actual flow computation all processors communicate data for a common point directly with each other.

The approach of embedding the interface into the source code of each flow solver has been chosen for its efficiency in the communication process. Alternative solutions would be to use a third code, which organizes the communication between the flow solvers, or to limit the peer-to-peer communication to the root processes of each flow solver. While the latter two solutions are usually easier to implement, they cause more communication processes and slow down the computation.

2.4. *Boundary Conditions*

The definition of the boundary conditions requires special attention, especially on the LES side, due to the different physical modeling approaches. Since on the LES side a part of the turbulent energy spectrum is resolved, the challenge is to regenerate and preserve the turbulence at the boundaries. At the LES outflow, a body force method has been developed to impose RANS solutions at the outflow of the LES domain (Schlüter *et al.* 2002a; Schlüter *et al.* 2004b).

At the LES inflow boundary, the challenge is to prescribe transient turbulent velocity profiles from ensemble-averaged RANS data. Simply adding random fluctuations to the RANS profiles miss the temporal and spatial correlations of real turbulence and are dissipated very quickly. Instead, a data-base of turbulent fluctuations is created by an auxiliary LES computation of a periodic turbulent pipe flow. The LES inflow boundary condition can then be described by scaling the data base solution to the RANS mean profiles and velocity fluctuations (Schlüter *et al.* 2004a).

On the RANS side, inlet and exit boundary condition are applied using the time-averaged solution from the LES side. More advanced boundary conditions are under investigation (Kim *et al.* 2004).

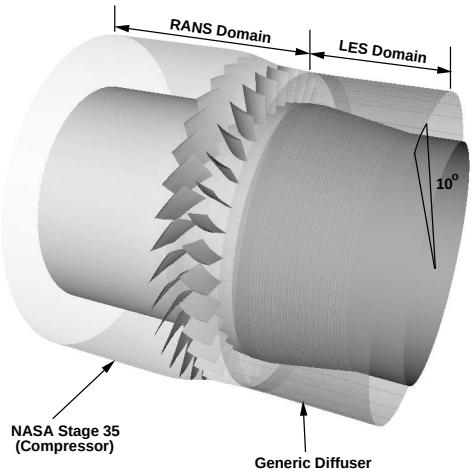

FIGURE 2. Geometry of coupled NASA stage 35/prediffuser domain.

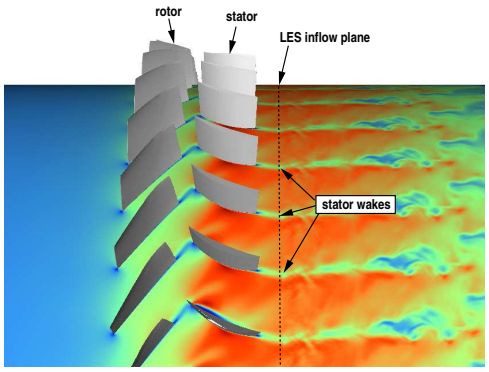

FIGURE 3. Integrated RANS-LES of compressor/prediffuser: Velocity distribution at the 50% plane. Close-up of the interface.

2.5. *Validation*

In the past, we have reported the validation of the flow solvers and the interface. The multi-block RANS flow solver TFLO has been in use for turbomachinery applications for several years. The description of the flow solver and some validation studies have been reported by Yao *et al.* (Yao *et al.* 1998; Yao *et al.* 2000). The unstructured LES flow solver CDP has been validated separately with a focus on combustor simulations (Ham *et al.* 2003; Moin & Apte 2004; Wu *et al.* 2004). The validation for the interface has been performed for integrated simulations on simplified geometries (Schlüter & Pitsch 2002b; Schlüter *et al.* 2003b; Schlüter *et al.* 2004d). The necessary boundary conditions for integrated simulations have been validated in detail (Schlüter *et al.* 2004a; Schlüter *et al.* 2004b; Kim *et al.* 2004).

3. Integrated RANS-LES of the NASA Stage 35/Diffuser

In this section we demonstrate the value of coupled RANS-LES computations for gas turbine applications. The test-case is that of the NASA Stage 35 compressor that we extended behind the stators with a diffuser. This geometry has been studied by Schlüter *et al.* (2003d ; 2004c). Previous studies have demonstrated the capability of the integrated RANS-LES approach to simulate this kind of geometry. Here, we want to focus on demonstrating the advantages such an approach may give in comparison to simulations of the single components.

3.1. *Geometry*

The compressor geometry for the computed test-case corresponds to that of a modified NASA Stage 35 experimental rig, which consists of a rotor with 46 rotor blades and a stator with 36 stators vanes. In order to simplify this geometry, the rotor stage has been rescaled to a 36 blade count, which allows to compute an axisymmetric segment of 10° using periodic boundary conditions at the corresponding azimuthal planes.

For this integrated computation, the rotor tip-gap has been closed in order to decrease the overall computational costs. The inclusion of the tip-gap is addressed in the TFLO

flow solver and poses no additional problem from the integration point of view. The RANS time step was chosen to resolve one blade passing with 50 intervals.

On the LES side, we use the structured LES flow solver developed at CTR. A more comprehensive description of the geometry, the mesh topology and the flow conditions, as well as some results on the main flow features (see also Fig. 3) can be found in Schlüter *et al.* (2003d).

Here, we assess the value of integrated RANS-LES simulations for this geometry. We will perform an integrated RANS-LES simulation of the entire domain. Then, we will use the computed flow field at the inlet of the diffuser to define the inflow boundary conditions for a separate, uncoupled LES simulation of the diffuser. The comparison of the integrated RANS-LES with the separate LES will give an insight on the importance of the flow development in the compressor on the diffuser flow.

3.2. *Results*

The integrated RANS-LES computations were carried out using 64 processors for TFLO and 16 processors for the structured LES flow solver. Eight blade passings were computed in 60 hours of wall clock time using an IBM Power3. The uncoupled LES computations were performed on 32 processors in 10 hours wall clock time computing a physical time-span equivalent to 5 blade passings.

Figure 4 compares the flow development in the diffuser for the two different simulations. The solid lines represent the uncoupled LES computation. The inlet velocity profile and the level of turbulence has been specified according to the time-averaged RANS solution at the outlet of the compressor. This solution has been retrieved from the integrated solution and is used to specify the inlet boundary conditions of an the uncoupled LES computation. The turbulence in this inlet plane is added to the mean velocity profile using the method of Schlüter *et al.* (2004d) using the identical turbulence inflow data base as in the integrated RANS-LES. The profiles of velocity fluctuations contain the turbulence modeled by the RANS turbulence model as well as the long-wave flow modulation, which is resolved in the RANS computation. The dashed lines are from the LES domain of the coupled RANS-LES computation, which means, that at each RANS time step the LES inflow is updated according to the unsteady solution in the compressor.

Comparing the velocity profiles at the inlet plane, we can see that both solutions are identical. However, further downstream both solutions are distinctively different.

The profiles of the velocity fluctuations show a similar behavior. At the inlet, both profiles are identical. Here, already shortly downstream, the velocity fluctuations are much larger in the integrated RANS-LES computation. This can be explained with the fact that in the integrated RANS-LES unsteady flow features from the compressor are transfered to the LES. This results in temporarily stronger gradients. The production of turbulence is determined as: $P = \overline{u_i' u_j'} \frac{\partial \bar{u}_i}{\partial x_j}$ and depends on these gradients. Hence, in the coupled RANS-LES simulation the RANS simulation does not only provide turbulent energy in its turbulence model, but also the potential to create more turbulence in the unsteady mean velocity gradients. In the current case, the additional turbulence production leads to a different turbulence field which results in a different mean flow field than in the uncoupled LES computation. This demonstrated that in the current case of the NASA Stage 35/diffuser the use of an integrated RANS-LES can improve the prediction of the diffuser flow.

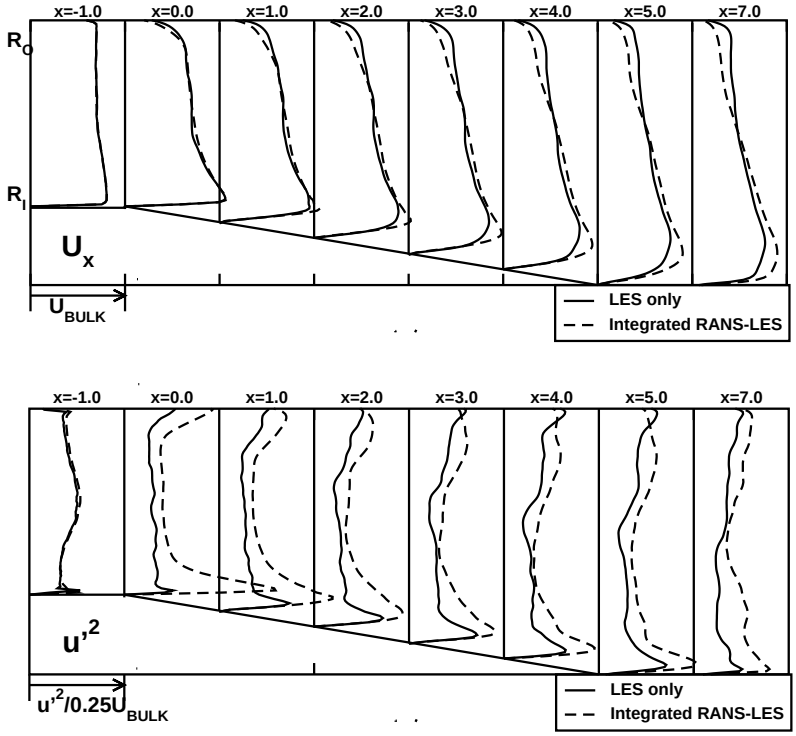

FIGURE 4. Velocity profiles in the diffuser; Solid lines: LES only; Dashed lines: RANS-LES; Above: axial velocity; Below: axial velocity fluctuations

3.3. *Pratt & Whitney Engine Geometry*

In the previous sections we presented the coupled RANS-LES approach and its application to a simplified compressor geometry. Here, we want to demonstrate this approach using a real engine geometry.

The geometry considered is that of a Pratt & Whitney aircraft engine (Fig. 5 & 6). Here, we present a simulation of the last stage of the high pressure compressor consisting of one rotor and the exit guide vanes (EGV) using the RANS approach. This RANS simulation is coupled with a LES of the prediffuser and the entire combustor. We chose to simulate the entire combustor including the fuel injector, since the flow blockage by the fuel injector and the resulting flow split is considered to be important for the performance of the diffuser (Barker & Carrotte 2001a; Barker & Carrotte 2001b; Klein 1995). However, the flow in the combustion chamber is non-reactive. The computation of reactive flows has been already demonstrated for this geometry (Moin & Apte 2004), but we consider it as not necessary for the purpose of the present demonstration.

The geometry is a 20° segment of the full engine geometry, which means that we compute one fuel injector. The blade count of the last stage of the compressor was rescaled to fit the 20° segment, and four rotor blades and seven exit guide vanes are computed in total. The RANS mesh consists of 500,000 cells in a structured multi-block mesh.

The complexity of the combustor geometry requires the use of the unstructured LES flow solver CDP. The combustor mesh consists of 3,000,000 unstructured mesh cells and

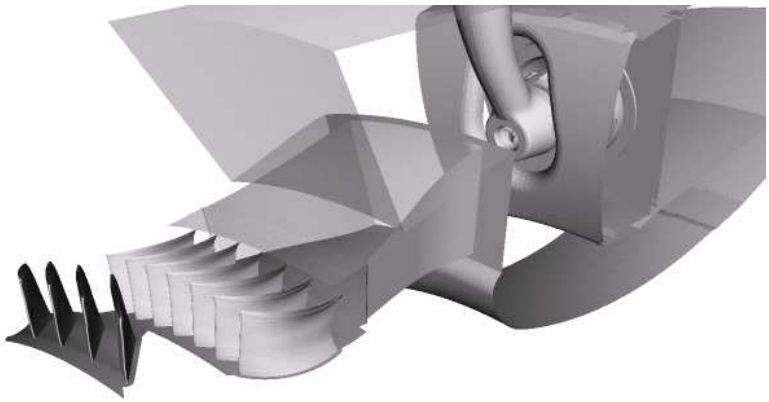

FIGURE 5. Geometry of Pratt & Whitney test case: In the front, the segment of the compressor (4 rotor blades, 7 exit guide vanes) is shown. The flow leaving the compressor enters the prediffuser box before it enters a plenum in front of the fuel injector.

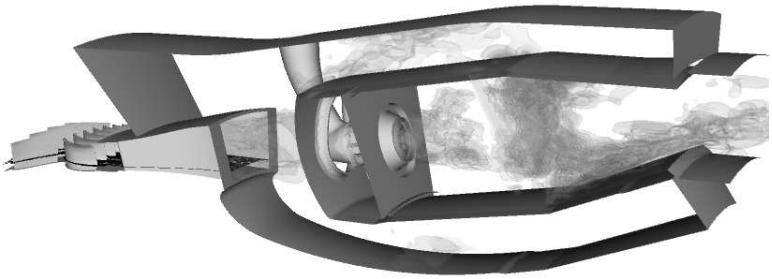

FIGURE 6. Geometry and flow visualization in the combustor. Note the compressor stage upstream of the diffuser. Smoke visualization demonstrates flow features of the cold flow.

is refined in the diffuser part. The mesh resolution in the prediffuser was chosen to correspond approximately to the coarse mesh resolution of the diffuser simulation (Wu *et al.* 2004).

The computation of 10 blade passings was performed using 128 processors on an IBM SP3. One blade passing needed 10 hours wall clock time. The entire computation was performed within one week.

Figures 7 and 8 show a flow visualization of this computation. For this visualization, the computed 20° segment is shown several times in different azimuthal locations in order to present a picture of a 360° engine. In the combustor, isosurfaces of the axial velocity demonstrate the level of detail of the flow simulation in the combustor. In the compressor and the prediffuser, a clip plane at 50% span of the exit guide vane (EGV) shows the axial velocity distribution. The most dominant flow feature at the interface is the propagation of the wakes of the EGV into the prediffuser. The wakes create large scale turbulent structures inside the prediffuser. Figure 9 shows a close-up of the axial velocity contours at the interface.

This computation of the Pratt & Whitney real engine geometry is the first of its kind. Simulations of this portion of a gas turbine usually encounter difficulties, either in the description of the compressor flow, which can be computed only by a RANS approach, or the representation of the diffuser flow, which needs to capture the possible presence of flow detachment accurately and is largely improved by the use of LES.

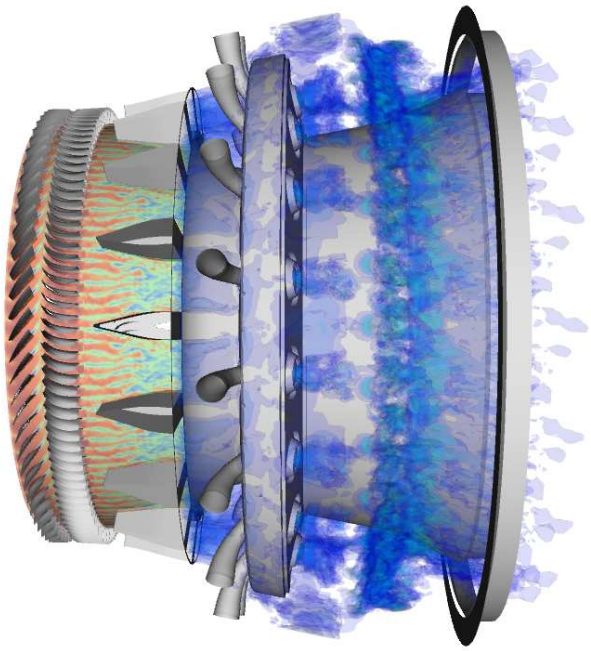

FIGURE 7. Isocontours of the axial velocity at the 50% plane in the compressor and diffuser. Isosurfaces of axial velocity in the combustor. A 20° segment is computed.

The current state-of-the-art in diffuser simulations uses either radial profiles obtained from experiments or steady state data from uncoupled RANS simulations of the compressor. The integrated simulation allows not only to obtain a more precise representation of the compressor flow, but also to simulate the geometries accurately without the need of input from experiments.

4. Conclusions

In this study we presented an approach to couple two separate flow solvers, one based on the RANS approach, the other based on LES, to improve flow predictions of complex flows. As an example, we investigated the flow leaving the compressor and entering the diffuser. We have validated the interface and the flow solvers extensively in previous studies. Here, we applied the multi-code coupling approach to a compressor-combustor geometry.

First, a computation of a simplified compressor/diffuser geometry demonstrated the basic flow features of such a geometry and showed the value of coupled RANS-LES for this application.

Then, the approach was applied to a real engine geometry. Basic flow features of this flow configuration were identified.

The integrated RANS-LES environment provides a computational test bench for the assessment of complex flow interactions, such as those of the compressor/combustor coupling in an aircraft gas turbine engine.

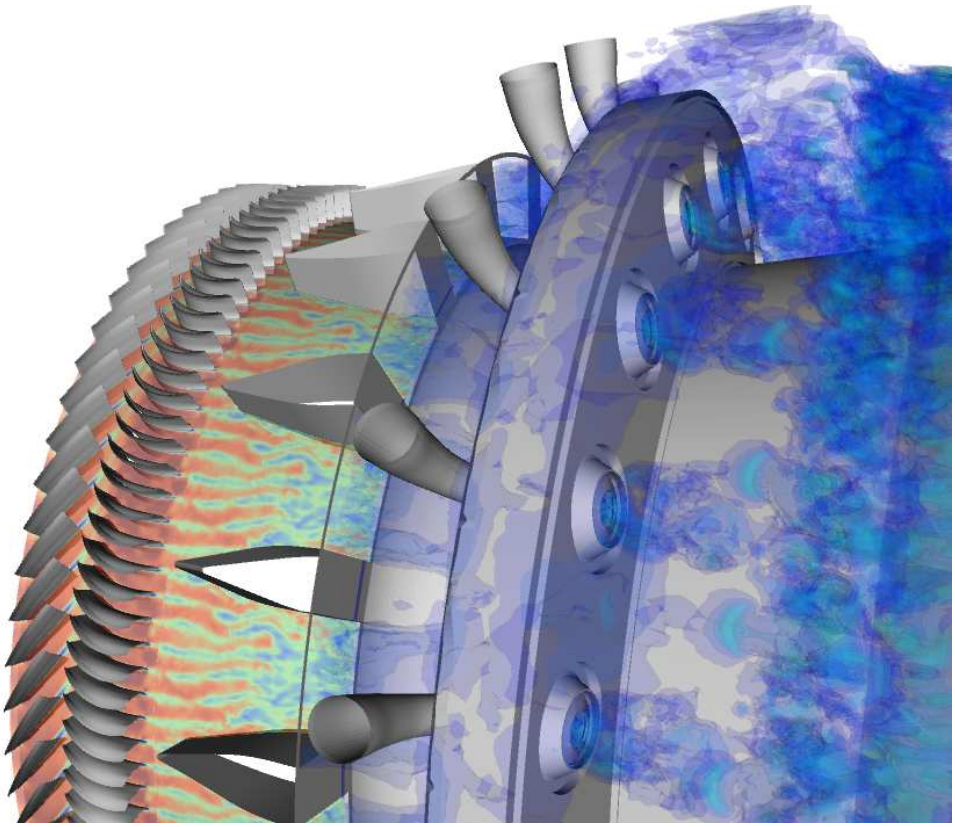

FIGURE 8. Close-up: Isocontours of the axial velocity at the 50% plane in the compressor and diffuser. Isosurfaces of axial velocity in the combustor. A 20° segment is computed.

5. Acknowledgments

We wish to thank the US Department of Energy for the support under the ASC program.

We also thank Dr. Saadat Syed, Dr. Jinzhang Feng and Dr. Stephen Krautheim from Pratt & Whitney for providing the engine geometry, helpful comments and discussions.

REFERENCES

ADAMIDIS P., BECK, A., BECKER-LEMGAU, U., DING, Y, FRANZKE, M., HOLTHOFF, H., LAUX, M., MÜLLER, A. MÜNCH, M., REUTER, A., STECKEL, B., TILCH, R. 1998 Steel strip production - a pilot application for coupled simulation with several calculation systems. *Journal of Materials Processing Technology*, (80-81):330–336, 1998.

J. J. ALONSO, L. MARTINELLI, AND A. JAMESON 1995 Multigrid unsteady Navier-Stokes calculations with aeroelastic applications. *AIAA Paper* 95-0048

BARKER, A. G., AND CARROTTE, J. F. 2001A Influence of compressor exit conditions on combustor annular diffusers, Part 1: Diffuser performance. *Journal of Propulsion and Power*, **17**, No. 3, 678-686.

BARKER, A. G., AND CARROTTE, J. F. 2001B Influence of compressor exit conditions

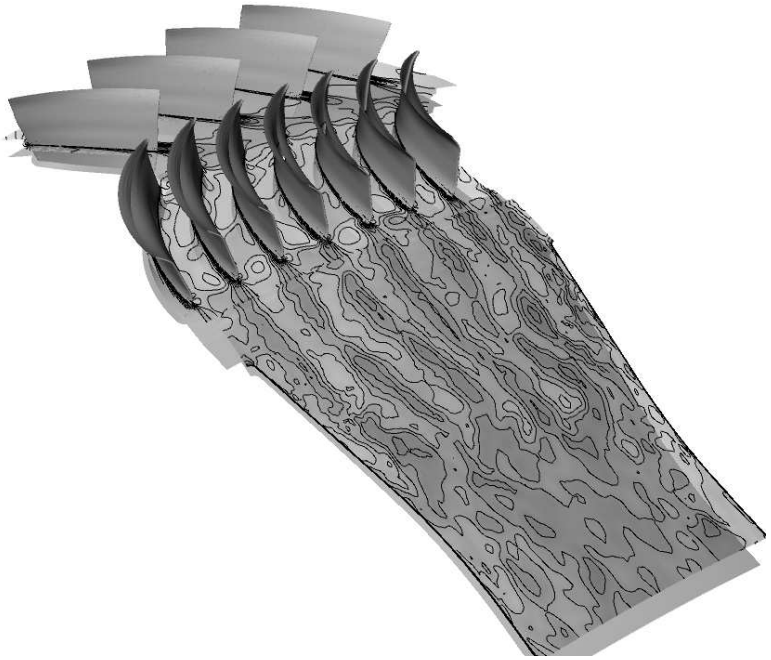

FIGURE 9. Isocontours of the axial velocity at the 50% plane in the compressor and diffuser. Close up of the interface.

on combustor annular diffusers, Part 2: Flow redistribution. *Journal of Propulsion and Power*, **17**, No. 3, 687-694.

BATTEN, P., GOLDBERG, U., CHAKRAVARTHY, S. 2002 LNS-an approach towards embedded LES. *AIAA paper*, (AIAA 2002-0427), 2002. 40th AIAA Aerospace Sciences Meeting and Exhibit, January 2002, Reno, NV.

A. BELOV, L. MARTINELLI, AND A. JAMESON 1996 Three-dimensional computations of time-dependent incompressible flows with an implicit multigrid-driven algorithm on parallel computers. In *Proceedings of the 15th International Conference on Numerical Methods in Fluid Dynamics, Monterey, CA*

CONSTANTINESCU, G., MAHESH, K., APTE, S., IACCARINO, G., HAM, F., AND MOIN, P. 2003 A new paradigm for simulation of turbulent combustion in realistic gas turbine combustors using LES. *ASME Turbo Expo 2003*, GT2003-38356, 2003.

DAVIS, R., YAO, J.,CLARK, J. P. , STETSON, G,ALONSO, J. J., JAMESON, A., HALDEMAN, C., AND DUNN, M. 2002 Unsteady interaction between a transsonic turbine stage and downstream components. *ASME Turbo Expo 2002*, GT-2002-30364.

FERZIGER, J. H. 1996 *New Tools in Turbulence Modelling*, volume New Tools in Turbulence Modelling of *Les edition physique*, chapter 2 Large eddy simulation: an introduction and perspective, pages 29–47. Springer, 1996.

GERMANO, M., PIOMELLI, U., MOIN, P. & CABOT, W., 1991 A dynamic subgrid-scale eddy viscosity model. *Phys. Fluids* A **(3)**, 1760-1765.

HAM, F., APTE, S., IACCARINO, G., WU, X., HERRMANN, M., CONSTANTINESCU, G., MAHESH, K., MOIN, P. 2003 Unstructured LES of reacting multiphase flows in realistic gas turbine combustors. *CTR Annual Research Briefs*, pages 139–160, 2004. Center for Turbulence Research, Stanford.

JAMESON, A. 1991 Time dependent calculations using multigrid, with applications to unsteady flows past airfoils and wings. *AIAA paper* 91-1596

KIM, S., SCHLÜTER, J. U., WU, X., ALONSO, J. J., PITSCH, H. 2004 Integrated simulations for multi-component analysis of gas turbines: RANS boundary conditions. *AIAA Paper*, (AIAA 2004-3415), July 2004.

KLEIN, A. 1995 Characteristics of combustor diffusers. *Prog. Aerospace Sci.*, 31:171–271, 1995.

MOIN, P., APTE, S. 2004 Large-eddy simulation of realistic gas turbine combustors. *AIAA Paper*, (AIAA 2004-0330), January 2004.

POINSOT, T., SCHLÜTER, J., LARTIGUE, G., SELLE, L., KREBS, W., HOFFMANN, S. 2001 Using large eddy simulations to understand combustion instabilities in gas turbines. *IUTAM Symposium on Turbulent Mixing and Combustion*, pages 1–8, 2001. Kingston, Canada 2001.

SAGAUT, S. 2002 *Large eddy simulation for incompressible flows.* Springer, Berlin, 2 edition, 2002.

SCHLÜTER, J. U., PITSCH, H., MOIN, P., 2002A Consistent boundary conditions for integrated LES/RANS simulations: LES outflow conditions. *AIAA paper* 2002-3121

SCHLÜTER, J., PITSCH, H. 2002B Integration of LES and RANS flow solvers: Interface validation. *CTR Annual Research Briefs*, 2002. Center for Turbulence Research, Stanford.

SCHLÜTER, J. U., PITSCH, H., MOIN, P., 2003A Boundary conditions for LES in coupled simulations. *AIAA paper*, (AIAA-2003-0069), 2003.

SCHLÜTER, J., SHANKARAN, S., KIM, S., PITSCH, H., ALONSO, J. J., 2003B Towards multi-component analysis of gas turbines by CFD: integration of RANS and LES flow solvers. *ASME paper*, (ASME GT2003-38350), 2003. ASME Turbo Expo 2003, June 16-19, 2003, Atlanta, GA.

SCHLÜTER, J., SHANKARAN, S., KIM, S., PITSCH, H., ALONSO, J. J., 2003C Integration of RANS and LES flow solvers for simultaneous flow computations. *AIAA paper*, (AIAA 2003-0085), 2003.

SCHLÜTER, J. U., WU, X., KIM, S., ALONSO, J. J., PITSCH, H. 2003D Integrated RANS-LES computations of turbomachinery components: Generic compressor/diffuser. *CTR Annual Research Briefs*, pages 357–368, 2003.

SCHLÜTER, J. U., PITSCH, H., MOIN, P., 2004A Large eddy simulation inflow conditions for coupling with Reynolds-averaged flow solvers. *AIAA Journal*, 42(3):478–484, March 2004.

SCHLÜTER, J. U., PITSCH, H., MOIN, P., 2004B Outflow conditions for integrated Large-Eddy simulation/Reynolds-averaged Navier-Stokes simulations. *accepted for publication to AIAA Journal*, 2004.

SCHLÜTER, J. U., WU, X., KIM, S., ALONSO, J. J., PITSCH, H. 2004C Integrated RANS-LES computations of gas turbines: Compressor-diffuser. *AIAA Paper*, (AIAA 2004-0369), January 2004.

SCHLÜTER, J. U., WU, X., KIM, S., ALONSO, J. J., PITSCH, H. 2004D A framework for coupling Reynolds-averaged with large eddy simulations for gas turbine applications. *Journal of Fluids Engineering*, submitted, 2004.

SHANKARAN, S., LIOU, M.-F., LIU, N.-S., DAVIS, R., ALONSO, J. J. 2001 A multi-code-coupling interface for combustor/turbomachinery simulations. *AIAA paper*, (AIAA 2001-0974), 2001.

SMAGORINSKY 1963 General circulation experiments with the primitive equations, I, the basic experiment. *Mon. Weather Rev.*, 91(3):99–152, 1963.

SPALART 1963 Trends in turbulence treatments. *AIAA paper*, (AIAA 2000-2306), 2000. Fluids 2000, June, Denver, CO.

TRENBERTH, K. E. 1992 *Climate System Modeling.* Cambridge, New York, 1992. chapter 9.

VEYNANTE, D., POINSOT, T. 1996 Reynolds averaged and large eddy simulation modeling for turbulent combustion. In *New Tools in Turbulence Modelling*, Les edition physique. Springer, pp 105–140

WU, X., SCHLÜTER, J., MOIN, P., PITSCH, H., IACCARINO, G, HAM, F., 2004 Identification of an internal layer in a diffuser. *CTR Annual Research Briefs*, 2004. Center for Turbulence Research, Stanford.

YAO, J., JAMESON, A., ALONSO, J. J., LIU, F. 2000 Development and validation of a massively parallel flow solver for turbomachinery flows. *AIAA paper* 00-0882

YAO, J., JI, S., LIU, F., JENNIONS, I. K. 1998 Computation of a steady flow in a turbomachinery stage by third-order accurate high-resolution scheme. *AIAA paper* 98-3561

Variational multiscale large eddy simulation of turbulent flows using a finite volume method

By V. Gravemeier

1. Motivation and objectives

The variational multiscale method represents a general approach for problems in computational mechanics which give rise to broad ranges of scales, see Hughes *et al.* (1998). The basic concept differentiates a predefined number of scale groups. This theoretical framework has also been applied to the problem of the incompressible Navier-Stokes equations in Hughes *et al.* (2000) in order to facilitate large eddy simulation (LES) of turbulent flows. In Collis (2001) and Gravemeier (2003), the variational multiscale method for LES has recently been broadened by raising the number of separated scale groups to three. Such a three-scale separation accounts specifically for large resolved scales, small resolved scales, and unresolved scales.

Apart from the initial separation and potentially different treatment of the respective scale ranges, two important aspects characterize the variational multiscale LES. Firstly, a variational projection separates scale ranges within the variational multiscale method rather than a spatial filter as in traditional LES. Secondly, the (direct) influence of the subgrid-scale model is confined to the small resolved scales. Thus, the large resolved scales are solved as a direct numerical simulation (DNS), i.e. without any (direct) influence of the modeling term. Of course, the large resolved scales are still influenced indirectly by the subgrid-scale model due to the inherent coupling of all scales.

At this stage, it should be pointed out that the variational multiscale method is essentially a theoretical framework for the separation of scales. Corresponding practical implementations within the variational multiscale framework are still rare. For such practical methods, it is crucial that a clear separation of the different scale ranges is actually achieved. The scale-separating approach developed in this work is implemented into the CDP-α code. Underlying this code is a finite volume method particularly suited for applications on unstructured grids. Please consult e.g. Ham *et al.* (2003) for further information concerning CDP-α. Within this computational environment, the separation of scales is developed in this work. A general class of scale-separating operators based on combined multigrid operators in a two-grid procedure is proposed here in order to replace spatial filters or their discrete analogs, respectively, which are widely used in classical LES. One particular representative of this class has the important property of a projector. A projector of this type has also been addressed in Koobus & Farhat (2004) as well as Vreman (2004).

The proposed methods of this work are applied to the case of a turbulent channel flow and compared to the DNS data in Moser *et al.* (1999). Turbulent channel flow has already served as one of the first test cases for variational multiscale LES in Hughes *et al.* (2001). That study was later complemented by Oberai & Hughes (2002) reporting the case $Re_\tau = 590$. A further study in Jeanmart & Winckelmans (2002) compares the subgrid-scale modeling approach of the variational multiscale method with other modeling approaches in the context of a turbulent channel flow. All of the aforementioned studies have one

important aspect in common: the use of a spectral method with higher-order accuracy in the homogeneous x_1-x_3-planes of the channel. In this work, the method applied is of second-order accuracy overall without any special treatment for the homogeneous planes of the channel. With regard to future applications in more complex geometries, performance of the variational multiscale LES within such a numerical environment is the more relevant test case, since spectral methods are by no means suited to such applications. The introduction of a generally larger numerical error due to the use of a second-order accurate method, combined with a relatively coarse discretization, has been investigated in Kravchenko & Moin (1997) at a high Reynolds number channel flow ($Re_\tau = 1000$). Similar evaluations have also been reported in Shah & Ferziger (1995) for a flow at very high Reynolds number $Re_\tau = 1800$ as well as in Terracol *et al.* (2001) for flows at Reynolds numbers $Re_\tau = 180$ and $Re_\tau = 590$.

This work basically follows the general guideline expressed in the idea that there exists an inherent link between, on the one hand, *physically motivated turbulence modeling* and, on the other hand, *numerically motivated modeling to account for inevitable errors due to an inadequate discretization*. A combined strategy relying on this observation has already been pointed out as a very promising tool in Collis (2001) and Gravemeier (2003). A detailed study of the approach to be presented in this work has recently been completed in Gravemeier (2004).

2. Variational three-scale formulation

A variational form of the incompressible Navier-Stokes equations reads

$$B_{NS}\left(\mathbf{v},q;\mathbf{u},p\right) = \left(\mathbf{v},\mathbf{f}\right)_\Omega \qquad \forall\left(\mathbf{v},q\right) \in \mathcal{V}_{\mathbf{u}p} \tag{2.1}$$

where $\mathcal{V}_{\mathbf{u}p}$ denotes the combined form of the weighting function spaces for velocity and pressure in the sense that $\mathcal{V}_{\mathbf{u}p} := \mathcal{V}_{\mathbf{u}} \times \mathcal{V}_p$. The bilinear form $B_{NS}\left(\mathbf{v},q;\mathbf{u},p\right)$ on the left hand side is hereby defined as

$$\begin{aligned} B_{NS}\left(\mathbf{v},q;\mathbf{u},p\right) = & \int_\Omega \mathbf{v}\frac{\partial \mathbf{u}}{\partial t}\,\mathrm{d}\Omega + \int_\Omega \mathbf{v}\nabla\cdot\left(\mathbf{u}\otimes\mathbf{u}\right)\,\mathrm{d}\Omega + \int_\Omega \mathbf{v}\nabla p\,\mathrm{d}\Omega \\ & - \int_\Omega \mathbf{v}\nu\Delta\mathbf{u}\,\mathrm{d}\Omega - \int_\Omega q\nabla\cdot\mathbf{u}\,\mathrm{d}\Omega \end{aligned} \tag{2.2}$$

where $\mathbf{v}$ and q denote the weighting functions. The L_2-inner product in the domain Ω on the right hand side is defined as usual:

$$\left(\mathbf{v},f\right)_\Omega = \int_\Omega \mathbf{v}f\,\mathrm{d}\Omega \tag{2.3}$$

The scales of the problem are now separated into three scale ranges as proposed in Collis (2001), Gravemeier (2003), and Gravemeier *et al.* (2004): the large resolved scales, small resolved scales, and unresolved scales. In terms of the underlying weighting and solution function spaces $\mathcal{V}_{\mathbf{u}p}$ and $\mathcal{S}_{\mathbf{u}p}$, this scale separation yields

$$\mathcal{V}_{\mathbf{u}p} = \overline{\mathcal{V}}_{\mathbf{u}p} \otimes \mathcal{V}'_{\mathbf{u}p} \otimes \hat{\mathcal{V}}_{\mathbf{u}p} \tag{2.4}$$

$$\mathcal{S}_{\mathbf{u}p} = \overline{\mathcal{S}}_{\mathbf{u}p} \otimes \mathcal{S}'_{\mathbf{u}p} \otimes \hat{\mathcal{S}}_{\mathbf{u}p} \tag{2.5}$$

According to this, the weighting functions read

$$\mathbf{v} = \overline{\mathbf{v}} + \mathbf{v}' + \hat{\mathbf{v}}; \quad q = \overline{q} + q' + \hat{q} \tag{2.6}$$

and, analogously, the solution functions are composed as

$$\mathbf{u} = \overline{\mathbf{u}} + \mathbf{u}' + \hat{\mathbf{u}}; \quad p = \overline{p} + p' + \hat{p} \tag{2.7}$$

Due to the linearity of the weighting functions, the variational equation (2.1) may now be decomposed into a system of three variational equations reading

$$B_{NS}\left(\overline{\mathbf{v}}, \overline{q}; \overline{\mathbf{u}} + \mathbf{u}' + \hat{\mathbf{u}}, \overline{p} + p' + \hat{p}\right) = \left(\overline{\mathbf{v}}, \mathbf{f}\right)_\Omega \qquad \forall \left(\overline{\mathbf{v}}, \overline{q}\right) \in \overline{\mathcal{V}}_{\mathbf{u}p} \tag{2.8}$$

$$B_{NS}\left(\mathbf{v}', q'; \overline{\mathbf{u}} + \mathbf{u}' + \hat{\mathbf{u}}, \overline{p} + p' + \hat{p}\right) = \left(\mathbf{v}', \mathbf{f}\right)_\Omega \qquad \forall \left(\mathbf{v}', q'\right) \in \mathcal{V}'_{\mathbf{u}p} \tag{2.9}$$

$$B_{NS}\left(\hat{\mathbf{v}}, \hat{q}; \overline{\mathbf{u}} + \mathbf{u}' + \hat{\mathbf{u}}, \overline{p} + p' + \hat{p}\right) = \left(\hat{\mathbf{v}}, \mathbf{f}\right)_\Omega \qquad \forall \left(\hat{\mathbf{v}}, \hat{q}\right) \in \hat{\mathcal{V}}_{\mathbf{u}p} \tag{2.10}$$

Furthermore, it is assumed that

$$B_{NS}\left(\overline{\mathbf{v}}, \overline{q}; \hat{\mathbf{u}}, \hat{p}\right) \approx 0 \tag{2.11}$$

relying on a clear separation of the large-scale space and the space of unresolved scales. Likewise, the opposite projection is assumed to be

$$B_{NS}\left(\hat{\mathbf{v}}, \hat{q}; \overline{\mathbf{u}}, \overline{p}\right) \approx 0 \tag{2.12}$$

This leads to a simplified equation system by changing (2.8) to

$$B_{NS}\left(\overline{\mathbf{v}}, \overline{q}; \overline{\mathbf{u}} + \mathbf{u}', \overline{p} + p'\right) = \left(\overline{\mathbf{v}}, \mathbf{f}\right)_\Omega \qquad \forall \left(\overline{\mathbf{v}}, \overline{q}\right) \in \overline{\mathcal{V}}_{\mathbf{u}p} \tag{2.13}$$

and (2.10) to

$$B_{NS}\left(\hat{\mathbf{v}}, \hat{q}; \mathbf{u}' + \hat{\mathbf{u}}, p' + \hat{p}\right) = \left(\hat{\mathbf{v}}, \mathbf{f}\right)_\Omega \qquad \forall \left(\hat{\mathbf{v}}, \hat{q}\right) \in \hat{\mathcal{V}}_{\mathbf{u}p} \tag{2.14}$$

whereas (2.9) remains unchanged.

It is not intended to resolve anything called unresolved *a priori*. Taking into account the effect of the unresolved scales onto the small scales is the only desire. Some alternatives lend themselves for this purpose as shown in Gravemeier (2003), but the focus here will be on the subgrid viscosity approach as a usual and well-established way of taking into account the effect of unresolved scales in classical LES. The small-scale equation (2.9) then reads

$$B_{NS}\left(\mathbf{v}', q'; \overline{\mathbf{u}} + \mathbf{u}', \overline{p} + p'\right) - \left(\mathbf{v}', \nu^T \Delta \mathbf{u}'\right)_\Omega = \left(\mathbf{v}', \mathbf{f}\right)_\Omega \qquad \forall \left(\mathbf{v}', q'\right) \in \mathcal{V}'_{\mathbf{u}p} \tag{2.15}$$

Due to assumption (2.11), the subgrid viscosity term directly acts only on the small resolved scales. Indirect influence on the large resolved scales, however, is ensured due to the coupling of the large- and the small-scale equations. Appropriate modeling approaches for the subgrid viscosity ν^T will be discussed in section 4. Note that the reason for introducing a model term in the variational formulation is mathematically different from the usual necessity of introducing a model term due to the appearance of a subgrid-scale stress tensor in the strong formulation of the Navier-Stokes equations in a classical LES. Nevertheless, the physical necessity to account for the missing effect of unresolved scales onto the resolved scales is the same in both cases.

The variational equations above may serve as the starting point for either a finite element formulation or a finite volume formulation, but the focus here is on the finite volume method. The presupposition for the application of the finite volume method is a discretization of the domain Ω into n_{cv} control volumes Ω_i $(i = 1, ..., n_{cv})$ with control volume boundaries Γ_i. The weighting functions are chosen to be

$$\mathbf{v}^h = \sum_i \mathbf{v}_i^h; \quad q^h = \sum_i q_i^h \tag{2.16}$$

where

$$\mathbf{v}_i^h = \mathbf{1}; \quad q_i^h = 1 \qquad \text{in} \quad \Omega_i \tag{2.17}$$

and zero elsewhere. In (2.17), $\mathbf{1}$ explicitly means that each component of $\mathbf{v}_i^h$ is of unit value. The characteristic control volume length of the discretization is h. With these definitions at hand, the variational equation (2.1) may likewise be formulated for each $\mathbf{v}_i^h$ and q_i^h such that

$$B_{NS}\left(\mathbf{v}_i^h, q_i^h; \mathbf{u}^h, p^h\right) = \left(\mathbf{v}_i^h, \mathbf{f}\right)_\Omega \qquad \forall \left(\mathbf{v}_i^h, q_i^h\right) \in \mathcal{V}_{\mathbf{u}p}^h \tag{2.18}$$

where the bilinear form on the left hand side is obtained from (2.2) after applying Gauss' theorem to the convective term, the pressure term, the viscous term, and the continuity term according to

$$\begin{aligned} B_{NS}\left(\mathbf{v}_i^h, q_i^h; \mathbf{u}^h, p^h\right) = & \int_\Omega \mathbf{v}_i^h \frac{\partial \mathbf{u}^h}{\partial t} \, \mathrm{d}\Omega + \int_{\Gamma_i} \mathbf{v}_i^h \left(\mathbf{u}^h \otimes \mathbf{u}^h\right) \cdot \mathbf{n} \, \mathrm{d}\Gamma + \int_{\Gamma_i} \mathbf{v}_i^h p^h \mathbf{n} \, \mathrm{d}\Gamma \\ & - \int_{\Gamma_i} \mathbf{v}_i^h \nu \mathbf{n} \cdot \nabla \mathbf{u}^h \, \mathrm{d}\Omega - \int_{\Gamma_i} q_i^h \mathbf{u}^h \cdot \mathbf{n} \, \mathrm{d}\Omega \end{aligned} \tag{2.19}$$

where Γ_i denotes the boundary of the support of $\mathbf{v}_i^h$ and q_i^h, respectively, and $\mathbf{n}$ the respective outward normal vector of unit length to this boundary of support.

The scale separation to be presented in section 3 relies on a level of complete resolution indicated by the characteristic control volume length h. In terms of the velocity, this reads

$$\mathbf{u}^h = \left(\overline{\mathbf{u}} + \mathbf{u}'\right)^h \tag{2.20}$$

With respect to this complete resolution level, a large-scale resolution level is identified *a priori*. This level is characterized by the control volume length $\overline{h}$ and, accordingly, yields a large-scale velocity $\overline{\mathbf{u}}^h$. The small-scale velocity is consistently defined as

$$\mathbf{u}'^h = \mathbf{u}^h - \overline{\mathbf{u}}^{\overline{h}} \tag{2.21}$$

Accordingly, a large-scale weighting function

$$\overline{\mathbf{v}}^{\overline{h}} = \sum_i \overline{\mathbf{v}}_i^{\overline{h}} \tag{2.22}$$

where

$$\overline{\mathbf{v}}_i^{\overline{h}} = \mathbf{1} \qquad \text{in} \quad \overline{\Omega}_i \tag{2.23}$$

and zero elsewhere is introduced. $\overline{\Omega}_i$ denotes the i-th control volume of the discretization with the characteristic control volume length $\overline{h}$. Reunifying the large-scale equation (2.13) and the small-scale equation (2.15) with the subgrid viscosity term on the basis of the preceding finite volume formulation yields a final equation which may be written in compact form with the help of (2.21) as

$$\begin{aligned} & B_{NS}\left(\mathbf{v}_i^h, q_i^h; \overline{\mathbf{u}}^h, p^h\right) - \left(\mathbf{v}_i'^h, \nu^T \mathbf{n} \cdot \nabla \mathbf{u}'^h\right)_{\Gamma_i'} \\ & = B_{NS}\left(\mathbf{v}_i^h, q_i^h; \overline{\mathbf{u}}^h, p^h\right) - \left(\mathbf{v}_i^h, \nu^T \mathbf{n} \cdot \nabla \left(\mathbf{u}^h - \overline{\mathbf{u}}^{\overline{h}}\right)\right)_{\Gamma_i} + \left(\overline{\mathbf{v}}_i^{\overline{h}}, \nu^T \mathbf{n} \cdot \nabla \left(\mathbf{u}^h - \overline{\mathbf{u}}^{\overline{h}}\right)\right)_{\overline{\Gamma}_i} \\ & = \left(\mathbf{v}_i^h, \mathbf{f}\right)_\Omega \qquad \forall \left(\mathbf{v}_i^h, q_i^h\right) \in \mathcal{V}_{\mathbf{u}p}^h; \quad \overline{\mathbf{v}}_i^{\overline{h}} \in \overline{\mathcal{V}}_{\mathbf{u}p}^{\overline{h}} \end{aligned} \tag{2.24}$$

where the boundary Γ_i is split up into a large-scale boundary $\overline{\Gamma}_i$ and, accordingly, a small-scale boundary subject to

$$\Gamma_i' = \Gamma_i - \overline{\Gamma}_i \tag{2.25}$$

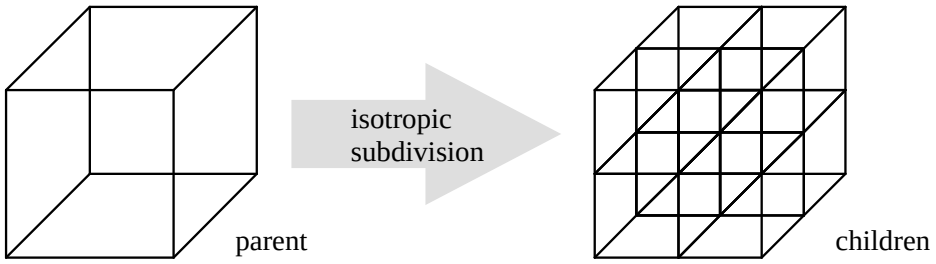

FIGURE 1. Parent hexahedron with 8 child hexahedra

These boundaries are illustrated in the figure at the end of the subsequent section. The inherent scale separation remains obvious in (2.24) merely due to the subgrid viscosity term.

3. Separation of scales

As a geometrical basis for the present approach, two grids are created: a coarser grid, which is called the 'parent' grid, and a finer grid, which is called the 'child' grid. The child grid is obtained by an isotropic hierarchical subdivision of the parent grid similar to the procedure described in Mavriplis (1997). In contrast to the usual parent-child relationship in multigrid solvers where the parent needs to know only the number of its children, a complete parent-child knowledge base is set up here, i.e. every parent knows about every child and vice versa. Hybrid unstructured meshes may contain tetrahedra, hexahedra, prisms, and pyramids. However, only two different types of faces, namely triangles and quadrangles, occur for these 4 different types of control volumes. Based on the fact that a factor of 2 is most often used in a dynamic modeling procedure for the relation of the cutoff length scale for the large resolved scales to the one for all resolved scales, an subdivision procedure using this factor is chosen. Both a parent triangular face and a parent quadrangular face subdivided isotropically result in four child faces of the same type. For the actual 3-D control volumes, isotropic subdivision of either a parent tetrahedron or hexahedron, for example, both results in 8 children. A parent hexahedron along with its 8 child hexahedra is depicted in Fig. 1. Illustrations of subdivided tetrahedra, prisms, and pyramids may be found in Mavriplis (1997). Obviously, this kind of refinement is not restricted to a subdivision by factor 2. Other integer factors (*e.g.*, 3 or 4) may be applied, and result in considerably lower ratios of the spaces containing the large resolved scales to the spaces containg the small resolved scales.

The general class of scale-separating operators based on multigrid operators reads

$$\overline{\mathbf{u}}^h = S^m\left[\mathbf{u}^h\right] = P \circ R\left[\mathbf{u}^h\right] = P\left[\overline{\mathbf{u}}^{\overline{h}}\right] \tag{3.1}$$

where the scale-separating operator S^m consists of the sequential application of a restriction operator R and a prolongation operator P. Applying the restriction operator on $\mathbf{u}^h$ yields a large-scale velocity $\overline{\mathbf{u}}^{\overline{h}}$ defined at the degrees of freedom of the parent grid which is then prolongated in order to obtain a large-scale velocity $\overline{\mathbf{u}}^h$ defined at the degrees of freedom of the child grid. Various restriction operators as well as prolongation operators may be used in (3.1). However, the attention is focused on two special combinations of restriction and prolongation operators. Both of them rely on the same restriction operator, but apply different prolongation operators afterwards. The restriction operator is

defined to be a volume-weighted average over all the child control volumes within one parent control volume subject to

$$\overline{\mathbf{u}}_j^{\overline{h}} = \frac{\sum_{i=1}^{n_{cop}} |\Omega_i| \, \mathbf{u}_i^h}{\sum_{i=1}^{n_{cop}} |\Omega_i|} \tag{3.2}$$

where $\overline{\mathbf{u}}_j^{\overline{h}}$ denotes the large-scale velocity at the center of the parent control volume $\overline{\Omega}_j$ and n_{cop} the number of child control volumes in $\overline{\Omega}_j$. The first prolongation operator P^p yields a constant prolongation, i.e.

$$\overline{\mathbf{u}}_i^h = P^p \left[\overline{\mathbf{u}}_j^{\overline{h}}\right]_i = \overline{\mathbf{u}}_j^{\overline{h}} \qquad \forall \Omega_i \subset \overline{\Omega}_j \tag{3.3}$$

and zero elsewhere. The scale-separating operator defined as

$$S^{pm} := P^p \circ R \tag{3.4}$$

has the property of a projector indicated by the additional superscript p. The second prolongation operator considered in this work yields a linear prolongation subject to

$$\overline{\mathbf{u}}_i^h = P^s \left[\overline{\mathbf{u}}_j^{\overline{h}}\right]_i = \overline{\mathbf{u}}_j^{\overline{h}} + \nabla^{\overline{h}} \overline{\mathbf{u}}_j^{\overline{h}} \, (\overline{\mathbf{r}}_j - \mathbf{r}_i) \qquad \forall \Omega_i \subset \overline{\Omega}_j \tag{3.5}$$

and zero elsewhere. The vectors $\mathbf{r}_i$ and $\overline{\mathbf{r}}_j$ denote geometrical vectors pointing to the centers of the child control voume Ω_i and the parent control volume $\overline{\Omega}_j$, respectively. $\nabla^{\overline{h}}$ describes the discrete gradient operator on the parent grid. Due to this, values from neighbouring parent control volumes and, consequently, child control volumes contained in these neighbouring parent control volumes influence the final large-scale value in the child control volume Ω_i. Hence, P^s does not provide us with a projective scale-separating operation as shown in Gravemeier (2004). It rather produces some kind of smoothing prolongation, which is indicated by the additional superscript s. The complete scale-separating operator is defined as

$$S^{sm} := P^s \circ R \tag{3.6}$$

Nevertheless, S^{sm} exhibits a fundamentally different character than usual discrete smooth filters.

The validity of (2.24) in a complete sense with respect to the subgrid viscosity term remains to be analyzed. In Gravemeier (2004), it is demonstrated that discrete smooth filters, in contrast to the scale-separating operators based on combined multigrid operators, do not satisfy (2.24) in a strict sense due to the fact that the third term in the second line of (2.24) cannot be represented. Nevertheless, there is also a crucial difference between S^{pm} and S^{sm} in this context: there is no large-scale (subgrid) viscous flux for S^{pm} across the small-scale boundary subject to (2.25), see Gravemeier (2004). As a result, (2.24) may be specified for S^{pm} as

$$B_{NS}\left(\mathbf{v}_i^h, q_i^h; \overline{\mathbf{u}}^h, p^h\right) - \left(\mathbf{v}_i'^h, \nu^T \mathbf{n} \cdot \nabla \mathbf{u}^h\right)_{\Gamma_i'} = \left(\mathbf{v}_i^h, \mathbf{f}\right)_\Omega \tag{3.7}$$

In Fig. 2, the definition of large- and small-scale boundaries in the finite volume method is visualized for the 2-D case. The large-scale weighting function $\overline{\mathbf{v}}^{\overline{h}}$ is exclusively defined on the large-scale boundaries belonging to the parent control volume as shown in Fig. 2(a). The small-scale weighting function $\mathbf{v}'^h$ is exclusively defined on the inner boundaries of the child control volumes, see Fig. 2(b).

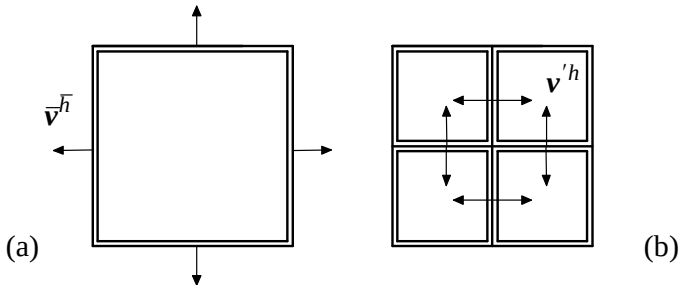

FIGURE 2. Geometrical locations of weighting functions in the FVM for a 2-D case: (a) large-scale; (b) small-scale

4. Subgrid-scale modeling within the multiscale environment

Adopting the usual filter-related notation for the Smagorinsky model to the underlying situation where the resolved part of the velocity is defined by the discretization with characteristic length scale h, the subgrid viscosity can be expressed as

$$\nu^T = (C_S h)^2 \left|\varepsilon\left(\mathbf{u}^h\right)\right| \tag{4.1}$$

The actual evaluation of (4.1) is performed in every control volume using the respective characteristic length scale, so that a value for ν^T in every control volume is obtained. Despite the well-known flaws of the constant-coefficient Smagorinsky, the integration of this simple model within the framework of the variational multiscale method has already led to good results for a number of test cases. The present study focuses on the specific modification of the model restricting the dependence on the small scales subject to

$$\nu^T = (C_S h)^2 \left|\varepsilon\left(\mathbf{u}'^h\right)\right| = (C_S h)^2 \left|\varepsilon\left(\mathbf{u}^h - \overline{\mathbf{u}}^h\right)\right| \tag{4.2}$$

which has been named 'small-small' model in Hughes *et al.* (2000) and seems to be the most natural version within the multiscale formalism. The constant C_S is chosen to be 0.1.

The dynamic modeling procedure proposed in Germano *et al.* (1991) enables a computation of the constant C_S as a function of time and position. It is interesting to note that the dynamic modeling procedure already distinguishes large resolved scales, small resolved scales, and unresolved scales explicitly. This mirrors the type of scale separation in the variational three-scale formulation.

Due to the pointwise formulation of the classical Germano identity, the dynamic procedure starts with a spatially discretized strong form of the Navier-Stokes equations. The spatially discretized momentum equation reads

$$\frac{\partial \mathbf{u}^h}{\partial t} + \nabla \cdot \left(\mathbf{u}^h \otimes \mathbf{u}^h\right) + \nabla p^h - \nu \Delta \mathbf{u}^h + \nabla \cdot \tau^h = \mathbf{f}^h \tag{4.3}$$

where the subgrid-scale stress tensor is defined as

$$\tau^h = (\mathbf{u} \otimes \mathbf{u})^h - \mathbf{u}^h \otimes \mathbf{u}^h \tag{4.4}$$

Note that in (4.3)-(4.4) the ususal filtered formulation is replaced by the actual implicit scale-separation based on the chosen discretization with characteristic length scale h. The 'test filter' is replaced by the scale-separating operators of section 3. Thus, the analog of the 'subtest'-scale stress tensor can be expressed as

$$\overline{\tau}^h = \overline{(\mathbf{u} \otimes \mathbf{u})}^h - \overline{\mathbf{u}}^h \otimes \overline{\mathbf{u}}^h = S\left[(\mathbf{u} \otimes \mathbf{u})^h\right] - S\left[\mathbf{u}^h\right] \otimes S\left[\mathbf{u}^h\right] \tag{4.5}$$

With regard to the child grid discretization level, the following may be stated:

$$\mathbf{L}^h = \overline{\tau}^h - \overline{\tau^h} = \overline{\tau}^h - S\left[\tau^h\right] \tag{4.6}$$

where $\mathbf{L}^h$ can be obtained as

$$\mathbf{L}^h = \overline{\mathbf{u}^h \otimes \mathbf{u}^h} - \overline{\mathbf{u}}^h \otimes \overline{\mathbf{u}}^h = S\left[\mathbf{u}^h \otimes \mathbf{u}^h\right] - S\left[\mathbf{u}^h\right] \otimes S\left[\mathbf{u}^h\right] \tag{4.7}$$

by inserting (4.4) and (4.5) into (4.6). Assuming the Smagorinsky model as an appropriate modeling term at both discretization levels and accounting for the fact that the Smagorinsky model is basically a 'trace-free' model in the context of incompressible flow, (4.6) is modeled as follows:

$$\begin{aligned} \mathrm{dev}\mathbf{L}^h &= \mathbf{L}^h - \frac{1}{3}\mathrm{tr}\mathbf{L}^h\mathbf{I} \\ &= -2\left(C_S h\right)^2 S\left|\left[\varepsilon\left(\mathbf{u}^h\right)\right]\right| S\left[\varepsilon\left(\mathbf{u}^h\right)\right] + S\left[2\left(C_S h\right)^2 \left|\varepsilon\left(\mathbf{u}^h\right)\right| \varepsilon\left(\mathbf{u}^h\right)\right] \end{aligned} \tag{4.8}$$

where $\mathbf{I}$ denotes the identity tensor, and modeling is obviously confined to the deviatoric part of the tensor $\mathbf{L}^h$. It is now assumed that C_S is at least constant over one control volume of the parent grid. Hence, (4.8) may be rewritten as

$$\begin{aligned} \mathrm{dev}\mathbf{L}^h &= \left(C_S h\right)^2 \left[2S\left[\left|\varepsilon\left(\mathbf{u}^h\right)\right| \varepsilon\left(\mathbf{u}^h\right)\right] - 2\left(\frac{\overline{h}}{h}\right)^2 S\left|\left[\varepsilon\left(\mathbf{u}^h\right)\right]\right| S\left[\varepsilon\left(\mathbf{u}^h\right)\right]\right] \\ &= \left(C_S h\right)^2 \mathbf{M}^h \end{aligned} \tag{4.9}$$

The calculation of the constant expression $\left(C_S h\right)^2$ on the right hand side of (4.9) aims to minimize the error tensor

$$\mathbf{E}^h = \mathrm{dev}\mathbf{L}^h - \left(C_S h\right)^2 \mathbf{M}^h \tag{4.10}$$

Using the least-squares approach proposed by Lilly (1992), the formula for the constant expression reads

$$\left(C_S h\right)^2 = \frac{\mathrm{dev}\mathbf{L}^h \mathbf{M}^h}{\mathbf{M}^h \mathbf{M}^h} \tag{4.11}$$

from which the actual constant C_S may be evaluated. Gravemeier (2004) discusses an alternative procedure based on the classical Germano identity which makes use of the special form of the scale-separating operators and yields only values for C_S related to the control volumes of the parent grid. The essential differences between this strategy and a new approach based on the so-called *variational Germano identity* of Oberai & Wanderer (2004) are also addressed.

5. Numerical example: turbulent channel flow

Three different methods are compared:

- the dynamic Smagorinsky (DS) model based on the classical Germano identity in the usual non-multiscale application,
- the constant-coefficient Smagorinsky (CMS) model in the 'small-small' version (4.2) within the multiscale environment subject to (2.24), and
- the dynamic Smagorinsky (DMS) model in the 'small-small' version (4.2) based on the classical Germano identity within the multiscale environment subject to (2.24).

All of these methods are investigated for the scale-separating operators S^{pm} and S^{sm}. The results are compared to simulations with discrete smooth filters based on the trapezoidal rule as well as the Simpson rule denoted S^{tf} and S^{sf}, respectively. In the following diagrams, the abbreviation DMS-PM, for instance, indicates the variational multiscale LES incorporating a dynamic Smagorinsky model with the scale-separating operator S^{pm} applied. Results are also reported for simulations using the constant-coefficient Smagorinsky model in a non-multiscale environment (CS) as well as applying no model at all (NM). It must be emphasized that CMS is merely the combination of these last two approaches by applying no model to the large resolved scales and the constant-coefficient Smagorinsky model to the small resolved scales.

Based on results of Gravemeier (2004), the characteristic length scale ratio for all DS and DMS simulations is set to 2.5 for S^{pm} and 2.0 for S^{sm}. For S^{tf} and S^{sf}, ratios of 2 and 1.5, respectively, are applied. The computational effort required for the various methodological combinations is also evaluated. In this brief, results are reported only for the case $Re_\tau = 590$ with a relatively coarse discretization of 64 control volumes in each coordinate direction. Gravemeier (2004) provides a detailed description of the numerical setup as well as the results for three other cases.

In order to compare the various methods, the scale-separating operator S^{pm} is used for DS, CMS, and DMS, since it is the most important operator of this work due to its projective property. Figs. 3 and 4 depict the mean streamwise velocity profile and the turbulent kinetic energy, respectively. The larger numerical error introduced by a second-order accurate method in combination with a relatively coarse discretization already mentioned in section 1 comes into play for all methods applied. Surprisingly however, the lower accuracy of the basic method affects CMS-PM to a far lesser extent than the other methods towards the channel center. It is considerably closer to the DNS profile in this part of the channel than NM, DS-PM, and DMS-PM. DMS-PM shows no improvement in comparison to NM, and DS-PM performs even slightly worse. Despite the higher accuracy in the inertial layer (usually expected to start at $x_2^+ = 30$), CMS-PM slightly underpredicts the velocity profile in the buffer layer (usually expected to range from $x_2^+ = 5$ to $x_2^+ = 30$). The profile for the turbulent kinetic energy shows a much better agreement for the height of the peak in comparison to the DNS profile than the other methods. Of course, CS is far worse than all other methods with respect to both aspects of the flow.

An objective comparison of the computational effort for the simulations using the aforementioned methods is difficult, since it strongly depends on the amount of computational time spent within the actual solvers in CDP-α. These time measures can vary considerably from one calculation to another. Thus, only approximate measures for the necessary computational effort are reported as a mean value of the actual simulation times covering all calculations in Gravemeier (2004). Setting the computational effort for NM to 1.0, the relative measures for CS, DS-PM, CMS-PM, and DMS-PM are circa 1.10, 1.15, 1.10, and 1.15, respectively. Thus, CMS in combination with PM is a very efficient method computationally, even more efficient than DS. Taking into account different scale-separating operators, the numbers increase drastically for CMS and DMS however.

A second important issue concerns the differences between the various scale-separating operators. In Figs. 5 and 6, the mean streamwise velocity and the turbulent kinetic energy, respectively, for four different scale-separating operators applied with DS, CMS, or DMS are pictured. There are hardly any differences visible for DMS in Fig. 5(c), but the scale-separating operators PM and SM perform better than TF and SF in the

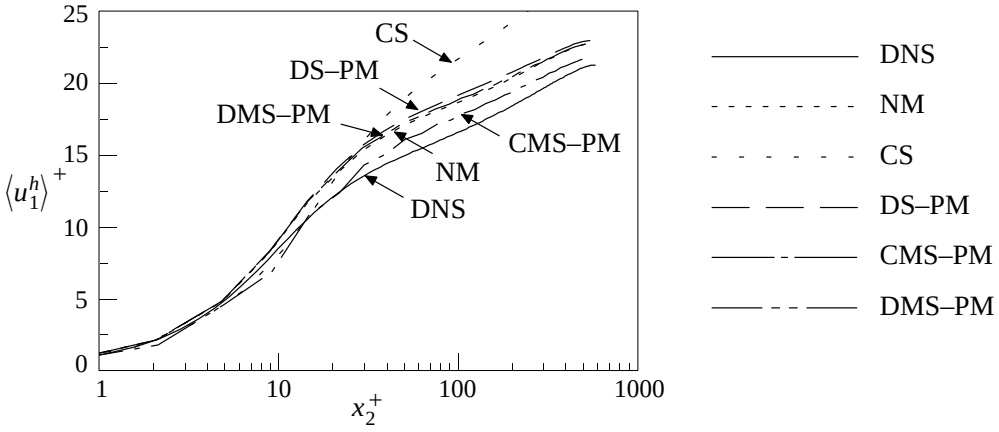

FIGURE 3. Comparing methods (pm-separation): mean streamwise velocity.

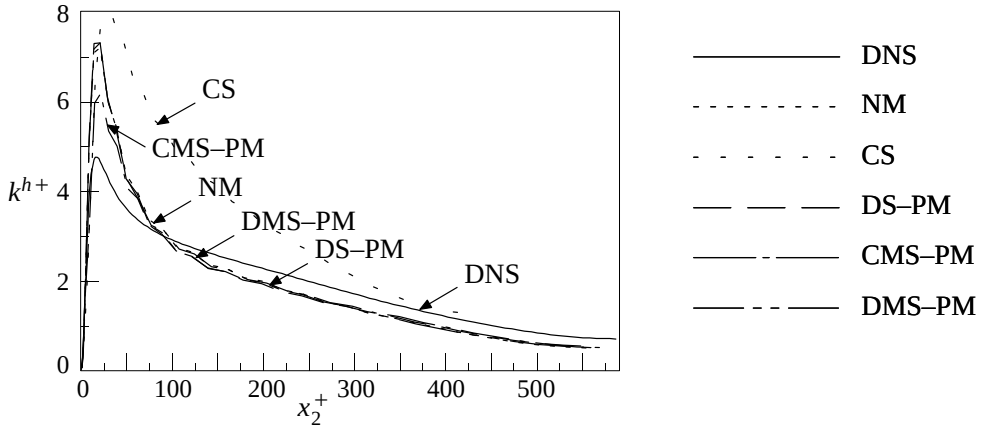

FIGURE 4. Comparing methods (pm-separation): turbulent kinetic energy.

context of DS, see Fig. 5(a). This presumption is, at least to a certain degree, reinforced for the turbulent kinetic energy profiles in Figs. 6(a) and (c). A remarkable difference between the projective scale-separating operator PM and the other operators shows up in the context of CMS for the mean streamwise velocity particularly as well as for the turbulent kinetic energy profile, although to a lesser degree, see Figs. 5(b) and 6(b). Thus, the favourable behaviour of CMS-PM in the inertial layer as well as the slightly underpredictive performance in the buffer layer and parts of the viscous sublayer seems to be attributed to CMS only depending on this specific scale-separating operator.

Specifying the necessary computational effort for the various scale-separating operators results in the following approximate numbers. Setting the relative computational simulation time for the operator PM to 1.0, the measures for SM, TF, and SF are approximately 1.25, 1.40, and 2.50, respectively. In particular, SF in this implementation is an extremely time-consuming operator and is, therefore, not recommended for further use. The reason for the additional effort linked with such non-projective operators can be traced back to a necessary call of the scale-separating routine at the beginning of each Gauss-Seidel iteration step in the solution procedure for the momentum equation.

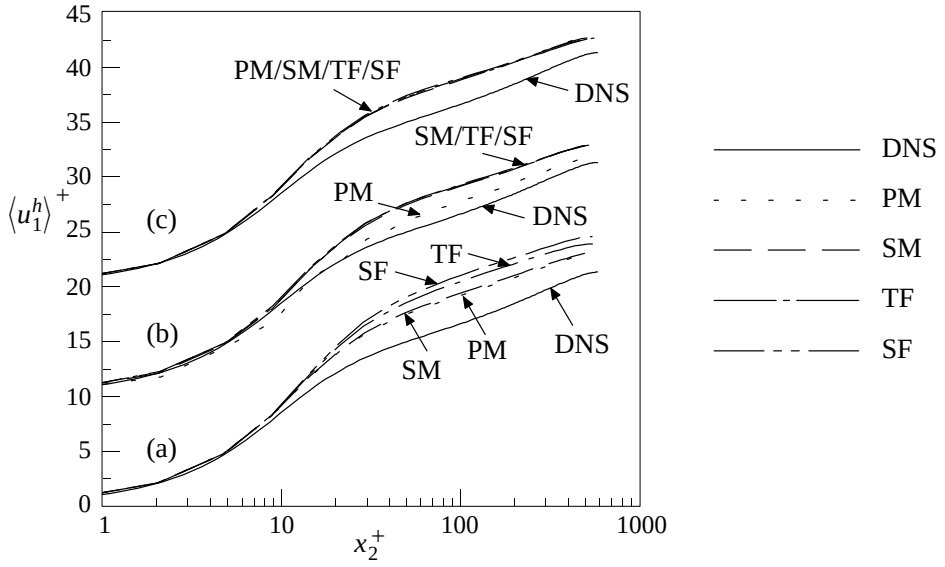

FIGURE 5. Comparing scale-separating operators: mean streamwise velocity: (a) DS; (b) CMS ($\langle u_1^h \rangle^+ +10$); (c) DMS ($\langle u_1^h \rangle^+ +20$).

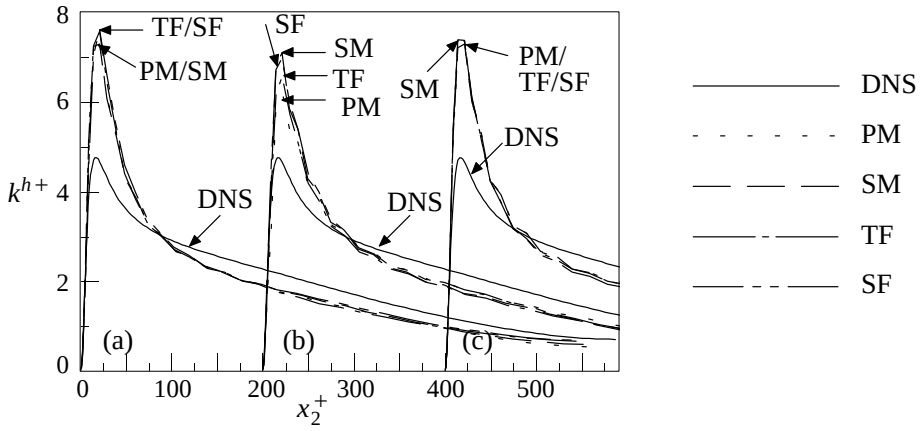

FIGURE 6. Comparing scale-separating operators: turbulent kinetic energy: (a) DS; (b) CMS ($x_2^+ +200$); (c) DMS ($x_2^+ +400$).

This call is required to determine the updated large-scale velocity field for the residual calculation. This is not necessary for PM.

In order to analyze the specific behaviour of CMS-PM in comparison to all other scale-separating operator in the context of CMS, the small scales are extracted and investigated explicitly in this section. Figs. 7 and 8 depict the mean streamwise small-scale velocity and the small-scale turbulent kinetic energy, respectively. The small-scale velocity of CMS-PM shows an oscillating behaviour with large amplitudes particularly in the buffer layer. For CMS-SM, the frequency of the oscillation is about the same, but the amplitudes are considerably smaller. In case of CMS-TF and CMS-SF, one oscillation period can be seen at most throughout half-width of the channel with the amplitude being larger for CMS-TF than for CMS-SF. As expected, the largest small-scale turbulent kinetic

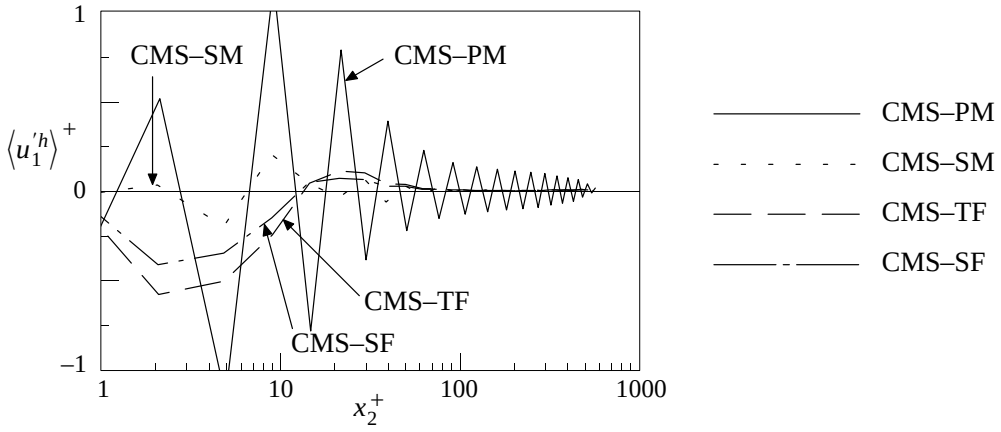

FIGURE 7. Comparing scale-separating operators for CMS: mean streamwise small-scale velocity.

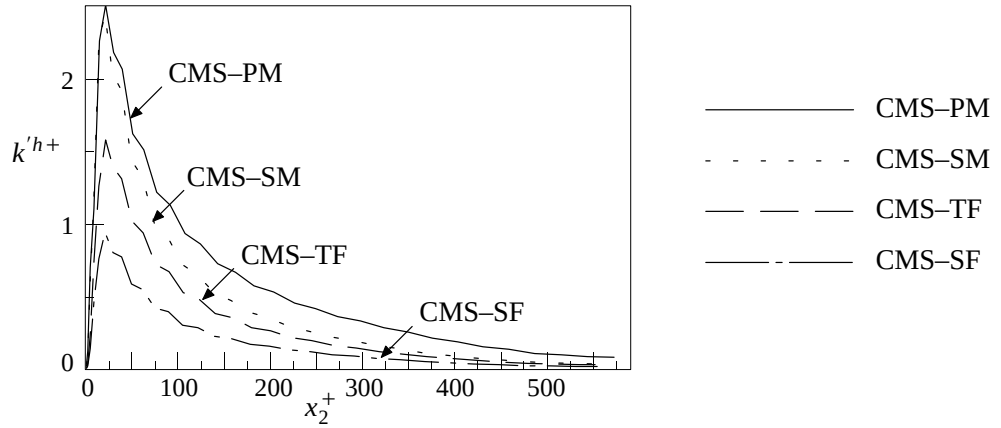

FIGURE 8. Comparing scale-separating operators for CMS: small-scale turbulent kinetic energy.

energy is obtained for CMS-PM (although the peak is also matched by CMS-SM) and the smallest one for CMS-SF, see Fig. 8. This indicates a measure for the amount of small scales extracted by the respective scale-separating operator and has been quantified in Gravemeier (2004).

6. Conclusions and future plans

A general class of scale-separating operators based on combined multigrid operators and suited for variational multiscale LES both with dynamic and constant-coefficient based subgrid-scale modeling has been proposed. These operators may also be used for the dynamic modeling procedure in a classical LES. Only one of these scale-separating operators exhibits the important property of a projector allowing fulfillment of the theoretical assumption for a clear scale separation within the variational multiscale method. All of the scale-separating operators have been implemented in a second-order accurate, energy-conserving finite volume method particularly suited for applications on hybrid unstructured grids in complex geometries. Dynamic and non-dynamic methods based on

the various scale-separating operators have been tested for the case of a turbulent channel flow at two different Reynolds numbers and for two different discretizations for each of these two Reynolds number flows. Several important observations have been made and summarized in Gravemeier (2004). With respect to certain crucial flow features, the simple constant-coefficient Smagorinsky model based variational multiscale method in combination with the projective operator has shown remarkable results. In particular, it represents a very efficient methodical combination with regard to the important aspect of computational cost.

Four subsequent projects growing from this study are currently underway or planned for the near future. First, the investigation of an alternative approach for dynamic subgrid-scale modeling based on the variational Germano identity is currently underway. In contrast to the classical Germano identity, this identity appears to be more consistent with the variational LES formulation. Second, the performance of the scale-separating operators based on combined multigrid operators will be investigated in the context of more challenging turbulent flows. These flow configurations will be characterized by an even larger range of subgrid scales than in the present investigation in order to provide an even more challenging test for variational multiscale LES. Currently, it is planned to use the turbulent flow in a planar asymmetric diffuser as such an additional test case. Third, the suitability of a more sophisticated approach for dynamic subgrid-scale modeling according to Ghosal *et al.* (1995) in the framework of variational multiscale LES will be investigated. Fourth, it is planned to address wall modeling approaches in this context.

7. Acknowledgements

The partial support by the Alexander von Humboldt-Foundation through a Feodor Lynen Fellowship is gratefully acknowledged. The author would like to express his sincere appreciation to Frank Ham for providing a basic version of the code CDP-α for the simulation of incompressible flows which the developments of this work are built upon. The author is also grateful to Parviz Moin and Gregory Burton for helpful discussions.

REFERENCES

Collis, S. S. 2001 Monitoring unresolved scales in multiscale turbulence modeling. *Phys. Fluids* **13**, 1800-1806.

Germano, M., Piomelli, U., Moin, P. & Cabot, W. H. 1991 A dynamic subgrid-scale eddy vicosity model. *Phys. Fluids* **3**, 1760-1765.

Ghosal, S., Lund, T. S., Moin, P. & Akselvoll, K. 1995 A dynamic localization model for large-eddy simulation of turbulent flows. *J. Fluid Mech.* **286**, 229-255.

Gravemeier, V. 2003 The variational multiscale method for laminar and turbulent incompressible fow. *PhD Thesis*, Report No. 40, Institute of Structural Mechanics, University of Stuttgart, Germany.

Gravemeier, V. 2004 Scale-separating operators for variational multiscale large eddy simulation of turbulent flows. *Preprint.*

Gravemeier, V., Wall, W. A. & Ramm, E. 2004 A three-level finite element method for the instationary incompressible Navier-Stokes equations. *Comput. Methods Appl. Mech. Engrg.* **193**, 1323-1366.

Ham, F., Apte, S., Iaccarino, G., Wu, X., Herrmann, M., Constantinescu,

G., MAHESH, K. & MOIN, P. 2003 Unstructured LES of reacting multiphase flows in realistic gas turbine combustors. *Annual Research Briefs - 2003*, Center for Turbulence Research, Stanford University and NASA Ames Research Center, 139-160.

HUGHES, T. J. R., FEIJOO, G. R., MAZZEI, L. & QUINCY, J.-B. 1998 The variational multiscale method - a paradigm for computational mechanics. *Comput. Methods Appl. Mech. Engrg.* **166**, 3-24.

HUGHES, T. J. R., MAZZEI, L. & JANSEN, K. E. 2000 Large eddy simulation and the variational multiscale method. *Comput. Visual. Sci.* **3**, 47-59.

HUGHES, T. J. R., OBERAI, A. A. & MAZZEI, L. 2001 Large eddy simulation of turbulent channel flows by the variational multiscale method. *Phys. Fluids* **13**, 1784-1799.

JEANMART, H. & WINCKELMANS, G. S. 2002 Comparison of recent dynamic subgrid-scale models in turbulent channel flow. *Proceedings of the Summer Program 2002*, Center for Turbulence Research, Stanford University and NASA Ames Research Center, 105-116.

KOOBUS, B. & FARHAT, C. 2004 A variational multiscale method for the large eddy simulation of compressible turbulent flows on unstructured meshes - application to vortex shedding. *Comput. Methods Appl. Mech. Engrg.* **193**, 1367-1383.

KRAVCHENKO, A. G. & MOIN, P. 1997 On the effect of numerical errors in large eddy simulations of turbulent flows. *J. Comput. Phys.* **131**, 310-322.

LILLY, D. K. 1992 A proposed modification of the Germano subgrid-scale closure method. *Phys. Fluids* **4**, 633-635.

MAVRIPLIS, D. J. 1997 Adaptive meshing techniques for viscous flow calculations on mixed element unstructured meshes. *ICASE-Report 97-20*, NASA Langley Research Center, Hampton, VA.

MOSER, R. D., KIM, J. & MANSOUR, N. N. 1999 Direct numerical simulation of turbulent channel flow up to $Re_\tau = 590$. *Phys. Fluids* **11**, 943-945.

OBERAI, A. A. & HUGHES, T. J. R. 2002 The variational multiscale formulation of LES: channel flow at $Re_\tau = 590$. *AIAA Paper 2002-1056*, Reno, NV, January 14-17, 2002.

OBERAI, A. A. & WANDERER, J. 2004 A dynamic approach for evaluating parameters in a numerical method. *Preprint*, submitted for publication in Int. J. Numer. Meth. Engrg.

TERRACOL, M., SAGAUT, P. & BASDEVANT, C. 2001 A multilevel algorithm for large-eddy simulation of turbulent compressible flows. *J. Comput. Phys.* **167**, 439-474.

SHAH, K. B. & FERZIGER, J. H. 1995 A new non-eddy viscosity subgrid-scale model and its application to channel flow. *Annual Research Briefs - 1995*, Center for Turbulence Research, Stanford University and NASA Ames Research Center, 73-90.

VREMAN, A. W. 2004 The adjoint filter operator in large-eddy simulation of turbulent flow. *Phys. Fluids* **16**, 2012-2022.

Large-eddy simulation of passive-scalar mixing using multifractal subgrid-scale modeling

By G.C. Burton

1. Motivation and introduction

Turbulent mixing of a passive scalar is important to a number of processes of interest to industry and science, including multiphase flows and the dispersion of pollutants in atmospheric flows. Turbulent mixing also is of particular interest to the modeling of reacting flows, since turbulence is known to mix reactants in an extremely rapid manner, which may greatly influence the rate and efficiency of the reactive processes. While experimental and/or field work may continue to provide certain insights into the characteristics of these flows, their analysis may be difficult, time consuming or expensive to conduct. As a result, the practicing engineer and scientist has turned in the past decade to numerical simulation to develop a more detailed understanding of turbulent flows. In this context, large eddy simulation has been shown to be a promising approach to numerically simulate many turbulent flows. However, most current subgrid-scale models used for LES fail to recover the detailed spatial structure of the stress and energy transfer fields of such flows. These factors, however, may be of particular importance for modeling processes that occur principally in the subgrid scales, such as energy-dissipation, scalar-dissipation and chemical reactions.

Recently, Burton & Dahm (2004 *a,b*) have introduced multifractal modeling for large-eddy simulation, which derives a structural model for the subgrid velocities u_i^{sgs} based on the demonstrated multifractal structure of the subgrid vorticity field $\boldsymbol{\omega}^{sgs}$, and uses this to close the filtered Navier-Stokes momentum equation. The method shows special promise because, at modest computational cost, multifractal LES has been shown to recover the detailed spatial structure of the subgrid-energy production $\mathcal{P}(\mathbf{x},t)$ field with high accuracy ($\rho \geq 0.997$). Importantly the multifractal modeling approach may be applied to other turbulence modeling problems. Thus, the multifractal structure of the passive-scalar dissipation field in high Re turbulence, already confirmed by previous studies, may be used to develop a model for the filtered passive-scalar transport equation. In this report, the derivation of such a model is set out in detail, as well as *a priori* tests of the model against DNS data, and *a posteriori* tests in which the model is employed in large-eddy simulations of the turbulent mixing of a passive scalar. These tests indicate that multifractal modeling holds great promise for the accurate simulation of turbulent mixing of passive conserved scalar quantities.

2. Derivation of a multifractal model for the filtered passive-scalar flux

2.1. *Background*

For large-eddy simulation, the filtered passive-scalar transport equation without source term may be expressed as

$$\frac{\partial \overline{\zeta}}{\partial t} + \frac{\partial}{\partial x_j}\,\overline{\overline{u}_j\,\overline{\zeta}} - D\frac{\partial^2 \overline{\zeta}}{\partial x_j \partial x_j} = -\frac{\partial}{\partial x_j}\,\sigma_j^*\,, \tag{2.1}$$

where D is the coefficient of scalar diffusivity, and where

$$\sigma_j^* \equiv \overline{\overline{u}_j \, \zeta^{sgs}} + \overline{u_j^{sgs} \, \overline{\zeta}} + \overline{u_j^{sgs} \, \zeta^{sgs}}. \tag{2.2}$$

Equations (2.1) and (2.2) involve filtered nonlinear interactions between the resolved and subgrid velocities $\overline{u}_j$ and u_j^{sgs} on the one hand, and the resolved and subgrid passive-scalar concentrations $\overline{\zeta}$ and ζ^{sgs} on the other, and require some form of modeling. One approach is to evaluate the terms in σ_j^* from a structural model that provides the subgrid velocity components u_j^{sgs} and the subgrid-scalar concentrations ζ^{sgs}. Burton & Dahm (2004 *a,b*) have proposed such a model for u_j^{sgs} based on the multifractal structure of the vorticity field in high Reynolds-number turbulence. The approach involves describing the spatial distribution of subgrid vorticity magnitude by a multifractal cascade and the distribution of subgrid vorticity orientations by an additive decorrelation cascade. An expression for the subgrid velocity components can be derived by applying the Biot-Savart operator to this representation of the subgrid vorticity, which after some analysis takes the form:

$$u_j^{sgs} \approx \mathcal{B} \, u_j^{\Delta}, \tag{2.3}$$

where

$$\mathcal{B} \equiv 0.47 \; 2^{-\frac{2\mathcal{N}}{3}} \left[2^{\frac{4\mathcal{N}}{3}} - 1 \right]^{\frac{1}{2}}, \tag{2.4}$$

where u_j^{Δ} is the velocity field associated with the smallest resolved scale Δ, and where the number of cascade steps in the subgrid field is given by

$$\mathcal{N} \equiv \log_2(\Delta / \lambda_\nu). \tag{2.5}$$

A similar model for the concentrations of a conserved passive scalar ζ^{sgs} may be developed based on the multifractal structure of the passive-scalar dissipation field in high Reynolds number turbulence.

2.2. *Overview*

Fundamental considerations indicate that gradient-magnitude fields in turbulent flows, such as the passive-scalar energy dissipation field, given by

$$\chi(\mathbf{x}, t) \equiv -D \, \nabla\zeta \cdot \nabla\zeta(\mathbf{x}, t), \tag{2.6}$$

will display multifractal scale-similarity. This structure arises as the result of the repeated stretching and folding provided by the strain-rate and vorticity fields within turbulent flows. Such repeated stretching and folding may be represented by a stochastic multiplicative cascade, in which a scale-invariant distribution of multipliers $\mathcal{M}$ maps the given field from one scale to the next as the cascade proceeds. In one dimension, such a multiplicative cascade is given generically by

$$\mu(x) = \mu_o(x) \, 2^{\mathcal{N}} \prod_{n=1}^{\mathcal{N}} \mathcal{M}_n \, (x), \tag{2.7}$$

where the mass-density field is given by $\mu(x)$, the initial mass distribution averaged over the domain is $\mu_o(x)$ and the number of repetitions in the cascade is given by $\mathcal{N}$.

A number of prior experimental studies have confirmed that the passive-scalar dissipation field in high Reynolds-number turbulence does in fact exhibit multifractal scale-similarity over inertial-range scales (Prasad *et al.* 1988; Prasad & Sreenivasan 1989;

Frederiksen *et al.* 1997), and from this a unique distribution of scale-invariant multipliers $\mathcal{M}$ that distributes the scalar dissipation field of (2.6) according to (2.7). This multifractal structure may therefore be used to derive a model for a dynamically-passive conserved-scalar field at the subgrid scales $\zeta^{sgs}(\mathbf{x},t)$ that closes (2.1). The derivation involves representing the spatial distribution of the subgrid-scalar gradient field $\nabla\zeta^{sgs}$ by two cascades: (a) a multiplicative multifractal cascade for scalar gradient magnitudes $|\nabla\zeta^{sgs}|$ and (b) an additive decorrelation cascade for scalar-gradient orientations $\hat{\mathbf{e}}^{sgs}_{\nabla\zeta}$. This representation for the scalar gradient field is then inverted using Green's function to recover the subgrid-scalar concentrations ζ^{sgs}. The following derivation parallels in most substantial respects the derivation of the multifractal model for the subgrid velocity field u_j^{sgs} set forth in Burton & Dahm (2004*a*).

2.2.1. *The scalar-gradient magnitude cascade*

Specifying the scalar-gradient magnitude in each subgrid-scale cell first requires determining the total amount of subgrid-scalar dissipation χ^{sgs} over the LES grid cell Δ. This may be determined from Kolmogorov scaling arguments, assuming that the grid-scale Δ falls within the inertial range. Following K41 theory the scalar-dissipation spectrum $\mathcal{X}(k)$ exhibits power-law scaling in the inertial range of high Reynolds-number turbulence as

$$\mathcal{X}(k) \sim k^1. \tag{2.8}$$

Thus the total amount of subgrid-scalar dissipation can be determined by integrating the scalar-dissipation spectrum from the smallest-resolved scale k_Δ to the viscous scale k_ν, giving

$$\chi^{sgs} = \int_{k_\Delta}^{k_\nu} \mathcal{X}(k)\, dk = \kappa\, \chi^\Delta \left[\left(\frac{k_\nu}{k_\Delta} \right)^2 - 1 \right], \tag{2.9}$$

where

$$\kappa \equiv (1 - \alpha^{-2})^{-1}. \tag{2.10}$$

Using (2.9) requires estimating the average magnitude of scalar-dissipation χ^Δ in the resolved flow between filter scale Δ and some larger inertial-range scale $\alpha\,\Delta$. This may be accomplished by determining the value of the scalar field ζ^Δ, and then differentiating the field locally to determine $\nabla\zeta^\Delta$ and from this obtaining

$$\chi^\Delta \equiv -D\, \nabla\zeta^\Delta \cdot \nabla\zeta^\Delta. \tag{2.11}$$

For sufficiently small α, (2.11) provides a reasonably accurate estimate of the true nonlinear quantity χ^Δ given that the contribution of the scalar gradient magnitude at other scale ranges to the product at scale Δ will be small at high Reynolds number (see Burton & Dahm, 2004*a*).

Combining (2.9), (2.10) and (2.11), the subgrid-scalar dissipation magnitude distributed over each grid cell may be described by a three-dimensional stochastic binomial cascade, giving the amount of subgrid-scalar gradient magnitude in each inner scale cell as

$$|\nabla\, \zeta^{sgs}|(\mathbf{x},t) = \left[\chi^{sgs}\, (2^{\mathcal{N}})^3 \prod_{n=1}^{\mathcal{N}} \mathcal{M}_n(\mathbf{x},t) \right]^{\frac{1}{2}}, \tag{2.12}$$

where $\mathcal{N}$ from (2.5) is the number of cascade steps, and the multipliers $\mathcal{M}_n$ correspond to random samples from the scale-invariant distribution $P(\mathcal{M})$ for the scalar-dissipation field (*e.g.*, Frederiksen *et al.* 1997, 1998). This leads naturally to a multifractal subgrid-scalar dissipation field.

2.3. *The additive orientation cascade*

As discussed in Burton & Dahm (2004 *a*), substantial experimental and computational evidence indicates that the orientations of the subgrid velocity field are highly correlated with the orientations of the $\mathbf{u}^{\Delta}$ field. (*e.g.*, Bardina *et al.* 1983; Liu, Meneveau & Katz 1994; Domaradzki & Saiki 1997). For similar dynamic considerations, such behavior should also be apparent within the scalar-gradient field $\nabla\zeta$. To test the extent to which such correlations in fact exist, a DNS database of homogeneous isotropic turbulence including passive-scalar transport was generated, using a third-order in time, fourth-order in space finite-difference code. A series of initial simulations were made at a resolution of 128^3, corresponding to $Re_\lambda \approx 55$. These simulations were run until the field reached statistical stationarity, approximately $5t_o$, where t_o is the global eddy-turnover time. Filter width was selected at $\Delta = 2\pi/16$ approximately in the middle of the range over which log-linear behavior in the scalar-energy fluctuation field spectrum was seen to exist, as illustrated in Figure 1. Using this particular dataset, the correlations between the Δ-scale and subgrid-scale orientations of the scalar gradient field $\nabla\zeta^{\Delta/2}$ are found to be $\rho \sim 0.9$.

Using these findings, it is then possible to describe an additive decorrelation cascade by which the scalar gradient field $\nabla\boldsymbol{\zeta}$ orientations decorrelate isotropically at successively smaller scales from the local orientation of $\nabla\boldsymbol{\zeta}^{\Delta}$ at the smallest resolved scale in the LES, here denoted by the unit vector $\hat{\mathbf{e}}^{\Delta}_{\nabla\zeta}$. Between any two successive stages (n) and $(n+1)$ in the cascade, the corresponding vorticity orientations $(\hat{\mathbf{e}})_{n+1}$ and $(\hat{\mathbf{e}})_n$ thus deviate by stochastic spherical decorrelation angles θ and ϕ. Each component of the orientation unit-vector at stage $(n+1)$ is therefore determined as

$$(\hat{e}_i)_{n+1} \;=\; (\hat{e}_i)_n \;+\; f_i(\phi,\theta)_{n+1}, \tag{2.13}$$

where $f_1(\phi,\theta) = \sin\phi\,\cos\theta$, $f_2(\phi,\theta) = \sin\phi\,\sin\theta$ and $f_3(\phi,\theta) = \cos\phi - 1$. Since isotropy requires θ to be uniformly distributed, the θ dependence will vanish trivially in the expectation value $\langle\nabla\boldsymbol{\zeta}^{sgs}\rangle$ of the stochastic subgrid vorticity field. The ϕ distribution on the other hand should be strongly correlated with the multiplier values $\mathcal{M}$.

Based on the above considerations, a scalar-gradient intermittency factor $\mathcal{I}^s$ can be defined from a correlation between $\nabla\boldsymbol{\zeta}^{sgs}$ and $\nabla\boldsymbol{\zeta}^{\Delta}$ as

$$\mathcal{I}^s \;=\; \int_{\mathbf{x}'} \nabla\boldsymbol{\zeta}^{sgs}\cdot\nabla\boldsymbol{\zeta}^{\Delta}\; d^3\,\mathbf{x}' \;\Bigg/\; \int_{\mathbf{x}'} |\nabla\boldsymbol{\zeta}^{sgs}|\,|\nabla\boldsymbol{\zeta}^{\Delta}|\, d^3\,\mathbf{x}' \,. \tag{2.14}$$

The subgrid scalar gradient field $\nabla\boldsymbol{\zeta}^{sgs}$ after $\mathcal{N}$ cascade steps can then be expressed in terms of $\mathcal{I}^s(\mathcal{N})$ as

$$\nabla\boldsymbol{\zeta}^{sgs}(\mathbf{x},t) \;=\; |\nabla\boldsymbol{\zeta}^{sgs}|\,\left(\mathcal{I}^s(\mathcal{N})\,\hat{\mathbf{e}}^{\Delta}_{\nabla\zeta}(\mathbf{x},t) \;+\; (1-\mathcal{I}^s)\sum_{n=1}^{\mathcal{N}}\boldsymbol{\delta}^s_n\right) \tag{2.15}$$

where $\boldsymbol{\delta}^s_n$ are the scalar-gradient field decorrelation increments in the orientation cascade. Owing to the stochastic nature of both the multiplier values $\mathcal{M}_n$ in the magnitude cascade and the decorrelation increments $\boldsymbol{\delta}^s_n$ in the orientation cascade, the subgrid scalar gradient $\nabla\boldsymbol{\zeta}^{sgs}(\mathbf{x},t)$ is a stochastic field. From (2.15) its expectation value $\langle\nabla\boldsymbol{\zeta}^{sgs}\rangle$ involves correlations between the multipliers $\mathcal{M}_n$ and the increments $\boldsymbol{\delta}^s_n$. If the effect of

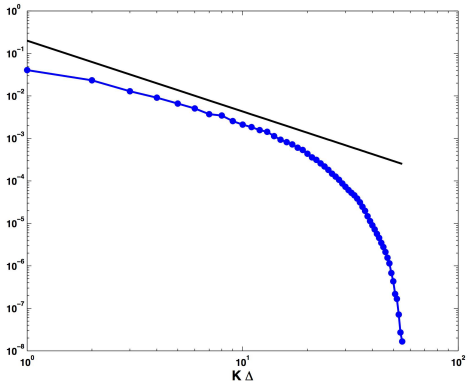

FIGURE 1. Scalar energy spectrum $\mathcal{S}(k) = frac12\zeta^2(k)$ from DNS database with $N = 128^3$ and $Re_\lambda \approx 55$ used for the *a priori* study of the multifractal model in section 4, below. Inertial-convective range scaling of $\mathcal{S}(k) \sim k^{-5/3}$ is apparent over at least one decade of length scales in the dataset.

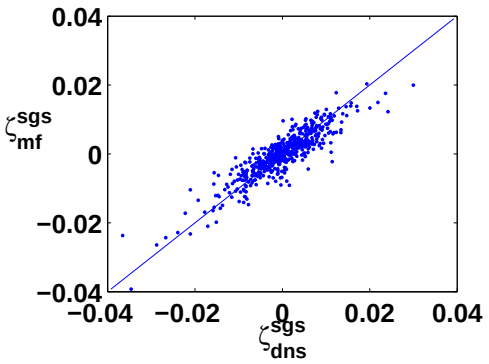

FIGURE 2. Scatterplot of DNS vs. model values for the filtered scalar concentrations $\overline{\zeta^{sgs}}$, from DNS database of $N = 128^3$ and $Re_\lambda \approx 55$. This is an important initial test for the validity of the model set out in (2.24) and (2.25). Model correlations are found to be $\rho \geq 0.90$ for the particular conditions considered.

these correlations is taken to be negligible, then

$$\langle \nabla\boldsymbol{\zeta}^{sgs} \rangle \;=\; \mathcal{I}^s(\mathcal{N})\,\langle |\nabla\boldsymbol{\zeta}^{sgs}| \rangle\,\hat{\mathbf{e}}^{\Delta}_{\nabla\zeta} \;+\; (1-\mathcal{I}^s)\,\langle |\nabla\boldsymbol{\zeta}^{sgs}| \rangle \sum_{n=1}^{\mathcal{N}} \langle \boldsymbol{\delta}^s_n \rangle\,. \tag{2.16}$$

Furthermore, if the decorrelation cascade is isotropic, then the expectation value of the increments in (2.16) vanishes, giving from (2.12)

$$\langle \nabla\boldsymbol{\zeta}^{sgs} \rangle \;=\; \mathcal{I}^s(\mathcal{N})\,\left(2^{\mathcal{N}}\right)^{\frac{3}{2}} \left\langle (\mathcal{M}_1 \cdots \mathcal{M}_{\mathcal{N}})^{\frac{1}{2}} \right\rangle\,(\chi^{sgs})^{1/2}\;\;\hat{\mathbf{e}}^{\Delta}_{\nabla\zeta}, \tag{2.17}$$

where χ^{sgs} comes from (2.9).

2.3.1. *Inversion using Green's Function*

The expectation value of the subgrid scalar concentrations $\langle \zeta^{sgs} \rangle$ is obtained from the corresponding subgrid scalar-gradient field $\langle \nabla\boldsymbol{\zeta}^{sgs} \rangle$ in (2.17) via the Green's function approach, as

$$\langle \zeta^{sgs} \rangle = \nabla \cdot \frac{1}{4\pi} \int_{\mathbf{x}'} \langle \nabla\boldsymbol{\zeta}^{sgs} \rangle\;\frac{1}{|\mathbf{x}-\mathbf{x}'|}\,d\mathbf{x}'\,. \tag{2.18}$$

Since the distribution $P(\mathcal{M})$ of the multipliers in $\langle \nabla\boldsymbol{\zeta}^{sgs} \rangle$ is the same everywhere, from (2.17) and (2.18) the expectation value becomes

$$\langle \zeta^{sgs} \rangle \;=\; \mathcal{I}(\mathcal{N})\,\left(2^{\mathcal{N}}\right)^{\frac{3}{2}} \left\langle (\mathcal{M}_1 \cdots \mathcal{M}_{\mathcal{N}})^{\frac{1}{2}} \right\rangle \left(\frac{\chi^{sgs}}{\chi^{\Delta}}\right)^{\frac{1}{2}} \nabla \cdot \frac{1}{4\pi} \int_{\mathbf{x}'} (\chi^{\Delta})^{1/2}\,\hat{\mathbf{e}}^{\Delta}_{\nabla\zeta}\;\frac{1}{|\mathbf{x}-\mathbf{x}'|}\,d\mathbf{x}'\,. \tag{2.19}$$

The Green's function integral in (2.19) is simply ζ^{Δ}, giving with (2.5) and (2.9)

$$\langle \zeta^{sgs} \rangle \;=\; \mathcal{I}(\mathcal{N})\;2^{\frac{3}{2}\mathcal{N}} \left\langle \mathcal{M}^{\frac{1}{2}} \right\rangle^{\mathcal{N}} \left[2^{\mathcal{N}}-1\right]^{\frac{1}{2}} \sqrt{\kappa}\;\zeta^{\Delta}\,, \tag{2.20}$$

where we have also made use of the fact that the multipliers are statistically independent.

From (2.20) the subgrid scalar concentration values ζ^{sgs} can be written as

$$\zeta_i^{sgs}(\mathbf{x},t) \approx \mathcal{I}^s(\mathcal{N})\,\mathcal{A}^s(\mathcal{N})\sqrt{\kappa}\,\zeta^{\Delta}(\mathbf{x},t) \tag{2.21}$$

where

$$\mathcal{A}^s \equiv 2^{\frac{3}{2}\mathcal{N}}\left\langle \mathcal{M}^{\frac{1}{2}}\right\rangle^{\mathcal{N}}\left[2^{\mathcal{N}}-1\right]^{\frac{1}{2}}. \tag{2.22}$$

2.3.2. *Final form of model*

The intermittency factor $\mathcal{I}^s$ from (2.14) that appears in (2.21) is implied by the required Re_Δ-independence of ζ^{sgs} as $Re_\Delta \to \infty$. As correspondingly $\mathcal{N} \to \infty$ this requires

$$\mathcal{I}^s(\mathcal{N}) \approx C_{\mathcal{I}^s}\,2^{-2\mathcal{N}}\left\langle \mathcal{M}^{\frac{1}{2}}\right\rangle^{-\mathcal{N}}. \tag{2.23}$$

The associated proportionality constant $C_{\mathcal{I}^s}$ should be universal, and can be obtained from *a priori* testing using the DNS data discussed above, with the result that $C_{\mathcal{I}^s} \approx 0.3$. Together with the multifractal model for the subgrid velocity components of (2.3) and (2.4), this gives the multifractal model for the subgrid scalar flux vector σ_j^* as

$$\sigma_j^* \approx \mathcal{D}\,\overline{\overline{u}_j\,\zeta^{\Delta}} + \mathcal{B}\,\overline{u_j^{\Delta}\,\overline{\zeta}} + \mathcal{B}\,\mathcal{D}\,\overline{u_j^{\Delta}\,\zeta^{\Delta}}, \tag{2.24}$$

where

$$\mathcal{D} \equiv 0.39\;2^{-\frac{2\mathcal{N}}{3}}\left[2^{\frac{4\mathcal{N}}{3}}-1\right]^{\frac{1}{2}} \tag{2.25}$$

where $\mathcal{B}$ is given by (2.4), and where $\mathcal{N}$ is from (2.5). This involves only quantities available from the resolved scales of the flow, thus closing the subgrid-scalar flux term in the passive-scalar transport equation in (2.1) and (2.2).

3. Numerical implementation of the passive-scalar flux model

Each of the filtered product terms appearing in (2.24) and (2.1) is calculated using an explicit Legendre box filter, following the method presented in Burton & Dahm (2004*a*). In brief, this approach approximates each velocity component and scalar term by a three-dimensional Legendre expansion, which for the resolved velocity component field is given as

$$\overline{u}_j(\mathbf{x}) \approx \sum_{l,m,n} a_{lmn}\,\Phi_l(x)\,\Phi_m(y)\,\Phi_n(z) \equiv \mathcal{G}_j(\mathbf{x}), \tag{3.1}$$

and for the Δ-scale velocity component as

$$u_j^{\Delta}(\mathbf{x}) \approx \sum_{l,m,n} b_{lmn}\,\Phi_l(x)\,\Phi_m(y)\,\Phi_n(z) \equiv \mathcal{H}_j(\mathbf{x}). \tag{3.2}$$

Legendre expansions for the resolved and Δ-scale passive-scalar concentrations, $\mathcal{G}^s$ and $\mathcal{H}^s$, are defined similarly. The filtered products in the subgrid-scalar flux vector σ_j^* in (2.24) are then explicitly evaluated by integrating over the grid cell volume as

$$\overline{\overline{u}_j\zeta^{\Delta}} \approx \frac{1}{\Delta^3}\int_{\Delta^3}\mathcal{G}_j(\mathbf{x})\,\mathcal{H}^s(\mathbf{x})\,d^3\mathbf{x} \tag{3.3}$$

$$\overline{u_j^{\Delta}\overline{\zeta}} \approx \frac{1}{\Delta^3}\int_{\Delta^3}\mathcal{H}_j(\mathbf{x})\,\mathcal{G}^s(\mathbf{x})\,d^3\mathbf{x} \tag{3.4}$$

$$\overline{u_j^{\Delta}\,\zeta^{\Delta}} \approx \frac{1}{\Delta^3}\int_{\Delta^3}\mathcal{H}_j(\mathbf{x})\,\mathcal{H}^s(\mathbf{x})\,d^3\mathbf{x}, \tag{3.5}$$

and similarly the explicit filter on the inertial term in (2.1) is evaluated as

$$\overline{\overline{u}_j\,\overline{\zeta}} \;\approx\; \frac{1}{\Delta^3}\int_{\Delta^3} \mathcal{G}_j(\mathbf{x})\,\mathcal{G}^s(\mathbf{x})\,d^3\mathbf{x}. \tag{3.6}$$

Equations (2.24) – (3.6) allow evaluation of σ_j^* and the nonlinear term $\overline{\overline{u}_j\,\overline{\zeta}}$ in (2.1), and together provide a complete statement of the multifractal subgrid-scale model for large-eddy simulation of the mixing of a conserved passive-scalar.

4. *A priori* evaluation of the multifractal passive-scalar flux model

Because multifractal modeling of the subgrid passive scalar concentrations, like the related velocity model, attempts to replicate the actual structure of the unknown subgrid field, its performance in actual large-eddy simulations can be accurately assessed by *a priori* testing, in which model values are compared with DNS or expermental data from one realization of the given flow field.† As a result, the model for the filtered scalar flux term of the previous section was first tested in the *a priori* sense against the DNS database described above.

The filtered scalar fields $\overline{\zeta}$ supplied to the subgrid-scale model were first used to construct the subgrid scalar concentration fields from (2.21), and the resulting fields then filtered at the scale Δ using the Legendre box filter to give the filtered subgrid scalar concentration components $\overline{\zeta^{sgs}}$. As can be seen by the scatterplot in Figure 2, the model values agree well with the DNS data, with correlations of $\rho \approx 0.90$. For purposes of an actual large eddy simulation, the most relevant *a priori* comparison is of the subgrid scalar flux vector σ^* from (2.24) and the complete scalar flux vector σ^T, where

$$\sigma^T \;\equiv\; \overline{\overline{u}_j\,\overline{\zeta}} \;+\; \mathcal{D}\,\overline{\overline{u}_j\zeta^{\Delta}} \;+\; \mathcal{B}\,\overline{u_j^{\Delta}\overline{\zeta}} \;+\; \mathcal{B}\mathcal{D}\,\overline{u_j^{\Delta}\,\zeta^{\Delta}}. \tag{4.1}$$

As indicated in Figure 3, the subgrid scalar σ^* correlations exceed $\rho \geq 0.9$ (*right column*), while for the complete scalar flux term σ^T correlations exceed $\rho \geq 0.995$ (P*left column*). The latter is the most relevant measure for an actual LES, since the complete σ^T is necessary to solve the passive-scalar transport equation, and since each term in (4.1) is implicated in energy transfer to the subgrid scales. Finally, corrrelations were also examined for the subgrid scalar energy production field, given by

$$\mathcal{P}^s \equiv \left[\overline{\overline{u}_j\,\overline{\zeta}} + \mathcal{D}\,\overline{\overline{u}_j\zeta^{\Delta}} + \mathcal{B}\,\overline{u_j^{\Delta}\overline{\zeta}} \;+ \mathcal{B}\mathcal{D}\,\overline{u_j^{\Delta}\,\zeta^{\Delta}}\right]\,\frac{\partial\overline{\zeta}}{\partial x_j}. \tag{4.2}$$

As illustrated in Figure 4, correlations for that portion of the subgrid-scalar energy transfer due to σ^* in (2.2) exceed $\rho = 0.90$, while for the complete scalar-energy production field given by (4.2) correlations exceed $\rho \geq 0.995$. This indicates that at least for the conditions considered here the multifractal model recovers the details of the spatial distribution of $P^s(\mathbf{x},t)$ with extremely high accuracy.

5. *A posteriori* evaluation of the multifractal passive-scalar flux model.

The multifractal model for the flux of a filtered passive scalar was next tested in actual large-eddy simulations of forced, periodic, homogeneous isotropic turbulence with passive

† This is in contrast to eddy-viscosity methods, which cannot recover the details in the subgrid stress or energy production fields, and thus in which *a priori* tests provide little guidance about the model's performance in an actual simulation.

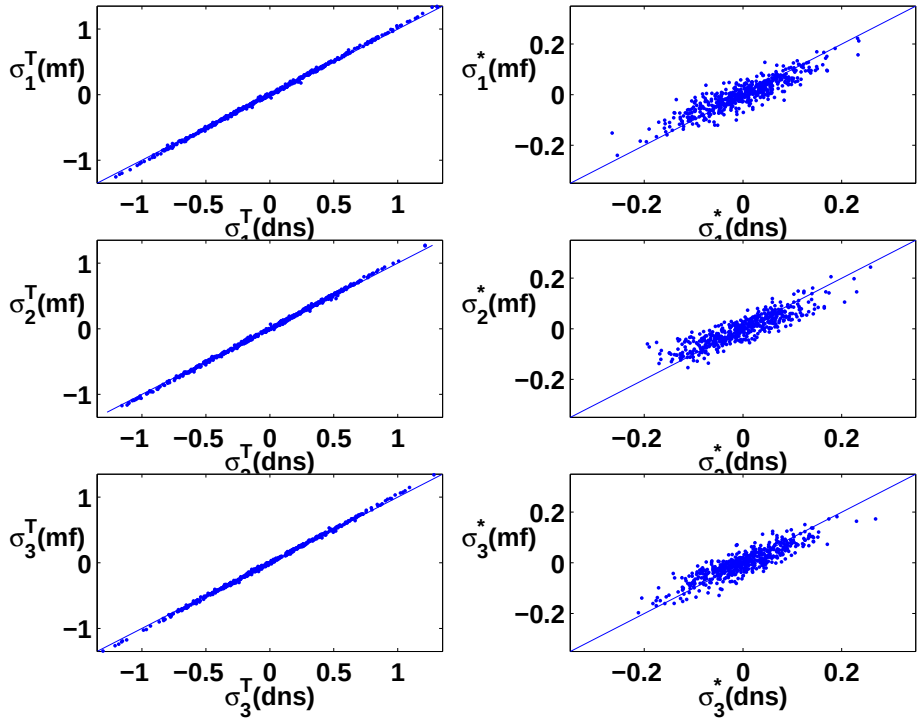

FIGURE 3. Scatterplot comparisons between DNS and model values for the full scalar flux σ^T given by (4.1), and that portion of the scalar flux involving the subgrid scalar concentrations ζ^{sgs} given in (2.2). Graphic indicates that correlations for σ_j^* exceed $\rho = 0.9$ (*right column*), while correlations for σ_j^T exceed $\rho = 0.995$ (*left column*). This indicates that the multifractal model produces exceedingly accurate representations of the scalar-inertial stress $\sigma^T(x,t)$ needed to solve the filtered passive-scalar transport equation of (2.1).

scalar mixing. The simulations were conducted at a resolution of $N = 32^3$, at $Re_\lambda \approx 160$ and a Schmidt number of $Sc = 1$. Details of the computational setup as well as the use of the backscatter limiter are given in Burton & Dahm (2004*b*).

The simulations were initiated by allowing an initial velocity field, randomized as to phase and with a kinetic energy spectrum scaling of $k^{-5/3}$ to reach a statistically stationary state, after which the passive-scalar field was introduced to the calculation. Various initialized states for the passive-scalar field have been implemented including a double-delta p.d.f. with concentrations near 0 and 1, where $\beta(\zeta) \equiv 0.5\,\delta(\zeta - 0) + 0.5\,\delta(\zeta - 1)$. Other simulations have been initialized with a normally distributed scalar concentration field in which the scalar energy field exhibited the traditional inertial-convective range power law scaling of $\mathcal{S}(k) \sim k^{-5/3}$. The simulations were then run to varying final times t_f where $4t_o \leq t_f \leq 20t_o$, where t_o is the global eddy-turnover time. Forcing for both the velocity and scalar fields is obtained by rescaling wave modes $|k| \leq 2$, so that a constant energy is maintained in those wavemodes throughout the simulation. Statistical measures were taken thereafter at a frequency of $2t_o$ to guarantee statistically independent samples of the flow field.

As illustrated in the time-evolution of the simulation in Figure 5 (*top*), the multifractal passive-scalar model runs stably over nearly 12 eddy turnover times, indicating that

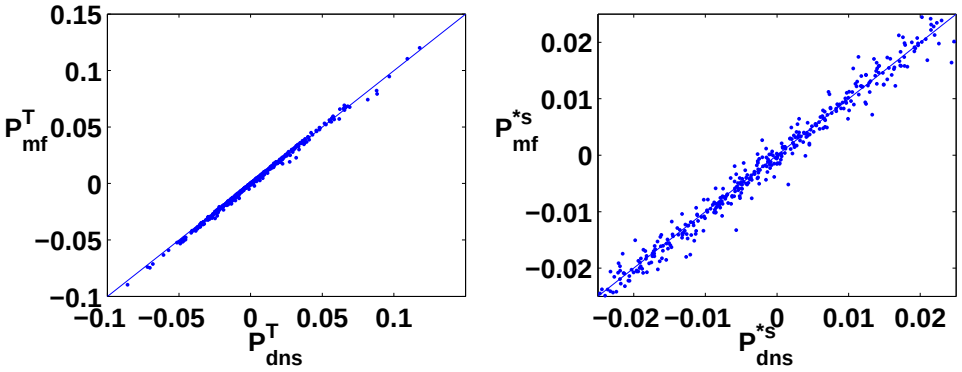

FIGURE 4. Scatterplots of scalar-energy production field comparing DNS values against the multifractal model given in (4.2). Graphic indicates that for the present DNS data, correlations exceed $\rho = 0.9$ for $\mathcal{P}^{*s}$ and $\rho = 0.995$ for the complete scalar energy production field $\mathcal{P}^{s}$ in (4.2) (*left and right columns respectively*).

the backscatter limiter for both the kinetic energy and scalar energy fields properly maintains resolved kinetic and scalar energies at physically realistic levels. In addition, the model reproduces the well-known result for flows where $Sc \approx 1$, that in the inertial-convective range, the scalar energy spectrum exhibits a power law scaling where $\zeta^2(k) \sim k^{-5/3}$, as shown in Figure 5 (*bottom*). This is a hallmark of high Reynolds number turbulence, as are the deviations from the Gaussian distribution for the skew components of the velocity gradient tensor illustrated in Figure 6. There it is evident that the flow field exhibits significant intermittency indicated by the log-linear tails of the velocity gradient magnitudes distributions. In addition Figure 7 illustrates the probability density functions for the scalar energy production (*left*) and kinetic energy production fields (*right*).

6. Future plans

6.1. *LES of passive-scalar mixing with mean scalar gradient*

Additional analysis must first be completed for the current case of forced periodic homogeneous isotropic turbulence. This includes evaluation of the scalar, scalar gradient and scalar dissipation distributions generated by LES with the multifractal model for given initial conditions of the scalar and velocity fields. Since the initial fields are randomized, it is crucial to establish within rigorous statistical bounds the performance of the model by running a number of simulations with constant parameters using different realizations of the given initial fields.

Thereafter, the model will be evaluated in the more sensitive and well-documented problem of high Reynolds-number turbulent mixing in the presence of a mean scalar gradient. Several DNS studies have been conducted of this flow regime (*e.g.,* Overholt & Pope 1996) and will provide the data against which the LES simulations will be compared. With a mean scalar gradient, the resolved-scale scalar energy equation is given by

$$\frac{1}{2}\frac{\partial}{\partial t}\overline{\zeta}^2 + \frac{\partial}{\partial x_j}\left(\overline{\zeta}\,\overline{u_j\,\zeta} + \overline{\zeta}\,\overline{u_j\,\alpha x_k} - D\,\overline{\zeta}\,\frac{\partial\overline{\zeta}}{\partial x_j}\right) = \left(\overline{u_j\,\zeta} + \overline{u_j\,\alpha x_k}\right)\frac{\partial\overline{\zeta}}{\partial x_j} - D\,\frac{\partial\overline{\zeta}}{\partial x_j}\,\frac{\partial\overline{\zeta}}{\partial x_j}, \tag{6.1}$$

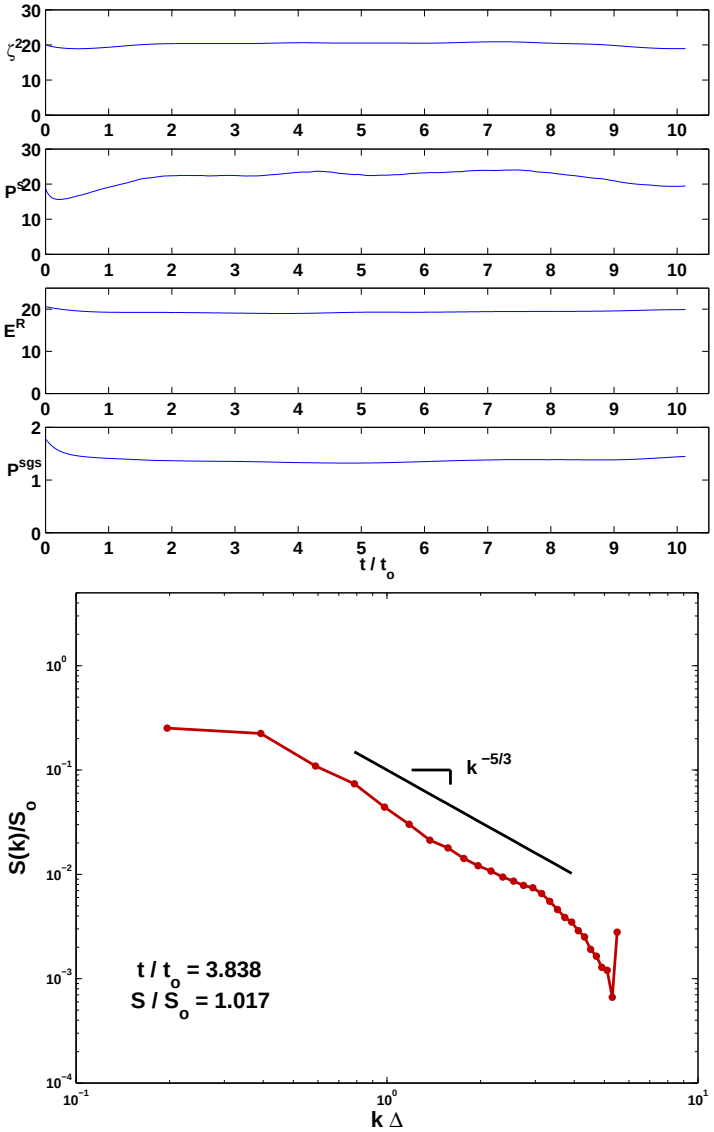

FIGURE 5. Large-eddy simulation with passive scalar mixing for $N = 32^3$, $Re_\lambda \approx 160$ and $Sc = 1$. (*Top frame, top to bottom:*) Evolution of resolved passive-scalar energy $\overline{\zeta}^2$, passive-scalar energy production P^s, resolved kinetic energy E^R, and kinetic energy production P^{sgs}, indicating that with the multifractal model and backscatter limiter the simulation runs stably to long integrated times. (*Bottom frame:*) Energy spectrum for resolved scalar concentrations $\frac{1}{2}\overline{\zeta^2}$, exhibiting the power law scaling $S(k) \sim k^{-5/3}$ characteristic of the inertial-convective range in high-Reynolds number turbulent scalar mixing.

where the total scalar field is expressed as

$$\zeta\,(\mathbf{x},t) \;=\; \left(\,\overline{\zeta} \;+\; \zeta^{sgs}\,\right)(\mathbf{x},t) \;+\; \alpha\, x_k\,, \tag{6.2}$$

and where α represents the mean scalar gradient imposed in the k-th component direc-

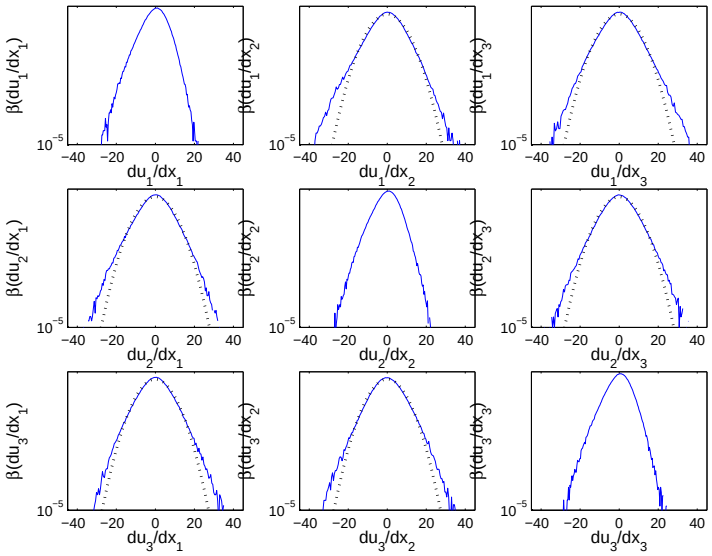

FIGURE 6. Probability distributions of the velocity gradient tensor from the LES of passive scalar mixing at $N = 32^3$ and $Re_\lambda \approx 160$ and $Sc = 1.0$. Note the significant deviation of the off-diagonal p.d.f.s from the Gaussian (dotted) indicating that the model is recovering significant intermittency seen in the resolved scales in real high Reynolds number turbulent flow, some three to four orders of magnitude smaller than the mean.

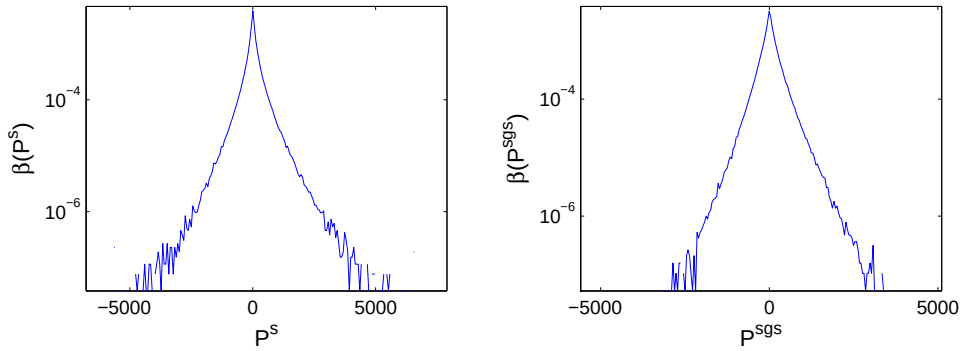

FIGURE 7. Probability distributions of the scalar energy production (*left*) and kinetic energy production (*right*) for LES using multifractal model developed in this paper.

tion. From (6.1), it is apparent that the mean gradient α imposes an additional source term on the scalar energy equation by the scalar flux working against the mean scalar gradient (Overholt & Pope 1996). Prior DNS studies have shown that the normalized scalar variance, dissipation time ratio, and the ratio of subgrid-scalar energy production to total scalar-energy dissipation all become independent of Reynolds number above $Re_\lambda \geq 180$. In addition, it has been demonstrated that the skewness of the scalar gradient in the direction of the imposed mean gradient may grow smaller with increasing Schmidt number (Yeung *et al.* 2002). The accuracy of the multifractal model will therefore be evaluated in the context of these well-established measures of passive-scalar mixing in fully developed turbulent flow with a mean scalar gradient.

6.2. *LES of free round jet with passive-scalar mixing*

Finally, the multifractal model will be incorporated into the modified JETCODE described in Burton (2004), so that the present modeling approach may be evaluated in the context of simulations involving passive-scalar mixing in a free round turbulent jet. Since turbulent jets are encountered in many practical combustion applications such as turbines, furnaces, and rocket engines, this configuration will provide an important test of the efficacy of multifractal modeling for a variety of practical turbulence modeling problems using large-eddy simulation.

REFERENCES

Bardina, J., Ferziger, J. H. & Reynolds, W. C. 1983 Improved turbulence models based on large eddy simulation of homogeneous, incompressible, turbulent flows. *Technical Report TF-19*, Thermosciences Div., Stanford University, Stanford, CA.

Burton, G. C. 2004 Large-eddy simulation of a free round jet using multifractal subgrid-scale modeling. *Annual Research Briefs 2004* Center for Turbulence Research, NASA/Stanford University.

Burton, G. C. & Dahm, W. J. A. 2004*a* Multifractal subgrid-scale modeling for large-eddy simulation. Part 1: model development and *a priori* testing. *Submitted to Phys. Fluids.*

Burton, G. C. & Dahm, W. J. A. 2004*b* Multifractal subgrid-scale modeling for large-eddy simulation. Part 2: backscatter limiting and *a posteriori* evaluation. *Submitted to Phys. Fluids.*

Domaradzki, J. A. & Saiki, E. M. 1997 A subgrid-scale model based on the estimation of unresolved scales of turbulence. *Phys. Fluids* **9** 2148-2164.

Frederiksen, R. D., Dahm, W. J. A. & Dowling, D. R. 1997 Experimental assessment of fractal scale similarity in turbulent flows. Part 3. Multifractal scaling. *J. Fluid Mech.* **338** 127-155.

Frederiksen, R. D., Dahm, W. J. A. & Dowling, D. R. 1998 Experimental assessment of fractal scale similarity in turbulent flows. Part 4. Effects of Reynolds and Schmidt numbers. *J. Fluid Mech.* **377** 169-187.

Liu, S., Meneveau, C. & Katz, J. 1994 On the properties of similarity subgrid-scale models as deduced from measurements in a turbulent jet. *J. Fluid Mech.* **275** 83-119.

Overholt, M. R. & Pope, S. B. 1996 Direct numerical simulation of a passive scalar with imposed mean gradient in isotropic turbulence *Phys. Fluids* **8** 3128-3148.

Prasad, R. R., Meneveau, C. & Sreenivasan, K. R. 1988 The multifractal nature of the dissipation field of passive scalars in fully turbulent flows. *Phys. Rev. Lett.* **61** 74-77.

Sreenivasan, K. R. & Prasad, R. R. 1989 New results on the fractal and multifractal structure of the large Schmidt number passive scalars in fully turbulent flows. *Physica D* **38** 322-329.

Yeung, P. K., Xu, S. & Sreenivasan, K. R. 2002 Schmidt number effects on turbulent transport with uniform mean scalar gradient *Phys. Fluids* **14** 4178-4191.

Large-eddy simulation of a free round jet using multifractal subgrid-scale modeling

By G.C. Burton

1. Motivation and objectives

The free round turbulent jet is perhaps the most extensively studied of the canonical free-shear turbulent flows. Turbulent jets are important to a variety of industrial applications such as fuel injectors, furnaces, and rocket engines. Owing to the difficulty, time and expense of conducting experimental studies of most turbulent flows, numerical simulation of the turbulent jet has been increasingly used to guide design and development work at the industrial level. It has also provided numerous insights into fundamental physical laws governing such flows. Reynolds-averaged Navier-Stokes (RANS) studies of such jets, in which only the time-averaged mean flow is explicitly calculated, have been used extensively in the past, but remain of only limited accuracy, and thus of limited usefulness, in the industrial design process. On the other hand, fully resolved studies (DNS) of turbulent flows, which could provide the needed precision, will remain for most flows encountered in engineering practice far beyond the capability of the most powerful computers for some decades to come. Midway between DNS and RANS lies the approach of large-eddy simulation (LES), which explicitly calculates the large-scale turbulent structures, while modeling the smaller unresolved scales. An accurate model for the small scales is needed for LES to provide a reliably accurate tool for practical turbulent flow problems. Most current models rely on an eddy-viscosity assumption that the smallest-resolved eddies in an LES remove energy from the resolved flow much like molecular viscosity at the smallest continuous scales in actual turbulence. Such models, even if roughly capturing the integrated transfer of energy to the subgrid scales, cannot reproduce the detailed spatial structure of the true energy transfer field $\mathcal{P}(x,t)$.

Recently Burton & Dahm (2004 *a,b*) have proposed a multifractal subgrid-scale model that does not rely on an eddy-viscosity assumption, but instead is derived from the multifractal structure of the vorticity field in high Reynolds-number turbulence. From this, a new, highly accurate model for the subgrid velocity field u_i^{sgs} has been proposed that permits explicit calculation of the nonlinear term $\overline{u_i\,u_j}$, thus closing the filtered Navier-Stokes equations. Prior LES of forced homogeneous isotropic turbulence using the multifractal model indicate that stable and remarkably accurate simulations may be obtained, including recovery of the detailed spatial structure of the subgrid energy-production field $\mathcal{P}^{sgs}(\mathbf{x},t)$, with $\rho \geq 0.995$ (Burton & Dahm 2004*b*). The work reported in the present paper involves refining and evaluating the accuracy of the multifractal model in the significantly more complex configuration of a free round turbulent jet.

2. Overview: Multifractal subgrid-scale modeling

A full development of multifractal subgrid-scale modeling for LES is given in Burton & Dahm (2004 *a,b*). Only the most important aspects of the modeling approach are summarized here.

2.1. *The subgrid-scale model*

Multifractal modeling derives a representation for the subgrid velocity field $\mathbf{u}^{sgs}(\mathbf{x},t)$ from a representation of the subgrid vorticity field $\boldsymbol{\omega}^{sgs}(\mathbf{x},t)$ using the Biot-Savart operator. The resulting subgrid velocity field is then used to solve explicitly the subgrid stress tensor τ_{ij}^* using the form of the filtered momentum equation given by

$$\frac{\partial \overline{u}_i}{\partial t} + \frac{\partial}{\partial x_j}\overline{\overline{u}_i\,\overline{u}_j} + \frac{1}{\rho}\frac{\partial \overline{p}}{\partial x_i} - \nu\frac{\partial^2 \overline{u}_i}{\partial x_j^2} = -\frac{\partial}{\partial x_j}\tau_{ij}^*, \tag{2.1}$$

where

$$\tau_{ij}^* \equiv \overline{\overline{u}_i\, u_j^{sgs}} + \overline{u_i^{sgs}\,\overline{u}_j} + \overline{u_i^{sgs}\, u_j^{sgs}}. \tag{2.2}$$

The derivation begins by noting that the enstrophy field $\frac{1}{2}\,\boldsymbol{\omega}\cdot\boldsymbol{\omega}(\mathbf{x},t)$ in high Reynolds number turbulence exhibits multifractal scale similarity over inertial range scales. Therefore, the spatial distribution of subgrid vorticity magnitude $|\boldsymbol{\omega}^{sgs}|(\mathbf{x},t)$ may be described by a multiplicative multifractal cascade. Similarly, DNS data indicates that the distribution of subgrid vorticity orientations $\mathbf{e}^{\boldsymbol{\omega}^{sgs}}(\mathbf{x},t)$ may be represented by an additive orientation cascade by which the subgrid vorticity field decorrelates isotropically from the smallest resolved field $\boldsymbol{\omega}^{\Delta}(\mathbf{x},t)$. The subgrid velocity field $\mathbf{u}^{sgs}(\mathbf{x},t)$ may then be determined by applying the Biot-Savart operator to this representation of the subgrid vorticity field. Since both the magnitude and orientation cascades are stochastic in nature, the resulting integral can be evaluated using probabilistic concepts with the result that the subgrid stress tensor τ_{ij}^* may be modeled as

$$\tau_{ij}^* \approx \mathcal{B}\left(\overline{\overline{u}_i\, u_j^{\Delta}} + \overline{\overline{u}_j\, u_i^{\Delta}}\right) + \mathcal{B}^2\,\overline{u_i^{\Delta}\, u_j^{\Delta}}, \tag{2.3}$$

where

$$\mathcal{B} \equiv 0.47\; 2^{-\frac{2\mathcal{N}}{3}}\left[2^{\frac{4\mathcal{N}}{3}} - 1\right]^{\frac{1}{2}}, \tag{2.4}$$

$\mathcal{N}$ represents the number of cascade iterations within the subgrid field given by

$$\mathcal{N} \equiv \log_2(\Delta/\lambda_\nu). \tag{2.5}$$

and where u_i^{Δ} is the velocity field associated with the smallest resolved scale Δ. This involves only quantities available from the resolved scales of the flow, thus closing the subgrid-stress term in the momentum equation in (2.1).

Each of the filtered products represented by the long overbars in (2.3) is explicitly evaluated as

$$\overline{\overline{u}_i\, u_j^{\Delta}} \approx \frac{1}{\Delta^3}\int_{\Delta^3} \mathcal{G}_i(\mathbf{x})\,\mathcal{H}_j(\mathbf{x})\,d^3\mathbf{x} \tag{2.6}$$

$$\overline{u_i^{\Delta}\, u_j^{\Delta}} \approx \frac{1}{\Delta^3}\int_{\Delta^3} \mathcal{H}_i(\mathbf{x})\,\mathcal{H}_j(\mathbf{x})\,d^3\mathbf{x}, \tag{2.7}$$

and the filtered product of the resolved velocity components in (2.1) is similarly evaluated as

$$\overline{\overline{u}_i\,\overline{u}_j} \approx \frac{1}{\Delta^3}\int_{\Delta^3} \mathcal{G}_i(\mathbf{x})\,\mathcal{G}_j(\mathbf{x})\,d^3\mathbf{x}. \tag{2.8}$$

The functions $\mathcal{G}_i(\mathbf{x})$ and $\mathcal{H}_i(\mathbf{x})$ are, respectively, Legendre expansions of $\overline{u}_i(\mathbf{x})$ and $u_i^{\Delta}(\mathbf{x})$

as

$$\overline{u}_i(\mathbf{x}) \approx \sum_{l,m,n} a_{lmn}\, \Phi_l(x)\, \Phi_m(y)\, \Phi_n(z) \equiv \mathcal{G}_i(\mathbf{x}) \tag{2.9}$$

$$u_i^{\Delta}(\mathbf{x}) \approx \sum_{l,m,n} b_{lmn}\, \Phi_l(x)\, \Phi_m(y)\, \Phi_n(z) \equiv \mathcal{H}_i(\mathbf{x}), \tag{2.10}$$

where the required cell-centered values of u_i^{Δ} are obtained from the cell-centered values of $\overline{u}_i(\mathbf{x})$ as

$$u_i^{\Delta} \equiv \overline{u}_i - a_{000}. \tag{2.11}$$

Equations (2.1) and (2.3) – (2.11) give a complete statement of the multifractal model for large-eddy simulation.

2.2. *Backscatter limiting*

Numerical errors introduced in the resolved scales during an actual simulation are reduced by introducing an explicit backscatter limiter in the flow calculation. This effectively decouples the role of the subgrid model from the additional burden of controlling the numerical error. The backscatter limiting is implemented by a small reduction in the local magnitude of only those stress components that contribute to local backscatter of energy from the subgrid scales to the resolved scales. Since $\mathcal{P} \equiv \mathcal{P}^* + \mathcal{P}^R$, where

$$\mathcal{P}^*(\mathbf{x},t) \equiv -\tau_{ij}^*\, \overline{S}_{ij} \tag{2.12}$$

and

$$\mathcal{P}^R(\mathbf{x},t) \equiv -\overline{\overline{u}_i\, \overline{u}_j}\, \overline{S}_{ij}, \tag{2.13}$$

the limiter first calculates each of the terms $\mathcal{P}_{(ij)}$ that contribute to the local subgrid production as

$$\mathcal{P}_{(ij)} \equiv -\left(\overline{\overline{u}_{(i)}\, \overline{u}_{(j)}} + \tau_{(ij)}^*\right) \overline{S}_{(ij)}\,, \tag{2.14}$$

where the subscript parentheses indicate that no summation is implied. Any of the local $\mathcal{P}_{(ij)}$ terms that are negative will contribute to local backscatter of energy, and thus only those terms are reduced as

$$\widehat{\mathcal{P}_{(ij)}} \equiv (1 - C_{\mathcal{B}})\, \mathcal{P}_{(ij)}\,, \tag{2.15}$$

where $0 \le C_{\mathcal{B}} \le 1$ is a prescribed backscatter-limiter coefficient. This has the effect of locally reducing the contribution to backscatter into the resolved scales by the amount $C_{\mathcal{B}}\, \mathcal{P}_{(ij)}$, which is largest where $\mathcal{P}_{(ij)}$ is most strongly negative and thus where the numerical errors are presumably also largest.

To implement this in the momentum equation in (2.1), for each (ij) in (2.14) for which $\mathcal{P}_{(ij)} < 0$, the corresponding production term $\mathcal{P}_{(ij)}$ is effectively replaced with $\widehat{\mathcal{P}_{(ij)}}$ from (2.15), by replacing the corresponding $\overline{\overline{u}_{(i)}\, \overline{u}_{(j)}}$ in (2.1) with the backscatter-limited value

$$\widehat{\overline{\overline{u}_{(i)}\, \overline{u}_{(j)}}} = (1 - C_{\mathcal{B}})\, \overline{\overline{u}_{(i)}\, \overline{u}_{(j)}}, \tag{2.16}$$

and replacing the corresponding $\tau_{(ij)}^*$ in (2.1) with the backscatter-limited value

$$\widehat{\tau_{(ij)}^*} = (1 - C_{\mathcal{B}})\, \tau_{(ij)}^*. \tag{2.17}$$

Altering the components in the momentum equation in this manner is equivalent to backscatter-limiting the subgrid energy production field $\mathcal{P}(\mathbf{x},t)$ as in (2.15). Note that the

limiter procedure could alternatively be implemented by an analogous forward-transfer accelerator, in which the backscatter reduction is replaced by a forward-transfer accelerator factor $(1 + C_{\mathcal{F}})$ for each (ij) in (2.14) for which $\mathcal{P}_{(ij)} > 0$.

3. Adaptive backscatter limiting for LES

3.1. *Motivation*

Prior studies have indicated that a backscatter reduction factor of $C_{\mathcal{B}} \approx 0.15$ provides reasonably optimal control of resolved energy levels for the specific case of periodic forced homogeneous isotropic turbulence for a resolution of $N = 32^3$ and a grid-cell Reynolds number of $Re_{\Delta} \approx 160$ (Burton & Dahm 2004*b*). However, in the more complex configurations seen in practical engineering development work such as the turbulent round jet, spatial and temporal variation in flow conditions may be significant during the simulation. As a result, it may prove advantageous to vary the value for $C_{\mathcal{B}}$ during the simulation. Thus before the multifractal model was used in an LES of a round jet, a method was developed and tested for adaptively determining the value for the backscatter coefficient $C_{\mathcal{B}}$. This adaptive approach is shown to eliminate globally numerical errors in subgrid-energy transfer during a simulation or to reduce local errors to the order of the spatial derivative operators.

3.2. *Resolved energy transport*

The kinetic energy of the resolved velocity field $\mathcal{E}(\mathbf{x},t) \equiv \frac{1}{2}\overline{u}_i\overline{u}_i$, as implemented in the multifractal model evolves according to

$$\frac{\partial}{\partial t}\,\mathcal{E}(\mathbf{x},t) \;=\; \frac{\partial}{\partial x_j}\,[\,\mathcal{R}_j\,] \;-\; \mathcal{D} \;-\; \mathcal{P}. \tag{3.1}$$

The flux vector $\mathcal{R}_j$ is given by

$$\mathcal{R}_j(\mathbf{x},t) \;\equiv\; -\left[\,\overline{u}_i\,\left(\,\overline{\overline{u}_i\,\overline{u}_j} \;+\; \tau^*_{ij}\,\right) \;+\; \overline{u}_i\,\frac{\overline{p}}{\rho}\,\delta_{ij} \;-\; \nu\,\frac{\partial\,\mathcal{E}}{\partial x_j}\,\right], \tag{3.2}$$

which appears in (3.1) in divergence form and thus has no effect on energy transfer between the resolved and subgrid scales. Only the resolved viscous dissipation $\mathcal{D}$ defined as

$$\mathcal{D}(\mathbf{x},t) \;\equiv\; 2\nu\,\overline{S}_{ij}\,\overline{S}_{ij} \tag{3.3}$$

and the subgrid energy production $\mathcal{P}$ defined as

$$\mathcal{P}(\mathbf{x},t) \;\equiv\; -\,\left(\,\overline{\overline{u}_i\,\overline{u}_j} \;+\; \tau^*_{ij}\,\right)\,\overline{S}_{ij}, \tag{3.4}$$

contribute to the exchange of energy between the resolved and subgrid scales. The subgrid production $\mathcal{P}$ in (3.4) may be broken down further into components contributing to the forward transfer of energy $\mathcal{P}^{\,forw}$ where,

$$\mathcal{P}^{forw} = \sum \mathcal{P}_{(ij)} \quad \forall\, \mathcal{P}_{(ij)} > 0 \tag{3.5}$$

and backscatter $\mathcal{P}^{\,back}$ where

$$\mathcal{P}^{back} = \sum \mathcal{P}_{(ij)} \quad \forall\, \mathcal{P}_{(ij)} < 0 \tag{3.6}$$

and where in (3.1)

$$\mathcal{P}(\mathbf{x},t) \;\equiv\; \mathcal{P}^{forw}(\mathbf{x},t) \;+\; \mathcal{P}^{\,back}(\mathbf{x},t)\,. \tag{3.7}$$

This gives the final energy transport equation as

$$\frac{\partial}{\partial t}\,\mathcal{E}(\mathbf{x},t) \;=\; \frac{\partial}{\partial x_j}\,[\,\mathcal{R}_j\,] \;-\; \mathcal{D} \;-\; \left(\mathcal{P}^{forw} + \mathcal{P}^{\,back}\right). \tag{3.8}$$

3.3. *Implementation of adaptive backscatter limiter*

We can however adaptively select a local backscatter reduction coefficient $C_{\mathcal{B}}(\mathbf{x},t)$ as follows. Equation 3.8 with the backscatter limiter can be stated as

$$\frac{\partial}{\partial t}\,\mathcal{E}(\mathbf{x},t) \;=\; \frac{\partial}{\partial x_j}\,[\,\mathcal{R}_j\,] \;-\; \mathcal{D} \;-\; \left(\mathcal{P}^{forw} + (\,1 \;-\; C_{\mathcal{B}})\;\mathcal{P}^{\,back}\right). \tag{3.9}$$

with all terms similarly defined as in the previous section. First, a target value is selected for energy transfer at a given location, which is taken to be the exact amount of resolved energy desired at a particular location at the next timestep as $\mathcal{E}^{exact}(\mathbf{x},t) \equiv \mathcal{E}^{(n+1)}(\mathbf{x},t)$. This target value may be taken from the value predicted by the multifractal subgrid model itself or from some other estimate, such as for example that predicted by the dynamic Smagorinsky model. With an initial guess for the coefficient as $C_{\mathcal{B}}^{(n)}$, the flow solver is then advanced one step in time giving an estimated new value for the resolved energy $\mathcal{E}^{*}$ as

$$\mathcal{E}^{(*)}(\mathbf{x},t) \;=\; \mathcal{E}^{(n)} \;+\; \Delta t\left[\frac{\partial}{\partial x_j}\,[\,\mathcal{R}_j\,] \;-\; \mathcal{D} \;-\; \mathcal{P}^{forw} - \beta\left(1 \;-\; C_{\mathcal{B}}^{(n)}\right)\,\mathcal{P}^{\,back}\right]^{(n)}, \tag{3.10}$$

where β is a relaxation factor, that may nominally be set to $\beta \;=\; 1$. Note, however, that in general the resulting value $\mathcal{E}^{(*)}(\mathbf{x},t) \neq \mathcal{E}^{exact}(\mathbf{x},t)$, due to the effect of numerical errors such as aliasing. Therefore, the error between this actual and the intended final kinetic energy is defined as

$$\epsilon \;\equiv\; \mathcal{E}^{(*)}(\mathbf{x},t) \;-\; \mathcal{E}^{exact}(\mathbf{x},t). \tag{3.11}$$

Usually $\epsilon \;>\; 0$, although this need not be the case. The numerical error now may be eliminated by adjusting the backscatter coefficient $C_{\mathcal{B}}$ in (3.10) through an iterative scheme described below. First, a new value for the coefficient for the next iteration is determined as

$$C_{\mathcal{B}}^{(n+1)} \;=\; C_{\mathcal{B}}^{(n)} + \Delta\, C_{\mathcal{B}}, \tag{3.12}$$

where

$$\Delta\, C_{\mathcal{B}}^{(n+1)} \equiv \frac{\epsilon}{\mathcal{P}^{back}}, \tag{3.13}$$

with ϵ and $\mathcal{P}^{back}$ as defined above. Using the new value $C_{\mathcal{B}}^{(n+1)}$, the estimated new energy may be calculated according to (3.10). This will produce an updated value for the energy transfer error ε in (3.11). The iteration scheme thus consists of iterating on the backscatter coefficient $C_{\mathcal{B}}^{(n)}$ value, as defined above until $\varepsilon \;\to\; 0$. This method is essentially a Newton-Raphson iterative scheme with

$$x^n \;-\; \frac{F(x^n)}{F'(x^n)} \;=\; x^{n+1}, \tag{3.14}$$

where the backscatter coefficient provides

$$x^n \;\equiv\; C_{\mathcal{B}}^{(n)}\,, \tag{3.15}$$

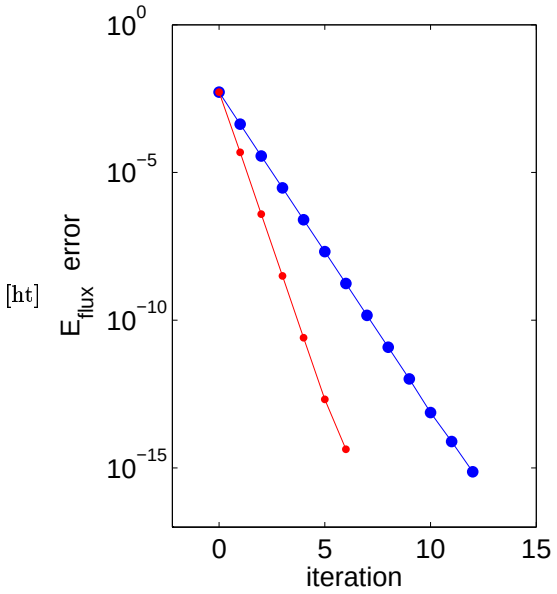

FIGURE 1. Rapid convergence to machine zero is evident for the iterative method described in this paper. (*Large dots:*) iteration with no relaxation. (*Small dots:*) iteration with small relaxation factor $\beta = 1.01$.

and the error in the final kinetic energy provides

$$F(x) \equiv \epsilon. \tag{3.16}$$

It can be shown that the iteration scheme converges to a unique solution if $C_{\mathcal{B}}^o$ is selected even with only marginal accuracy. Studies run to date indicate that iteration with some relaxation will very quickly drive $\epsilon \to 0$, as indicated in Fig. 1, below. The present method applies to the solution for a single global value of $C_{\mathcal{B}}$, in which all flux terms $\mathcal{R}_j$ in (3.10) sum to zero at the domain boundaries according to Gauss' theorem. The method also applies to a solver which employs a collocated storage arrangement for primitive flow variables, so that a unique value for the kinetic energy of the resolved scales can be determined in each computational control volume. If the scheme is used to solve for such a local value, the iteration scheme will only converge to the order of the error of the flux term.

On a staggered grid, in which separate control volumes are defined for each primitive flow variable (Harlow & Welch 1965), the method in (3.10) must be modified so that separate iterative systems are solved simultaneously for components of kinetic energy in each of the three coordinate directions. The transport equation for the i-th component contribution to kinetic energy is then given by

$$\frac{\partial}{\partial t}\,\mathcal{E}_i\,(\mathbf{x},t) \;=\; \frac{\partial}{\partial x_j}\left[\,\mathcal{R}_{(i)j}\,\right] \;-\; \mathcal{D}_i \;-\; \mathcal{P}_i \;-\; \mathcal{W}_i. \tag{3.17}$$

where $\mathcal{R}_{(i)j}$ is the i-th component of the flux vector in (3.2), and $\mathcal{D}_i$ and $\mathcal{P}_i$ are those portions of the dissipation and subgrid production fields that involve the i-th components of the fields in (3.3) and (3.4), respectively. The term $\mathcal{W}_i$ involves the interaction of the

stress field $\overline{u_i\, u_j}$ with the i-th components of the rotation tensor Ω_{ij} as

$$\mathcal{W}_i \;\equiv\; \overline{u_{(i)}\, u_j}\, \Omega_{(i)j} \tag{3.18}$$

where the rotation tensor is given by

$$\Omega_{ij} \;\equiv\; \frac{1}{2}\left(\frac{\partial u_j}{\partial x_i} - \frac{\partial u_i}{\partial x_j}\right) \tag{3.19}$$

and where the parentheses in (3.18) again indicate that summation is not implied over the particular component direction. The term in (3.18) accounts for solid-body rotation within the fluid that moves kinetic energy from one component direction to another. The iteration scheme of (3.10) on a staggered grid is then given as

$$\mathcal{E}_i^{(*)}(\mathbf{x},t) \;=\; \mathcal{E}_i^{(n)} \;+\; \Delta t\left[\frac{\partial}{\partial x_j}\left[\,\mathcal{R}_{(i)j}\,\right] \;-\; \mathcal{D}_i \;-\; \mathcal{W}_i \;-\; \mathcal{P}_i^{forw} - \left(1 \;-\; C_{\mathcal{B}}^{(n)}\right)\,\mathcal{P}_i^{back}\right]^{(n)}. \tag{3.20}$$

4. Differential backscatter limiting

The backscatter-limiter methodology has also been modified to more precisely capture the transfer of energy across all the resolved scales in the flow. This modification makes use of the significant information about the stress field contained in the product of the Legendre expansions in (2.6) – (2.8), and involves applying a backscatter reduction factor that varies with the order of each term within the Legendre product expansions.

4.1. *Overview of approach*

Because the multifractal model calculates the inertial stresses in (2.6) – (2.8) as volume integrals of the products of the Legendre expansions of the velocity component fields, the model simply consists of a linear summation of monomial terms. Thus, for example the cross-term stress in (2.6) can be expressed as

$$\overline{\overline{u}_i\, u_j^{\Delta}} \;\equiv\; \frac{1}{\Delta^3}\int_{\Delta^3}\sum_{n=1}^{N}\gamma_n\,\left(x_i^{(a)}x_j^{(b)}x_k^{(c)}\right)_n\,d\mathbf{x}^3, \tag{4.1}$$

where $(a),(b),(c)$ are the exponents representing the order of the term in each component direction, and γ represents the coefficient of the particular monomial term, with similar expressions for (2.7) and (2.8). Since the integration in (4.1) is symmetric about the canonical Legendre interval $I = [\,-1,\,1\,]$, odd-order (antisymmetric) terms will vanish in the integration. Thus the summation in (4.1) involves terms containing various combinations of constant, 2nd, and 4th order variables in each of the three coordinate directions x_i. Note also that any 4th order term appearing in (4.1) is generated only through the multiplication of the Legendre expansions and cannot arise directly from the Legendre expansions in (2.9) and (2.10) themselves, which of course contain basis functions up to second order. Such 4th-order terms correspond to aliased frequencies within the product summation.

4.2. *Implementation of differential backscatter limiting*

Rather than applying a constant backscatter-reduction coefficient $C_{\mathcal{B}}$ to all terms in (4.1) as has been done previously (Burton & Dahm 2004), the present approach instead applies different $C_{\mathcal{B}}$ reduction factors to individual summation terms depending on the order of the given term in (4.1). A number of variations were evaluated to determine

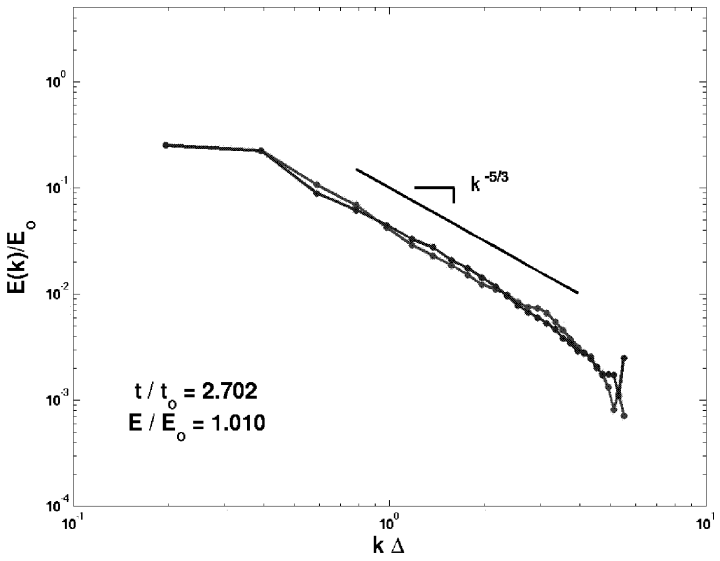

FIGURE 2. Resolved energy spectrum $E(k)$ from LES of forced, periodic homogeneous, isotropic turbulence where $N = 32$ and $Re_\Delta \approx 160$ with differential backscatter limiting described in section 4. Spectrum follows closely the K41 scaling $E(k) \sim k^{-5/3}$ over essentially the entire resolved spectrum.

the combination producing the most physical distribution of kinetic energy across all resolved wavenumbers. For the purposes of the free-round jet simulation, the following approach distributed kinetic energy within the resolved scales in closest accordance with classical equilibrium inertial range scalings:

- Non-aliased terms contributing to backscatter are left unchanged. Thus, where a, b and $c \leq 2$,

$$\forall \quad \left(\text{sign}(\gamma)\, x_i^{(a)} x_j^{(b)} x_k^{(c)}\right) \overline{S}_{ij} \geq 0 \quad \Rightarrow \quad C_{\mathcal{B}} = 0.0. \tag{4.2}$$

- Aliased terms contributing to backscatter are completely eliminated. Thus, where a, b or $c = 4$,

$$\forall \quad \left(\text{sign}(\gamma)\, x_i^{(a)} x_j^{(b)} x_k^{(c)}\right) \overline{S}_{ij} \geq 0 \quad \Rightarrow \quad C_{\mathcal{B}} = 1.0. \tag{4.3}$$

- Aliased terms contributing to the forward cascade of energy are amplified. Thus, where a, b or $c = 4$,

$$\forall \quad \left(\text{sign}(\gamma)\, x_i^{(a)} x_j^{(b)} x_k^{(c)}\right) \overline{S}_{ij} \leq 0, \quad \Rightarrow \quad C_{\mathcal{F}} = 3.0. \tag{4.4}$$

- Non-aliased terms contributing to the forward cascade of energy are left unchanged. Thus where, a, b and $c \leq 2$,

$$\forall \quad \left(\text{sign}(\gamma)\, x_i^{(a)} x_j^{(b)} x_k^{(c)}\right) \overline{S}_{ij} \leq 0 \quad \Rightarrow \quad C_{\mathcal{F}} = 0.0. \tag{4.5}$$

As illustrated in Fig. 2, the use of backscatter reduction that varies as a function of term order as described above produces an energy spectrum exhibiting Kolmogorov inertial-range scaling throughout the resolved scales.

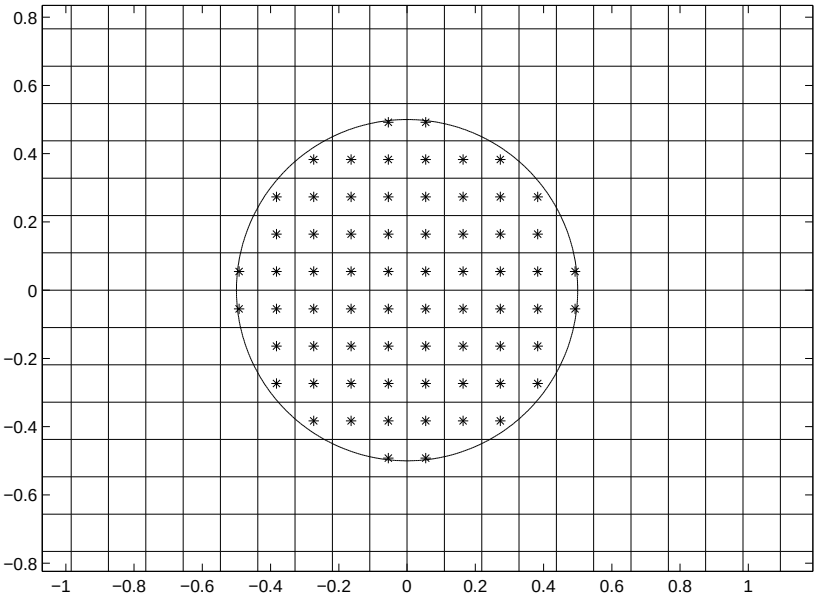

FIGURE 3. Detail of inlet geometry for turbulent jet for $128 \times 64 \times 64$. Cartesian mesh is used to retain the high accuracy of the Legendre interpolation matrices. A physically accurate inlet condition will be established by appropriate volume averaging of the inlet profile for those inlet cells intersecting the maximum inlet radius $D = 7$.

5. LES of a Free Round Turbulent Jet.

5.1. *Configuration and setup.*

Using the refinements to the multifractal subgrid-scale model discussed above in Sections 2 - 4, the structured JETCODE produced at the CTR has been modified to the following configuration to conduct the simulation of the free round turbulent jet. Initial validation simulations are being run at a resolution of $128 \times 64 \times 64$ on a regular Cartesian mesh. The regular mesh has been selected because it allows a single well-conditioned inverse Legendre matrix to be defined throughout the flow domain, which produces exceedingly accurate estimates for the resolved and Δ-scale tensor-product expansions in (2.9) and (2.10). The regular mesh also permits the use of 4th-order centered spatial derivative operators, permitting more accurate determination of the divergence of the backscatter stresses and the related resolved strain-rate fields. Time advancement is with a fully explicit 3rd-order Runge-Kutta scheme. The flow domain is periodic in both cross-stream coordinate directions, and set $\pm 7\,D$ from the centerline, where D is the width of the jet. This configuration has been shown to adequately minimize the impact of the cross-stream periodicity on the downstream development of the jet (da Silva & Métais 2002).

Inflow conditions will consist initially of a core plug flow with constant velocity U_{mean}, and a co-flow in the remainder of the inflow plane of $U_{cf} = 0.1\,U_{mean}$. As illustrated in Figure Fig. 5.1, inlet grid cells intersecting the maximum jet radius (*i.e.*, $r = D$) will contain an appropriate volume-averaged fraction of U_{mean} to ensure accurate implementation of the plug inflow condition. A second inflow condition will also be tested, consisting of the hyperbolic tangent profile (Michalke & Hermann 1982) for the jet core, which has been shown to be a realistic approximation of the actual inlet conditions found in experimental investigations (Freymuth 1966).

This condition is given by

$$U_{mean}(x_o, r) = \frac{U_o + U_{cf}}{2} - \frac{U_o - U_{cf}}{2} \tanh\left[\frac{1}{4}\frac{R}{\theta_o}\left(\frac{r}{R} - \frac{R}{r}\right)\right], \qquad (5.1)$$

where U_o is the centerline jet velocity, U_{cf} is the co-flow velocity and θ_o is the momentum thickness of the initial shear layer.

5.2. *Model evaluation*

Once the initial validation of the modified JETCODE is completed, the accuracy of the multifractal model will be evaluated in direct comparisons with the experimental data of Hussein *et al.* (1994) and others for those statistics traditionally used to evaluate turbulent jet evolution in the self-similar region. These include: (1) linear evolution of jet half-width with downstream location, given by $\delta_{0.5}(x) / D = C_d [\frac{x}{D} - \frac{x_o}{D}]$; (2) decay of the centerline velocity, given by $B_u^{-1} \equiv U_o / \langle u_x(x, r = 0)\rangle$; (3) streamwise-normal mean velocity profiles, given by $(U(r) - U_{cf}) / (U_o - U_{cf})$ as a function of $\eta = r / (x - x_o)$; (4) streamwise-normal Reynolds stress profiles for: streamwise normal stresses $u_x^2 / (U_o - U_{cf})^2$, radial normal stresses $u_r^2 / (U_o - U_{cf})^2$, tangential normal stresses $u_\theta^2 / (U_o - U_{cf})^2$, and streamwise-radial cross stresses $u_x\, u_r / (U_o - U_{cf})^2$; (5) downstream evolution and return to isotropy of the centerline Reynolds stresses $u_x^2(x) / (U_o - U_{cf})^2(x)$. These measures will provide a stringent quantified evaluation of the accuracy of multifractal modeling in the important and complex case of a free round turbulent jet.

5.3. *Additional studies: jet with passive-scalar mixing*

In many combustion problems, such as those arising from the development of systems like the rocket engine, gas turbine and internal combustion engine, the efficient mixing of fuel and oxidizer is accomplished through the use of turbulent jets, whose ability to mix fuel and oxidizer often largely determines the efficiency and stability of the combustion process. LES of such turbulent reacting flows often employ models for local reaction in the subgrid scales that are parameterized by resolved-scale quantities such as the filtered scalar concentrations $\langle\zeta\rangle$, the filtered scalar variance $\langle\zeta'^2\rangle$, and the filtered scalar dissipation rate $\langle 2D\nabla\zeta \cdot \nabla\zeta\rangle$ (See, *e.g.,* Rajagopalan & Tong 2003).

With the completion of the tests described above in section 5.2, the jet flow solver will be augmented with the related multifractal model for the filtered passive-scalar transport equation. That model, whose derivation and initial tests have been described elsewhere in this volume (Burton 2004), uses the multifractal structure of the passive-scalar energy dissipation field in high Reynolds number turbulence to close the filtered passive-scalar transport equation. Tests will compare the accuracy of the model against experimental or DNS data for the behavior of the scalar and scalar dissipation field in the scale-similar region of the jet (Dowling & Dimotakis 1990; Dowling 1991). Statistics to be evaluated will include (1) scale similarity of the normalized scaled concentration field, scalar variance and scalar dissipation rate versus scaled radial component $\eta \equiv r/(x - x_o)$, (2) scaled power spectra for scalar variance and scalar dissipation fields at given downstream and cross-stream locations and (3) probability density functions of scalar concentrations and scalar dissipation rates at the same downstream and cross-stream locations. Such measures will provide a rigorous evaluation of the accuracy of multifractal modeling for turbulent mixing in a complex shear flow seen in a wide range of practical engineering applications.

REFERENCES

BURTON, G. C. 2004 Large-eddy simulation of passive-scalar mixing using multifractal subgrid-scale modeling. *Annual Research Briefs 2004* Center for Turbulence Research, NASA/Stanford University.

BURTON, G. C., & DAHM, W. J. A. 2004 Multifractal subgrid-scale modeling for large-eddy simulation. Part 1: model development and *a priori* testing. *Submitted to Phys. Fluids.*

BURTON, G. C., & DAHM, W. J. A. 2004 Multifractal subgrid-scale modeling for large-eddy simulation. Part 2: backscatter limiting and *a posteriori* evaluation. *Submitted to Phys. Fluids.*

DOWLING, D. R. & DIMOTAKIS, P. E. 1990 Similarity of the concentration field of gas-phase turbulent jets. *J. Fluid Mech.* **218** 109-141.

DOWLING, D. R. 1991 The estimated scalar dissipation rate in gas-phase turbulent jets. *Phys. Fluids A* **9** 2229-2246.

FREYMUTH, P. 1966 On transition in a separated laminar boundary layer. *J. Fluid Mech.* **25**, 683.

HARLOW, F. W. & WELCH, J. E. 1965 Numerical calculation of time-dependent viscous incompressible flow of fluids with free surface. *Phys. Fluids* **8**, 2182-2189.

HUSSEIN, H. J., CAPP, S. P. & GEORGE, W. K. 1994 Velocity measurements in a high-Reynolds-number, momentum-conserving, axisymmetric, turbulent jet. *J. Fluid Mech.* **258**, 31-75.

MICHALKE, A. & HERMANN, G. 1982 On the inviscid instability of a circular jet with external flow. *J. Fluid Mech.* **114** 343.

RAJAGOPALAN, A. G. & TONG, C. 2003 Experimental investigation of scalar-scalar-dissipation filtered joint-density function and its transport equation. *Phys. Fluids* **15** 227-244/

DA SILVA, C. B., & MÉTAIS, O. 2002 Vortex control of bifurcating jets: A numerical study. *Phys. Fluids* **14**, 3798-3819.

Identification of an internal layer in a diffuser

By X. Wu, J. Schluter, P. Moin,
H. Pitsch, G. Iaccarino AND Frank Ham

1. Motivation and objectives

Identifying regions of self-preservation in representative non-equilibrium flows is useful for basic fluid mechanics as well as engineering computation. Townsend (1976) discussed the process that sudden changes in external conditions in boundary layers may result in an internal boundary layer that spreads from the section of change, and the layer outside the internal layer develops in almost the same way as in the original flow. Experimental evidence in support of this observation includes the boundary layer over a curved hill (Baskaran *et al.* 1987), and the boundary layer over a bump (Webster *et al.* 1996). In Baskaran *et al.*, streamwise pressure gradient changes rapidly from adverse to favorable at the leading edge, and separation occurs downstream of the summit. Internal layer was found downstream of the leading edge. The flow of Webster *et al.* remains attached, its streamwise pressure gradient changes suddenly from adverse to favorable at both the leading and trailing edges and internal layers were identified downstream of these two locations. They considered signatures of internal layer as knee points in the wall-normal profiles of streamwise turbulence intensity. In these two studies knee points emerge when the outer peak of streamwise turbulence intensity associated with upstream adverse pressure gradient decays rapidly under favorable pressure gradient and an inner peak establishes as a result of the internal layer. Obviously this process of knee point formation is specific to the hill or bump type of flows in which upstream strong adverse pressure gradient changes suddenly to favorable at the leading/trailing edges.

This paper describes an internal layer identified from an incompressible turbulent diffuser flow, as opposed to the internal layers previously identified in external boundary layer flows. The present internal layer emerges in the relaxation zone downstream of a sharp variation in streamwise pressure gradient: from mildly favorable to strongly adverse, then weakly adverse. Unlike those in Baskaran *et al.* and Webster *et al.*, the present internal layer does not display significant spreading into the central region of the flow. The flow in the region where internal layer forms exhibits certain characteristics similar to those observed the C-type of Couette-Poisuille turbulent flows.

Two laboratory incompressible diffuser flows have emerged in a number of fundamental and modeling studies on spatially developing complex internal turbulent flows, namely, the Azad diffuser (Azad 1996) and the Obi diffuser (Obi *et al.* 1993). The Azad diffuser is an axisymmetric conical geometry with a total divergence angle of 8° and with fully developed pipe flow at the inlet. The inlet Reynolds number based on friction velocity and pipe diameter is 12,400. Extensive measurements have been performed on this flow by Okwuobi & Azad (1973), Trupp *et al.* (1986) and Azad & Kassab (1989), among others. They found that sudden application of adverse pressure gradient at the diffuser throat affects the flow so drastically that the downstream mean and turbulent fields become unrecognizable in relation to the inlet condition. The Obi diffuser has an asymmetric planar configuration with a total expansion ratio of 4.7 and a single sided deflection wall

of 10°, see figure 1. The inlet was designed to be a fully developed turbulent channel flow, though in some of the experiments this condition was not achieved. The inlet Reynolds number based on friction velocity and channel half height is 500. Obi *et al.* (1993) studied the flow experimentally using a single component laser-Doppler anemometer. Buice & Eaton (1997) made hot-wire and pulsed-wire measurements in the Obi diffuser. Lindren *et al.* (2002) made measurements on a slightly modified geometry based on the Obi diffuser at a higher Reynolds number to study the control of flow separation. Lim & Choi (2004) performed shape optimization using the Obi diffuser as the base flow configuration. The Obi diffuser has also been used as a test flow in a number of computational studies. These include the Reynolds-averaged simulation of Durbin (1995) and Iaccarino (2001), as well as the large eddy simulation work of Kaltenbach *et al.* (1999). Previous investigations in the Azad diffuser emphasized the process of instantaneous flow reversal (Azad 1996): note that their time-averaged flow is not separated. Likewise, work in the Obi diffuser emphasized the unsteady process of separation on the lower deflected wall, e.g., see Kaltenbach *et al.* (1999). The focus of the present study is on the discovery of an internal layer over the upper flat wall of the Obi diffuser, a subject that has eluded attention in the previous diffuser studies which have focused on separation and reattachment over the lower deflected wall.

Aside from the obvious outstanding issue of identifying internal layers in internal flows, further flow physics questions can be raised with reference to the conditions under which internal layers may form, and the statistical and structural features of the internal layer, as well as possible connection between turbulent fluctuations inside internal layer and identifiable large scale motions in the central region of the flow. In addition, from the view point of basic fluid mechanics it is of interest to query whether it is possible to relate the characteristics of internal layer with any well-known fundamental equilibrium component flows. Furthermore, the original process described by Townsend (1976) needs further scrutiny: Does the layer outside the internal layer develop as in the original unperturbed flow? Does the internal layer emerge right at the streamwise section of change? In this work we attempt to address these flow physics questions using large eddy simulation.

2. Computational details

We consider incompressible fluid flow with constant density ρ in the Obi planar diffuser shown in figure 1. Unit length scale is h, the inlet channel half-height. The two transitional curvatures between the parallel walls and the inclined wall have the same radius of 19.4. The origin of the coordinate system is at the intersection of the deflected wall and the lower inlet channel wall. The curvature center associated with the upstream curved section is located at ($x = -1.7$, $y = -19.4$). The curvature center of the downstream curved section is at ($x = 43.7$, $y = 12.0$). The inlet plane is located at $x = -5$, and the outlet plane at $x = 100$. Spanwise dimension of the computational domain is $8h$.

Unit velocity scale is defined as the friction velocity u^* at the inlet. This then defines the unit time scale as $h/u^*_{x=-5}$. Reynolds number Re based on the unit length h and unit velocity $u^*_{x=-5}$ is 500. As in previous studies of the Obi diffuser, e.g., Buice & Eaton (1997) and Kaltenbach *et al.* (1999), the majority of the results to be presented in this paper were normalized by the inlet bulk velocity u_b defined as the area-averaged mean streamwise velocity at the $x = -5$ station.

The numerical methodology used to solve the filtered continuity and momentum equa-

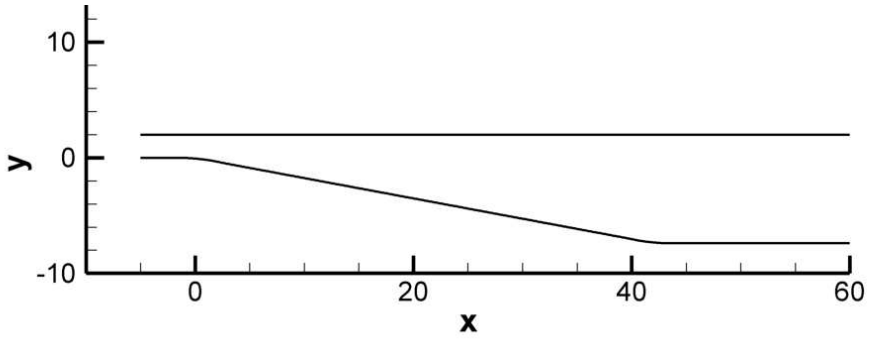

FIGURE 1. Cross-section of the asymmetric planar diffuser; the exit is at $x = 100$.

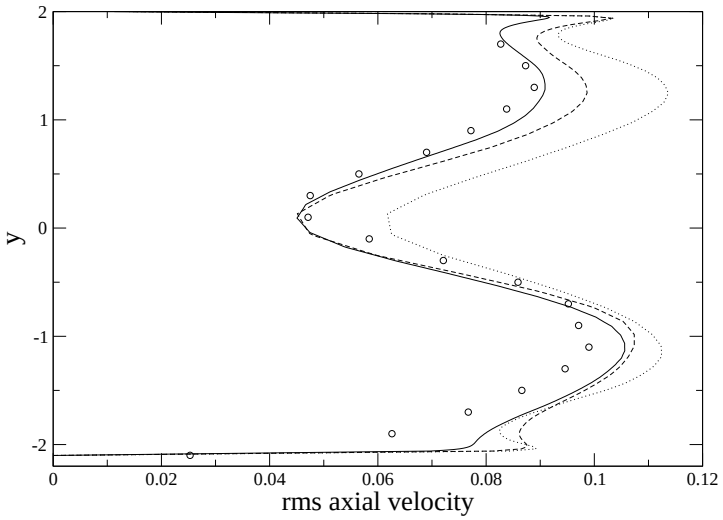

FIGURE 2. $\overline{u}'_{rms}/u_b$ versus y at $x = 11.96$ showing the effects of resolution and subgrid scale model on LES results. ∘ Buice & Eaton (1997); solid line: fine resolution; dashed line: coarse resolution; dotted line: coarse resolution without subgrid scale model.

tions is the unstructured fractional step method for large eddy simulation in complex geometries of Mahesh *et al.* (2004) with the dynamic subgrid-scale procedure of Germano *et al.* (1991). Velocities at the inflow boundary plane, $x = -5$, are from a separate LES of fully developed channel flow at $Re = 500$. Simulations were performed on two sets of hexahedral meshes. The fine mesh has $590(x) \times 100(y) \times 110(z)$ control volume cells. The coarse mesh has $360(x) \times 80(y) \times 80(z)$ control volume cells. Figure 2 shows the effects of grid resolution and subgrid-scale stress model on predicted rms velocity at $x = 11.96$.

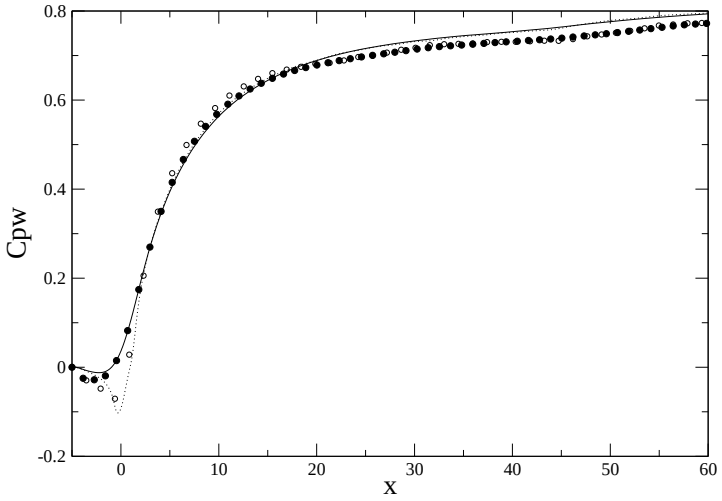

FIGURE 3. Wall static pressure coefficient C_{pw}. Kaltenbach *et al.* (1999): ∘ (lower wall); • (upper wall). Present LES: dotted line (lower wall); solid line (upper wall).

3. Results and discussion

Planar and conical diffusers have broadly similar wall static pressure distributions. A mildly favorable pressure gradient turns to sharply adverse at the diffuser throat, followed by a gradual decrease in the magnitude of adverse pressure gradient further downstream. Such similarity can be appreciated by comparing the C_{pw} results for the Obi diffuser in figure 3 with figure 4 of Okwuobi & Azad (1973) for the axisymmetric Azad diffuser. In figure 3 the change from strongly adverse to weakly adverse pressure gradient starts near $x = 10$, and in Okwuobi & Azad (1973) similar transition takes place approximately 8 pipe radii downstream of the throat, though the leveling off of C_{pw} is not as distinct as in the Obi diffuser. This pattern of C_{pw} for incompressible diffuser flows may be contrasted with the behavior of C_{pw} found in the hill/bump flows of Baskaran *et al.* (1987) and Webster *et al.* (1996). In Webster *et al.* there are two adverse to favorable pressure gradient changes where signatures of internal layers emerge. The magnitude of their favorable pressure gradient decreases further downstream of the trailing edge. The diffuser flow and the bump flow both experience sharp variation in streamwise pressure gradient followed by downstream relaxation. The difference is that the signs of the sudden changes are opposite. Given the fact that internal layer exists in the scenario where C_{pw} is from adverse to favorable, a query which naturally presents itself is whether internal layer can be found in the other scenario.

Skin friction coefficient C_f over the upper flat wall in the Obi diffuser displays a long plateau extending from $x = 15$ to 45 (figure 4). The plateau is bound by a sharp drop from $x = 0$ to 10 upstream and a more gradual decline downstream of $x = 45$. In the plateau region, friction velocity is approximately 0.43, and 1 viscous wall unit corresponds to $0.0047h$. Broadly similar streamwise variation of C_f exists in the Azad diffuser, see figure 17 of Azad (1996). Though in his flow the sharp drop of C_f near the diffuser throat is followed by an additional slower decrease rather than a distinct plateau. In Webster *et al.* (1996) two sudden jumps in C_f are found at the locations where pressure gradient

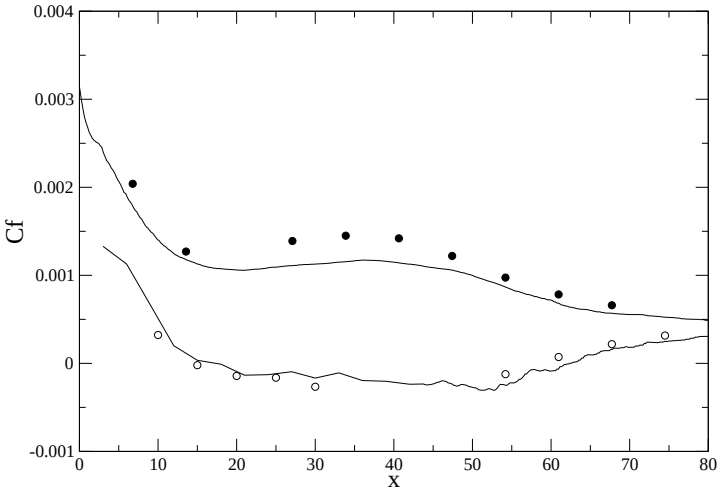

FIGURE 4. Skin friction coefficients. Buice & Eaton (1997): ○ lower wall, • upper flat wall; solid lines are from the present LES.

changes from adverse to favorable. Downstream of their trailing edge C_f settles into a minor descending slope and signature of internal layer is distinct in this region. Abrupt increase in C_f implies quasi-step changes in the near-wall mean velocity gradient. Thus, production terms which are directly dependent on this gradient in the transport equations for second-order turbulence statistics will be expected to show large increases in the near-wall region, for example, streamwise intensity. The argument that a quasi-step increase in C_f selectively modifies near-wall shear production of turbulent stresses and leads to signatures of an internal layer explains well the internal layers identified in Webster *et al.* (1996) and Baskaran *et al.* (1987), but is not directly applicable in the present diffuser flow. This is because near the upper flat wall of Obi diffuser there is no quasi-step increase in C_f. Instead, C_f has a prolonged plateau which is preceded by a rapid decrease. Although the overall trend of C_f in the Obi diffuser is drastically different from that in the Webster bump, both flows nevertheless show regions of stabilized positive skin friction downstream of sections of sudden change. Again, the signs of the sudden changes are opposite. The stabilized C_f in the relaxation region suggests newly established level of near-wall mean velocity gradient, which may be the driving factor in the formation of an internal layer. Obviously if the sharp drop in C_f on the upper wall of the Obi diffuser is severe enough to cause separation there can be no internal layer. It is expected that internal layer, if it does exist in the Obi diffuser, will be less pronounced than that in the bump flow of Webster *et al.* (1996).

The newly established level of near-wall mean velocity gradient after sudden change implied by figure 4 can be more directly seen from figure 5 and figure 6 in which $\langle\overline{u}\rangle/u_b$ at a number of x stations is plotted against the y coordinate. Experimental data of Buice & Eaton (1997) and Obi *et al.* (1993) are also shown for comparison. For example in figure 6 the near-wall slope of $\langle\overline{u}\rangle/u_b$ decreases from $x = 6.4$ to 10.4, remains nearly constant from $x = 18.4$ to 38.4, and decreases further from $x = 42.4$ to 58.4. The mean velocity distributions are consistent with the sharp drop in C_f followed by a prolonged

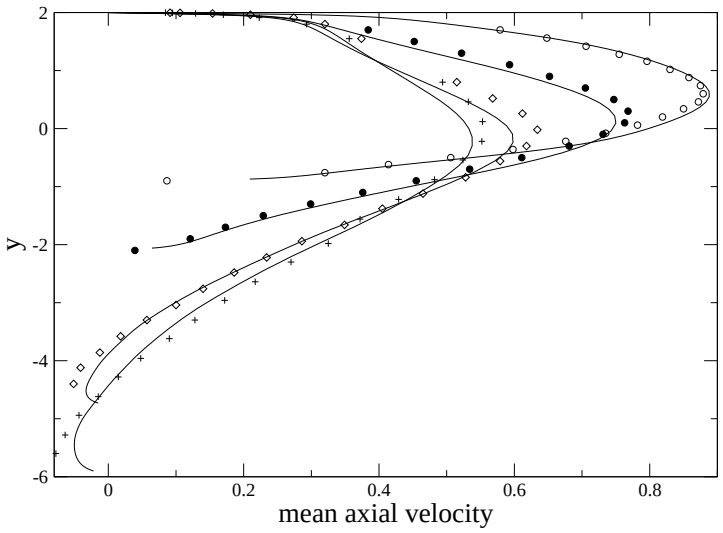

FIGURE 5. $\langle\overline{u}\rangle/u_b$ versus y. Symbols are from Buice & Eaton (1997) and lines are present LES. $\circ$ $x = 5.18$, $\bullet$ $x = 11.96$, $\diamond$ $x = 27.1$, $+$ $x = 33.86$.

plateau spanning from $x = 15$ to 45 shown in figure 4. On the scales adopted in the figures, mean velocity profiles near the top flat wall exhibits nearly discontinuous abrupt change of curvature at $y \approx 1.8$ for those streamwise stations located within the range from $x = 11.96$ to 38.4. In addition, along the wall-normal direction from the abrupt change to approximately $y = 0$, $\langle\overline{u}\rangle/u_b$ displays linear slopes at these streamwise stations. In this paper we will refer this region as the flow outside the internal layer, the outer flow, or the core region. The linearity of mean velocity in the core region is significant because it implies that the velocity difference is only a function (not necessarily linear) of distance to the wall for the outer flow, thereby satisfying a crucial condition in Millikan's reasoning for the existence of logarithmic velocity profile in the overlap region for the flow underneath the core flow. Based on the results of figure 4, figure 5 and figure 6, we can predict that in the C_f plateau region underneath the core flow the mean velocity profiles are logarithmic.

The above prediction is put to test in figure 7 by plotting the mean velocity $\langle\overline{u}\rangle^+$ against wall distance $(2-y)^+$ using wall units. Using the friction velocity suggested in figure 4 it can be shown that $y = 1.8$ corresponds to approximately 45 wall units at each of the selected five x locations. From $(2-y)^+ = 20$ to 80 the $\langle\overline{u}\rangle^+$ profiles at these five streamwise stations collapse onto a logarithmic curve with the well-known slope of $1/0.4$. Very close to the wall $(2-y)^+ < 10$ the usual Law of the Wall is satisfied. We consider one of the properties of the present internal layer is that the mean velocity obeys self-similar Log Law and Law of the Wall inside the internal layer, and varies linearly with distance from the wall outside the internal layer. It may be possible to further collapse the $\langle\overline{u}\rangle/u_b$ profiles at different streamwise locations outside the internal layer in the core region of the flow. For scaling of mean velocity in adverse pressure gradient boundary layers, see the work of Na & Moin (1998) and references therein. Scaling in simple equilibrium internal flows was discussed in a recent paper of Nakabayashi *et al.* (2004).

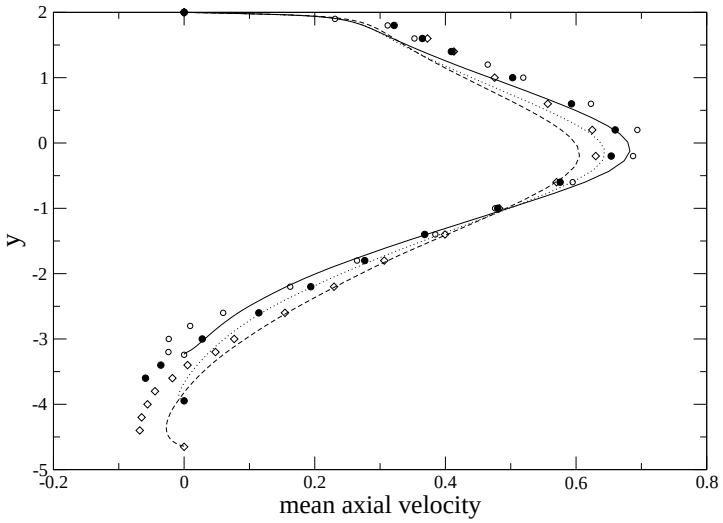

FIGURE 6. $\langle\overline{u}\rangle/u_b$ versus y. Symbols are from Obi *et al.* (1993) and lines are present LES. $\circ$ solid $x = 18.4$, $\bullet$ dotted $x = 22.4$, $\diamond$ dashed $x = 26.4$.

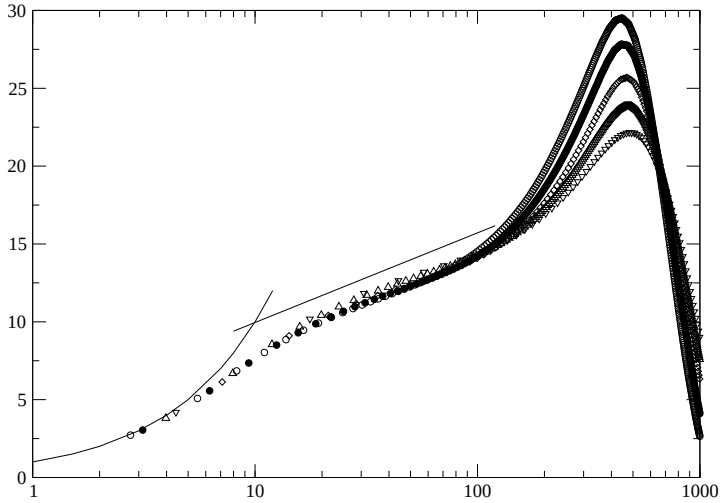

FIGURE 7. $(2-y)^+$ versus $\langle\overline{u}\rangle^+$. $\circ$ $x = 18.4$, $\bullet$ $x = 22.4$, $\diamond$ $x = 26.4$, $\triangle$ $x = 30.4$, $\triangledown$ $x = 34.4$; solid lines are $\langle\overline{u}\rangle^+ = y^+$ and $\langle\overline{u}\rangle^+ = 2.5 \ln y^+ + 4.2$.

Mean streamwise velocity and its wall-normal gradient near the top wall at $x = 20$ are presented in figure 8. In the region of $1 < y < 2$ and $18 < x < 38$ the present mean velocity profiles exhibit similar characteristics to those in the C-type of Couette-Poiseuille turbulent flows measured by Nakabayashi *et al.*, compare figure 8 with the sketch shown in figure 9. The inflectional point where second-order wall-normal mean

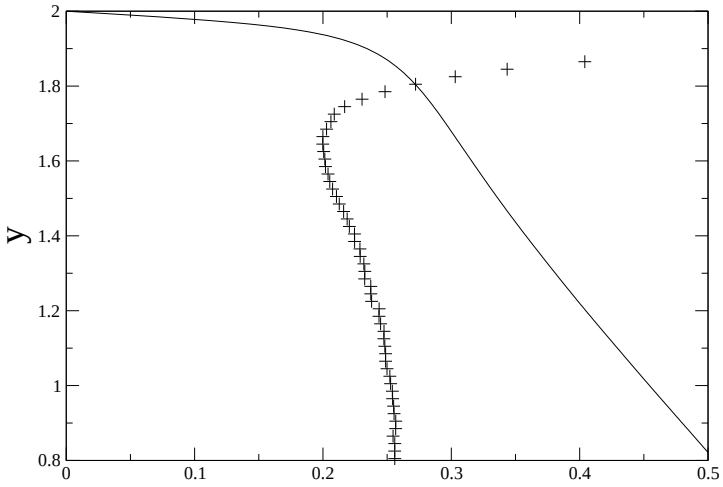

FIGURE 8. Mean velocity and its wall-normal gradient versus y near the top wall at $x = 20$. Solid line: $\langle\overline{u}\rangle/u_b$; +: $-1/u_b\partial\langle\overline{u}\rangle/\partial y$.

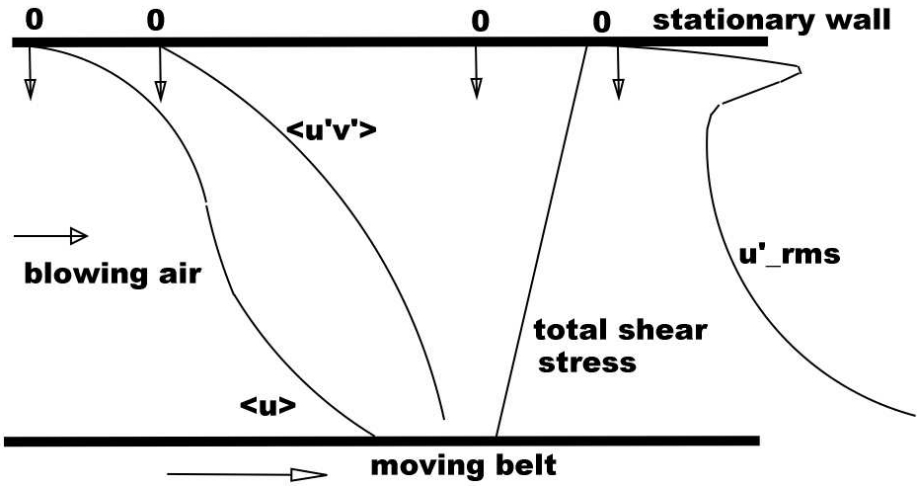

FIGURE 9. Sketch of the C-type of Couette-Poiseuille turbulent flows, following the experimental data of Nakabayashi *et al.* (2004).

velocity gradient changes sign is less apparent from the distribution of $\langle\overline{u}\rangle/u_b$ in the present diffuser flow compared to that indicated by figure 9 for the C-type of flow. However the profile of $\partial\langle\overline{u}\rangle/\partial y$ shown in figure 8 clearly demonstrates that the inflection is located at approximately $y = 1.7$. The effect on mean velocity of the lower moving wall in the C-type of flow is accomplished in the present diffuser flow by the high speed fluid beyond the core region, i.e., $y < 1$. Thus if the C-type of Couette-Poiseuille turbulent flows can be considered approximately as a distant prototype in the region of $1 < y < 2$

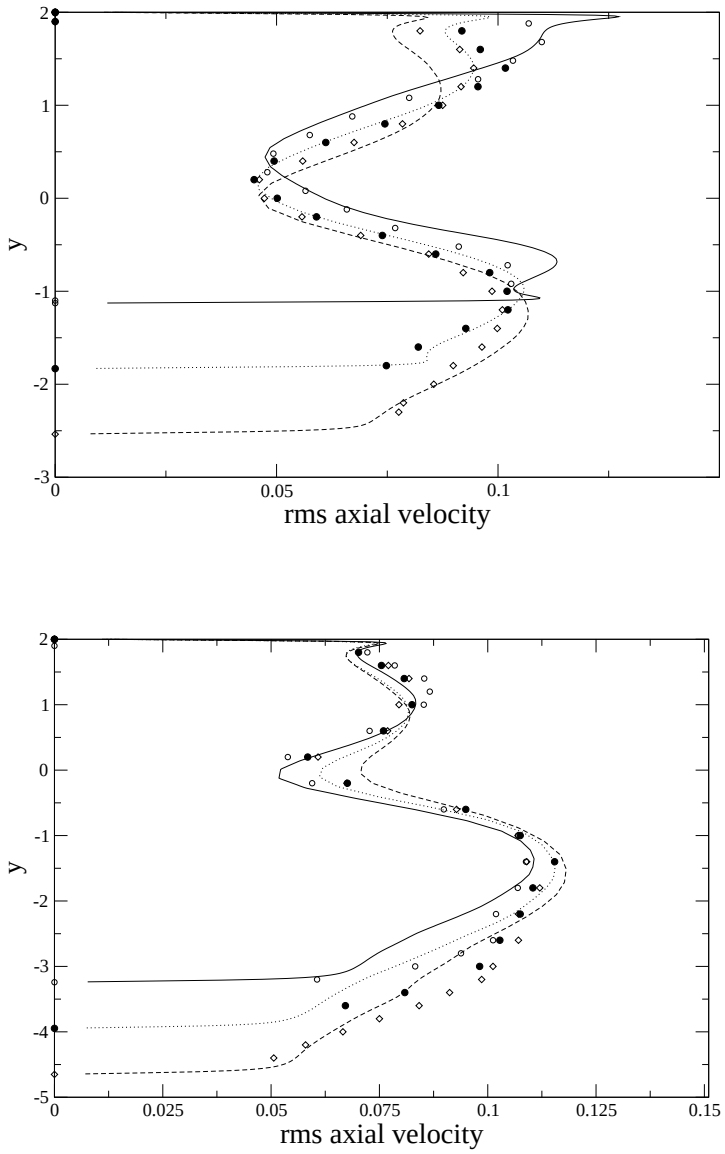

FIGURE 10. $\overline{u}'_{rms}/u_b$ versus y. Symbols are from Obi *et al.* (1993) and lines are present LES. Upper: ∘ solid $x = 6.4$, • dotted $x = 10.4$, ⋄ dashed $x = 14.4$; Lower: ∘ solid $x = 18.4$, • dotted $x = 22.4$, ⋄ dashed $x = 26.4$.

and $18 < x < 38$, the linearly varying high speed fluid flow away from the top wall is then one of the driving components in the internal layer formation process because it provides the necessary mechanism for mean velocity inflection in this particular flow.

In the flow over a bump of Webster *et al.* (1996), prior to the sudden change of C_{pw} near the trailing edge the level of u'_{rms} is elevated and its peak displaced away from the

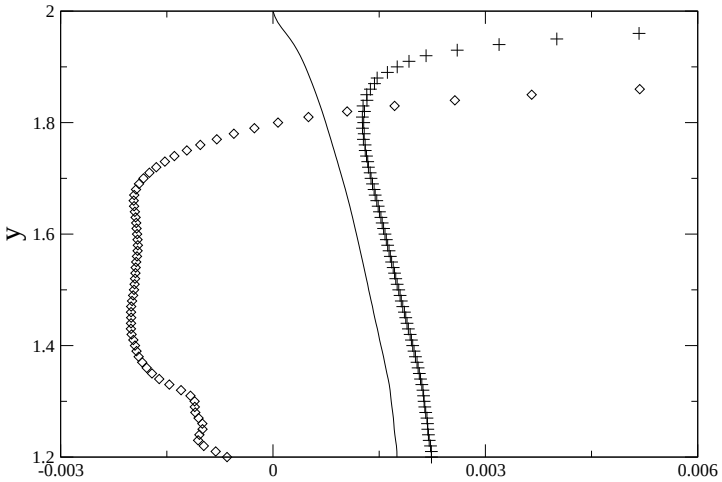

FIGURE 11. Shear stress and its wall-normal gradient versus y near the top wall at $x = 20$. Solid line: Reynolds shear stress $\langle \overline{u}' \overline{v}' \rangle / u_b^2$; +: total shear stress $\langle \overline{u}' \overline{v}' \rangle / u_b^2 - 1/Re u_b \partial \langle \overline{u} \rangle / \partial y$; $\diamond$: wall-normal gradient of total shear stress.

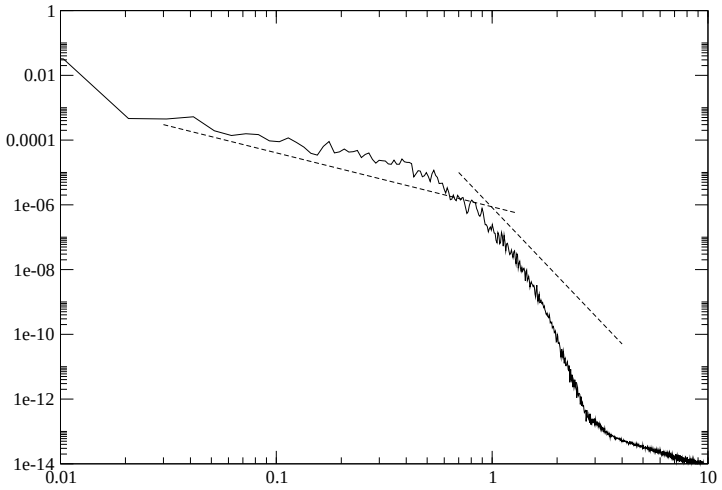

FIGURE 12. Periodogram estimator of frequency spectrum E_{11}/u_b^2 as a function of f/u_b at $x = 30$, $y = 1.8$ and $z = 1$. The left and right dashed lines represent the $-5/3$ and -7 slopes, respectively.

wall to the central region of the boundary layer. As the streamwise pressure gradient changes from adverse to favorable an inner peak of u'_{rms} appears while the outer peak due to upstream adverse pressure gradient diminishes rapidly under the effect of newly imposed favorable pressure gradient so that the wall-normal profiles of u'_{rms} show knee points, i.e., sharp turning, at the edge of internal layer. Sudden application of strong

adverse pressure gradient at the throat of the Obi diffuser significantly elevates $\overline{u}'_{rms}$ near the upper flat wall, the local peak value at the throat is nearly 100% larger than the inlet peak. But this elevated peak decays rapidly back to the original inlet peak level by $x = 10$ as a result of the leveling off of C_{pw} shown in figure 3. This process of rise and decay corresponds to the precipitous drop and subsequent stabilization in C_f discussed in figure 4. Under the effect of adverse pressure gradient, the elevated $\overline{u}'_{rms}$ in the region away form the wall bifurcates away from the inner peak and forms an outer peak. This outer peak is the one commonly observed when boundary layer responds to adverse pressure gradient. It shifts away from the wall with increasing streamwise distance from $x = 6.4$ to 14.4. This process can be discerned from figure 10. Because the flow is still under the influence of weak adverse pressure gradient downstream of $x = 10$ the outer peak does not decay as quickly as in Baskaran *et al.* and Webster *et al.*. Thus, in the Obi diffuser, internal layer signatures may also include a valley bottom at $y \approx 1.8$ separating the inner and outer peaks. The streamwise range within which such a signature is distinct is from $x = 15$ to 40, consistent with figure 7. Comparison of the computed turbulence intensity with experimental data further downstream of the last x station in figure 10 is less satisfactory; this is very similar to findings from Kaltenbach *et al.* (1999) and the other computational studies of the Obi diffuser. Kaltenbach *et al.* commented that the data of Obi *et al.* (1993) downstream of $x = 40$ are only of qualitative value for validation because of a possible scaling problem. No inflectional points can be found in the Reynolds shear stress and wall-normal intensity profiles.

The notion that the present internal layer together with its surrounding environment bears certain resemblance to the fundamental C-type of Couette-Poiseuille turbulent flows is reinforced by considering the characteristics of second-order turbulence statistics in these two flows. The $\overline{u}'_{rms}$ profiles close to the top wall in figure 10 bear remarkable resemblance to those shown in figure 14 of Nakabayashi *et al.* (2004). The valley between the inner and outer peaks in the present discussion is termed as plateau region by Nakabayashi *et al.*. Reynolds shear stress similarity between these two types of flows can be appreciated by comparing the $\langle u'v' \rangle$ profile in figure 11 with those in figure 4 of Nakabayashi *et al* (2004). Note the absence of inflection in the Reynolds shear stress profiles for both flows. Apparently, the total shear stress in the present diffuser flow at $x = 20$ close to the top wall has different behavior from that in the C-type of Couette-Poiseuille turbulent flows. This reflects the fact that the present flow is not one-dimensional and fully developed as assumed in the C-type of Couette-Poiseuille turbulent flows. The wall-normal gradient of total shear stress shown in figure 11 also serves as a measure for identification of internal layer. In adverse pressure gradient boundary layer flows it is approximately equal to the streamwise gradient of total pressure. Outside the internal layer the total pressure on a streamline continues to change slowly as in the upstream flow, whereas inside the internal layer under adverse pressure gradient the total pressure increase along a streamline, being equal at the wall to the static pressure. In the present flow the location at which the total shear stress gradient changes sign serves as one the markers for the edge of the internal layer.

Velocity signals were recorded at selected points for a duration of 32,000 time steps. The raw records were processed using the data windowing technique of Press *et al.*. (1992). The computed periodogram estimator of the power spectrum with data windowing E_{11}/u_b^2 is presented in figure 12. Normalization follows convention so that the spectrum axis has a dimension of unit length h, and the horizontal frequency axis has a dimension of h^{-1}. The extent within which the slope of E_{11} agrees with the $-5/3$ inertial

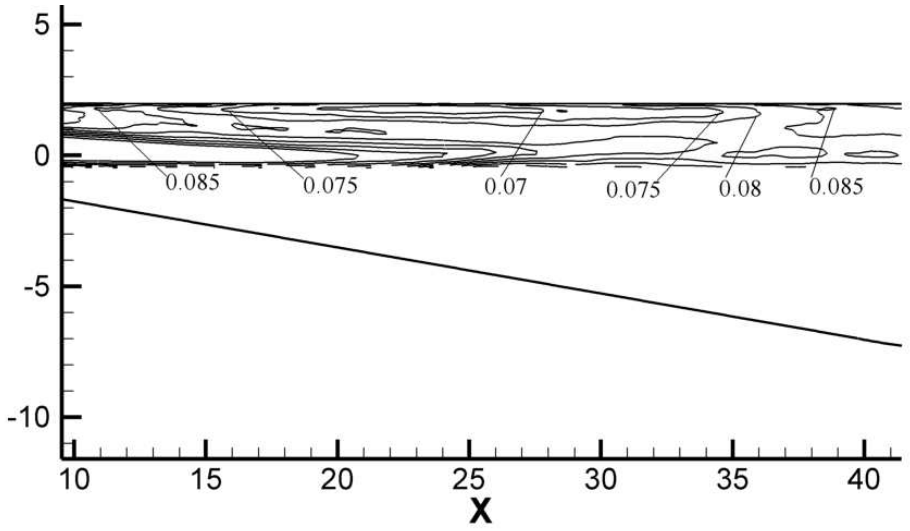

FIGURE 13. Visualization of the internal layer using contours of rms axial turbulence intensity.

subrange law is impressive. In addition, a modest extent of -7 slope is also evident. Grid spacing limits the highest frequency that can be locally resolved in the simulation, and this represents an implicit filter that is imposed by the grid on the flow field (Mittal & Moin 1997). Based on the streamwise grid spacing and the local value of mean streamwise velocity $\langle\overline{u}\rangle$, the normalized Nyquist critical frequency f_c/u_b is approximately 1.2. Spectrum results at higher frequencies may therefore be ignored on the figure.

The internal layer itself is visualized in figure 13 using contours of rms axial turbulence intensity. An imaginary nearly horizontal line connecting the local tips of the contours close to the top wall can be considered approximately as the outer edge of the internal layer.

4. Conclusions

In the concluding remarks of Azad & Kassab (1989), it was commented that *"it may also be conjectured that there is a new growth of a layer in the diffuser wall underneath the retarded, fully developed flow coming from the pipe into the diffuser"*. Our results near the upper wall region of the asymmetric planar Obi diffuser supports their conjecture, albeit at a much lower Reynolds number and also with qualifications.

The new layer is identified as an internal layer but with slow growth. Mean streamwise velocity possesses a well-defined logarithmic slope inside the internal layer until 80 wall units, and varies linearly with wall-normal distance outside the internal layer. One of the statistical indicators of an internal layer is inflectional characteristic in the wall-normal profile of streamwise turbulence intensity. This may take the concrete form of knee-point as reported in the external flow over a hill (Baskaran *et al.* 1987), or valley as found in the present internal flow through a planar diffuser. Internal layers have a tendency to emerge in the relaxation zone downstream of a sudden change in streamwise pressure gradient. Examples of such abrupt change in pressure gradient include the adverse to favorable drop at the trailing edge of the bump of Webster *et al.* (1996), as well as the favorable to adverse jump at the throat regions of the Azad diffuser (Okwuobi & Azad 1973) and the

Obi diffuser. Obviously one prerequisite for internal layer formation is that the abrupt change in pressure gradient may not lead to flow separation, though instantaneous flow reversal is not precluded. We argue that it is possible to relate the occurrence of internal layer to the skin-friction coefficient C_f, which is directly related to the near-wall mean velocity gradient. For instance, a step increase in C_f is found after the trailing edge of the Webster bump corresponding to the adverse to favorable streamwise pressure gradient transition, followed by a gradual leveling off. Over the upper wall of the Obi diffuser, a rapid drop in C_f corresponding to the favorable to adverse pressure gradient jump is followed by a leveling off downstream of $x = 15$. The establishment and stabilization of a new level of C_f signals the birth of internal layer and may be considered as an indicator.

Approximately speaking, the present internal layer and the outer flow associated with it together constitute a distant analogue to the fundamental C-type of Couette-Poiseuille turbulent flows studied recently by Nakabayashi *et al.* (2004). They share broadly similar characteristics of mean and second-order turbulence statistics, but the total shear stress profiles are distinctly different. The role of the lower moving wall in the C-type flow is substituted by the high speed fluid in the central region of the diffuser where the mean velocity $\langle\overline{u}\rangle$ varies linearly with wall-normal coordinate. In this sense the linearly varying high speed flow in the outer region provides the necessary mean flow inflection mechanism for the fluid close to the wall, and may be regarded as one of the driving components in the present internal layer process. The location at which the total shear stress gradient changes sign serves as one the markers for the edge of the internal layer.

Clarifications should be added with reference to the discussion of Townsend (1976) that sudden changes in external conditions in boundary layers may result in an internal boundary layer that spreads from the section of change, and the layer outside the internal layer develops in almost the same way as in the original flow. The results from this study suggest that internal layers may emerge in the relaxation zone downstream of a sudden change in streamwise pressure gradient. Furthermore, the layer outside the internal layer does not behave as if it were unperturbed, i.e., in the same way as in the original flow. On the contrary the flow outside the internal layer displays distinct relaxation characteristics consistent with the removal of strong pressure gradient. Admittedly such observations are limited to the internal layers arising from sudden changes in streamwise pressure gradient. Other perturbation mechanisms, e.g., change in surface roughness, probably will result in an internal layer process not entirely the same as described in this paper.

Acknowledgments

Discussions with Juan Alonso, Sourabh Apte, Peter Bradshaw, George Constantinescu, Massimiliano Fatica, Sangho Kim, Krishnan Mahesh and Cliff Wall are acknowledged. This work is supported by the Advanced Scientific Computing program of the United States Department of Energy. The simulations were performed on the IBM terascale parallel machines at San Diego Supercomputing Center and at Lawrence Livermore National Laboratory.

REFERENCES

Azad, R.S. 1996, Turbulent flow in a conical diffuser: a review. *Experimental Thermal and Fluid Science* **13**, 318–337. Special issue for Peter Bradshaw 60th birthday.

AZAD, R.S. & KASSAB, S.Z. 1989, Turbulent flow in a conical diffuser: overview and implications. *Phys. Fluids* **A1**, 564–573.

BASKARAN, V., SMITS, A.J. & JOUBERT, P.N. 1987, A turbulent flow over a curved hill. Part 1. Growth of an internal boundary layer. *J. Fluid Mech.* **182**, 47–83.

BUICE, C.U. & EATON, J.K. 1997, Experimental investigation of flow through an asymmetric plane diffuser. *Ph.D. Thesis*, Department of Mechanical Engineering, Stanford University.

DURBIN, P.A. 1995, Separated flow computations with the $k-\epsilon-v^2$ model. *AIAA J.* **33**, 659–664.

GERMANO, M., PIOMELLI, U., MOIN, P. & CABOT, W.H. 1991, A dynamic subgrid-scale eddy viscosity model. *Phys. Fluids A* **3**, 1760–1765.

IACCARINO, G. 2001, Prediction of a turbulent separated flow using commercial CFD codes. *J. Fluids Eng.* **123**, 819–828.

KALTENBACH, H.J., FATICA, M., MITTAL, R., LUND, T.S. & MOIN, P. 1999, Study of flow in a planar asymmetric diffuser using large eddy simulation. *J. Fluid Mech.* **390**, 151–185.

LIM, S. & CHOI, H. 2004, Optimal shape design of a two-dimensional asymmetric diffuser in turbulent flow. *AIAA J.* **42**, 1154–1169.

LINDGREN, B., TORNBLOM, O. & JOHANSSON, A.V. 2002, Flow facility design and experimental studies of wall-bounded turbulent shear flows. *Ph.D. Thesis*, Royal Institute of Technology, Stockholm, Sweden.

MAHESH, K., CONSTANTINESCU, G. & MOIN, P. 2004, A numerical method for large eddy simulation in complex geometries. *J. Comp. Phys.* **197**, 215–240.

MITTAL, R. & MOIN, P. 1997, Suitability of upwind biased finite difference schemes for large eddy simulation of turbulent flows. *AIAA J.* **35**, 1415–1417.

NA, Y. & MOIN, P. 1998, Direct numerical simulation of a separated turbulent boundary layer. *J. Fluid Mech.* **370**, 175–202.

NAKABAYASHI, K., KITOH, O. & KATOH, Y. 2004, Similarity laws of velocity profiles and turbulence characteristics of Couette-Poiseuille turbulent flows. *J. Fluid Mech.* **507**, 43–69.

OBI, S., AOKI, K. & MASUDA, S. 1993, Experimental and computational study of turbulent separating flow in an asymmetric plane diffuser. *Ninth Symp. Turbulent Shear Flows, Kyoto, Japan, August 16-19.*

OKWUOBI, P.A.C. & AZAD, R.S. 1973, Turbulence in a conical diffuser with fully developed flow at entry. *J. Fluid Mech.* **57**, 603–622.

PIERCE, C.D. & MOIN, P. 2004, Progress variable approach for large-eddy simulation of non-premixed turbulent combustion. *J. Fluid Mech.* **504**, 73–97.

PRESS, W.H., TEUKOLSKY, S.A., VETTERLING, W.T. & FLANNERY, B.P. 1992, *Numerical Recipes in FORTRAN.* Cambridge University Press.

TOWNSEND, A.A. 1976 *The Structure of Turbulent Shear Flow.* Cambridge University Press.

TRUPP, A.C., AZAD, R.S. & KASSAB, S.Z. 1986 Near wall velocity distributions within a straight conical diffuser. *Experiments in Fluids* **4**, 319–331.

WEBSTER, D., DEGRAAFF, D. & EATON, J.K. 1996 Turbulence characteristics of a boundary layer over a two-dimensional bump. *J. Fluid Mech.* **320**, 53–69.

LES prediction of pressure fluctuations on a low speed airfoil

By M. Wang, S. Moreau†, G. Iaccarino, AND M. Roger‡

1. Motivation and objectives

The noise generated by flow over a lifting surface is a major concern in many engineering applications. Examples include propeller noise, rotor noise, wind turbine noise, fan noise, and noise from wings and hydrofoils. Even in the absence of disturbances in the incoming stream, an airfoil (blade) can be noisy due to the unsteady and turbulent boundary layers and wake generated around the profile and their interaction with it, particularly in the trailing-edge region. This so called self-noise, or trailing-edge noise, is a major contributor to the overall noise in rotating machines and generally defines the lower bound of noise (Wright 1976).

Trailing-edge noise is much more powerful than the noise radiated by turbulent flows of comparable intensity in free space. This is because when turbulent boundary layer eddies are convected past the trailing edge, their aeroacoustic source characteristics are modified by the edge, resulting in a more efficient conversion of flow energy to acoustic energy. The theoretical framework for predicting trailing-edge noise has long been established (see, for example, Ffowcs Williams & Hall 1970; Crighton & Leppington 1971; Howe 1978). In recent years, aided by the rapid increase in computing power, a number of numerical studies have been performed using Lighthill's theory (Lighthill 1952) in conjunction with large-eddy simulation (LES) of the near field (Wang & Moin 2000; Manoha, Troff & Sagaut 2000; Oberai, Roknaldin & Hughes 2002). Wang & Moin (2000) computed the flow over a model airfoil used by Blake (1975) in a trailing-edge aeroacoustic experiment at chord Reynolds number of 2.1×10^6, and obtained reasonable agreement with experimental measurements in terms of velocity and unsteady surface pressure statistics as well as radiated noise spectra. To save computational cost, the simulation was limited to the rear 40% of the airfoil and a spanwise width of just 50% of the airfoil thickness (1.2% chord). In addition, there is uncertainty about the velocity boundary conditions because of wind tunnel installation effects, which can cause the flow to deviate from that in free space (Moreau *et al.* 2003).

The objective of the present work is to further assess the predictive capability of LES for airfoil self noise. A new experiment was performed at Ecole Centrale de Lyon (ECL) to provide data for comparison with numerical solutions. In the experiment, described in Roger & Moreau (2004*a*) and Moreau *et al.* (2003), an industrial cambered airfoil (fan blade) is placed at the exit of an open-jet anechoic wind tunnel, as shown in figure 1. The airfoil, designed to achieve low drag by controlling the chordwise diffusion, is known as the controlled diffusion (CD) profile. Far-field acoustic spectra are measured along with the spatial-temporal statistics of surface pressure fluctuations, including the frequency spectra, coherence and phase. The unsteady surface pressure is of interest because it is used to predict the far-field noise in certain aeroacoustic models based on the classical

† Valeo Motors and Actuators, France
‡ Ecole Centrale de Lyon, France

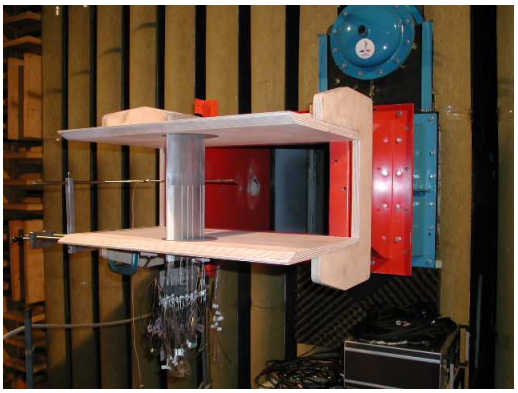

FIGURE 1. Experimental setup in the ECL open-jet facility.

diffraction theory (Amiet 1976; Brooks & Hodgson 1981; Roger & Moreau 2004*b*). It can also induce blade vibration which is an additional source of noise. From a fundamental point of view, both the unsteady surface pressure and radiated acoustic pressure are generated by the same velocity source filed, and hence an accurate prediction of the surface pressure, particularly near the trailing edge, is indicative of the quality of the flow solution for far-field computation. In this article, we present a validation and analysis of the spatial-temporal statistics of the fluctuating surface pressure field. The far-field noise radiation will be computed and presented in the future.

The numerical simulation follows closely the experimental flow conditions. The Reynolds number based on chord and maximum nozzle exit velocity is 1.5×10^5. At this relatively low Reynolds number, it is feasible to perform LES with the entire airfoil, although the details of laminar-to-turbulence transition in the nose region may not be captured accurately. It is argued, and later confirmed, that as long as the location of the transition is captured approximately, the subsequent development of the boundary layer and hence the trailing-edge noise and surface pressure fluctuations are relatively insensitive to the transition process. Several angles of attack (α), measured with respect to the nozzle axis, are considered in the experiment, among which we choose $\alpha = 8°$ in the numerical simulation.

2. Accomplishments

2.1. *Computational approach*

It has been shown by Moreau *et al.* (2003) that the flow around an airfoil in an open-jet wind tunnel facility differs significantly from that around an isolated airfoil in a uniform stream. In the former case, the airfoil is immersed in a jet of finite width, which is deflected by the circulation created by the airfoil. This can have a large impact on the airfoil loading and its aeroacoustic properties. To account for the effect of jet-airfoil interaction, one possible approach is to include both the jet and airfoil in the simulation. This would, however, make the LES computationally very expensive if not impossible, and add considerable complexity to the problem.

To facilitate the LES while matching closely the experimental conditions, we use an approach which incorporates Reynolds-averaged Navier-Stokes (RANS) solutions into the computation as illustrated in figure 2. First, a RANS simulation is performed in a large

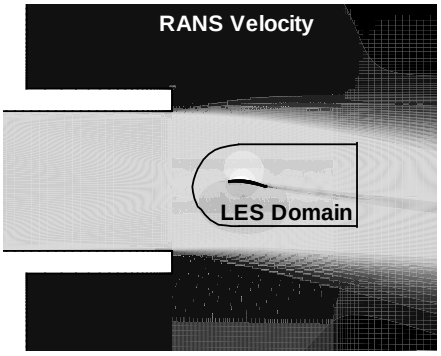

FIGURE 2. Schematic of LES domain embedded in a RANS solution field. The contours, ranging from -0.04 (dark) to 1.25 (light), indicate the streamwise velocity.

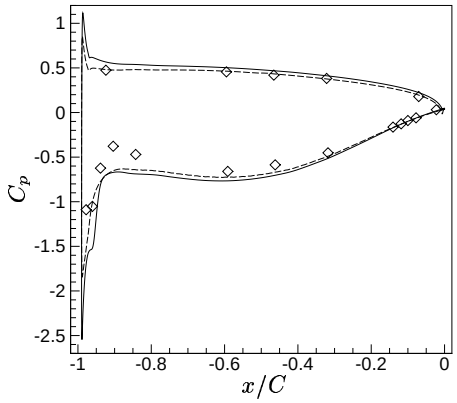

FIGURE 3. Pressure coefficient along the airfoil surface. ——— , LES; - - - - , RANS; ◇ , Experiment.

computational domain which includes the airfoil, the nozzle and the jet. The velocities obtained from the RANS calculation are used to provide boundary conditions for the LES, performed in a smaller domain embedded in the potential core of the jet. A similar method was employed previously by Wang and Moin (2000). As shown in figure 3, the pressure coefficient from LES is in reasonable agreement with those from RANS and experiment, indicating that this approach provides high fidelity in terms of global flow conditions. In order to allow for a reasonably large LES domain within the jet core, the largest nozzle available in the ECL facility was employed. The jet width at the nozzle exit is 50 cm, or 3.69 times the airfoil chord C.

In the LES, we solve the spatially filtered, incompressible Navier-Stokes equations in conjunction with the dynamic subgrid scale model (Germano *et al.* 1991; Lilly 1992) using an energy-conserving, hybrid finite-difference/spectral code described in Wang & Moin (2000). The numerical scheme utilizes second-order central differences in the streamwise and cross-stream directions, and Fourier collocation in the spanwise direction. The time advancement is of the fractional step type in combination with the Crank-Nicholson method for viscous terms and third order Runge-Kutta scheme for the convective terms. The Poisson equation for pressure is solved using a multigrid iterative procedure. Simulations are performed on a C-mesh with $960 \times 84 \times 64$ cells, covering a region of size $4C$ (streamwise, x) $\times$ $2.5C$ (cross-stream, y) $\times$ $0.1C$ (spanwise, z). Except in the vicinity of the leading edge, the near-wall grid resolution on the suction side is $\Delta x^+ \leq 34$, $\Delta y^+ \leq 1.1$, and $\Delta z^+ \leq 20$ in wall units, which is adequate for LES. Resolution on the pressure side is considerably coarser because the boundary layer is laminar. The boundary conditions consist of the no-slip condition on the airfoil surface, convective outflow condition in the exit plane, steady RANS velocities along the outer "C" boundary, and periodic boundary conditions in the spanwise direction.

2.2. *Results*

2.2.1. *Flow-field characteristics*

Figure 4 depicts the iso-contours of the streamwise velocity in a given spanwise plane at a given time instant. It shows a laminar boundary layer on the lower (pressure) side

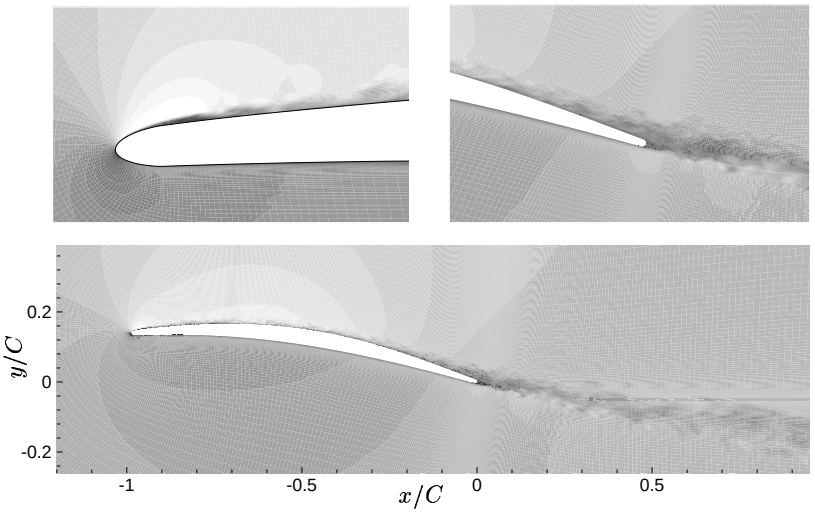

FIGURE 4. Instantaneous streamwise velocity in a spanwise plane. 25 contour levels ranging from -0.27 (dark) to 1.47 (light) are plotted.

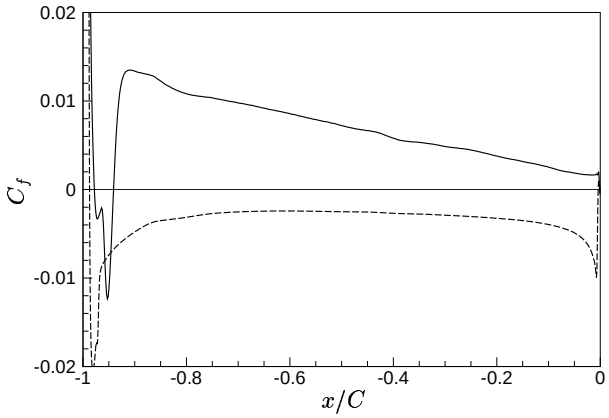

FIGURE 5. Distribution of skin friction coefficient (computed relative to maximum inlet velocity) along the airfoil. ——— , suction side; - - - - , pressure side.

of the airfoil, and a transitional and turbulent boundary layer on the upper (suction) side. Transition on the suction side is triggered by an unsteady laminar separation near the nose, as illustrated clearly in the leading-edge close-up in figure 4. The leading-edge separation is quantitatively identified in figure 5 as a region of negative skin friction coefficient C_f. The streamwise extent of the mean separation bubble is approximately $3.7\%C$. After reattachment the suction side boundary layer evolves downstream into a fully turbulent one. Like its laminar counterpart on the pressure side, the turbulent boundary layer remains attached as it passes the trailing edge despite the strong adverse pressure gradient. There is no obvious coherent vortex shedding at the present angle of attack. These qualitative features of the flow are in agreement with experimental observations.

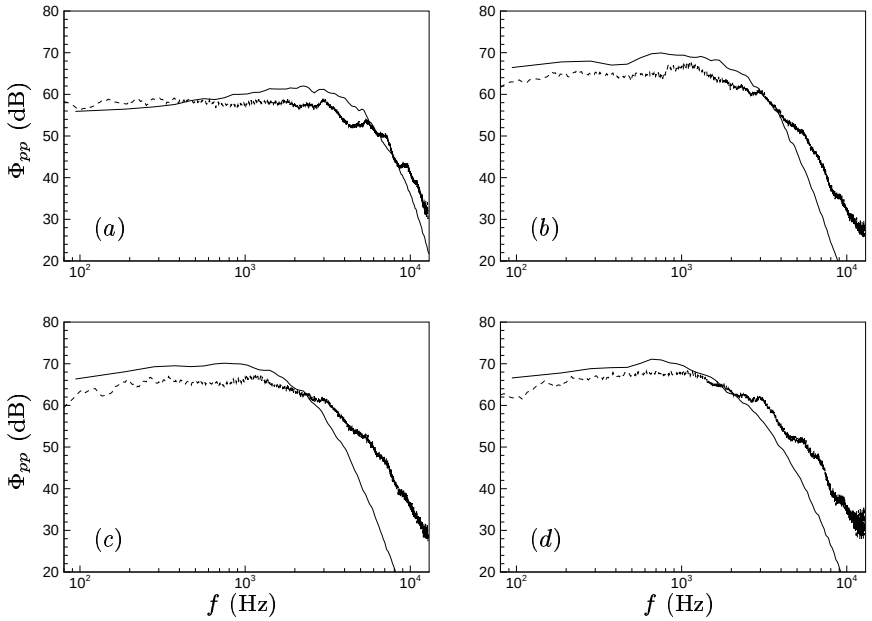

FIGURE 6. Frequency spectra of pressure fluctuations on the suction side of airfoil surface at (*a*) $x_c/C = -0.60$, (*b*) $x_c/C = -0.14$, (*c*) $x_c/C = -0.08$, and (*d*) $x_c/C = -0.02$. ——— , LES; – – – – , Experiment.

2.2.2. *Frequency spectra of surface pressure fluctuations*

The frequency spectra of pressure fluctuations on the suction side of the airfoil surface are shown in figures 6 and 7. To facilitate comparisons with the experimental data, dimensional frequencies (in Hz) and spectra (in dB, relative to the reference pressure of 2×10^{-5} Pa) are used. The reference velocity (U_0) and density (ρ_0), taken at the center of nozzle exit, are 16 m/s and 1.25 kg/m^3, respectively, and the airfoil chord is $C = 0.1356$ m. Since the airfoil has an angle of attack, it is convenient to define a chordwise coordinate x_c, which is related to the x-coordinate (cf. figure 4) by $x_c = x/\cos\alpha$, to identify the measurement stations. Along this coordinate the nose is located at $x_c/C = -1$ and the trailing-edge is at $x_c/C = 0$.

Plotted in figure 6 are comparisons with experimental measurements at four stations: $x_c/C = -0.60, -0.14, -0.08, -0.02$. The first station (figure 6*a*) is in the front half of the airfoil. At this location the pressure spectrum already exhibits turbulent boundary layer characteristics and is in good agreement with experimental measurements. Similar spectral shapes are observed at downstream locations. The last three stations shown in figure 6(*b–d*) are located in the trailing-edge region. Their pressure spectra show overall agreement with the experimental data. In general, LES is seen to overpredict the spectral level by 2 to 4 dBs relative to the experiment in the low to intermediate frequency range. At the high frequency end the LES spectra drop off more rapidly, suggesting that the boundary layer lacks very small scale structures. This is not atypical of LES predictions (e.g. Wang & Moin 2000; 2002), although somewhat surprising given the good grid resolution employed in the computation and the fact that high frequency contents are much better captured at the upstream location shown in figure 6*a*.

A useful observation from figure 6(*b–d*) is that the pressure spectra exhibit only small

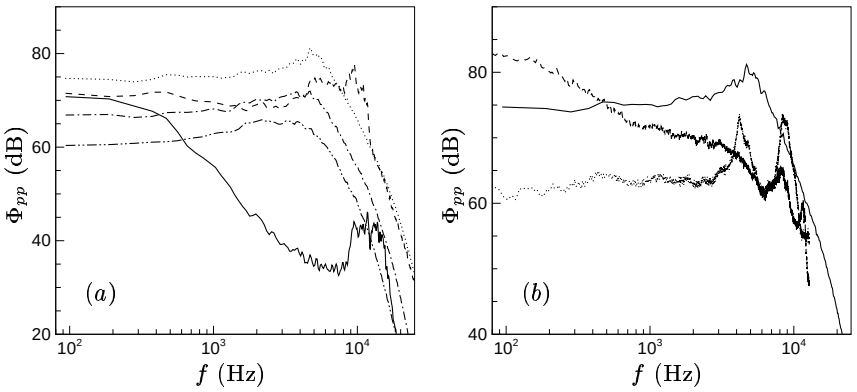

FIGURE 7. Frequency spectra of pressure fluctuations on the suction surface in the leading-edge area. (a) LES results at five chordwise locations: ——— , $x_c/C = -0.99$; - - - - , $x_c/C = -0.97$; ····· , $x_c/C = -0.95$; — - — , $x_c/C = -0.91$; — · — , $x_c/C = -0.85$. (b) Comparison with experimental measurements at $x_c/C = -0.95$: ——— , LES; - - - - , measurement 1; ····· , measurement 2.

variations in the trailing-edge region (within the last 15% chord). This is important for the aeroacoustic prediction models based on pressure diffraction theory (e.g. Amiet 1976; Brooks & Hodgson 1981, Roger & Moreau 2004*b*), which utilize the frequency spectrum of wall pressure at a single point near the trailing edge as an input. The exact location is arbitrary as long as the spectrum is not affected by the edge diffraction. This approach necessarily requires the boundary layer to be self-similar so that the wall pressure spectrum does not exhibit strong sensitivity to the streamwise position. The spectra obtained for the present flow exhibit this property despite the adverse pressure gradient, indicating that this modeling approach is suitable for the far-field noise prediction.

In contrast to the trailing-edge area, the pressure spectrum in the leading-edge region shows extremely strong dependence on position. Figure 7*a* depicts the frequency spectra at locations $x_c/C = -0.99$, -0.97, -0.95, -0.91, and -0.85. The first station is upstream of the unsteady separation, and hence the spectrum lacks high frequency contents. The second station is inside the separation, and the other three are downstream of reattachment. The spectral levels are highly elevated inside the separation and immediately following the reattachment as a result of the shear layer motions and laminar breakdown. It should be pointed out that the detailed transition process, including the precise locations of separation and reattachment, is strongly dependent on incoming flow disturbances. No free-stream turbulence is provided in the computation, whereas in the experiment, the residual turbulence level in the incident flow is approximately 0.8% of the mean velocity. The experimental pressure spectra in the leading-edge region show significant variations from one measurement to another. As an example, two sets of measurements at the same location, $x_c/C = -0.95$, are plotted in figure 7*b* along with the LES solution. The discrepancies among the three curves are very large. An accurate simulation of the leading-edge region would require a precise characterization of the incoming turbulence as well as very accurate numerics. However, given the non-repeatability even among experimental measurements, such a task may prove very challenging.

The root-mean-square (rms) value of pressure fluctuations p_{rms}, normalized by the local mean wall shear stress τ_w, is plotted in figure 8 along the suction surface. The curve

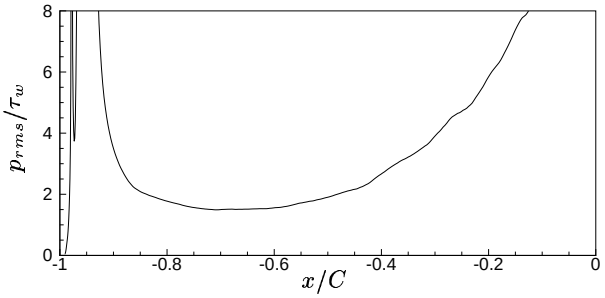

FIGURE 8. Variation of p_{rms}/τ_w along the airfoil suction surface, computed using LES.

is truncated in the nose and trailing-edge regions because of the exceedingly small τ_w values caused by flow separation and adverse pressure gradient. In the region $-0.8 \leq x/C \leq -0.4$, the pressure gradient is nearly zero (cf. figure 3), and p_{rms}/τ_w varies from 1.5 to 2.7. This is consistent with previous numerical and experimental values for equilibrium turbulent boundary layers at similar low Reynolds numbers (e.g. Choi & Moin 1990).

2.2.3. *Correlation and coherence*

The evolution of the spatial and temporal scales in the turbulent boundary layer is reflected in the space-time correlation of the fluctuating surface pressure, depicted in figure 9 as a function of temporal and spanwise spatial separations at four streamwise locations $x_c/C = -0.60$, -0.23, -0.02, and 0. A significant growth of the spanwise and temporal scales is observed from the first station to the third, as a result of the thickening of the boundary layer which is accelerated by the adverse pressure gradient. A similar growth in streamwise scales can be inferred from the temporal scales through Taylor's hypothesis. The last station, $x_c/C = 0$, is in the back of the trailing edge, which is blunt on a small scale (see figure 4). The decorrelation spatial and temporal scales at this location (figure 9*d*) are found to be much larger than those of its close neighbor, $x_c/C = -0.02$ (figure 9*c*). Note that the spanwise correlation coefficient in figure 9 decays to between 0.1 and 0.2 over a maximum separation equal to one half of the periodic spanwise domain size. This is, while not ideal, considered reasonable for this flow and much better than in some related studies (e.g. Wang & Moin 2000). To test the sensitivity of the correlation to spanwise domain size, a separate simulation with twice the spanwise domain size but coarser grid resolution has been conducted. The results show only a marginal improvement, and the minimum spanwise correlation remains larger than 0.1.

An important parameter in trailing-edge noise prediction (both modeling and computation) is the coherence length scale of the source field in the spanwise direction, since it represents the size of a source region which radiate independently from sources in neighboring regions in a statistical sense. The coherence is essentially the two-point correlation coefficient in the frequency domain, defined as

$$\gamma^2(\mathbf{x}, \mathbf{r}, \omega) = \frac{|\Phi_{pp}(\mathbf{x}, \mathbf{r}, \omega)|^2}{|\Phi_{pp}(\mathbf{x}, 0, \omega)||\Phi_{pp}(\mathbf{x} + \mathbf{r}, 0, \omega)|}, \tag{2.1}$$

where the cross spectrum function Φ_{pp} is the Fourier transform of the space-time cross

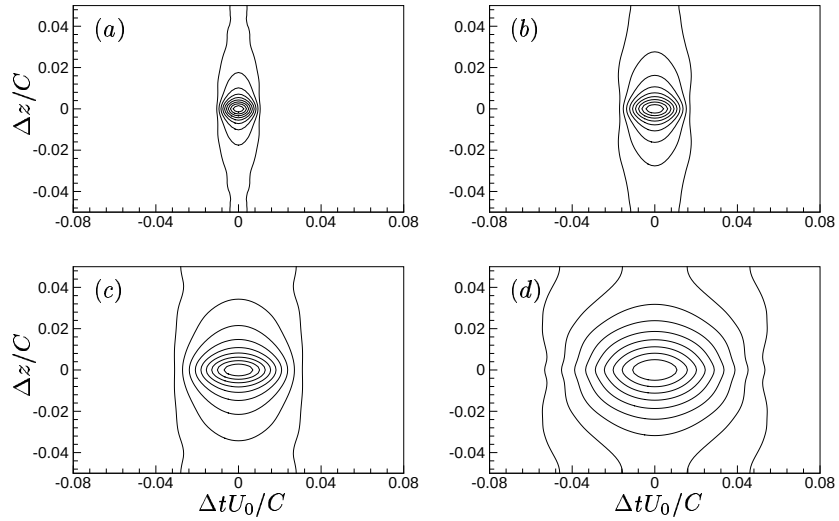

FIGURE 9. Contours of space-time correlation of the fluctuating pressure on the suction surface as a function of spanwise and temporal separations, at streamwise locations (*a*) $x_c/C = -0.60$, (*b*) $x_c/C = -0.23$, (*c*) $x_c/C = -0.02$, and (*d*) $x_c/C = 0$ (trailing edge). Contour values are from 0.1 to 0.9, with increment 0.1.

correlation function

$$\Phi_{pp}(\mathbf{x}, \mathbf{r}, \omega) = \int_{-\infty}^{\infty} \langle p(\mathbf{x}, t) p(\mathbf{x} + \mathbf{r}, t + \tau) \rangle e^{-i\omega\tau} d\tau. \tag{2.2}$$

Figure 10 shows the surface pressure coherence as a function of spanwise separation and frequency, at locations $x_c/C = -0.60$ and -0.02. These two contour plots should be contrasted with the corresponding correlation plots in figure 9*a* and figure 9*c*, respectively. It is observed that the increased spanwise correlation near the trailing edge is a low frequency effect. The higher frequency components near the trailing edge are in fact less correlated (having smaller coherence length) than their upstream counterparts.

In figure 11*a*, a comparison is made between the experimental and computed values of the spanwise coherence of fluctuating surface pressure at the near trailing-edge point $x_c/C = -0.02$. Two spanwise separations, $\Delta z/C = 0.02$ and 0.04, are considered. The LES results are shown to predict the higher frequency behavior of the coherence but not the low frequency value. It appears that the coherence at low frequencies, particularly for relatively large separations as measured in the experiment, is extremely sensitive to sample size and numerical errors. In figure 11*b* the coherence at the same location is plotted as a function of spanwise separation for five discrete frequencies. The rapid decay of the coherence with spanwise separation, even at low frequencies (see also figure 10), indicates that the current spanwise computational domain size allows the capturing of a statistically independent acoustic source region and the computation of coherence length scales; both are key to the computation of radiated noise. However, the accuracy of the lower frequency coherence needs to be improved.

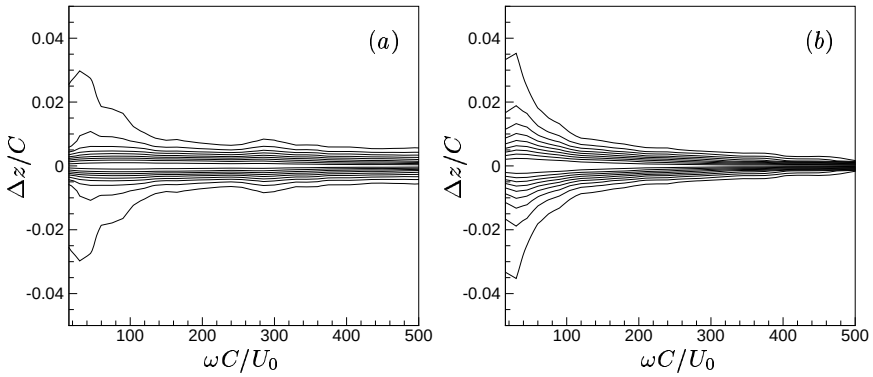

FIGURE 10. Contours of spanwise coherence of the fluctuating pressure on the suction surface as a function of frequency and spanwise separation, at streamwise locations (*a*) $x_c/C = -0.60$ and (*b*) $x_c/C = -0.02$. Contour values are from 0.1 to 0.9, with increment 0.1.

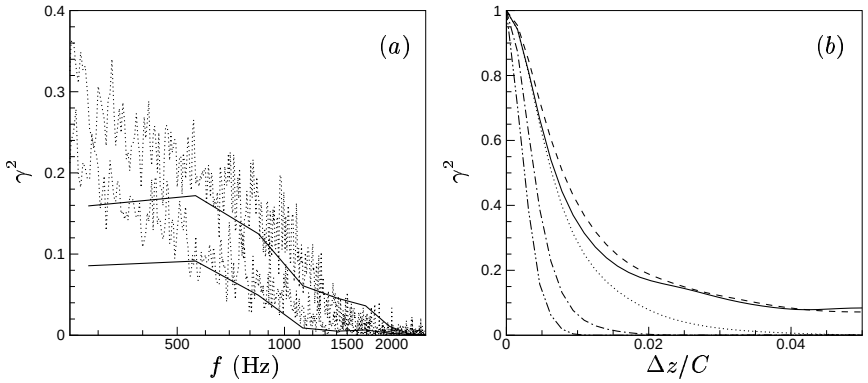

FIGURE 11. Spanwise coherence of fluctuating pressure on the suction surface at $x_c/C = -0.02$. (*a*) Coherence plotted against frequency in Hz: ——— , LES; ····· , experiment. Upper curves are for spanwise separation $\Delta z/C = 0.02$, and lower curves are for $\Delta z/C = 0.04$. (*b*) Coherence plotted against spanwise separation: ——— , $\omega C/U_0 = 15$ (281 Hz); – – – – , $\omega C/U_0 = 30$ (563 Hz); ····· , $\omega C/U_0 = 60$ (1126 Hz); — – — , $\omega C/U_0 = 120$ (2252 Hz); — ·· — , $\omega C/U_0 = 240$ (4503 Hz).

3. Summary and future plans

In this work large-eddy simulation has been employed to study the space-time characteristics of the fluctuating pressure on a thin, cambered airfoil at 8° angle of attack. The computational results are compared with concurrent experimental measurements carried out at ECL in terms of the frequency spectra and spanwise coherence. The relatively low Reynolds number of 1.5×10^5 based on chord allows the simulation to be performed with the entire airfoil in the computational domain. Transition is triggered naturally by unsteady laminar separation near the nose.

To replicate faithfully the experimental flow conditions in the simulation, a RANS calculation is first performed in an open-jet wind tunnel configuration. The resulting velocity profiles are then used to define the boundary conditions for LES in a smaller, C-mesh domain within the core of the jet. This approach is shown to provide the correct

global flow condition in terms of airfoil loading. The precise turbulent inflow condition, which can affect the leading-edge transition, is not prescribed. It is found that the pressure spectrum beneath the fully developed turbulent boundary layer is insensitive to the details of the upstream transition process, as long as the location of the transition is captured approximately.

The LES flow field is characterized by an attached laminar boundary layer on the pressure side of the airfoil and a transitional and turbulent boundary layer on the suction side, in agreement with experimental observations. A spectral analysis of the fluctuating surface pressure field shows reasonable agreement with experimental values in the mid- and aft-sections of the airfoil. In the nose region, characterized by unsteady separation and transition, the flow and wall-pressure fluctuations are highly sensitive to small inflow perturbations. Their spatial-temporal statistics are difficult to measure experimentally or predict computationally with certainty. LES is also shown to be capable of predicting the spanwise coherence of the surface pressure field to reasonable satisfaction compared with the experiment except at the low frequency end, where statistical convergence is difficult to reach. In addition to the validation study using experimental data, a preliminary analysis of the spatial and temporal structures of the unsteady pressure field and their evolution has been carried out.

In the future we plan to further validate and analyze the LES solutions using recently acquired hot-wire measurements in the wake. We will also compute the noise radiation to the far-field using Lighthill's aeroacoustic theory.

REFERENCES

AMIET, R. K. 1976 Noise due to turbulent flow past a trailing edge. *J. Sound Vib.* **47**, 387–393.

BLAKE, W. K. 1975 *A Statistical Description of Pressure and Velocity Fields at the Trailing Edge of a Flat Strut.* DTNSRDC Report 4241, David Taylor Naval Ship R & D Center, Bethesda, Maryland.

BROOKS, T. F. & HODGSON, T. H. 1981 Trailing edge noise prediction from measured surface pressures. *J. Sound Vib.* **78**, 69–117.

CHOI, H. & MOIN, P. 1990 On the space-time characteristics of wall-pressure fluctuations. *Phys. Fluids A* **2**, 1450–1460.

CRIGHTON, D. G. & LEPPINGTON, F. G. 1971 On the scattering of aerodynamic noise. *J. Fluid Mech.* **46**, 577–597.

FFOWCS WILLIAMS, J. E. & HALL, L. H. 1970 Aerodynamic sound generation by turbulent flow in the vicinity of a scattering half plane. *J. Fluid Mech.* **40**, 657–670.

GERMANO, M., PIOMELLI, U., MOIN, P. & CABOT, W. H. 1991 A dynamic subgrid-scale eddy viscosity model. *Phys. Fluids A* **3**, 1760–1765.

HOWE, M. S. 1978 A review of the theory of trailing edge noise. *J. Sound Vib.* **61**, 437–465.

LIGHTHILL, M. J. 1952 On sound generated aerodynamically; I. General theory. *Proc. Roy. Soc. London Ser. A* **211**, 564–587.

LILLY, D. K. 1992 A proposed modification of the Germano subgrid scale closure method. *Phys. Fluids A* **4**, 633–635.

MANOHA, E., TROFF, B. & SAGAUT, P. 2000 Trailing edge noise prediction using large eddy simulation and acoustic analogy. *AIAA J.* **38**, 575–583.

MOREAU, S., HENNER, M., IACCARINO, G., WANG, M. & ROGER, M. 2003 Analysis of flow conditions in free-jet experiments for studying airfoil self-noise. *AIAA J.* **41**, 1895–1905.

OBERAI, A. A., ROKNALDIN F. & HUGHES T. J. R. 2002 Computation of trailing-edge noise due to turbulent flow over an airfoil. *AIAA J.* **40**, 2206–2216.

ROGER, M. & MOREAU, S. 2004*a* Broadband self-noise from loaded fan blades. *AIAA J.* **42**, 536–544.

ROGER, M. & MOREAU, S. 2004*b* Back-scattering correction and further extensions of Amiet's trailing-edge noise model. Part I: Theory. *J. Sound Vib.*, in press.

WANG, M. & MOIN, P. 2000 Computation of trailing-edge flow and noise using large-eddy simulation. *AIAA J.* **38**, 2201–2209.

WANG, M. & MOIN, P. 2002 Dynamic wall modeling for large-eddy simulation of complex turbulent flows. *Phys. Fluids* **14**, 2043–2051.

WRIGHT, S. E. 1976 The acoustic spectrum of axial flow machines. *J. Sound Vib.* **45**, 165–223.

A space-time correlation theory for turbulent shear flows

By G.W. He† AND M. Wang

1. Motivations and objectives

The objective of this research is to investigate the large-eddy simulation (LES) prediction of velocity space-time correlations in turbulent shear flows. In the application of LES methodology to aeroacoustics (e. g. Wang & Moin 2000; Colonius & Lele 2005), Lighthill's acoustic analogy (Lighthill 1952) is often used to compute the far-field noise. According to Lighthill's theory, the acoustic intensity radiated by a turbulent flow depends on the space-time correlations of the Lighthill stresses, which are related to the space-time correlations of velocity fluctuations based on Proudman's (1952) analysis. Our previous research (He, Rubinstein & Wang 2002; He, Wang & Lele 2004) shows that the space-time correlations in isotropic turbulence are determined by the instantaneous wavenumber energy spectrum and the sweeping velocity; the latter is the root mean square of total energy. Therefore, if LES with an appropriate SGS model captures the time evolution of the energy spectrum, the space-time correlation, and hence noise, is expected to be computed correctly. However, realistic flows are not isotropic and homogeneous. In turbulent shear flows, the space-time correlations are no longer dominated by the sweeping velocity. Thus, an accurate prediction of the energy spectrum is not the only requirement for SGS modeling. The convection and shear may cause additional effects on space-time correlations, which must be accounted for by the SGS models.

In this study, we investigate the space-time correlations in turbulent shear flows. An elliptic hypothesis is proposed to model the space-time correlations in the streamwise direction. It is shown that Taylor's hypothesis is a linear approximation to the correlation contours, whereas the elliptic hypothesis is a second order approximation to the contours. An analytical expression for space-time correlations is formulated from the elliptic hypothesis, which relates the space-time correlations to two-point spatial correlations and propagation velocities. The propagation velocities are neither the sweeping velocity nor the mean velocity in general. The results will be used to guide a subsequent computation aimed at elucidating the SGS modeling effect on space-time correlations in turbulent shear flows.

2. Main results

The space-time correlation in a statistically stationary and homogeneous flow is defined as

$$R(r,\tau) = \langle u_i(\mathbf{x},t)u_i(\mathbf{x}+\mathbf{r},t+\tau)\rangle, \tag{2.1}$$

† Permanent address: Laboratory for Nonlinear Mechanics, Institute of Mechanics, Chinese Academy of Sciences, Beijing, 100080, China; Email: hgw@lnm.imech.ac.cn and ghe@ctr.stanford.edu

where u_i is a component of velocity fluctuation $\mathbf{u}$ and τ is the temporal separation. No summation over repeated indices is implied unless otherwise indicated. For notational simplicity, the index on the correlation function R has been dropped. In the present analysis, we limit spatial separation to the streamwise direction: $\mathbf{r} = (r, 0, 0)$, in which turbulence is statistically homogeneous. In previous studies of the space-time correlations, velocity fluctuations are frequently considered to be convected by a propagation velocity V such that

$$R(r, \tau) = R(r - V\tau, 0). \tag{2.2}$$

If the fluctuations are convected in frozen patterns, the propagation velocity is the mean velocity. This is the result from Taylor's well-known hypothesis. Eq. (2.2) also implies that

$$R(r, \tau) = \int E(k) \cos[k(r - V\tau)] dk, \tag{2.3}$$

which indicates that the space-time correlation is determined by the wavenumber energy spectrum $E(k)$ and propagation velocity. Therefore, if LES can predict both the wavenumber energy spectrum and propagation velocity, it can predict the space-time correlations. However, Taylor's hypothesis is a rather crude approximation and may fail in flows with a strong shear (Lumley 1965). It is desirable to derive a more general and accurate model for the space-time correlations in turbulent shear flows.

Consider an iso-correlation contour $R(r, \tau) = C$, where C is constant. If we can find a point $(r_c, 0)$ on the contour, it implies that $R(r, \tau) = R(r_c, 0)$. Therefore, the space-time correlations are determined by the spatial correlation $R(r, 0)$ and the solution of the equation $R(r, \tau) = R(r_c, 0)$. Both numerical simulations (Kim & Hussain 1993) and experiments (Wills 1964) have shown that in turbulent shear flows the correlation contours form closed curves with a single peak at the origin $(r, \tau) = (0, 0)$. The contours decrease in value with increasing r or τ, and decay to zero as r or τ goes to infinite. This ensures the existence of a solution to the equation $R(r, \tau) = R(r_c, 0)$. The most prominent feature of the contours is that they have a preferred direction.

The correlation contours can be reasonably approximated by second order algebraic curves. A higher-order approximation can be introduced if necessary. Based on the experimental and numerical observations, we propose an elliptic approximation, i.e. the contours of space-time correlations are ellipses. The ellipses can be obtained by Taylor's expansion of the space-time contours $R(r, \tau) = C$

$$R_{rr} r^2 + 2R_{r\tau} r\tau + R_{\tau\tau} \tau^2 = C, \tag{2.4}$$

where the subscripts denote derivatives evaluated at $r = 0$ and $\tau = 0$. Note that $R_\tau(0, 0) = R_r(0, 0) = 0$ because the flow is statistically stationary and homogeneous in the direction of separation. $R(0, 0)$ has been absorbed into C. Suppose that (r, τ) and $(r_c, 0)$ are the two points on the ellipse, that is $R(r, \tau) = R(r_c, 0)$, we obtain

$$r_c = \sqrt{r(r - 2V_l\tau) + V_t^2 \tau^2}, \tag{2.5}$$

where

$$V_l = -R_{r\tau}(R_{rr})^{-1}, \tag{2.6}$$

$$V_t^2 = R_{\tau\tau}(R_{rr})^{-1}. \tag{2.7}$$

Here V_l is the same propagation velocity defined by Wills (1964). V_t also has the dimension

of velocity and may thus be considered as a propagation velocities. As a result, we have

$$R(r,\tau) = R\left(\sqrt{r(r-2V_l\tau)+V_t^2\tau^2}, 0\right) \tag{2.8}$$

Eq. (2.8) implies that the space-time correlations in a turbulent shear flow can be determined from the spatial correlations and appropriately defined propagation velocities.

In the degenerate case of $R_{rr}R_{\tau\tau} - R_{r\tau}^2 = 0$, (2.5) can be simplified to

$$r_c = r - V_l\tau, \tag{2.9}$$

which is Taylor's hypothesis. It is now clear that Taylor's hypothesis is a linear approximation to the correlation contours, which is the degenerate case of the elliptic hypothesis. If there exists a dominant propagation velocity, the ellipse is very flat in the direction normal to the propagation direction. This means that the ratio of two principal axes of the ellipse, $R_{rr}R_{\tau\tau} - R_{r\tau}^2$, is negligibly small. Thus, Taylor's hypothesis is a good approximation.

The two velocities in (2.5) can be analytically calculated from the Navier-Stokes equations using the Taylor expansion technique (Gotoh & Kaneda 1991; Kaneda 1993). In the following, we derive the first propagation velocity as an example. We start with the incompressible Navier-stokes equations

$$\begin{aligned} &\frac{\partial \mathbf{v}}{\partial t} + (\mathbf{v}\cdot\nabla)\mathbf{v} = -\frac{1}{\rho}\nabla p + \nu\nabla^2\mathbf{v}, \\ &\nabla\cdot\mathbf{v} = 0, \end{aligned} \tag{2.10}$$

where ν is the kinematic viscosity and ρ is the density, hencefore absorbed into pressure. The velocity $\mathbf{v}$ and pressure p are decomposed into their mean parts, $\mathbf{U}$ and P, and their fluctuation parts, $\mathbf{u}$ and p', such that

$$\begin{aligned} \mathbf{v} &= \mathbf{U} + \mathbf{u}, \\ p &= P + p'. \end{aligned} \tag{2.11}$$

For simplicity, we consider parallel flows whose mean velocity has the form $\mathbf{U} = (U_1(x_2), 0, 0)$. The velocity and pressure fluctuations must then satisfy

$$\begin{aligned} \frac{\partial u_i}{\partial t} &= -U_1(x_2)\frac{\partial u_i}{\partial x_1} - u_2\frac{\partial U_1(x_2)}{\partial x_2}\delta_{i1} - u_j\frac{\partial u_i}{\partial x_j} + \left\langle u_j\frac{\partial u_i}{\partial x_j}\right\rangle - \frac{\partial p'}{\partial x_i} + \nu\frac{\partial^2 u_i}{\partial x_j\partial x_j}, \\ p' &= -\nabla^{-2}\frac{\partial^2}{\partial x_i\partial x_j}\left[U_1\delta_{i1}u_j + U_1\delta_{j1}u_i + u_iu_j - \langle u_iu_j\rangle\right]. \end{aligned} \tag{2.12}$$

Note that in (2.12), the summation convention over repeated indices applies. From the definition of the space-time correlation, we can calculate

$$R_{rr} = \left\langle u_i(\mathbf{x},t)\frac{\partial^2 u_i(\mathbf{x}+\mathbf{r},t+\tau)}{\partial r^2}\right\rangle_{r=\tau=0} = -\left\langle \frac{\partial u_i(\mathbf{x},t)}{\partial x_1}\frac{\partial u_i(\mathbf{x},t)}{\partial x_1}\right\rangle \tag{2.13}$$

$$R_{r\tau} = \left\langle u_i(\mathbf{x},t)\frac{\partial^2 u_i(\mathbf{x}+\mathbf{r},t+\tau)}{\partial r\partial \tau}\right\rangle_{r=\tau=0} = -\left\langle \frac{\partial u_i(\mathbf{x},t)}{\partial x_1}\frac{\partial u_i(\mathbf{x},t)}{\partial t}\right\rangle \tag{2.14}$$

Substituting (2.12) into (2.14) leads to

$$R_{r\tau} = U_1(x_2)\left\langle \frac{\partial u_i(\mathbf{x},t)}{\partial x_1}\frac{\partial u_i(\mathbf{x},t)}{\partial x_1}\right\rangle + \frac{\partial U_1(x_2)}{\partial x_2}\delta_{i1}\left\langle u_2(\mathbf{x},t)\frac{\partial u_1(\mathbf{x},t)}{\partial x_1}\right\rangle$$

$$-\frac{1}{2\pi}\iiint \frac{\partial U_1(y_2)}{\partial y_2}\left\langle \frac{\partial u_2(\mathbf{y},t)}{\partial y_1}\frac{\partial u_i(\mathbf{x},t)}{\partial x_1}\right\rangle \frac{y_i - x_i}{|\mathbf{x}-\mathbf{y}|}d\mathbf{y} \tag{2.15}$$

where the velocity fluctuations are assumed to be homogeneous and their triple correlations and the viscous terms are ignored.

Therefore, the first propagation velocity is

$$V_l = U_1(x_2) + \frac{\partial U_1(x_2)}{\partial x_2}\delta_{i1}\left\langle u_2\frac{\partial u_1}{\partial x_1}\right\rangle \left\langle \frac{\partial u_i}{\partial x_1}\frac{\partial u_i}{\partial x_1}\right\rangle^{-1}$$
$$-\frac{1}{2\pi}\iiint \frac{\partial U_1(y_2)}{\partial y_2}\left\langle \frac{\partial u_2(\mathbf{y},t)}{\partial y_1}\frac{\partial u_i(\mathbf{x},t)}{\partial x_1}\right\rangle \frac{y_i - x_i}{|\mathbf{x}-\mathbf{y}|}d\mathbf{y}\left\langle \frac{\partial u_i}{\partial x_1}\frac{\partial u_i}{\partial x_1}\right\rangle^{-1} \tag{2.16}$$

Expression (2.16) shows that the propagation velocity V_l is dominated by the mean velocity if the shear rate is relatively small. However, when the shear rate is large, the contribution from the second term can be significant. This observation is in agreement with the numerical results in channel flows obtained by Kim and Hussain (1993): the propagation velocity for most of the outer layer is essentially identical to the local mean velocity, whereas the propagation velocity in the near-wall region is about one half of the mean velocity at the center of the channel, which is larger than the local mean velocity. Therefore, the space-time correlations in turbulent shear flows present additional requirements to LES beyond the wavenumber energy spectra.

3. Future work

An elliptic approximation for space-time correlations in turbulent shear flows has been proposed. According to this approximation, the space-time correlations of velocity fluctuations are determined by the two-point spatial correlations and the propagation velocities. It is also shown that Taylor's hypothesis is a linear approximation to the space-time correlations. To accurately predict the space-time correlations, one must accurately predict the spatial correlations and the propagation velocities.

Future work will include the numerical verification of the elliptic hypothesis in turbulent shear flows. The space-time correlations will be evaluated in a channel flow using DNS and LES with different SGS models. The results obtained will be analyzed in terms of propagation velocities. These fluctuating quantities to be analyzed include velocity, pressure and the Lighthill stress tensor.

REFERENCES

COLONIUS, T. & LELE, S.K. 2004 Computational aeroacoustics: progress on nonlinear problems of sound generation. To be published in *Prog. Aerospace Sci.*

GOTOH, T. & KANEDA, Y. 1991 Lagrangian velocity autocorrelation and eddy viscosity in two-dimensional anisotropic turbulence. *Phys. Fluids A* **3**, 2426–2437.

HE, G.-W., RUBINSTEIN, R. & WANG, L.-P. 2002 Effects of subgrid scale modeling on time correlations in large eddy simulation. *Phys. Fluids* **14**, 2186–2193.

HE, G.-W., WANG, M. & LELE, S.K. 2004 On the computation of space-time correlations by large eddy simulation, *Phys. Fluids* **16**, 3859–3867.

KANEDA, Y. 1993 Lagrangian and Eulerian time correlations in turbulence. *Phys. Fluids A* **5**, 2835–2845.

KIM, J. & HUSSAIN, F 1993 Propagation velocity of perturbations in turbulent channel flow. *Phys. Fluids A* **5**, 695–706.

LIGHTHILL, M.J. 1952 On sound generated aerodynamically: I. General theory. *Proc. R. Soc. Lond. A* **211**, 564–587.

LUMLEY, J.L. 1965 Interpretation of time spectra measured in high-intensity shear flows. *Phys. Fluids* **8**, 1056-1062.

PROUDMAN, I. 1952 The generation of sound by isotropic turbulence. *Proc. R. Soc. Lond. A* **214**, 119–132.

WANG, M. & MOIN, P. 2000 Computation of trailing-edge flow and noise using large eddy simulation. *AIAA J.* **38**, 2201–2209.

WILLS, J.A.B. 1964 On convection velocities in turbulent shear flows. *J. Fluid Mech.* **20**, 417–432.

A multilevel formulation to simulate particulate flows

By S. V. Apte

1. Motivation and objectives

Many engineering problems involve two-phase flows, where particles of different shapes, sizes, and densities in the form of droplets, solid particles, or bubbles are dispersed in a continuum (gaseous or liquid) fluid. Numerical simulations of these flows commonly employ Lagrangian description for the dispersed phase and Eulerian formulation for the carrier phase. Depending on the volumetric loading of the dispersed phase two regimes are identified: dilute ($d_p << l$) and dense ($d_p \approx l$), where d_p is the particle diameter, and l the inter-particle distance. Furthermore, the grid resolution (Δ) used for solution of the carrier phase could be such that the particles are *subgrid* ($d_p << \Delta$) or *resolved* ($\Delta < d_p$) (cf. figure 1). Clearly, different numerical approaches are necessary to simulate various regimes of the flow. In addition, these regimes may occur in the same simulation, e.g. DNS or LES of wall-bounded turbulent flows with moderate particle loadings. Near the wall, the grid resolution in the wall-normal direction is extremely fine ($d_p > \Delta$) to capture the small scales of turbulence, and the particles move slowly thus increasing their residence time and number density near the wall and decreasing the inter-particle distance ($l \approx d_p$), whereas away from the wall the grid resolution is coarse and the inter-particle distance is large. A multi-level approach capable of addressing all regimes is needed.

Typical simulations involving millions of dispersed particles employ "point-particle" approach for dilute particle-loadings (Apte *et al.* 2003a; Apte *et al.* 2003b; Segura *et al.* 2004) where the forces on the dispersed phase are computed through model coefficients and the effect of particles on the carrier phase is represented by a force applied at the *centroid* of the particle. Although this approach has been shown to give good results for swirling, separated flows (Apte *et al.* 2003a), it fails to properly capture turbulence modulation in wall-bounded flows (Segura *et al.* 2004). If the volumetric loading is high or the particle size is greater than Kolmogorov scale, simple drag/lift laws for particle motion (used in the point-particle approach) do not capture the unsteady wake effects (Burton & Eaton 2003). Apte *et al.* (2003c) (henceforth CTR-ARB03) performed simulations of Poisuille flow with large spherical particles arranged in layers at the bottom of the channel. It was shown that the point-particle approach was unable to provide any lift to the particles in this shearing flow. Accounting for volumetric effects of the spherical particles was important to obtain lift and fluidization of the channel as observed in fully resolved DNS studies (Choi & Joseph 2001; Patankar *et al.* 2001). The formulation developed in Apte *et al.* (2003c) is applicable to dense as well as dilute regimes (here the effect of volume fraction will be negligible). However, it requires that the size of particles is *less* than the grid control volume.

If $d_p >> \Delta$, the particle-domain is completely resolved by the grid, and forces on the particle should be computed directly. A variety of approaches based on distributed Lagrange multipliers (DLM)/fictitious domain method (Glowinski *et al.* 1999; Patankar *et*

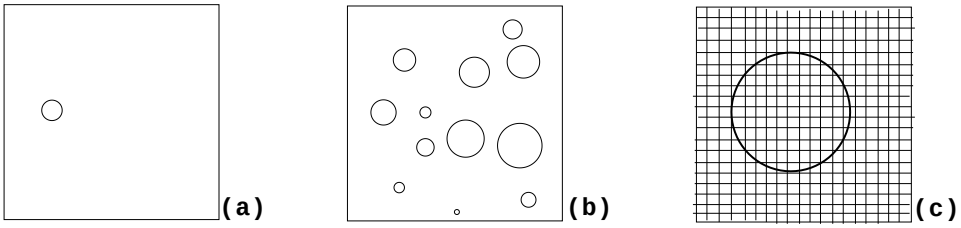

FIGURE 1. Regimes of particulate flows in Eulerian-Lagrangian simulations: a) dilute, b) dense, c) resolved

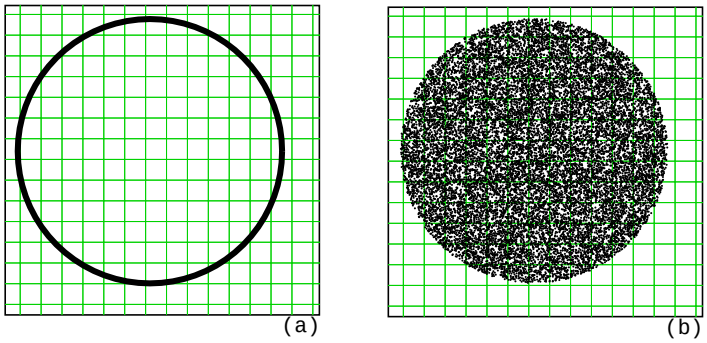

FIGURE 2. Use of material points to describe the particle domain: a) original sphere, b) sphere replaced by material points. Each material point has an associated volume (and thus a length scale) so that the total volume of all material points is equal to the original particle.

al. 2000), arbitrary Lagrangian-Eulerian (ALE) formulation (Hu *et al.* 2001), immersed boundary based direct forcing method (Kajishima & Takagi 2002), fast computation techniques based on DLM (Patankar 2001; Sharma & Patankar 2004) have been developed and applied to simulate these types of "resolved" particulate flows. For turbulent flow simulation of large number of particles, two approaches stand-out because of their easy implementation and fast computation: a) Kajishima & Takagi (2002) (henceforth KT02) and b) Patankar (2001). The formulation due to KT02 is explicit in terms of particle momentum coupling and is first-order accurate in time, however, has been shown to give good results for particle-turbulence interactions. Patankar (2001) developed a formulation which is implicit for particle momentum coupling. We attempt to extend the framework developed in CTR-ARB03 by investigating the resolved particle regime. The emphasis in this work is to develop a formulation for resolved particles, which can be directly used in conjunction with formulation described in CTR-ARB03, and thus can be used to compute all regimes encountered in particulate flows. We first investigate the formulation based on KT02 and propose modifications/improvements.

2. Governing equations

We assume that the particle size, d_p, is much larger than the grid spacing, Δ, as shown in figure (1c). We also assume that the particles are rigid. The grid used is kept fixed

and part of the control volumes occupy the particle domain. Following the notation used in CTR-ARB03, Θ_g and Θ_p represent the carrier and dispersed phase volume fractions, respectively, and $\Theta_p + \Theta_g = 1$. We define the composite velocity as,

$$\mathbf{u} = \Theta_g \mathbf{u}_g + (1 - \Theta_g)\, \mathbf{u}_p \tag{2.1}$$

where $\mathbf{u}_g$ is the fluid velocity vector, and $\mathbf{u}_p = \mathbf{U}_p + \omega_p \times \mathbf{r}$ the particle velocity. Here, $\mathbf{U}_p$ is the translational velocity and ω_p the angular velocity of rigid body rotation. Equation (2.1) represents the volume-weighted velocity at the interfacial control volumes. For no-slip and non-permeable interface, $\mathbf{u}_g = \mathbf{u}_p$, the Navier-Stokes equations for an incompressible fluid with rigid particles become:

$$\bigtriangledown \cdot \mathbf{u} = 0 \tag{2.2}$$

$$\rho_g(\frac{\partial \mathbf{u}}{\partial t} + \mathbf{u} \cdot \bigtriangledown \mathbf{u}) = - \bigtriangledown p + \mu_g \bigtriangledown \cdot \left(\bigtriangledown \mathbf{u} + (\bigtriangledown \mathbf{u})^T \right) + \rho_g \mathbf{g} + \mathbf{F} \tag{2.3}$$

where μ_g is the dynamic viscosity of fluid, $\mathbf{g}$ the gravitational force, and $\mathbf{F}$ the force acting to enforce the rigid-body motion within the particle domain. If the particle is moving with a velocity of $\mathbf{u}_p$, the fluid velocity inside the particle domain ($\Theta_p = 1$) should be $\mathbf{u} = \mathbf{u}_p$. The force imposing this condition is given as $\mathbf{F}_p = \rho_g(\mathbf{u}_p - \mathbf{u})/\Delta t$. In KT02, a first order approximation is used for the force in the region $0 < \Theta_p < 1$ to give,

$$\mathbf{F} = \rho_g \Theta_p \frac{\mathbf{u}_p - \mathbf{u}}{\Delta t} \tag{2.4}$$

This force is applied to the centroid of the grid control volumes. In this work, we present a better representation of the force to impose rigid body motion in the particle domain as shown below.

2.1. *Volume fraction and interphase force*

In order to compute the volume fraction (Θ_p) we replace each particle by N_m "material points" distributed over the entire particle domain as shown in figure 2. Each material point has an associated volume such that the total volume of the material points is equal to the particle volume. The centroid of a material point cannot be inside the volume of another. The volume fraction is easily obtained as

$$\Theta_p\,(\mathbf{x}) = \sum_{k=1}^{N_m} V_k \mathcal{G}_\sigma\,(\mathbf{x} - \mathbf{x}_k) \tag{2.5}$$

where the summation is over all material points N_m. Here $\mathbf{x}_k$ is the particle location, $\mathbf{x}$ the centroid of a control volume, and V_k the volume of each material point. The function $\mathcal{G}_\sigma$ is the interpolation operator given as

$$\mathcal{G}_\sigma(\mathbf{x}_p) = \frac{1}{\left(\sigma\sqrt{2\pi}\right)^3} exp\left[-\frac{\sum_{i=1}^{3} (x_i - x_{p,i})^2}{2\sigma^2} \right]. \tag{2.6}$$

The Gaussian interpolation operator is normalized to satisfy $\int_V \mathcal{G}_\sigma \left(\S - \S_\| \right) dV = 1$, where V is the grid control volume and the filter-width (σ) is proportional to the grid size. This enforces mass (or volume) conservation over the material points. It should be noted that, the particle surface is diffused by this procedure over a length-scale of the order of the grid spacing (Δ), and its effect on the flow is reduced with increased grid resolution. We believe that for the purpose of capturing unsteady wake effects in turbulent flows with many particles, this approximation is sufficient and is verified later. In KT02,

volume fraction is computed by approximating the sphere by a polygon enclosing the sphere and obtained by drawing tangents to the spherical surface in each control volume. In turn, the effective total volume of the sphere is increased. Similar, error is introduced at the particle interface.

The force acting on the fluid phase is given as

$$\mathbf{F}\left(\mathbf{x}\right) = \sum_{k=1}^{N_m} V_k \rho_g \mathcal{G}_\sigma \left(\frac{\mathbf{u}_{p,k} - \mathbf{u}}{\Delta t} \right). \tag{2.7}$$

This interpolation procedure gives a smoother force field near the particle surface. The main advantages of using Gaussian interpolation and material points are: a) the interphase force and volume fractions can be readily evaluated for *arbitrary* shaped particle, b) the material points move as a rigid body, thus they do not change their positions relative to each other and recomputing volume fraction field does not require any expensive computation of finding the intersections of particle surface with grid nodes, and c) same interpolation scheme was used to compute force and volume fraction in simulations of dilute and dense particulate flow (CTR-ARB03).

3. Numerical Algorithm

The above system of equations is solved using the fractional step algorithm on unstructured grids as described by Mahesh *et al.* (2004). The steps are summarized below:

- **Step 1:** Compute the volume fraction field using equation 2.5.
- **Step 2:** Advance the fluid momentum equations without the interphase force, $\mathbf{F}$.

$$\frac{\rho_g u_i^* - \rho_g u_i^n}{\Delta t} + \frac{1}{2V} \sum_{\text{facesofcv}} \left[u_{i,f}^n + u_{i,f}^* \right] g_N^{n+1/2} A_f = \frac{1}{2V} \sum_{\text{facesofcv}} \mu_f \left(\frac{\partial u_{i,f}^*}{\partial x_j} + \frac{\partial u_{i,f}^n}{\partial x_j} \right) A_f \tag{3.1}$$

where f represents the face values, N the face-normal component, $g_N = \rho_g u_N$, and A_f is the face area.

- **Step 3:** Compute the force on material points:

$$\mathbf{F}_{p|\mathbf{x}_{p,k}} = \rho_g \left(\frac{\mathbf{u}_p^n - \mathbf{u}_{\mathbf{x}_{p,k}}^*}{\Delta t} \right) \tag{3.2}$$

where $\mathbf{u}^*$ is interpolated to the material point k of a particle.

- **Step 4:** Project force from material points onto the grid control volume using equation 2.7.
- **Step 5:** Correct the velocity field within the particle domain by imposing the force:

$$\rho_g \widehat{u}_i = \rho_g u_i^* + F_i \Delta t \tag{3.3}$$

- **Step 6:** Interpolate the velocity fields to the faces of the control volumes and solve the Poisson equation for pressure:

$$\bigtriangledown^2 \left(p \Delta t \right) = \frac{1}{V} \sum_{\text{facesofcv}} \rho_g \widehat{u_{i,f}} A_f \tag{3.4}$$

- **Step 7:** Reconstruct the pressure gradient, compute new face-based velocities, and update the cv-velocities using the least-squares interpolation used by Mahesh *et al.*

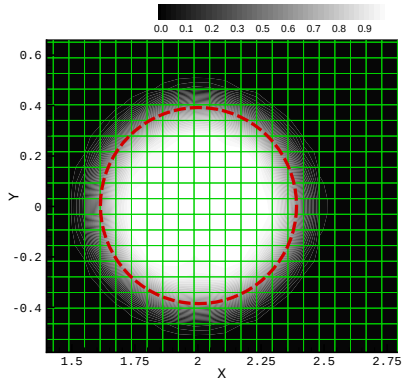

FIGURE 3. Distribution of particle volume fraction field for a single sphere on uniform grid.

(2004):

$$\frac{\rho_g \left(u_i^{n+1} - \widehat{u}_i\right)}{\Delta t} = -\frac{\partial p}{\partial x_i} \tag{3.5}$$

- **Step 8:** Advance the particle velocity. The total force $\mathbf{F}$ acting on a particle is simply the summation $(\sum_{k=1}^{N_m} \mathbf{F}_p V_k)$ over all material points. Similarly, torque acting at each material point is given as, $\mathbf{T} = \sum_{k=1}^{N_m} (\mathbf{F}_p \times \mathbf{r}_{p,k}) V_k$, where $\mathbf{r}_{p,k}$ is the position vector of the each material point from the particle centroid:

$$m_p u_{p,i}^{n+1} = m_p u_{p,i}^n - \Delta t F_{p,i} + m_p g_i \tag{3.6}$$

$$I_p \omega_{p,i}^{n+1} = I_p \omega_{p,i}^n - \Delta t T_{p,i} \tag{3.7}$$

where m_p is the particle mass, I_p the moment of inertia, $u_{p,i}$ and $\omega_{p,i}$ the particle translational and angular velocities, respectively.

- **Step: 9** Advance the particle positions:

$$x_{p,i}^{n+1} = x_{p,i}^n + \frac{\Delta t}{2}\left(u_{p,i}^n + u_{p,i}^{n+1}\right) \tag{3.8}$$

The above formulation is similar to the one given in KT02 with some key differences: a) we compute the volume fraction and force acting on the particle as described in section 2.1. The forces acting at the material points within each particle are interpolated onto the Eulerian grid by a Gaussian interpolation operator to give smoother representation of the field (see equation 2.7), b) the rigid body motion to the fluid velocity is imposed before the incompressibility constraint (KT02 impose Step 3 after solving the Poisson equation). This way the flowfield over the computational domain satisfies the incompressibility constraint exactly, however, rigid-body motion within the particle domain is imposed only approximately, and c) the volume fraction computation is applicable to any arbitrary shaped particle.

4. Results

We investigate the above formulation by simulating flow over a *fixed* sphere at different Reynolds numbers and compare the predicted drag coefficients with experimental data. The computational domain is a rectangular box of dimension $8 \times 8 \times 8\ m$ and the sphere

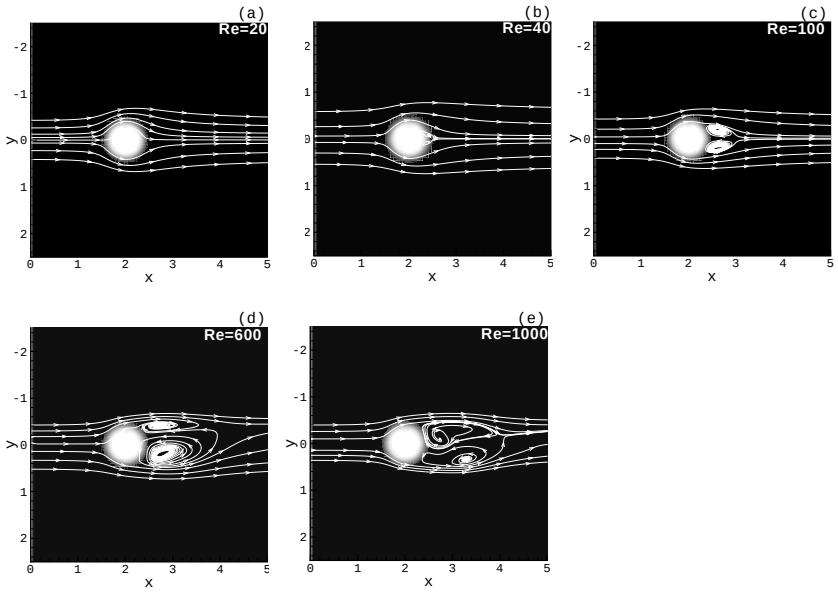

FIGURE 4. Instantaneous streamlines for flow over a stationary sphere at different Reynolds numbers: a) Re=20, b) Re=40, c) Re=100, d) Re=600, and e) Re=1000. Also shown are the contours of particle volume fraction, Θ_p.

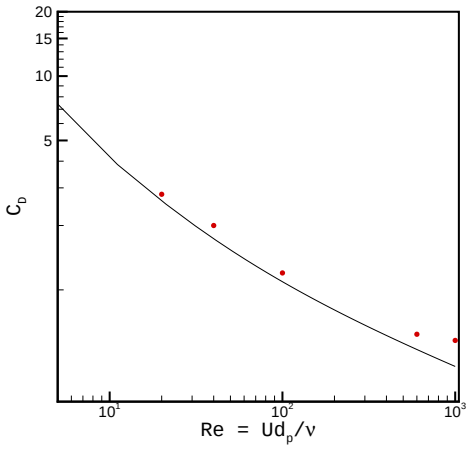

FIGURE 5. Comparison of drag coefficient for flow over a fixed sphere: ——— non-linear drag law Clift *et al.* (1978), ∘ present.

diameter is $d_p = 0.8\ m$ with its centroid located at [2,0,0]. The computational grid consists of uniform, cubic elements of size $128 \times 128 \times 128$ giving approximately 11 grid cells in each direction over the particle domain ($d_p/\Delta = 11$). We impose uniform fluid velocity at the inlet, convective boundary condition at the exit and periodic conditions in the y and z directions.

Figure 3 shows the distribution of particle volume fraction together with the sphere

surface. It shows that Θ_p is smoothed over the particle boundary and covers a domain larger than the actual particle size by one grid cell. Increased resolution reduces this spread. We used 5000 material points uniformly distributed over the particle domain to compute the volume fraction field, however, out tests indicate that fewer material points are enough to provide the volume fraction field. Flow over the fixed sphere was simulated at six different Reynolds numbers ($Re = \rho_g d_p U/\mu_g$) over a range of $20-1000$. The particle was fixed by specifying $\mathbf{u}_p^n = 0$ in Step 3 of the formulation and the equations for particle motion are not necessary (Steps 8 and 9). Figure 4 shows the instantaneous streamlines at different Reynolds numbers. The flowfield is symmetric for low Reynolds numbers and unsteady vortex shedding is observed for higher Reynolds numbers ($>$ 200). Figure 5 compares the drag coefficients at different Reynolds numbers with the experimental curve fit, $C_d = \frac{24}{Re}\left(1 + 0.15Re^{0.687}\right)$ obtained from Clift *et al.* (1978). The drag coefficient obtained from present simulations is within 5-15% of the experimental data with maximum error obtained at $Re = 1000$. Overprediction of drag is due to the spreading of the particle domain as shown in figure 3. Similar results have been reported in KT02.

5. Discussion

A formulation for simulating *resolved* particles ($d_p >> \Delta$) is developed based on the work by Kajishima & Takagi (2002). Regions where particles are *subgrid* ($d_p < \Delta$), can be captured by using the formulation developed in CTR-ARB03. Thus, different regimes encountered in particle-laden flows in the same simulation can be handled. The resolved particle domain is replaced by material points which do not move relative to each other. Forces acting at the material points are interpolated to the Eulerian grid using a Gaussian interpolation operator. It was observed that the present formulation predicts the drag on a fixed sphere correctly and captures unsteady wake effects with grid resolution (d_p/Δ) of the order 10.

Based on this work, a simple extension to the standard point-particle approach can be devised. In LES or DNS of particle-laden channel flows the typical grid resolution in the wall-normal direction is $3-10\ d_p$ (see Segura *et al.* 2004). With point-particle approach, all of the interphase force is applied at the particle centroid. In regions with high grid resolution, one may use material points to represent the particles. This will distribute the interphase force over a length scale comparable to the particle diameter. In addition, flow modification due to wake-effects can be captured by material points with sufficient grid resolution.

The formulation presented here is explicit for momentum coupling and first order accurate in time. The temporal accuracy can be increased by performing iterations per time-step over the fluid and particle equations, however, is costly. Explicit coupling is undesirable as it may give rise to instabilities and unphysical oscillations in drag/lift forces. As shown by Patankar 2001 (also Sharma & Patankar 2004) an implicit momentum coupling with little increase in computational time is possible and should be used. Our future effort will focus on combining the present approach with their implicit algorithm to develop a robust and accurate numerical scheme for simulations of particle/turbulence interactions in complex flows.

6. Acknowledgement

Discussions and communications with Prof. Neelesh Patankar (Northwestern University) are grately appreciated.

REFERENCES

APTE, S. V., MAHESH, K., MOIN, P., & OEFELEIN, J.C. 2003a Large-eddy simulation of swirling particle-laden flows in a coaxial-jet combustor. *Int. J. Mult. Flow* **29**, 1311-1331.

APTE, S. V., GOROKHOVSKI, M. & MOIN, P. 2003b LES of atomizing spray with stochastic modeling of secondary breakup *Int. J. Mult. Flow* **29**, 1503-1522.

APTE, S. V., MAHESH, K., & LUNDGREN, T. 2003c

BURTON, T. M. & EATON, J. K. 2003 Fully resolved simulations of particle-turbulence interaction. *Rep. No. TSD–151*, Dept. of Mech. Engr., Stanford University.

CLIFT, R., GRACE, J.R., & WEBER, M.E. 1978 Bubbles, drops, and particles. Academic Press, New York.

CHOI, H.G., & JOSEPH, D.D. 2001 Fluidization by lift of 300 circular particles in plane Poisuille flow by direct numerical simulation. *J. Fluid. Mech.* **438**, 101–128.

GLOWINSKI, R., PAN, T.-W., HESLA, T. I., & JOSEPH, D. D. 1999 A distributed Lagrange multiplier/fictitious domain method for particulate flows. *Int. J. Multiphase Flow* **25**, 755–794.

HU, H. H., PATANKAR, N. A., & ZHU, M. Y., 2001. Direct numerical simulations of fluid-solid systems using Arbitrary Lagrangian-Eulerian technique. *J. Comp. Phys.* **169**, 427–462.

KAJISHIMA, T., & TAKIGUCHI, S. 2002 Interaction between particle clusters and particle-induced turbulence. *J. Heat Fluid Flow*, **23**, pp. 639–646.

MAHESH, K., CONSTANTINESCU, G., & MOIN, P. 2004 A New Time-accurate Finite-Volume Fractional-Step Algorithm for Prediction of Turbulent Flows on Unstructured Hybrid Meshes. *J. Comp. Phy.* **197**, 215–240.

MOIN, P, & APTE, S.V. 2005 LES of multiphase reacting flows in complex combustors *AIAA J.* to appear.

PATANKAR, N. A. 2001b Lagrangian numerical simulation of particulate flows. *Int. J. Multi. Flow* **27**, 1685-1706.

PATANKAR, N. A., SINGH, P., JOSEPH, D. D., GLOWINSKI, R., & PAN, T.-W. 2000. A new formulation of the distributed Lagrange multiplier/fictitious domain method for particulate flows. *Phy. Fluids*, **9**, 3786–3807.

PATANKAR, N. A., HUANG, P. Y., KO, T., & JOSEPH, D. D. 2001 Lift-off of a single particle in Newtonian and viscoelastic fluids by direct numerical simulation, J. FLUID MECH. **438**, 67–100.

SHARMA, N., & PATANKAR, N. A. 2004 A fast computation technique for the direct numerical simulation of rigid particulate flows. *J. Comp. Phy.*, in press.

SEGURA, J. C., EATON, J. K. & OEFELEIN, J. C. 2004 Predictive capabilities of particle-laden LES. *Rep. No. TSD–156*, Dept. of Mech. Engng., Stanford University.

A presumed pdf model for droplet evaporation/condensation in complex flows

By S. Apte AND S. Ghosal†

1. Motivation and objectives

In many multiphase flow problems, the condensed phase (liquid or solid) exists in the form of a cloud of droplets of heterogeneous size in an ambient gas undergoing time dependent (often turbulent) motion. One example is the problem of the formation and growth of ice crystals in the "contrails" of aircraft [Paoli *et al.* 2002 - henceforth cited as CTR-SP0]. Other examples include, atmospheric aerosols (Binkowski & Shankar, 1995), rain drops in clouds (Shaw 2003), and, the fuel vapor from evaporating drops of hydrocarbon fuel in spray combustion engines (Moin & Apte 2005). In order to be specific, we shall assume here that the condensed phase is a liquid that undergoes evaporation.

The need for modeling the spray arises in both LES and DNS. In DNS, the size of a computational grid is typically within an order of magnitude of the Kolmogorov scale. However, if particle sizes and the average distance between particles is much smaller than this, then clearly some kind of a statistical description of the particles need to be adopted so as not to increase the computational effort by many orders of magnitude. In LES the size of the computational grid is somewhere intermediate between the integral scale and the Kolmogorov scale. Here once again some statistical modeling is needed if particle sizes and the distance between them are much smaller than the LES grid.

In this report the statistical description based on a 'presumed pdf' (henceforth PPDF) outlined in CTR-SP02 is worked out in detail for a specific evaporation model and for a lognormal form of the presumed pdf. The predictions are checked against a full numerical simulation that does not involve any statistical modeling. The general formalism had been presented in Sec 4.1 of CTR-SP02 and need not be reported here. We will assume the results presented in that earlier report and also adopt the notation used there.

2. The Model

The simplest nontrivial model follows from assuming that the "presumed pdf" is a two parameter distribution depending on the first two moments m_1 and m_2 in addition to the droplet density $N_p = m_0$. Then the time evolution of N_p, m_1 and m_2 are described by equations (4.2) and (4.3) of CTR-SP02‡ with the series of moment equations truncated at $k = 2$. In order to obtain explicitly the source terms we need to specify (a) the analytical form of the presumed pdf and (b) the evaporation/condensation model.

2.1. *Evaporation Law*

We will assume that the fluid droplets are spherical and at a fixed temperature T_0. Further, the local thermal field around a droplet is described by spherically symmetric

† Northwestern University

‡ please note that (4.3) in CTR-SP02 has a typographic error, it should read $\frac{\partial m_k}{\partial t} + \nabla \cdot (m_k \mathbf{u}) = k \int_0^\infty r^{k-1} n_p \dot{r}\, dr$

solutions of $\nabla^2 T = 0$ with the far field temperature matched to $T(\mathbf{x}, t)$, the temperature at the location of the particle in the absence of the drop. Any cooling effect on the gas due to particle evaporation is neglected. The rate of inflow of heat to the droplet can then be easily calculated. If one assumes that this energy is expended in raising the temperature of the liquid to its boiling point and evaporating some of the liquid, then, the change of droplet radius is given by

$$\frac{dr}{dt} = -\frac{\Lambda(T - T_0)}{r} \tag{2.1}$$

where Λ is a constant determined by properties of the gas and the liquid:

$$\Lambda = \frac{k_g/\rho_\ell}{L + C_\ell(T_* - T_0)} \tag{2.2}$$

where k_g is the thermal diffusivity of the gas, L is the latent heat of vaporization, ρ_ℓ is the liquid density, C_ℓ is the liquid specific heat and T_* is the temperature at the boiling point.

2.2. *The Presumed PDF*

The form of the presumed pdf ϕ for the distribution of particle sizes will be assumed lognormal;

$$n_p = \phi(r; m_0, m_1, m_2) = \frac{N_p}{\sigma r\sqrt{2\pi}} \exp\left[-\frac{1}{2\sigma^2}\left(\ln(r/r_p)\right)^2\right] \tag{2.3}$$

where the parameters N_p, r_p and σ^2 are easily seen to be related to m_0, m_1 and m_2 through the relations

$$m_0 = N_p; \qquad m_1 = N_p r_p \exp(\sigma^2/2); \qquad m_2 = N_p r_p^2 \exp(2\sigma^2). \tag{2.4}$$

The mean particle radius $\langle r\rangle$ and the variance of the particle radius $\langle \Delta r^2\rangle$ may be easily shown to be related to r_p and σ by the relations

$$\sigma^2 = \ln\left[1 + \frac{\langle \Delta r^2\rangle}{\langle r\rangle^2}\right]; \qquad r_p^2 = \frac{\langle r\rangle^4}{\langle r\rangle^2 + \langle \Delta r^2\rangle}. \tag{2.5}$$

If $\langle \Delta r^2\rangle \ll \langle r\rangle^2$ we get $r_p \approx \langle r\rangle$ and $\sigma^2 \approx \langle \Delta r^2\rangle / r_p^2 = \langle \Delta r^2\rangle / \langle r\rangle^2$; the variance normalized by the square of the mean.

2.3. *Time Evolution of Distribution Parameters*

The right hand sides of equations (4.3) in CTR-SP02 may be explicitly evaluated using the presumed pdf (2.3) and the evaporation law (2.1). Further, using (2.4) the equations can be transformed into a form that uses N_p, r_p and σ^2 in place of m_0, m_1 and m_2 as dependent variables:

$$\frac{D}{Dt}\left(\frac{N_p}{\rho}\right) = 0, \qquad \frac{Dr_p}{Dt} = \mathcal{S}_r, \qquad \frac{D\sigma^2}{Dt} = \mathcal{S}_\sigma, \tag{2.6}$$

where the source terms $\mathcal{S}_r$ and $\mathcal{S}_\sigma$ are given by

$$\mathcal{S}_r = -\frac{\Lambda(T - T_0)}{r_p}\left\{2 - \exp(-2\sigma^2)\right\}, \qquad \mathcal{S}_\sigma = \frac{2\Lambda(T - T_0)}{r_p^2}\left\{1 - \exp(-2\sigma^2)\right\}. \tag{2.7}$$

Using the continuity equation, the equations (2.6) can also be expressed in conservative form, which may be more suited for numerical methods such as finite volume approaches. Equations (2.6) determine the value of the parameters N_p, r_p and σ^2 at any time.

Knowing these three parameters at any given point in space, "P", the PDF of drop sizes in the neighborhood of "P" is determined by (2.3). Thus, any desired quantity related to the interaction between the gas phase variables (resolved) and condensed phase (unresolved) may be calculated. For example, if droplet evaporation is a source of combustible vapors, then we may write

$$\rho \frac{DY_F}{Dt} = -\omega + \nabla \cdot (k_F \nabla Y_F) + S \tag{2.8}$$

where Y_F is the vapor mass fraction, ω is the rate of removal of vapor mass due to chemical reaction, k_F is a diffusion coefficient and the source term due to liquid evaporation from the droplets is

$$S = -\int_0^\infty n_p \dot{r}(4\pi r^2)\rho_\ell \, dr = 4\pi\Lambda\rho_\ell(T - T_0)N_p r_p \exp(\sigma^2/2). \tag{2.9}$$

To obtain the expression on the right hand side, $\dot{r}$ and n_p was substituted from (2.1) and (2.3) the integral was evaluated in order to sum the contributions from all droplet sizes. Equations (2.6) and (2.8) may be solved together to account for the gas as well as the condensed phase without the need for following the motion of each particle in the condensed phase.

2.4. *Physical Interpretation*

The first of equations (2.6) simply means that the total number of droplets in a material volume of fluid does not change. The density in the denominator takes account of the fact that the volume of the material element could vary if the flow is compressible. At first sight this conclusion may seem to be in conflict with the fact that droplets may evaporate completely! However, this paradox is only superficial since in the language of PDFs droplets never evaporate "completely", rather, the distribution function n_p shifts continuously towards smaller and smaller particle sizes ($r_p \to 0$) so that the total mass in the condensed phase goes arbitrarily close to zero. Thus, the right hand side of (2.9) would be "machine zero" after sufficient time has evolved; whether one describes this situation by saying "all droplets have evaporated" or the "distribution function has become extremely localized around $r = 0$" is of course just a matter of linguistics.

The interpretation of the second of equations (2.6) is clearest if one considers the initial PDF of drop sizes to be narrowly peaked around the mean size: $\langle \Delta r^2 \rangle \ll \langle r \rangle^2$. In this case, as pointed out before, $r_p \approx \langle r \rangle$ and $\sigma^2 \approx \langle \Delta r^2 \rangle / r_p^2 = \langle \Delta r^2 \rangle / \langle r \rangle^2 \ll 1$. Therefore, the source terms of the equations for r_p and σ^2 in (2.6) may be simplified:

$$\frac{Dr_p}{Dt} = \mathcal{S}_r \approx -\frac{\Lambda(T - T_0)}{r_p}(1 + 2\sigma^2), \qquad \frac{D\sigma^2}{Dt} = \mathcal{S}_\sigma \approx \frac{4\Lambda(T - T_0)}{r_p^2}\sigma^2. \tag{2.10}$$

Thus, if $\sigma = 0$ initially, it remains zero and the mean droplet size remains exactly equal to the size of any droplet in the monodisperse cluster since the evolution equation for r_p is the same as (2.1) for an individual drop. However, if σ^2 is small but nonzero, these equations predict (a) the mean of the distribution shifts to the left *faster* than the radius of an individual droplet of radius r_p (b) the variance of the distribution increases rapidly. The physical reason behind these predictions may be found in the evaporation law (2.1) according to which small droplets get smaller *faster* than large ones. Indeed, if one considers three droplets of radii $r_1 < r_2 < r_3$ then since r_1 decreases faster than r_3, $r_1 - r_3$ would get larger with time, that is the spread of the distribution increases. Also, if initially r_2 was the mean of r_1 and r_3, at later times the mean would be less than r_2,

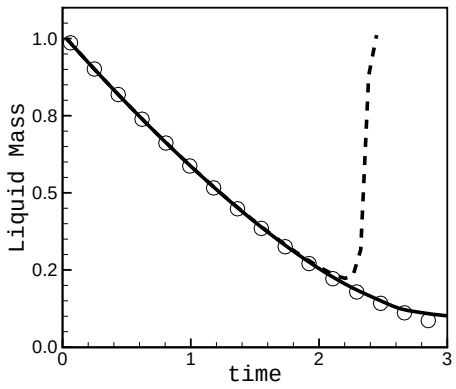

FIGURE 1. Temporal evolution of total mass of droplets in a Taylor-vortex flow for $\sigma = 0.1$: $\circ$ DNS, – – – model with $\mathcal{S}_\sigma$ given by equation (2.6), ——— model with $\mathcal{S}_\sigma$ given by equation (3.5).

that is the average of the distribution decreases faster than an average sized drop. This is indeed what equations (2.10) predicts.

3. A Problem with the model and its resolution

Figure 1 shows the change of total mass in the liquid phase as predicted by equations (2.6) in a swirling 'Taylor-vortex' flow with an inhomogeneous initial temperature distribution. The details of the simulation are discussed in the following section. Here it suffices to point out that the predicted liquid mass is in close agreement with the full DNS of the system until very late times when apparently some kind of instability develops causing the liquid mass to *increase* rapidly - a completely unphysical prediction - since each individual droplet is evaporating!

3.1. *Physical mechanism for anomalous growth*

The instability is not a numerical one but its source is in the equations (2.6) themselves. To see this, first note that the total volume of liquid in the condensed phase in the entire domain (Ω) at a given instant may be expressed as

$$V(t) = \int_\Omega dV \int_0^\infty n_p \frac{4}{3}\pi r^3 \, dr = \frac{4}{3}\pi \int_\Omega dV \; N_p r_p^3 \exp\left(\frac{9}{2}\sigma^2\right) \tag{3.1}$$

where the second equality follows on substituting the expression (2.3) for n_p and performing the radial integration. As a particular case, suppose that system is homogeneous (N_p, r_p, σ are position independent). Further suppose there is no flow so that $D/Dt = \partial/\partial t$ in (2.6). In this case it is easy to show that

$$\frac{1}{V}\frac{dV}{dt} = \frac{3\Lambda(T - T_0)}{r_p^2}[1 - 2\exp(-2\sigma^2)]. \tag{3.2}$$

When $\sigma \ll 1$ the right hand side is negative (assuming $T > T_0$ everywhere) but as σ becomes large the sign of the term in [ ] changes and the volume of the condensed phase

starts to increase! This is the source of the observed late time instability apparent in figure 1.

3.2. *Resolution of the difficulty*

First note that $V(t)$ is related to the third moment $m_3(\mathbf{x},t)$ of the distribution:

$$V(t) = \frac{4}{3}\pi \int_\Omega dV\ m_3(\mathbf{x},t). \tag{3.3}$$

Now according to equation (4.3) of CTR-SP02 m_3 actually has an evolution equation:

$$\frac{\partial m_3}{\partial t} + \nabla\cdot(m_3\mathbf{u}) = 3\int_0^\infty r^2 n_p \dot{r}\ dr \tag{3.4}$$

with a source term that is always negative as long as $\dot{r} < 0$. The problem with our model is that we *discarded* this moment equation (together with all higher moments) in order to achieve a "closure". Thus, in the current model, the behavior of "m_3" is a derived quantity determined by the dynamics of m_0, m_1, m_2 and the presumed PDF, and there is nothing in those lower order equations to ensure that V would decrease for evaporating droplets.

The nature of the difficulty also suggests a resolution. If one were to adopt a moment closure at the level of m_3 and assume that the presumed PDF $\phi = \phi(m_0, m_1, m_2, m_3)$, then the equation for m_3 would ensure that V does not increase. Actually we can achieve the same result within the lognormal formalism itself, if we notice that the lognormal form of the presumed PDF with three independent parameters requires that we retain *any three* of the equations of the moment hierarchy, *not necessarily the first three*! We will therefore modify our closure assumption by enforcing the moment equations for m_0, m_1 and m_3 and dropping all the rest. This is no more or no less justified than our original closure but it does have the advantage that the physically important moment m_3 is calculated directly from its evolution equation.

With this modification, the form of our basic model (2.6) remains unaltered, except for the formula for the source term which now becomes:

$$\mathcal{S}_\sigma = \frac{2}{3}\frac{\Lambda(T-T_0)}{r_p^2}\left\{2 - \exp(-2\sigma^2) - \exp(-4\sigma^2)\right\}. \tag{3.5}$$

If the calculation leading up to (3.2) is repeated with the modified source term, it is readily verified that this time $\dot{V} < 0$. In fact one need not assume statistical homogeneity or that $\mathbf{u} = 0$, in general,

$$\frac{dV}{dt} = -4\pi \int_\Omega r_p N_p \Lambda(T-T_0)\exp(\sigma^2/2)\ d\mathbf{x} \tag{3.6}$$

which implies that $\dot{V} < 0$ as long as $T > T_0$ everywhere. Thus, stability is assured and indeed when the simulation is repeated with the new source term (3.5), the liquid mass decreases monotonically and in good agreement with experimental data as shown in figure 1.

Another interesting property of equation (3.5) is that when $\sigma^2 \ll 1$, both the right hand side of (3.5) and the second of equations (2.10) evaluate to

$$\mathcal{S}_\sigma \approx \frac{4\Lambda(T-T_0)}{r_p^2}\sigma^2. \tag{3.7}$$

Thus, at low dispersions, enforcing the equation for m_3 automatically enforces the equation for m_2, until the dispersion gets very large.

4. Numerical Experiments

The PPDF model (2.6) with the modified source term (3.5) is used to simulate a cloud of evaporating droplets in the presence of a temperature gradient in a two-dimensional decaying Taylor vortex flow. Preliminary results are also presented for the case of forced isotropic turbulence in a box. The flows considered here are periodic and solved in a periodic box of dimensionless length 2π. The reference length and velocity scales used in the computation are 1 m and 1 m/s, respectively, giving a reference time-scale of 1 s. Results are compared with direct numerical simulations using Lagrangain tracking of all droplets.

4.1. *Decaying Taylor Vortex*

The initial conditions for the velocity components are:

$$u(x, y, 0) = -\pi \cos x \sin y \tag{4.1}$$

$$v(x, y, 0) = \pi \sin x \cos y \tag{4.2}$$

and initial temperature distribution is

$$T = T_{min} + \Delta T \, |1 - x/\pi| \tag{4.3}$$

$$\Delta T = T_{max} - T_{min} \tag{4.4}$$

We use isopropyl alcohol as the liquid phase, and we take $T_{min} = 355\ K$ (the boiling point of isopropyl alcohol) and $\Delta T = 2250\ K$, representative of the typical temperatures achieved in turbulent combustion. Figure 2 shows the initial streamlines and the temperature field. The Reynolds number is $Re = 50,000$ and we use 32×32 grid points for this two-dimensional calculation. To test the model's predictions we performed a DNS by tracking 122880 droplets which were initially randomly distributed over the computational domain. Approximately 120 droplets were obtained per control volume providing statistically meaningful results. For DNS, the initial droplet sizes in each control volume were sampled from the lognormal distribution (2.3) with a mean droplet radius of 250 microns. Two cases with different variances ($\sigma = 0$ and 0.1) were investigated. Using the properties of isopropyl alcohol (Reid *et al.* 1987) the droplet life-time of a $r_0 = 250$ micron size drop can be estimated as,

$$t_e = \frac{r_0^2}{2\Lambda \, (T_{max} - T_0)} \approx 0.23\, s \tag{4.5}$$

This is shorter than an eddy turn over time ($\sim$ 1 s) and much shorter than the viscous decay time of the eddies ($\sim 157,000$ sec), so that for the duration of the computation, the vortices are essentially stationary in time.

4.1.1. *Case 1:* $\sigma = 0$

For this case, at the initial time, the computational domain was seeded with droplets of a uniform size (250 μm). Figure 3 shows the time evolution of the droplet radius averaged over the entire domain, the total liquid mass in the droplets, and the fuel vapor mass fraction obtained from DNS and the model. All of these global averages are seen to be predicted very accurately by the model.

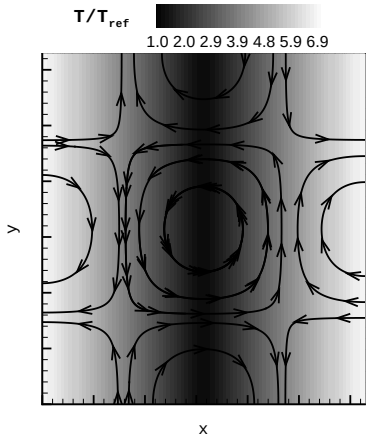

FIGURE 2. Initial streamlines and temperature distribution in a 2D Taylor-vortex flow: $T_{ref} = T_{min}$.

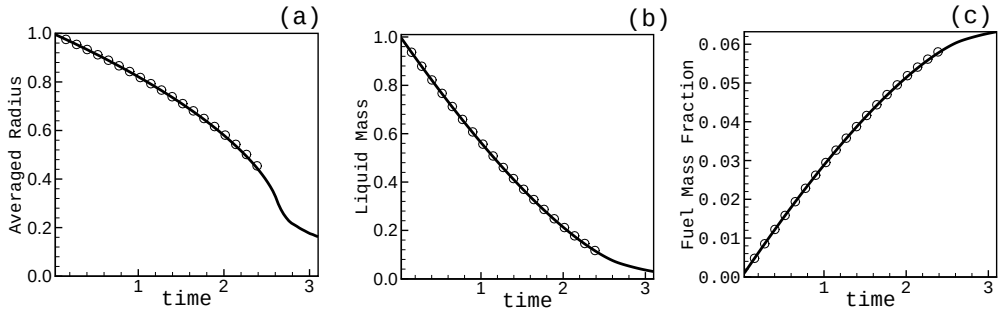

FIGURE 3. Temporal evolution of global quantities for $\sigma = 0$: ∘ DNS, ——— PPDF, (a) Volume average of mean droplet radius (b) total liquid mass (both normalized by respective initial values) and (c) fuel mass fraction, Y_F.

4.1.2. *Case 2:* $\sigma = 0.1$

Keeping the flow conditions the same as in case 1, we introduce a small variance ($\sigma = 0.1$) in the initial droplet size distribution. For DNS, droplets in each control volume were sampled from a lognormal distribution giving a scatter of ± 50 μm around the mean droplet radius of 250 μm. Figure 4 shows the instantaneous distribution of fuel mass fraction obtained from DNS and the model at a later time. The time-evolution of the total liquid mass and fuel mass fraction in the computational domain (figure 5) also show good agreement with the DNS. However, at large times, the mean droplet radius obtained using PPDF is lower than that of DNS (figure 5). This could be an artifact of our sampling procedure, since in DNS particles that have become too small are discarded so they are no longer counted in the calculation of the mean. The loss of these small values could upwardly bias the mean.

Next we calculate the average droplet radius within each control volume. Figure 6 shows the scatter plot of the mean droplet radius at each control volume obtained from the DNS and the model. At $t = 0$, the mean droplet radii in all control volumes obtained

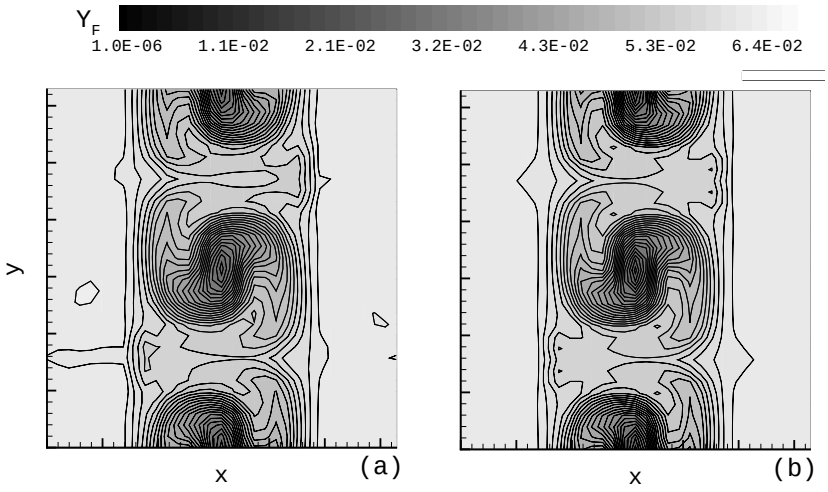

FIGURE 4. Contour plot of fuel mass fraction Y_F at $t = 2.5$ for $\sigma = 0.1$: (a) DNS, (b) PPDF

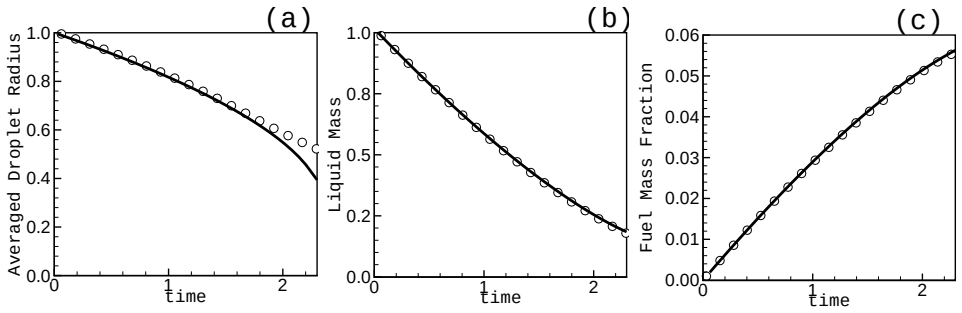

FIGURE 5. Temporal evolution of global quantities for $\sigma = 0.1$: ∘ DNS, —— PPDF, (a) Volume average of droplet radius, (b) total liquid mass (both normalized by respective initial values) and (c) mean fuel mass fraction in volume, $\langle Y_F \rangle$.

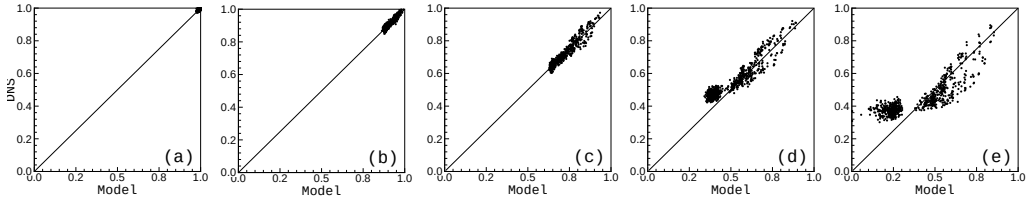

FIGURE 6. Correlation analysis between the DNS and PPDF for droplet radius averaged over a control volume. Scatter plot shows mean radius at each grid cell: a) $t = 0$, b) $t = 0.75$, c) $t = 1.5$, d) $t = 2$, e) $t = 2.5$

from both DNS and model are the same. The small scatter is due to discrete sampling of droplet sizes in DNS. With time, the mean droplet size in certain control volumes decreases more rapidly due to evaporation and the scatter plot shifts to the left towards zero radius, but the predictions from the two simulations are closely correlated. At large

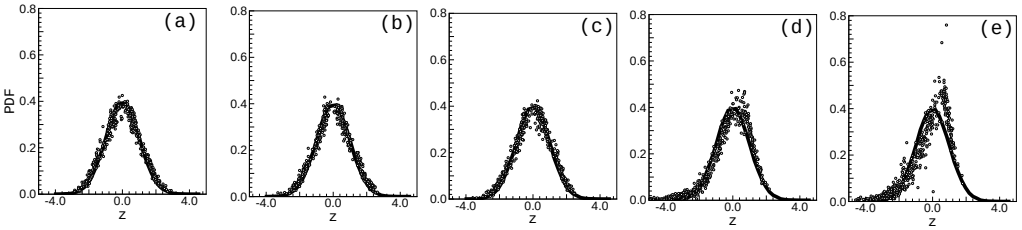

FIGURE 7. Test of the validity of the lognormal distribution of droplet radius; plot of $z = (\ln r - \ln r_p)/\sigma$ (x-axis) against PDF (y-axis), ∘ PPDF: at (a) $t = 0$ (b) $t = 0.75$ (c) $t = 1.5$ (d) $t = 2$ (e) $t = 2.5$, ——— Standard normal distribution (zero mean & unit variance).

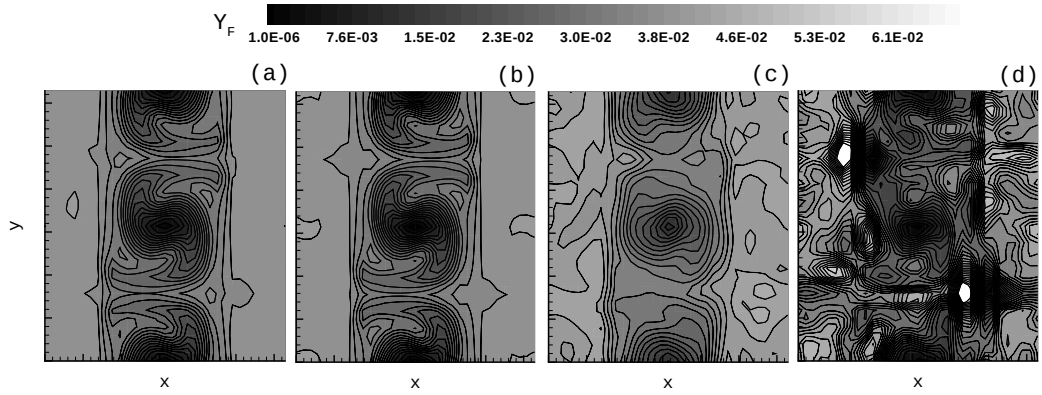

FIGURE 8. Instantaneous profiles of fuel mass fraction. Comparison of PPDF predictions with standard Lagrangian Parcel Tracking (LPT) at $t = 2.4$: a) DNS, b) PPDF, c) LPT1; 6144 parcels, d) LPT2; 256 parcels.

times, the mean droplet radius from DNS is generally higher than that obtained from the model. This is partly because of the fact that droplets smaller than a threshold were removed in the DNS resulting in higher mean of the droplet radius. Local liquid mass, on the other hand, shows good correlation between the model and the DNS mainly because droplets of size less than the threshold contribute little to the mass in a control volume.

Figure 7 shows the pdf of the variable $z = (\ln r - \ln r_p)/\sigma$ which should follow the unit normal distribution if r is distributed lognormally. The data was obtained from the DNS at times corresponding to those in figure 6. From the DNS, we collect all droplets in a control volume, and use the data to determine r_p and σ for that control volume. Then the variable z is calculated for each particle, the results binned and plotted. The same procedure is repeated for each control volume. As shown in figure 7, initially the pdf collapses on top of the standard normal distribution. With time, there are some small deviations but the distribution does remain close to lognormal until most of the liquid has evaporated.

4.1.3. *PPDF or Lagrangian Parcels Tracking (LPT)?*

In simulations of practical gas-turbine combustor, the spray is represented by computational particles or 'parcels' each representing a fixed number of droplets. Each parcel carries with it properties: velocity, mass, radius, temperature etc. equal to that of some

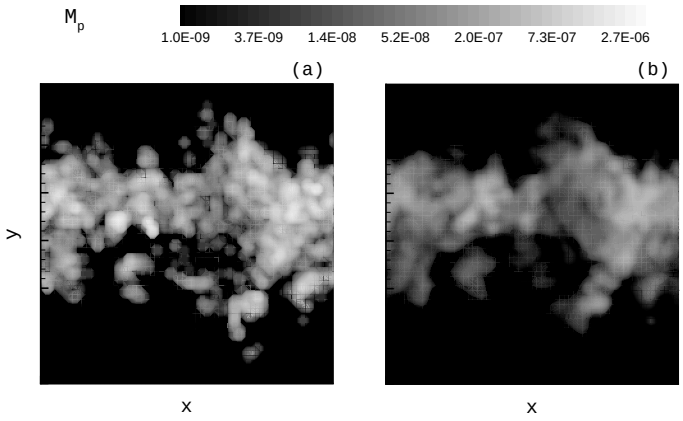

FIGURE 9. Instantaneous profiles of liquid mass dispersed in isotropic turbulence: a) DNS, b) PPDF

'average' particle in the cloud that it represents (Apte *et al.* 2003a, Apte *et al.* 2003b). Replacing a large clump of particles by a single 'proxy' in this way reduces the computational cost to manageable levels. The accuracy of the algorithm as well as its computational cost is inversely correlated to the number of particles that a parcel represents. In order to compare the PPDF model with the LPT approach in regards to accuracy as well as computational cost, two separate simulations were run with the LPT method using the conditions corresponding to case 2 of the Taylor-vortex flow. We will call these cases (a) LPT1: 3072 parcels each representing 40 droplets and (b) LPT2: 128 parcels each representing 960 droplets. They both correspond to the same number (122, 880) of droplets present in the DNS. These numbers are typical of a realistic spray simulation in complex combustors (Moin & Apte 2005). Figure 8 shows the instantaneous distributions of fuel vapor mass fraction obtained from DNS, PPDF, LPT1, and LPT2. It is seen that the accuracy in predicting the evolution of fuel mass fraction degrades considerably as one goes from 40 to 960 drops per parcel. Table 4.1.3 shows the comparison of CPU time per 100 iterations on a single processor of Origin2000 for the four different approaches. It should be noted that the PPDF and LPT1 have comparable computational cost, with the PPDF approach actually producing somewhat better agreement with DNS at a cost that is slightly lower than the LPT1 simulation.

Method	DNS	PPDF	LPT1	LPT2
CPUs in second per 100 iterations	1200	75	85	50

4.2. *Forced Isotropic Turbulence*

The PPDF model was used to simulate forced isotropic turbulence with temperature gradients at $Re_\lambda = 40$ on a 64^3 grid. The initial temperature profile was chosen as

$$T = T_{min} + \Delta T\,|1 - y/\pi| \tag{4.6}$$

where $\Delta T = T_{max} - T_{min} = 2000\ K$ and $T_{min} = 700\ K$. The configuration is representative of the interaction between a turbulent flame and a sprinkler system. The droplets that are introduced in a narrow band of thickness $\Delta y = 0.03 \times (2\pi)$ around $y = 0$. They may be thought of as originating from a sprinkler at $y = 0$ and being subsequently

convected by the turbulent flow as they evaporate and cool the system. Figure 9 shows an instantaneous map of the liquid mass in droplets obtained from the DNS and the model. Preliminary results show good agreement with the DNS data. A more systematic analysis for this turbulent flow case is in progress.

5. Discussion

The model developed here is based on certain assumptions which are valid to a greater or lesser approximation depending on the physical system being described. Let us bring together here these various assumptions, discuss under what conditions they are valid and how the current theory may be expanded (if possible) when the assumptions fail to be valid.

First, we wrote down a continuity equation in phase space for the PDF $n_p(\mathbf{x}, r, t)$: (4.3) of CTR-SP02. This equation is valid provided that

(a) the external field $\mathbf{u}$ varies on a length scale that is very much larger than Δ, the scale on which n_p itself varies.

(b) there exists no processes that would result in abrupt changes in particle radii (i.e. collisions, coalesence and break up of droplets).

(c) the particles move with the local flow velocity.

Both (a) and (b) are reasonable if $a \ll d \ll \eta$ where a is a characteristic particle radius, d is a typical separation and η is the Kolmogorov scale. If $d \sim \eta$ and one is solving a DNS then the PDF approach is of course superfluous since one has only a few particles per grid and one might as well track them individually and not rely on any modeling. If on the other hand one is describing the system at a courser level, such as an LES then $\Delta \gg d$ and $d \sim \eta$ or $d \gg \eta$. In this case the velocity in (4.3) of CTR-SP02 need to be decomposed into a slowly varying part and a second rapidly varying term. If one assumes that the latter (the rapidly varying part) has a net diffusive effect (the "Fokker-Planck Approximation") then the moment equations get modified through the appearance of a term $\alpha \nabla^2 m_k$ (where $\alpha > 0$) on the right hand side and $\mathbf{u}$ is identified as the smooth part of the velocity field. Thus, such a modification of the theory would extend it to situations such as LES where $\mathbf{u}$ has a smooth and a fluctuating component. If $a \sim d$ then assumption (b) is no longer valid because of collisions between particles. Unlike the case of collisions between rigid spheres, there exists no simple "collision operator" for the coalescence and break up of fluid drops. In a turbulent fluid statistical break up models such as those due to Kolmogorov predict an equilibrium distribution n_p^{eq} that is lognormal (Kolmogorov 1941, Gorokhovski 2001). If the system is not very far from equilibrium a linearized collision operator $(n_p - n_p^{eq})/\tau$ (where τ is a timescale parameter) may be used and the moment equations should be modified to account for such a term. The approximation is not likely to be valid far from equilibrium. Fortunately in many combustor systems there are separate zones characterizing droplet break up and evaporation and the current model might be useful in the latter zone while the break up region is handled by a different approach. The third assumption is the assumption of zero particle inertia. Its accuracy depends on the Reynolds number based on particle radius being small. The violation of this assumption leads to important phenomena that are well known (Reade & Collins 2000).

Secondly we assumed that the system has a "universal behavior" in the sense that the PDF has a certain prescribed form (such as lognormal) the only thing that varies with position and time are the finite set of moments $m_0, \ldots, m_n$ that specify the distribution.

Such 'self-similarity' is well known in systems with many degrees of freedom, the case of an ideal gas being a familiar example. In that case, the velocity distribution is "locally Maxwellian" everywhere, the parameters of the Maxellian obey certain moment equations which are the familiar Navier-Stokes-Fourier equations of classical gas dynamics. The self-similarity in the gas dynamic example follows from the smallness of the duration of collisions compared to the time between collisions. The smallness of the ratio of these two time-scales imply a collapse to a center manifold the evolution on which is described by the Navier-Stokes-Fourier equations. In our case, we do not have an asymptotic formalism such as the Chapman-Enskog development to systematically prove such a self-similar behavior but rather such behavior is assumed apriori, an assumption that is open to critique and subject to experimental test.

Thirdly we assumed lognormality and the evaporation law (2.1). These assumptions are the least fundamental and are only incidental to the particular test cases we chose to run. Both statistical arguments as well as experimental data exists to support the hypothesis that in dense two phase turbulent flows, the distribution of droplet sizes is well approximated by the lognormal distribution. Therefore, if we wish to model the zone beyond the break up zone where droplet evaporation dominates droplet break up, the lognormal assumption is a reasonable one at least for the particles entering our computational zone. Subsequently, evaporation could change the shape of the distribution, and the accuracy of the model would depend on whether or not droplet evaporation is essentially complete before substantial departure from lognormality becomes an issue. If it does become an issue, then one will need to replace ϕ by a more detailed model. Finally, equation (2.1) was chosen for illustrative purposes only. Models that capture much finer details of the particle evaporation or condensation process are well known in atmospheric physics. A modified evaporation law may also be desirable for a technical reason: equation (2.1) has the feature, that the radius of a droplet goes to zero in finite time $t = t_e$ which leads to a small denominator problem in equations (2.6) unless the droplet radius is artificially prevented from going to zero. However, a better way of avoiding the singularity is to modify the evaporation law (2.6), for example:

$$\frac{dr}{dt} = -\frac{\Lambda(T - T_0)}{r}\{1 - \exp(-r/b)\} \tag{5.1}$$

eliminates the finite time singularity. Here b is to be chosen as a length so small that the mass of liquid droplets of radius less than b is essentially zero for all physical purposes. The incorporation of these more complicated evaporation models involves only the practical difficulty of evaluating more complicated integrals for the source terms.

6. Acknowledgement

The work reported here was performed in the summer of 2004 during which time one of us (S.G.) was supported as a visitor at the Center for Turbulence Research.

REFERENCES

Apte, S. V., Gorokhovski, M. & Moin, P. 2003a LES of atomizing spray with stochastic modeling of secondary breakup *Int. J. Mult. Flow* **29**, 1503–1522.

Apte, S. V., Mahesh, K., Moin, P., & Oefelein, J.C. 2003b Large-eddy simulation of swirling particle-laden flows in a coaxial-jet combustor. *Int. J. Mult. Flow* **29**, 1311–1331.

BINKOWSKI, F.S., & SHANKAR, U. 1995 The regional particulate matter model 1. Model description and preliminary results, *J. Geo. Res.*, **100**: D12, 26191–26209.

GOROKHOVSKI M.A. 2001. The stochastic lagrangian model of drops breakup in the computation of liquid sprays, Atom. & Sprays, **11** (5): 505–520.

KOLMOGOROV A.N. 1941 On the log-normal distribution of particles sizes during breakup process, *Dokl. Akad. Nauk. SSSR, XXXI*, **2**: 99–101.

MOIN, P, & APTE, S.V. 2005 LES of multiphase reacting flows in complex combustors. *to appear in AIAA J.*

PAOLI, R., HÉLIE, J., POINSOT, T.J., & GHOSAL, S. 2002 Contrail formation in aircraft wakes using large-eddy simulations. *Proceedings of the CTR Summer Program*, Stanford University, Stanford.

READE, W. C. & COLLINS, L. R. 2000 Effect of preferential concentration on turbulent collision rates. *Phys. Fluids* **12**, 2530–2540.

REID, R.C., PRAUSNITZ, J.M., AND POLING, B.E., 1987 The Properties of Gases and Liquids. McGraw Hill, Boston.

SHAW, R. 2003 Particle-turbulence interactions in atmospheric clouds. *Ann. Rev. Fluid Mech.*, **35**, 183–227.

Spreading laws for diffusion in a low-Reynolds-number channel

By J. Jiménez†,

1. Introduction

It was shown by del Álamo *et al.* (2004) and by Jiménez, del Álamo & Flores (2004) that the spectral energy densities of the streamwise velocity fluctuations in turbulent channels contain relatively-narrow ridges at long wavelengths, scaling as $\lambda_z \sim \lambda_x^{1/3}$ in the viscous and buffer sublayers, and as $\lambda_z \sim \lambda_x^{1/2}$ in the logarithmic region. The wavelengths λ_x and λ_z in those expressions can be interpreted as characteristic streamwise and spanwise dimensions of individual velocity structures, and it was argued by those authors that those two laws could be explained by the spreading of wakes left in the mean velocity profile by compact wall-normal-velocity structures.

It has indeed often been noted that, for long streamwise structures, the equations for the streamwise and for the flow-normal velocity components approximately decouple, and that the former can be approximated as a passive species advected by the latter (Orlandi & Jiménez 1994). In a turbulent flow this advection can approximately be represented as a turbulent diffusion. It was shown by del Álamo *et al.* (2004) that reasonable assumptions on the advection velocity of the generating structures and on the effective eddy viscosity yield spreading rates which agree quantitatively with the spectral square-root behavior observed in the logarithmic layer. It was also noted by Jiménez, del Álamo & Flores (2004) that the cube-root law is the similarity solution for diffusion in a uniform shear under the effect of a constant diffusion coefficient, both of which are reasonable assumptions near the wall. Finally, the physical structure of the wakes in the logarithmic region was isolated by means of conditional statistics in del Álamo *et al.* (2005), and supporting evidence for wakes in the buffer layer was provided by Jiménez, del Álamo & Flores (2004).

On the other hand, the coexistence of two different power laws remains to our knowledge undocumented in other flows, and would benefit from a quantitative theoretical explanation in at least one case. Since diffusion in turbulent channels, which requires delicate modelling of the effective diffusion coefficients at various flow locations, remains complicated, we will present here the analysis of the spanwise spreading of a mixing layer in a laminar low-Reynolds flow, and we will show that it already contains the two power-law regimes.

That shear influences diffusion is well known. Taylor (1953, 1954) showed in two classic papers that the effective diffusion coefficient of a solute is strongly modified when the mixing occurs in a shear flow. His analysis deals with the experimentally-important case in which the solute is injected as a plug filling a tube, and the diffusion is nominally streamwise. It therefore competes with the advection by the sheared streamwise velocity, which generates a wall-normal concentration gradient that is responsible for the enhanced diffusion. Recently Baroud *et al.* (2002) implemented a different experimental

† School of Aeronautics, Universidad Politécnica, 28040 Madrid, Spain

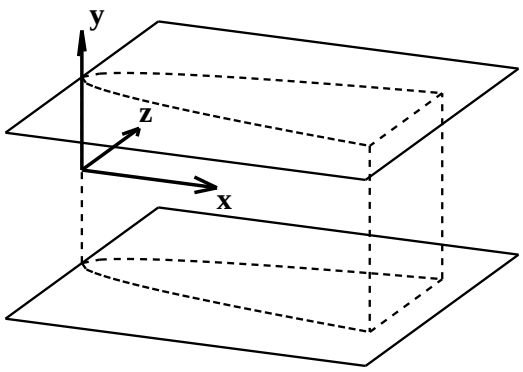

FIGURE 1. Problem geometry

configuration in which the diffusion happens in a narrow channel in which two streams of different solute concentration are injected side by side in the spanwise direction. The conditions are such that, although the Reynolds number of the flow is low enough for the mean velocity profile to be considered parabolic, the Péclét number of the solute is large, and the lateral diffusion occurs slowly. Since the longitudinal evolution of the mixing layer is then also slow, its interaction with the streamwise shear is weaker than in the plug case, but its growth is still modified. It is indeed clear that, were it not for the wall-normal diffusion, the mixing layer would grow at different rates at different wall distances, corresponding to the different local velocities. In this paper we analyze the diffusion of a solute under those conditions in enough detail to allow the experimental arrangement to be used in the determination of molecular diffusion coefficients. As discussed above a secondary motivation is to document the dependence on the wall distance of the spreading exponents, and to compare it with the ones observed in wall turbulence.

2. Basic scaling

Consider a channel between two parallel plates located at $y = \pm h$, and denote by $\widetilde{x}$ and $\widetilde{z}$ the streamwise and spanwise coordinates (see figure 1). Normalize the parabolic velocity profile U with its maximum, and the coordinates with h, so that $U = 1 - y^2$. Two streams with different concentrations of a passive scalar c are initially at $\widetilde{z} > 0$ and $\widetilde{z} < 0$, and come together at $\widetilde{x} = 0$. The diffusion equation for c is

$$Pe\,(1-y^2)\partial_x c = \partial_{\widetilde{x}\widetilde{x}} c + \partial_{yy} c + \partial_{\widetilde{z}\widetilde{z}} c, \tag{2.1}$$

where $Pe = U_c h/\kappa \gg 1$, and κ is the diffusivity of c. We will assume that there is no diffusion flux into the walls, so that

$$\partial_y c = 0, \text{ at } y = \pm 1, \tag{2.2}$$

and that the mixing takes place between

$$c = \pm 1/2, \text{ at } \widetilde{z} = \pm\infty. \tag{2.3}$$

Note that, since the problem is linear and homogeneous in $\widetilde{z}$, the same analysis can applied to the spreading of an initially-thin contaminant layer by differentiating everything with respect to $\widetilde{z}$.

As long as $\widetilde{x} \gg 1$ the streamwise diffusion term is negligible with respect to the other

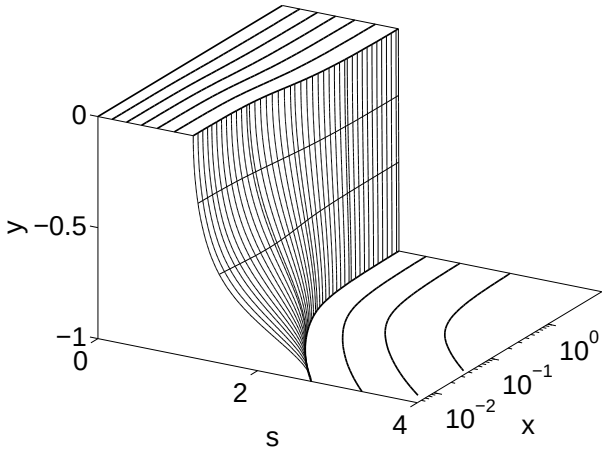

FIGURE 2. Numerical solution of (2.4), for $s > 0$ and $y < 0$. The wall is at the bottom, and the channel center at the top. The flow is from bottom–left to top–right. The isosurface represented is $c = 0.3$. The isolines on the top plane are $c = 0.05(0.05)0.3$, and those at the bottom plane are $c = 0.3(0.05)0.45$.

two directions, and can be neglected. The spreading of the mixing layer involves the balance of the streamwise advection with the spanwise diffusion, which have to be of the same order. If $\widetilde{x} = O(L)$, the spanwise scale then has to be $\widetilde{z} = O(L/Pe)^{1/2}$. There is a natural scaling, $L = Pe$, in which the three remaining terms of (2.1) are of comparable magnitude. Defining stretched coordinates $x = \widetilde{x}/Pe$ and $z = \widetilde{z}/Pe^{1/2}$, we get

$$(1 - y^2)\partial_x c = \partial_{yy} c + \partial_{zz} c + O(Pe^{-2}). \tag{2.4}$$

The leading order of this equation is parameter-free, and can be integrated numerically. The solution is symmetric with respect to $y = 0$, and antisymmetric with respect to $z = 0$, and is shown in figure 2 as a function of the scaled x, of y, and of the usual similarity variable for two-dimensional diffusion problems

$$s = z/x^{1/2}. \tag{2.5}$$

It has been computed using a second-order Crank-Nicholson marching code, using 200 grid points in y, and between 200 and 800 points in z, depending on the distance to the origin. The step in x was refined to insure grid independence in the critical region of small x. The solution in the figure corresponds to the overlap of three different computations at three different x-ranges, and the lack of discontinuities between the ranges was used as a criterion for numerical convergence.

At the central plane the solution follows fairly well the square-root law, but near the wall it spreads faster, specially at the early stages of the mixing. Even at the central plane there is a transition in the growth rate around $x = 1$. To understand that behavior we consider next the two limits in which x is either much smaller or much larger than one.

3. The near limit, $\widetilde{x} \ll Pe$

This is the relevant experimental case when $Pe \gg 1$, because further downstream the mixing layer grows enough to interfere with the lateral walls of the apparatus. When

$x \ll 1$, the longitudinal transport and the transverse diffusion are the dominant terms in (2.4), and it is natural to attempt an expansion of the form

$$c = c_{n,0} + x c_{n,1} + \dots, \tag{3.1}$$

where the coefficient are functions of y and of s. They satisfy

$$\partial_{ss} c_{n,k} + (1-y^2)\left(\frac{s}{2}\partial_s c_{n,k} - k c_{n,k}\right) = -\partial_{yy} c_{n,k-1}, \tag{3.2}$$

which is a well-ordered hierarchy in which y appears only as a parameter. In the leading-order equation for $c_{n,0}$ the right-hand side vanishes, and the solution can be written immediately as

$$c_{n,0} = \frac{1}{2}\mathrm{erf}\,(Z/2), \tag{3.3}$$

where

$$Z = s(1-y^2)^{1/2}. \tag{3.4}$$

Equation (3.3) satisfies the boundary conditions for c at $z \to \pm\infty$, but not the zero-flux conditions (2.2) at the walls.

Consider the neighborhood of the lower wall, and define the distance to the wall as $y' = y + 1$. When $y' \ll 1$ the velocity is $U \approx 2y'$, and $c_{n,0}$ behaves as $y'^{1/2}$. In this region the width of the mixing layer given by (3.3) is $z = O([x/y']^{1/2})$, and there is a boundary layer of thickness $y' = O(x^{1/3})$ in which the wall-normal diffusion cannot be neglected. The three terms in (3.2) are then of the same order, and there are new similarity variables

$$\eta = y'/x^{1/3}, \tag{3.5}$$

and

$$\zeta = z/x^{1/3}, \tag{3.6}$$

in terms of which (3.2) becomes

$$\partial_{\eta\eta} c + \partial_{\zeta\zeta} c + \frac{2}{3}\eta(\eta\partial_\eta c + \zeta\partial_\zeta c) = O(x^{1/3}). \tag{3.7}$$

The error term in the right-hand side is due primarily to the expansion of U near the wall in terms of η. The concentration c must satisfy (2.2) at $\eta = 0$, and (2.3) at $\zeta = \pm\infty$. When $\eta \gg 1$, it also has to match the $y \ll 1$ limit of the outer solution (3.3),

$$c_{n,0} \approx \frac{1}{2}\mathrm{erf}\,[\zeta(\eta/2)^{1/2}]. \tag{3.8}$$

This is a parameter-free elliptic problem that can be solved numerically. Its solution, c_{BL}, is antisymmetric with respect to $\zeta = 0$, and is shown graphically in figure 3(a). It has been obtained in the domain $\zeta = (0, 8)$ and $\eta = (0, 6)$, using a straightforward second-order finite-difference code with a grid of 200×250 points. It tends to (3.8) away from the wall, but it does not become infinitely wide in ζ at the wall.

Note that the higher-order terms of the expansion for c_n become increasing singular near the wall. While the only singularity of $c_{n,0}$ comes from the similarity variable Z, the next term

$$c_{n,1} = -\frac{Z(3+3y^2+y^2Z^2)}{12\sqrt{\pi}(1-y^2)^3}\mathrm{e}^{-Z^2/4}, \tag{3.9}$$

has an extra factor factor y'^{-3}. It is easy to show that $c_{n,k}x^k$ behaves near the wall as $(x/y'^3)^k = \eta^{-3k}$. Since Z is also approximately $\zeta\eta^{1/2}$ in that limit, it follows that the

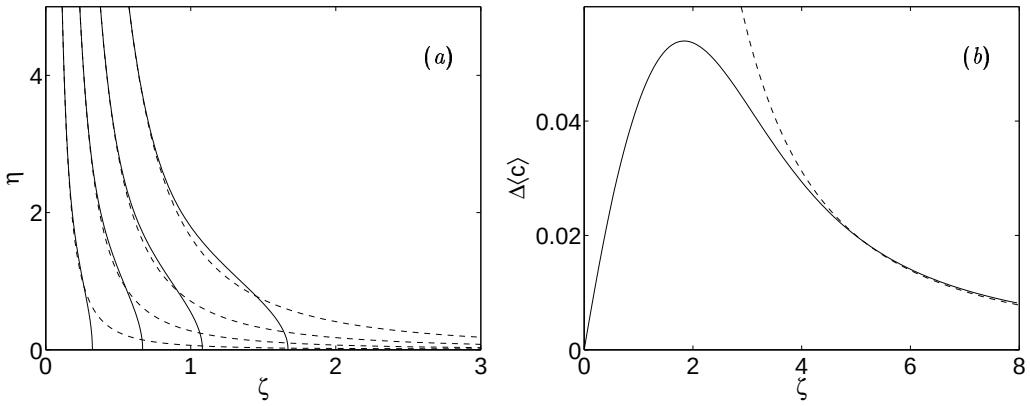

FIGURE 3. (*a*) Similarity solution for the boundary layer near the lower wall. ——— , similarity solution; ---- , outer solution (3.8). The contours are $c_{BL} = 0.1(0.1)0.4$. (*b*) Correction to the vertically-integrated concentration due to the boundary layer. ——— , $\langle c_{BL} - c_n \rangle$; ---- , large-$\zeta$ limit, $0.5/\zeta^2$.

inner limit of the outer solution is a function of ζ and η which has contributions from all the orders in the expansion (3.3). It is however clear from the previous discussion that the contributions to this function of the higher-order terms decay quickly as η increases, and that the boundary-layer solution can be matched safely to $c_{n,0}$ as long as the matching is done far enough. On the other hand, this is a problem in which the only way to avoid singularities in the higher-order terms is to use in the right-hand side of (3.2) the composite solutions formed by the lower-order boundary-layer and outer solutions, instead of just by the outer ones (Van Dyke 1964). This has no effect in the outer region, where the inner and outer solution coincide but, within the boundary layer where $\partial_{yy} c_{BL} = O(x^{-2/3})$, the correction $x c_1$ is $O(x^{1/3})$. This was already suggested by (3.7).

What is often measured in experiments is the vertically-integrated concentration

$$\langle c \rangle = \frac{1}{2} \int_{-1}^{1} c \, \mathrm{d}y. \tag{3.10}$$

It can be written in the present case as

$$\langle c \rangle \approx \langle c_{n,0} \rangle + x^{1/3} \langle \Delta c \rangle = \frac{\sqrt{\pi}}{8} s \exp(-s^2/8) \left[\mathrm{I}_0(s^2/8) + \mathrm{I}_1(s^2/8) \right] + x^{1/3} \langle \Delta c \rangle, \tag{3.11}$$

where I_0 and I_1 are Bessel functions. The correction $\langle \Delta c \rangle$ due to the boundary layers is

$$\langle \Delta c \rangle(\zeta) = \int_0^\infty (c_{BL} - c_{n,0}) \, \mathrm{d}\eta, \tag{3.12}$$

and is given in figure 3(*b*). For $\zeta \gg 1$ the solution c_{BL} is everywhere close to its asymptotic value 1/2, and (3.12) is mostly due to the integral of c_n, which can be evaluated exactly. That limit, $\langle \Delta c \rangle \approx 1/2\zeta^2$, is included in figure 3(*b*) for comparison.

Because $\langle c_n \rangle(s)$ and $\langle \Delta c \rangle(\zeta)$ depend differently on x it is impossible to express the composite solution in terms of a single similarity variable but, since (3.11) and (3.12) only hold in the limit $x \ll 1$, it is usually possible to write asymptotically valid expressions

for most quantities. Consider for example the 'slope' thickness defined by

$$\delta_s = \frac{c_\infty - c_{-\infty}}{\langle c \rangle'_{\widetilde{z}}}, \tag{3.13}$$

where $c'_{\widetilde{z}}$ stands for $\partial_{\widetilde{z}} c$ at $\widetilde{z} = 0$. Using the expressions above,

$$\delta_s^{-1} = \langle c_n \rangle'_s x^{-1/2} + \langle \Delta c \rangle'_\zeta \approx \frac{\sqrt{\pi}}{8} x^{-1/2} + 0.0551, \tag{3.14}$$

where $\langle c_n \rangle'_s$ follows from (3.11), and $\langle \Delta c \rangle'_\zeta$ has been estimated numerically from figure 3(b). Similar expressions can be obtained for other product thicknesses.

4. The limit $\widetilde{x} \gg Pe$

When $x \gg 1$, the mixing layer becomes much wider than h, and the dominant diffusion term is the one normal to the wall. We then look for expansions of the form,

$$c = c_{f,0} + x^{-1} c_{f,1} + \dots, \tag{4.1}$$

where the coefficients are again functions of s and y, and satisfy,

$$\partial_{yy} c_{f,k+1} = -\partial_{ss} c_{f,k} - (1 - y^2) \left(\frac{s}{2} \partial_s c_{f,k} + k c_{f,k} \right). \tag{4.2}$$

To leading order $\partial_{yy} c_{f,0} = 0$ and, from the boundary conditions (2.2), it follows that $c_{f,0}$ is only a function of s. To obtain it we must go to the next order, where

$$\partial_{yy} c_{f,1} = -(1 - y^2) \frac{s}{2} \partial_s c_{f,0} - \partial_{ss} c_{f,0}. \tag{4.3}$$

The correction $c_{f,1}$ also has to satisfy the Neumann conditions (2.2) at $y = \pm 1$, and it follows from the integration of (4.3) between the two walls that this is only possible if

$$\langle (1 - y^2) \rangle \frac{s}{2} \partial_s c_{f,0} + \partial_{ss} c_{f,0} = \frac{s}{3} \partial_s c_{f,0} + \partial_{ss} c_{f,0} = 0, \tag{4.4}$$

from where we write immediately

$$c_0 = \langle c_0 \rangle = \frac{1}{2} \mathrm{erf}\, (s/\sqrt{6}). \tag{4.5}$$

Note that the similarity variable in (4.5) is the same as the one for $\langle c_n \rangle$ in the previous section, but that the spreading rate is different. The first-order correction $c_{f,1}$ can be obtained by integrating (4.3) with respect to y, and contains an unknown additive function of s that has to satisfy a diffusion equation similar to (4.4), but the solution is now uniformly valid across the channel, and the correction is everywhere $O(x^{-1})$. To leading order, the mixing layer thickness is

$$\delta_s = (6\pi x)^{1/2}. \tag{4.6}$$

In figure 4(a) the evolution of the slope thickness obtained from the numerical solution of (2.4) is compared with the asymptotic expressions (3.14) and (4.6). The approximation is much better in the downstream case than in the one near the origin, in agreement with the different orders of the corrections which have been neglected, but the solution deviates little in general from a square-root growth law.

Note that we could have written the similarity variable s in these formulas with an arbitrary shift in the origin of x, since the approximation in this section does not hold

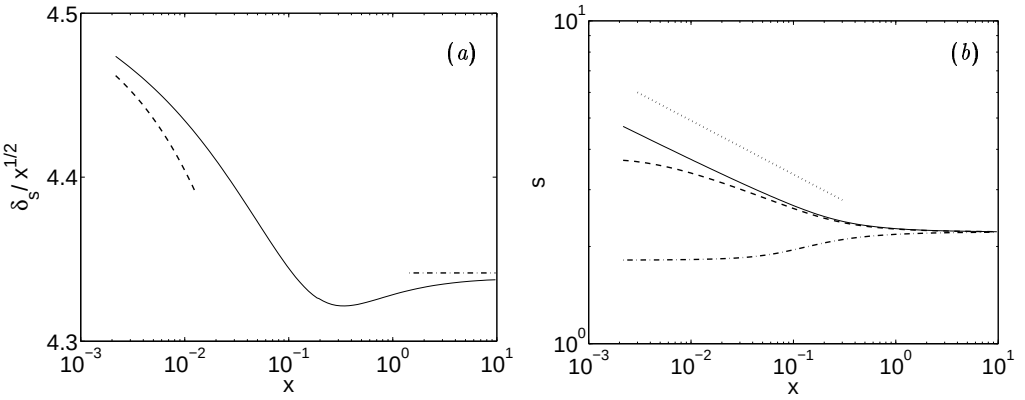

FIGURE 4. (*a*) Slope thickness of the mixing layer, scaled with $x^{1/2}$. ——— , numerical result; - - - - , small-x limit (3.14); —·— , large-x limit (4.6). (*b*) Lateral position of the isosurface $c = 0.4$, scaled with $x^{1/2}$, for different wall distances. ——— , $y' = 0.01$; - - - - , $y' = 0.15$; —·— , central plane. $y' = 1$. The dotted line corresponds to $z \sim x^{1/3}$.

at the physical origin of the mixing region. Any shift in the virtual origin can however be expected to be at most $x_0 = O(1)$, and would only appear in a large-x expansion as a term of $O(x^{-1})$.

The growth of the mixing layer at different distances from the wall is summarized in figure 4(*b*), which is compiled from the numerical results. The square-root growth appears as a constant in this plot, and it is the one followed by the layer in the central plane. The two different constants at small and large downstream locations correspond to the two outer solutions (3.8) and (4.5). Near the wall the layer follows initially the $x^{1/3}$ growth law, and only joins the square-root behavior when the mixing layer becomes vertically uniform farther downstream. The behavior of the intermediate location at $y' = 0.15$ is interesting. That wall distance is initially within the outer core of the channel, and follows approximately the square-root law. It then changes to an $x^{1/3}$ behavior as it is swallowed by the growth of the wall boundary layer, and it only returns to $x^{1/2}$ in the downstream limit in which the layer uniformizes.

5. Conclusions

We have shown that the spreading of a spanwise discontinuity of a passive scalar in a laminar channel is modified by the wall-normal diffusion due to the variation of the advection velocity with the distance to the wall. Because the spreading is orthogonal to the shear, this effect is weaker than in the case of longitudinal diffusion in tubes, but it has several experimentally-relevant effects. First, the spreading in the central plane is always approximately like $\widetilde{x}^{1/2}$, but the reasons are different near the origin and far from it, and the multiplicative constants change accordingly. Near the origin the wall-normal diffusion is negligible in this central region, but it becomes dominant far downstream, where the layer is much wider than the channel thickness. The layer then becomes uniform in the wall-normal direction, and behaves as if the advection velocity were constant and equal to the bulk velocity.

Near the origin the wall-normal diffusion is only important in boundary layers that develop near each wall. They have widths and heights of the order of $(\widetilde{x}/Pe)^{1/3}$, and they account for corrections of that order to the square-root behavior of the vertically-

integrated scalar profiles. The transition between the two regimes occurs at $\widetilde{x}/h \approx Pe$, when the wall layers fill the whole channel. We have given numerical results which can be used to interpret experiments.

We have noted that similar spreading laws are found in the growth of the structures of the streamwise velocity of turbulent channels. The effect of the wall-normal shear should also be their origin in that case, but there are extra complications connected with the variation of the eddy viscosity with the wall distance. That case will be the subject of a future study.

This work was supported in part by CICYT, under grant BPI2003-03434, and also the Department of Energy under the ASC program. I am grateful to S. Lele for his careful critique of an early version of this manuscript.

REFERENCES

DEL ÁLAMO, J.C., JIMÉNEZ, J., ZANDONADE, P. & MOSER, R.D. 2004 Scaling of the energy spectra of turbulent channels, *J. Fluid Mech.* **500**, 135–144.

DEL ÁLAMO, J.C., JIMÉNEZ, J., ZANDONADE, P. AND MOSER, R.D. 2005 Attached and detached vortex clusters in the logarithmic region, submitted *J. Fluid Mech.*

BAROUD, C.N., OKKELS, F., MÉNÉTRIER & TABELING, P. 2002 Reaction-diffusion dynamics: Confrontation between theory and experiment in a microfluidic reactor. *Phys. Rev.* E **67**, 060104-1.

JIMÉNEZ, J., DEL ÁLAMO, J.C. & FLORES, O. 2004 The large-scale dynamics of near-wall turbulence, *J. Fluid Mech.* **505**, 179–199.

ORLANDI, P. AND JIMÉNEZ, J. 1994 On the generation of turbulent wall friction, *Phys. Fluids* **6**, 634-641.

TAYLOR, G.I. 1953 Dispersion of soluble matter in solvent flowing slowly through a tube. *Proc. Roy. Soc. London* A **219**, 186–203.

TAYLOR, G.I. 1954 Conditions under which a solute in a stream of solvent can be used to measure molecular diffusion. *Proc. Roy. Soc. London* A **225**, 473–477.

VAN DYKE, M. 1964 *Perturbation methods in fluid mechanics*, Associated Press, 93–97.

Consistent hybrid LES-FDF formulation for the simulation of turbulent combustion

By V. Raman, H. Pitsch AND R. O. Fox †

1. Motivation and objectives

The numerical simulation of turbulent reactive flows is a complex and challenging problem with widespread practical use. Recent breakthroughs in algorithmic techniques and the drastic increase in computing power have provided us with the tools to understand the complex interaction between turbulence and chemical reactions. In the past decade, the use of the large-eddy simulation (LES) technique has made it possible to make accurate predictions of turbulent flows even for complex configurations. On the other hand, the treatment of combustion is mainly through models similar to that uses in the Reynolds-Averaged NS methods (RANS) like flamelet models or conditional moment closure type approximations. Although these models work well for systems that exhibit little or no extinction, a higher-dimensional multi-scalar model is required to describe slow and extinction chemistry. The transported-filtered density function (FDF) (Colucci *et al.* 1998) method provides a natural starting point for such detailed description. The FDF technique has the key advantage that the reaction source term of the scalars appears closed and requires no modeling.

Though a joint velocity-composition FDF transport equation can be formulated, numerical implementations of this high-dimensional system pose stability and feasibility issues. To overcome this problem, a hybrid approach is used where the velocity and turbulence fields are solved using an Eulerian scheme (like RANS or LES), while the scalar transport is handled using the FDF approach. Although the FDF technique has been widely used in the RANS context, almost all the applications involve steady-state flows. Since LES is inherently transient, the coupled LES-FDF method needs to maintain temporal accuracy. Due to the statistical nature of the FDF scheme, such a coupled scheme poses numerical accuracy issues.

Hence, in order to establish the accuracy of a LES-FDF implementation, a robust consistency criterion is formulated. Based on redundant density fields carried by the Eulerian as well as the Lagrangian part of the solver, it is required that the evolution of all such density fields should be equivalent. The theoretical development guarantees such an equivalence. The current implementation of the LES-FDF scheme is then used to verify this equivalence in the context of a numerical simulation of a variable density complex flow problem.

2. Hybrid LES-FDF scheme

In the hybrid scheme implemented here, the LES technique is based on a low-Mach number approximation-based finite-volume scheme. Further details of the LES implementation can be found elsewhere (Pierce 2001; Pierce & Moin 2004). The Lagrangian method uses stochastic particles to evolve the FDF.

† Iowa State University

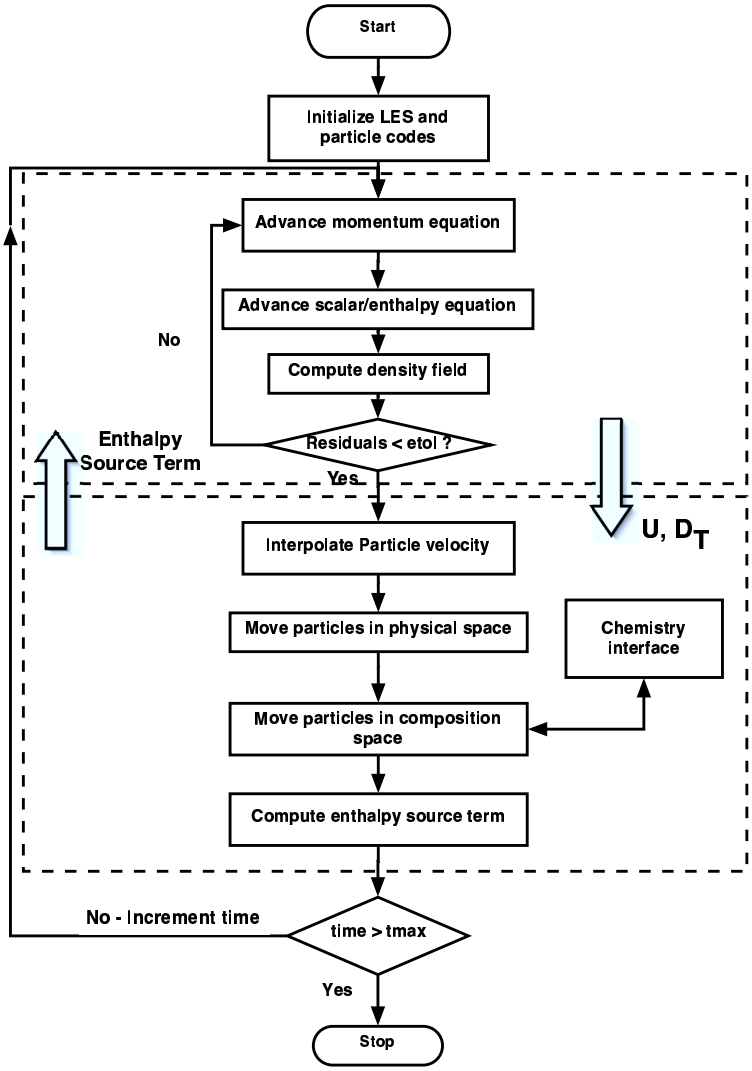

FIGURE 1. Flowchart showing the coupled LES-FDF simulation with feedback.

The particle method is obtained from the fundamental FDF transport equation. The FDF in a variable density flow can be defined as:

$$F_L(\boldsymbol{\psi};\mathbf{x},t) = \int_{-\infty}^{+\infty} \rho(\mathbf{y},t)\,\xi[\boldsymbol{\psi},\boldsymbol{\phi}(\mathbf{y},t)]\,G(\mathbf{y}-\mathbf{x})\,d\mathbf{y}, \tag{2.1}$$

$$\xi[\boldsymbol{\psi},\boldsymbol{\phi}(\mathbf{y},t)] = \delta[\boldsymbol{\psi}-\boldsymbol{\phi}(\mathbf{y},t)], \tag{2.2}$$

where δ is an N-dimensional delta function for an N-species system and $\boldsymbol{\psi}$ is the sample space variable in the composition domain. The FDF definition yields the following property:

$$\int_{-\infty}^{+\infty} F_L d\boldsymbol{\psi} = \int_{-\infty}^{+\infty} \rho(\mathbf{y},t)\,G(\mathbf{y}-\mathbf{x})\,d\mathbf{y} = \overline{\rho}. \tag{2.3}$$

Similarly, the filtered mean of any scalar Q_ϕ can be defined as:

$$\widetilde{Q_\phi} = \int_{-\infty}^{+\infty} Q_\phi(\boldsymbol{\psi}, \mathbf{y}, t) F_L d\boldsymbol{\psi} = \frac{1}{\overline{\rho}} \int_{-\infty}^{+\infty} \rho\left(\mathbf{y}, t\right) Q_\phi\left(\mathbf{y}, t\right) G\left(\mathbf{y} - \mathbf{x}\right) d\mathbf{y}. \tag{2.4}$$

Using these definitions, the transport equation for the joint composition FDF can be written as (Colucci *et al.* 1998; Jaberi *et al.* 1999)

$$\frac{\partial F_L}{\partial t} + \frac{\partial}{\partial \mathbf{x}}\left(\widetilde{\mathbf{u}} F_L\right) + \frac{\partial}{\partial \mathbf{x}}\left(\widetilde{\mathbf{u}'|\boldsymbol{\psi}} F_L\right) = -\frac{\partial}{\partial \boldsymbol{\psi}}\left[\left(\frac{1}{\overline{\rho}}\overline{\nabla \cdot \rho D \nabla \boldsymbol{\phi}|\boldsymbol{\psi}} + \mathbf{S}(\boldsymbol{\psi})\right) F_L\right], \tag{2.5}$$

where $\widetilde{\mathbf{u}}$ is the filtered velocity field, $\widetilde{\mathbf{u}'|\boldsymbol{\psi}}$ is the sub-filter velocity fluctuation conditioned on the scalar, $\overline{\nabla \cdot \rho D \nabla \boldsymbol{\phi}|\boldsymbol{\psi}}$ is the conditional micromixing term, and $\mathbf{S}$ is the reaction source term. The conditional velocity term is modeled using the gradient-diffusion hypothesis to give

$$\widetilde{u_i'|\boldsymbol{\psi}} F_L = -\overline{\rho} D_T \frac{\partial F_L/\rho}{\partial x_i}. \tag{2.6}$$

The conditional mixing term is closed using the Interaction-by-Exchange-with-the-Mean (IEM) model (Villermaux 1986).

$$\overline{\nabla \cdot \rho D \nabla \boldsymbol{\phi}|\boldsymbol{\psi}} = \nabla \cdot \overline{\rho} D \nabla \widetilde{\boldsymbol{\phi}} - \frac{\overline{\rho} C_\phi}{\tau}\left(\boldsymbol{\psi} - \widetilde{\boldsymbol{\phi}}\right), \tag{2.7}$$

where C_ϕ is scalar-to-mechanical time-scale ratio and τ is a turbulence time scale. In the present study we set $C_\phi = 2$ (Peters 2000) and use a turbulent-diffusivity-based time scale (Colucci *et al.* 1998).

The high dimensionality of the FDF equation makes finite-differencing-based solution techniques infeasible. A stochastic approach (Pope 2000) is used where the filtered momentum equations are solved using conventional grid-based techniques (like LES) while the FDF equation is solved using a particle-based Monte-Carlo approach. The Lagrangian approach uses a large ensemble of notional particles to represent the fluid. These particles evolve using a set of stochastic differential equations obtained from the above FDF transport equation. The stochastic differential equations are functions of the filtered LES flow fields. Hence, the Lagrangian system uses the filtered fields from the LES solver to advance the notional particles. Using the particle properties, mean fields are constructed that are fed back to the LES solver. The LES solver then advances the flow using these mean fields. Figure 1 shows the flowchart of the hybrid algorithm.

Typically, the Lagrangian system provides the filtered density field that is then used by the LES solver. However, the stochastic nature of the FDF scheme leads to large statistical fluctuations in the filtered density field. Direct feedback of this noisy field usually leads to numerical instabilities. Here, to increase the robustness of the feedback algorithm, an additional enthalpy equation is used. Following (Muradoglu *et al.* 1999), we define the equivalent enthalpy, h as

$$h(\boldsymbol{\psi}) = \frac{\gamma}{\gamma - 1}\frac{P_0}{\rho(\boldsymbol{\psi})}, \tag{2.8}$$

where γ is the ratio of the specific heats, P_0 is the operating pressure. Since the equivalent enthalpy is only a function of the local thermochemical composition, the transport equation for h can be derived from the FDF transport equation.

$$\frac{\partial \overline{\rho}\widetilde{h}}{\partial t} + \frac{\partial}{\partial \mathbf{x}}\left(\overline{\rho}\widetilde{\mathbf{u}}\widetilde{h}\right) = \frac{\partial}{\partial \mathbf{x}}\left(\overline{\rho}\left(D + D_T\right)\frac{\partial \widetilde{h}}{\partial \mathbf{x}}\right) + \overline{\rho}\left(\widetilde{h_\alpha S_\alpha} - \frac{1}{2\tau} C_\phi \overline{\rho} \widetilde{h_\alpha \phi''_\alpha}\right), \tag{2.9}$$

$$h_\alpha = \frac{\partial h}{\partial \phi_\alpha}, \tag{2.10}$$

where α represents the components of the N-dimensional composition array. It is evident that the physical transport terms in this equation can be treated in the same way as a conserved scalar equation. The source terms, however, are not known and need to be provided by the FDF solver. In terms of the particle properties, the source term is the change of enthalpy of the particles due to reaction and mixing (Muradoglu *et al.* 1999):

$$\widetilde{S_h} = \overline{\rho}\left(\widetilde{h_\alpha S_\alpha} - \frac{1}{2\tau} C_\phi \overline{\rho} h_\alpha \widetilde{\phi"}_\alpha\right). \tag{2.11}$$

Once the equivalent enthalpy is known, the density field is found using the relation obtained by filtering Eq. 2.8:

$$\overline{\rho} = \frac{\gamma}{\gamma - 1}\frac{P_0}{\widetilde{h}}, \tag{2.12}$$

where the low-Mach number assumption has been used to remove the pressure fluctuations. This density field is then used to advance the LES flow solver. It is found that this feedback mechanism is numerically stable and does not lead to large spikes in the $d\overline{\rho}/dt$ term that appears in the continuity equation.

To increase statistical accuracy, large particle numbers are needed making such methods computationally expensive. Numerical implementation of the LES-FDF scheme is an algorithmic challenge and novel techniques are used to reduce the computational expense of these schemes (Raman *et al.* 2004). A major issue in such implementations is to consistently couple a stochastic FDF scheme and a deterministic Eulerian scheme. Though steady-state-based flow solvers have been successfully used (Muradoglu *et al.* 1999), a consistent algorithm for a temporally variant system (like the LES-based approach) has not been studied in detail so far. Here we propose a criterion for a consistent implementation and test it with a challenging reacting flow problem.

3. Consistency requirements

In the Lagrangian particle-based system, the computational domain is decomposed into a large number of notional particles that represent the fluid. The particles are initially distributed uniformly and evolve in space and time using stochastic differential equations (Pope 2000). Each particle carries information about its location, a composition vector and a representative weight. In order to pass information from and to the LES solver, particle mean fields are obtained by a weighted summation process involving particle properties in a given computational cell. The particle weight is initially assigned to be a fraction of the local fluid mass such that the sum of the particle weights in a computational cell equals the cell fluid mass.

$$w_k = \frac{V_i \overline{\rho}_i}{N_p}, \tag{3.1}$$

where w_k is the particle weight, V_i is the cell volume, $\overline{\rho}_i$ is the fluid density in cell i, and N_p is the number of particles in the cell. As the particles evolve with time, the sum of the weights of the particles in a given cell is dependent on the enforcement of the continuity equation. The particle weight has no direct evolution equation and will follow the particle trajectory. At any time step, the particle-weights based density can be obtained by using the sum of particle weights in a given cell.

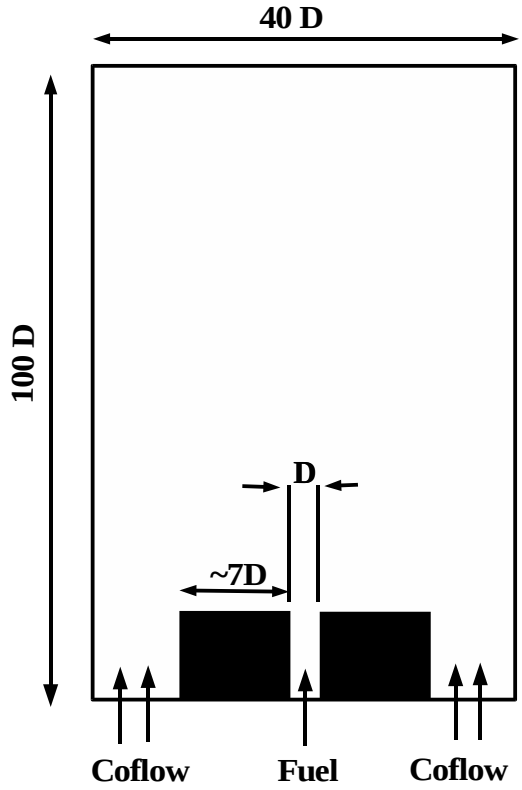

FIGURE 2. Schematic of the bluff-body flame configuration. The jet diameter D is 3.6 mm.

$$\overline{\rho}_w = \frac{1}{V_i} \sum_{i=1}^{N_p} w_k. \tag{3.2}$$

In addition to the particle weight, a mean density can also be obtained from the particle composition vector based on thermochemical properties.

$$\overline{\rho}_p^{-1} = \frac{\sum_{k=1}^{N_p} w_k / \rho\left(\boldsymbol{\phi}_k\right)}{\sum_{k=1}^{N_p} w_k}, \tag{3.3}$$

where $\rho(\boldsymbol{\phi})$ is the thermochemical density computed using the particle composition. The initial conditions are chosen such that $\overline{\rho} = \overline{\rho}_p$ at $t = 0$. As the particles evolve in space and time, the density fields evolve through different equations, though indirectly, they should all satisfy the continuity equation. By construction (Raman *et al.* 2004), the thermochemical density ($\overline{\rho}_p$) and the LES density ($\overline{\rho}$) evolve closely. This is ensured by solving an ancillary enthalpy transport equation using Eulerian schemes. The source term

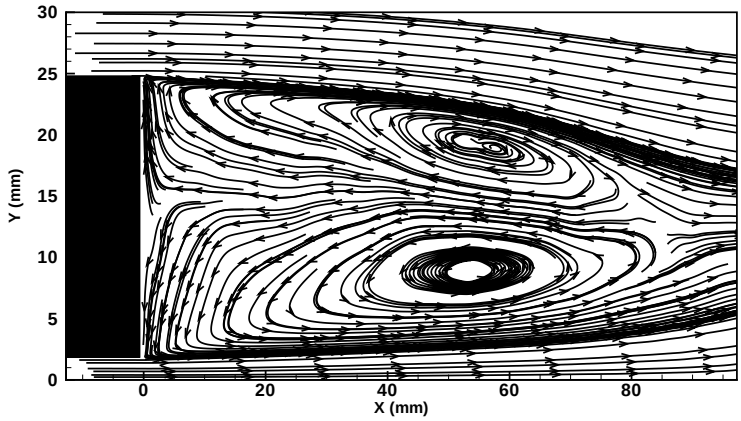

FIGURE 3. Streamtraces of the time-averaged velocity vector showing the counter-rotating vortices.

for the enthalpy equation is provided using the particle properties. The Eulerian density is obtained directly using this enthalpy field (Muradoglu *et al.* 1999).

On the other hand, the particle weights-based density ($\overline{\rho}_w$) evolves with the particle motion. Based on the continuity equation, it can be shown (Pope 2000) that for the particles to be uniformly distributed, the particle-weights-based density should be equivalent to the Eulerian density field. However, the stochastic evolution scheme will make the particle-based mean fields noisy. Hence a strict equality can be obtained only by time-averaging a statistically stationary field. Finite particle number density can also introduce a bias in the mean fields. This will lead to a progressive divergence of the particle-weights-based density field from the Eulerian field. Such a bias will be readily observed through particle agglomeration in certain sections of the grid and depletion of particles in other regions. The sampling error induced by such low particle number density will further increase the error in mean-field estimation.

A consistent algorithm should hence maintain the equivalence of the three density fields described above. It is noted that this amounts to a consistent evolution of the zeroth moment of the FDF-transport equation. The accuracy of the scheme can be tested using higher-order moments of the same equation. For the single-scalar flamelet model used here, the first moment of the scalar can be evolved simultaneously by both the particle and Eulerian systems. Such a moments-based validation procedure ensures a robust yet simple way of demonstrating the accuracy of the numerical implementation. We will illustrate the validation criteria using an experimental flame next.

4. Numerical test

A bluff-body stabilized experimental flame is simulated using the LES-FDF scheme. The methane/hydrogen fuel jet is separated from the coflow of air by a solid body (Fig. 2). The presence of this bluff-body induces strong recirculation zones that stabilize the flame. In fact, time-averaged streamtraces (Fig. 3) show the presence of two counter-rotating vortices that help mix the coflow with the fuel. The interaction of the high-velocity jets with the slow recirculating fluid creates high shear rates where the reaction is controlled predominantly by mixing. This complex unsteady reacting flow makes an ideal candidate

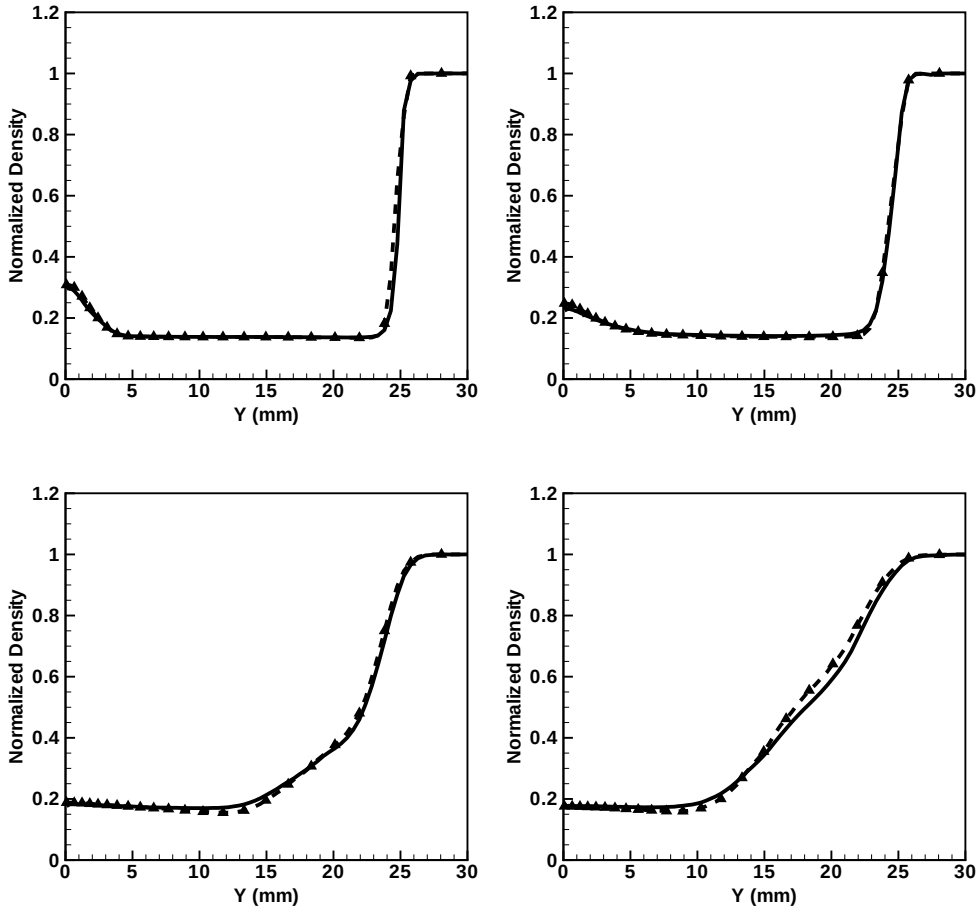

FIGURE 4. Comparison of density obtained from particle weights (dashed line), particle composition (solid line) and LES flow solver (symbols). The four plots are at downstream locations of (top) 13, 30, (bottom) 65, and 90 mm, respectively. The density values have been normalized by the density of the coflow.

for testing the LES-FDF scheme. A computational domain of $256 \times 128 \times 32$ is used along with a nominal particle number density of 15 per cell. Combustion is described using a laminar flamelet chemistry.

The FDF solver was initialized with 15 particles per cell. During the course of the simulation, the total number of particles in the domain was in the range of 10.5–21 million. The simulations were started from cold-flow-converged results, after which the mixture was ignited using the flamelet solution. All simulations were continued for 7 flow-through times, where each flow through time is defined by the time it takes for a particle to travel along the centerline from the inflow to the exit of the domain. The simulation is time-averaged for 1.5 flow-through times starting at two different time-steps separated by 1 flow-through time. The two time-averaged profiles differed by less than 2 % for the mixture-fraction radial profiles ensuring that statistical stationarity has been reached.

The LES-FDF simulation took roughly 200 hours on an 8-processor 600 MHz computer to reach statistical stationarity.

Figure 4 shows time-averaged radial profiles of the three density fields. The density profiles show very good agreement indicating that the FDF implementation is accurate. It was further confirmed that the time-averaged particle number density was constant indicating that there was no long term accumulation of statistical errors. This trend continues at further downstream positions as well.

Figures 5 and 6 show the time-averaged mixture-fraction and RMS mixture-fraction radial profiles at different axial locations. To aid in the comparison, the Eulerian mixture-fraction and RMS mixture-fraction fields obtained from the finite-volume solution of the scalar transport equation are also included. It is observed that the mean mixture-fraction profiles obtained from the FDF solver and the Eulerian solver show excellent agreement with one another and the experimental data as well. The near-bluff-body profile shows a flat profile in the recirculation zone, further affirming the large-scale mixing in this region. The sharp decay of the mixture fraction near the edge of the bluff body is a region of large temperature changes, and consequently large density gradients. At $X = 30\,\mathrm{mm}$, the recirculation region is slightly overpredicted, indicated by the large mixture-fraction values as compared to experiments as well as a sharper decay at the outer vortex signifying a thin reaction zone. Further downstream, the profiles are in much better agreement with the experimental data. At $X = 90\,\mathrm{mm}$, the profiles indicate a tendency of the flame to be narrower than the experimental observation. This is a direct consequence of the grid coarsening to limit the number of computational cells, and leads to the faster decay of the axial velocity.

The RMS profiles show good agreement with experimental data, although certain discrepancies are noticed near the centerline. In general, it is observed that the results agree well with the Eulerian computation as well. At the first axial position considered, the FDF as well as Eulerian calculation show the right RMS profile indicating that the large-scale recirculation has been captured accurately. It is noted that the sub-filter or the unresolved variance in this zone is very small since the large-scale mixing renders the fluid homogeneous. Similar trends are observed at $X = 30$, and $45\,\mathrm{mm}$, but the extent of the recirculation zone in the radial direction decreases as implied by the streamtrace profile (Fig 3). At $X = 65\,\mathrm{mm}$, the secondary peak in the mixture-fraction RMS corresponding to the end of the recirculation zone is captured very accurately. Further downstream, the peak in the RMS profile is shifted towards the centerline which is consistent with the mixture-fraction profiles that indicate a narrower jet spreading than the experimental observation.

It is observed that the RMS profile from the FDF calculation at $X = 30\,\mathrm{mm}$ and $X = 45$ mm show a peak near the centerline that is much larger than the experimental data. One explanation for this behavior is the reduction of accuracy of the particle tracking near the centerline. The LES solver uses a semi-implicit form, where the radial and azimuthal directions are treated implicitly, and are hence independent of the CFL criteria accounting for the radial and azimuthal components. However, the particle method is fully explicit implying that in regions where the CFL criteria computed based on the radial or azimuthal velocity is not satisfied, the errors could be significant. It was found from an analysis of the turbulent-diffusivity profile that such an event is more likely to occur in the region where the central fuel jet breaks down. For this flow, this region varied from $X = 25\,\mathrm{mm}$ to $X = 60\,\mathrm{mm}$. It is noted that the CFL criterion is not violated at each time step, but the additive errors due to frequent violation of this condition led to a spurious

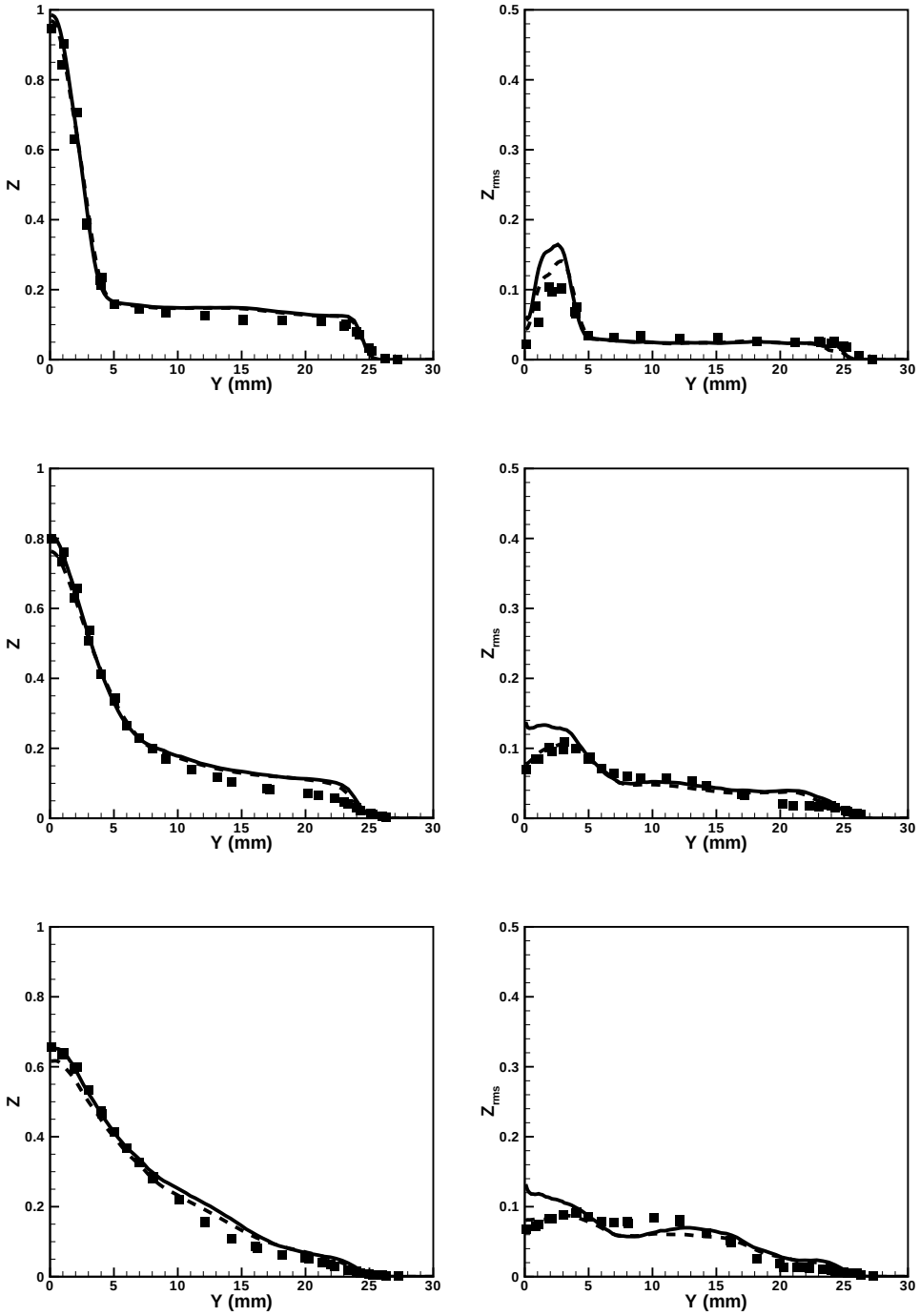

FIGURE 5. Comparison of mean mixture fraction and RMS mixture fraction profiles with experimental data at different axial locations. From top to bottom, $X = 13$, 30, and 45 mm. Symbols are experimental data, solid lines show FDF-based results and dashed lines show beta-function-based Eulerian calculation.

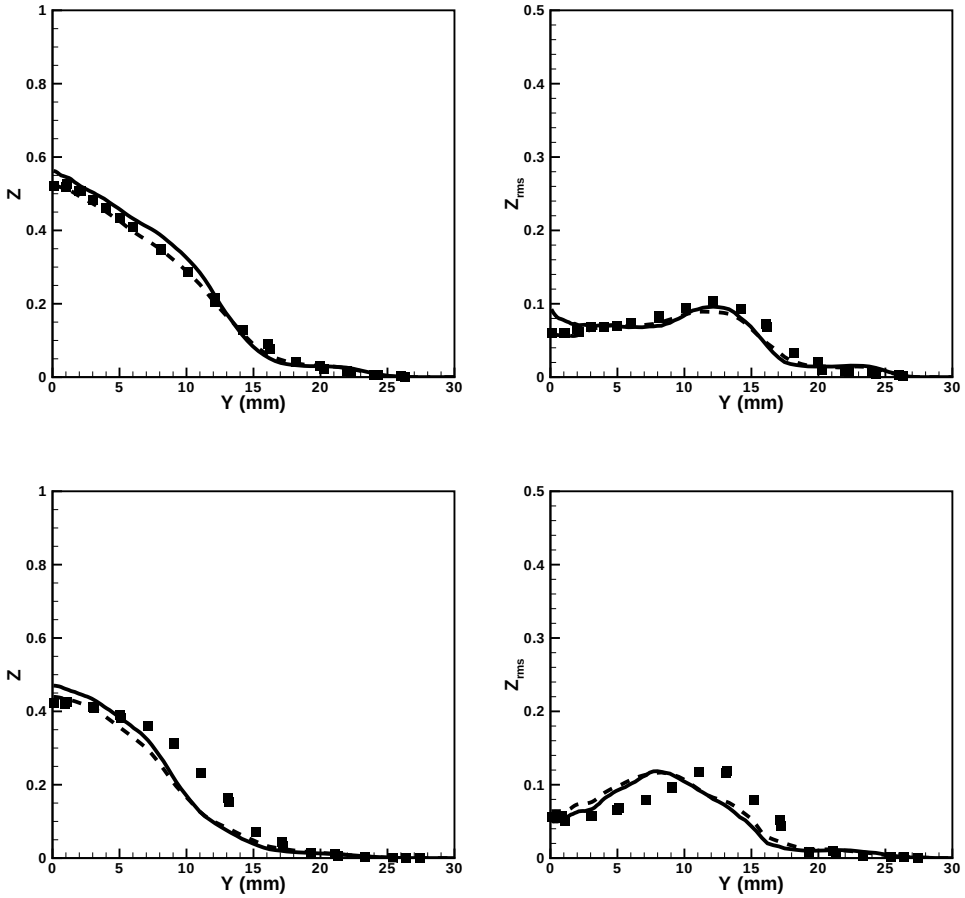

FIGURE 6. Comparison of mean mixture fraction and RMS mixture fraction profiles with experimental data at different axial locations. From top to bottom, $X = 65$ and 90 mm. Symbols are experimental data, solid lines show FDF-based results and dashed lines show beta-function-based Eulerian calculation.

increase in the RMS fluctuation. Since the purpose of this study is to establish the hybrid technique as a viable tool for practical flows, no further evaluations are reported on this observation. Although not reported here, increase in the nominal particle number density decreased this error. Currently, a multi-step fractional-stepping algorithm is being tested to overcome this problem.

5. Conclusion

A consistent hybrid LES-FDF scheme has been developed and implemented for variable density flows. The LES-FDF scheme has been validated by using a density-based consistency condition. An experimental flame configuration was used to test the validation scheme. Currently, direct integration of the chemical source term is being used with a detailed chemical mechanism to fully exploit the advantages of the LES-FDF technique.

REFERENCES

Colucci, P. J., Jaberi, F. A. & Givi, P. 1998 Filtered density function for large eddy simulation of turbulent reacting flows. *Physics of Fluids* **10** (2), 499–515.

Jaberi, F. A., Colucci, P. J., James, S., Givi, P. & Pope, S. B. 1999 Filtered mass density function for large-eddy simulation of turbulent reacting flows. *Journal of Fluid Mechanics* **401**, 85–121.

Muradoglu, M., Jenny, P., Pope, S. B. & Caughey, D. A. 1999 A consistent hybrid finite-volume/particle method for the PDF equations of turbulent reactive flows. *Journal of Computational Physics* **154**, 342–371.

Peters, N. 2000 *Turbulent Combustion*. Cambridge University Press.

Pierce, C. D. 2001 Progress-variable approach for large-eddy simulation of turbulence combustion. PhD thesis, Stanford University.

Pierce, C. D. & Moin, P. 2004 Progress-variable approach for large-eddy simulation of non-premixed turbulent combustion. *Journal of Fluid Mechanics* **504**, 73–97.

Pope, S. B. 2000 *Turbulent Flows*. Cambridge University Press.

Raman, V., Pitsch, H. & Fox, R. O. 2004 A consistent hybrid les-fdf scheme for the simulation of turbulent reactive flows. *Submitted to Comb. and Flame*

Villermaux, J. 1986 Micromixing phenomena in stirred reactors. In *Encyclopedia of Fluid Mechanics*, chap. 27. Gulf, Houston, TX.

Conditional filtering method for large eddy simulation of turbulent nonpremixed combustion

By S.H. Kim AND H. Pitsch

1. Motivation and objectives

In the fast chemistry limit of turbulent nonpremixed combustion, turbulence does not affect the local flame structure and a reactive scalar is given as a function of the mixture fraction, which describes mixing of fuel and oxidizer (Bilger 1980). This assumption allows the statistics of reactive scalars to be determined from those of the mixture fraction. Although the fast chemistry limit gives a leading order solution for turbulent nonpremixed combustion, the separation of time scales is not generally acceptable due to a wide spectrum of time scales involved in turbulence and chemical reactions.

Turbulent straining enhances scalar gradients and diffusive heat loss from flames to surrounding fluid parcels. Scalar dissipation rate, which measures the diffusive mixing rate, is a critical parameter to describe the nonequilibrium effects. With excessive scalar dissipation rate, nonpremixed flames may be locally extinguished. The extinguished flames may be reignited by diffusive transfer of heat and radicals from burning flames, when the scalar dissipation rate falls below a certain level. The modeling of local extinction and reignition requires detailed description of transient response of local flame structure to scalar dissipation fluctuations.

Large eddy simulation (LES) offers two advantages over the Reynolds averaged Navier Stokes (RANS) approach in computation of turbulent flames. First, mixing processes can be predicted with improved accuracy because large scale structures, which dominates global mixing characteristics, are resolved in LES. Second, LES can capture the transient response of the local flame structure to the unsteadiness of the flow field on the order of resolved time scale or longer. This makes LES attractive for the computation of turbulent flames, in which nonlinear interactions of turbulence and chemical reactions are of critical importance, e.g., local extinction and reignition in turbulent nonpremixed flames.

Subgrid scale modeling of combustion processes in LES is a prominent research topic. A subgrid scale model usually adopts the scale invariance assumption, which implies that certain features of physical processes are invariant in different length scales (Meneveau & Katz 2000). This assumption works well when the major part of subgrid scale contributions comes from length scales just smaller than the filter width. The scale invariance assumption is, therefore, not relevant to subgrid scale combustion processes, which mostly occur at the dissipative scales. The filterered density function method (Jaberi *et al.* 1999), the linear eddy model (Kerstein 1992), the laminar flamelet model (Pitsch 2002), the conditional source term estimation (Bushe & Steiner 1999) and the progress-variable approach (Pierce & Moin 2004) have been proposed as a subgrid combustion model.

The conditional moment closure (CMC) model solves the conditional moments of reactive scalars to resolve the closure problem of nonlinear chemical reactions (Bilger 1993; Klimenko 1990; Klimenko & Bilger 1999). In a turbulent nonpremixed flame, fluctuations of reactive scalars are primarily associated with those of the mixture fraction. Nonlinear

chemical reactions can, therefore, be closed using statistics conditioned on the mixture fraction. The first-order CMC model, which assumes that fluctuations of the reactive scalars about the conditional means are small enough for chemical reactions to be closed using the conditional means, has been successfully applied to turbulent nonpremixed flames with low levels of local extinction (Kim *et al.* 2000; Smith *et al.* 1995). Refined approaches, such as second-order closure and double conditioning are being investigated for application to significant local extinction (Kim *et al.* 2002; Kim & Huh 2004; Kronenberg 2004; Cha & Pitsch 2002). Although the CMC model has been extensively studied for RANS, there have been few studies in the context of LES (Bushe & Steiner 1999).

The objective of this study is to develop a subgrid combustion model for turbulent nonpremixed flames with local extinction and reignition, based on the concept of CMC. In what follows, the conditionally filtered equations for reactive scalars are derived and closure assumptions are discussed. The integrated conditional filtering for a reacting shear layer is introduced. The closure assumptions and the performance of the model are tested with direct numerical simulation (DNS) data of reacting mixing layers.

2. Mathematical formulation

2.1. *Conditional filtering*

Conventional filtering smoothes out all small scale details and filtered chemical reaction rates are generally not well reconstructed from the (conventionally) filtered scalar field. In turbulent nonpremixed flames the mixture fraction, which describes the extent of mixing of fuel and oxidizer, is a key quantity to describe the flame structure (Klimenko & Bilger 1999). Here we adopt density weighted filtering conditioned on iso-surfaces of the mixture fraction to resolve small scale mixing and chemical reactions in a nonpremixed flame:

$$\overline{\phi|\eta}(\eta,\mathbf{x},t) \equiv \frac{\int_V \rho\phi(\mathbf{x},t)\delta(\xi(\mathbf{x},t)-\eta)G(\mathbf{x}-\mathbf{x}';\Delta_f)d\mathbf{x}'}{\int_V \rho\delta(\xi(\mathbf{x},t)-\eta)G(\mathbf{x}-\mathbf{x}';\Delta_f)d\mathbf{x}'}, \tag{2.1}$$

where $G(\mathbf{x}-\mathbf{x}';\Delta_f)$ is a filtering function of specified width, Δ_f. We assume constant filter width so that the filtering operation commutes with differentiation. δ is the Dirac delta function and ξ is the mixture fraction. In Eq. (2.1), filtering is made only on iso-η surfaces because of the weighting with $\delta(\xi(\mathbf{x},t)-\eta)$. This decouples physical processes across a flame from those on a flame surface. The denominator of Eq.(2.1) is the subgrid probability density function (PDF) of the mixture fraction, P_ξ, weighted by the conditionally filtered density. The density weighted filtered value of ϕ can be calculated by integration in η space:

$$\widetilde{\phi} = \frac{\int_0^1 \rho_\eta \overline{\phi|\eta} P_\xi(\eta)d\eta}{\overline{\rho}}, \tag{2.2}$$

where $\overline{\rho}$ is the filtered density.

2.2. *Conditionally filtered equation*

The conditionally filtered equation for a reactive scalar can be derived using the transport equation for the δ function:

$$\begin{aligned}\frac{\partial \rho \delta_\eta}{\partial t} + \nabla \cdot (\rho \mathbf{v} \delta_\eta) &= -\frac{\partial \delta_\eta \nabla \cdot (\rho D \nabla \xi)}{\partial \eta} \\ &= -\frac{\partial^2 \rho \delta_\eta N}{\partial \eta^2} - \frac{\partial \nabla \cdot (\rho \delta_\eta D \nabla \xi)}{\partial \eta},\end{aligned} \tag{2.3}$$

where $\delta_\eta \equiv \delta(\xi(\mathbf{x}, t) - \eta)$. D is the molecular diffusivity. The molecular diffusivity is assumed to be equal for all scalars here. $N \equiv D \nabla \xi \cdot \nabla \xi$ is the scalar dissipation rate. Multiplying Eq. (2.3) by Y_i and adding the equation for Y_i multiplied by δ_η gives

$$\begin{aligned}\frac{\partial \rho \delta_\eta Y_i}{\partial t} + \nabla \cdot (\rho \delta_\eta \mathbf{v} Y_i) = \rho \delta_\eta \omega_i &- \frac{\partial^2 \rho \delta_\eta N Y_i}{\partial \eta^2} + 2 \frac{\partial \rho \delta_\eta D \nabla \xi \cdot \nabla Y_i}{\partial \eta} \\ &- \frac{\partial \nabla \cdot (\rho \delta_\eta D \nabla Y_i)}{\partial \eta} + \nabla \cdot (\delta_\eta \rho D \nabla Y_i),\end{aligned} \tag{2.4}$$

where ω_i is the chemical reaction rate of species i. Filtering Eq. (2.4) gives

$$\begin{aligned}\frac{\partial \rho_\eta P_\xi \overline{Y_i|\eta}}{\partial t} &+ \nabla \cdot (\rho_\eta P_\xi \overline{\mathbf{v} Y_i|\eta}) \\ &= \rho_\eta P_\xi \overline{\omega_i|\eta} - \frac{\partial^2 \rho_\eta P_\xi \overline{N Y_i|\eta}}{\partial \eta^2} \\ &+ 2 \frac{\partial \rho_\eta P_\xi \overline{D \nabla \xi \cdot \nabla Y_i|\eta}}{\partial \eta} \\ &- \frac{\partial \nabla \cdot (\rho P_\xi \overline{Y_i D \nabla \xi)|\eta}}{\partial \eta} + \nabla \cdot (\rho_\eta P_\xi \overline{D \nabla Y_i|\eta}).\end{aligned} \tag{2.5}$$

To identify the resolved part of the equation, we substitute the decompositions, $Y_i \equiv \overline{Y_i|\eta} + Y_i'$, $\mathbf{v} \equiv \overline{\mathbf{v}|\eta} + \mathbf{v}'$ and $N \equiv \overline{N|\eta} + N'$, into Eq. (2.5). This gives

$$\begin{aligned}\frac{\partial \rho_\eta P_\xi \overline{Y_i|\eta}}{\partial t} &+ \nabla \cdot (\rho_\eta P_\xi \overline{\mathbf{v}|\eta}\ \overline{Y_i|\eta}) \\ &= \rho_\eta P_\xi \overline{\omega_i|\eta} - \frac{\partial^2 \rho_\eta P_\xi \overline{N|\eta}\ \overline{Y_i|\eta}}{\partial \eta^2} \\ &+ 2 \frac{\partial}{\partial \eta} \left(\rho_\eta P_\xi \overline{N|\eta} \frac{\partial \overline{Y_i|\eta}}{\partial \eta} \right) + \rho_\eta P_\xi F_i + \rho_\eta P_\xi M_i,\end{aligned} \tag{2.6}$$

where

$$F_i \equiv \frac{1}{\rho_\eta P_\xi} \left[-\nabla \cdot (\rho_\eta P_\xi J_i^{\mathbf{x}}) + \frac{\partial \rho_\eta P_\xi J_i^\eta}{\partial \eta} \right] \tag{2.7}$$

$$J_i^{\mathbf{x}} \equiv -\overline{\mathbf{v} Y_i|\eta} + \overline{\mathbf{v}|\eta}\ \overline{Y_i|\eta} \tag{2.8}$$

$$J_i^\eta \equiv \frac{1}{\rho_\eta P_\xi} \left[-\frac{\partial \rho_\eta P_\xi \left(\overline{N Y_i|\eta} - \overline{N|\eta}\ \overline{Y_i|\eta} \right)}{\partial \eta} + 2 \left(\overline{D \nabla Y_i \cdot \nabla \xi|\eta} - \overline{N|\eta} \frac{\partial \overline{Y_i|\eta}}{\partial \eta} \right) \right] \tag{2.9}$$

$$M_i \equiv \frac{1}{\rho_\eta P_\xi} \left[-\frac{\partial \nabla \cdot (\rho_\eta P_\xi \overline{Y_i D \nabla \xi|\eta})}{\partial \eta} + \nabla \cdot (\rho_\eta P_\xi \overline{D \nabla Y_i|\eta}) \right]. \tag{2.10}$$

The conditionally filtered equations for other reactive scalars can be obtained by the same procedure.

2.3. *Primary closures*

F_i represents the subgrid transport of reactive scalars in ($\mathbf{x}$,η) space: $J_i^{\mathbf{x}}$ for $\mathbf{x}$ space and J_i^{η} for η space. It plays an important role in reignition of locally extinguished flames and stablization of lifted diffusion flames. Extinguished flames are reignited through transfer of heat and species from burning flames. Reignition may occur by the edge flame propagation along iso-surfaces of the mixture fraction and also by diffusion normal to the iso-η surfaces following flame folding (Sripakagorn *et al.* 2004). These interactions between neighboring flames are represented by F_i in the conditionally filtered equation. When we assume that flame propagation along the isopleth is the most important mechanism for reignition and flame stablization, F_i can be approximated as

$$F_i \approx -\frac{1}{\rho_\eta P_\xi}\nabla\cdot(\rho_\eta P_\xi J_i^{\mathbf{x}}). \tag{2.11}$$

Next we are concerned with the closure of M_i. It can be easily shown that

$$\nabla\cdot[\rho D\nabla(\delta_\eta Y_i)] = -\frac{\partial\nabla\cdot(\rho\delta_\eta D\nabla Y_i)}{\partial\eta} + \nabla\cdot(\delta_\eta\rho D\nabla Y_i). \tag{2.12}$$

When the density and the molecular diffusivity are constant, we have

$$\nabla\cdot[\rho D\nabla(P_\xi\overline{Y_i|\eta})] = -\frac{\partial\nabla\cdot(\rho P_\xi D\overline{\nabla Y_i|\eta})}{\partial\eta} + \nabla\cdot(P_\xi\rho D\overline{\nabla Y_i|\eta}). \tag{2.13}$$

The term, M_i, therefore, represents the molecular transport of $\overline{Y_i|\eta}$ on iso-η surfaces. The molecular transport is much smaller than the turbulent transport and usually neglected in RANS of high Reynolds number flows. However, in LES, the molecular transport term can be of the same order as the unresolved subgrid one. Based on Eq. (2.13) we propose the following closure for M_i:

$$M_i \approx \nabla\cdot[\rho_\eta D_\eta\nabla(P_\xi\overline{Y_i|\eta})], \tag{2.14}$$

where $D_\eta \equiv \overline{D|\eta}$.

2.4. *Closure of chemical reaction rates*

In turbulent nonpremixed flames, fluctuations of reactive scalars are primarily associated with those of the mixture fraction. However, fluctuations of reactive scalars on iso-η surfaces, which are much smaller than those in $\mathbf{x}$ space, can be significant when turbulent time scales are of the order of chemical ones. Assuming that fluctuations on iso-η surfaces occur on the large scales, the conditionally filtered reaction rate can be calculated as

$$\overline{\omega_i(\rho,\mathbf{Y},T)|\eta} \approx \omega_i(\rho_\eta,\overline{\mathbf{Y}|\eta},\overline{T|\eta}). \tag{2.15}$$

2.5. *Integrated conditional filtering for a reacting shear layer*

The conditionally filtered quantity may not be properly evaluated with negligible subgrid scale probability. For example, when we take measurements at the locations far from the axis of a turbulent jet diffusion flame, we seldom observe mixtures with $\xi \approx 1$ and have difficulty in evaluating conditionally filtered quantities at $\eta \approx 1$. The conditionally filtered equation is valid over the whole flow field but becomes trivial when P_ξ is negligible. It is physically meaningful in a small volume in the four-dimensional probability space,

Case	Da	q	l/u'	l/l_K	Δ/l_K	Re_λ	Grid
H1	2.52E+4	$\alpha c_p T_0$	1.03	27.1	1.37	47	192×128×128
H2	7.57E+4	$\alpha c_p T_0$	1.03	27.1	1.37	47	192×128×128
H3	1.51E+5	$\alpha c_p T_0$	1.03	27.1	1.37	47	192×128×128
C1	2.06E+3	0	1.03	27.1	1.37	47	192×128×128
C2	4.0E+3	0	0.80	50.2	1.72	73.5	256×256×256

TABLE 1. Characteristics of the simulations (l: integral length scale, l_K: Kolmogorov length scale, u': r.m.s. velocity, Δ: grid spacing, Re_λ: Taylor scale Reynolds number, $Da \equiv A\rho_0 l/u'$, ρ_0: reference density)

$(\mathbf{x}, \eta)$, where P_ξ is not negligible. Here, integrated conditional filtering is introduced as an alternative for Eq. (2.1), which is computationally less expensive and solves the low probability problem:

$$\overline{\phi|\eta}^*(\eta, x_2, x_3, t) \equiv \frac{\int_{-\infty}^{\infty} w \int_V \phi(\mathbf{x},t)\delta(\xi(\mathbf{x},t)-\eta)G(\mathbf{x}-\mathbf{x}';\Delta_f)d\mathbf{x}'dx_1}{\int_{-\infty}^{\infty} w \int_V \delta(\xi(\mathbf{x},t)-\eta)G(\mathbf{x}-\mathbf{x}';\Delta_f)d\mathbf{x}'dx_1}, \tag{2.16}$$

where $\mathbf{x} = (x_1, x_2, x_3)$. w is the weighting factor that depends on the coordinate system. The integration direction depends on the case, but should go through the flame brush. In a round jet flame $x_1 = w = r$, where r is the radial coordinate. The equation for $\overline{Y_i|\eta}^*$ can be written as

$$\begin{aligned}\frac{\partial \rho_\eta^* P_\xi^* \overline{Y_i|\eta}^*}{\partial t} &+ \nabla\cdot(\rho_\eta^* P_\xi^* \overline{\mathbf{v}|\eta}^* \overline{Y_i|\eta}^*) \\ &= \rho_\eta^* P_\xi^* \overline{\omega_i|\eta}^* - \frac{\partial^2 \rho_\eta^* P_\xi^* \overline{N|\eta}^* \overline{Y_i|\eta}^*}{\partial \eta^2} \\ &+ 2\frac{\partial}{\partial\eta}\left(\rho_\eta^* P_\xi^* \overline{N|\eta}^* \frac{\partial \overline{Y_i|\eta}^*}{\partial\eta}\right) + \rho_\eta^* P_\xi^* F_i^* + \rho_\eta^* P_\xi^* M_i^*,\end{aligned} \tag{2.17}$$

where the superscript, $*$, represents the integrated quantity. This is the conservative form of the conditionally filtered species equation. Using the equation for P_ξ^* we obtain

$$\frac{\partial \overline{Y_i|\eta}^*}{\partial t} + \overline{\mathbf{v}|\eta}^* \cdot \nabla \overline{Y_i|\eta}^* = \overline{N|\eta}^* \frac{\partial^2 \overline{Y_i|\eta}^*}{\partial \eta^2} + \overline{\omega_i|\eta}^* + F_i^* + \nabla\cdot(D_\eta^* \nabla \overline{Y_i|\eta}^*), \tag{2.18}$$

where $\rho_\eta^* P_\xi^*$ is assumed to have a weak spatial dependence. This equation has a similar form to the Eulerian laminar flamelet model of Pitsch (2002), but includes the subgrid transport term, F_i^*, and the molecular transport term, which are neglected in the Eulerian flamelet model. Closure of F_i^* will be addressed in a subsequent section.

3. Direct numerical simulation

DNS was performed to validate the present formulation. The simulated flow field is a shear-free, temporally developing mixing layer. Initially separated fuel and oxidizer mix in the presence of decaying turbulence, and react according to a single-step reaction:

$$F + O \rightarrow 2P$$

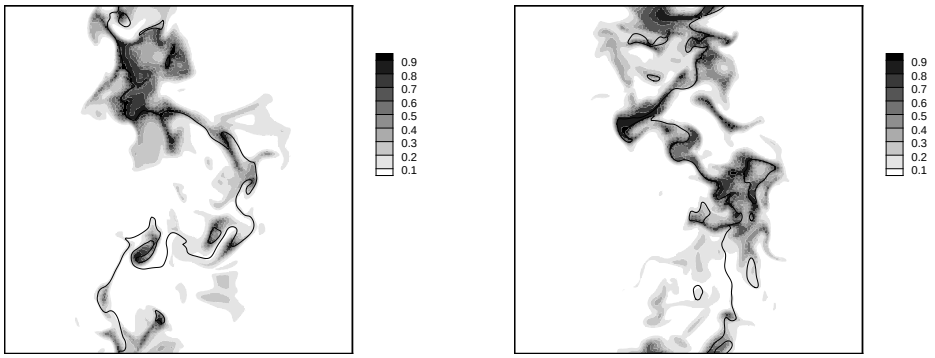

FIGURE 1. Instantaneous fields of the product mass fraction on two $x_1 - x_2$ planes for C2 (The line represents the stoichiometric surface).

where F, O and P represent fuel, oxidant and product, respectively. The stoichiometric mixture fraction is 0.5 and the reaction rate is given by

$$\omega = A\rho Y_F Y_O \exp\left(-\frac{\beta}{(1+\alpha\theta)}\right) \tag{3.1}$$

where Y_F and Y_O represent the mass fractions of fuel and of oxidizer, respectively. $\theta \equiv (T - T_0)/(T_f - T_0)$ is the nondimensional temperature, where T_f and T_0 represent the adiabatic flame temperature and reference temperature, respectively. The heat release parameter, $\alpha \equiv T_f/T_0 - 1$, is given by $q/(c_p T_0)$, where q and c_p are heat release per unit mass and the specific heat at constant pressure, respectively. $\beta \equiv T_a/T_0$ is the nondimensional activation temperature, where T_a is the activation temperature. Chemical parameters used here are α=6 and β=28. The pre-exponential factor, A, is adjusted to control the level of local extinction.

The fully compressible Navier-Stokes equations are solved with the conservation equations of the mass fractions of the fuel and the oxidizer. A low storage fourth-order Runge-Kutta method is used for time integration, while spatial derivatives are evaluated with a sixth-order compact finite difference scheme (Kennedy *et al.* 2000; Lele 1992). The computation domain is periodic in the x_2 and x_3 directions, while it has nonreflecting boundaries in the x_1-direction (Poinsot & Lele 1992). Table 1 shows characteristics of the simulations. The initial Mach number based on the r.m.s. velocity fluctuations and the temperature of fuel and oxidizer is below 0.1 for all the cases, so that compressibility effects are negligible. The nondimensional temperature, θ, is set to be the product mass fraction for the constant density cases, C1 and C2. The dynamic viscosity is a constant for the given case here. C1, C2 and H2 have a similar level of local extinction. The level of local extinction for H3 is lower than that for H2 , while that for H1 is more significant.

4. Results and discussion

Figure 1 shows the instantaneous fields of the product mass fraction on an $x_1 - x_2$ plane for the case, C2, at $\tau \approx 2$, where the nondimensional time, τ, is normalized by the initial eddy turn over time. There is significant local extinction in Fig. 2. The extinguished part

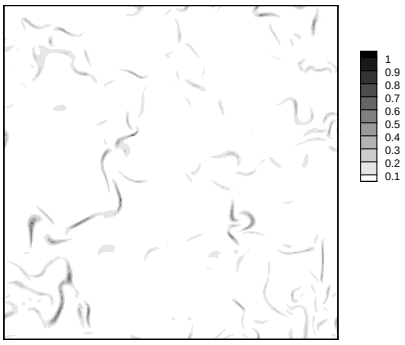

FIGURE 2. Distribution of the scalar dissipation rate on an $x_2 - x_3$ plane for C2.

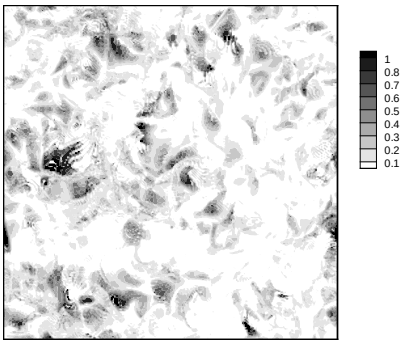

FIGURE 3. Distribution of the scalar dissipation rate averaged in the x_1-direction with the condition of $0.4 < \xi < 0.6$ for C2.

of the flame surface is of large scale and is not much distorted by small scale eddies, indicating that extinction processes are dominated by large scale structures in this case. The product concentration is high near a vortex core where the scalar dissipation is low. Note that the variation of Y_P along the stoichiometric surface is significant near the vortex core. Rolling up of the flame surface makes extinguished and burning flames be closer around the vortex core.

The underlying assumption of the conditional filtering method is that fluctuations of reactive scalars on iso-surfaces of the mixture fraction are primarily due to large scale fluctuations of the scalar dissipation rate. The justification of this assumption has been discussed in Pitsch (2002). For a further validation, we need to investigate the length scales of scalar dissipation fluctuations on iso-η surfaces. Figure 2 shows the distribution of the scalar dissipation rate in an x_2-x_3 plane for the case, C2, at $\tau \approx 2$. High scalar dissipation rates are associated with thin sheet-like structures in Fig. 2. The length scales of scalar dissipation rate across flames are much smaller than those along flame surfaces. Figure 3 shows the distribution of the integrated scalar dissipation rates on the stoichiometric surfaces for C2. Scalar dissipation rates for $0.4 < \xi < 0.6$ are averaged in the x_1-direction. Note that the structures with high scalar dissipation rates have a range of length scales and that higher scalar dissipation rates are associated with large scale structures. Nonpremixed flames are sensitive to the spatial and temporal fluctuations of the scalar dissipation rate. With excessive scalar dissipation rate, nonpremixed flames may be locally extinguished and flame holes appear. Capturing high scalar dissipation events is crucial to predict the extinction process. Although high scalar dissipation rates are concentrated in a very small fraction of the fluid, these are mainly associated with counter-flowing large scale structures that carry high and low values of the scalar (Warhaft 2000; Shriman & Siggia 2000). The major part of high scalar dissipation events can, therefore, be captured from a resolved large scale field, while filtering smoothes out highest scalar dissipation events.

Figure 4(a) shows the conditionally filtered reaction rates, $\overline{\omega|\eta_{st}}$, for H2 at $\tau \approx 2$, where the subscript, st, denotes stoichiometric conditions. A top hat filter with a filter width of $\Delta_f = 8\Delta$ was used. The predicted reaction rates are in excellent agreement with the filtered DNS data in Fig. 4(a), while they are slightly overpredicted for a small

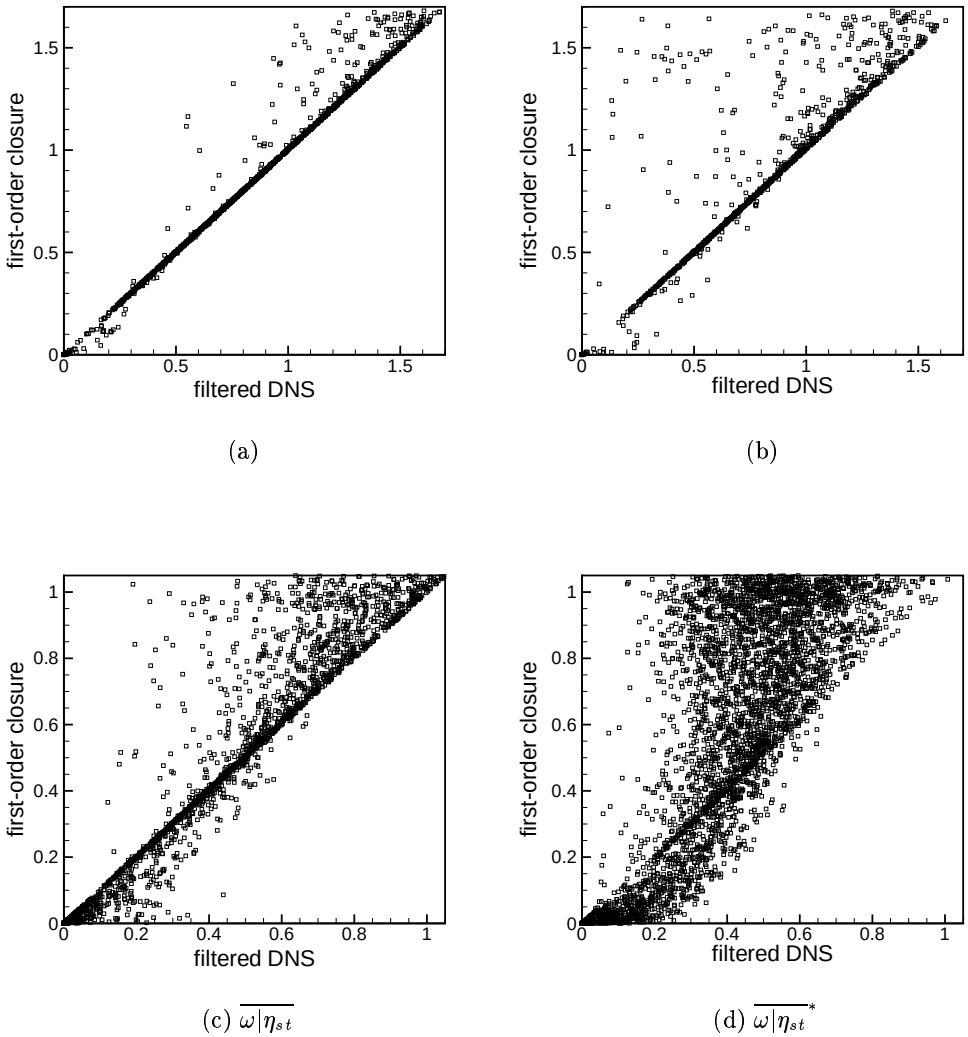

FIGURE 4. Correlation for conditionally filtered reaction rates at the stoichiometric mixture fraction (a) $\overline{\omega|\eta_{st}}$ for H2 (b) $\overline{\omega|\eta_{st}}^{*}$ for H2 (c) $\overline{\omega|\eta_{st}}$ for C2 (d) $\overline{\omega|\eta_{st}}^{*}$ for C2. ($\Delta_f/\Delta = 8$)

fraction of points with higher reaction rates. The overprediction of the reaction rates occurs in the region close to interface between burning and extinguished flames. In that region the conditional subgrid fluctuations of reactive scalars are large enough for the higher order correlations to be nonnegligible. The first-order closure tends to overpredict the reaction rates when the reactive scalars fluctuate near the maximum reaction rate. Figure 4(b) shows the integrated reaction rate, $\overline{\omega|\eta_{st}}^{*}$, for H2. The overall agreement is similar to that for $\overline{\omega|\eta_{st}}$. Figure 4(c) shows the conditionally filtered reaction rates, $\overline{\omega|\eta_{st}}$, for C2 at $\tau \approx 2$. The prediction is well correlated with the filtered DNS, while it is more scattered than in H2. Here, in addition to the overprediction at higher reaction rates,

Δ_f/Δ	4	8	12	16	24
H1	0.9995	0.9955	0.9868	0.9728	0.9426
H2	0.9983	0.9881	0.9550	0.9313	0.8361
H3	0.9979	0.9880	0.9723	0.9461	0.8730
C1	0.9986	0.9905	0.9765	0.9606	0.9247
Δ_f/Δ	4	8	16	32	48
C2	0.9909	0.9552	0.8871	0.7940	0.7367

TABLE 2. Correlation coefficients for $\overline{\omega|\eta_{st}}$

Δ_f/Δ	4	8	12	16	24
H1	0.9695	0.9486	0.9324	0.9132	0.8819
H2	0.9371	0.8739	0.8325	0.6928	0.5164
H3	0.9801	0.9229	0.8621	0.7933	0.6952
C1	0.9480	0.9182	0.9014	0.8744	0.8467
Δ_f/Δ	4	8	16	32	48
C2	0.8345	0.8098	0.7978	0.7785	0.7476

TABLE 3. Correlation coefficients for $\overline{\omega|\eta_{st}}^*$

the reaction rates are underpredicted at lower reaction rates. In Fig. 4(d) the accuracy of the integrated reaction rate for C2 is not as good as for H2.

The correlation coefficients between the filtered DNS data and the model prediction for all the test cases are shown in Table 2:

$$C = \frac{\langle \overline{\omega|\eta_{st}}\ \omega(\overline{\mathbf{Y}|\eta_{st}}, \overline{T|\eta_{st}})\rangle - \langle \overline{\omega|\eta_{st}}\rangle \langle \omega(\overline{\mathbf{Y}|\eta_{st}}, \overline{T|\eta_{st}})\rangle}{\sqrt{(\langle \overline{\omega|\eta_{st}}^2\rangle - \langle \overline{\omega|\eta_{st}}\rangle^2)(\langle \omega(\overline{\mathbf{Y}|\eta_{st}}, \overline{T|\eta_{st}})^2\rangle - \langle \omega(\overline{\mathbf{Y}|\eta_{st}}, \overline{T|\eta_{st}})\rangle^2)}} \tag{4.1}$$

The correlation coefficients are above 0.9 except for C2, when the filter width, Δ_f, is smaller than the integral length scale, l. For C2 the correlation coefficient remains about 0.9 when $\Delta_f < 0.5l$. Accuracy of the first-order closure is not much affected by the level of local extinction. Note that the correlation coefficient decreases slowly with Δ_f. This implies that the grid spacing for conditionally filtered equations can be larger than that for the flow field, which significantly reduces the computational cost for solving the conditionally filtered equations. Table 3 shows the correlation coefficients for $\overline{\omega|\eta_{st}}^*$. The integration direction is x_1 and $w = 1$. The correlation coefficients remains about 0.8 when $l/\Delta_f < 0.5$, which are lower than those for $\overline{\omega|\eta_{st}}$. Due to the integration, $\overline{\omega|\eta}^*$ contains the contribution of the subgrid fluctuations along the x_1-direction. The subgrid fluctuations along the x_1-direction are more significant for C2, which has higher Reynolds number.

Conditional filtering adds a new independent variable in the system of equations, which substantially increases the computational cost. However, the computational cost can be reduced when the characteristics of the conditionally filtered equation are properly considered. $P_\xi(\eta_{st})$ has a very narrow distribution as compared with the thickness of the mixing layer as in Fig. 1. Since all the terms in the conservative form of the conditionally filtered equations are weighted by P_ξ, only a small region of $(\mathbf{x}, \eta)$ space is *active*. We do not need to solve the equations in the region where P_ξ is negligible. In addition, according

to the results in Table 2, the filter width for the conditionally filtered equations can be larger than that for the flow field. Another way to reduce the computational cost is the integrated conditional filtering approach. In this approach, the number of independent variables is reduced by one due to integration in one spatial coordinate.

The integrated conditional filtering equation, Eq. (2.18), is solved to validate the performance of the model. $\overline{N|\eta}^*$ and $\overline{\mathbf{v}|\eta}^*$ are taken from the DNS data to avoid ambiguity in the modeling of the flow and mixing field. The conditional subgrid scale flux, $J_i^{\mathbf{x}*}$, is modeled by an eddy diffusivity model:

$$J_i^{\mathbf{x}*} \approx -D_t \nabla \overline{Y_i|\eta}^* \tag{4.2}$$

where D_t is given by

$$D_t = c_q \Delta_f^2 \sqrt{2\overline{S}_{ij}^* \overline{S}_{ij}^*}. \tag{4.3}$$

$\overline{S}_{ij}$ is the filtered strain rate tensor. Although a dynamic model could be used to determine the value of c_q, a constant value of $c_q = 0.1$ has been used here. Because $\rho_\eta^* P_\xi^*$ has a weak spatial dependence, F_i^* can be approximated as

$$F_i^* \approx \nabla \cdot (D_t \nabla \overline{Y_i|\eta}^*). \tag{4.4}$$

The filter width is taken as $\Delta_f = 8\Delta$. The physical domain is discretized into 32×32 grid points, while 50 grid points are used in mixture fraction space.

The spatial distributions of $\overline{Y_P|\eta_{st}}^*$ at $\tau \approx 2$ are shown in Fig. 5. The present method predicts the location and size of flame holes for H1 with good accuracy, while the minimum of $\overline{Y_P|\eta_{st}}^*$ in the flame holes is overpredicted due to the filtering. Flame holes with large length scales are also well predicted for C2.

The variation of the conditional average in a transverse direction is small in a turbulent shear layer (Klimenko 1995). *A priori* tests show that the variation of the conditionally filtered quantity is not as small as that of the conditional average. As shown in Fig. 2, due to the folding of the flame surface, burning and extinguished flamelets can coexist in the integration direction. The averages have then contributions from the flames with different strain rate history, which causes errors in the integrated approach. The variation of the conditional average is not significant because flame surfaces fluctuate in the shear layer.

Although the present method underpredicts large excursions of a reactive scalar from the conditionally filtered value, it can reproduce the major part of extinction processes, which are associated with large scale structures. Pitsch (2002) showed in LES of a turbulent methane/air jet flame that the prediction of pollutant formation can be improved by considering large scale fluctuations of the scalar dissipation rate. The subgrid fluctuations of scalar dissipation could be considered by second-order closure of conditionally filtered reaction rates (Klimenko & Bilger 1999; Kim *et al.* 2002; Kim & Huh 2004).

5. Conclusions

The conditional filtering method is proposed as a subgrid combustion model in LES of turbulent nonpremixed combustion. Filtering conditioned on iso-surfaces of the mixture fraction is adopted to resolve small scale mixing and chemical reactions in nonpremixed combustion. The conditionally filtered equation is derived and *a priori* tests are performed to validate the closure assumptions and the model performance.

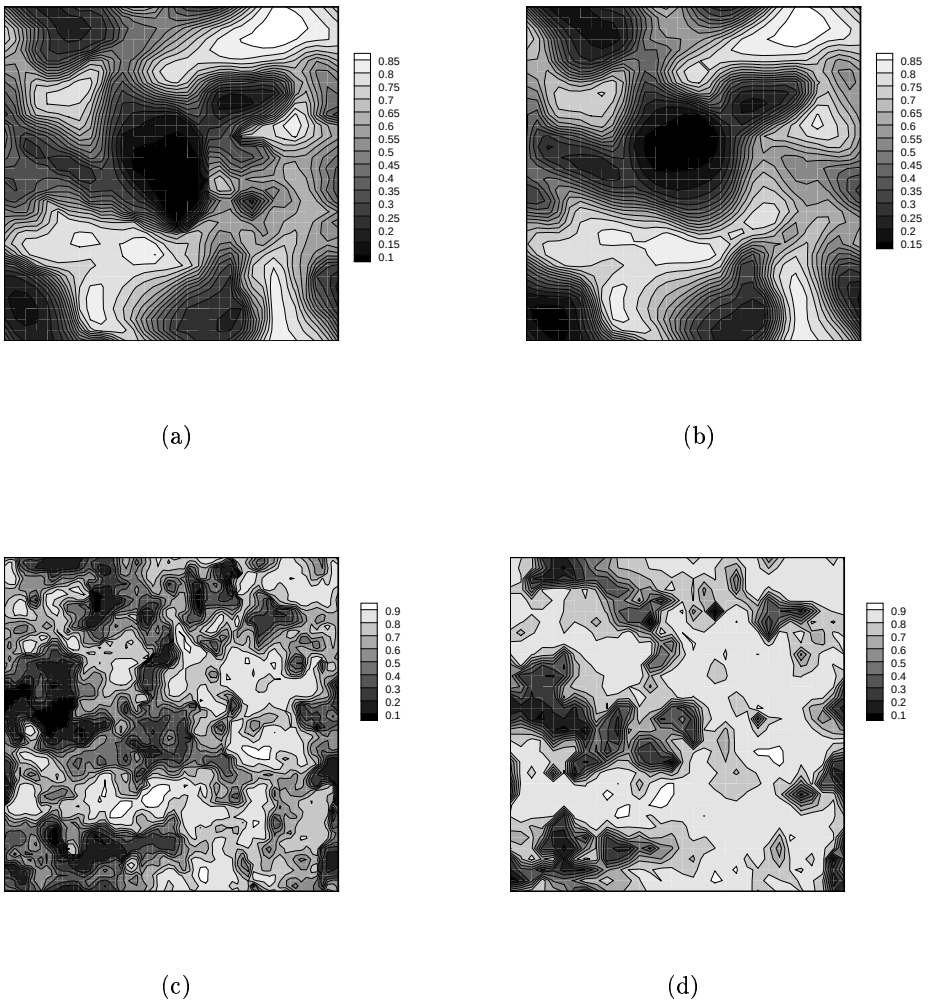

FIGURE 5. Distribution of conditionally filtered mass fraction of product at the stoichiometric mixture fraction: (a) filtered DNS data for H1 (b) conditional filtering method for H1 (c) filtered DNS data for C2 (d) conditional filtering method for C2.

The first-order closure of the reaction rate performs well when the filter width is less than half the integral length scale in the present cases. The effects of the subgrid fluctuations become more important as the filter width increases. Accuracy of the first-order closure is not sensitive to the level of local extinction in contrast to first-order CMC for RANS. The integrated conditional filtering approach is introduced to reduce the computational cost and to resolve the low probability problem in the conditional filtering method. While the assumption of homogenity in the integration direction is not as good as in the conditional average, the integrated formulation is shown to well represent the extinction process caused by large scale fluctuations of the scalar dissipation rate.

REFERENCES

BILGER, R. W. 1980 *Turbulent Reacting Flows* (Libby, P. A., Williams, F. A. Ed.), Springer-Verlag, Berlin, pp.65-113.

BILGER R. W. 1993 Conditional moment closure for turbulent reacting flow. *Phys. Fluids* **A5** 436-444.

BUSHE, W. K. & STEINER, H. 1999 Conditional moment closure for large eddy simulation of nonpremixed turbulent reacting flows. *Phys. Fluids* **11**, 1896-1906.

CHA, C. M. & PITSCH, H. 2002 Higher-order conditional moment closure modelling of local extinction and reignition in turbulent combustion. *Combust. Theory Modelling* **6**, 425-437.

JABERI, F. A., COLUCCI, P. J., JAMES, S., GIVI, P. & POPE, S. B. 1999 Filtered mass density function for large-eddy simulation of turbulent reacting flows. *J. Fluid. Mech.* **401**, 85.

KENNEDY, C. A., CARPENTER, M. H. & LEWIS, R. M. 2000 Low-storage, explicit Runge-Kutta schemes for the compressible Navier-Stokes equations. *Appl. Nume. Math.* **35**, 177.

KERSTEIN, A. R. 1992 Linear eddy model of turbulent transport, Part 7. Finite rate chemistry and multi stream mixing. *J. Fluid Mech.* **240**, 289.

KIM, S. H., HUH, K. Y. & LIU, T. 2000 Application of the elliptic conditional moment closure model to a two-dimensional nonpremixed methanol bluff-body flame. *Combust. Flame* **120**, 75-90.

KIM, S. H., HUH, K. Y. & BILGER, R. W. 2002 Second-order conditional moment closure modelling of local extinction and reignition in turbulent nonpremixed hydrocarbon flames.*Proc. Combust. Inst.* **29**, 2131.

KIM, S. H. & HUH, K. Y. 2004 Second-order conditional moment closure modelling of turbulent piloted jet diffusion flames. *Combust. Flame* **138**, 336-352.

KLIMENKO, Y. 1990 Multicomponent diffusion of various admixtures in turbulent flow. *Fluid Dynamics*, **25**, 327-334.

KLIMENKO, Y. 1995 Note on the conditional moment closure in turbulent shear flows. *Phys. Fluids* **7(2)** 446-448.

KLIMENKO, A. Y. & BILGER, R. W. 1999 Conditional moment closure for turbulent combustion. *Prog. Energy Combust. Sci.* **25** 595.

KRONENBERG, A. 2004 Double conditioning of reactive scalar transport equations in turbulent nonpremixed flames. *Phys. Fluids* **16** 2640-2648.

LELE, S. K. 1992 Compact finite difference schemes with spectral-like resolution. *J. Comp. Phys.* **103**, 16.

MENEVEAU, C. & KATZ, J. 2000 Scale-invariance and turbulence models for large eddy simulation. *Annu. Rev. Fluid Mech.* **32**, 1.

PIERCE, C. D. & MOIN, P. 2004 Progress-variable approach for large-eddy simulation of non-premixed turbulent coombustion *J. Fluid Mech.* **504** 73.

PITSCH, H. 2002 Improved pollutant predictions in large-eddy simulation of turbulent nonpremixed combustion by considering scalar dissipation fluctuations *Proc. Combust. Inst.* **29** 1971.

POINSOT, T. J. & LELE, S. K. 1992 Boundary conditions for direct numerical simulations of compressible viscous flows.*J. Comp. Phys.* **101** 104.

SHRIMAN, B. I. & SIGGIA, E. D. 2000 Scalar turbulence. *Nature(London)* **405** 639.

SMITH, N. S. A., BILGER, R. W., CARTER, R. D., BARLOW, R. S. & CHEN, J. Y. 1995 A comparison of CMC and PDF modelling predictions with experimental nitric oxide LIF/Raman measurements in a turbulent H_2 jet flame. *Combust. Sci. Tech.* **105** 357-375.

SRIPAKAGORN, P., MITARAI, S., KOSALY, G. & PITSCH, H. 2004 Extinction and reignition in a diffusion flame: a direct numerical study *J. FLuid Mech.* bf 518 231-259.

WARHAFT, Z. 2000 Passive scalars in turbulent flows.*Annu. Rev. Fluid Mech.* **32** 203.

DNS of lean premixed turbulent spherical flames with a Flamelet Generated Manifold

By R. J. M. Bastiaans, J. A. van Oijen†, S. M. Martin, L. P. H. de Goey† AND H. Pitsch

1. Motivation and objectives

The present research is concerned with the direct numerical simulation (DNS) and analysis of turbulent propagation of premixed flame kernels. The simulations are direct in the sense that the smallest scales of motion are fully resolved, while the chemical kinetics are solved in advance and parameterized in a table by the method of the flamelet generated manifolds (FGM) (Van Oijen 2002). The state of the reactions are assumed to be directly linked to a single progress variable. The conservation equation for this progress variable is solved using DNS, with the unclosed terms coming from the table. This allows the use of detailed chemical kinetics without having to solve the individual species conservation equations.

Turbulent premixed combustion of gaseous fuels is one of the most important energy conversion processes today, but its physics are not fully understood (e.g. Driscoll 2003). On the one hand a detailed knowledge is required to understand the behavior of the conversion process and the efficiency and formation of pollutants. On the other hand this insight is needed to obtain the parameterizations that are essential in developing accurate models for large scale simulations. One of the most important processes to understand is the physics of turbulent flame wrinkling. Flame wrinkling is very important because it determines both the total flame surface area as well as the local modulation of the mass burning rate.

Here a lean premixed turbulent expanding flame kernel is studied. Lean premixed combustion is becoming the method of choice for ground based gas turbine combustors due to several advantages. The high percentage of air results in complete combustion, reducing emissions of hydrocarbons and carbon monoxide. The excess air also results in lower combustion temperatures and as a consequence low emissions of nitrogen oxides. Therefore, significant research on turbulent premixed combustion has been performed under lean conditions. Some examples of these investigations are the experimental study of Shepherd *et al.* (2002) and the numerical study of Bell *et al.* (2002). The research of Shepherd *et al.* (2002) indicates that even when the smallest turbulent scales are smaller then the flame thickness there is no significant flame front broadening, i.e. combustion remains within the thin reaction fronts regime. This result is confirmed by an analysis of experimental low swirl burner results of De Goey *et al.* (2004). In the numerical experiments of Bell *et al.* (2002), which includes semi-detailed kinetics, it was concluded that flame wrinkling is the dominant factor for increasing the turbulent flame speed.

From a numerical point of view, the setup of a flame kernel is relatively straight forward. There are no walls and due to the expansion of the kernel itself, all boundaries are considered as outflow boundaries. The initial turbulence is decaying, as is the case in

† Combustion Technology, Eindhoven University of Technology, The Netherlands, www.combustion.tue.nl

most practical combustion applications. However, not many researchers have used flame kernels for the study of premixed turbulent combustion. Of particular interest is the research of Jenkins & Cant (2002), Gashi *et al.* (2004) and Thévenin (2004). The latter study is associated with rich flames, which are not addressed here. Jenkins & Cant (2002) studied the evolution of shape parameters in terms of flame normals and curvatures by means of DNS combined with single step chemistry. One of their conclusions is that at low turbulence intensities there is a tendency to favor spherical over cylindrical curvature. In the study of Gashi *et al.* (2004), the numerical simulations of Jenkins & Cant (2002) were extended and supplemented by experimental PLIF observations for both methane and hydrogen combustion at stoichiometric and lean conditions. The result of the study is a qualitatively good agreement between the simulations and experiments.

Combustion at lean premixed conditions, like in ground-based gas-turbines, predominantly takes place in the flamelet and thin-reaction zones regimes of premixed combustion using Peters (2000) definitions. Consequently, this is the starting point for the development of many models. Several flamelet based models have been developed for premixed combustion in the flamelet regime. The first and most well-known models were derived by assuming that the flame-front is infinitely thin (Bray & Moss 1977). An efficient flamelet model is based on the G-equation (Peters 2000). The G-equation is a kinematic equation which can be used to follow the average position, brush thickness and wrinkling of the flame front. Peters very recently extended the G-equation model for combustion in the thin-reaction zones regime. The model is efficient since it is not sensitive to the internal structure of the turbulent flame brush.

Flame stretch is an important parameter that is recognised to have a determining effect on the burning velocity in premixed flames. In the past this effect has not been taken into account in the flamelet approach for turbulent combustion in a satisfying manner. The laminar burning velocity, which is largely affected by stretch, is an important parameter for modelling turbulent combustion. Flame stretch is also responsible for the creation of flame surface area, affecting the consumption rate as well. In the turbulent case, stretch rates vary significantly in space and time. An expression for the stretch rate is derived directly from its mass-based definition by De Goey & Ten Thije Boonkkamp (1999),

$$K = \frac{1}{M}\frac{dM}{dt}, \tag{1.1}$$

where M is the amount of mass in an arbitrary control volume moving with the flame velocity:

$$M = \int_{V(t)} \rho dV. \tag{1.2}$$

On the basis of this definition, a model for the influence of stretch and curvature on the mass burning rate has been developed. In a numerical study by Groot & De Goey (2002), it was shown that this model, with a slight reformulation, shows good agreement with calculations for spherically expanding laminar flames. This formulation, for the ratio of the actual mass burning rate at the inner layer, m_{in}, relative to the unperturbed mass burning rate at the inner layer, m_{in}^0 (for unity Lewis numbers), reads

$$\frac{m_{\mathrm{in}}}{m_{\mathrm{in}}^0} = 1 - \mathit{Ka}_{\mathrm{in}}, \tag{1.3}$$

with the integral Karlovitz number being a function of flame stretch (Eq. 1.1), flame

surface area, σ, and a progress variable, $\mathcal{Y}$,

$$\mathit{Ka}_{\rm in} := \frac{1}{\sigma_{\rm in} m^0_{\rm in}} \left(\int_{s_u}^{s_b} \sigma \rho K \mathcal{Y} ds - \int_{s_{\rm in}}^{s_b} \sigma \rho K ds \right). \tag{1.4}$$

The integrals have to be taken over paths normal to the flame and s_u, s_b and $s_{\rm in}$ are the positions at the unburned side, the burned side and the inner layer, respectively. The flame surface area, σ, is related to the flame curvature, κ, which is related to the flame normals, n_i on the basis of the progress variable, $\mathcal{Y}$,

$$n_i = -\frac{\partial \mathcal{Y}/\partial x_i}{\sqrt{\partial \mathcal{Y}/\partial x_j \partial \mathcal{Y}/\partial x_j}}, \tag{1.5}$$

$$\kappa = \frac{\partial n_i}{\partial x_i} = -\frac{1}{\sigma}\frac{\partial \sigma}{\partial s}. \tag{1.6}$$

In turbulent premixed combustion the total fuel consumption is a result of the combined effect of flame surface increase and local modulation of the mass burning rate. In the present study the latter will be investigated on the basis of Eq. 1.3 and possible parameterizations thereof, i.e. models for the Karlovitz integral, Eq. 1.4.

2. Methodology

In this section the governing equations and the numerical treatment are presented. Followed by the construction of the initial fields.

2.1. *Numerical method*

Freely expanding flames are modelled in a turbulent flow field using DNS. More detailed information about the DNS program can be found in Bastiaans *et al.* (2001) and Groot (2003). The governing equations are,

$$\frac{\partial \rho}{\partial t} + \frac{\partial}{\partial x_i}(\rho u_i) = 0$$

$$\rho \frac{\partial u_j}{\partial t} + \rho u_i \frac{\partial u_j}{\partial x_i} = -\frac{\partial p}{\partial x_j} + \frac{\partial \sigma_{ij}}{\partial x_i}$$

$$\rho \bar{c}_v \frac{\partial T}{\partial t} + \rho u_i \bar{c}_v \frac{\partial T}{\partial x_i} = \frac{\partial}{\partial x_i}\left(\lambda \frac{\partial T}{\partial x_i}\right) - p\frac{\partial u_i}{\partial x_i} + \sigma_{ij}\frac{\partial u_i}{\partial x_j} +$$
$$\Sigma_\alpha \left[[R_\alpha T - h_\alpha]\,\dot{\rho}_\alpha + \rho R_\alpha T D_{\alpha m} \frac{\partial^2 Y_\alpha}{\partial x_i^2} + \frac{\partial Y_\alpha}{\partial x_i}\frac{\partial \rho R_\alpha T D_{\alpha m}}{\partial x_i} - \rho D_{\alpha m}\frac{\partial Y_\alpha}{\partial x_i}\frac{\partial\,[R_\alpha T - h_\alpha]}{\partial x_i}\right]$$

$$\rho \frac{\partial Y_\alpha}{\partial t} + \rho u_i \frac{\partial Y_\alpha}{\partial x_i} = \frac{\partial}{\partial x_i}\left(\frac{\lambda}{Le_\alpha \bar{c}_p}\frac{\partial Y_\alpha}{\partial x_i}\right) + \dot{\rho}_\alpha \tag{2.1}$$

with

$$\sigma_{ij} = \mu\left(\frac{\partial u_i}{\partial x_j} + \frac{\partial u_j}{\partial x_i} - \frac{2}{3}\delta_{ij}\frac{\partial u_k}{\partial x_k}\right); \qquad p = \rho R T. \tag{2.2}$$

The viscosity of the mixture is computed with Sutherland's law and the ratio of the thermal conductivity and the heat capacity at constant pressure (λ/c_p) is assumed to be a function of temperature only (Smooke & Giovangigli 1991). The species heat capacities are tabulated in polynomial form. Unity Lewis numbers are assumed for all species in order to prevent differential diffusion effects from obscuring the direct effects of stretch and curvature on the mass burning rate.

The equations are in fully compressible form and are solved in a three-dimensional cubic computational domain with a length of 12 mm and 254 grid points uniformly distributed in each direction. This gives a mesh size of approximately 0.0472 mm in each direction. For the spatial discretization of second derivatives, the sixth order accurate compact finite difference method of Lele (1992) is used. First order derivatives connected to advection are treated by a compact fifth order finite difference method, developed by De Lange (2004). The time integration is performed explicitly with a compact storage third-order Runge-Kutta method. A time step of order 10^{-8} is used to satisfy the stability criteria.

The boundary conditions are modelled with the Navier-Stokes Characteristic Boundary Conditions (NSCBC) of Poinsot & Lele (1992). The initial flame kernels are expanding at atmospheric conditions, which means that all boundaries of the cubic computational domain are modelled as outlet boundaries to prevent pressure build-up in the domain. Therefore, partially-reflecting outlet boundaries are required, imposing a fixed pressure far away.

To make the DNS computations affordable, the FGM method of Van Oijen (2002) is used to describe the reaction kinetics. FGM can be considered a combination of the flamelet approach and the intrinsic low-dimensional manifold (ILDM) method of Maas & Pope (1992) and is similar to the Flame Prolongation of ILDM (FPI) introduced by Gicquel *et al.* (2000). FGM is applied similarly to ILDM. However, the thermo-chemical data-base is not generated by applying the usual steady-state relations, but by solving a set of 1D convection-diffusion-reaction equations describing the internal flamelet structure. The main advantage of FGM is that diffusion processes, which are important near the interface between the preheat zone and the reaction layer, are taken into account. This leads to a very accurate method for (partially) premixed flames that uses fewer controlling variables than ILDM. The manifold used in this paper is based on the GRI3.0 kinetic mechanism with 53 species and 325 reversible reactions (Smith *et al.* 1999).

The mass fraction of carbon dioxide, which is monotonically increasing, is used as the single controlling variable (progress variable). Since pressure, enthalpy and element mass fractions are constant in these flames, they are not needed as additional controlling variables. A large portion of the terms and parameters in the governing equations, Eq. 2.1, are given by the manifold. These items include the source term for the progress variable, the source term for the temperature equation, which is given by all the terms in the summation over species (the large term in square brackets), the viscosity, conductivity, specific gas constant, the heat capacity at constant volume and the ratio of heat capacities.

2.2. *Initial conditions*

The initial conditions are a laminar spherical flame superimposed on a turbulent field. There is no forcing in the simulation, so the turbulence will decay in time. In order to select a physical condition to be considered one normally refers to a certain region of the premixed combustion regime diagram given by (Peters 2000) among others. Given a certain chemistry, the regime is given by the applied turbulence in terms of the amplitude

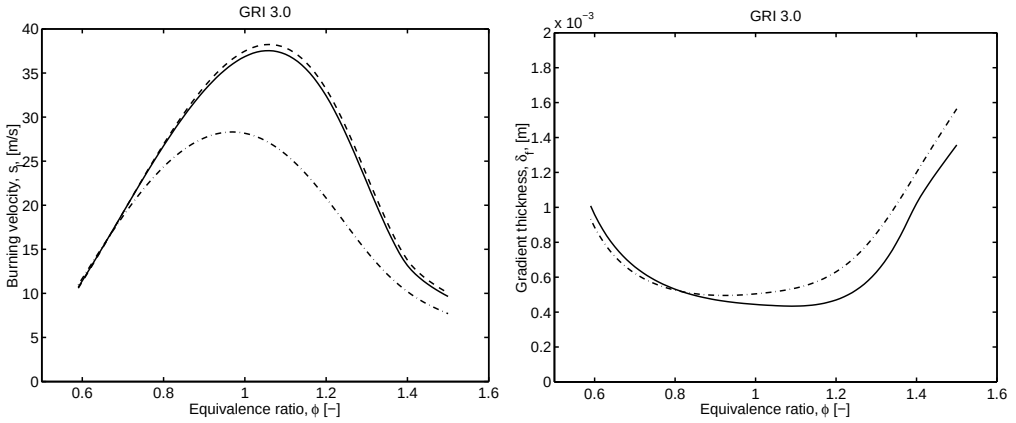

FIGURE 1. Burning velocity and flame gradient thickness from simulation of laminar methane air combustion as function of equivalence ratio based on GRI3.0 at 300 K and $1.013250{\cdot}10^5$ Pa. Left: Burning velocity using full GRI3.0 kinetics (drawn line), mixture average Lewis numbers approximation (dashed) and $Le_i = 1$ approximation (dash-dotted). Right: Flame gradient thickness, full GRI3.0 (drawn) and $Le_i = 1$ approximation (dash-dotted).

of the velocity fluctuations and the mean turbulent coherence length given by the Taylor integral scale. The procedure to initialize the turbulence starts with drawing random numbers for a stream function. This field is subsequently filtered multiple times by means of a top-hat filter. This results in a smooth field in which derivatives can be approximated with sufficient accuracy and a certain Taylor scale depending on the number of filter operations. It must be remarked that the number of filter operations generally is of the order of 100, so that the effective filter is an accurate approximation of a Gaussian. In order to keep disturbances away from the domain boundaries, the resulting field is windowed with a tanh function, decreasing from 1 to 0 at a diameter of 0.8 times the domain size and with a width of 0.05 times the domain size. Subsequently, derivatives are taken from the stream function to obtain the velocity components of a solenoidal field.

The chemistry is chosen due to the large interest in the power industry in lean premixed combustion engines and there is detailed knowledge of its chemical kinetics. Therefore premixed combustion of a methane/air mixture is used, with an equivalence ratio of $\phi = 0.7$. An additional advantage for lean methane chemistry is that the flame speed and the flame thickness are equal for the full GRI3.0 kinetics, and for the case in which these kinetics are used with a $Le_i = 1$ approximation (as can be observed from simulations using CHEM1D (2002), displayed in figure 1). We will use the $Le_i = 1$ approximation in the present study. The advantage is that the results will not be obscured by differential diffusion effects.

Our objective is to analyse the flame dynamics in a well defined and sufficiently resolved case. The most interesting region in the regime diagram with respect to the objective of the present study is the transition from the thin reaction zones regime towards the distributed reactions zone regime. It is expected that somewhere in this region the FGM method (as used in the present mode with only one progress variable, based on the ratio of the CO_2 mass fraction and its equilibrium value) loses its validity. In this study we will restrict ourselves to conditions where the use of just one progress variable is still a good assumption. Additionally, the simulations are constrained by geometrical and numerical conditions.

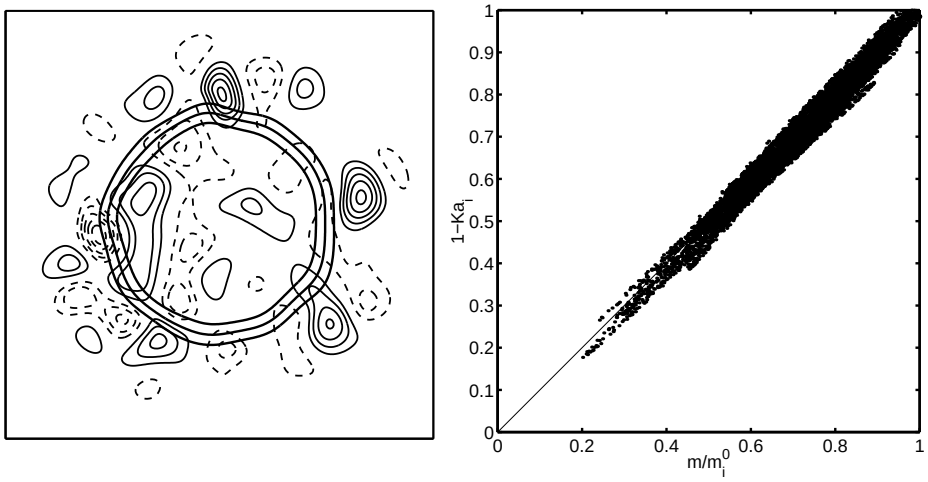

FIGURE 2. Case C1, left: Vorticity contours (positive and negative values indicated by solid and dashed lines, respectively) and progress variable (thick lines, values 0.2, 0.5, 0.8), right: Correlation of the actual mass burning rate with the basic model (result of 52000 flamelets found in the domain).

Since the domain size depends on the starting field of the controlling variable (progress variable), a relevant initial flame kernel must be chosen. For this reason and for comparison of turbulent results with a laminar undisturbed flame development, the evolution of the initial laminar spherical flame kernel is calculated with detailed chemistry as well. Again, the CHEM1D (2002) code was used, but now using spherical coordinates. The starting condition is a flat adiabatic flame at the same conditions, which is converted geometrically to a spherical flame with a very small radius. It is assumed that this kernel adjusts itself in time to a sort of self-similar laminar flame kernel.

3. Results

In this section the test cases are presented, followed by the flamelet analysis. The section closes with the presentation of results.

The first simulation, denoted C1, is a lean case with an equivalence ratio of $\phi = 0.7$, domain size of 12 mm, an initial flame kernel radius of approximately 2.9 mm, turbulent fluctuations of $u' = 0.4$ m/s and a turbulence length scale of ℓ_t=1.15 mm. In order to allow for very mild perturbations, initially we study the results at a time equal to 0.026τ, with $\tau = \ell_t/u' = 2.9ms$, taken from the start of the simulation. The time of growth of the laminar flame kernel to the initial DNS size was about 5 ms. The burning velocity of a flat unstretched flame with respect to the unburnt mixture is equal to $s_L^0 = 18.75$ cm/s and the corresponding mass burning rate is $m^0 = 0.213$ kg/m^{2}s. The progress variable is taken to be the carbon dioxide mass fraction, normalized with the maximum adiabatic value. At the left side of figure 2 is a cross section of the field. The contours of the progress variable are deformed only very mildly. It is observed that the scale of the vorticity patches are larger then the integral flame thickness. For this field the mass burning rate is analyzed as a reference case.

Additional analyses are performed in order to assess the basic model (Eq. 1.4) under varying physical conditions. The test cases are listed in table 1. In case C2, the effect of

Case	ϕ	u' $[m/s]$	ℓ_t $[mm]$	δ_f $[mm]$	L $[mm]$	r_{ini} $[mm]$	grid	$Re_t = u'\ell_t/s_L^0\delta_f$	tu'/ℓ_t
C1	0.7	0.40	1.15	0.614	12	2.9	254^3	4.0	0.026
C2	0.7	0.40	1.15	0.614	12	2.9	125^3	4.0	0.026
C3	1.0	0.60	0.89	0.475	12	2.9	254^3	4.0	0.026
C4	0.7	0.70	0.77	0.614	20	3.9	254^3	4.7	0.026
C5	0.7	1.31	0.94	0.614	12	2.9	254^3	10.7	0.026
C6	0.7	1.30	0.66	0.614	12	2.9	254^3	7.5	0.026

TABLE 1. Physical properties correspondig to the different simulations

grid resolution is investigated. It is assumed that the FGM method is valid in the flamelet regime if the progress variable is approximated with enough accuracy. Since all lengths scales of the gradients of primary variables (i.e. the variables that are solved in the present DNS calcualations) are of the same order, this will yield satisfactory solutions. In order to assess the influence of the chemistry a stoichiometric case, C3, is selected, in which the same ratio of the turbulent velocity fluctuations compared to the laminar flame speed, and the turbulent integral length scale compared to the initial flame thickness as used for cases C1 and C2. For the stoichiometric case at unity Lewis numbers the burning velocity is $s_L^0 = 28.17$ cm/s and the corresponding mass burning rate is $m^0 = 0.316$ kg/m^{2}s. An additional case is given by the simulation of an increased initial flame kernel in a larger domain, C4. Here also the effective resolution is decreased. In addition, cases are chosen with increased velocity fluctuations and decreased length scales, cases C5 and C6, respectively.

In the analysis, the stretch rate defined by,

$$\rho K = \frac{\partial}{\partial x_i}(\rho s_L n_i), \tag{3.1}$$

is evaluated by using the relation for the local burning velocity s_L,

$$s_L = \frac{\left(\frac{\partial}{\partial x_i}\left(\frac{\lambda}{Le\bar{c}_p}\frac{\partial \mathcal{Y}}{\partial x_i}\right) + \dot{\rho}\right)}{\left|\frac{\partial \mathcal{Y}}{\partial x_i}\right|}, \tag{3.2}$$

which is a consequence of the combination of the conservation equation for $\mathcal{Y}$ with the kinematic equation for $\mathcal{Y}$. The latter defines the flame speed u_{if} and then the relation for the flame velocity, $u_{if} = u_i + s_L n_i$, can be used to arrive at Eq. 3.2.

Now the actual mass burning rate can be compared to model-values. This is performed by looking for points in the domain that are close to the inner layer and interpolate from there in the direction of positive and negative gradient of the progress variable, with steps of 1/20 times the gridsize. All relevant variables are interpolated over these flamelets and these flamelets are analysed to determine the burning velocity of Eq. 3.2 and the model of the mass burning rate given by Eq. 1.4. For the present simulations these analyses lead to lots of starting points (e.g. for case C1: 52000) and thus resulting flamelets. For case C1 the correlation is depicted on the right side of figure 2. This shows that the model is a relatively accurate description of the actual mass burning rate. Deviations of the actual

Case	C1	C2	C3	C4	C5	C6
Mean	0.0072	0.0081	0.0075	0.0091	0.0107	0.0094
RMS	0.0215	0.0202	0.0216	0.0236	0.0336	0.0280

TABLE 2. Differences of the mass burning rate with the basic model.

mass burning rate compared to the model (Eq. 1.4) are given in table 2 for all six cases. It is seen that the mean error for all cases is about 0.01 or less, with a root mean square value of 0.02 to 0.03 (without normalization). It can be concluded that the model is a good description for all the present cases. Moreover, the grid coarsening shows no real deterioration, indicating that all cases are sufficiently resolved.

Starting from this point approximations to Eq. 1.4 can be considered. First, one can consider the case in which the surface area is taken to be constant, $\sigma = \sigma_{\text{in}}$ as used frequently in the literature,

$$\mathcal{K}a'_{\text{in}} := \frac{1}{m^0_{\text{in}}} \left(\int_{s_u}^{s_b} \rho K \mathcal{Y} ds - \int_{s_{\text{in}}}^{s_b} \rho K ds \right). \tag{3.3}$$

An improved model can be constructed by assuming that the curvature is not a function of the distance s, but that it remains constant equal to the inner layer value $\kappa = \kappa_{\text{in}}$. By integrating Eq. 1.6 this yields for the surface

$$\sigma = \exp\left(-\kappa_{\text{in}}(s - s_{\text{in}})\right). \tag{3.4}$$

A third approximation is that the iso-planes of the progress variable are concentric, either cylindrical or spherical yielding

$$\sigma = \left(\frac{\xi/\kappa_{\text{in}} - s}{\xi/\kappa_{\text{in}}} \right)^{\xi}, \tag{3.5}$$

in which ξ takes the value 2 for spherical curvature and 1 for cylindrical curvature. This has to be limited for distances s beyond the concentric origin, $s > \xi/\kappa_{\text{in}}$, at which $\sigma = 0$.

The result of the approximations are given in table 3 for all cases. It is observed that the constant flame surface conjecture gives rise to relatively large error. There is a systematic over-prediction of about 0.05 (without normalization) of the mass burning rate with this model and the fluctuations are of the same order of magnitude. The other approximations give much better results. For the mean differences the spherical approximation, $\xi = 2$, is superior compared to the cylindrical model, $\xi = 1$, and for most cases also compared to the constant curvature model. However, this is not really substantiated when looking at the accompanying fluctuations. For the better resolved cases, C1 and C3, the mean difference is best predicted by the $\xi = 2$ model, but again the accompanying fluctuations are much larger than the model deviation. This suggests that it is not a real improvement. With respect to the fluctuations it seems that constant curvature gives the smallest deviations. Additionally, it can be observed that the constant curvature estimation gives slight under-predictions, whereas the concentric cases give systematic increased values of the mass burning rate. Moreover it can be seen that the stoichiometric case (C3) gives

Case	C1	C2	C3	C4	C5	C6
$\sigma = \sigma_{\text{in}}$						
Mean	-0.0537	-0.0519	-0.0340	-0.0496	-0.0653	-0.0810
RMS	0.0552	0.0473	0.0373	0.0641	0.0772	0.1004
$\kappa = \kappa_{\text{in}}$						
Mean	0.0062	0.0055	0.0029	0.0026	0.0082	0.0079
RMS	0.0103	0.0085	0.0055	0.0173	0.0186	0.0338
$\xi = 2$						
Mean	-0.0011	-0.0006	-0.0007	-0.0075	-0.0037	-0.0141
RMS	0.0114	0.0101	0.0074	0.0313	0.0224	0.0540
$\xi = 1$						
Mean	-0.0059	-0.0050	-0.0032	-0.0115	-0.0101	-0.0219
RMS	0.0169	0.0142	0.0098	0.0333	0.0281	0.0556

TABLE 3. Differences of the mass burning rate determined by the basic model compared to the approximations.

the smallest deviations for any of the present approximations. This indicates that the choice of progress variable for the lean case might not be the best choice.

For closer inspection of all realizations in the field, case C6 is chosen in which the deviations are largest. Correlation plots are shown in figure 3. For this case the basic model does not deviate significantly from the results in figure 2, the only difference being that the range of values is extended more to the origin of the plot. Moreover some features, as indicated above, are clearly reflected like the under-prediction of the constant surface case. Furthermore the predictions of the concentric cases are less robust compared to the constant curvature model. The latter however gives deviations at small mass burning rates. This is also observed, to a lesser degree, in the concentric spherical approximation. Near the origin the cylindrical model seems to perform better. This is in agreement with observations of Jenkins & Cant (2002), who found that at higher turbulence levels, curvature in premixed turbulent combustion of flame kernels tends to cylindrical modes of deformation of the flame front.

It is obvious that all models do not fit to the true values because no local information on the flame geometry is taken into account in the approximations. If local geometric information is taken into account a much better agreement would be possible and will be a topic of further research. At larger times in the evolution, e.g. case C6, it was found that the basic model Eq. 1.4, gives good correlations (at $t = 0.087\tau$ mean deviation 0.08, rms values of 0.24), see figure 4, whereas all approximations are starting to deteriorate

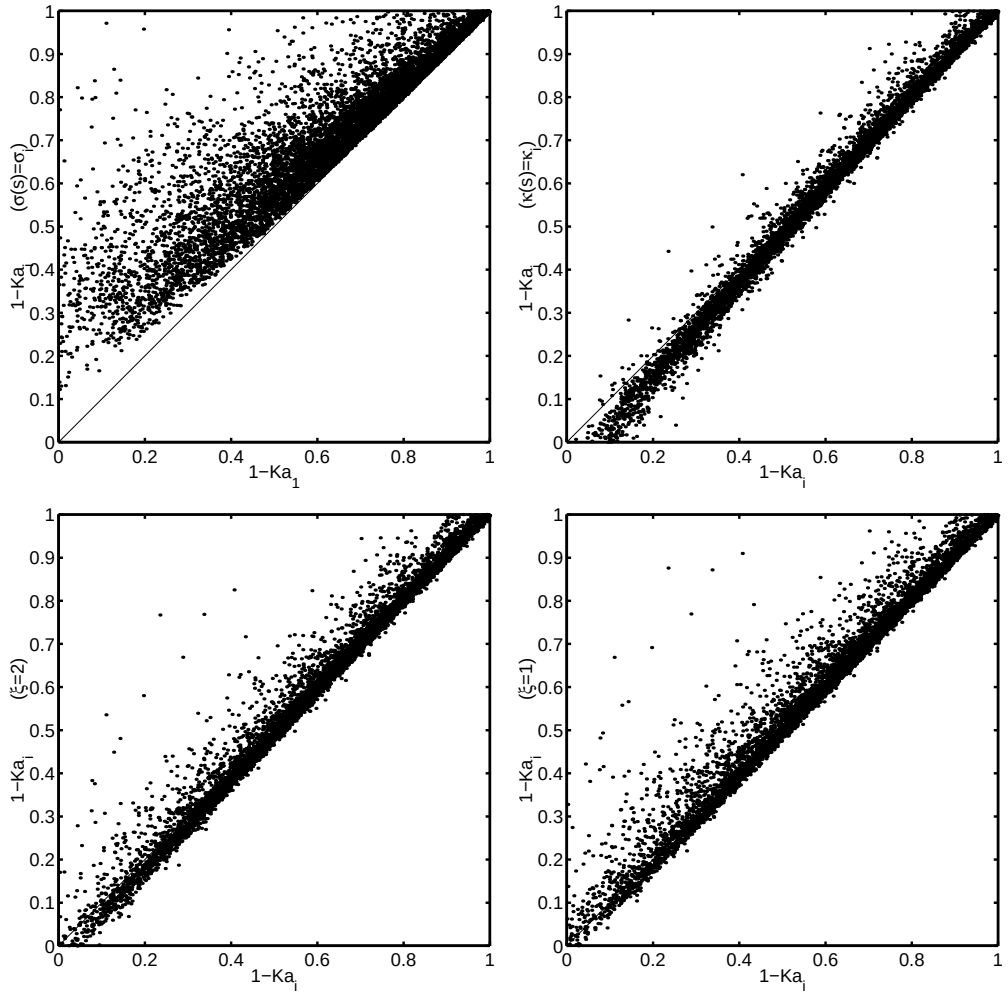

FIGURE 3. Case C6, Correlation of the actual mass burning rate with the approximations, top left: $\sigma = \sigma_{\rm in}$, top right: $\kappa = \kappa_{\rm in}$, bottom left: $\xi = 2$, bottom right: $\xi = 1$ (result of 60000 flamelets found in the domain).

severely. In this case the curvatures have large values, the associated values of radii are within the flame thickness, $\delta_{\rm f}$, as shown in the figure (at the right).

4. Future plans

From the previous results it can be concluded that the method of FGM in combination with DNS calculations looks very encouraging. It appears that the FGM is a promising technique to reduce the chemistry and obtain accurate results for the flow, thermodynamics and species. However, apart from a validation in terms of laminar burning velocity, a direct validation is not present for turbulent cases. With respect to this, more validation is needed and the strategy for this will be twofold. By applying a suitable kinetics model with a limited number of species, a DNS can be conducted. This system can be reduced and validated directly against the results of the detailed chemistry calculations. A sec-

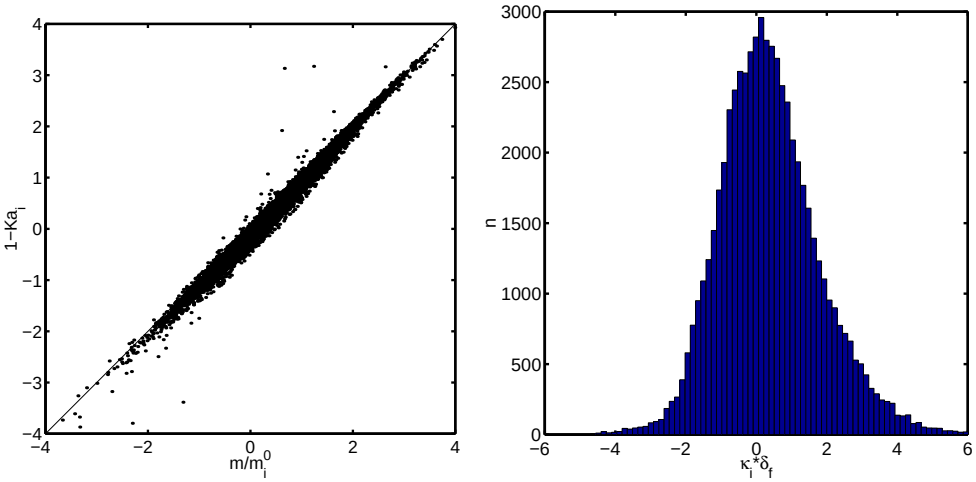

FIGURE 4. Results of case C6 at time $t = 0.087\tau$, left: correlation of the actual mass burning rate with the basic model, right: PDF of inner layer curvatures.

ond method is to increase the dimension of the manifold. It must be studied how many controlling variables are required for a certain accuracy of the predictions. This again can be performed in the framework of the previously mentioned full chemistry DNS.

REFERENCES

BASTIAANS, R. J. M., SOMERS, L. M. T. & DE LANGE, H. C. 2001 DNS of non-premixed combustion in a compressible mixing layer. In B.J. Geurts, editor, *Modern Simulation Strategies for Turbulent Flow*, R.T. Edwards Publishers, Philadelphia, 247-261.

BELL, J. B., DAY, M. S. & GRCAR, J. F. 2002 Numerical simulation of premixed turbulent methane combustion. *Proc. Comb. Inst.*, **29**, 1987-1993.

BRAY, K. N. C. & MOSS, J. B. 1977 A unified statistical model of the premixed turbulent flame. *Acta Astronautica*, **4**, 291-319.

CHEM1D 2002 A one dimensional flame code. Eindhoven University of Technology, http://www.combustion.tue.nl/chem1d.

DRISCOLL, J.F. 2003 Premixed Turbulent Combustion - Current Knowledge and New Challenges. *Invited Presentation at the 3rd Joint Meeting of the U.S. Sections of the Combustion Institute*, Chicago (IL), March 16, 2003.

GASHI, S., HULT, J., JENKINS, K.W., CHAKRABORTY, N., CANT, R.S. & KAMINSKI, C.F. 2004 Curvature and wrinkling of premixed flame kernels - comparisons of OH PLIF and DNS data. *Proc. Comb. Inst.*, **30**, In press.

GICQUEL, O., DARABIHA, N. & THEVENIN, D. 2000 Laminar premixed hydrogen/air counter flow flame simulations using flame propagation of ILDM with preferential diffusion. *Proc. Combust. Inst.* **28**, 1901-1908.

DE GOEY, L. P. H. 2000 Premixed turbulent combustion theory. Technical report, TUE-W, sabbatical visit at the RWTH-Aachen

DE GOEY, L. P. H. & TEN THIJE BOONKKAMP, J. H. M. 1997 A mass-based definition of flame stretch for flames with finite thickness. *Comb. Sci. Tech.*, **122**, 399-405.

DE GOEY, L. P. H. & TEN THIJE BOONKKAMP, J. H. M. 1999 A flamelet description of premixed laminar flames and the relation with flame stretch. *Comb. Flame*, **119**, 253-271.

DE GOEY, L. P. H., PLESSING, T., HERMANNS, R. T. E. & PETERS, N. 2004 Analysis of the flame thickness of turbulent flamelets in the thin reaction zones regime. In *Proc. Combust. Inst.*, **30** In press.

GROOT, G. R. A. 2003 Modelling of propagating spherical and cylindrical premixed flames. Ph.D. thesis, Eindhoven University of Technology.

GROOT, G. R. A. & DE GOEY, L.P.H. 2002 A computational study of propagating spherical and cylindrical premixed flames. *Proc. Combust. Institute*, **29**, 1445-1451.

JENKINS, K.W. & CANT, R.S. 2002 Curvature effects on flame kernels in a turbulent environment. *Proc. Comb. Inst.*, **29**, 2023-2029.

DE LANGE, H. C. 2004 Personal communication Eindhoven University of Technology.

LELE, S. K. 1992 Compact Finite Difference Schemes with Spectral-like Resolution. *J. Comput. Phys.* **103**, 16-42.

MAAS, U. & POPE, S. B. 1992 Simplifying Chemical Kinetics: Intrinsic Low-Dimensional Manifolds in Composition Space. *Combust. Flame* **88**, 239-264.

MARBLE, F. & BROADWELL, J. 1977 The coherent flame model for trubulent chemical reactions. TRW-9-PU Project Squid, Purdue University West Lafayette.

VAN OIJEN, J.A. 2002 Flamelet-Generated Manifolds: Development and Application to Premixed Laminar Flames. Ph.D. thesis, Eindhoven University of Technology, The Netherlands.

VAN OIJEN, J. A. & DE GOEY, L. P. H. 2002 Modelling of premixed counterflow flames using the flamelet-generated manifold method. *Combust. Theory Modelling*, **6**, 463-478.

VAN OIJEN, J. A., GROOT, G. R. A., BASTIAANS, R. J. M. & DE GOEY, L. P. H. 2004 A flamelet analysis of the burning velocity of premixed turbulent expanding flames. *Proc. Comb. Inst.*, **30**, In press.

POINSOT, T. J. & S. K. LELE 1992 Boundary Conditions for Direct Simulations of Compressible Viscous Flows. *J. Comput. Phys.* **101**, 104-129.

PETERS, N. 2000 *Turbulent combustion.* Cambridge University Press.

SHEPHERD, I. G., CHENG, R. K., PLESSING, T., KORTSCHIK, C. & PETERS, N. 2002 Premixed flame front structure in intense turbulence. *Proc. Comb. Inst.*, **29**, 1833-1840.

SMITH, G. P., GOLDEN, D. M., FRENKLACH, M., MORIARTY, N. W., EITENEER, B., GOLDENBERG, M., BOWMAN, C.T., HANSON, R. K., SONG, S., GARDINER JR., W. C., LISSIANSKI, V.V. & Z. QIN, Z. 1999 http://www.me.berkeley.edu/gri_mech/

SMOOKE, M. D. & GIOVANGIGLI V. 1991 Formulation of the Premixed and Non-premixed Test Problems. In *Lecture Notes in Physics*, **384**, 1-28.

THÉVENIN, D. 2004 Three-dimensional direct numerical simulations and structure of expanding turbulent methane flames. *Proc. Comb. Inst.*, **30**, In press.

Numerical simulations of spray flames

By R. Kurose, O. Desjardins, M. Nakamura†, F. Akamatsu† AND H. Pitsch

1. Motivation and objectives

Spray combustion is utilized in a number of engineering applications such as energy conversion and propulsion devices. It is, therefore, necessary to precisely predict the spray combustion behavior in designing and operating the equipment. However, since spray combustion is a complex phenomenon in which dispersion of the liquid fuel droplets, evaporation, and chemical reaction of the fuel vapor with oxidizer take place interactively at the same time, the underlying physics governing these processes has not been well understood.

Direct numerical simulations (DNS) directly solve conservation equations for the carrier gaseous phase and Lagrangian equations for dispersed droplet dynamics and can be used for discussing the detailed spray combustion mechanism. However, few of such studies have been done even for low Reynolds numbers and simple geometries, because such simulations can be quite expensive.

Likewise, although large-eddy simulations (LES) are becoming a standard tool to study and predict single-phase gaseous combustion fields (e.g., Huang *et al.* 2003; Pierce & Moin 2004; Selle *et al.* 2004), the number of LES studies of two-phase combustion fields is very limited. Recently, Kurose & Makino (2003) applied LES to a turbulent jet flame of solid fuel and investigated the interactions among the dispersion, evaporation and combustion of solid-fuel particles. Ham *et al.* (2003) also performed LES of a spray combustion field in a realistic gas turbine combustor. The small number of papers on LES of two-phase combustion is attributed not only to the high computational cost, but also to the lack of experimental data for the validation.

In LES modeling of gaseous fuel combustion, the widely-used flamelet models (Peters 1984, 2000) have been extensively validated in different formulations, such as the steady-flamelet model (Cook *et al.* 1997), the unsteady-flamelet models (Pitsch & Steiner 2000; Pitsch 2002), and the flamelet/progress-variable approach (Pierce & Moin 2004). However, for spray combustion, the mixture fraction, which characterizes the mixing field, is not a conserved scalar anymore. Evaporation changes the mixing field, and especially the scalar dissipation rate. A proper formulation accounting for all the effects has not yet been developed. In addition, the validity of the standard approach for representing a group of droplets so called parcel to reduce the computational cost should be carefully studied, since the use of the parcels may deteriorate the numerical accuracy. In fact, it was demonstrated that the spray combustion behavior varies with the number of parcels (Nakamura *et al.* 2004), and it is expected that this phenomenon can be explained in terms of the droplet group combustion theory (Chiu & Liu 1977; Chiu *et al.* 1982).

The purpose of this work is twofold. First, the spray combustion behavior is studied by a two-dimensional DNS of spray flames formed in a laminar counterflow. The droplet group combustion theory (Chiu & Liu 1977; Chiu *et al.* 1982) is discussed in detail. The

† Osaka University

second aim of this work is to apply LES with the flamelet/progress-variable approach to a spray jet flame and validate the technique. Qualitative results are presented and compared with experimental observations.

2. Two-dimensional direct numerical simulation of spray flames stabilized in a laminar counterflow

2.1. *Field description and numerical method*

The computational setup for DNS of a spray flame in a laminar counter flow is designed to match the experiment of Hwang *et al.* (2000), and the numerical details are described in Nakamura *et al.* (2004). The computational domain analyzed in this study is shown in Figure 1. The dimensions are 20 mm × 40 mm. There are two burner ports with the widths of 20 mm on both the upper and lower sides, and the separation distance between the ports is 20 mm. The origin of the calculation domain is located at the center of the upper burner port. From the upper port of -10 $\leq y \leq$ 10 mm, atmospheric air (T = 300K, P = 0.1013 MPa, and oxygen mass fraction Y_{O_2} = 0.2357) is issued at a velocity of 0.4 m/s. From the lower port, a premixture of atmospheric air and n-decane ($C_{10}H_{22}$) vapor (equivalence ratio, ϕ = 0.6) is issued in the region of -3 $\leq y \leq$ 3 mm, and atmospheric air is issued in the region of -10 $\leq y \leq$ -3 mm and 3 $\leq y \leq$ 10 mm at the velocity of 0.4 m/s. The stretch ratio of the laminar counterflow is 40 1/s. The n-decane ($C_{10}H_{22}$) spray is injected from the upper port in the range of -3 $\leq y \leq$ 3 mm at the velocity of 0.4 m/s.

Gaseous species considered in the calculations are O_2, N_2, CO_2, H_2O, and $C_{10}H_{22}$, and their transport properties and thermodynamic data are obtained from CHEMKIN (Kee *et al.* 1986, 1989). Properties of liquid n-decane are obtained from Reid *et al.* (1977). The governing equations considered for the gaseous phase (mass, momentum, energy and species mass) are discretized and solved by the finite volume method using the SIMPLE algorithm (Patankar 1980). Dispersed droplets are tracked in a Lagrangian manner. It is assumed that the density of the droplets is much larger than that of the continuous phase such that only drag and gravity are significant. The effect of fluid shear on fluid force acting on the droplets (Saffman 1965; Kurose & Komori 1999), droplet breakup and collision, and dense particulate effects (Ham *et al.* 2003; Apte *et al.* 2003) are neglected. It is well known that the drag is reduced by evaporation. This effect is taken into account using the method by Kurose *et al.* (2003). Mass, heat and momentum interchanges between the carrier gas and dispersed droplet phases are calculated by the PSI-Cell model (Crowe *et al.* 1977). For the droplet evaporation, a non-equilibrium Langmuir-Knudsen evaporation model is employed (Miller & Bellan 1999).

Although the time-averaged equivalence ratio of the spray, ϕ_l, was 0.42 in the experiment (Hwang *et al.* 2000; Nakamura *et al.* 2004), this value was considered to vary periodically with time due to the unsteadiness of the fuel injection system. Hence, the computations are performed for four different spray equivalence ratios of ϕ_l = 0.21, 0.42, 0.84 and 1.26. The initial droplet size distribution is the same as that obtained by the PDA (phase Dopper anemometer) measurement (Figure 2), and the initial position of each droplet is determined randomly. The calculation domain (0 $\leq x \leq$ 20 mm, -20 $\leq y \leq$ 20 mm) is divided into 200 × 400 equally spaced computational cells in x and y directions, respectively, which generates the actual control volume size of 100 μm × 100 μm. The calculation time step is set at 0.1 ms.

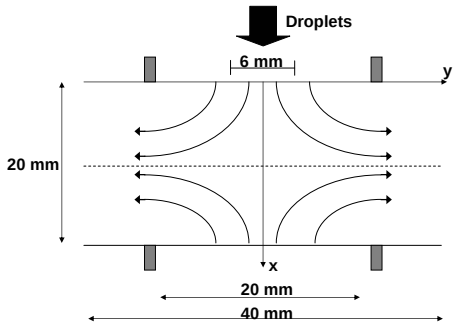

FIGURE 1. Computational domain for DNS of spray flames in a laminar counterflow.

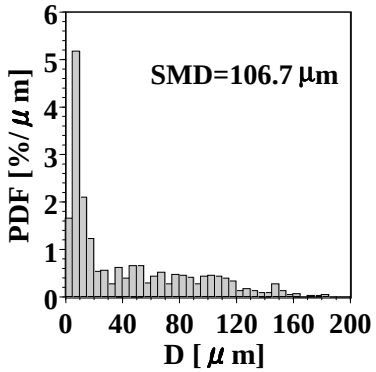

FIGURE 2. Initial droplet size distribution.

2.2. *Results and discussion*

Figure 3 shows the time-averaged axial (x direction) profiles of gaseous temperature, T, and axial velocity, u, respectively (at $y = 0$). The solid, dashed, dotted and dash-doted lines show the results of spray flames for $\phi_l = 0.21$, 0.42, 0.84 and 1.26, respectively. In general, as ϕ_l increases, the high T region expands, which is expected because the heat of reaction of the added spray increases with increasing ϕ_l. However, in the upper part of the high T region of $0.3 \leq x/L_x \leq 0.55$ (L_x is the separation difference between the ports), the value of T tends to decrease for high spray equivalence ratios of $\phi_l = 0.84$ and 1.26. It is also observed that, in accordance with the T profile, the difference in u between $\phi_l = 0.84$ and 1.26 is less for the upper region ($x/L_x \approx 0.4$) than that for the lower region ($x/L_x \approx 0.75$).

To investigate the spray combustion behavior in detail and clarify the reason why the gaseous temperature decreases for high spray equivalence ratio in the region of $0.3 \leq x/L_x \leq 0.55$, the instantaneous combustion fields for $\phi_l = 0.21$, 0.42, 0.84 and 1.26 are shown in Figure 4. Gas phase temperature, T, combustion reaction rate, R_F, and gas phase equivalence ratio, ϕ, are illustrated, and the droplet location is superimposed on each figure. The high combustion reaction rate around $x/L_x = 0.75$ in the figure of R_F (indicated by arrow F) is due to the flame of the premixed gases supplied from the lower port. The photograph of the flame obtained from the experiment, which, as will be explained later, is considered to correspond to the adjacent numerical condition, is also shown (Nakamura *et al.* 2004). It is found that, with increasing ϕ_l, the number of droplet entering the high temperature region increases, and the combustion behavior changes drastically. That is, while the droplets for low spray equivalence ratio of $\phi_l = 0.21$ monotonically evaporate and burn individually, those for higher spray equivalence ratio experience two different combustion zones, as shown in the distributions of R_F and ϕ. Firstly, for the high spray-equivalence-ratio cases of $\phi_l = 0.84$ and 1.26, the high R_F zone appears around the front surface of the high T region at $x/L_x = 0.35$ (indicated by arrow C). Although the droplets continuously evaporate even in the upstream region of

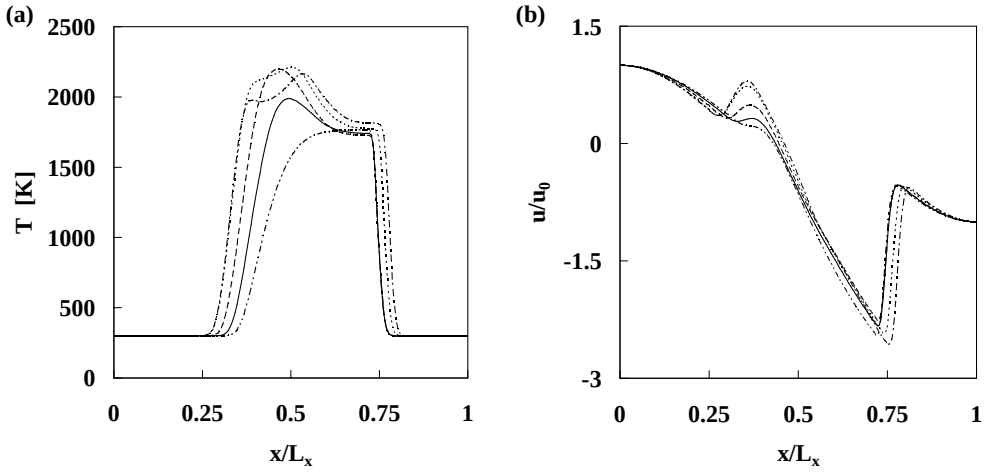

FIGURE 3. Time-averaged axial profiles of gaseous temperature and axial velocity: (a) temperature, T; (b) axial velocity, u; solid line, $\phi_l = 0.21$; dashed line, $\phi_l = 0.42$; dotted line, $\phi_l = 0.84$; dash-dotted line, $\phi_l = 1.26$; dash-double-dotted line, gaseous flame.

this zone (see the figure of ϕ), combustion does not occur until the fuel vapor reaches this zone. It can be said that a "premixed-like combustion" takes place in this zone, since the fuel vapor mixes with air before reaction starts. Subsequently, in the downstream region of $0.35 \leq x/L_x \leq 0.5$ (between arrows C and E), there appears a "diffusion-like combustion" zone, where the evaporation and combustion of the residual droplets penetrating the "premixed-like combustion" zone takes place at the same time.

Furthermore, this "diffusion-like combustion" is apparently divided into two different combustion types. The residual droplets in the high T region evaporate and burn individually in the upper region ($0.35 \leq x/L_x \leq 0.4$ (between arrows C and D)), but burn as clusters of some droplets in the lower region ($0.4 \leq x/L_x \leq 0.5$ (between arrows D and E)). The difference in the combustion type can be explained by Figure 5, which shows the instantaneous axial profiles of gaseous temperature, T, mass fraction of O_2 and $C_{10}H_{22}$, Y_{O_2} and $Y_{C_{10}H_{22}}$, and combustion reaction rate, R_F, on the A and B section in Figure 4. The oxygen is abundant in the upper region of $0.35 \leq x/L_x \leq 0.4$, but almost zero in the lower region of $0.4 \leq x/L_x \leq 0.5$. Therefore, the fuel vapor generated in the high T region rapidly reacts with the oxygen and is consumed in the former condition, whereas it is not consumed in the latter condition. Consequently, the high fuel vapor lumps containing some droplets burn from the outer surface, where the oxygen is abundant.

This phenomenon, in which the droplets burn as a cluster, is known as droplet group combustion. According to Chiu & Liu (1977) and Chiu *et al.* (1982), there are four modes in spray flames, i.e., (1) single droplet combustion mode, in which droplets burn as a single droplet, (2) internal group combustion mode, in which group flames appear inside the droplet group (droplets inside the group flame only just evaporate and droplets outside the group flame burn as a single droplet), (3) external group combustion mode, in which the group flame encloses the whole droplet group, and (4) external sheath combustion mode, in which a non-evaporation region (low temperature region) is found inside the evaporation region in the droplet group. These modes change from the single droplet

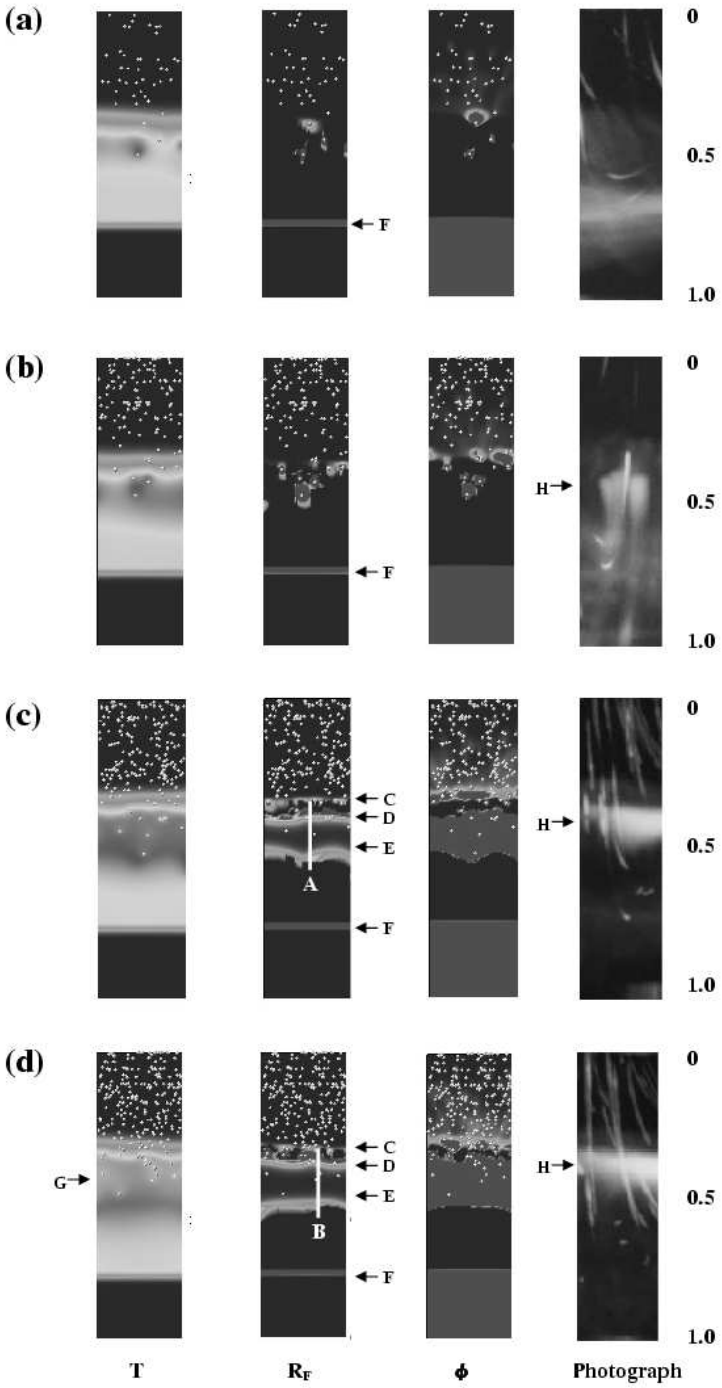

FIGURE 4. Instantaneous distributions of gaseous temperature, T, combustion reaction rate, R_F, gaseous equivalence ratio, ϕ, and photograph in the central region of counterflow ($-0.15 \leq y/L_x \leq 0.15$): (a) $\phi_l = 0.21$; (b) $\phi_l = 0.42$; (c) $\phi_l = 0.84$; (d) $\phi_l = 1.26$.

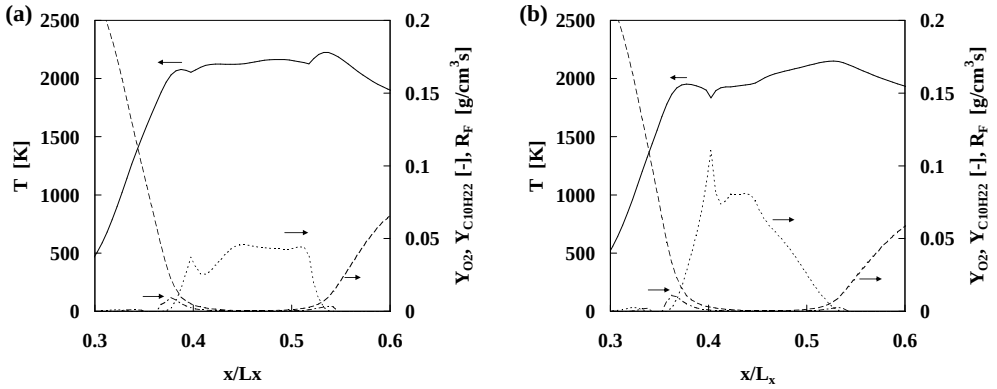

FIGURE 5. Instantaneous profiles of gaseous temperature, T, mass fractions of O_2 and $C_{10}H_{22}$, Y_{O_2} and $Y_{C_{10}H_{22}}$, and combustion reaction rate, R_F, on the A and B section in Figure 4: (a) $\phi_l = 0.84$; (b) $\phi_l = 1.26$; solid line, T; dashed line, Y_{O_2}; dotted line, $Y_{C_{10}H_{22}}$; dash-dotted line, R_F.

combustion mode to the external sheath combustion mode, as the group combustion number, G, increases.

In Figure 4, for the highest spray-equivalence-ratio cases of $\phi_l = 1.26$, low temperature lumps containing some droplets appear (see arrow G in the temperature profile in Figure 5). This is becasue that this combustion belongs to the external sheath combustion mode. The decrease of the gaseous temperature for high spray equivalence ratios of $\phi_l = 0.84$ and 1.26 in the upper part of the high T region of $0.3 \leq x/L_x \leq 0.55$, as shown before, is considered to be caused by the group combustion behavior. The reason why the gaseous temperature decreases in the droplet group is due to the heat exchange between droplets and gaseous phase, which is referred to as the evaporative cooling effect. The temperature of droplets is much lower than that of the gaseous phase. Moreover, as the evaporation of droplets proceeds, the heat of vaporization reduces the droplet temperature. This low gaseous temperature leads to the low reaction rates. Thus, droplet group combustion, which tends to appear in the regions of high droplet number density and low oxygen concentration, delays the combustion reactions.

As mentioned earlier, although the time-averaged equivalence ratio of the spray, ϕ_l, was 0.42 in the experiment, this value was considered to vary with time. Hence, the flame photograph, which seems to correspond to each numerical condition, is selected in Figure 4. In the photographs, blue and luminous flames indicate premixed and diffusion combustion (the flames are shown in white and the luminous flames are indicated by arrows H), respectively, since the lumination originates from soot radiation, which is generated under very rich conditions, such as those encountered in diffusion flames. It seems that the computed results generally agree with the experimental observations. For the high spray equivalence ratios of $\phi_l = 0.84$ and 1.26, the sizes and positions of the computed group combustion flames correspond to those of the luminous flames.

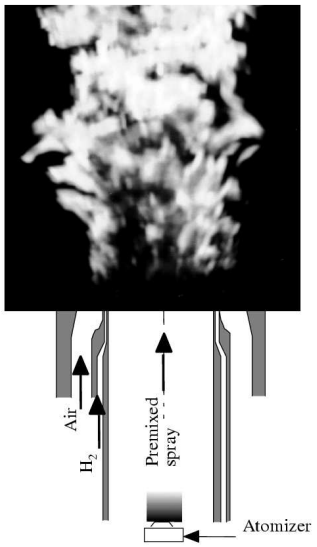

FIGURE 6. Premixed-spray jet flame (Akamatsu *et al.* 1996).

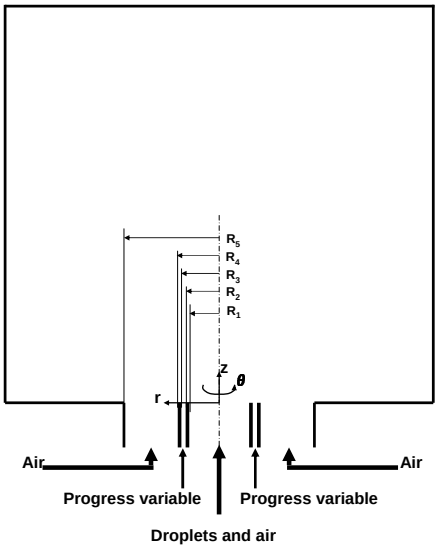

FIGURE 7. Computational domain for LES of a spray jet flame.

3. Large-eddy simulation of a spray jet flame

3.1. *Field description and numerical method*

The spray jet flame considered here has first been experimentally investigated by Nakabe *et al.* (1988, 1991, 1994) and the detailed flame behavior has been studied by Akamatsu *et al.* (1996, 1997) using several kinds of optical measurement techniques. The spray jet flame is a non-swirling piloted jet flame stabilized in a two-phase stream with minimum slip between gas and droplets, for which a long mixing length from a spray atomizer to burner outlet is given (Figure 6). It is called premixed-spray jet flame. A liquid fuel atomized by an air-blast atomizer placed upstream is issued in air from the central port of the annular pilot burner. This premixed-spray jet flame has the advantage that complicated phenomena such as dense particle flow effects and spray breakup, collision, and deformation (e.g., Ham *et al.* 2003; Apte *et al.* 2003) can be neglected in the computations.

The computations performed in this study are designed to match the experimental setup (Akamatsu *et al.* 1996, 1997). The computational domain is shown in Figure 7. The computational domain normalized by the burner radius (R_5) is -1 $\leq$ z $\leq$ 10, 0 $\leq$ r $\leq$ 6 and 0 $\leq \theta \leq 2\pi$ in the axial, radius and azimuthal directions (R_1 = 26.35 mm, R_2 = 27.35 mm, R_3 = 28.35 mm, R_4 = 29.35 mm, R_5 = 40.45 mm). In the experiments, kerosene is used as the liquid fuel, hydrogen is supplied from the annular pilot burner, and air is provided from the surrounding annulus to suppress the expansion of the stream lines. In this preliminary test, however, n-heptane is assumed as the liquid fuel, and the annular pilot burner to ignite and stabilize the spray flame is modeled by a stream of hot combustion products. The nominal bulk velocity of the central and surrounding air is 5.5 m/s.

The numerical procedure is essentially the same as that of Pierce and Moin (2001). A structured grid in cylindrical coordinates is used. The primary breakup of the liquid jet is not computed. Instead, the initial droplet size distribution obtained by the PDA measurement is used. The simplified model by Oefelein (1997) is used for droplet evaporation.

The size of the grid is $272 \times 128 \times 96$ nodes in the axial, radial, and azimuthal directions, respectively, and the grid is refined near the solid boundaries. The parcels representing about 20 droplets are tracked, which yields around 0.7 million parcels in the domain.

3.2. *Results and discussion*

Figures 8 and 9 show the instantaneous distributions of mixture fraction and product mass fraction together with the droplet distribution. Only mixture fractions and product mass fractions larger than 0.05 are shown. The spray jet flame is found to be stabilized by the product mass fraction issued from the annular pilot burner. For both the mixture fraction and product mass fraction, high concentration regions are observed around the spray jet, which means that combustion proceeds from the outside of the spray jet. Although not apparent only from these figures, in the upstream region near the burner, most of the droplets evaporate on the edge of the spray jet and hardly penetrate into the outer high product mass fraction area. In the downstream region of the spray jet, on the other hand, some droplets are found to separate from the main spray jet and move into the high product mass fraction area as clusters, as shown in Figure 10. A similar behavior was observed in the previous experiment by Tsushima *et al.* (see Figure 11). The numerical results also illustrate that, for the droplet cluster in the high product mass fraction area, the high temperature droplets tend to cover the low temperature droplets. This trend seems to correspond to the earlier described mode (3) or (4) , which suggests that the present LES is capable of capturing the droplet group combustion behavior. However, quantitative validation using an improved droplet evaporation model and chemical mechanism for a better kerosene surrogate would be essential to fully validate the technique.

4. Conclusions and future work

This paper presented the detailed behavior of spray flames by analysing 2-D DNS data for burning liquid fuel spray in a laminar counterflow. The droplet group combustion model (Chiu & Liu 1977) was explicitly demonstrated. It was also verified that the droplet group combustion tends to appear in the region of high droplet number density and low oxygen concentration and that it delays evaporation and combustion of the fuel droplets.

LES with the flamelet/progress-variable approach was applied to a spray jet flame, and preliminary test case results were shown. The spray jet flame was stabilized by supplying the progress variable from the annular pilot burner, and corresponding the experimental observations, the group combustion-like behavior was observed.

Future work will focus on the validation study for the LES technique of spray jet flames. First of all, an improved droplet evaporation model and a chemical mechanism for a kerosene surrogate will be implemented in the LES code. Our detailed experimental data for the premixed-spray jet flame (e.g. gaseous velocity, temperature, main species concentrations, droplet size, and droplet number density) will allow us to understand

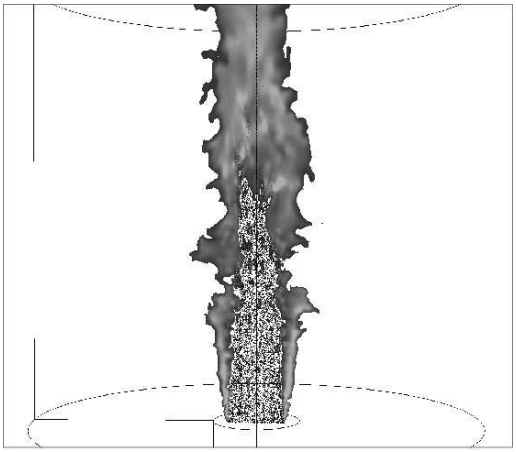

FIGURE 8. Instantaneous distributions of mixture fraction and droplets.

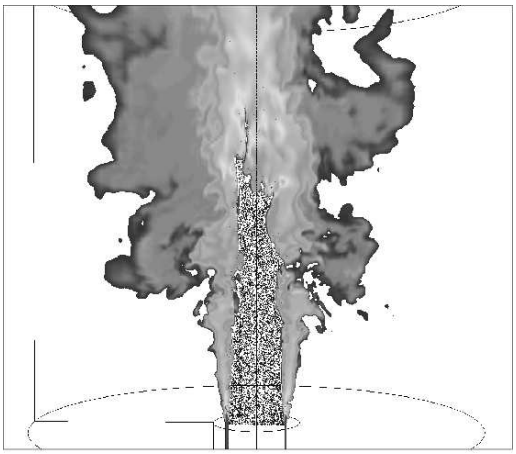

FIGURE 9. Instantaneous distributions of product mass fraction and droplets.

the accuracy of the existing models associated with droplet evaporation and combustion, and to develop improved models.

Acknowledgments

The authors are grateful to Drs. Sourabh Apte and Scott Martin for many helpful discussions and their comments on this manuscript. They also thank to Prof. Masashi Katsuki of Osaka University for many useful discussions. RK would like to thank Prof. Parviz Moin for providing a part of his expenses during his stay at Stanford through the Center for Turbulence Research Senior Visiting Fellow Program.

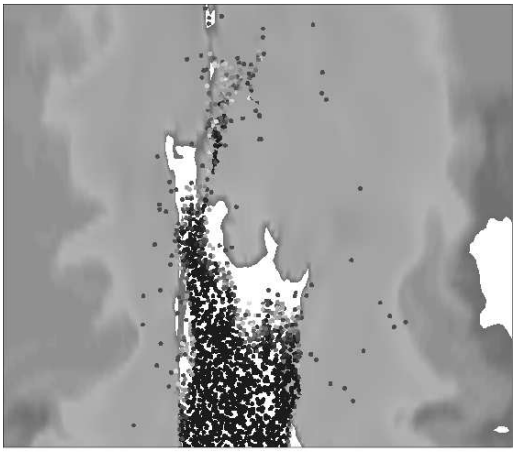

FIGURE 10. Magnified instantaneous distributions of product mass fraction and droplets.

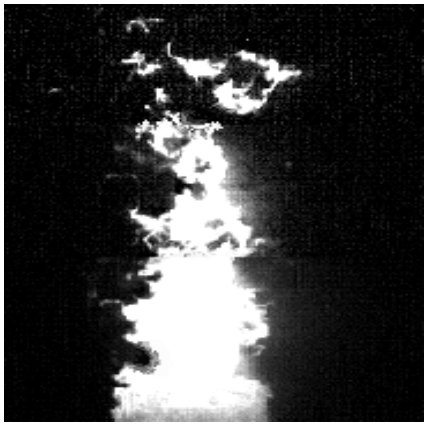

FIGURE 11. Droplet distribution obtained by experiment (Tsushima *et al.* 1998).

REFERENCES

AKAMATSU, F., MIZUTANI, Y., KATSUKI, M., TSUSHIMA, S. & CHO, Y. D. 1996 Measurement of local group combustion number of droplet clusters in a premixed spray stream. *Proc. of the Combustion Institute* **26**, 1723-1729.

AKAMATSU, F., MIZUTANI, Y., KATSUKI, M., TSUSHIMA, S., CHO, Y. D. & NAKABE, K. 1997 Group combustion behavior of droplets in a premixed-spray flame. *Atomization and Sprays* **7**, 199-218.

APTE, S. V., GOROKHOVSKI, M. & MOIN, P. 2003 LES of atomizing spray with stochastic modeling of secondary breakup. *Int. J. Multiphase Flow* **29**, 1503-1522.

CHIU, H. H. & LIU, T. M. 1977 Group combustion of liquid droplets. *Combust. Sci. Tech.* **17**, 127-142.

CHIU, H. H., KIM, H. Y. & CROKE, E. J. 1982 International group combustion of liquid droplets. *Proc. of the Combustion Institute* **19**, 971-980.

COOK, A. W., RILEY, J. J. & KOSÁLY, G. 1997 A laminar flamelet approach to subgrid-scale chemistry in turbulent flow. *Combust. Flame* **109**, 332-341.

CROWE, C. T., SHARMA M. P. & STOCK, D. E. 1977 The particle-source-in cell (PSI-CELL) model for gas-droplet flows. *Trans. ASME, J. of Fluids Eng.* **99**, 325-332.

HAM, F., APTE, S.V., IACCARINO, G., WU, X., HERRMANN, S., CONSTANTINESCU, G., MAHESH, K. & MOIN, P. 2003 Unstructured LES of reacting multiphase flows in realistic gas turbine combustors. *Annual Research Briefs-2003*, Center for Turbulence Research, NASA Ames/Stanford University, 139-160.

HUANG, Y., SUNG, H.-G., HSIEH, S.-Y. & YANG, Y. 2003 Large-eddy simulation of combustion dynamics of lean-premixed swirl-stabilized combustor. *J. Propul Power* **19**, 782-794.

HWANG, S.-M., SAITOH, H., TAKADA, S., AKAMATSU, F. & KATSUKI, M. 2000 Observation of Spray Flame Stabilized in a Laminar Counterflow Field. *Proc. of 38th Japanese Combustion Symposium*, 201-202, in Japanese.

KEE, R. J., DIXON-LEWIS, G., WARNATZ, J., COLTRIN, M. E. & MILLER, J. A. 1986 A fortran computer code package for the evaluation of gas-phase multicomponent transport properties. *SANDIA Report*, SAND86-8246.

KEE, R. J., RUPLEY, F. M. & MILLER, J. A. 1989 Chemkin-II: A fortran chemical kinetics package for the analysis of gas phase chemical kinetics. *SANDIA Report*, SAND89-8009B.

KUROSE, R. & KOMORI, S. 1999 Drag and lift forces on a rotating sphere in a linear shear flow. *J. Fluid Mech.* **384**, 183-206.

KUROSE, R., MAKINO, H., KOMORI, S., NAKAMURA, M., AKAMATSU, F. & KATSUKI, M. 2003 Effects of outflow from surface of sphere on drag, shear lift, and scalar diffusion. *Phys. Fluids* **15**, 2338-2351.

KUROSE, R. & MAKINO, H. 2003 Large eddy simulation of a solid-fuel jet flame. *Combust. Flame* **135**, 1-16.

MILLER, R. S. & BELLAN, J. 1999 Direct numerical simulation of a confined three-dimensional gas mixing layer with one evaporating hydrocarbon-droplet-laden stream. *J. Fluid Mech.* **384**, 293-338.

NAKABE, N., MIZUTANI, Y., HIRANO, T. & TANIMURA, S. 1988 Burning characteristics of premixed sprays and gas-liquid coburning mixtures. *Combust. Flame* **74**, 39-51.

NAKABE, N., MIZUTANI, Y., HIRANO, T. & FUJIOKA, H. 1991 An experimental study on detailed flame structure of liquid fuel sprays with and without gaseous fuel. *Combust. Flame* **84**, 3-14.

NAKABE, N., MIZUTANI, Y., AKAMATSU, F. & FUJIOKA, H. 1994 Observation of droplets group combustion in terms of simultaneous measurement of Mie-scattering and spectral luminosity of spray flame. *Atomization Sprays* **84**, 3-14.

NAKAMURA, M., AKAMATSU, F., KUROSE, R. & KATSUKI, M. 2004 Combustion mechanism of liquid fuel spray entering gaseous flame front, in preparation for submission.

OEFELEIN, J. C. 1997 Simulation and analysis of turbulent multiphase combustion processes at high pressures. Ph.D. Thesis, The Pennsylvania State University, University Park, Pa.

PATANKAR, S. V. 1980 *Numerical Heat Transfer and Fluid Flow*, McGraw-Hill.

PETERS, N. 1984 Laminar diffusion flamelet models in non-premixed turbulent combustion. *Prog. Energy Combust. Sci.* **10**, 319-339.

PETERS, N. 2000 *Turbulent Combustion*, Cambridge University Press.

PIERCE, C. D. & MOIN, P. 2001 Progress-variable approach for large-eddy simulation of turbulent combustion. *Mech. Eng. Dept. Rep.* **TF-80**, Stanford University.

PIERCE, C. D. & MOIN, P. 2004 Progress-variable approach for large-eddy simulation of non-premixed turbulent combustion. *J. Fluid Mech.* **504**, 73-97.

PITSCH, H. & STEINER, H. 2000 Large-eddy simulation of a turbulent piloted methane/air diffusion flame (Sandia flame D). *Phys. Fluids* **12**, 2541-2554.

PITSCH, H. 2002 Improved pollutant predictions in large-eddy simulations of turbulent non-premixed combustion by considering scalar dissipation rate fluctuations. *Proc. of the Combustion Institute* **29**, 1971-1978.

REID, R. C., PRAVSNITZ, J. M. & SHERWOOD, T. K. 1977 *The Properties of Gases and Liquids, third edition*, McGraw-Hill, New York.

SAFFMAN, P. G. 1965 The lift on a small sphere in a shear flow. *J. Fluid Mech.* **22**, 385-400, and 1968 Corrigendum **31**, 624.

SELLE, L., LARTIGUE, G., POINSOT, T., KOCH, R., SCHILDMACHER, K.-U., KREBS, W., PRADE, B., KAUFMANN, P. & VEYNANTE, D. 2004 Compressible large eddy simulation of turbulent combustion in complex geometry on unstructured meshes. *Combust. Flame* **137**, 489-505.

TSUSHIMA, S., SAITOH, H., AKAMATSU, F. & KATSUKI, M. 1998 Observation of combustion characteristics of droplet clusters in a premixed-spray flame by simultaneous monitoring of planar spray images and local chemiluminescence. *Proc. of the Combustion Institute* **27**, 1967-1974.

Frequency integrated radiation models for absorbing and scattering media

By J.F. Ripoll AND A.A. Wray†

1. Motivation and objectives

The objective of this work is to contribute to the simplification of existing radiation models used in complex emitting, absorbing, scattering media. The application in view is the the computation of flows occuring in such complex media, such as certain stellar interiors or combusting gases. In these problems, especially when scattering is present, the complexity of the radiative transfer leads to a high numerical cost, which is often avoided by simply neglecting it. This complexity lies partly in the strong dependence of the spectral coefficients on frequency (Modest 2003; Siegel & Howell 2001). Models are then needed to capture the effects of the radiation when one cannot afford to directly solve for it. In this work, the frequency dependence will be modeled and integrated out in order to retain only the average effects. A frequency-integrated radiative transfer equation (RTE) will be derived. In it, the absorption and scattering will be treated through the use of mean coefficients (Siegel & Howell 2001 and references in it). To obtain these coefficients, it is needed to assume a form for the intensity, which we take to be the maximum entropy closure (Minerbo 1978). Such an intensity is a function of the macroscopic radiative energy and flux and accounts for the variations of radiation in the considered medium. Models for mean absorption, mean isotropic scattering, and mean non-isotropic scattering coefficients will be proposed in the case where the various spectral coefficients can be written as polynomial functions of the frequency. Some of these models have already been derived and tested for non-scattering media in (Ripoll *et al.* 2001; Ripoll & Wray 2004a). They are here extended to the general case of emitting, absorbing, and scattering media. A direct application will be given for soot, which follows a linear frequency law for absorption; isotropic and incoming scattering spectral models are also here roughly approximated by a linear law. Macroscopic radiation models will also be derived with absorption and scattering coefficients since they constitute an alternative to the use of the RTE in cases where this equation is too costly to solve, as in many coupled problems. Finally, we believe another application of these models could be for radiating flows occuring in dusty media.

2. A frequency integrated RTE with mean coefficients

2.1. *Generalities*

The radiative transfer equation (RTE) describes the evolution of the radiative intensity within a emitting, absorbing, and scattering medium and is given by

$$\frac{1}{c}\partial_t I + \mathbf{\Omega}\cdot\nabla I = \sigma^a(\nu)\mathcal{B}(\nu,T) - \sigma^a(\nu)I - \sigma^{is}(\nu)I + \frac{\sigma^s(\nu)}{4\pi}\int_{\mathbf{\Omega}'} I(\mathbf{\Omega}')\Phi(\nu,\mathbf{\Omega}\rightarrow\mathbf{\Omega}')d\mathbf{\Omega}' \quad (2.1)$$

† NASA Ames Research Center

where the intensity $I = I(t, \mathbf{r}, \mathbf{\Omega}, \nu)$ is a function of the time t, the position $\mathbf{r}$, the direction of propagation $\mathbf{\Omega}$, and the frequency ν. Here c is the velocity of light, $\sigma^a(\nu)$ is the spectral absorption coefficient, $\sigma^{is}(\nu)$ the spectral isotropic scattering coefficient, $\sigma^s(\nu)$ the spectral incoming scattering coefficient, and $\mathbf{\Omega}'$ the original direction of radiation scattered into $\mathbf{\Omega}$. The Planck radiative intensity $\mathcal{B}$ describes the isotropic emission of the medium at the frequency ν and temperature T by

$$\mathcal{B}(\nu, T) = \frac{2h\nu^3}{c^2}\left[\exp(\frac{h\nu}{kT}) - 1\right]^{-1} \tag{2.2}$$

where h is the Planck constant, k the Boltzmann constant, and ν the frequency. We assume in this paper that the phase function of scattering $\Phi(\nu, \mathbf{\Omega} \to \mathbf{\Omega}')$ can be expressed as

$$\Phi(\nu, \mathbf{\Omega} \to \mathbf{\Omega}') = \alpha(\nu) + \beta(\nu)\mathbf{\Omega} \cdot \mathbf{\Omega}' + \gamma(\nu)(\mathbf{\Omega} \cdot \mathbf{\Omega}')^2 + \eta(\nu)\delta(\mathbf{\Omega} - \mathbf{\Omega}') \tag{2.3}$$

where $\delta(\cdot)$ is the Dirac delta function, and the coefficients, α, β, γ, and η are all in general functions of the frequency. They must be defined such that the following normalization property holds:

$$\frac{\sigma^s(\nu)}{4\pi}\int_{\mathbf{\Omega}} \Phi(\nu, \mathbf{\Omega} \to \mathbf{\Omega}')d\mathbf{\Omega} = \sigma^{is}(\nu). \tag{2.4}$$

2.2. *Derivation of the RTE with mean coefficients*

By integrating the RTE over frequency and introducing the quantity† $J(t, \mathbf{r}, \mathbf{\Omega}) = \int_0^\infty I(t, \mathbf{r}, \mathbf{\Omega}, \nu)\, d\nu \equiv \langle I \rangle_\nu$, we obtain

$$\begin{aligned}\frac{1}{c}\partial_t J + \mathbf{\Omega} \cdot \nabla J = &\langle \sigma^a(\nu)\mathcal{B}(\nu, T)\rangle_\nu - \langle \sigma^a(\nu) I\rangle_\nu - \langle \sigma^s(\nu) I\rangle_\nu \\ &+ \langle \frac{\sigma^s(\nu)}{4\pi}\int_{\mathbf{\Omega}'} I(\mathbf{\Omega}')\Phi(\nu, \mathbf{\Omega} \to \mathbf{\Omega}')d\mathbf{\Omega}' \rangle_\nu.\end{aligned} \tag{2.5}$$

We now introduce the following mean absorption and scattering coefficients:

$$\sigma_P^{e,\nu}(T) = \frac{\langle \sigma^a(\nu)\mathcal{B}(\nu, T)\rangle_\nu}{\langle \mathcal{B}(\nu, T)\rangle_\nu} \tag{2.6}$$

$$\sigma_E^{a,\nu}(t, \mathbf{r}, \mathbf{\Omega}) = \frac{\langle \sigma^a(\nu) I(t, \mathbf{r}, \mathbf{\Omega}, \nu)\rangle_\nu}{\langle I(t, \mathbf{r}, \mathbf{\Omega}, \nu)\rangle_\nu} \tag{2.7}$$

$$\sigma_E^{is,\nu}(t, \mathbf{r}, \mathbf{\Omega}) = \frac{\langle \left[\sigma^{is}(\nu) - \sigma^s(\nu)\eta(\nu)/4\pi\right] I(t, \mathbf{r}, \mathbf{\Omega}, \nu)\rangle_\nu}{\langle I(t, \mathbf{r}, \mathbf{\Omega}, \nu)\rangle_\nu} \tag{2.8}$$

$$\sigma_E^s(t, \mathbf{r}) = \frac{\langle \sigma^s(\nu)\alpha(\nu) I(t, \mathbf{r}, \mathbf{\Omega}', \nu)\rangle_{\nu, \mathbf{\Omega}'}}{\langle I(t, \mathbf{r}, \mathbf{\Omega}', \nu)\rangle_{\nu, \mathbf{\Omega}'}} \tag{2.9}$$

$$\sigma_F^s(t, \mathbf{r}, \mathbf{\Omega}) = \frac{\langle \sigma^s(\nu)\beta(\nu)\mathbf{\Omega} \cdot \mathbf{\Omega}' I(t, \mathbf{r}, \mathbf{\Omega}', \nu)\rangle_{\nu, \mathbf{\Omega}'}}{\langle \mathbf{\Omega} \cdot \mathbf{\Omega}' I(t, \mathbf{r}, \mathbf{\Omega}', \nu)\rangle_{\nu, \mathbf{\Omega}'}} \tag{2.10}$$

$$\sigma_G^s(t, \mathbf{r}, \mathbf{\Omega}) = \frac{\langle \sigma^s(\nu)\gamma(\nu)(\mathbf{\Omega} \cdot \mathbf{\Omega}')^2 I(t, \mathbf{r}, \mathbf{\Omega}'\nu)\rangle_{\nu, \mathbf{\Omega}'}}{\langle (\mathbf{\Omega} \cdot \mathbf{\Omega}')^2 I(t, \mathbf{r}, \mathbf{\Omega}', \nu)\rangle_{\nu, \mathbf{\Omega}'}} \tag{2.11}$$

where the superscripts *e, a, is,* and *s* designate respectively emission, absorption, isotropic scattering, and scattering. We define $\chi(\nu) \equiv \sigma^s(\nu)\eta(\nu)/(4\pi\sigma^{is}(\nu))$. Using these definitions and without any assumptions other than the form of the phase function (2.3), the

† We will denote the integration of a function f over the variables X, Y, Z as $\langle f \rangle_{X,Y,Z}$

frequency-integrated RTE becomes

$$\frac{1}{c}\partial_t J+\mathbf{\Omega}\cdot\nabla J=\frac{\sigma_P^{e,\nu}}{4\pi}aT^4-\sigma_E^{a,\nu}J-\sigma_E^{is,\nu}J+\frac{1}{4\pi}\int_{\mathbf{\Omega}'}J(\mathbf{\Omega}')(\sigma_E^s+\sigma_F^s\mathbf{\Omega}\cdot\mathbf{\Omega}'+\sigma_G^s(\mathbf{\Omega}\cdot\mathbf{\Omega}')^2)\,d\mathbf{\Omega}' \tag{2.12}$$

where the constant $a=8\pi^5k^4/(15h^3c^3)$. It should be noted that the mean scattering coefficients in the integral do not depend on $\mathbf{\Omega}$, unlike $\sigma_E^{a,\nu}$ and $\sigma_E^{is,\nu}$.

As a simplifying approximation, we now eliminate the $\mathbf{\Omega}$ dependence of the two mean coefficients σ_E^a and σ_E^{is}. This can be done by simply approximating the numerator and denominator in (2.7) and (2.8) by their $\mathbf{\Omega}$-integrated forms. Alternately, we integrate 2.12 indefinitely over $\mathbf{\Omega}$, using the polar variables $\mu=\cos\theta$ and ϕ, to obtain

$$\begin{aligned}\int\frac{1}{c}\partial_t J+\mathbf{\Omega}\cdot\nabla J\,d\mu\,d\phi=&\frac{\sigma_P^{e,\nu}}{4\pi}aT^4\mu\phi-\frac{\int\langle\sigma^a(\nu)I(t,\mathbf{r},\mathbf{\Omega},\nu)\rangle_\nu\,d\mu\,d\phi}{\int\langle I(t,\mathbf{r},\mathbf{\Omega},\nu)\rangle_\nu\,d\mu\,d\phi}\int J\,d\mu\,d\phi\\&-\frac{\int\langle\sigma^{is}(\nu)\left[1-\chi(\nu)\right]I(t,\mathbf{r},\mathbf{\Omega},\nu)\rangle_\nu\,d\mu\,d\phi}{\int\langle I(t,\mathbf{r},\mathbf{\Omega},\nu)\rangle_\nu\,d\mu\,d\phi}\int J\,d\mu\,d\phi\\&+\int\frac{1}{4\pi}\int_{\mathbf{\Omega}'}J(\mathbf{\Omega}')(\sigma_E^s+\sigma_F^s\mathbf{\Omega}\cdot\mathbf{\Omega}'+\sigma_G^s(\mathbf{\Omega}\cdot\mathbf{\Omega}')^2)\,d\mathbf{\Omega}'\,d\mu\,d\phi\end{aligned} \tag{2.13}$$

We now replace the indefinite integrals in the numerator and denominator of the second and third terms on the rhs of (2.13) with definite integrals over the full 4π of $\mathbf{\Omega}$ and then differentiate the resulting equation with respect to μ and ϕ.

This approximation allows us to define the following new mean absorption and scattering coefficients σ_P^e, σ_E^a, and σ_E^{is}, the last two being approximations of $\sigma_E^{a,\nu}$ and $\sigma_E^{is,\nu}$ respectively:

$$\sigma_P^e(T)=\frac{\langle\sigma^a(\nu)\mathcal{B}(\nu,T)\rangle_{\nu,\mathbf{\Omega}}}{\langle\mathcal{B}(\nu,T)\rangle_{\nu,\mathbf{\Omega}}}=\sigma_P^{e,\nu}(T) \tag{2.14}$$

$$\sigma_E^a(t,\mathbf{r})=\frac{\langle\sigma^a(\nu)I(t,\mathbf{r},\mathbf{\Omega},\nu)\rangle_{\nu,\mathbf{\Omega}}}{\langle I(t,\mathbf{r},\mathbf{\Omega},\nu)\rangle_{\nu,\mathbf{\Omega}}}\simeq\frac{\langle\sigma^a(\nu)I(t,\mathbf{r},\mathbf{\Omega},\nu)\rangle_{\nu,4\pi}}{\langle I(t,\mathbf{r},\mathbf{\Omega},\nu)\rangle_{\nu,4\pi}}=\sigma_E^{a,\nu} \tag{2.15}$$

$$\begin{aligned}\sigma_E^{is}(t,\mathbf{r})=&\frac{\langle\sigma^{is}(\nu)\left[1-\chi(\nu)\right]I(t,\mathbf{r},\mathbf{\Omega},\nu)\rangle_{\nu,\mathbf{\Omega}}}{\langle I(t,\mathbf{r},\mathbf{\Omega},\nu)\rangle_{\nu,\mathbf{\Omega}}}\\\simeq&\frac{\langle\sigma^{is}(\nu)\left[1-\chi(\nu)\right]I(t,\mathbf{r},\mathbf{\Omega},\nu)\rangle_{\nu,4\pi}}{\langle I(t,\mathbf{r},\mathbf{\Omega},\nu)\rangle_{\nu,4\pi}}=\sigma_E^{is,\nu}.\end{aligned} \tag{2.16}$$

The elimination of the $\mathbf{\Omega}$ dependence of the mean absorption coefficients constitutes our first approximation. It is not strictly necessary to the closure: one could choose to not make it. The three mean incoming scattering coefficients are unchanged from (2.9)-(2.11). The frequency-integrated RTE with these approximations becomes

$$\begin{aligned}\frac{1}{c}\partial_t J+\mathbf{\Omega}\cdot\nabla J=&\frac{\sigma_P^e}{4\pi}aT^4-\sigma_E^aJ-\sigma_E^{is}J\\&+\frac{1}{4\pi}\int_{\mathbf{\Omega}'}J(\mathbf{\Omega}')(\sigma_E^s+\sigma_F^s\mathbf{\Omega}\cdot\mathbf{\Omega}'+\sigma_G^s(\mathbf{\Omega}\cdot\mathbf{\Omega}')^2)d\mathbf{\Omega}'\,.\end{aligned} \tag{2.17}$$

We now introduce the following macroscopic quantities: the radiative energy given by

$$E_R(t,\mathbf{r})=\frac{1}{c}\left\langle I(t,\mathbf{r},\mathbf{\Omega},\nu)\right\rangle_{\nu,\Omega}=\frac{1}{c}\left\langle J(t,\mathbf{r}\mathbf{\Omega})\right\rangle_\Omega \tag{2.18}$$

the radiative flux

$$\mathbf{F}_R(t,\mathbf{r}) = \langle \mathbf{\Omega}\, I(t,\mathbf{r},\mathbf{\Omega},\nu)\rangle_{\nu,\Omega} = \langle \mathbf{\Omega}\, J(t,\mathbf{r},\mathbf{\Omega})\rangle_{\Omega} \tag{2.19}$$

and finally the radiative pressure

$$\mathbf{P}_R(t,\mathbf{r}) = \frac{1}{c}\langle \mathbf{\Omega}\otimes\mathbf{\Omega}\, I(t,\mathbf{r},\mathbf{\Omega},\nu)\rangle_{\nu,\Omega} = \frac{1}{c}\langle \mathbf{\Omega}\otimes\mathbf{\Omega}\, J(t,\mathbf{r},\mathbf{\Omega})\rangle_{\Omega} \tag{2.20}$$

It should be noted that in (2.17) these moments appear in the integral term of the scattering. This term can then be absorbed in the definition of the moments and the integrated RTE written as

$$\begin{aligned}\frac{1}{c}\partial_t J + \mathbf{\Omega}\cdot\nabla J = {} & \frac{\sigma_P^e}{4\pi} aT^4 - \sigma_E^a J - \sigma_E^{is} J \\ & + \frac{1}{4\pi}\big(c\sigma_E^s E_R + \sigma_F^s \mathbf{F}_R\cdot\mathbf{\Omega} + c\sigma_G^s \sum_{i,j=1..3} P_R^{i,j}\Omega^i\Omega^j\big).\end{aligned} \tag{2.21}$$

For this equation four remarks should be given. First, the introduction of the mean coefficients allows expressing the scattering term as a function of the moments. Integrations of the intensity are still needed in order to compute the moments, and in that sense the formulations (2.17) and (2.21) are equivalent. Second, if the phase function has moments of order higher than 2, this will introduce moments of order higher than the pressure in the scattering term. Third, if the intensity used in the mean incoming scattering coefficients is the exact one, then the incoming scattering term is exact. Finally, this equation has been derived with two assumptions relative to the absorption and isotropic scattering terms, namely (2.15) and (2.16).

The frequency-integrated RTE (2.21) will be closed in the next section by proposing expressions for the mean coefficients σ_P^e, σ_E^a, σ_E^{is}, σ_E^s, σ_F^s, and σ_G^s in terms of the microscopic spectral coefficients σ^a, σ^{is}, σ^s, α, β, γ, and η.

2.3. *Closure of the radiative equation with mean coefficients*

The mean coefficients (2.15), (2.16), (2.9), (2.10), and (2.11) are closed in this section by assuming a particular functional form for the intensity used in their definitions. For σ_E^a for instance, it is assumed that

$$\sigma_E^a = \frac{\langle \sigma^a(\nu) I(t,\mathbf{r},\mathbf{\Omega},\nu)\rangle_\nu, 4\pi}{\langle I(t,\mathbf{r},\mathbf{\Omega},\nu)\rangle_{\nu,4\pi}} \simeq \frac{\langle \sigma^a(\nu) I^*(t,\mathbf{r},\mathbf{\Omega},\nu)\rangle_{\nu,4\pi}}{\langle I^*(t,\mathbf{r},\mathbf{\Omega},\nu)\rangle_{\nu,4\pi}} = \sigma_E^{a\,*} \tag{2.22}$$

where the assumed intensity is denoted I^*. Similarly we assume that

$$\sigma_E^{is} \simeq \sigma_E^{is\,*}, \quad \sigma_E^s \simeq \sigma_E^{s\,*}, \quad \sigma_F^s \simeq \sigma_F^{s\,*}, \quad \sigma_G^s \simeq \sigma_G^{s\,*} \tag{2.23}$$

where the designation * for the mean coefficients, $\sigma_E^{a\,*}$, $\sigma_E^{is\,*}$, $\sigma_E^{s\,*}$, $\sigma_F^{s\,*}$, and $\sigma_G^{s\,*}$, indicates that the intensity I has been replaced by the pseudo-intensity I^*.

If we now assume that, at a microscopic level, the spectral absorption coefficient σ^a can be approximated as a sum of polynomial functions of frequency: $\sigma^a(\nu) = \sum_{i=1}^N C_i^a \nu^{i-3}$, it follows that

$$\sigma_P^e = \sum_{i=1}^N \sigma_{P\,i}(C_i^a, T) \quad \text{and} \quad \sigma_E^{a\,*} = \sum_{i=1}^N \sigma_{E\,i}^*(C_i^a, T_R, \mathbf{f}) \tag{2.24}$$

where $\sigma_{P\,i}$ and $\sigma_{E\,i}$ will be derived in the next section (Eqs. (2.32) and (2.38)). In particular, it will be shown that they depend on the radiative temperature T_R and on the anisotropic factor $\mathbf{f}$ defined below.

If the spectral scattering coefficient can also be written as $\sigma^{is}(\nu)\,[1-\chi(\nu)] = \sum_{i=1}^{N} C_i^{is}\nu^{i-3}$, then the isotropic mean scattering coefficient can be then written in terms of σ_{Ei} (see Eq. (2.38) in the next section) and is given by

$$\sigma_E^{is\,*} = \sum_{i=1}^{N} \sigma_{Ei}^{*}(C_i^{is}, T_R, \mathbf{f}) \tag{2.25}$$

Now let us assume that the incoming spectral scattering coefficients can also be approximated as sums of polynomial functions:

$$\sigma^s(\nu)\alpha(\nu) = \sum_{i=1}^{N} C_i^{\alpha,s}\nu^{i-3},\ \sigma^s(\nu)\beta(\nu) = \sum_{i=1}^{N} C_i^{\beta,s}\nu^{i-3},\ \text{and}\ \sigma^s(\nu)\gamma(\nu) = \sum_{i=1}^{N} C_i^{\gamma,s}\nu^{i-3} \tag{2.26}$$

then we have

$$\sigma_E^{s\,*} = \sum_{i=1}^{N} \sigma_{Ei}^{*}(C_i^{\alpha,s}, T_R, \mathbf{f}),\quad \sigma_F^{s\,*} = \sum_{i=1}^{N} \sigma_{Fi}^{*}(C_i^{\beta,s}, T_R, \mathbf{f}),\quad \sigma_G^{s\,*} = \sum_{i=1}^{N} \sigma_{Gi}^{*}(C_i^{\beta,s}, T_R, \mathbf{f}). \tag{2.27}$$

Finally, using these models for the mean absorption coefficients, the frequency-integrated RTE in its closed form is given by

$$\frac{1}{c}\partial_t J + \mathbf{\Omega}\cdot\nabla J = \frac{\sigma_P^e}{4\pi} aT^4 - \sigma_E^{a\,*} J - \sigma_E^{is\,*} J + \frac{1}{4\pi}(c\sigma_E^{s\,*} E_R + \sigma_F^{s\,*}\mathbf{F}_R\cdot\mathbf{\Omega} + c\sigma_G^{s\,*}\sum_{i,j=1..3} P_R^{i,j}\Omega^i\Omega^j) \tag{2.28}$$

where all the mean coefficients are defined in terms of the functions σ_{Ei}^{*}, σ_{Fi}^{*} , and σ_{Gi}^{*} defined in the following section.

2.4. *Computation of the mean coefficients*

The pseudo-intensity which is used in the definition of the mean coefficients is obtained from the maximization of the radiative entropy (Minerbo 1978; Fort 1997) and is given by

$$I^*(t,\mathbf{r},\mathbf{\Omega},\nu) = \frac{2h\nu^3}{c^2}\left[\exp(\frac{h\nu}{kT^*(\mathbf{\Omega})}) - 1\right]^{-1} \tag{2.29}$$

with $T^*(\mathbf{\Omega}) = 1/(B(1-\mathbf{A}\cdot\mathbf{\Omega}))$ and $\mathbf{A}$ and B defined by

$$\mathbf{A} = \frac{2-\sqrt{4-3\|\mathbf{f}\|^2}}{\|\mathbf{f}\|^2}\mathbf{f},\quad B = \frac{1}{T_R}\left[\frac{3+\|\mathbf{A}\|^2}{3(1-\|\mathbf{A}\|^2)^3}\right]^{\frac{1}{4}}. \tag{2.30}$$

These two coefficients are defined from the macroscopic quantities T_R, the radiative temperature, and $\mathbf{f}$, the anisotropic factor. The radiative temperature is defined in terms of the radiative energy by $E_R = aT_R^4$, and the anisotropic factor is given by $\mathbf{f} = \mathbf{F}_R/(cE_R)$.

Let us assume that a polynomial approximation in frequency of the spectral absorption and scattering coefficients can be done. Such a coefficient is chosen to have the following form

$$\sigma(\nu) = \sum_{i=1}^{N} C_i\nu^{i-3} \tag{2.31}$$

where C_i are constants which depend on the gaseous medium considered, the volume fraction of the main species, the pressure, etc.

First, the well-known Planck mean absorption coefficient is computed from the Planck function (see Ripoll *et al.* 2001):

$$\sigma_P(T) = \frac{\langle \sigma(\nu)\mathcal{B}(\nu,T)\rangle_{\nu,\Omega}}{\langle \mathcal{B}(\nu,T)\rangle_{\nu,\Omega}} = \sum_{i=1}^{N} \sigma_{Pi}(C_i,T) = \frac{15}{\pi^4} \sum_{i=1}^{N} i!\ C_i\ \zeta(i+1) \left(\frac{kT}{h}\right)^{i-3} \tag{2.32}$$

(2.33)

Second, the three mean coefficients σ_E^*, σ_F^*, and σ_G^* are defined by

$$\sigma_E^*(t,\mathbf{r}) = \frac{\langle \sigma(\nu) I^*(t,\mathbf{r},\mathbf{\Omega},\nu)\rangle_{\nu,\mathbf{\Omega}}}{\langle I^*(t,\mathbf{r},\mathbf{\Omega},\nu)\rangle_{\nu,\mathbf{\Omega}}} \tag{2.34}$$

$$\sigma_F^*(t,\mathbf{r},\mathbf{\Omega}) = \frac{\langle \sigma(\nu)\mathbf{\Omega}\cdot\mathbf{\Omega}' I^*(t,\mathbf{r},\mathbf{\Omega}',\nu)\rangle_{\nu,\mathbf{\Omega}'}}{\langle \mathbf{\Omega}\cdot\mathbf{\Omega}' I^*(t,\mathbf{r},\mathbf{\Omega}',\nu)\rangle_{\nu,\mathbf{\Omega}'}} = \frac{\mathbf{\Omega}\cdot\langle \sigma(\nu)\mathbf{\Omega}' I^*(t,\mathbf{r},\mathbf{\Omega}',\nu)\rangle_{\nu,\mathbf{\Omega}'}}{\mathbf{\Omega}\cdot\langle \mathbf{\Omega}' I^*(t,\mathbf{r},\mathbf{\Omega}',\nu)\rangle_{\nu,\mathbf{\Omega}'}} \tag{2.35}$$

$$\sigma_G^*(t,\mathbf{r},\mathbf{\Omega}) = \frac{\langle \sigma(\nu)(\mathbf{\Omega}\cdot\mathbf{\Omega}')^2 I^*(t,\mathbf{r},\mathbf{\Omega}',\nu)\rangle_{\nu,\mathbf{\Omega}'}}{\langle (\mathbf{\Omega}\cdot\mathbf{\Omega}')^2 I^*(t,\mathbf{r},\mathbf{\Omega}',\nu)\rangle_{\nu,\mathbf{\Omega}'}}. \tag{2.36}$$

It should be noticed here that in I^* the $\mathbf{\Omega}$ dependence is only present through a scalar product with the vector $\mathbf{A}$. This greatly simplifies σ_F as follows. The vector $\langle \mathbf{\Omega}' I^*(t,\mathbf{r},\mathbf{\Omega}',\nu)\rangle_{\mathbf{\Omega}'}$ necessarily has the form $X(t,\mathbf{r},\nu)\,\mathbf{A}(t,\mathbf{r})$, where X is a scalar, which leads to

$$\sigma_F^*(t,\mathbf{r}) = \frac{\langle \sigma(\nu) X(t,\mathbf{r},\nu)\rangle_{\nu}}{\langle X(t,\mathbf{r},\nu)\rangle_{\nu}} \tag{2.37}$$

Thus, σ_F^* does not depend on $\mathbf{\Omega}$.

Moreover, the simple form of I^* leads to analytical expressions for σ_E and σ_F, though the computation is not detailed here (see Ripoll *et al.* 2001). These coefficients have also been tested and validated for simple 1D problems (see Ripoll & Wray 2004a). They are given by:

$$\begin{aligned}\sigma_E^*(T_R,\mathbf{f}) &= \sum_{i=1}^{N} \sigma_{Ei}^*(C_i,T_R,\mathbf{f}) \\ &= \frac{45}{2\pi^4} \sum_{i=1}^{N} (i-1)!\ C_i\ \zeta(i+1) \left(\frac{k}{hB(1-\|\mathbf{A}\|^2)}\right)^{i-3} \frac{P_E^i(\|\mathbf{A}\|)}{\|\mathbf{A}\|}\end{aligned} \tag{2.38}$$

$$\begin{aligned}\sigma_F^*(T_R,\mathbf{f}) &= \sum_{i=1}^{N} \sigma_{Fi}^*(C_i,T_R,\mathbf{f}) \\ &= \frac{45}{8\pi^4} \sum_{i=1}^{N} (i-2)!\ C_i\ \zeta(i+1) \left(\frac{k}{hB(1-\|\mathbf{A}\|^2)}\right)^{i-3} \frac{P_F^i(\|\mathbf{A}\|)}{\|\mathbf{A}\|^3}\end{aligned} \tag{2.39}$$

with

$$P_E^i(\|\mathbf{A}\|) = ((1+\|\mathbf{A}\|)^i - (1-\|\mathbf{A}\|)^i)/(3+\|\mathbf{A}\|^2) \tag{2.40}$$

$$P_F^i(\|\mathbf{A}\|) = (1-\|\mathbf{A}\|)^i(i\|\mathbf{A}\|+1) + (1+\|\mathbf{A}\|)^i(i\|\mathbf{A}\|-1) \tag{2.41}$$

with ζ the Riemann Zeta function and $\mathbf{A}$ and B given in (2.30)†. The derivation of σ_G

† for i real but non-integer, these expressions are valid provided $i!$ is replaced with $\Gamma(i+1)$

involves the pressure tensor and is much more complex. We have

$$\sigma_G^s = \frac{\langle \sigma(\nu) \sum_{j,k} \Omega_j \Omega'_j \Omega_k \Omega'_k I^* \rangle_{\nu,\Omega'}}{\langle \sum_{j,k} \Omega_j \Omega'_j \Omega_k \Omega'_k I^* \rangle_{\nu,\Omega'}} \quad j,k = 1..3 \tag{2.42}$$

Following the same developments as in Ripoll *et al.* 2001, it is found that

$$\sigma_G^*(T_R, \mathbf{f}) = \sum_{i=1}^{N} \sigma_{Gi}^*(C_i, T_R, \mathbf{f}) \tag{2.43}$$

$$= \frac{45}{2\pi^4} \sum_{i=1}^{N} (i-3)!\; C_i\; \zeta(i+1) \left(\frac{k}{hB(1-\|\mathbf{A}\|^2)} \right)^{i-3} \frac{P_G^i(\mathbf{\Omega}, \|\mathbf{A}\|)}{\|\mathbf{A}\|^5} \tag{2.44}$$

where $P_G^i(\mathbf{A}, \|\mathbf{\Omega}\|)$ is given by

$$\begin{aligned} P_G^i = {} & \frac{(1-\|\mathbf{A}\|)^i}{1-\|\mathbf{A}\|^2+4(\mathbf{A}\cdot\mathbf{\Omega})^2} \big[(1-\|\mathbf{A}\|^2)\|\mathbf{A}\|^2 + (\|\mathbf{A}\|^2-3)(\mathbf{A}\cdot\mathbf{\Omega})^2 \\ & + i\|\mathbf{A}\| \big[(1+\|\mathbf{A}\|)\|\mathbf{A}\|^2 - (\|\mathbf{A}\| i + 3)(\mathbf{A}\cdot\mathbf{\Omega})^2\big]\big] \\ & + \frac{(1+\|\mathbf{A}\|)^i}{1-\|\mathbf{A}\|^2+4(\mathbf{A}\cdot\mathbf{\Omega})^2} \big[(\|\mathbf{A}\|^2-1)\|\mathbf{A}\|^2 + (3-\|\mathbf{A}\|^2)(\mathbf{A}\cdot\mathbf{\Omega})^2\big) \\ & + i\|\mathbf{A}\| \big[(1-\|\mathbf{A}\|)\|\mathbf{A}\|^2 + (\|\mathbf{A}\| i - 3)(\mathbf{A}\cdot\mathbf{\Omega})^2\big]\big] \end{aligned} \tag{2.45}$$

It should be noticed here that the Planck mean σ_P is a function of the volume fractions C_i and of the temperature, while the effective mean coefficients σ_E^*, σ_F^* are functions of C_i and of both the radiative temperature and anisotropic factor. In addition, σ_G^* is dependent on the scalar product between a vector parallel to the flux and the direction $\mathbf{\Omega}$.

The mean coefficients have been introduced to avoid the cost of the frequency integration. Thus, to be useful, the numerical cost of evaluating the mean coefficients and of the iterations needed to solve for J must be lower than that of these time integrations. The coefficients which are proposed here are analytic and should have low computational cost. Furthermore, the three coefficients $\sigma_{E,F,G}^*$ have common parts (see (2.38)-(2.44)). For absorbing media, it has been found that fewer than 6 iterations to solve the RTE were needed in the cases studied (Ripoll & Wray 2004a), which indicates that this method does not have a high numerical cost.

3. The linear case: application to soot

The apparent complexity of the coefficients in the previous section is only due to the polynomial expansion in frequency. For sooty media the absorption dependence is linear, and in this case the coefficients turn out to be quite simple.

The linear spectral absorption and isotropic scattering coefficients are written as

$$\sigma^e(\nu) = C^e \nu, \quad \sigma^a(\nu) = C^a \nu, \quad \text{and} \quad \sigma^{is}(\nu)\,[1-\chi(\nu)] = C^{is}\nu \tag{3.1}$$

As a rough approximation, we here also assume that the scattering follows a linear law†. The spectral scattering coefficients are then written as

$$\sigma^s(\nu)\alpha(\nu) = C^{\alpha,s}\nu, \quad \sigma^s(\nu)\beta(\nu) = C^{\beta,s}\nu, \quad \text{and} \quad \sigma^s(\nu)\gamma(\nu) = C^{\gamma,s}\nu. \tag{3.2}$$

† More complex models, such as in Houf 1999, could also be treated but would need to introduce higher order terms in frequency

We define for convenience the following coefficients:

$$C_P^x = 360\frac{k\zeta_5}{\pi^4 h}C^x \tag{3.3}$$

where x is a variable which will alternatively take the value a, e, is, (α,s), (β,s), (γ,s) below. The Planck absorption coefficient becomes then

$$\sigma_P^e(T) = \sigma_{P4}(C^e,T) = 360\ C^e\frac{k\zeta_5}{\pi^4 h}T = C_P^e\,T \tag{3.4}$$

Using (2.38), (2.39), (2.44) for $i=4$, and the definition (3.1), the general form for the mean coefficients is given by

$$\sigma_{E4}^*(C^x,T_R,\mathbf{f}) = \ 3C_P^x\frac{1+\|\mathbf{A}\|^2}{B(1-\|\mathbf{A}\|^2)(3+\|\mathbf{A}\|^2)} = C_P^x\,T_R\,G_E(\mathbf{f}) \tag{3.5}$$

$$\sigma_{F4}^*(C^x,T_R,\mathbf{f}) = \ \frac{C_P^x}{4}\frac{5+\|\mathbf{A}\|^2}{B(1-\|\mathbf{A}\|^2)} = C_P^x\,T_R\,G_F(\mathbf{f}) \tag{3.6}$$

$$\sigma_{G4}^*(C^x,T_R,\mathbf{f}) = C_P^x\frac{(1-\|\mathbf{A}\|^2+6(\mathbf{A}\cdot\mathbf{\Omega})^2)}{B(1-\|\mathbf{A}\|^2)(1-\|\mathbf{A}\|^2+4(\mathbf{A}\cdot\mathbf{\Omega})^2)} = C_P^x\,T_R\,G_G(\mathbf{f},\mathbf{\Omega}) \tag{3.7}$$

where the functions $G_{E,F,G}$ are obtained by using the definitions (2.30) in (3.5)-(3.7). Hence, the mean absorption and isotropic scattering coefficients are given in the linear case by

$$\sigma_E^{a\,*} = \sigma_{E4}^*(C^a,T_R,\mathbf{f}) = C_P^a\,T_R\,G_E(\mathbf{f}) \tag{3.8}$$

$$\sigma_E^{is\,*} = \sigma_{E4}^*(C^{is},T_R,\mathbf{f}) = C_P^{is}\,T_R\,G_E(\mathbf{f}) \tag{3.9}$$

and the incoming mean scattering coefficients are given by

$$\sigma_E^{s\,*} = \sigma_{E4}^*(C^{\alpha,s},T_R,\mathbf{f}) = C_P^{\alpha,s}\,T_R\,G_E(\mathbf{f}) \tag{3.10}$$

$$\sigma_F^{s\,*} = \sigma_{F4}^*(C^{\beta,s},T_R,\mathbf{f}) = C_P^{\beta,s}\,T_R\,G_F(\mathbf{f}) \tag{3.11}$$

$$\sigma_G^{s\,*} = \sigma_{G4}^*(C^{\gamma,s},T_R,\mathbf{f},\mathbf{\Omega}) = C_P^{\gamma,s}\,T_R\,G_G(\mathbf{f},\mathbf{\Omega}). \tag{3.12}$$

The integrated RTE,

$$\frac{1}{c}\partial_t J+\mathbf{\Omega}\cdot\nabla J = \frac{\sigma_P^e}{4\pi}aT^4-\sigma_E^{a\,*}J-\sigma_E^{is\,*}J+\frac{1}{4\pi}(c\sigma_E^{s\,*}E_R+\sigma_F^{s\,*}\mathbf{F}_R\cdot\mathbf{\Omega}+c\sigma_G^{s\,*}\sum_{i,j=1..3}P_R^{i,j}\Omega^i\Omega^j) \tag{3.13}$$

becomes using the previous definitions :

$$\begin{aligned}\frac{1}{c}\partial_t J+\mathbf{\Omega}\cdot\nabla J = &\frac{C_P^a}{4\pi}aT^5-C_P^aT_RG_E(\mathbf{f})J-C_P^{is}T_RG_E(\mathbf{f})J\\ &+\frac{T_R}{4\pi}(cC_P^\alpha G_E(\mathbf{f})E_R+C_P^\beta G_F(\mathbf{f})\mathbf{F}_R\cdot\mathbf{\Omega}+cC_P^\gamma G_G(\mathbf{f},\mathbf{\Omega})\sum_{i,j=1..3}P_R^{i,j}\Omega^i\Omega^j).\end{aligned} \tag{3.14}$$

If isotropy is assumed for the functions $G_{E,F,G}$, the following simpler form is obtained:

$$\begin{aligned}\frac{1}{c}\partial_t J+\mathbf{\Omega}\cdot\nabla J = &\frac{C_P^a}{4\pi}aT^5-C_P^aT_RJ-C_P^{is}T_RJ\\ &+\frac{T_R}{4\pi}(cC_P^\alpha E_R+C_P^{\beta\,\prime}\mathbf{F}_R\cdot\mathbf{\Omega}+cC_P^\gamma\sum_{i,j=1..3}P_R^{i,j}\Omega^i\Omega^j)\end{aligned} \tag{3.15}$$

with $C_P^{\beta'} = 5/4C_P^{\beta}$. In Ripoll & Wray 2004a, it was found that the function G_E played an important role. Eq. 3.15 should hence not be used for radiating flows where the anisotropy $\|f\|$ is larger than 0.3.

4. Macroscopic radiation models for absorbing and scattering media

We show in this section that the mean coefficients can be easily included in macroscopic moment models. We define the three first moments with respect to direction as

$$E_R^{\mathbf{\Omega}}(t,\mathbf{r},\nu) = \frac{1}{c}\left\langle I(t,\mathbf{r},\mathbf{\Omega},\nu)\right\rangle_{\Omega} \tag{4.1}$$

$$\mathbf{F}_R^{\mathbf{\Omega}}(t,\mathbf{r},\nu) = \left\langle \mathbf{\Omega}\, I(t,\mathbf{r},\mathbf{\Omega},\nu)\right\rangle_{\Omega} \tag{4.2}$$

$$\mathbf{P}_R^{\mathbf{\Omega}}(t,\mathbf{r},\nu) = \frac{1}{c}\left\langle \mathbf{\Omega}\otimes\mathbf{\Omega}\, I(t,\mathbf{r},\mathbf{\Omega},\nu)\right\rangle_{\Omega} \tag{4.3}$$

The first moment equation is obtained by integrating Eq. (2.1) with respect to $\mathbf{\Omega}$. We obtain

$$\partial_t E_R^{\mathbf{\Omega}} + \nabla\cdot\mathbf{F}_R^{\mathbf{\Omega}} = 4\pi c\sigma^a(\nu)\mathcal{B} - c\sigma^a(\nu)E_R^{\mathbf{\Omega}} \tag{4.4}$$

where the incoming and isotropic scattering have canceled using the normalization property (2.4).

Multiplying (2.1) by $\mathbf{\Omega}$, and integrating with respect to it, using the phase function definition (2.3), we obtain

$$\frac{1}{c}\partial_t\mathbf{F}_R^{\mathbf{\Omega}} + c\nabla\cdot\mathbf{P}_R^{\mathbf{\Omega}} = -(\sigma^a(\nu) + \sigma^{is}(\nu)(1-\chi(\nu)) - \sigma^s(\nu)\frac{\beta(\nu)}{3})\mathbf{F}_R^{\mathbf{\Omega}}. \tag{4.5}$$

The following three equalities have been used:

$$\int \Omega_i\, d\mathbf{\Omega} = 0, \quad \int \Omega_i\Omega_j\, d\mathbf{\Omega} = 4\pi/3\delta_{ij}, \quad \int \Omega_i\Omega_j\Omega_k\, d\mathbf{\Omega} = 0. \tag{4.6}$$

Using definitions (2.18), (2.19), and (2.20), the integration of (4.4) over frequency gives

$$\partial_t E_R + \nabla\cdot\mathbf{F}_R = ca\left(\sigma_P^e T^4 - \sigma_E^a E_R\right) \tag{4.7}$$

where models σ_P^e and $\sigma_E^a \simeq \sigma_E^{a\,*}$ were given previously in (2.24).

Integrating (4.5) over frequency leads to the second moment equation

$$\frac{1}{c}\partial_t\mathbf{F}_R + c\nabla\cdot\mathbf{P}_R = -(\sigma_F^a + \sigma_F^{is} - \frac{1}{3}\sigma_F^{\beta})\mathbf{F}_R, \tag{4.8}$$

for which the models for the mean coefficients are

$$\sigma_F^a \simeq \sigma_F^{a\,*} = \sum_{i=1}^{N}\sigma_{Fi}(C_i^a, T_R, \mathbf{f}) \tag{4.9}$$

$$\sigma_F^{is} \simeq \sigma_F^{is\,*} = \sum_{i=1}^{N}\sigma_{Fi}(C_i^{is}, T_R, \mathbf{f}) \tag{4.10}$$

$$\sigma_F^{\beta} \simeq \sigma_F^{\beta\,*} = \sum_{i=1}^{N}\sigma_{Fi}(C_i^{\beta,s}, T_R, \mathbf{f}) \tag{4.11}$$

where σ_{Fi} is defined in (2.39).

Closure of the macroscopic model (4.7)-(4.8) is achieved by modeling the radiative

pressure in (4.8). In many different closures the pressure is written as $\mathbf{P_R} = \mathbf{D_R}(\mathbf{f})E_R$, where $\mathbf{D_R}(\mathbf{f})$ is the Eddington tensor (Ripoll & Wray 2004b).

Combining the steady forms of (4.8) and (4.7) to eliminate the flux $\mathbf{F}_R$ leads to the general Milne-Eddington equations

$$-\nabla\cdot\left(\frac{1}{(\sigma_F^a+\sigma_F^{is}-\frac{1}{3}\sigma_F^\beta)}\nabla\cdot(\mathbf{D}_R E_R)\right)=\sigma_P^e a T^4-\sigma_E^a E_R\ . \tag{4.12}$$

Or, similarly, by eliminating the energy E_R, one obtains

$$-\nabla\cdot\left(\frac{\mathbf{D}_R}{\sigma_E}\ \nabla\cdot\mathbf{F}_R\right)+(\sigma_F^a+\sigma_F^{is}-\frac{1}{3}\sigma_F^\beta)\mathbf{F}_R=-c\vec{\nabla}\cdot\left(\frac{\sigma_P^e}{\sigma_E^a}\mathbf{D}_R a T^4\right)\ . \tag{4.13}$$

We have two main comments on the model (4.7)-(4.8); they also apply to the formulation (4.12)-(4.13). First, the normalization property (2.4) eliminates the pressure term coming from the scattering in the first moment equation (4.7). Second, the contribution of the incoming scattering integrated over direction only enters through the first order and delta-function parts of the scattering function in (4.13), since the zero and second order terms vanish.

5. On the use of these models and their numerical costs

The models presented here will be useful when the solution for frequency dependent intensities cannot be done due to its cost. This is usually the case for coupled problems. We now give a discussion on reducing the computational cost of the models presented here.

First, when using mean coefficients, it is possible to reduce the computational cost by noticing that when the radiation is isotropic and close to equilibrium, the coefficients $\sigma_{E,G}$ are equal to the Planck mean and σ_F to $(i+1/4)\sigma_P$. There is hence no need to evaluate the complex expressions for $\sigma_{E,F,G}$, and they should be simply replaced by their limits. More generally, these limits can be extended to $\|f\|<0.1$ when $T\simeq T_R$. In the case where the radiation is isotropic but $T\neq T_R$, the limit that should be taken is also the Planck mean but evaluated at T_R instead of T†. It should also be noticed that the form of the mean coefficients proposed here, in terms of $\mathbf{A}$ and B, should be retained. As a matter of fact, this choice allows checking the different limits and avoids introducing singularities. For instance, (2.30) can directly be replaced by their limits, respectivelly $A=0$ and $B=1/T$, for $\|f\|<0.1$.

The solution of the RTE with mean coefficients requires iteration since the mean coefficients are nonlinear functions of I. The required number of iterations has been found to be small in many simple cases (Ripoll & Wray 2004a), but one could be tempted to reduce it further. In the case of using such an equation for coupled problems, the previous time step provides excellent starting values for the iterative solution so that the required number of iterations should be lower, perhaps only one or two. Another alternative in this case could be not to iterate the RTE at all, i.e., to lag it in time, assuming that a small difference between the opacity and the intensity due to their non-synchronization in time with the fluid motion will not strongly affect the solution. This is likely when a global convergence process of the hydrodynamics and radiation to a steady state leads to synchronizing all the variables at the end. For the very first iteration, the Planck limit seems to be a good initial condition. It should also be noticed here that the moment model

† as was shown in (3.15) in the linear case

(4.7)-(4.8) can similarly be solved by using the mean coefficients from the previous time step of the radiation loop or of the hydrodynamics loop in coupled problems.

6. Conclusion

The objective of this work was to propose a simple model accounting for radiation in complex emitting, absorbing, and scattering media. To do that, models for mean absorption and mean isotropic and incoming scattering coefficients have been proposed in the case where the various spectral coefficients can be written in terms of polynomial functions. Some of these models were previously derived and validated (Ripoll *et al.* 2001, Ripoll & Wray 2004a) for non-scattering media; they have been extended here to the general case. An integrated RTE which uses these coefficients has been derived where the integral scattering term has been absorbed into the modeling. Such a form of the RTE is much less costly to solve than the RTE in its non-modeled form. Macroscopic moment radiation models, written in their hyperbolic or diffusive forms, have also been derived using these coefficients. The particular case where the spectral coefficients are linear in frequency has been treated. This case is particularly important for soot and hence for combustion applications. It has also been explained how such models can be used at a lower cost by reducing the number of iterations needed. We believe the formulations proposed here could be used in many complex or coupled problems, like flows radiating in dusty media, where, for instance, isotropic and non-isotropic scattering are usually disregarded and neglected due to their computational cost.

REFERENCES

FORT, J. 1997 Information-theoretical approach to radiative transfer. *Phys. A.*, **243**, 275-303.

HOUF, W. G. 1999 The effect of scattering by soot aggregates on radiative transfer in large-scale hydrocarbon pool fires. *Sandia Nat. Lab. report*, SAND99-8254.

LEVERMORE, D. 1984 Relating Eddington factors to flux limiters. *Jour. of Quant. Spectrosc. & Radiat. Transfer*, **32(2)**, 149-160.

MINERBO, G. N. 1978 Maximum entropy eddington factors. *J. Quant. Spectrosc. Radiat. Transfer* **20**, 541-545.

MODEST, M.F. 2003 Radiative heat transfer. 3rd ed., McGraw-Hill.

RIPOLL, J.-F., DUBROCA, B. & DUFFA, G. 2001 Modelling radiative mean absorption coefficients. *Comb. Th. and Mod.* **5** (3), 261–275.

RIPOLL, J.-F., DUBROCA, B., AUDIT, E. 2002 A factored operator method for solving coupled radiation-hydrodynamics models. *Trans. Theory and Stat. Phys.*, **31**(4-6), 531-557.

RIPOLL, J.-F., WRAY, A. A. 2004 The radiative transfer equation with mean absorption coefficients. *Proceedings of the 4^{th} symposium of radiative transfer*, submitted.

RIPOLL, J.-F., WRAY, A. A. 2004 On closure models for radiative pressure. *Proceedings of the 4^{th} symposium of radiative transfer*, submitted.

SIEGEL, R. C. & HOWELL, J. R. 2001 *Thermal radiation heat transfer*. 4^{th} Ed., Taylor and Francis.

SYMTH, K. C., SHADDIX C. R. 1996 The Elusive history of $\tilde{m} = 1.57 - 0.56i$ for the refractive index of soot. *Comb. and Flame*, **107**, 314-320.

Macroscopic modeling and computation of radiation for a 2m diameter pool fire

By J.F. Ripoll

1. Motivation and objectives

In large pool fires, radiation is the predominant mode of heat transfer (Cox 1995; Tieszen 2001), and its computation is usually time consuming. The use of macroscopic moment models (Modest 2003; Siegel & Howell 2001), which have a lower cost than directly solving the radiative transfer equation (RTE), is thus very attractive. In this paper, the M_1 radiation model, sometimes referred to as *Maximum entropy closure* see (Minerbo 1978; Levermore 1984; Fort 1997; Brunner & Holloway 2001), is chosen to model the radiation field generated by a synthetic fire (Brown & Blanchat 2003).

The first goal of this work is to show the ability of the M_1 model to solve a real fire case occuring in a complex geometry. The fire considered here occurs in the FLAME facility of Sandia Albuquerque, and the particular and complex geometry of this facility will be taken into account. A discussion of the radiative characteristics of the fire will be given to show the coherence of the modeling.

Average opacities, also called effective mean absorption coefficients, are of outstanding importance for radiation modeling. They allow one to take into account, at a macroscopic level, the frequency dependence of the spectral opacity. For fires this spectral coefficient is mainly determined from the soot volume fraction and is linear in frequency. As a result, the mean absorption coefficients are different from the Planck mean absorption coefficient, which constitutes their usual approximation. In this paper, new effective mean absorption coefficients, derived in (Ripoll *et al.* 2001), are used to model the opacity field.

The opacity field is obtained from a computation using the Sandia Vulcan code and accounts for both gas and soot radiation. From this, a global coefficient representative of a mixture of soot and gas is derived and used in the computation of the emission and absorption coefficients.

The first part of this article is a description of the M_1 model, the mean absorption coefficients used therein, and the numerical scheme used for its solution. The second part is devoted to the validation of the M_1 results. In the particular case of two concentric black cold spheres cooling a hot, emitting gas, the solution obtained by the M_1 model is compared to the analytic solution. In the third part, results of the computation of the synthetic fire are given and discussed.

2. Radiative transfer equations

2.1. *The* $\mathbf{M_1}$ *radiative model*

The M_1, or Maximum entropy closure, radiative model (Minerbo 1978; Levermore 1984; Fort 1997; Brunner & Holloway 2001) describes the evolution of the radiative energy E_R

and the radiative flux $\vec{F}_R$ of a non-scattering medium at temperature T.

$$\partial_t E_R + \vec{\nabla} \cdot \vec{F}_R = c\big[\sigma a T^4 - \sigma E_R\big] \tag{2.1a}$$

$$\frac{1}{c}\partial_t \vec{F}_R + c\ \vec{\nabla} \cdot \left(\vec{\vec{D}}_R\ E_R\right) = -\sigma\ \vec{F}_R \tag{2.1b}$$

where c is the speed of light and σ the opacity. The radiative flux has three components in $\mathbb{R}^3$, $\vec{F}_R = (F_R^x,\ F_R^y,\ F_R^z)^T$. The Eddington tensor $\vec{\vec{D}}_R$ is computed from the Eddington factor χ and the anisotropic factor $\vec{f} = (f_x,\ f_y,\ f_z)^T = \vec{F}_R/(cE_R)$:

$$\vec{\vec{D}}_R = \frac{\vec{\vec{P}}_R}{E_R} = \frac{1-\chi}{2}\ \vec{\vec{Id}} + \frac{3\chi - 1}{2}\ \vec{n} \otimes \vec{n} \ \text{ with } \vec{n} = \frac{\vec{f}}{\|f\|} \tag{2.2}$$

where $\vec{\vec{Id}}$ denotes the identity matrix, $\vec{\vec{P}}_R$ is the radiative pressure, and $\otimes$ stands for the dyadic product. The Eddington factor $\chi(\vec{f})$ is a function of the Euclidian norm of $\vec{f}$, $\|f\|$†

$$\chi(\vec{f}) = \frac{3 + 4\|f\|^2}{5 + 2\sqrt{4 - 3\|f\|^2}}. \tag{2.3}$$

The radiative temperature is defined from the radiative energy by

$$T_R = \left(\frac{E_R}{a}\right)^{\frac{1}{4}} \quad \text{with} \quad a = \frac{8}{15}\frac{\pi^5 k^4}{h^3 c^3} \tag{2.4}$$

where k is the Boltzmann constant and h the Planck constant.

2.2. *Computation of mean absorption coefficients*

When the spectral coefficients can be written as polynomial functions of the frequency, it is possible to derive closed formulas for the mean absorption coefficients using the following pseudo-intensity I^* (Ripoll *et al.* 2001):

$$I^* = I(\nu, T^*(\vec{\Omega})) = \frac{2h\nu^3}{c^2}\left[\exp\left(\frac{h\nu}{kT^*(\vec{\Omega})}\right) - 1\right]^{-1} \tag{2.5}$$

where h is the Planck constant, k the Boltzmann constant, ν the frequency, $\vec{\Omega}$ the direction of propagation, and $T^*(\vec{\Omega}) = T/(B(1 - \vec{A}\cdot\vec{\Omega}))$ with $\vec{A}$ and B defined by

$$\vec{A} = \frac{2 - \sqrt{4 - 3\|f\|^2}}{\|f\|^2}\vec{f}, \tag{2.6}$$

$$B = \frac{T}{T_R}\left[\frac{3 + \|A\|^2}{3(1 - \|A\|^2)^3}\right]^{\frac{1}{4}} \tag{2.7}$$

This pseudo-intensity has a Planckian form and maximizes the radiative entropy (or minimizes the mathematical entropy) under the constraint of the reconstruction of the two radiative moments (Minerbo 1978; Fort 1997; Brunner & Holloway 2001). $\vec{A}$ and B are given by this constraint.

When the spectral absorption coefficient is frequency dependent, i.e. when the medium is not gray, this intensity can also be used to define the associated effective absorption coefficients σ_E and σ_F, which are given below.

† $\|g\|$ denotes the Euclidian norm of a vector $\vec{g}$.

For sooty flames, such that the size of the soot particles is much smaller than the mean free path (Rayleigh approximation), the spectral absorption coefficient is linear in frequency, becoming simply $\sigma(\nu) = C_1\nu$, where C_1 depends on the soot volume fraction C_s and is defined in (Smith & Shaddix 1996) by

$$C_1 = \frac{1}{c}\frac{36\pi n\, p\, C_s}{(n^2 - p^2 + 2)^2 + 4n^2p^2},$$

where the values $n \simeq 1.57$ and $p = 0.56$ of (Smith & Shaddix 1996) are used. Hence C_1 is a linear function of the soot volume fraction: $C_1 = 8.33 \times 10^{-9}\, C_s$.

The well-known Planck mean absorption coefficient, σ_P, is given by

$$\sigma_P(T) = \frac{\langle \sigma(\nu)\mathcal{B}(\nu, T)\rangle_{\nu,\Omega}}{\langle \mathcal{B}(\nu, T)\rangle_{\nu,\Omega}} \tag{2.8}$$

where $\mathcal{B}$ is the Planck function and $\langle\mathcal{B}\rangle_{\nu,\Omega}$ denotes the integration of $\mathcal{B}$ over frequency ν and direction Ω. The effective mean absorption coefficients, σ_E and σ_F, are defined and modeled by

$$\sigma_E(t, \mathbf{r}) = \frac{\langle \sigma(\nu) I(t, \mathbf{r}, \mathbf{\Omega}, \nu)\rangle_{\nu,\mathbf{\Omega}}}{\langle I(t, \mathbf{r}, \mathbf{\Omega}, \nu)\rangle_{\nu,\mathbf{\Omega}}} \simeq \frac{\langle \sigma(\nu) I^*(t, \mathbf{r}, \mathbf{\Omega}, \nu)\rangle_{\nu,\mathbf{\Omega}}}{\langle I^*(t, \mathbf{r}, \mathbf{\Omega}, \nu)\rangle_{\nu,\mathbf{\Omega}}} \tag{2.9}$$

$$\sigma_F(t, \mathbf{r}) = \frac{\langle \sigma(\nu)\mathbf{\Omega} I(t, \mathbf{r}, \mathbf{\Omega}, \nu)\rangle_{\nu,\mathbf{\Omega}}}{\langle \mathbf{\Omega} I(t, \mathbf{r}, \mathbf{\Omega}, \nu)\rangle_{\nu,\mathbf{\Omega}}} \simeq \frac{\langle \sigma(\nu)\mathbf{\Omega} I^*(t, \mathbf{r}, \mathbf{\Omega}, \nu)\rangle_{\nu,\mathbf{\Omega}}}{\langle \mathbf{\Omega} I^*(t, \mathbf{r}, \mathbf{\Omega}, \nu)\rangle_{\nu,\mathbf{\Omega}}} \tag{2.10}$$

and are functions of time t and position r. These integrals are computed in (Ripoll *et al.* 2001) and are given by:

$$\sigma_P = 360\; C_1 \frac{k\zeta_5}{\pi^4 h} T = C_P\, T \quad \text{with} \quad C_P = 360\frac{k\zeta_5}{\pi^4 h} C_1 \tag{2.11}$$

$$\sigma_E = 1080 C_1\; \frac{k\zeta_5 T(1 + \|A\|^2)}{h\pi^4 B(3 + \|A\|^2)(1 - \|A\|^2)} \;=\; 3\sigma_P \frac{1 + \|A\|^2}{B(3 + \|A\|^2)(1 - \|A\|^2)}, \tag{2.12}$$

$$\sigma_F = 90 C_1 \frac{k\zeta_5 T(5 + \|A\|^2)}{h\pi^4 B(1 - \|A\|^2)} = \frac{\sigma_P}{4}\frac{5 + \|A\|^2}{B(1 - \|A\|^2)}. \tag{2.13}$$

Using (2.6) and (2.7), the coefficients become

$$\sigma_E = C_P\, G_E(f)\, T_R \quad \text{and} \quad \sigma_F = C_P\, G_F(f)\, T_R \tag{2.14}$$

with

$$G_E(f) = \frac{3}{4}\frac{\left(-1 + \sqrt{4 - 3\|f\|^2}\right)^{1/4}\left(\|f\|^2 - 4 + 2\sqrt{4 - 3\|f\|^2}\right)\|f\|}{\sqrt{\|f\|^2 - 2 + \sqrt{4 - 3\|f\|^2}}\left(-2 + \sqrt{4 - 3\|f\|^2}\right)} \tag{2.15}$$

$$G_F(f) = \frac{1}{4}\frac{\left(-1 + \sqrt{4 - 3\|f\|^2}\right)^{1/4}\left(\|f\|^2 + 4 - 2\sqrt{4 - 3\|f\|^2}\right)}{\sqrt{\|f\|^2 - 2 + \sqrt{4 - 3\|f\|^2}}\|f\|}. \tag{2.16}$$

The M_1 radiative model with mean coefficients becomes

$$\partial_t E_R + \vec{\nabla}\cdot\vec{F}_R = c\left[\sigma_P a T^4 - \sigma_E E_R\right] \tag{2.17a}$$

$$\frac{1}{c}\partial_t \vec{F}_R + c\;\vec{\nabla}\cdot\left(\vec{\vec{D}}_R\; E_R\right) = -\sigma_F\;\vec{F}_R \tag{2.17b}$$

2.3. *Numerical Schemes*

The M_1 model with mean coefficients can be reformulated in a conservative form as follows (Ripoll *et al.* 2002):

$$\partial_t U_R + \nabla_x\ F(U_R) + \nabla_y\ G(U_R) + \nabla_z\ H(U_R) = S_R(U_R, T) \tag{2.18}$$

where

$$U_R = \left(E_R,\ \frac{1}{c}\ F_R^x,\ \frac{1}{c}\ F_R^y,\ \frac{1}{c}\ F_R^z \right) \tag{2.19}$$

$$F(U_R) = (\ F_R^x,\ cD_R^{xx}E_R,\ cD_R^{xy}E_R,\ cD_R^{xz}E_R\ ) \tag{2.20}$$

$$G(U_R) = (\ F_R^y,\ cD_R^{yx}E_R,\ cD_R^{yy}E_R,\ cD_R^{yz}E_R)\,, \tag{2.21}$$

$$H(U_R) = (\ F_R^z,\ cD_R^{zx}E_R,\ cD_R^{zy}E_R,\ cD_R^{zz}E_R)\,, \tag{2.22}$$

$$S_R(U_R, T) = \left(\ c\left(a\sigma_P T^4 - \sigma_E E_R\right),\ -\sigma_F F_R^x,\ -\sigma_F F_R^y,\ -\sigma_F F_R^z\ \right). \tag{2.23}$$

Thus, given a computational field covered with a mesh of control volumes, the partial differential equations can be integrated on these polyhedra. Using Green's formula, this system is discretized in time by an explicit scheme.

$$\frac{U_{R_{i,j,k}}^{n+1} - U_{R_{i,j,k}}^{n}}{\Delta t} + \frac{\mathcal{F}_{i+1/2,j,k}^{n} - \mathcal{F}_{i-1/2,j,k}^{n}}{\Delta x} \tag{2.24}$$

$$+\frac{\mathcal{G}_{i,j+1/2,k}^{n} - \mathcal{G}_{i,j-1/2,k}^{n}}{\Delta y} + \frac{\mathcal{H}_{i,j,k+1/2}^{n} - \mathcal{H}_{i,j,k-1/2}^{n}}{\Delta z} = S_R(U_{R_{i,j,k}}^{n}). \tag{2.25}$$

In order to compute the convective terms, an upwind flux-limited scheme, the HLLE scheme (Hirsch 1990), using Roe's approximate Riemann solver, is used. This scheme applied to the M_1 model approximates the divergence as follows:

$$\begin{aligned}\frac{\mathcal{F}_{i+1/2,j,k}^{n+1} - \mathcal{F}_{i-1/2,j,k}^{n+1}}{\Delta x} = &\frac{1}{2\ \Delta x}\left(F_{i+1,j,k}^{n+1} + F_{i,j,k}^{n+1} - c\ \left(U_{R_{i+1,j,k}}^{n+1} - \ U_{R_{i,j,k}}^{n+1}\right)\right) \\ &- \frac{1}{2\ \Delta x}\left(F_{i,j,k}^{n+1} + F_{i-1,j,k}^{n+1} - c\ \left(U_{R_{i,j,k}}^{n+1} - \ U_{R_{i-1,j,k}}^{n+1}\right)\right)\end{aligned} \tag{2.26}$$

$\mathcal{G}$ and $\mathcal{H}$ are obtained similarly to $\mathcal{F}$ by permutation of i, j, and k. A second order correction which is needed to obtain better accuracy is given in (Ripoll *et al.* 2001).

3. Numerical Validation

This section is devoted to the numerical validation of the M_1 model and of the solver used.

The geometry for this test is the annular region between two concentric spheres. The inner sphere has a radius $R_i = 1.0$ and the outer sphere has radius $R_o = 1.6$. Both spheres have unit transmissivity (zero emissivity) and are exposed to cold black surroundings $I_i = I_o = 0$. The scattering coefficient within the annulus is zero while the absorption coefficient and retardation factor are set to unity. The annulus also has a uniform heat generation rate of $Q = 4\pi$.

With an uncertainty of 0.0005%, the steady state radiative energy is given in (Burns

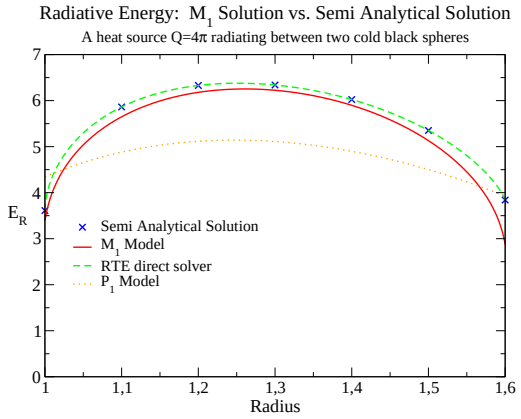

FIGURE 1. Hot gaz radiating between 2 concentric Spheres

2003) as

r	$E_R(r)$	r	$E_R(r)$	r	$E_R(r)$	r	$E_R(r)$
1.0	3.6108	1.2	6.3288	1.4	6.0233	1.6	3.8398
1.1	5.8619	1.3	6.3390	1.5	5.3508		

(3.1)

For the M_1 solver, a domain of 1000 nodes is used to obtain mesh convergence. The steady state solution is converged in time, and the final residue is 10^{-15}.

The solution found by the M_1 solver is in very good agreement with the semi-analytical values and with the solution given by a RTE solver, see Fig. 1. It may also be seen that the M_1 closure constitutes an improvement, compared to a simple closure like P_1, which in this case gives an inaccurate solution. The non-symmetry of the solution and the position of the maximum value, at $r = 1.2$ for the RTE solver and at $r = 1.25$ for M_1, indicates that the three dimensional geometry is well computed. These results demonstrate the accuracy of the method and its solver.

4. Computation of radiation for a pool fire

The domain of computation, describing a quarter of the geometry of the FLAME facility at Sandia Albuquerque, is shown in Fig. 2(left) (Brown & Blanchat 2003). The domain is three dimensional, but can roughly be considered axisymmetric due to the circular bowl containing the fuel and the circular facility for the entering air. All results plotted are in the plane $x = 0.05$, but the computations are done in 3D. The synthetic fire has been computed by A. Brown (Brown & Blanchat 2003) of Sandia Albuquerque. The mesh used for the computation is $31 \times 31 \times 93$. The wall and the bowl are simulated by a very large opacity, $1000\,m^{-1}$, where radiation cannot propagate. The domain is hence considered completely open, and the opacity σ, playing the role of walls, will regulate the radiation field. It must be noticed here that the exact position of the bowl, where the fuel burns, is spread out vertically over two cells, centered at $z = -0.05$ and $z = -0.15$. The first computational cells adjacent to it are $z \in [0., 0.1]$ (white zone), centered at $z = 0.05$.

In Fig. 2(right), the profile of the temperature of the synthetic fire is given. Four zones

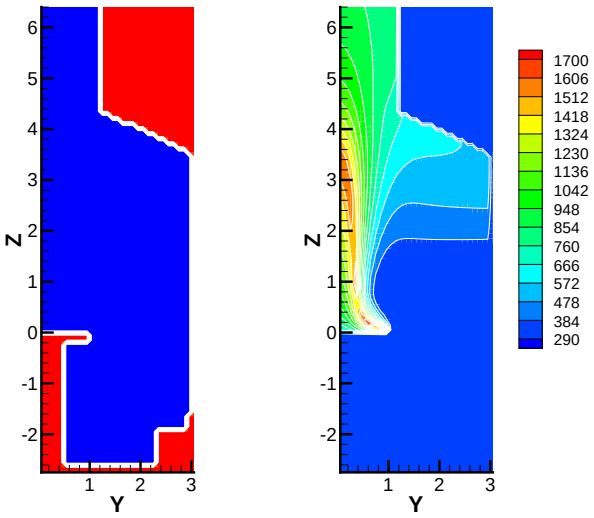

FIGURE 2. 2D cut of the computationnal domain (left); T (right)

can be seen: (1) the flame zone, delimited by the flame front where the temperature is higher, (2) the hot gas region, flowing in the chimney, (3) a moderately high temperature region on the right of the fire (between $400K$ and $700K$), where the opacity is small but not zero, generated by gas trapped by the too small size of the chimney, and (4) a region of quasi-ambient-temperature situated below the bowl. It is assumed that the absorption coefficient σ_s, provided by Sandia, has been determined from a Planck absorption coefficient in which a mixture of soot and gas is considered to radiate with the same optical properties as soot. This last assumption constitutes the main approximation since gaseous flame mixtures are, unlike soot, not gray media. This approximation allows us to determine the volume fraction Y_m of the mixture soot+gas as follows:

$$\sigma_s \simeq \sigma_P(Y_m, T) = C_m Y_m T \simeq C_s Y_m T \tag{4.1}$$

Then $Y_m = \sigma_s/(C_s T)$ gives the mixture fraction of our mixture and is plotted in Fig. 3.

The opacity of the fire is now considered as given from this mixture, and the three mean coefficients $\sigma_P(Y_m, T)$, $\sigma_E(Y_m, T_r, \|f\|)$, and $\sigma_F(Y_m, T_r, \|f\|)$ are used in this computation. These coefficients are plotted in Fig. 4-6. For each of these three figures, the high opacity zone in the flame is shown on the left: the maximal value reaches $10\,m^{-1}$ (zones higher than 10 are red and must be disregarded). The low opacity region, between $1\,m^{-1}$ and $0.1\,m^{-1}$, present close to the fire and in the chimney, is plotted on the right (here zones higher than 1 are red and must be disregarded). The steady state profile of both radiative temperature and energy computed with M_1 are given in Fig. 7. An important remark can immediately be given: the model does not propagate radiation below the bowl, as can be the case with other models, like P_1. The flame zone of the fire admits a high radiative temperature, but lower than the gas temperature, signifying a strong emission in this region. Furthermore, the moderately high temperature region absorbs a small quantity of radiation. The three components of the flux are plotted in Fig. 8. On the left, it can be checked that the x-component of the flux is very low compared to the others, signifying that the profile can be considered as nearly cylindrically symmetric.

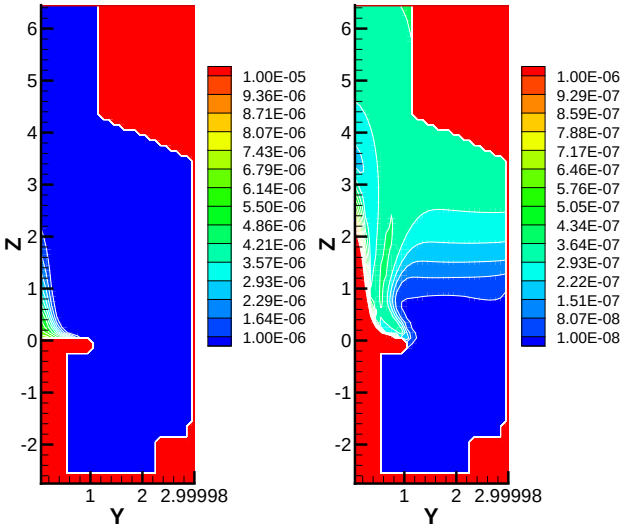

FIGURE 3. Y_m, high volume fraction regions (left), Y_m, low volume fraction opacity regions (right)

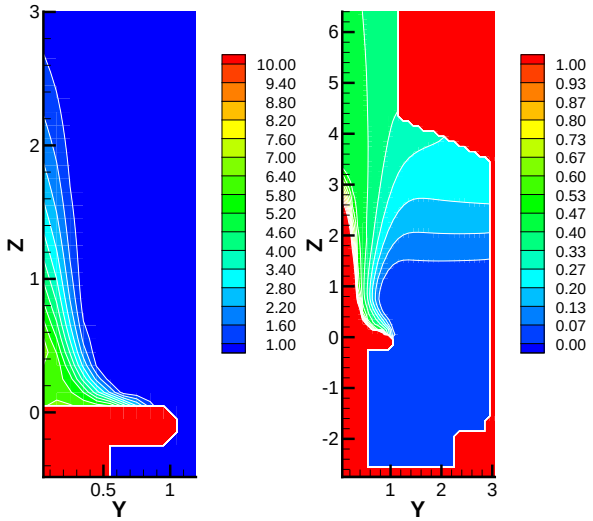

FIGURE 4. σ_P, high opacity regions (left) σ_P, low opacity regions (right)

Moreover the symmetry around to the z-axis can be checked. In Fig. 8(center)-(right), very close to the bowl, a region of negative fluxes can be seen, indicating that the bowl is heated by radiation. Radiation propagates clearly in the direction of the chimney and in the direction of the right wall. Two high temperature zones, one very close to the bowl and the other at $3\,m$ high, emit strongly in both chimney and wall directions, see Fig. 8(right).

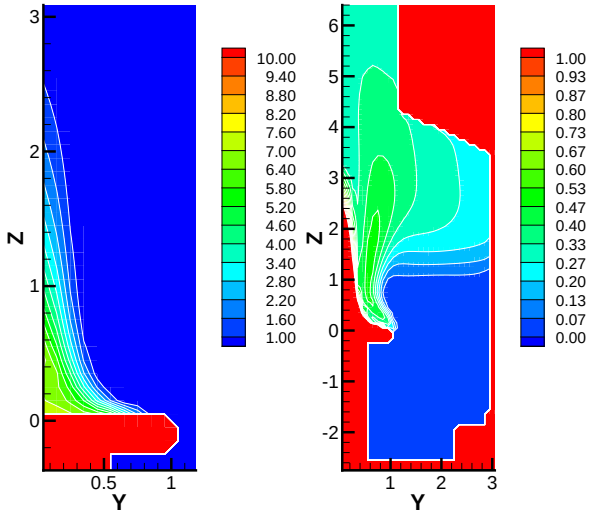

FIGURE 5. σ_E, high opacity regions (left) σ_E, low opacity regions (right)

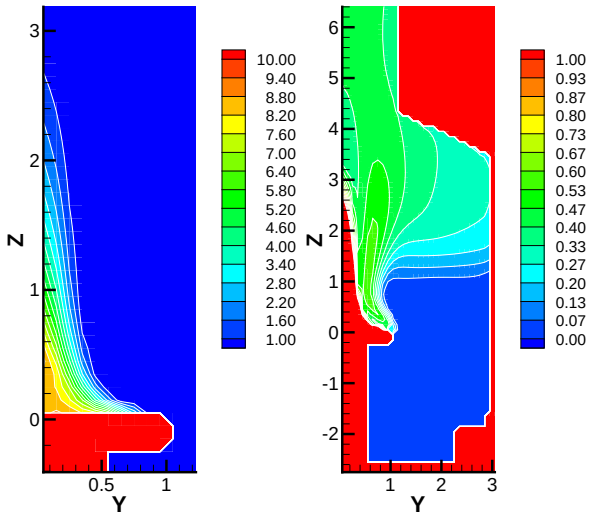

FIGURE 6. σ_F, high opacity regions (left) σ_F, low opacity regions (right)

In Fig. 9(left), the flux vector $\vec{V} = (F_R^y, F_R^z)$ is plotted. The three directions of propagation mentioned before are confirmed: toward the chimney, the wall, and the bowl. An important remark is that radiation does not propagate below the bowl in a pathological way, as we would find using some diffusion methods. In this region, where the opacity is almost zero, it can be seen that no dominant radiation occurs. The anisotropic factor in Fig. 9(center) indicates an isotropic region, central to the fire, where, due to symmetry around the z-axis, the fluxes are very small or zero. At one meter from the center of

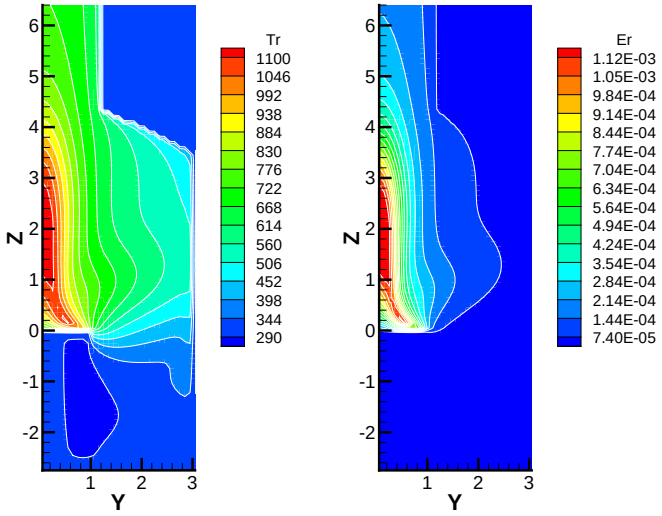

FIGURE 7. T_R (left), E_R (right)

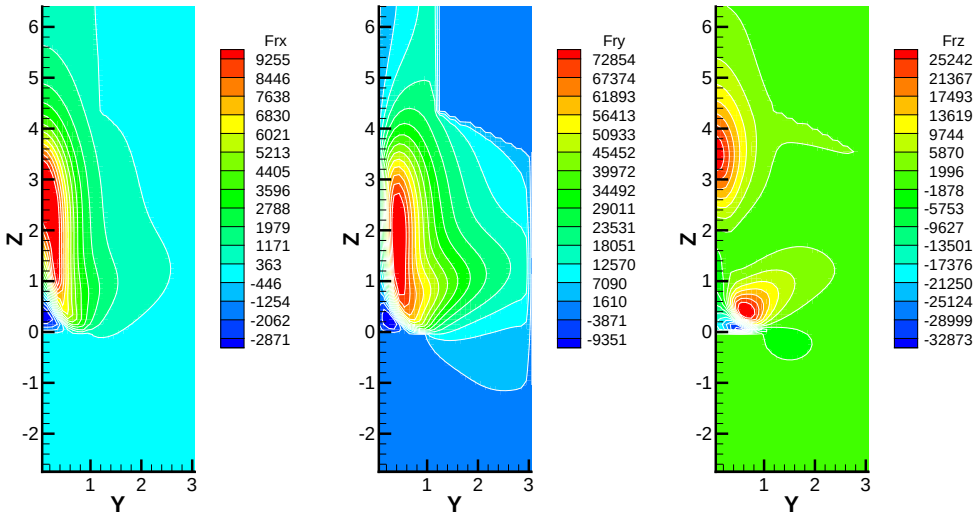

FIGURE 8. F_R^x (right); F_R^y (center); F_R^z (left)

the fire, radiation becomes anisotropic and, from there, isotropic models, like P_1, should not be used. The most anisotropic region is situated far from the fire, close to the wall, almost below the bowl, and "*sees*" the fire through a small window. The small opacity and angle of view explain this anisotropy region where $\|f\|$ reaches its maximal value of 0.94.

In Fig. 10, the radiative net heat flux, i.e. $c(\sigma_P a T^4 - \sigma_E E_R)$, which is the coupling term intervening in the energy conservation equation of Navier-Stokes (modulo the sign)

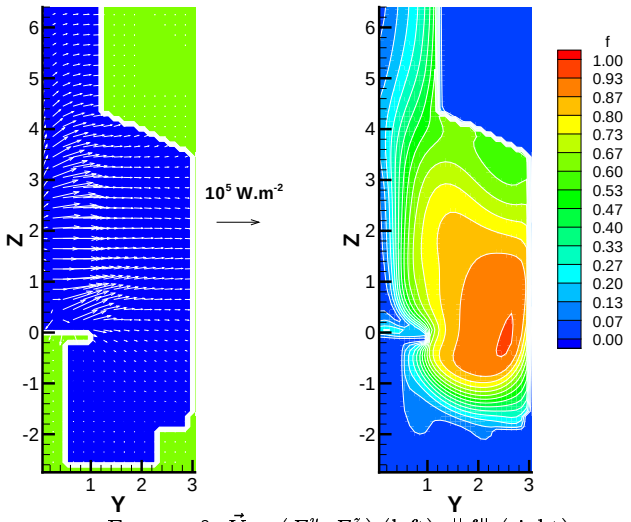

FIGURE 9. $\vec{V} = (F_R^y, F_R^z)$ (left); $||f||$ (right)

is plotted. Three ranges of scale have been chosen in order to differentiate the absorption zones from the emission ones. In the first figure, Fig. 10(left), the blue zone must be disregarded, as must be the red one in the next figure, and both blue and red ones in the third figure. In Fig. 10(left), the non-blue region of the flame zone indicates a strong region of emission. In Fig. 10(center), exactly in the first cells adjacent to the bowl, a strong absorption region can be seen. This indicates that the bowl is heated by the fire in a strong way, where we know it participates in an important way in the vaporization of the fuel. The vaporization process conditions the whole fire flow, and it is hence particularly important to predict it accurately. An accurate computation of the absorption of radiation is thus very important in this region. Moreover, a few centimeters higher, the hot gas in the flame cone region, not yet reacting, also absorbs heat from the flame zone. Finally it can be noticed that the wall of the chimney absorbs some heat as well. In Fig. 10(right) are plotted the regions where a low but non-negligible absorption occurs. The fire is bounded to the right by an absorption zone, which confines the heat. The right wall absorbs some heat as well. Finally, below the bowl, neither absorption or emission occurs.

5. Conclusion

A model of radiation using a moment method has been proposed for fires. The models for the transport of radiation, for the computation of the opacities, and their discretizations have been presented. A pool fire occuring in a complex geometry has been computed by this model. The results are found to be coherent and consistent. This model thus seems to constitute a good alternative to the solving of radiation by direct RTE methods, which are more costly. This work constitutes the preliminary results of a much bigger project involving the collaboration of NASA Ames, Sandia Albuquerque, and Ecole des Mines d'Albi. In this project, the radiation of a fire, which is comparable to the one studied

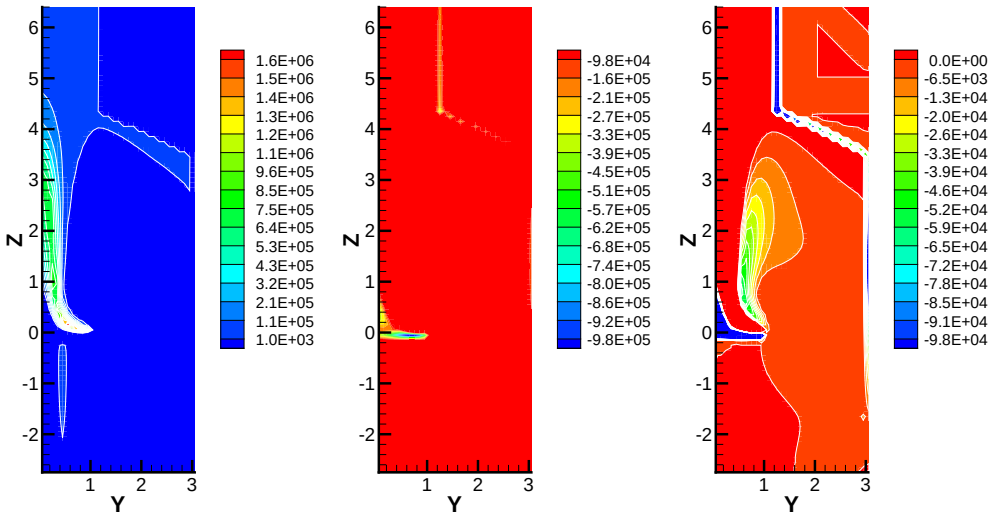

FIGURE 10. Positive net heat flux (left); Strong negative net heat flux (center); Low negative net heat flux (right)

here, will be solved by several methods, including this one, and compared (Jensen *et al.* 2004).

Acknowledgments

The author would like to thank Dr. Alexander Brown of Sandia National Laboratories who provided the temperature and opacity profiles of the fire which has been used in this work. Particular thanks are addressed to Dr. Kirk Jensen and Dr. Sheldon Tieszen of Sandia National Laboratories for their extensive technical discussions and support.

REFERENCES

BROWN, A.L., & BLANCHAT, T.K. 2003 A validation quality heat flux dataset for large pool fires. *2003 ASME Summer Heat Tansfer Conference, Las Vegas HT2003-40249.*

BRUNNER, T. A., HOLLOWAY, J. P. 2003 One-dimensional Riemann solvers and the maximum entropy closure. *Jour. Quant. Spectrosc. Radiat. Transfer*, **69**, 543-566.

BURNS, S. P. 2003 SYRINX User manual. Preprint in progress, Sandia National Laboratories, Albuquerque.

COX, G. 1995 Combustion fundamentals of fires. Academic Press.

FORT, J. 1997 Information-theoretical approach to radiative transfer. *Phys. A.*, **243**, 275-303.

HIRSCH, C. 1990 Numerical Computation of Internal and External Flows. Nb. 1-2. *Wiley Interscience Publication.*

JENSEN, K. A., RIPOLL, J.-F., WRAY, A. A., JOSEPH, D., EL-HAFI, M. 2004 Radiative transfer modeling of a large pool fire by discrete ordinates, discrete transfer, ray

tracing, Monte Carlo, and moment methods. *Proceedings of the center for turbulence research summer programm*, in preparation.

LEVERMORE, D. 1984 Relating Eddington factors to flux limiters. *Jour. of Quant. Spectrosc. & Radiat. Transfer*, **32(2)**, 149-160.

MINERBO, G. N. 1978 Maximum entropy eddington factors. *J. Quant. Spectrosc. Radiat. Transfer* **20**, 541–545.

MODEST, M.F. 2003 Radiative heat transfer. 3rd ed., McGraw-Hill.

RIPOLL, J.-F., DUBROCA, B. & DUFFA, G. 2001 Modelling radiative mean absorption coefficients. *Comb. Th. and Mod.* **5** (3), 261–275.

RIPOLL, J.-F., DUBROCA, B., AUDIT, E. 2002 A factored operator method for solving coupled radiation-hydrodynamics models. *Trans. Theory and Stat. Phys.*, **31**(4-6), 531-557.

SIEGEL, R. C. & HOWELL, J. R. 2001 *Thermal radiation heat transfer*. 4^{th} Ed., Taylor and Francis.

SYMTH, K. C., SHADDIX C. R. 1996 The Elusive history of $\tilde{m} = 1.57 - 0.56i$ for the refractive index of soot. *Comb. and Flame*, **107**, 314-320.

TIESZEN, S. R. 2001 On the fluid mechanics of fires *Annu. Rev. Fluid Mech.*, **33**, 33-67.

Direct numerical simulation of turbulent condensation in clouds

By R. Paoli AND K. Shariff †

1. Motivation and objectives

Clouds are responsible for precipitation, scattering and absorption of electromagnetic energy, and cloud particles serve as sites for chemical reactions. To properly incorporate these processes in cloud-resolving codes or climate models, the crucial quantity required is the droplet size spectrum $n(r)$ within a computational cell, defined such that $n\,dr$ gives the number of particles in the cell having radii between r and $r + dr$. The role of turbulence in clouds has been the object of intensive investigation in the atmospheric science community over the last forty years. (Consult the reviews by Pinsky & Khain 1997, Vaillancourt & Yau 2000, and Shaw 2003). Turbulence has three effects on the development of the droplet size spectrum: (i) During the initial phase of condensational growth it causes each particle to experience a different fluctuating supersaturation as it is transported and this leads to a broadening of the spectrum (Cooper 1989). (ii) Turbulence causes particles to cluster when they become large enough that particle inertia becomes important; this clustering eventually influences the size spectrum during the coagulation phase. (iii) Finally, during the coagulation phase, turbulence increases the number of particle encounters. The present work aims to further elucidate the first of these effects with a view to developing sub-grid models for it. In the atmospheric sciences literature, this effect is referred to as "stochastic condensation."

The first step in current approaches for modeling stochastic condensation (see for example Khvorostyanov & Curry 1999*a*) is to write down the transport equation,

$$\frac{\partial f}{\partial t} + \frac{(\partial f u_j)}{\partial x_j} = \frac{\partial (f\,\dot{r})}{\partial r}, \tag{1.1}$$

for the particle size distribution $f(\mathbf{x}, r, t)$. Here $f(\mathbf{x}, r, t)d\mathbf{x}\,dr$ gives the number of particles in the four dimensional phase space volume $d\mathbf{x}\,dr$ at $(\mathbf{x}, r)$. The next step follows the standard approach for Reynolds averaging. Decomposing variables into mean and fluctuating parts, $f = \overline{f} + f'$, $r = \overline{r} + r'$, and averaging the entire equation leads to the appearance of covariances like $\overline{u_j' f'}$ or $\overline{\dot{r}' f'}$ which are modeled using a mixing length approach. Khvorostyanov & Curry (1999*b*) were able to obtain a solution for $\overline{f}$ in terms of gamma functions which is an attractive result as many observed cloud-droplet distribution can be fitted with gamma distributions (Shaw 2003). One of the assumptions made by those authors was to use a linear relation between droplet growth rate and supersaturation fluctuations, $\dot{r}' \sim S'$, based on the analysis by Srivastava (1989) and heuristic considerations about the equivalence between Brownian motion of small particles and the motion of turbulent eddies.

In this brief, we investigate the turbulent condensation of a population of droplets by means of direct numerical simulation. To that end, a coupled Navier-Stokes/Lagrangian

† NASA Ames Research Center, Moffett Field, CA 94035

solver is used (see Paoli *et al.* 2004) where each particle is tracked and its growth by water vapor condensation is monitored exactly. The main goals of the study are to find out whether turbulence broadens the droplet size distribution, as observed in *in situ* measurements. The second issue is to understand if and for how long a correlation between the droplet radius and the local supersaturation exists for the purpose of modeling subgrid scale microphysics in cloud-resolving codes.

This brief is organized as follows. In Sec. 2 the governing equations are presented, including the droplet condensation model. The implementation of the forcing procedure is described in Sec. 3. The simulation results are presented in Sec. 4 together with a sketch of a simple stochastic model for turbulent condensation. Conclusions and the main outcomes of the study are given in Sec. 5.

2. Governing equations

The dimensionless forced compressible Navier-Stokes equations are

$$\frac{\partial \rho}{\partial t} + \frac{\partial (\rho u_j)}{\partial x_j} = 0 \tag{2.1}$$

$$\frac{\partial (\rho u_i)}{\partial t} + \frac{\partial (\rho u_i u_j)}{\partial x_j} + \frac{\partial p}{\partial x_i} = \frac{1}{Re}\frac{\partial \tau_{ij}}{\partial x_j} + \rho f_i,\ i = 1, \ldots, 3 \tag{2.2}$$

$$\frac{\partial (\rho E)}{\partial t} + \frac{\partial [(\rho E + p) u_j]}{\partial x_j} = \frac{1}{Re}\frac{\partial (u_i \tau_{ij})}{\partial x_j} - \frac{1}{Re\, Pr} C_p \frac{\partial Q_j}{\partial x_j} + \rho W \tag{2.3}$$

$$\frac{\partial (\rho Y_n)}{\partial t} + \frac{\partial (\rho Y_n u_j)}{\partial x_j} = \frac{1}{Re\, Sc_n}\frac{\partial^2 Y_n}{\partial x_j^2} + \rho \omega_n + \rho q_n,\ n = 1, 2. \tag{2.4}$$

Here ρ is the density, $\mathbf{u} = [u_1, u_2, u_3]$ is the velocity vector, p is the pressure, E is the total energy, $\mathbf{Q} = [Q_1, Q_2, Q_3]$ is the heat flux vector given by Fourier's law, C_p being the non-dimensional specific heat at constant pressure. The quantity τ_{ij} is the shear stress tensor, and $Y_n, n = 1, 2$ are scalar fields, Y_1 being the temperature T and Y_2 the vapor mass fraction Y_v, while ω_n are physical source terms for Y_n. In the case of water vapor ($Y_2 = Y_v$), $\omega_2 = \omega_v$ represents the removal of vapor due to condensation. Quantities are made non-dimensional using reference values: ρ_{ref} for the density, a_{ref} for the velocity, p_{ref} for the pressure, l_{ref} for length, T_{ref} for temperature, μ_{ref} for the dynamic viscosity, and $C_{p,\mathrm{ref}}$ for the specific heat. The Reynolds number is defined as $Re = a_{\mathrm{ref}}\, l_{\mathrm{ref}}/(\mu_{\mathrm{ref}}/\rho_{\mathrm{ref}})$. The Schmidt number is defined as $Sc_n = \mu_{\mathrm{ref}}/\rho_{\mathrm{ref}} D_n$, where D_n is the diffusivity of scalar n. For atmospheric conditions vapor diffusivity (given in Pruppacher & Klett 1997, p. 503 is not too different from thermal diffusivity and so we chose $Sc = 0.75$ for both vapor and temperature. Finally, the terms $\rho f_j, \rho W$, ρq_1 , and ρq_2 in (2.2)-(2.4) represent forcing of momentum, total energy, temperature and vapor, respectively and are described in detail in the next section.

The use of compressible equations to simulate atmospheric clouds requires some comment since use of the incompressible or Boussinesq equations is more common. The rms u' of velocity fluctuations in clouds is of the order of 1 to a few meters per second (MacPherson & Isaac 1977). For $u' = 3$ m/s and speed of sound $a = 300$ m/s, the turbulence Mach number $M_t = u'/a = 0.01$. If we were to choose a similar M_t for the simulations, the CFL criterion would lead to a time step that is very small compared with the flow time. Instead we chose $M_t \simeq 0.05$ for the simulations. This leaves the velocity field essentially incompressible, but allows one to run with an affordable time step. However, in weakly

compressible flow, temperature fluctuations are induced by pressure fluctuations and are proportional to M_t^2. Furthermore the mechanisms for temperature fluctuations in the atmosphere are not unrelated to flow induced pressure fluctuations. Thus we have no right to derive the temperature from the energy E which obeys (2.3). For this reason, temperature is obtained independently by solving a scalar transport equation for $Y_1 \equiv T$.

2.1. *Particle treatment*

Due to their small size (less than about ten microns during the condensation phase), the relaxation time $\tau_p = 4\rho_p r^2/18\mu$ of particles is short compared to the smallest turbulence time scale. They can then be treated as tracers which follow the gas according to

$$\frac{d\mathbf{x}_p}{dt} = \mathbf{u}(\mathbf{x}_p, t). \tag{2.5}$$

Gas variables at a particle location $\mathbf{x}_p$ are estimated by linear interpolation, using the values at the nodes of the surrounding cell (see Boivin *et al.* 1998 for details). For the law of droplet growth by condensation we start with equation (15.74) in Seinfeld & Pandis (1997) and ignore the solute contribution to the equilibrium vapor pressure over the drop. We retain the latent heat term as well as the curvature contribution (Kelvin effect) and the kinetic corrections to effective vapor and temperature diffusivities. (We verified *a posteriori* that the last two contributions are negligible for drops $\gtrsim 1\mu$m). We are thus left with

$$\frac{dr}{dt} = \frac{\alpha(r,T)S}{r} \tag{2.6}$$

where $S = Y_v - Y_v^s(T)$ is the local supersaturation with respect to water and $\alpha(r,T)$ is a coefficient that depends on temperature and droplet size. Saturation conditions are obtained from the fit by Sonntag (1994)

$$p_v^s = p\,X_v^s = \exp(\,a_1 \ln T + a_2\,T^{-1} + a_3 + a_4\,T + a_5\,T^2) \tag{2.7}$$

where the mass fraction $Y_v^s(T)$ and molar fraction $X_v^s(T)$ at saturation are related by $Y_v^s = X_v^s/(X_v^s + (1 - X_v^s)\,W_{air}/W_v)$, with $W_{air}/W_v = 28.85/18.01 = 1.6$.

2.2. *Numerical method*

The gas transport equations (2.1)–(2.4) are discretized in physical space by means of the sixth order compact scheme by Lele (1992). They are advanced in time together with (2.5)–(2.6), using a 3rd order Runge-Kutta scheme. Periodic boundary conditions are used in the three directions of the computational cube which has sides $L_{box} = 2\,\pi$. The code is parallelized using domain decomposition with MPI as the communication protocol.

3. Turbulence forcing

In order to obtain a statistically stationary velocity field, a body force $\mathbf{f}(\mathbf{x},t) = [f_1(\mathbf{x},t), f_2(\mathbf{x},t), f_3(\mathbf{x},t)]$ is applied to the momentum equations. Physically, this represents the effect of processes such as turbulence production by shear and the turbulent cascade which occur on scales larger than the computational box. To preserve universality of the smallest scales of turbulence, only the (low) vector-valued wavenumbers $\mathbf{k}$ within the sphere $k \equiv |\mathbf{k}| \leq k_f$ are forced. The force is represented as a finite Fourier

series (see Eswaran & Pope 1988a)

$$\mathbf{f}(\mathbf{x},t) = \sum_{k\le k_f} e^{\mathrm{i}\mathbf{k}\cdot\mathbf{x}}\,\hat{\mathbf{f}}(\mathbf{k},t) \tag{3.1}$$

where $\hat{\mathbf{f}}(\mathbf{k},t) = [\hat{f}_1(\mathbf{k},t), \hat{(}f_2\mathbf{k},t), \hat{f}_3(\mathbf{k},t)]$ and $\hat{f}_j(\mathbf{k},t) \equiv f_j^R(\mathbf{k},t) + \mathrm{i}\, f_j^I(\mathbf{k},t)$ is the Fourier transform corresponding to $\mathbf{k} = k_0\,[l,m,n]$ ($k_0 = 2\pi/L_{box} = 1$ being the fundamental wavenumber), while the summation is intended over the three components, $l = -N/2 + 1,..,N/2$; $m = -N/2+1,..,N/2$; $n = -N/2+1,..,N/2$, with the condition $k = k_0(l^2 + m^2 + n^2)^{1/2} \le k_f$. At each wavenumber, $\hat{\mathbf{f}}(\mathbf{k},t)$ is obtained from the divergence-free projection

$$\hat{\mathbf{f}}(\mathbf{k},t) = \hat{\mathbf{g}}(\mathbf{k},t) - (\mathbf{k}\cdot\hat{\mathbf{g}}(\mathbf{k},t)/k^2)\,\mathbf{k}, \tag{3.2}$$

of the three-dimensional stochastic process $\hat{\mathbf{g}}(\mathbf{k},t) = [\hat{g}_1(\mathbf{k},t), \hat{g}_2(\mathbf{k},t), \hat{g}_3(\mathbf{k},t)]$ which is composed of six independent Uhlenbeck-Ornstein (UO) processes corresponding to the real and imaginary parts of $\hat{g}_j(\mathbf{k},t) = g_j^R(\mathbf{k},t) + \mathrm{i}\, g_j^I(\mathbf{k},t), j = 1,\ldots,3$. These processes are governed by the Langevin stochastic differential equation (Lemons 2002),

$$dg_j^{R,I}(\mathbf{k},t) \equiv g_j^{R,I}(\mathbf{k},t+dt) - g_j^{R,I}(\mathbf{k},t) = -\frac{g_j^{R,I}(\mathbf{k},t)}{\tau_f}\,dt + N_t^{t+dt}(0,1)\sqrt{2\,\sigma_f^2\frac{dt}{\tau_f}} \tag{3.3}$$

where τ_f and σ_f are, respectively, the autocorrelation time and standard deviation of all processes, while $N_t^{t+dt}(0,1)$ is a normally distributed random number with zero mean and unit variance associated with the time interval $[t;t+dt]$. From (3.3) it can be easily shown that each UO process has zero ensemble-mean and is exponentially auto-correlated with time lag τ_f, i.e.

$$\left\langle g_j^{R,I}(\mathbf{k},t)\right\rangle = 0 \tag{3.4}$$

$$\left\langle g_i^{R,I}(\mathbf{k},t)\, g_j^{R,I}(\mathbf{k},t+s)\right\rangle = \sigma_f^2\delta_{ij}^{R,I}e^{-s/\tau_f}. \tag{3.5}$$

Using the condition that f_j be real (i.e. $f_j^R(-\mathbf{k}) = f_j^R(\mathbf{k})$, $f_j^I(-\mathbf{k}) = -f_j^I(\mathbf{k})$) and the requirement $\int_V f_j\,dV = 0$ that the force not change the net linear momentum (i.e. $f_j^R(0) = f_j^I(0) = 0$), one has for the forcing terms f_j and W in (2.2) and (2.3)

$$f_j(\mathbf{x},t) = 2\sum_{l=1}^{N/2}\sum_{m=1}^{N/2}\sum_{n=1}^{N/2}\left[f_j^R(\mathbf{k},t)\cos(\mathbf{k}\cdot\mathbf{x}) - f_j^I(\mathbf{k},t)\sin(\mathbf{k}\cdot\mathbf{x})\right], \quad k\le k_f \tag{3.6}$$

$$W(\mathbf{x},t) = \sum_{j=1}^{3} f_j(\mathbf{x},t)\,u_j(\mathbf{x},t) - \int_V \sum_{j=1}^{3} f_j(\mathbf{y},t)\,u_j(\mathbf{y},t)\,dV(\mathbf{y}). \tag{3.7}$$

The quantity W represents the work done by the force and must be added in compressible flows to maintain consistency between the momentum and energy equations (see e.g. Kida & Orzag 1991). In the statistically stationary state the amount of work done by the forcing equals viscous dissipation to heat. The integral term in (3.7) removes thermal energy in the mean and is necessary to keep the mean internal energy in the computational box from monotonically increasing due to viscous heating.

3.1. *Scalar forcing*

Let us now consider the forcing terms q_n in the scalar equations (2.4), and for the sake of clarity neglect the subscript n which simply identifies the scalar (temperature or

water vapor). The same stochastic forcing as described above is used in (2.4) to drive temperature and vapor fluctuations at the large scales. In actual clouds it is convection and mixing between air parcels, and radiation, etc. that drive the fluctuations. Following the usual approach, one can decompose $q(\mathbf{x},t)$ as

$$q(\mathbf{x},t) = \sum_{k\le k_f} e^{\mathrm{i}\mathbf{k}\cdot\mathbf{x}}\,\hat{q}(\mathbf{k},t), \quad \text{with} \quad \hat{q}(\mathbf{k},t) \equiv q^R(\mathbf{k},t) + \mathrm{i}\,q^I(\mathbf{k},t), \tag{3.8}$$

where $q^R(\mathbf{k},t)$ and $q^I(\mathbf{k},t)$ are chosen to be UO processes defined by

$$dq^{R,I}(\mathbf{k},t) = -\frac{q^{R,I}(\mathbf{k},t)}{\tau_q}\,dt + N_t^{t+dt}(0,1)\sqrt{2\,\sigma_q^2\frac{dt}{\tau_q}}, \tag{3.9}$$

Using the fact that $q(\mathbf{x},t)$ is real one obtains finally

$$q(\mathbf{x},t) = 2\sum_{l=1}^{N/2}\sum_{m=1}^{N/2}\sum_{n=1}^{N/2}\left[q^R(\mathbf{k},t)\cos(\mathbf{k}\cdot\mathbf{x}) - q^I(\mathbf{k},t)\sin(\mathbf{k}\cdot\mathbf{x})\right], \quad k\le k_f. \tag{3.10}$$

In (3.9), we chose $\tau_q = \tau_f$ assuming that the same process, namely large eddies, drive scalar and velocity fluctuations. The ampltitude parameter σ_q could be obtained by requiring that the standard deviation of the resulting scalar field (temperature or vapor concentration) be in the range of atmospheric values. Strictly speaking this can only be verified *a posteriori*, however, one can obtain a good prediction of the resulting variance by using the assumption of a particle system, as often done in the simulation of turbulent flows (see Pope 2000). In these kinds of methods, the flow is regarded as an ensemble of fluid particles each carrying a different value for the scalar Y which evolves according to a Langevin equation

$$dY(t) = -\frac{Y(t) - \langle Y\rangle(t)}{\tau_m}\,dt + \sum_{k=1}^{N_f/2}\left[q^R(k,t) + q^I(k,t)\right] \tag{3.11}$$

$$dq^{R,I}(k,t) = -\frac{q^{R,I}(k,t)}{\tau_q}\,dt + N_t^{t+dt}(0,1)\sqrt{2\,\sigma_q^2\frac{dt}{\tau_q}} \tag{3.12}$$

where N_f indicates all forced modes. The first term in (3.11) is a classical exchange-with-the-mean mixing model, τ_m being the mixing time (usually taken to be the integral time scale τ_e of the flow) which is assumed to be equal to forcing time scale, $\tau_m = \tau_f$. From (3.11) one may then derive

$$\frac{d\langle Y\rangle}{dt} = \sum_{k=1}^{N_f/2}\left\langle\left[q^R(k,t) + q^I(k,t)\right]\right\rangle = 0 \tag{3.13}$$

$$\frac{d\,\sigma_Y^2}{dt} = -2\,\frac{\sigma_Y^2}{\tau_m} + 2\sum_{k=1}^{N_f/2}\left\langle Y\left[q^R(k,t) + q^I(k,t)\right]\right\rangle. \tag{3.14}$$

Using (3.4)-(3.5) and (3.9), one finally gets to

$$\langle Y\rangle = \text{const} \equiv \langle Y\rangle_0 \tag{3.15}$$

$$\sigma_Y^2(t) = N_f\frac{\sigma_q^2\tau_e^2}{2}\left(1 - e^{-2t/\tau_e} - \frac{2t}{\tau_e}\,e^{-2\,t/\tau_e} - \frac{t^2}{\tau_e^2}\,e^{-2\,t/\tau_e}\right) \tag{3.16}$$

N	Re	$u' = \sqrt{2/3K}$	L_e/L_{box}	Re_λ	$k_{max}\eta$	$\sigma_{Y_1}/\langle Y_1\rangle$	$\sigma_{Y_2}/\langle Y_2\rangle$
64	2000	0.05	0.162	49	1.15	0.001	0.001
128	3333	0.05	0.162	69	1.68	0.001	0.001

TABLE 1. Flow-field parameters

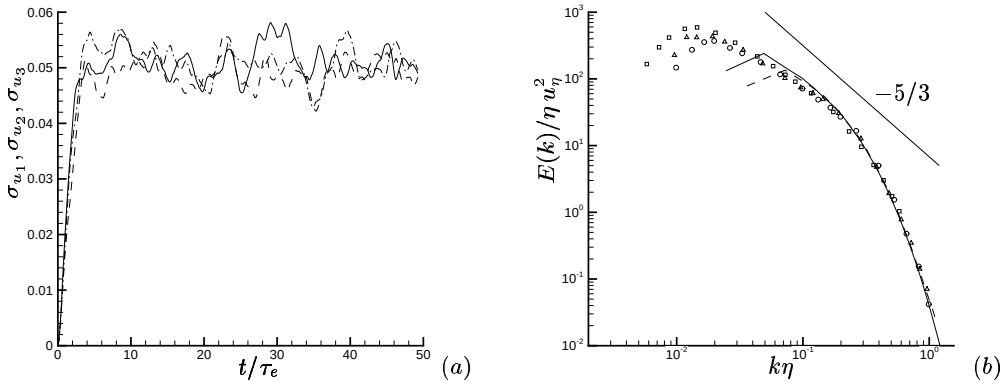

FIGURE 1. (a) Evolution of the standard deviation of the three componets of the velocity field. Particles are introduced at $t/\tau_e = 10$ when the velocity field is statistically stationary. (b) Energy spectra normalized by the Kolmogorov length η and velocity u_η. Solid line: 128^3 simulation; dashed line: 64^3 simulation; symbols: $Re_\lambda \simeq 69$ grid-turbulence experiments of Comte-Bellot & Corrsin (1971).

which shows that σ_Y achieves a stationary value σ_{Y_∞} which satisfies

$$\sigma_q = \frac{\sigma_{Y_\infty}}{\tau_e}\left(\frac{2}{N_f}\right)^{1/2}. \tag{3.17}$$

This relation can be used to design σ_q, knowing some characteristic values for σ_{Y_∞} in the atmosphere. For temperature ($Y \to Y_1 \equiv T$) and vapor concentration ($Y \to Y_2 \equiv Y_v$), Kulmala *et al.* (1997) report $\sigma_{T_\infty} \approx 0.3\,\mathrm{K}$ and $\sigma_{Y_{v\infty}} \approx 1.4 \times 10^{-5}$, which give, for the present simulations, $\sigma_{q_1} = 2.2 \times 10^{-3}$, and $\sigma_{q_2} = 1.0 \times 10^{-6}$. We verified *a posteriori* that these choices did indeed lead to the desired fluctuation levels (see next section).

4. Simulation Results

For each simulation a statistically stationary turbulent flow is first generated according to the method described above. The radius of the sphere of forced wavenumbers is $k_f = \sqrt{8}$, giving a total of $N_f = 92$ forced modes. The standard deviation and autocorrelation time scale of the stochastic forcing were chosen to be, respectively, $\sigma_f = 1.339 \times 10^{-4}$ and $\tau_f = 20.8$ (the same as in Eswaran & Pope 1998b). The resulting turbulence statistics of the flow are provided in Table 1, where $k_{max} \equiv \pi N/L_{box}$, $K = 1/2\,(\sigma_{u_1}^2 + \sigma_{u_2}^2 + \sigma_{u_3}^2)$ is the turbulent kinetic energy, $L_e \equiv L_{11}$ is the longitudinal integral length scale, $Re_\lambda = u'\lambda/\nu$ is the Reynolds number based on the Taylor microscale λ (see Pope 2000 for details). These statitsics were obtained by averaging over samples collected between $t = 10\,\tau_e$,

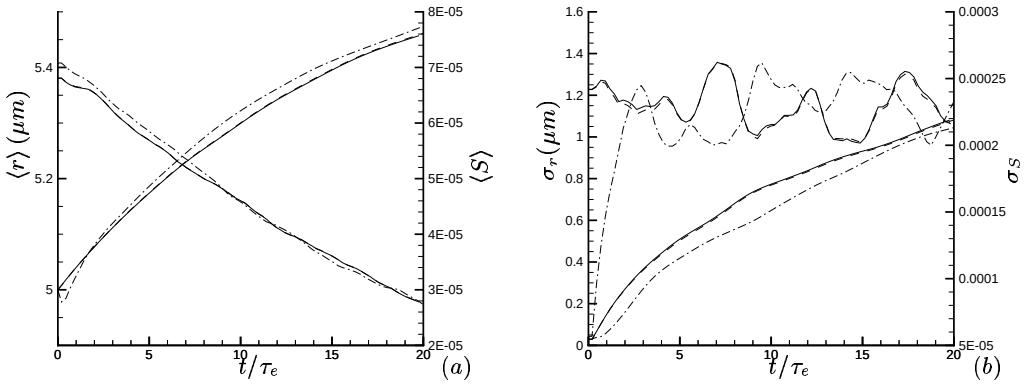

FIGURE 2. Evolution of the statistics of droplet radii r and supersaturation S. (a) Mean values $\langle r\rangle$ and $\langle S\rangle$. The three rising curves show $\langle r\rangle$ while the three falling curves show $\langle S\rangle$. (b) Standard deviations σ_r and σ_S. The three rising curves show σ_r while the three fluctuating curves show σ_S. Line types: ——— , vapor equation is forced throughout (case 1); - - - - , vapor forcing is removed at particle insertion (case 2); —·— , vapor equation is unforced throughout and the vapor field when particles are inserted is set to be random Gaussian (case 3).

when the velocity fluctuations reach their statistically stationary value, up to about $t = 50\,\tau_e$; see Fig. 1a. This figure shows that velocity fluctuations are isotropic; this was also confirmed by examining the two-point longitudinal and transverse correlation functions (not shown). The bulk of the simulations were performed on a 64^3 grid; the rest employed a 128^3 grid which gives a higher Re_λ and allows validation of the method against the grid-turbulence experiments of Comte-Bellot & Corrsin (1971) (see Fig. 1b).

Scalar equations are also forced with the same method, with the means set to $\langle T\rangle = 292K$ and $\langle Y_v\rangle = 0.01415$, respectively. The resulting standard deviations are $\sigma_T \simeq 0.29K$ and $\sigma_{Y_v} \simeq 1.4 \times 10^{-5}$, which are in the range of atmospheric values reported in the literature (see Kulmala *et al.* 1997).

At $t/\tau_e = 50$, $N_p = 96^3$ droplets are randomly distributed in the computational domain and time is then reset to zero. Their number was chosen to satisfy two major constraints: first, it must be high enough that accurate Lagrangian statistics can be obtained, and second, the particle spacing $\lambda = (Vol/N_p)^{1/3}$ must be of the same order of the Kolmogrov scale as in clouds (see Sec. 1). This was indeed verified in the present DNS where $\lambda = 2\pi/96 = 0.67\,\Delta$ or $\lambda = 1.8\,\eta$ (for the 64^3 simulations).

The reference length is taken to be $l_{\rm ref} = 2.5$ cm which implies a dimensional box size of 15.7 cm (for a kinematic viscosty of air $\nu_{\rm ref} = \mu_{\rm ref}/\rho_{\rm ref} = 1.5 \times 10^{-5}\,{\rm m}^2/{\rm s}$, this also sets a reference velocity $a_{\rm ref} = \nu_{\rm ref}\,Re/l_{\rm ref} = 1.2\,{\rm m/s}$, and turbulent fluctuations $\sigma_{u_j} a_{\rm ref} \simeq 6\,{\rm cm/s}$). The droplets are initially monodisperse with radius $r_0 = 5\,\mu$m.

Figure 2 shows the time evolution of the statistics of droplet size and of the local supersaturation. Three cases were run with different types of forcing of the vapor field. Each case is shown using a different line type and is described in the caption. As the mean radius $\langle r\rangle$ increases by condensation, the mean supersaturation $\langle S\rangle$ decreases due to mass conservation. However, their standard deviations are quite different: σ_r increases, up to about $1\,\mu$m while σ_S fluctuates about a certain value. Apart for a short transient in case 3 which is due to the adjustment of water vapor to the turbulent flow, the insensitivity

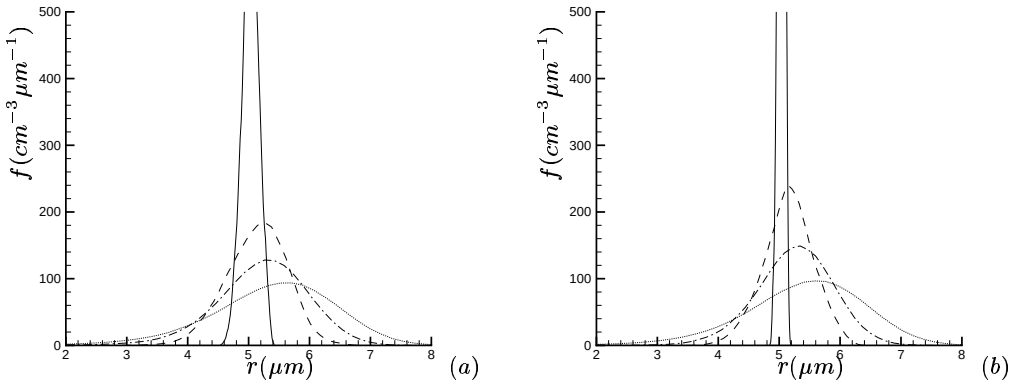

FIGURE 3. Time evolution of droplet size distribution: (a) Case 1; (b) Case 3; ——— , $t = 0.25\,\tau_e$; - - - - , $t = \tau_e$; —·— , $t = 2\,\tau_e$; ····· , $t = 5\,\tau_e$.

of the results to vapor forcing implies that in the present simulations supersaturation fluctuations are mainly controlled by temperature fluctuations.

The increase in σ_r reflects broadening of the droplet size spectrum, as is often observed in cloud measurements (Shaw 2003). This is further shown in Fig. 3 where the distribution of particle radius is plotted at various instants. The mechanism of broadening is that each individual droplet absorbs a fraction of the available supersaturation, depending on the local thermodynamic conditions and water vapor concentration, and grows with its own rate, according to (2.6). Integrating the latter gives

$$r^2(t) = r_0^2 + \int_0^t 2\alpha S(t)\,dt \tag{4.1}$$

which shows that the square of the radius r depends on the time history of supersaturation S. In particular, for two droplets i and j and for a short time t the difference in the radius goes like $r_i^2 - r_j^2 \sim t(S_i - S_j)$. Equation (4.1) also indicates that r and S initially develop a correlation but subsequently turbulent fluctuations decorrelate them. This is clearly shown in Fig. 4 where the correlation coefficient $C_{rS} = \langle r'S' \rangle / \sigma_r \sigma_S$ (S' being evaluated at particle locations) is shown for the two cases with and without forcing the vapor transport equation. The figure shows that, at least for the present Re_λ and dissipation rate, the correlation coefficient is > 0.5 up to $t \equiv \tau_{1/2} = 5\,\tau_e$. It is interesting to compare $\tau_{1/2}$ with the characteristic condensation time for a cloud, which coincides with the supersaturation absorption time (see Khvorostyanov & Curry 1999a), $\tau_f = (4\pi \langle r \rangle_0 D_2 N_p / Vol)^{-1}$. In non-dimensional form, this is $\tau_f = 167 \simeq 8\tau_e$, or $\tau_f \simeq 1.6\,\tau_{1/2}$ for the current simulations. Figure 5 shows scatter plots of r and S at different times for case 1. As the previous figure, they show that $S'/\sigma_S \approx r'/\sigma_r$ up to $t \simeq 2\tau_e$. This result may be used to model the droplet microphysics at the sub-grid scale level in cloud resolving LES, as mentioned e.g. by Paoli & Shariff (2003), and discussed next.

4.1. *Towards a stochastic model of condensation*

One goal of this work was to study the correlation between droplet radius and local supersaturation in a cloud and, eventually, to model it for application in cloud-resolving LES codes. The object of this section is to propose a modeling methodology.

The concept of fluid particles has already been used in Sec. 3 to derive a simple re-

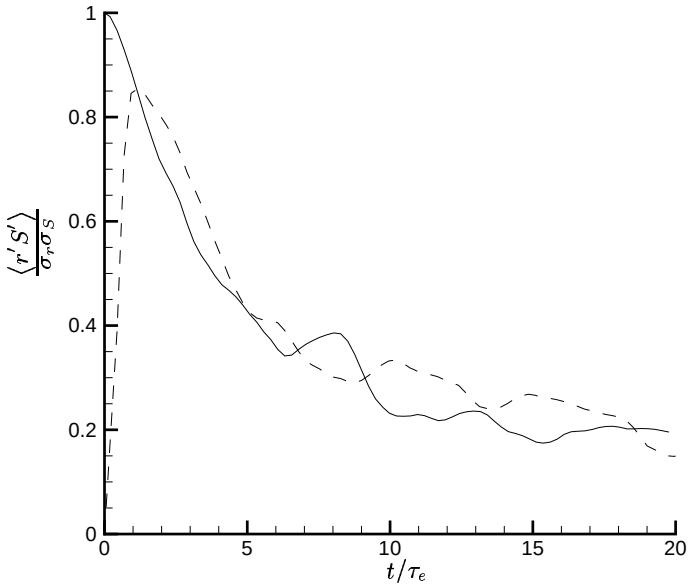

FIGURE 4. Temporal evolution of the radius-supersaturation correlation coefficient: solid line, case 1; dashed line, case 3.

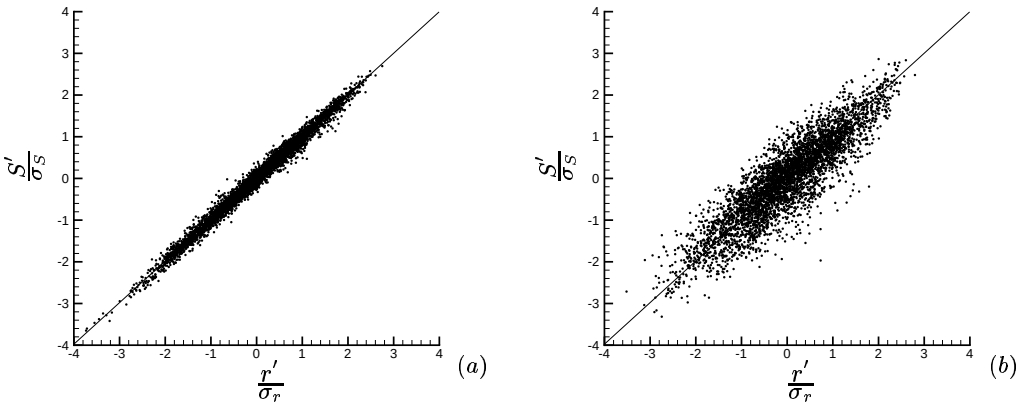

lation between σ_q and σ_{Y_∞}. The same approach is used here for a system of physical droplets, as they have negligible inertia and exactly follow fluid particles. Thus, averaging over droplets is equivalent to volume averaging provided the number of droplets is "sufficiently" high. This has been verified for the present simulations. Assuming a statistically stationary temperature forcing and neglecting water vapor forcing, one can use a Lagrangian formulation to describe temperature and vapor evolution around a physical droplet,

$$dY_v = -\frac{Y_v - \langle Y_v\rangle}{\tau_e}\,dt - 4\pi\alpha\rho_w n_p r^2 \dot{r} \tag{4.2}$$

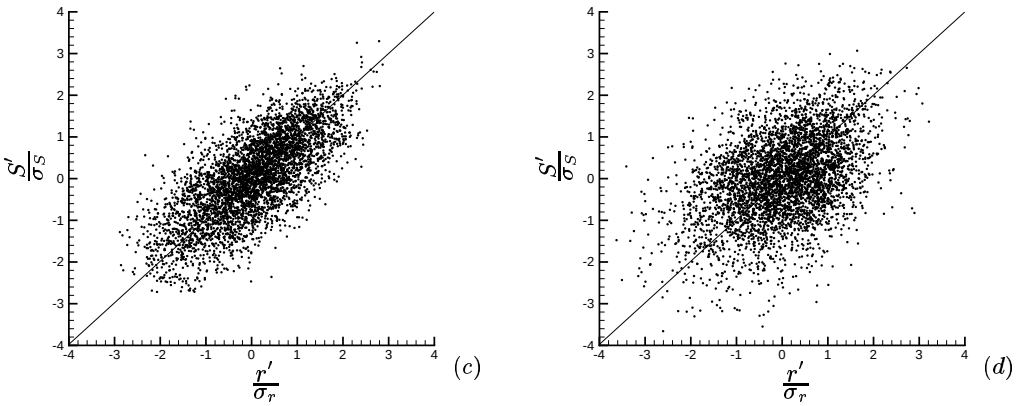

FIGURE 5. Evolution of the scatter plot of droplet radius and supersaturation for case 1 ($r' \equiv r - \langle r \rangle$, $S' \equiv S - \langle S \rangle$): (a) $t = 0.25\,\tau_e$; (b) $t = \tau_e$; (c) $t = 2\,\tau_e$; (d) $t = 5\,\tau_e$.

$$dT = -\frac{T - \langle T \rangle}{\tau_e}\,dt + \sqrt{2\sigma_{T_\infty}^2\,\frac{dt}{\tau_e}}\,N_t^{t+dt}(0,1) \tag{4.3}$$

where n_p is the droplet number density and ρ_w is the water density. Expanding the supersaturation S in (2.7) around the ambient temperature T_∞, one gets after some algebra

$$Y_s(T) \simeq Y_s(T_\infty) + \left(\frac{dY_s}{dT}\right)_{T_\infty}(T - T_\infty) = Y_s(T_\infty)\left[1 + \varphi_\infty (T - T_\infty)\right] \tag{4.4}$$

with $\varphi_\infty = a_1\,T_\infty^{-1} - a_2\,T_\infty^{-2} + a_4 + 2a_5\,T_\infty$. Substituting the latter into Eqs. (4.2) and (4.3) and rewriting for completeness the equation for the growth of droplet radius gives

$$dS = -\frac{S - \langle S \rangle}{\tau_e}\,dt + \varphi_\infty\,Y_s(T_\infty)\sqrt{2\sigma_{T_\infty}^2\,dt} - 4\pi\alpha\rho_w n_p r^2 \dot{r} \tag{4.5}$$

$$dr = \frac{\alpha S}{r}\,dt \tag{4.6}$$

Taking the average of these equations over a population gives

$$\frac{d\langle S \rangle}{dt} = -4\pi\alpha\rho_w n_p \langle S\,r \rangle = -4\pi\alpha\rho_w n_p \left(\langle S \rangle \langle r \rangle + C_{Sr}\,\sigma_r \sigma_S\right) \tag{4.7}$$

$$\frac{d\langle r^2 \rangle}{dt} = \frac{d\langle r \rangle^2}{dt} + \frac{d\langle \sigma_r^2 \rangle}{dt} = 2\alpha \langle S \rangle . \tag{4.8}$$

The problem then is to close, using information from the DNS, the covariances that appear when taking higher moments of r and S (such as, for example, the correlation between r' and S'). This represents the object of our current research.

5. Conclusions

In this brief, a direct numuerical simulation of the turbulent condensation of a population of droplets was perfomed using a coupled Navier-Stokes/Lagrangian code. Forcing of the small wavenumbers was used to sustain velocity, vapor, and temperature fluctuations. The resulting supersaturation fluctuations were responsible for the broadening of

the droplet size distribution in agreement with *in situ* measurements. Finally, a sketch of a possible approach for modeling the correlation between droplet size and supersaturation for use in cloud resolving LES was presented.

Computational resources were provided by the NAS Supercomputing Division at NASA Ames Research Center which is gratefully aknowledged. The first author wishes to thank the Center for Turbulence Research for its hospitality during his post-doctoral stay at NASA Ames and Stanford University.

REFERENCES

Boivin, M., Simonin, O. & Squires, K. D. 1998 Direct numerical simulation of turbulence modulation by particles in isotropic turbulence *J. Fluid Mech.*, **375**, 235–263.

Comte-Bellot, G. & Corrsin, S. 1971 Simple Eulerian time correlation of full and narrow band velocity signals in isotropic turbulence. *J. Fluid Mech.*, **48**, 273–337.

Cooper, W. A. 1989 Effects of variable droplet growth histories on droplet size distributions. Part I: Theory *J. Atmos. Sci.* **46**, 1301–1311.

Eswaran, V. & Pope, S. B. 1988a An examination of forcing in direct numerical simulations of turbulence. *Comput. Fluids*, **16**, 257–278.

Eswaran, V. & Pope, S. B. 1988b Direct numerical simulation of the turbulent mixing of a passive scalar. *Phys. Fluids*, **31**, 506–520.

Khvorostyanov, V. I. & Curry, J. A. 1999*a* Toward the theory of stochastic condensation in clouds. Part I: A general kinetic equation. *J. Atmos. Sci.*, **56**, 3985–3996.

Khvorostyanov, V. I. & Curry, J. A. 1999*b* Toward the theory of stochastic condensation in clouds. Part II: Analytical solutions of the gamma-distribution type *J. Atmos. Sci.*, **56**, 3997-4012.

Kida, S. & Orszag, S. A. 1991 Energy and spectral dynamics in forced compressible turbulence. *J. Sci. Comp.*, **5**, 85–125.

Kulmala, M., Rannik, U., Zapadinsky, E., Clement, C. 1997 The effect of saturation fluctuations on droplet growth. *J. Aerosol Sci.*, **28**, 1395–1409.

Lele, S. K. 1992 Compact finite difference scheme with spectral-like resolution. *J. Comp. Phys.*, **103**, 16–42.

Lemons, D. S. 2002 *An Introduction to Stochastic Processes in Physics.* The Johns Hopkins University Press.

MacPherson, J. I., & Isaac, G. A. 1977 Turbulent characteristics of some Canadian cumulus clouds. *J. Appl. Meteor.*, **16** , 81–90.

Paoli, R., & Shariff, K. 2003 Particle size distributions in atmospheric clouds. *CTR Annual Research Briefs*, 39–47.

Paoli, R., Hélie, J. & Poinsot, T. 2004 Contrail formation in aircraft wakes. *J. Fluid Mech.*, **504** 361–373.

Pinsky, M. B. & Khain, A. P. 1997 Turbulence effects on droplet growth and size distribution in clouds- A review. *J. Aerosol Sci.*, **28**, 1177–1214.

Pope, S. B. 2000 *Turbulent Flows.* Cambridge University Press.

Pruppacher, H. R. & Klett, J. D. 1997 *Microphysics of Clouds and Precipitation.* Kluwer Academic Publishers, Dordrecht, The Netherlands.

SEINFELD, J. N. & PANDIS, S. N. 1997 *Atmospheric Chemistry and Physics: From Air Pollution to Climate Change.* John Wiley & Sons Inc.

SHAW, R. A. 2003 Particle-Turbulence Interactions in Atmospheric Clouds. *Annu. Rev. Fluid Mech.* **35**, 183–227.

SONNTAG, D. 1994 Advancements in the field of hygrometry. *Meteorol. Z.* **3**, 51–66.

SRIVASTAVA, R. C. 1989 Growth of cloud Drops by Condensation: A criticism of currently accepted theory and a new approach. *J. Atmos. Sci.*, **46**, 869–887.

VAILLANCOURT, P. A. & YAU, M. K. 2000 Review of Particle-Turbulence Interactions and Consequences for Cloud Physics. *Bull. Am. Meteorol. Soc.*, **81**, 285–298.

Droplet growth by turbulent coagulation

By N. Riemer AND A.S. Wexler †

1. Motivation and objectives

Rain formation and the role of clouds in climate and atmospheric chemistry are closely linked to the evolution of the cloud droplet spectra. Our understanding of these processes is still fragmentary (Beard & Ochs 1993; Pinsky *et al.* 2000). This implies that the treatment of clouds leads to large uncertainties in weather and climate predictions.

Cloud droplets are initially produced by condensation of water vapor onto nuclei. Condensation alone, however, cannot form drops that are large enough to precipitate. In the absence of the ice phase this requires the coagulation of smaller droplets resulting in a larger drop. The process of coagulation relies on relative velocities between the droplet. One mechanism to provide relative velocities is the gravitational settling of the droplets. The larger droplets fall faster and collect smaller droplets on their way. However, this does not describe the real situation in a cloud sufficiently since the droplets are transported in a turbulent environment which results in relative velocities that will deviate from the mere differences of the terminal velocities in calm air.

Recent literature agrees that the in-cloud turbulence can enhance the collision kernel and hence the droplet growth significantly. However, the quantitative treatment of these processes represents a fundamental gap in our understanding of cloud microphysics. Although the potential importance of turbulence for droplet growth has been noted by Arenberg (1939) more than 60 years ago, progress has been slow in this area. At present, turbulence effects on cloud microphysics are ignored in most current cloud models.

Air turbulence in clouds can modify the collision process in at least four ways. First, particle inertia leads to increased relative velocities and less correlated velocity directions (acceleration effect). Second, the wind field shear produces collisions between particles even with the same inertia (shear effect). The acceleration and the shear effect are often referred to as the transport effect. Third, coagulation rates are enhanced due to local concentration increases for particle response times on the order of the Kolmorgorov scale. For this phenomenon the terms "preferential concentration" or "accumulation effect" have been coined. Fourth, turbulence can also impact the local droplet-droplet hydrodynamic interactions.

Since turbulence also influences the fields of temperature and water vapor it may impact condensational growth due to the turbulence induced fluctuations in supersaturation (see for instance the article by Paoli & Shariff (2004), this issue). This process, however, is beyond the scope of this paper.

Depending on the relation between the governing time scales of the fluid and the particle response times, the impact of the transport and accumulation effects varies. The transport effect is most dominant if the particle response time τ_p is on the order of the flow integral time scale T_e, whereas the accumulation effect is most dominant if τ_p is on the order of the Kolmogorov time scale τ_k (Wang *et al.* 2000; Reade & Collins 2000).

† Department of Mechanical and Aeronautical Engineering, University of California, Davis, U.S.A

Maxey (1987) first showed the phenomenon of preferential concentration, which was expanded by Squires & Eaton (1991) and Wang & Maxey (1993). Sundaram & Collins (1996) introduced the pair correlation function to quantify the effect of preferential concentration in the collision kernel. Since this work, further efforts have been made by Wang *et al.* (1998), Wang *et al.* (2000) and Zhou *et al.* (2001) to develop a model for the collision kernel on the basis of the solution of the Navier-Stokes equations using direct numerical simulations (DNS).

Pinsky & Khain (1997) brought the concept of preferential concentration to the atmospheric science community as a phenomenon that could play an important role in cloud microphysics. Indeed, several authors measured the existence of small-scale concentration fluctuations in clouds which strengthens the hypothesis that preferential concentration is also present in the atmosphere (Brenguier & Chaumat 2001; Kostinski & Shaw 2001).

Laboratory studies are rare compared to the theoretical ones, especially in the parameter range that relates to atmospheric clouds. Obviously, it is not feasible to cover the entire turbulent kinetic energy spectrum present in natural clouds with laboratory experiments. Woods *et al.* (1972), Jonas & Goldsmith (1972) and Neizvestny & Kobzunenko (1986) all conclude from their experiments that turbulence enhances drop collision. However, their experiments were limited to relatively small collector drops. Vohl *et al.* (1999) confirmed for larger collector drops that the droplets grow faster in turbulent flow compared to laminar flow.

As outlined in the brief literature review above, many of the theoretical studies have been devoted to the derivation of collision kernels. Few studies, however, investigate the resulting development of droplet size distributions (Park *et al.* 2002; Pinsky & Khain 1997). In light of the recent DNS-derived kernels we explore the possible impact of turbulence on the droplet size distribution for atmospheric conditions systematically, approaching the problem in two steps.

First, we will consider a Lagrangian box model of a cloud parcel simulating the evolution of the cloud droplet size distribution under the assumption that only coagulation is occuring. We will employ the coagulation kernel presented by Zhou *et al.* (2001), since their parameterization covers the accumulation and the transport effects. By applying this parameterization to atmospheric conditions, the potential influence of turbulent coagulation on droplet growth is evaluated.

In the second step, we will expand this model to a 1D-column model so that condensation, and transport processes such as turbulent diffusion and sedimentation can also be included.

In the following section the calculation of the turbulent collision kernel is outlined. Section 3 presents numerical results of the box model simulations, and Section 4 presents results of column model. Finally, future work is addressed in Section 5.

2. The collision kernel

Zhou *et al.* (2001) provide a model to predict the geometric collision kernel in a bidisperse system for a turbulent fluid, which is derived from DNS. This model includes both the turbulent transport effect and the accumulation effect. In this work we apply this kernel to calculate the development of cloud droplet spectra under atmospheric conditions. The following section outlines the calculation of the collision kernel in a turbulent fluid.

The ensemble average of the collision kernel $K_t(r_1, r_2)$ for two particles with radii r_1

and r_2 in a turbulent fluid can be expressed in a generalized form by Sundaram & Collins (1997):

$$K_t(r_1, r_2) = E_t \Gamma_0 \frac{\langle |w_r(r_1, r_2)| \rangle}{\langle |w_{r,\mathrm{shear}}(r_1, r_2)| \rangle} g_{12}(R), \tag{2.1}$$

where $R = r_1 + r_2$ is the collision radius and

$$\Gamma_0 = \sqrt{\frac{8\pi}{15}} R^3 \frac{v_k}{\eta} \tag{2.2}$$

is the collision kernel for zero-inertia particles according to Saffman & Turner (1956), with the Kolmogorov velocity scale $v_k = (\nu\epsilon)^{\frac{1}{4}}$, where ν is the kinematic viscosity of the fluid and ϵ is the dissipation rate. The Kolmogorov length scale is $\eta = (\nu^3/\epsilon)^{\frac{1}{4}}$, and E_t is the turbulent collection efficiency. The notation $\langle |w_r(r_1, r_2)| \rangle$ denotes the ensemble-averaged magnitude of the relative velocity of particles with radii r_1 and r_2.

The collection efficiency E_t is defined as the product of the collision efficiency $E_{\mathrm{col},t}$ and the coalescence efficiency $E_{\mathrm{coa},t}$. The collision efficiency represents the ratio of the actual number of collisions to the number for complete geometric sweep-out. However, collision does not guarantee coalescence. The coalescence efficiency accounts for this fact and is defined as the ratio of the number of coalescences to the number of collisions.

The hydrodynamic interactions of droplets in turbulent flow are highly uncertain, but there are indications that the collision efficiency is larger in turbulence than in calm air (Pinsky *et al.* 1999). In our study we retain the value $E_{\mathrm{col},t} = 1$. An estimation of the impact of $E_{\mathrm{col},t} < 1$ based on the work of Pinsky *et al.* (1999) is given in Riemer & Wexler (2004).

Even less is known about the coalescence efficiency in turbulent flow, $E_{\mathrm{coa},t}$. Laboratory studies of small colliding droplets show that the coalescence efficiency is close to 1 if the droplets are charged and an electrical field is present (Rogers & Yau 1989). Because weak fields and charges exist in natural clouds, we therefore assume $E_{\mathrm{coa},t} = 1$ for the sake of simplicity.

The term $\langle |w_r(r_1, r_2)| \rangle / \langle |w_{r,\mathrm{shear}}(r_1, r_2)| \rangle$ with its two components – shear and acceleration – represents the turbulent transport effect by

$$\begin{aligned} \langle |w_{r,\mathrm{shear}}(r_1, r_2)| \rangle &= \sqrt{\tfrac{2}{15\pi}} v_k \tfrac{R}{\eta}, \qquad \tfrac{\langle |w_r(r_1,r_2)| \rangle}{\langle |w_{r,\mathrm{shear}}(r_1,r_2)| \rangle} = \left[1 + 15 \tfrac{w_{r,\mathrm{accel}}^2}{v_k^2} \left(\tfrac{\eta}{R}\right)^2\right]^{\frac{1}{2}} \\ \frac{w_{r,\mathrm{accel}}^2}{v_k^2} &= C_w(\phi) \left(\tfrac{u'}{v_k}\right)^2 \tfrac{\gamma}{\gamma - 1} \left((\theta_1 + \theta_2) - \tfrac{4\theta_1\theta_2}{(\theta_1+\theta_2)} \sqrt{\tfrac{1+\theta_1+\theta_2}{(1+\theta_1)(1+\theta_2)}}\right) \times \\ &\qquad \left[\tfrac{1}{(1+\theta_1)(1+\theta_2)} - \tfrac{1}{(1+\gamma\theta_1)(1+\gamma\theta_2)}\right], \end{aligned} \tag{2.3}$$

where $\theta_i = 2.5\tau_p(r_i)/T_e$ $(i = 1, 2)$ is proportional to the ratio of particle response time $\tau_p = 2\rho_p r_i^2/(9\nu\rho)$ to flow integral time $T_e = u'^2/\epsilon$. Here, ρ_p is the particle density, ρ the fluid density, r_i particle radius and u' the fluid r.m.s. velocity fluctuation.

Equation (2.3) is developed on the basis of the formulation by Kruis & Kusters (1997). To fit their numerical results, Zhou *et al.* (2001) introduced the function $C_w(\phi) = 1.0 + 0.6 \exp\left[-(\phi - 1)^{1.5}\right]$ and the factor $\gamma = \phi \times 0.183 u'^2/\sqrt{\epsilon\nu}$ with $\phi = \max(\theta_2/\theta_1, \theta_1/\theta_2)$.

The factor

$$g_{12}(R) = 1 + \rho_{12} \sqrt{g_{11}(R) - 1} \sqrt{g_{22}(R) - 1} \tag{2.4}$$

is the bidisperse radial distribution function at contact and accounts for the accumulation

$$
\begin{aligned}
y_0(\alpha) &= 18\alpha^2 \\
y_1(\alpha) &= 0.36\alpha^{2.5}\exp(-\alpha^{2.5}) \\
y_2(\alpha) &= 0.24\exp(-0.5\alpha) \\
y_3(\alpha) &= 0.013\exp(-0.07\alpha) \\
z_0(\alpha) &= \tfrac{1}{2}\left[1+\tanh\tfrac{\alpha-0.5}{0.25}\right] \\
z_1(\alpha) &= \tfrac{1}{2}\left[1+\tanh\tfrac{\alpha-1.25}{0.1}\right] \\
z_2(\alpha) &= \tfrac{1}{2}\left[1+\tanh\tfrac{\alpha-6.5}{2.5}\right]
\end{aligned}
$$

TABLE 1. Auxiliary functions for the radial distribution function g_{ii}

effect, which is governed by the monodisperse radial distribution functions g_{ii} (i=1,2; no summation implied) and the concentration correlation coefficient

$$\rho_{12} = 2.6\exp(-\psi) + 0.205\exp(-0.0206\psi)\frac{1}{2}(1+\tanh(\psi-3)). \tag{2.5}$$

where $\psi = \max(\tau_{p2}/\tau_{p1}, \tau_{p1}/\tau_{p2})$ and

$$g_{ii} = 1 + y_0(\alpha)[1-z_0^2(\alpha)] + R_\lambda z_0^2(\alpha)\{y_1(\alpha)[1-z_1(\alpha)] + y_2(\alpha)z_1(\alpha) + y_3(\alpha)z_2(\alpha)\}. \tag{2.6}$$

The functions $y_0(\alpha)$, $y_1(\alpha)$, $y_2(\alpha)$, $y_3(\alpha)$, $z_0(\alpha)$, $z_1(\alpha)$ and $z_2(\alpha)$ are given in Table 1. Here, the argument $\alpha = \tau_{pi}/\tau_k$ is the Stokes number where $\tau_k = \sqrt{\nu/\epsilon}$ is the Kolmogorov time scale.

The monodisperse radial distribution function g_{ii} scales with the Taylor-microscale Reynolds number, which is defined as $R_\lambda = u'\lambda/\nu$ with the transverse Taylor microscale $\lambda = \sqrt{15\nu u'^2/\epsilon}$. The linear dependence of g_{ii} on R_λ is based on the results of DNS, which only cover a range of low Reynolds numbers compared to atmospheric conditions. The extrapolation of this relationship to high Reynolds numbers introduces some uncertainty which we must keep in mind when interpreting our results.

Zhou *et al.* (2001) employ furthermore the following assumptions in their model: The size of the particles is on the order of or less than the Kolmogorov length scale η. The particle volume fraction and mass loading are sufficiently low so that the presence of the particles does not impact the gas turbulence. These assumptions are valid for clouds as established in Section 2.1.

Moreover, their DNS do not include the effect of gravity. In the atmosphere, clearly both turbulence and gravitation effect the size distribution. Therefore it is necessary to formulate a collision kernel that includes both mechanisms. The usual approach for modeling the impact of several coagulation mechanisms, for instance Brownian motion and gravitational settling, is simply adding the individual kernels. As Butuirat & Kielkiewicz (1996) show this method gives satisfactory results. However if the accumulation effect is also involved, the formulation of the resulting kernel requires more caution because sedimentation might counteract the clustering effect (Vaillancourt & Yau 2000). The overall effect of the interaction of gravitation and turbulence on the coagulation of particles is still not very well understood at this stage and represents an area where further research is needed.

Unless otherwise indicated, we will consider the effect of gravity and turbulence separately. To estimate the interaction of these processes, we simply add the turbulent and

sedimentation kernels. Clearly, this approach is only preliminary and will be improved as research progresses.

In our investigation the sedimentation kernel $K_s(r_1, r_2)$ for calm air will be employed for comparison, which is given by:

$$K_s(r_1, r_2) = \pi(r_1 + r_2)^2 E_s |v_T(r_1) - v_T(r_2)|. \tag{2.7}$$

Here, E_s is the collision efficiency for calm air for which we use the values provided by Hall (1980), and $v_T(r_1)$, $v_T(r_2)$ are the terminal velocities of the droplets in calm air.

2.1. *Calculation of the size distributions*

The stochastic collection equation describes the evolution of a colliding and coalescing cloud droplet size distribution (Pruppacher & Klett 1997):

$$\begin{aligned} \frac{\partial n(m,t)}{\partial t} &= \tfrac{1}{2} \int_{m_0}^{m} n(m_c, t) K(m_c, m') n(m', t) dm' \\ &\quad - \int_{m_0}^{\infty} n(m, t) K(m, m') n(m', t) dm', \end{aligned} \tag{2.8}$$

where $n(m,t)$ is the drop number distribution function at time t and $K(m_c, m')$ is the collection kernel describing the rate at which a droplet of mass $m_c = m - m'$ is collected by a droplet of mass m' forming a droplet of mass m. The following transformation of variables leads to the stochastic collection equation for the mass size distribution $g(y,t)$ (Berry 1967):

$$g(y,t)dy = m\, n(m,t) dm, \quad n(m,t) = \frac{1}{3m^2} g(y,t), \tag{2.9}$$

where $y = \ln r$, and r is the radius of droplets with mass m.

$$\begin{aligned} \frac{\partial g(y,t)}{\partial t} &= \tfrac{1}{2} \int_{y_0}^{y} \tfrac{m^2}{m_c^2 m'} g(y_c, t) K(y_c, y') g(y', t) dy' \\ &\quad - \int_{y_0}^{\infty} g(y,t) \tfrac{K(y,y')}{m'} g(y', t) dy'. \end{aligned} \tag{2.10}$$

As the initial cloud droplet distribution we use a Gamma function of the form $n(m, t = 0) = L_w / \bar{m}^2 \exp(-m/\bar{m})$, where L_w is the total cloud water content, and $\bar{m}$ is the mean droplet mass. Assuming spherical droplets, $\bar{m}$ and the mean droplet radius $\bar{r}$ are related by $\bar{m}(r) = 4/3\pi\rho_p \bar{r}^3$, where ρ_p is the water density.

For our simulations, L_w is set to 1 g m^{-3}, typical for warm rain clouds and $\bar{r}$ to 10 μm, a typical cloud droplet size. This means that the assumptions mentioned above (low mass loading and particles smaller than or on the order of η) hold. Solution of the stochastic collection equation (2.10) uses the flux method by Bott (1998), which has been proved to be both efficient and mass conservative. For the collection kernel K we employ the turbulent collision kernel K_t as described in Section 2 for different atmospheric conditions and compare the results to those obtained with the kernel for sedimentation in calm air K_s (equation (2.7)).

Cloud dissipation rates ϵ depend on cloud type and age. The values range from 10 cm^2 s^{-3} for stratus clouds to several 100 cm^2 s^{-3} for cumili and 1000 cm^2 s^{-3} for cumulonimbus clouds (Pruppacher & Klett 1997).

Figure 1 shows measured dissipation rates ϵ in clouds with the corresponding r.m.s. velocity u' (MacPherson & Isaac 1977). From dimensional arguments, a cubic relation

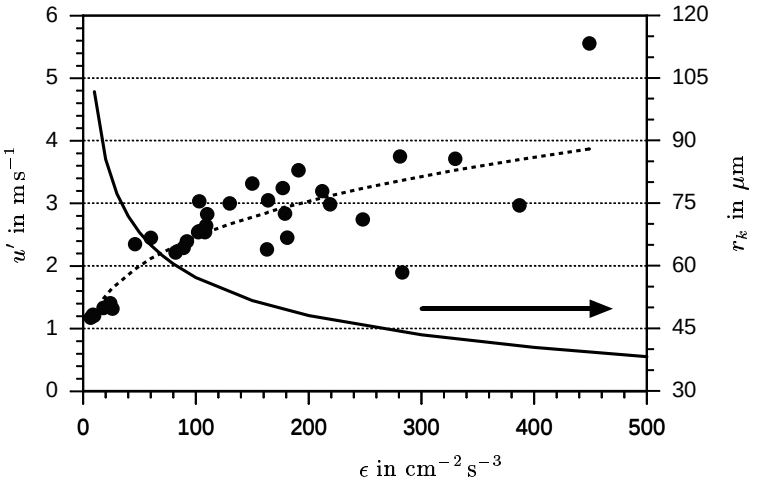

FIGURE 1. Full circles: Measured values of u' and ϵ in clouds (MacPherson & Isaac 1977), dashed line: fit of measured data, solid line: particle radius for which $\tau_p = \tau_k$ (see text for details).

between ϵ and u' is expected, since

$$\epsilon = \frac{u'^3}{L}, \tag{2.11}$$

as long as the characteristic length scale L is relatively constant. The dashed line shows the fit to the data points for $L = 1500$ m. The solid line shows the radius r_k that fulfills the condition $\tau_p(r_k) = \tau_k(\epsilon)$, showing that the accumulation effect is important.

Clearly, for values of ϵ that occur in the atmosphere, the values for r_k are in the range of observed cloud droplet sizes. Therefore the accumulation effect is expected to be significant for droplets between 30 μm and 100 μm. The transport effect, however, is less important since $\tau_p = T_e$ applies for unreasonably large particle sizes under atmospheric conditions.

In the following, the values of $\epsilon = 300$ cm^2 s^{-3} and $u' = 3.5$ m s^{-1} are used for the base case, which fulfill equation (2.11) and represent in-cloud turbulence of moderate to high intensity.

3. Box model simulations

In this section we evaluate the influence of turbulence on the evolution of the drop size spectra if only coagulation is considered. Figure 2a shows the turbulent coagulation kernel K_t according to equation (2.1) for the base case, and figure 2b shows the relative differences $(K_t - K_s)/K_s$ to the sedimentation kernel K_s according to equation (2.7). Given equation (2.7), it is clear that K_s depends both on the absolute and on the relative particle sizes. In particular, since it depends on the relative velocity it becomes large if the sizes of the colliding droplets are different and zero for equally sized droplets. The turbulent coagulation kernel K_t exhibits a distinct local maximum for the combination of droplet radii near 65 μm and 250 μm using the base case values for ϵ and u'. The exact position as well as the magnitude of this maximum depend on ϵ and u'. It shifts to larger radii for smaller dissipation rates, which means that higher dissipation rates enhance the coagulation process at an earlier stage. Note that the local maximum in the 65 to 250 μm size range is not of primary importance for the onset of effective coagulation.

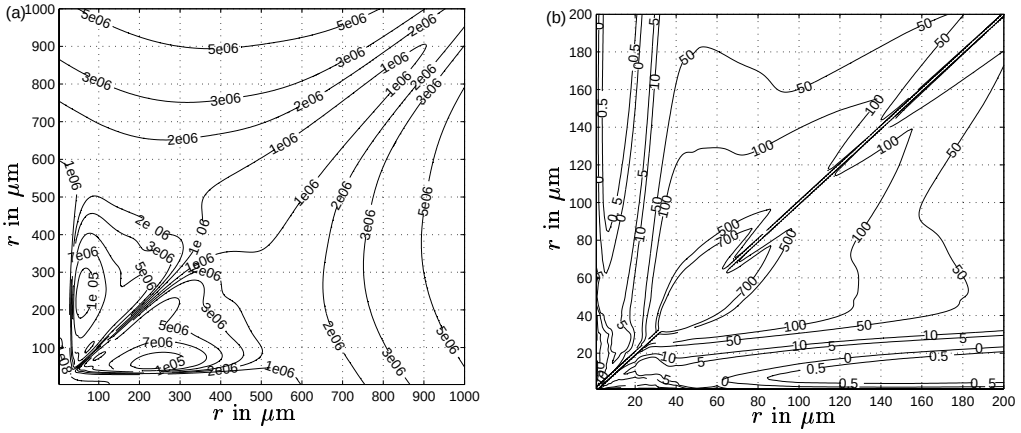

FIGURE 2. (a) K_t in $\mathrm{m^3\,s^{-1}}$ for $\epsilon = 300\ \mathrm{cm^2\,s^{-3}}$ and $u' = 3.5\ \mathrm{m\,s^{-1}}$. (b) Relative differences $(K_t - K_s)/K_s$. K_t as in figure 2. Note the different scale of the axis compared to figure 2a.

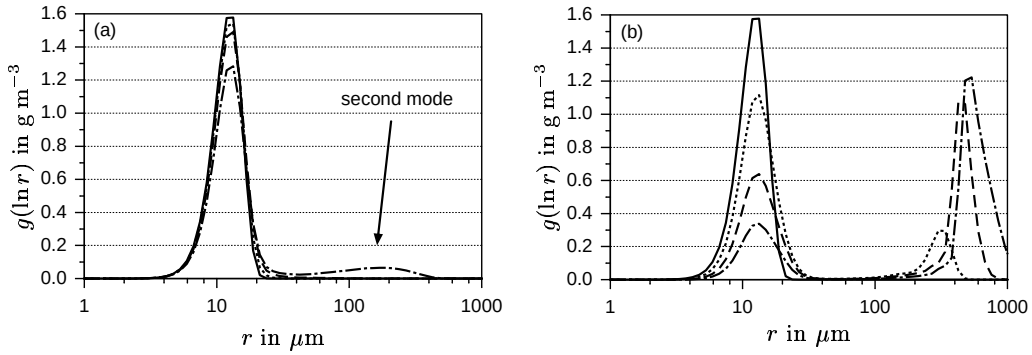

FIGURE 3. (a) Temporal evolution of the mass size distribution with sedimentation kernel according to Hall (1980). (b) Same as (a) but with turbulent kernel (base case). ——— : start, · · ·: 10 min., – – – – : 20 min., — · —: 30 min.

To be effective, turbulent coagulation must help particle grow through the 10-40 μm gap. Below this size range condensation grows particles effectively, above this size range settling coagulation becomes an effective mechanism for particle growth. Indeed figure 2 shows that K_t is by about a factor of 5-10 larger than K_s in this size range. Moreover, turbulent coagulation is also effective for same-sized particles.

We can therefore expect that the impact of turbulent coagulation is especially significant in the initial stage of the development of the cloud whereas the impact decreases for large cloud droplets or rain drops.

Figure 3 shows the temporal evolution of the mass distribution $g(\ln r)$ for the sedimentation kernel and for the turbulent kernel for the base case. For the sedimentation kernel (figure 3a) a second mode appears only after about 30 minutes. At $t = 30$ min, most of the mass (97 %) is still distributed over the droplet size range smaller than 100 μm, confirming the well known fact that sedimentation alone cannot explain the fast formation of large droplets. For the turbulent kernel (figure 3b), the second mode forms already after 10 minutes, because the turbulent coagulation kernel of Zhou *et al.* (2001) accelerates the formation of large drops. For simulation times around one hour, the sedimentation and

turbulent kernels predict similar distributions, supporting the finding that turbulence is especially important for the early stage of the development of the cloud. If the combined sedimentation and turbulent kernel is considered, the second mode becomes visible after only 5 minutes, and after 30 minutes 96 % of the mass is transferred to sizes larger than 100 μm (not shown here).

The temporal evolution of the size distribution shows a strong sensitivity to the dissipation rate. We will address this point in section 4.

4. 1D simulations

With the boxmodel presented in section 3 only the impact of coagulation has been studied and we found that turbulent coagulation can accelerate rain formation significantly. In the real atmosphere, however, condensation is also an important process – in fact condensation is the governing process in the early stage of droplet growth. Additionally, transport processes such as turbulent diffusion and sedimentation take place. The question arises if the result of the previous section still holds considering the interaction of these processes.

To address this question, we consider a column of air parcels with a prescribed aerosol distribution that undergoes an updraft (e.g. cooling) process. For the set up of the base case and the initial condition see table 2.

The size distribution of the aerosol particles (solid line in figure 4a) is initially prescribed in each grid box. We use 100 logarithmically spaced bins to discretize the size distribution with respect to radius. At the start of the simulation the water content of the aerosol particles is calculated according to equilibrium conditions assuming that the aerosol consists of ammonium sulfate. As a consequence of the ascent of the column supersaturation is reached and a proportion of the aerosol particles are activated serving as cloud condensation nuclei (CCN). The processes of condensation/evaporation, coagulation, turbulent diffusion and sedimentation shape the size distribution and feed back on the supersaturation of the system. We assume a constant updraft velocity and do not consider entrainment processes.

The following set of equations describes the system: As the column rises, the potential temperature θ and the specific humidity q change according to:

$$\frac{\partial \theta}{\partial t} = \frac{\partial}{\partial z}\left(K_h \frac{\partial \theta}{\partial z}\right) - \left(\frac{p_0}{p}\right)^{0.286} \frac{L_v}{c_{pa}\rho}\left(\frac{\partial}{\partial t} q\right)_{\text{phase}}, \tag{4.1}$$

$$\frac{\partial q}{\partial t} = \frac{\partial}{\partial z}\left(K_h \frac{\partial q}{\partial z}\right) + \frac{1}{\rho}\left(\frac{\partial}{\partial t} q\right)_{\text{phase}}. \tag{4.2}$$

Here K_h is the eddy diffusivity for heat, c_{pa} is the specific heat of dry air at constant pressure, L_v is the latent heat of condensation, p is the pressure, and ρ is the air density.

Changes of the size distribution of the water mass g_w are calculated as follows:

$$\begin{aligned}\frac{\partial g_w}{\partial t} = &\frac{\partial}{\partial z}\left(K_h \frac{\partial g_w}{\partial z}\right) - \frac{\partial}{\partial z}\left(v_t g_w\right) \\ &+ H g_w - \frac{1}{3}\frac{\partial}{\partial y}(H g_w) + \left(\frac{\partial g_w}{\partial t}\right)_{\text{coa}}\end{aligned} \tag{4.3}$$

The last term corresponds to coagulation and is defined in equation (2.10). The second term of the right hand side describes sedimentation with terminal velocity v_t.

Updraft velocity	1 ms^{-1}
Vertical gridsize	20 m
Total column height	500 m
Initial aerosol distribution	see figure 4
Eddy diffusivity	10 m^2s^{-1}
Dissipation rate	300 cm^2s^{-3}
r.m.s. velocity	3 ms^{-1}
Relative humidity	from 91 % (layer 1, bottom) increasing to 99.6 % (layer 25, top)
Temperature	from 285 K (layer 1) decreasing with wet-adiabatic lapse rate

TABLE 2. Model parameters and initial conditions

The third and fourth terms specify the condensation/evaporation with the condensation/evaporation rate H defined as

$$H = \frac{1}{m(r)} \frac{\partial m(r)}{\partial t} \tag{4.4}$$

here m is the mass of a particle of size r.

The growth rate $\partial m/\partial t$ of the particles is calculated according to Majeed and Wexler (2001).

$$\frac{\partial m(r)}{\partial t} = \frac{4\pi r D_v' M_w p^\circ(T)/(RT)\,[\mathrm{RH} - \exp(\mathrm{A} - \mathrm{B})]}{1 + (4\pi r D_v' M_w p^\circ(T)/(RT))(L_v M_w/(RT))(L_v/(4\pi r k_a' T))\exp(A - B)},$$

with

$$A = \frac{2M_w\sigma_w}{RT_a\rho_w r}, \quad B = \nu_m \frac{M_w}{M_s}\frac{m_s}{m_d - m_p}, \tag{4.5}$$

where M_w is the molecular weight of water vapor, M_s the molecular weight of the solute, R the universal gas constant, D_v' the water diffusivity corrected for non-continuum effects, T the temperature of the environment, T_a the droplet temperature, $p^\circ(T)$ the water saturation pressure at T, RH the relative humidity, L_v the latent heat of water, k_a' the thermal conductivity corrected for non-continuum effects, σ_w the air-water surface tension, ρ_w the water density, ν_m the number of ions per solute molecule, m_s, m_d and m_p the masses of solute, droplet and dry particle.

A corresponding equation can be formulated for the aerosol mass distribution. Since we do not consider chemical processes the terms for condensation/evaporation vanish.

$$\frac{\partial g_a}{\partial t} = \frac{\partial}{\partial z}\left(K_h \frac{\partial g_a}{\partial z}\right) - \frac{\partial}{\partial z}(v_t g_w) + \left(\frac{\partial g_a}{\partial t}\right)_{\mathrm{coa}} \tag{4.6}$$

The term due to the phase change of water vapor in equations 4.1 and 4.2 may be obtained by integrating over the whole droplet spectrum :

$$\left(\frac{\partial q}{\partial t}\right)_{\mathrm{phase}} = \int_0^\infty H g_w - \frac{1}{3}\frac{\partial}{\partial y}(H g_w)\mathrm{d}y \tag{4.7}$$

For solving these equations we apply operator splitting. The terms for turbulent diffu-

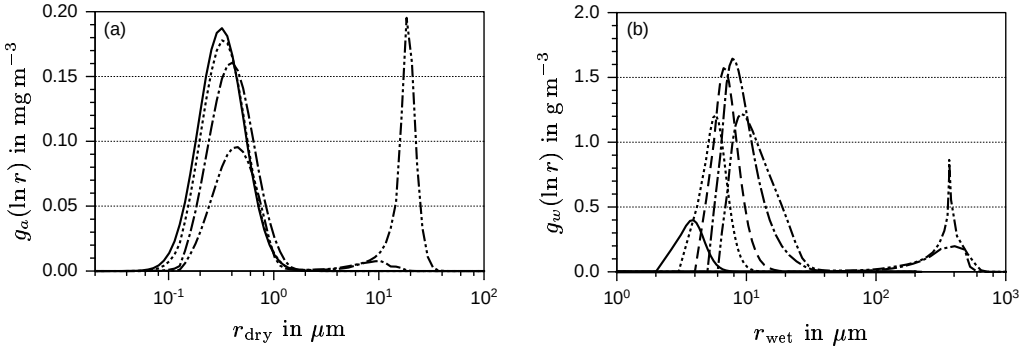

FIGURE 4. (a) Temporal development of the dry aerosol mass size distribution, layer 6, base case. ——— : start, · · ·: 15 min., — · —: 25 min., — · · —: 30 min. (b) Same as figure 4a but for water mass size distribution. ——— : 7 min., · · ·: 15 min., - - - - : 20 min., — · —: 25 min., — · · —: 30 min.

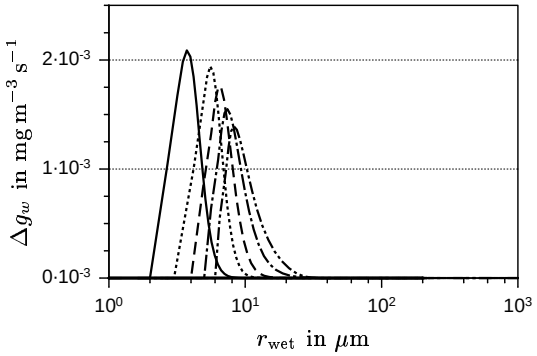

FIGURE 5. Rates of change of the water mass size distribution due to condensation. ——— : 7 min., · · ·: 15 min., - - - - : 20 min., — · —: 25 min., — · · —: 30 min.

sion are solved with an implicit scheme, for the sedimentation terms we use the advection algorithm according to Dhaniyala & Wexler (1996).

Coagulation is treated as following: For the dry aerosol mass we use a fixed grid with respect to the dry particle radius and apply the method by Bott (1998). The associated water is moved from bin to bin accordingly assuming an internal mixture of the whole droplet.

For the condensation of water we use a moving grid. The advantage of this hybrid approach (e.g. fixed grid for coagulation, moving grid for condensation) is that it avoids numerical diffusion as it occurs when treating condensation on a fixed grid. It also ensures that the aerosol mass is regenerated after evaporation, which is important for the investigation of aerosol processing.

Figure 4a shows the temporal development of the dry aerosol mass size distribution in layer 6 for the base case. Starting from the initial distribution, the dry aerosol mass is transferred to larger radii over the course of the simulation due to the coagulation process. The corresponding development of the water mass distribution in figure 4b shows that large droplets are formed after 25 min. To understand the development of the size distribution it is necessary to analyse which process is most important at various

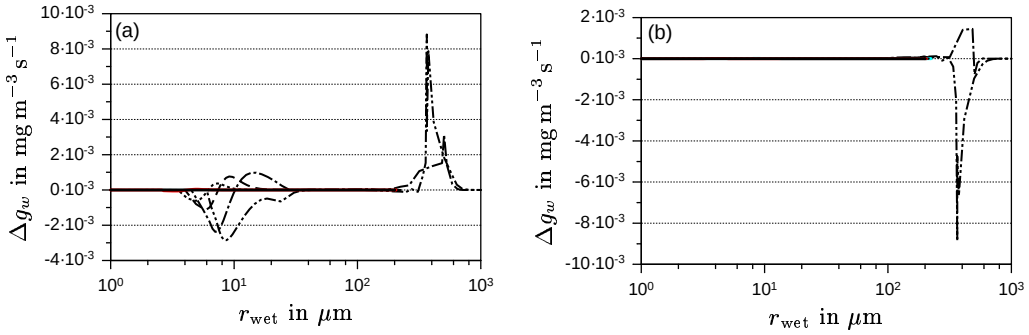

FIGURE 6. (a) Rates of change of the water mass size distribution due to coagulation. (b) Same as (a) but for sedimentation. ——— : 7 min., ···: 15 min., - - - - : 20 min., — · —: 25 min., — · · —: 30 min.

times over the course of the simulation. Figure 5 and 6 display these processes for this purpose. As seen from figure 5 condensation is dominant for the size range below 20 μm and therefore most important for the early stages of the simulation. Figure 6a shows that after 25 min. coagulation takes over and shifts the mass from sizes below 20 μm to those above 100 μm. As seen in figure 6b sedimentation becomes important once the droplets have attained a critical size of about 300 μm. This process eventually removes the water and associated CCN from the column.

Figure 7a shows the sensitivity towards the turbulence intensity. All size distributions are shown at t=30 min. The case without turbulent coagulation (coagulation only due to sedimentation) is included for comparison. For this case we see the results of the box model study confirmed. The size distribution is still very narrow and does not show any formation of larger size droplets. For $\epsilon = 100$ cm^2 s^{-3} the second maximum is not apparent, but a broadening towards the right is noticable. For both $\epsilon = 300$ cm^2 s^{-3} and $\epsilon = 500$ cm^2 s^{-3} large droplets are formed. For $\epsilon = 500$ cm^2 s^{-3} the formation occurs already ealier in the simulation so that at t=30 min. more water mass has been removed from the column due to sedimentation.

Finally we want to address the uncertainty concerning the Reynolds number dependence of the coagulation kernel. As mentioned in section 2 some uncertainty is introduced in the calculation of the coagulation kernel since we assume that the radial distribution function g_{12} depends linearly on the Reynolds number. While this assumption holds for the range of Reynolds numbers that are covered in DNS, it is unknown if this would still be the case for Reynolds numbers in the atmosphere or if g_{12} would level off after some (likewise unknown) threshold value is reached. Such behavior has been found for other problems in turbulence. For instance Belin *et al.* (1997) have shown for the velocity gradient distributions in turbulence that a change in the dependence of the parameters of the distributions on the Reynolds number can be found around $R_\lambda = 700$. To estimate the sensitivity in our model we carry out an additional simulation where R_λ in equation (2.6) is set artificially to 700 while ϵ and u' are set to the base case values. The result in figure 7b shows that compared to figure 4b, the development of large droplets is clearly delayed. However, compared to the case with coagulation due to sedimentation only strong acceleration of the large droplet formation within the first 30 min. can still be noticed.

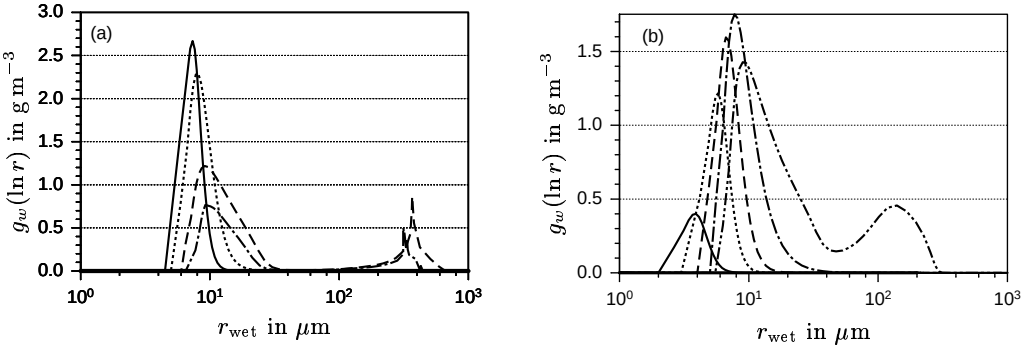

FIGURE 7. (a) Size distribution of water mass for different dissipation rates, t = 30 min. ——— : no turbulence, $\cdots$: 100 cm^2 s^{-3}, – – – – : 300 cm^2 s^{-3}, – · –: 500 cm^2 s^{-3}. (b) Temporal development of the water mass size distribution with R_λ set to 700. ——— : 7 min., $\cdots$: 15 min., – – – – : 20 min., – · –: 25 min., – · · –: 30 min.

5. Conclusions and future work

In this paper we have investigated the impact of turbulence on the development of cloud droplet spectra. In a two-step approach we have shown first that – compared to the effect of sedimentation in calm air only – even moderate turbulence can enhance the formation of large droplets significantly. The largest impact of turbulence is expected for similar sized particles and/or for particles in the size range smaller than 100 μm. Here, the collision kernel is enhanced by several orders of magnitude if turbulence is included, which accelerates the growth of droplets dramatically. By treating coagulation, condensation, turbulent diffusion and sedimentation in a 1D model we find the result confirmed. Turbulent coagulation appears to be the key mechanism that bridges the gap in transforming droplets into drops.

This model framework represents a powerful tool to investigate the impact of in-cloud turbulence on the various interactions of clouds and the Earth system. The validation of the model with observational data is currently underway.

Further plans should address the interaction of cloud microphysics with in-cloud chemistry. Current cloud chemical models predict a dependence of sulfate production on the droplet size distribution. However, the droplet dynamics in existing models does not account for the turbulence in clouds. Therefore, a focus of our research concerning the heterogeneous chemistry in clouds will be to quantify the sulfate production of clouds including the process of turbulent coagulation. In this context, it will be worthwhile to implement the cloud parcel model in a more comprehensive atmospheric model, such as a full 3D Large Eddy Simulation (LES) model, which provides the meteorological input data for the cloud microphysics model, and includes transport and coupling with atmospheric chemistry.

REFERENCES

ARENBERG, D. 1939 Turbulence as the major factor in the growth of cloud drops. *Bull. Amer. Meteor. Soc.* **20**, 444 – 448.

BEARD, K. & OCHS, H. 1993 Warm-rain initiation: An overview of microphysical mechanisms. *J. Appl. Meteorol.* **32**, 608 – 625.

BELIN, F., MAURER, J., TABELING, P. & WILLAIME, H. 1997 Velocity gradient distri-

butions in fully developed turbulence: An experimental study. *Phys. Fluids* **9**, 3843 – 3850.

BERRY, E. 1967 Cloud droplet growth by collection. *J. Atmos. Sci.* **24**, 688 – 700.

BOTT, A. 1998 A flux method for the numerical solution of the stochastic collection equation. *J. Atmos. Sci.* **55**, 2284 – 2293.

BRENGUIER, J.-L. & CHAUMAT, L. 2001 Droplet spectra broadening in cumulus clouds. Part I: Broadening in adiabatic cores. *J. Atmos. Sci.* **58**, 628 – 641.

BUTUIRAT, F. & KIELKIEWICZ, M. 1996 On additivity of coagulation kernels. *Ann. Nucl. Energy* **23**, 1091 – 1096.

DHANIYALA, S. & WEXLER, A. 1996 Numerical schemes to model condensation and evaporation of aerosols. *Atmos. Env.* **30**, 919 – 928.

HALL, W. 1980 A detailed microphysical model within a two-dimensional dynamic framework: Model description and preliminary results. *J. Atmos. Sci.* **37**, 2486 – 2507.

JONAS, P. & GOLDSMITH, P. 1972 The collection efficiencies of small droplets falling through a sheared air flow. *J. Fluid Mech.* **52**, 593 – 608.

KOSTINSKI, A. & SHAW, R. 2001 Scale-dependent droplet clustering in turbulent clouds. *J. Fluid Mech.* **434**, 389 – 398.

KRUIS, F. & KUSTERS, K. 1997 The collision rate of particles in turbulent flow. *Chem. Eng. Comm.* **158**, 201 – 230.

MACPHERSON, J. & ISAAC, G. 1977 Turbulent characteristics of some Canadian cumulus clouds. *J. Appl. Meteorol.* **16**, 81 – 90.

MAXEY, M. 1987 The gravitational settling of particles in homogeneous turbulence and random flow fields. *J. Fluid Mech.* **174**, 441 – 465.

NEIZVESTNY, A. & KOBZUNENKO, A. 1986 Effect of small scale turbulence on the coagulation growth rate of cloud droplets. *Izv. Atm. Ocean. Phys.* **22**, 481 – 487.

PAOLI, R. & SHARIFF, K. 2004 Direct numerical simulation of turbulent condensation in clouds. Annual Research Briefs, Center for Turbulence Research, NASA AMES/Stanford Univ.

PARK, S., KRUIS, F., LEE, K. & FISSAN, H. 2002 Evolution of particle size distributions due to turbulent and Brownian coagulation. *Aerosol Sci. Technol.* **36**, 419 – 432.

PINSKY, M. & KHAIN, A. 1997 Turbulence effects on droplet growth and size distribution in clouds — A review. *J. Aerosol Sci.* **28**, 1177 – 1214.

PINSKY, M., KHAIN, A. & SHAPIRO, M. 1999 Collision of small drops in a turbulent flow. Part I: Collision efficiency. Problem formulation and preliminary results. *J. Atmos. Sci.* **56**, 2585 – 2600.

PINSKY, M., KHAIN, A. & SHAPIRO, M. 2000 Stochastic effects of cloud droplet hydrodynamic interaction in an turbulent flow. *Atmos. Res.* **53**, 131 – 169.

PRUPPACHER, H. & KLETT, J. 1997 *Microphysics of Clouds and Precipitation*. Kluwer Academic Publishers.

READE, W. & COLLINS, L. 2000 Effect of preferential concentration on turbulent collision rates. *Physics of Fluids* **12**, 2530 – 2540.

RIEMER, N. & WEXLER, A. 2004 Droplets to drops by turbulent coagulation. *J. Atmos. Sci.* Accepted for publication.

ROGERS, R. & YAU, M. 1989 *A Short Course in Cloud Physics*. Butterworth-Heinemann.

SAFFMAN, P. & TURNER, J. 1956 On the collision of drops in turbulent clouds. *J. Fluid Mech.* **1**, 16 – 30.

SQUIRES, K. & EATON, J. 1991 Preferential concentration of particles by turbulence. *Phys. Fluids A* **3**, 1169 – 1179.

SUNDARAM, S. & COLLINS, L. 1996 Numerical considerations in simulation a turbulent suspension of finite-volume particles. *J. Comp. Phys.* **124**, 337 – 350.

SUNDARAM, S. & COLLINS, L. 1997 Collision statistics in an isotropic, particle-laden turbulent suspension I. Direct Numerical Simulations. *J. Fluid Mech.* **335**, 75–110.

VAILLANCOURT, P. & YAU, M. 2000 Review of particle-turbulence interactions and consequences for cloud physics. *Bull. Amer. Meteorol. Soc.* **81**, 285 – 298.

VOHL, O., MITRA, S., WURZLER, S. & PRUPPACHER, H. 1999 A wind tunnel study of the effects of turbulence on the growth of cloud drops by collision and coalescence. *J. Atmos. Sci.* **56**, 4088 –4099.

WANG, L.-P. & MAXEY, M. 1993 Settling velocity and concentration distribution of heavy particles in homogeneous isotropic turbulence. *J. Fluid Mech.* **335**, 27 – 68.

WANG, L.-P., WEXLER, A. & ZHOU, Y. 1998 Statistical mechanical description of turbulent coagulation. *Phys. Fluids* **10**, 2647 – 2651.

WANG, L.-P., WEXLER, A. & ZHOU, Y. 2000 Statistical mechanical description and modelling of turbulent collision of inertial particles. *J. Fluid Mech.* **415**, 117 – 153.

WOODS, J., DRAKE, J. & GOLDSMITH, P. 1972 Coalescence in a turbulent cloud. *Q. J. R. Meteorol. Soc.* **99**, 758 – 763.

ZHOU, Y., WEXLER, A. & WANG, L.-P. 2001 Modelling turbulent collision of bidisperse inertial particles. *J. Fluid Mech.* **433**, 77 – 104.

Topography modeling in atmospheric flows using the immersed boundary method

By I. Senocak, A.S. Ackerman †, D.E. Stevens ‡ AND N.N. Mansour

1. Motivation and objectives

Numerical simulation of flow over complex geometry needs accurate and efficient computational methods. Different techniques are available to handle complex geometry. The unstructured grid and the multi-block body-fitted grid techniques have been widely adopted for complex geometry in engineering applications. In atmospheric applications, terrain fitted single grid techniques have found common use. Although these are very effective techniques, their implementation, coupling with the flow algorithm, and efficient parallelization of the complete method are more involved than a Cartesian grid method. Oftentimes, the grid generation can be tedious and one needs to pay special attention in numerics to handle skewed cells for conservation properties. Researchers have long sought for alternative methods to ease the effort involved in simulating flow over complex geometry. A good example is the work by Peskin (1977). He has developed the immersed boundary method (IBM) to simulate blood flow in a heart/mitral valve system, where the boundary is represented by a body force and the equations are solved on a Cartesian grid. However, formulating a suitable body force term has proved to be a challenging issue.

In recent years, IBM has been significantly improved. Mohd-Yusof (1997) has proposed the direct forcing method in which the body force is implicitly taken into account by reconstructing the velocity field around the immersed boundary. Essentially, this new approach has eliminated the issue of explicit formulation of a suitable body force representing the boundary. IBM with the direct forcing approach has been further developed by adopting higher order reconstruction schemes, and it has been successfully applied to complex flow problems in engineering applications (e.g. flow over a truck, flow in piston cylinder assembly and flow in a stirred tank) by Fadlun *et al.* (2000); Verzicco *et al.* (2000); Iaccarino & Verzicco (2003). For high Reynolds number flow simulations, IBM coupled with an adaptive mesh refinement technique has been effective to provide the required near-wall resolution (Kalitzin & Iaccarino 2003). Adaptive mesh refinement helps reduce the overall number of computational nodes to achieve the desired near-wall resolution, but the problem can still be very demanding for higher Reynolds number flow simulations.

Wall/surface modeling in LES or the wall-function formulation in Reynolds-averaged Navier-Stokes (RANS)computations have been proposed to decrease the computational load due to near-wall resolution. In these approaches, coarse resolution grids can be employed, and no-slip conditions are not applied directly at the surface, because the implied stress would be overestimated on a coarse resolution grid. Instead, stresses at the surface are imposed as boundary conditions, alleviating the need to resolve the thin turbulent boundary layer. If one wants to extent the IB method for topography modeling

† NASA Ames Research Center
‡ Lawrence Livermore National Laboratory

in LES of atmospheric flows, for which numerical resolutions have been poor, then it is necessary to develop a reconstruction scheme that can take into account surface modeling. This issue has not been addressed within the context of IBM and it is one of our main objectives in this paper.

In what follows, we briefly describe the immersed boundary method, and apply it to low Reynolds number laminar flow cases to test our implementation. To take into the LES surface modeling issue within the IB method, we develop a reconstruction scheme based on the mean logarithmic wind profile assumption near the surface. To test this new scheme, we perform LES of a neutrally stratified atmosphere. Specifically, we compare the results of the IB method with the new reconstruction scheme to the results of the commonly adopted surface modeling approach, in which surface stresses are imposed as boundary conditions.

2. Governing equations

The governing equations for LES of a neutrally stratified atmospheric boundary layer are the filtered Navier-Stokes equations written as follows

$$\frac{\partial \bar{u}_i}{\partial x_i} = 0, \qquad \frac{\partial \bar{u}_i}{\partial t} + \frac{\partial (\bar{u}_i \bar{u}_j)}{\partial x_j} = \frac{\partial \bar{p}}{\partial x_i} + \epsilon_{ijk} f_j \bar{u}_k - \frac{\partial \tau_{ij}}{\partial x_j}, \tag{2.1}$$

where turbulent stresses are defined as $\tau_{ij} = \overline{u_i u_j} - \bar{u}_i \bar{u}_j$, f_j is the Coriolis parameter, ϵ_{ijk} is the permutation tensor, $\bar{u}$ and $\bar{p}$ are the filtered velocity and filtered dynamic pressure, respectively.

To solve the above governing equations, we use the LES atmospheric research code DHARMA. The numerical method adopted in DHARMA is described in detail in Stevens & Bretherton (1996) and Stevens *et al.* (2000). The governing equations are integrated using a forward-in-time projection method based on an explicit second-order Runge-Kutta scheme (Bell & Marcus 1992). The spatial discretisation is performed on a staggered grid. A third-order accurate upwind-biased monotonic scheme is used for the advection terms, whereas diffusion and pressure gradient terms are discretized using second-order accurate central differencing schemes. A direct solver (FFT) is utilized for solving the pressure Poisson equation, and the code has been parallelized to run on various platforms using MPI.

3. Subgrid scale turbulence modeling

Since the Reynolds number of a typical atmospheric boundary layer (ABL) flow is very high, LES of ABL with near-surface resolution is not a practical option with current computer resources. To alleviate this obstacle one resorts to LES with surface modeling. For a planar surface, a common approach is to set the vertical component of the velocity to zero, and to define the horizontal components of the turbulent stresses based on the mean logarithmic wind profile assumption (Moeng 1984). The surface stresses can be written as follows

$$\tau_{i3} = -\left(\frac{\kappa}{\ln \frac{z_1}{z_o}}\right)^2 |u| \bar{u}_i, \tag{3.1}$$

where z_1, u_i are the distance in the vertical direction and the velocity of the first grid point away from the surface, respectively. z_0 represents the roughness height. It should be noted that, in the immersed boundary method, we do not utilize the above approach

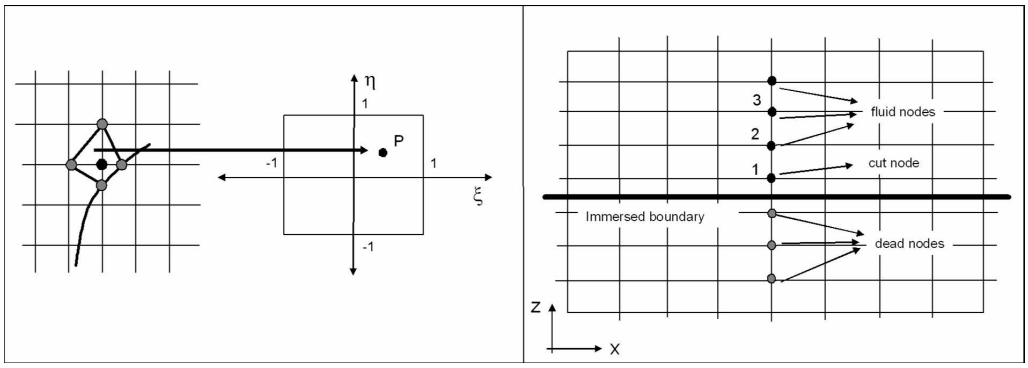

FIGURE 1. Schematics of the reconstruction schemes. Bilinear inverse interpolation (left), log-law (right)

for surface modeling. Instead, we employ the log-law reconstruction scheme, which is described in the next section.

Turbulent stresses that appear in equation 2.1 are modeled based on the Boussinesq eddy viscosity assumption. As discussed in Senocak *et al.* (2004), in LES of ABL near-surface models are needed to improve the predictions in the vicinity of the surface. Based on the results of that study we employ the hybrid RANS/LES model for the present computations. The hybrid RANS/LES model adopts the Prandtl's mixing length model (Prandtl 1925) near the surface and blends in with the dynamic Smagorinsky (Germano *et al.* 1991) away from the surface. The resulting form of the turbulent eddy viscosity can be written as

$$\nu_t = [(1 - \exp(-z/h))^2 \cdot (C\Delta^2) + \exp(-z/h)^2(\kappa z)^2]|S|, \tag{3.2}$$

where z is the distance from the surface, Δ is the filter width, κ is the von Karman constant with a value of 0.41, and $|S|$ is the magnitude of the strain rate tensor. The dimensionless parameter C is computed dynamically during the solution, making it a function of space and time (Germano *et al.* 1991). In the above equation h is the altitude, corresponding roughly to the upper edge of the surface layer. A value of $150(m)$ is used for the present computations. It should be mentioned that a logarithmic velocity profile is expected within the surface layer, which is approximately the bottom 10 percent of the atmospheric boundary layer height for neutrally stratified conditions (100 m -200 m) (Stull 1988).

4. Immersed boundary method

In IBM the solid boundary is represented by a body force F_i. The discretized form of the momentum equation given in 2.1 can be written as follows.

$$\frac{u_i^{n+1} - u_i^n}{\Delta t} = RHS_i + F_i, \tag{4.1}$$

where RHS_i includes the pressure gradient, convective, diffusive, and Coriolis terms. F_i is the body source term that gives the desired velocity at the boundary. In the direct forcing technique (Mohd-Yusof 1997; Fadlun *et al.* 2000) if the desired velocity at the

boundary is $u_i^{n+1} = V_i^{n+1}$ then one can write the explicit form of the body force as

$$F_i = -RHS_i + \frac{V_i^{n+1} - u_i^n}{\Delta t}. \tag{4.2}$$

Hence, instead of imposing the body force F_i explicitly to obtain the desired velocity at the boundary, one can impose the desired velocity and take into account the body force implicitly. For complex geometry, the boundary is not coincident with the Cartesian grid nodes, so one needs to reconstruct the velocity field using the values from neighboring nodes and the desired value at the boundary.

The steps involved in applying the immersed boundary method can be summarized as follows.

(*a*) Preprocessing: Determine the Cartesian cells that are cut by the boundary. Tag the nodes as *dead*, *fluid* and *cut*.

(*b*) Predictor stage: Solve the discretized momentum equations.

(*c*) Set zero velocity field on the *dead* nodes, and apply the reconstruction scheme on the *cut* nodes.

(*d*) Solve the pressure Poisson equation

(*e*) Update the velocity and the pressure field, and impose the reconstruction on the *cut* nodes.

Several reconstruction schemes have been suggested in literature (Fadlun *et al.* 2000; Iaccarino & Verzicco 2003). The simplest reconstruction scheme is the nearest neighbor. For instance, if we consider a 2-D geometry, a linear interpolation can be employed in either the x (horizontal) or the z (vertical) direction depending on the distance from the boundary. To preserve the local maxima or the minima a bilinear inverse interpolation can also be adopted. As depicted in the left part of figure 1, a quadrilateral element can be constructed from the neighboring nodes and the boundary surrounding the cut node. This quadrilateral element and the coordinate of the cut node is then mapped onto a square element, where an area weighted average is used to interpolate the value of the velocity at the cut node. A quadratic equation needs to be solved for this mapping, which can be derived as follows

$$x_P = \sum_{i=1}^{4} x_i N_i, \quad y_P = \sum_{i=1}^{4} y_i N_i,$$
$$N_i = \frac{1}{4}(1 + \xi\xi_i)(1 + \eta\eta_i), \quad \xi_i = \pm 1, \eta_i = \pm 1. \tag{4.3}$$

Eliminating ξ gives a quadratic equation for η.

$$a\eta^2 + b\eta + c = 0, \tag{4.4}$$

Upon solution of this equation the root that lies within the mapped zone is taken as the solution. A stable algorithm for bilinear inverse interpolation is given by Felippa (2004). However, the extension of this method to 3-D (trilinear inverse interpolation) is not straightforward. An iterative algorithm is needed to solve the set of equations defining the mapping of a hexahedral element to a cubic element

For high Reynolds number flows, both the nearest neighbor and the bilinear inverse interpolation schemes would require a very fine resolution near the boundary. The computational grid should be fine enough to resolve the viscous sublayer, where the velocity variation is physically linear. However, this is an overwhelming requirement, which is not

practical for atmospheric flows. Instead one should consider LES of atmospheric flows with surface modeling.

We propose the *log-law reconstruction scheme* for incorporating surface modeling into the immersed boundary method. It should be emphasized that this scheme addresses the surface modeling issue through reconstruction of the velocity field, whereas in the commonly adopted surface modeling approach turbulent stresses are imposed at the surface as boundary conditions. In the following, we explain the formulation of the log-law reconstruction scheme.

The log-law for a rough surface can be written as follows (Panofsky & Dutton 1984)

$$\frac{U}{u_*} = \frac{1}{\kappa} ln(\frac{z}{z_0}), \tag{4.5}$$

where z is the distance from the surface measured along the surface normal direction, z_0 is the roughness height, u_* is the friction velocity, and U is the magnitude of the velocity. Within the log-layer the friction velocity, u_* is constant in the surface normal direction. Using this property, one can write the following between two points lying on the same surface normal direction.

$$\frac{U_2}{U_1} = \frac{ln(z_2/z_0)}{ln(z_1/z_0)}, \tag{4.6}$$

The above formula is based on the magnitudes of the velocity. One needs to decompose it into velocity components in each direction (u, v, w), in order to impose the direct forcing in equation 4.1. For instance, if we consider a neutrally stratified atmospheric boundary layer over a planar surface, the velocity direction in the horizontal plane θ changes with altitude due to the rotation of the Earth. Since one has the magnitude of the velocity at hand due to equation 4.6, θ needs to be extrapolated from the fluid nodes to the cut node lying along the same vertical direction. The direction of the velocity on the horizontal plane is computed as follows

$$\theta = arctan(v/u) \tag{4.7}$$

For simplicity, we suggest a linear extrapolation to compute θ at the cut node. Once θ_{cut} is determined, then horizontal components of the velocity is computed as shown below

$$u = U \cos\theta_{cut}, \quad v = U \cos\theta_{cut} \tag{4.8}$$

The log-law reconstruction scheme in the case of a planar surface is described schematically on the right part of figure 1. In the preprocessing stage, first, the nodes are tagged as dead, fluid and cut. Next, the magnitude of the velocity at the cut node, numbered as 1, is updated based on equation 4.6, using the information from the fluid node numbered as 2. Then θ at fluid nodes 2 and 3 are computed based on equation 4.7. Using θ_2 and θ_3, a linear extrapolation gives θ_1, which is then used to compute the horizontal components of the velocity at the cut node, based on equation 4.8. Note that, the vertical component of the velocity (w) has zero value at the boundary and a linear interpolation is used to impose it on the cut node.

For a three dimensional complex surface the above scheme needs to be reformulated based on normal and tangential directions to the surface. We are currently working on extension of our scheme to complex topography.

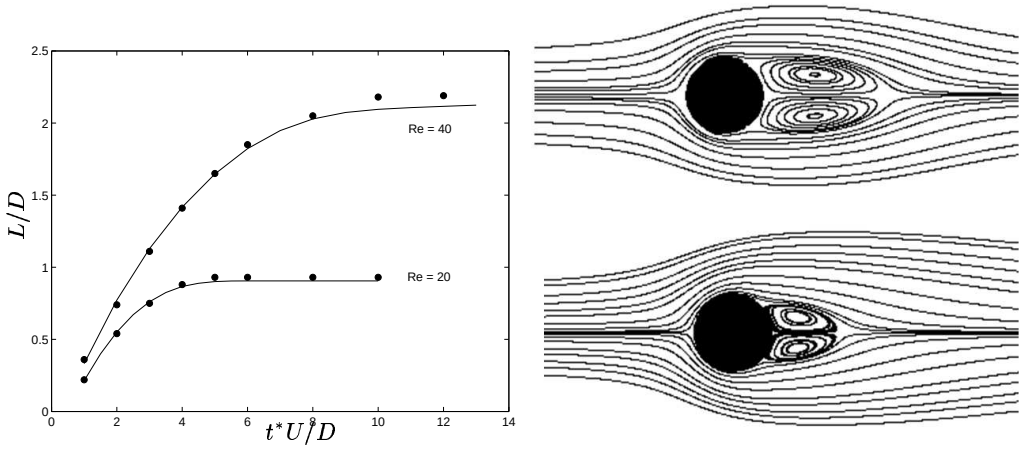

FIGURE 2. Time evolution of the recirculation zone length and the flow structure. ——— : present computations, • : experiment (Coutanceau & Bouard 1977*a*).

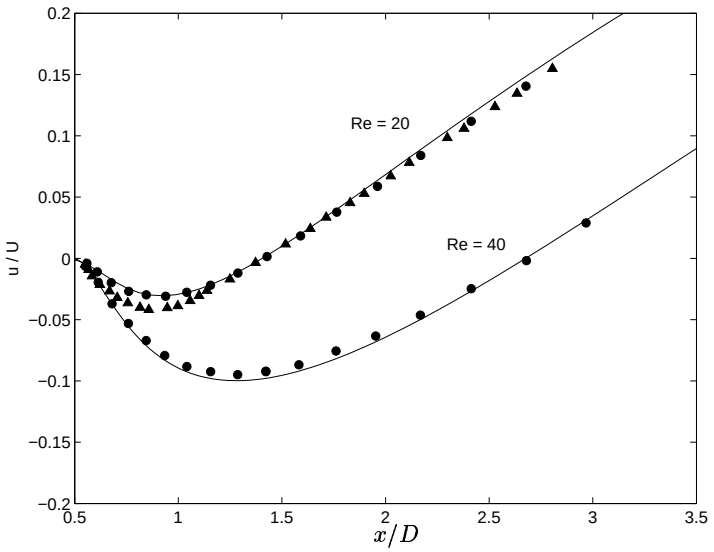

FIGURE 3. Streamwise component of the velocity field in the wake of the circular cylinder. ——— : present computations, • : computations of Nieuwstadt & Keller (1973), △ : experiment (Coutanceau & Bouard 1977*a*).

5. Results

In this section we, first, present results of low Reynolds number laminar flow computations adopting the linear reconstruction scheme in the IB method. Following this, we present results of LES of a neutrally stratified atmospheric boundary layer adopting the log-law reconstruction scheme in the IB method.

5.1. *Linear reconstruction scheme*

To test our implementation of the immersed boundary method, we perform simulations of laminar flow past circular cylinders and compare our results with the available exper-

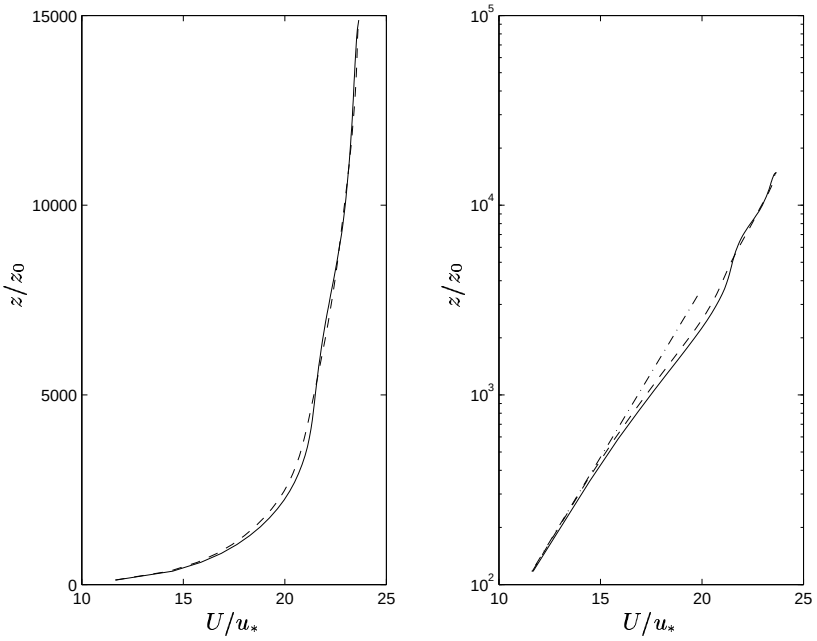

FIGURE 4. Comparison of the mean wind profiles. Linear plot (left), semi-log plot (right). ——— : surface-stress boundary condition, - - - - : immersed boundary with log-law reconstruction scheme, — · — : log-law

imental and computational studies in literature. We consider flows at Reynolds number of 20 and 40.The Reynolds number is defined as

$$Re = \frac{UD}{\nu}, \tag{5.1}$$

where U is the upcoming freestream velocity, D is the diameter of the circular cylinder, and ν is the kinematic viscosity of the fluid. The wake behind the circular cylinder becomes unsteady above Reynolds number of approximately 40, (Coutanceau & Bouard 1977*a*,*b*).

Figure 2 shows the time evolution of the length of the recirculation zone that forms in the wake at Reynolds number of 20 and 40. In figure 3, the streamvise component of the velocity is compared with both the experimental data of Coutanceau & Bouard (1977*a*)and the computational data of Nieuwstadt & Keller (1973).The present results obtained with the IB method agrees well with both the experimental and the computational data. We have also compared the results of linear reconstruction scheme with the results of bilinear inverse reconstruction scheme. Since the results are nearly identical, we do not include the comparisons in this study.

5.2. *Log-law reconstruction scheme*

To test the performance of IB method in LES of atmospheric flows, we consider a neutrally stratified atmospheric boundary layer. We compare the results of the IB method with log-law reconstruction scheme to the results obtained by adopting the surface-stress boundary condition approach, which is described in equation 3.1. For surface-stress boundary condtion approach, the computational domain size is 3000 m $\times$ 1500 m $\times$ 1500 m with 64 $\times$ 32 $\times$ 64 grid points uniformly distributed in x, y, and z directions, respectively. For

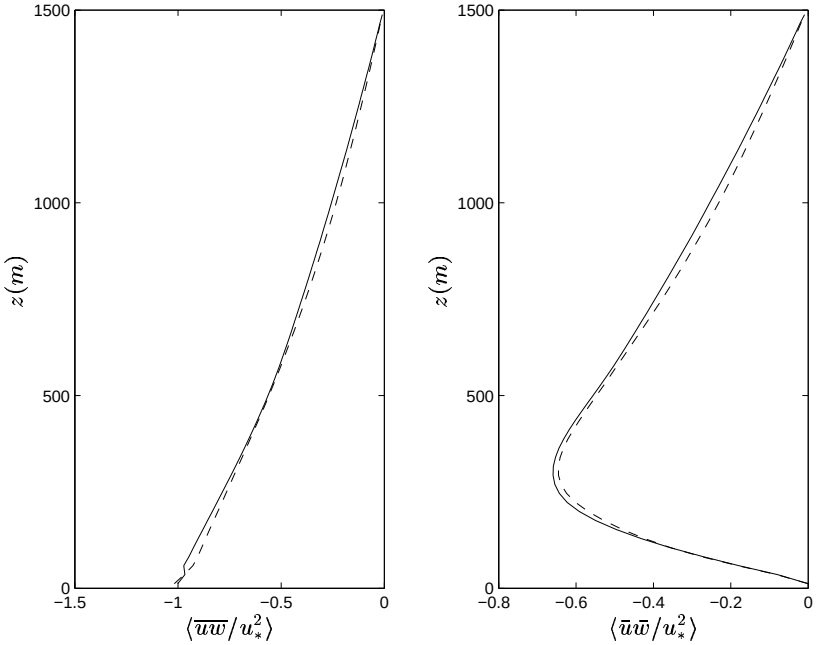

FIGURE 5. Comparison of streamwise component of the total (left) and resolved (right) stress. ——— : surface-stress boundary condition, – – – – : immersed boundary with the log-law reconstruction

immersed boundary simulations, we consider a domain height of $1687.5m$ with 72 grid nodes in the vertical direction. We place the immersed boundary at a height of $187.5m$ so that we have a computational domain, which is identical to the computational domain adopting the surface-stress boundary condition approach. The flow is driven by a mean pressure gradient that would balance a 10 ms^{-1} geostrophic wind in the x direction. Coriolis parameter is set equal to 10^{-4} s^{-1}, and the roughness parameter z_0 has a value of 0.1 m. A dimensionless time unit can be defined based on the Coriolis parameter$(1/f)$. The simulations were run over a period of $10f^{-1}$, and statistics are collected during the time period of last the $4f^{-1}$. Ensemble averaged vertical profiles have been obtained by collecting data at every 6×10^{-3} dimensionless units $(60secs)$, and averaging them both in time and in horizontal space.

In figures 4 and 5 the mean wind profile and the streamwise component of the total and the resolved stress obtained with the commonly adopted surface-stress boundary condition are compared with the results of IB method. Clearly, the IB method with the log-law reconstruction is able to reproduce the results of the surface stress boundary condition.

Figure 6 compares the spanwise components of the total stress and the velocity. The noticable differences seen in this plot is because of the extrapolation of the velocity direction in the IB method with log-law reconstruction, given in 4.7. As discussed in Senocak *et al.* (2004) the adoption of near-surface models results in non-vanishing spanwise component of the velocity. In that respect, the IB method with log-law reconstruction does a better job by predicting a lower value of the spanwise velocity.

Finally, we compare turbulent eddy viscosity profiles because it is an important quantity in atmospheric modeling. In figure 7, we see that the IB method with log-law recon-

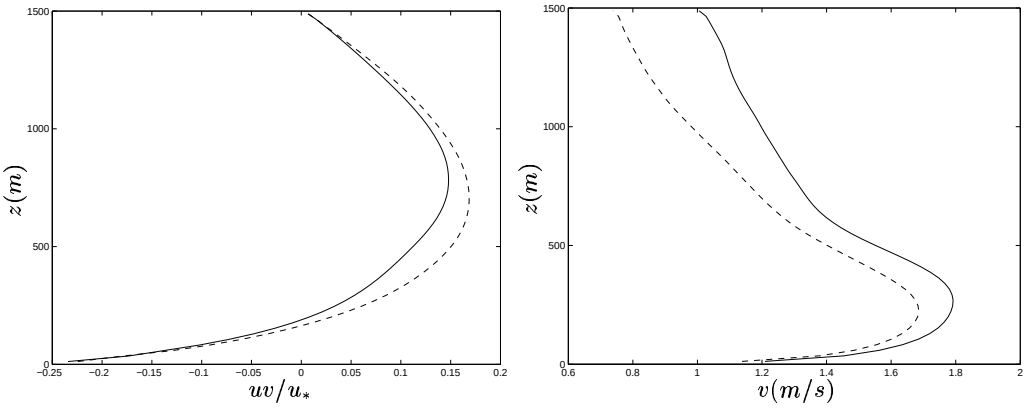

FIGURE 6. Comparisons of spanwise component of the total stress (left) and the velocity (right). ——— : surface stress boundary condition, – – – – : immersed boundary with the log-law reconstruction

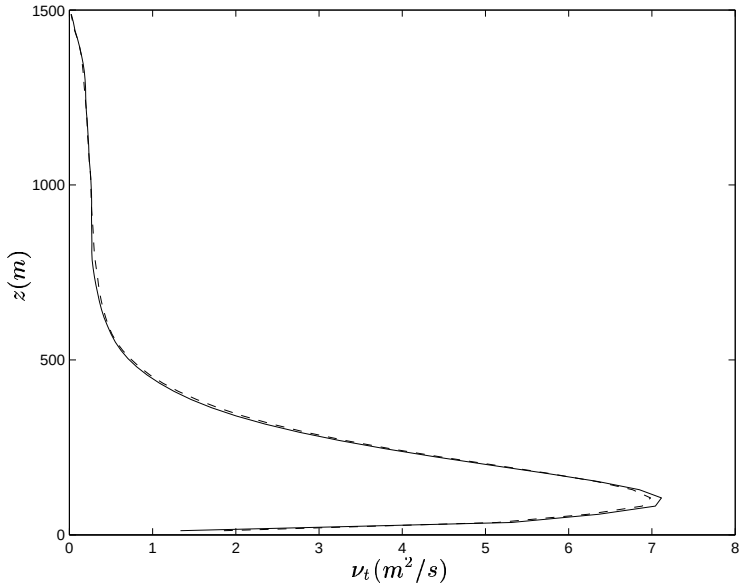

FIGURE 7. Comparison of turbulent eddy viscosity profiles. ——— : surface stress boundary condition, – – – – : immersed boundary with the log-law reconstruction

struction gives results that are almost identical to results of the surface-stress boundary condition.

6. Summary and conclusions

In this study, we have presented a Cartesian grid immersed boundary method for LES of a neutrally stratified atmospheric boundary layer flow. The IB method is appealing for atmospheric flow modeling because its implementation is easy and does not alter the computational structure of the Cartesian grid code, which can involve extensive modeling for cloud microphysics and radiation modeling.

For validation purposes, first, we have considered laminar flows over a circular cylinder

at low Reynolds numbers and demonstrated good agreements with available experimental and computational studies in literature. To address the surface modeling issue in LES of ABL using the immersed boundary method, we have proposed the log-law reconstruction scheme. This scheme enables us to employ the IB method for high Reynolds number flows without the need for fine near-surface resolution. We have shown that the IB method with log-law reconstruction scheme can produce results that are nearly identical to the results obtained with the commonly adopted surface-stress boundary condition approach.

Our future work will focus on applying the IB method to atmospheric flow problems that involve complex topography, cloud coverage and radiative energy transfer.

Acknowledgments

We thank Gianluca Iaccarino of Stanford University for helpful discussions on the immersed boundary method. We have also benefited from fruitful discussions with Tim Barth and Karim Shariff of NASA Ames Research Center.

REFERENCES

Bell, J. B. & Marcus, D. L. 1992 A second-order projection method for variable-density flows. *J. Comp. Phys.* **101**, 334–348.

Coutanceau, M. & Bouard, R. 1977*a* Experimental determination of the main features of the viscous flow in the wake of a circular cylinder in uniform translation. Part-1: Steady flow. *J. Fluid Mech.* **79**, 231.

Coutanceau, M. & Bouard, R. 1977*b* Experimental determination of the main features of the viscous flow in the wake of a circular cylinder in uniform translation. Part-2: Unsteady flow. *J. Fluid Mech.* **79**, 257.

Fadlun, E. A., Verzicco, R., Orlandi, P. & Mohd-Yusof, J. 2000 Combined immersed boundary finite difference methods for three-dimensional complex flow simulations. *J. Comp. Phys.* **161**, 35–60.

Felippa, C. A. 2004 Introduction to finite element methods. (http://titan.colorado.edu/courses.d/IFEM.d) Chapter 23, section 6.

Germano, M., Piomelli, U., Moin, P. & Cabot, W. H. 1991 A dynamic subgrid-scale eddy viscosity model. *Phys. Fluids* **3**, 1760–1765.

Iaccarino, G. & Verzicco, R. 2003 Immersed boundary technique for turbulent flow simulations. *Appl. Mech. Rev.* **56**, 331–347.

Kalitzin, G. & Iaccarino, G. 2003 Toward immersed boundary simulation of high Reynolds number flows. Annual Research Briefs, Center for Turbulence Research, NASA-Ames/Stanford Univ.

Moeng, C. H. 1984 A large-eddy simulation model for the study of planetary boundary-layer turbulence. *J. Atmos. Sci* **41**, 2052–2062.

Mohd-Yusof, J. 1997 Combined immersed boundary/B-spline methods for simulations of flows in complex geometries. Annual Research Briefs, Center for Turbulence Research, NASA-Ames/Stanford Univ.

Nieuwstadt, F. & Keller, H. B. 1973 Viscous flow past circular cylinders. *Comput. Fluids* **1**, 59.

Panofsky, H. A. & Dutton, J. A. 1984 *Atmospheric Turbulence*. John Wiley.

Peskin, C. S. 1977 Numerical analysis of blood flow in the heart. *J. Comp. Phys.* **25**, 220–252.

PRANDTL, L. 1925 Bericht uber die entstehung der turbulenz. *Z. Angew. Math. Mech.* **5**, 136–139.

SENOCAK, I., ACKERMAN, A. S., KIRKPATRICK, M. P., STEVENS, D. E. & MANSOUR, N. N. 2004 Study of near-surface models in large-eddy simulation of neutrally stratified atmospheric boundary layer. Annual Research Briefs, Center for Turbulence Research, NASA-Ames/Stanford Univ.

STEVENS, D. E., BELL, J. B., ALMGREN, A. S., BECKNER, V. E. & RENDLEMAN, C. A. 2000 Small-scale processes and entrainment in a stratocumulus marine boundary layer. *J. Atmos. Sci.* **57**, 567–581.

STEVENS, D. E. & BRETHERTON, C. S. 1996 A forward-in-time advection scheme and adaptive multilevel flow solver for nearly incompressible atmospheric flow. *J. Comp. Phys.* **129**, 284–295.

STULL, R. B. 1988 *An Introduction to Boundary Layer Meteorology*. Kluwer Academic Publishers.

VERZICCO, R., MOHD-YUSOF, J., ORLANDI, P. & HAWORTH, D. 2000 Large eddy simulation in complex geometric configurations using boundary body forces. *AIAA J.* **38**, 427–433.

Study of near-surface models in large-eddy simulations of a neutrally stratified atmospheric boundary layer

By I. Senocak, A.S. Ackerman †, M.P. Kirkpatrick ‡, D.E. Stevens ¶ AND N.N. Mansour

1. Motivation and objectives

Large-eddy simulation (LES) is a widely used technique in atmospheric modeling research, partly because of the difficulties involved in observational studies and field experiments to obtain information about the turbulent structure of the atmosphere (Stevens & Lenschow 2001). In LES, large, unsteady, three dimensional structures are resolved and small structures that are not resolved on the computational grid are modeled. A filtering operation is applied to distinguish between resolved and unresolved scales. Unresolved motions are believed to be universal, and simple models should be sufficient to parameterize them, provided that a major fraction of the energetic large scales are resolved by the spatial and temporal resolution (Sagaut 2002). However, this requirement becomes stringent to fulfill in the close proximity of the surface/wall. Traditionally, the no-slip boundary has been referred to as "wall" in engineering context, and as "surface" in atmospheric science context. We will use the latter terminology throughout the paper.

As the surface is approached anisotropy in turbulence structure increases and the length scale of the flow structures diminish rapidly, requiring too fine a spatial and a temporal resolution to numerically resolve a large fraction of the energetic scales. Hence, fully resolved LES of atmospheric or any other wall-bounded high Reynolds number flow would be extremely expensive in terms of computational resources. In fact, it is this obstacle that motivates surface/wall modeling research in LES. Furthermore, the roughness of the surface underlying the atmospheric boundary layer has always been a complicated issue, and needs to be considered in modeling too.

In surface modeling, no-slip boundary conditions are not applied directly because the implied stress would be overestimated on a coarse grid. The simplest surface model that has long been adopted in atmospheric boundary layer simulations assumes that the logarithmic law holds within the surface layer, and stresses are imposed as boundary conditions at the surface(Schumann 1975; Moeng 1986). Cabot, Jimenez & Baggett (1999) showed that such models have problems for high Reynolds number LES simulations with coarse numerical resolution. Cabot (1997) indicated that providing accurate mean surface stresses is not sufficient to overcome the overall poor predictions. He suggested that, given a coarse numerical resolution, typical subgrid-scale (SGS) models used in LES do not perform well to predict Reynolds stresses in the near-surface region accurately.

Boundary layer approximations have been proposed to extend the application of surface models for separating flows with adverse pressure gradient, (Balaras *et al.* 1996;

† NASA Ames Research Center
‡ University of Tasmania
¶ Lawrence Livermore National Laboratory

Cabot & Moin 2000). In this approach, a simplified set of turbulent boundary layer equations, adopting a Reynolds-averaged Navier-Stokes (RANS) type eddy viscosity, are solved on an embedded mesh near the wall. The surface stress is then calculated from the computed velocity profile. Within this framework, Wang & Moin (1992) utilized a dynamically adjusted mixing length eddy viscosity, and showed that their model performs significantly better than the simpler surface modeling approaches. Surface modeling for LES continues to be an active area of research for high Reynolds number flow, coarse resolution simulations. Latest research in this area focuses on incorporating suboptimal control theory to improve the predictive capability of the surface models (Templeton, Wang & Moin 2002).

In atmospheric boundary layer simulations, the practice has been to employ LES models away from the surface and make a transition towards ensemble-averaged (RANS) models as the surface is approached. This idea has been adopted through different formulations. For instance, Sullivan *et al.* (1994) proposed an eddy viscosity model in which the so-called isotropy factor controls the transition from LES to a RANS type simulation, and accounts for the anisotropy effects at the same time. Mason & Thomson (1992) introduced a modified length scale that is a matching between the LES filter size and the distance from the surface. Brown, Hobson & Wood (2001) suggested using a canopy model with the aim of overcoming the difficulties in surface modeling. Traditionally, canopy models have been adopted to study the effect of flow within the canopy layer. In this approach, instead of modifying the eddy viscosity or the length scale, additional turbulent stresses are added to the turbulent stresses that are already modeled by the LES SGS model. Chow & Street (2002) and Kirkpatrick *et al.* (2003) adopted the canopy model of Brown *et al.* (2001) for atmospheric boundary layer simulations, and reported improved predictions. We will refer to these models, in which additional stresses are added onto sugrid-scale models to improve the predictions in the vicinity of the surface, as "near-surface" models. We reserve the term "surface model" to include both the models for surface boundary condition and the near-surface models.

In what follows, we present two near-surface models that have found use in atmpspheric modeling. We also suggest a simpler eddy viscosity model that adopts Prandtl's mixing length model (Prandtl 1925) in the vicinity of the surface and blends in with the dynamic Smagorinsky model (Germano *et al.* 1991) away from the surface. We evaluate the performance of these surface model by simulating a neutrally stratified atmospheric boundary layer.

2. Governing equations

The governing equations for LES of a neutrally stratified atmospheric boundary layer are the filtered Navier-Stokes equations

$$\frac{\partial \bar{u}_i}{\partial x_i} = 0, \qquad \frac{\partial \bar{u}_i}{\partial t} + \frac{\partial (\bar{u}_i \bar{u}_j)}{\partial x_j} = \frac{\partial \bar{p}}{\partial x_i} + \epsilon_{ijk} f_j \bar{u}_k - \frac{\partial \tau_{ij}}{\partial x_j}, \tag{2.1}$$

where turbulent stresses are defined as $\tau_{ij} = \overline{u_i u_j} - \bar{u}_i \bar{u}_j$, f_j is the Coriolis parameter, ϵ_{ijk} is the permutation tensor, $\bar{u}$ and $\bar{p}$ are the filtered velocity and filtered dynamic pressure, respectively.

The lateral boundary conditions are periodic and a stress-free condition is imposed on the upper boundary. At the lower boundary, the vertical component of the velocity is set to zero and horizontal components of the turbulent stresses are defined based on the

mean logarithmic wind profile assumption as follows (Moeng 1984)

$$\tau_{i3} = -\left(\frac{\kappa}{\ln \frac{z_1}{z_o}}\right)^2 |u|\bar{u}_i, \tag{2.2}$$

where z_1, u_i and z_0 are the vertical spacing, the velocity of the first grid point away from the surface, and the roughness height, respectively. This type of boundary condition for the surface is a common practice in atmospheric modeling.

3. Subgrid-scale turbulence modeling

Turbulent stresses that appear in equation 2.1 are modeled based on the Boussinesq eddy viscosity assumption. The Smagorinsky eddy viscosity model (Smagorinsky 1963) is a popular approach to represent turbulent stresses

$$\tau_{ij} = -2Cl^2|\bar{S}|\bar{S}_{ij}, \tag{3.1}$$

where $|\bar{S}|$ is the magnitude of the filtered strain rate tensor, it is defined as

$$|\bar{S}| = \sqrt{2\bar{S}_{ij}\bar{S}_{ij}}, \qquad \bar{S}_{ij} = \frac{1}{2}\left(\frac{\partial \bar{u}_i}{\partial x_j} + \frac{\partial \bar{u}_j}{\partial x_i}\right). \tag{3.2}$$

In LES, the filter width $\Delta = (dx \cdot dy \cdot dz)^{1/3}$ is chosen as the length scale l in the eddy viscosity definition (equation 3.1). In the original Smagorinsky model, the dimensionless parameter C is an empirical constant, whereas in the dynamic Smagorinsky model (Germano *et al.* 1991), this parameter is computed dynamically during the solution, making it a function of space and time.

In the vicinity of the surface, the numerical resolution is generally limited and near-surface models are adopted to model the turbulent stresses properly. We consider three near-surface models, and provide a brief explanation of them in the following.

3.1. *Mason and Thomson Model*

This is an arbitrary and simple modification of the length scale in the eddy viscosity definition given by equation 3.1. Mason & Thomson (1992) have suggested using the following form as the length scale.

$$\frac{1}{l^2} = \frac{1}{\Delta^2} + \frac{1}{(\kappa z)^2} \tag{3.3}$$

where κ is the von Karman constant with a value of 0.41, and z is the distance from the surface.

3.2. *Canopy Stress Model*

Canopy models are usually adopted to model the structure of the flow within the canopy. Brown *et al.* (2001) have suggested using them as near-surface models in the case of coarse numerical resolution. In particular, we follow the implementation of Kirkpatrick *et al.* (2003). Canopy stresses near the surface are formulated as

$$\tau_{i3} = -\int_0^h C_s \cos\left(\frac{\pi z}{2h}\right) |u|u_i dz, \tag{3.4}$$

where C_s is a normalizing parameter. Specifically, C_s is the ratio of the surface stress at the bottom to the canopy stress at the first grid point. The canopy height h is taken to

be twice the streamwise grid spacing ($2dx$). Canopy stresses are added onto the turbulent stresses that are modeled with the dynamic Smagorinsky model.

3.3. *Hybrid RANS/LES model*

We adopt a hybrid RANS/LES approach as the third model. The motivation behind this model is that the surface stress boundary conditions represent ensemble-averaged quantities, because they are derived from the mean logarithmic wind profile. Hence, it is more meaningful to adopt a RANS type eddy viscosity formulation near the surface.

One can analytically show that the logarithmic wind profile can be derived from the following eddy viscosity definition (Panofsky & Dutton 1984)

$$\nu_t = \kappa u_* z, \tag{3.5}$$

where u_* is the friction velocity. The above form is also identical to the following definition

$$\nu_t = (\kappa z)^2 \frac{\partial U}{\partial z} = (\kappa z)^2 |S|. \tag{3.6}$$

Here, U is magnitude of the velocity vector. We apply the above definition in the vicinity of the surface, which guarantees a logarithmic wind profile, and switch to the dynamic Smagorinsky model away from the surface with the help of a blending function. This hybrid RANS/LES model can be written as

$$\nu_t = [(1 - \exp(-z/h))^2 \cdot (C\Delta^2) + \exp(-z/h)^2 (\kappa z)^2] |S| \tag{3.7}$$

Following the suggestion of van Driest (1956) an exponential form is selected as the blending function. Here h is the altitude, where the logarithmic wind profile is not expected further. As a rule of thump, a logarithmic velocity profile is expected within the surface layer, which is the bottom 10 percent of the atmospheric boundary layer height (100 m -200 m) (Stull 1988). $h = 150m$ is used for the present computations.

4. Numerical schemes

We use the LES atmospheric research code (DHARMA) for the present simulations. The numerical method adopted in DHARMA is described in detail in Stevens & Bretherton (1996) and Stevens *et al.* (2000). The governing equations are integrated using a forward-in-time projection method based on an explicit second-order Runge-Kutta scheme (Bell & Marcus 1992). The spatial discretization is performed on a staggered grid. A third-order accurate upwind-biased monotonic scheme is used for the advection terms, whereas diffusion and pressure gradient terms are discretized using second-order accurate central differencing schemes. A direct solver (FFT) is utilized for solving the pressure Poisson equation, and the code has been parallelized to run on various platforms using MPI.

5. Results

In this section, we present results from the simulation of neutrally stratified atmospheric boundary layer. The computational domain size is 3000 m $\times$ 1500 m $\times$ 1500 m with 64 $\times$ 32 $\times$ 64 grid points in x, y, and z directions, respectively. In the vertical direction, the grid points are clustered exponentially near the surface, where the first grid point for the horizontal component of the velocity is located at 4 m from the surface. The flow is driven by the Coriolis force that would balance a 10 ms^{-1} geostrophic

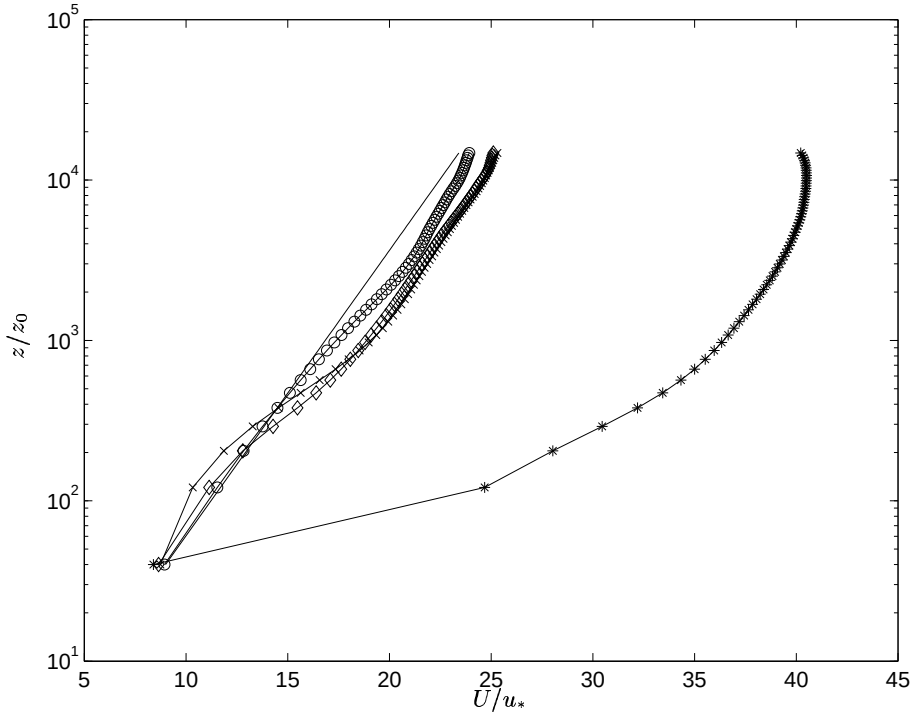

FIGURE 1. Comparison of mean wind profile. ——— : log-law, —∗— : no near-surface model, —○— : hybrid RANS/LES model, —◇— : canopy stress model, —×— : Mason-Thomson model

wind in the x direction. Coriolis parameter is set equal to $10^{-4}\ s^{-1}$, and the roughness parameter z_0 has a value of 0.1m. A dimensionless time unit can be defined based on the Coriolis parameter$(1/f)$. The simulations were run over a period of $10f^{-1}$, and statistics are collected during the time period of last the $4f^{-1}$. Ensemble averaged vertical profiles have been obtained by collecting data at every 6×10^{-3} dimensionless units $(60secs)$, and averaging them both in time and in horizontal space.

Andren *et al.* (1994) compared the performance of different LES computer codes to simulate a neutrally stratified atmospheric boundary layer. They concluded that results were more sensitive to the SGS model in the lower third of the boundary layer, and commonly used SGS models have failed to reproduce the logarithmic wind profile in the vicinity of the surface. Hence, satisfying the logarithmic wind profile near the surface has become one of the measures of good performance for an SGS model.

Figure 1 shows a comparison of the mean wind profiles for all the models considered in the present study. When no near-surface model is used, the dynamic Smagorinsky model produces an erroneous profile. This indicates that providing only the surface stress boundary condition is not sufficient to model the SGS motions near the surface in the case of high Reynolds number and coarse numerical resolution. This observation is in agreement with the findings of Cabot *et al.* (1999). It should be noted that the erroneous profile is not surprising because the essence of the dynamic Smagorinsky model is based on resolving the inertial subrange. This has not been satisfied with the current coarse

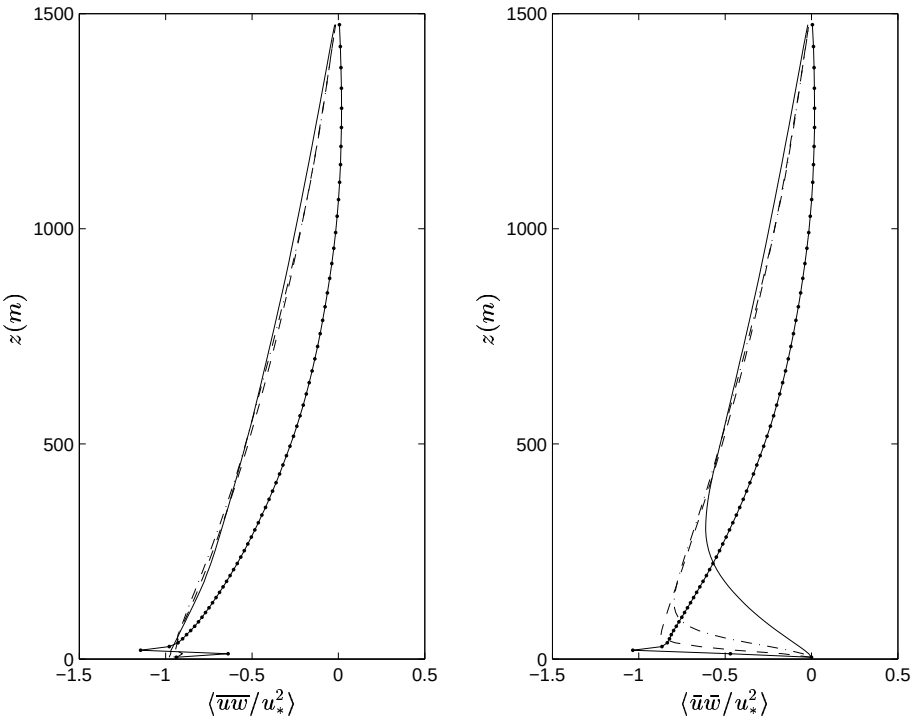

FIGURE 2. Comparison of streamwise component of the total (left) and resolved (right) stress. ··· : no near-surface model, ——— : hybrid RANS/LES model, — — — : canopy stress model, —·— : Mason-Thomson model

resolution. Hence, SGS models need augmentation to represent the unresolved scales near the surface.

The near-surface models considered in the present study, namely, Mason-Thomson model, the canopy stress model and the hybrid RANS/LES model are formulated to parameterize the unresolved scales near the surface. Both the canopy stress model and the hybrid RANS/LES model adopt the dynamic Smagorinsky model away from the surface, whereas the Mason-Thomson model adopts the original Smagorinsky model. As seen from figure 1, results obtained from these three near-surface models are much closer to the log-law profile. However, considerable differences exist among them. The best agreement with the log-law near the surface is achieved with the hybrid RANS/LES model, whereas the Mason and Thomson model gives the worst agreement. The hybrid RANS/LES model has the closest agreement, because the length scale is taken to be the distance from the surface in the model, which is known to give the log-law analytically. The canopy stress model follows the log-law close to the surface, but a significant deviation is observed further from the surface. This indicates that, canopy stresses should be distributed over a larger distance from the surface. We reiterate that, based on field experiments, a logarithmic velocity profile is expected in the surface layer, which is approximately the bottom 10 percent of the atmospheric boundary layer height (100 m -200 m).

The streamwise ($\langle \overline{uw}/u_*^2 \rangle$) component of the total and resolved turbulent stress profiles are compared in figure 2. By total stress, we mean the resolved turbulent stresses plus the modeled SGS turbulent stresses. As seen from this plot, simulations with surface models predict an almost linear variation of the total turbulent stress in agreement with surface

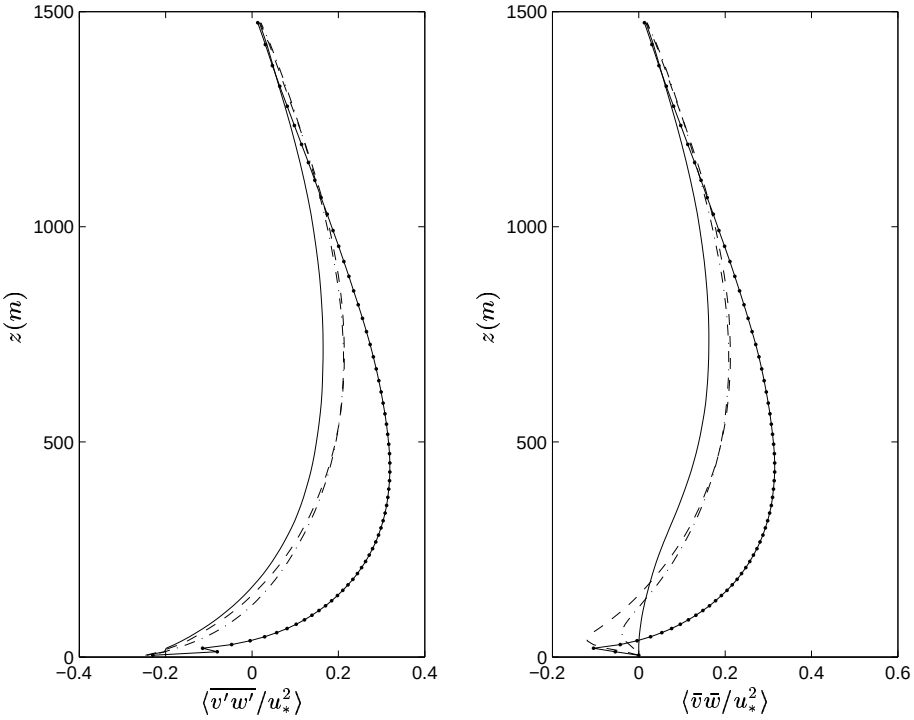

FIGURE 3. Comparison of spanwise component of the total (left) and resolved (right) stress. · · · : no near-surface model, ——— : hybrid RANS/LES model, — — — : canopy stress model, —·— : Mason-Thomson model

similarity theory (Garratt 1992). However, without a near-surface model, the dynamic Smagorinsky model does not predict a linear variation of the total turbulent stress and produces wiggles at the surface, indicating the need for near-surface modeling.

The resolved turbulent stresses are also shown in figure 2. Within the lower one fourth of the boundary layer, a large range of turbulent scales are modeled and not resolved with the hybrid RANS/LES model, whereas other surface models are effective only within the lower one tenth of the boundary layer. The extent of RANS modeling in the hybrid RANS/LES model is adjustable through the value of h in equation 3.7. We have found that $h = 150m$ is reasonable in terms of satisfying the logarithmic wind profile in accordance with experimental observations.

The differences among the three surface models are more pronounced in the spanwise ($\langle \overline{v'w'}/v_*^2 \rangle$) component of the total stress as shown in 3. This spanwise component of the total stress is generated due to the rotation of the Earth. The variation of the velocity vector with height is known as the Ekman spiral (Stull 1988).

As can be seen from figure 4, the spanwise component of the velocity is also affected because of differences in the distribution of the spanwise component of the total turbulent stress. With all three surface models, we see that the spanwise component of the velocity does not vanish at the top, whereas it vanishes in the case of the dynamic Smagorinsky model without a near-surface model. Apparently, nonvanishing spanwise velocity at the top is an outcome of employing the surface models. Since ensemble averaged quantities are obtained near the wall, fluctuations of the velocity field are damped due to the action of turbulent eddy viscosity or canopy stresses, effectively resulting in a laminar flow field.

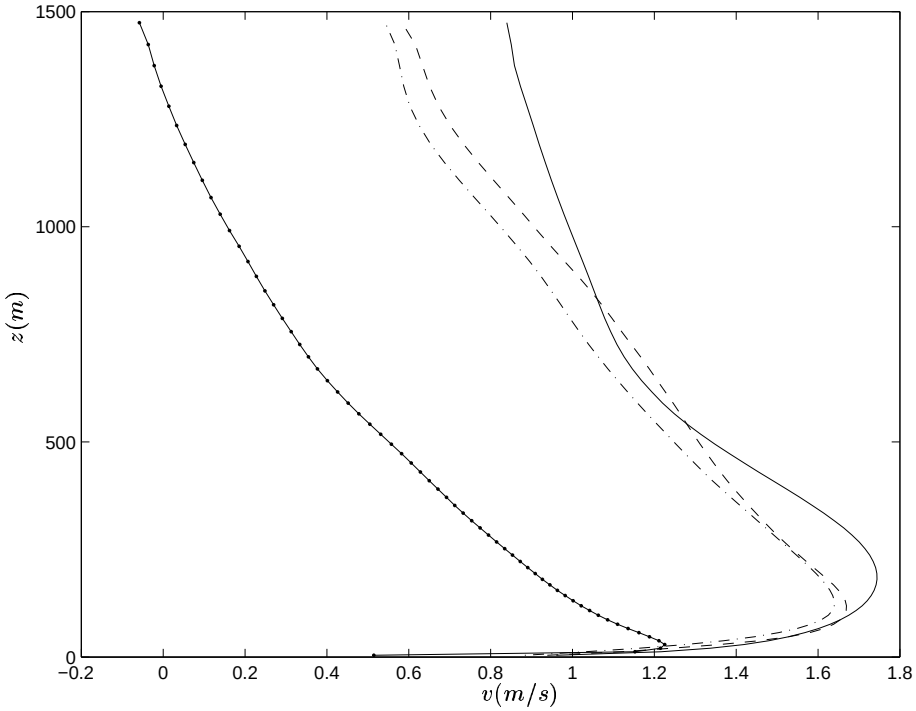

FIGURE 4. Comparison of spanwise component (v) of the velocity profiles. · · · : no near-surface model, ——— : hybrid RANS/LES model, — — — : canopy stress model, — · — : Mason-Thomson model

As a result, this ensemble averaged region acts like an artificial boundary layer for the flow field away from the surface that is modeled in the LES sense. Baggett (1998) have reported similar issues in LES of channel flow.

We present turbulent eddy viscosity profiles in figure 5. Away from the surface, identical profiles are obtained with the hybrid RANS/LES model and the canopy stress model. Near the surface, the eddy viscosity levels are much lower with the canopy stress model. This is because the model modifies the stress terms but not the eddy viscosity. On the other hand, eddy viscosity level is much higher near the surface with the hybrid RANS/LES model. With such high levels of eddy viscosity, turbulent motions near the surface are dampened, resulting in an ensemble averaged velocity field. Among all models, the Mason-Thomson predicts higher levels of eddy viscosity away from the surface, because it adopts the original Smagorinsky model in that region.

6. Summary and conclusions

In this study, we have performed large-eddy simulations of a neutrally stratified atmospheric boundary layer. Particularly, we have assessed the performance of different near-surface models in predicting the mean flow structure. The surface of our atmosphere is always rough and typical numerical resolutions that are utilized in atmospheric boundary layer modeling are too coarse near the surface to perform well-resolved large-eddy simulations. This necessitates additional modeling in the vicinity of the surface to take into account the unresolved turbulent flow, covering a large range of scales. We have

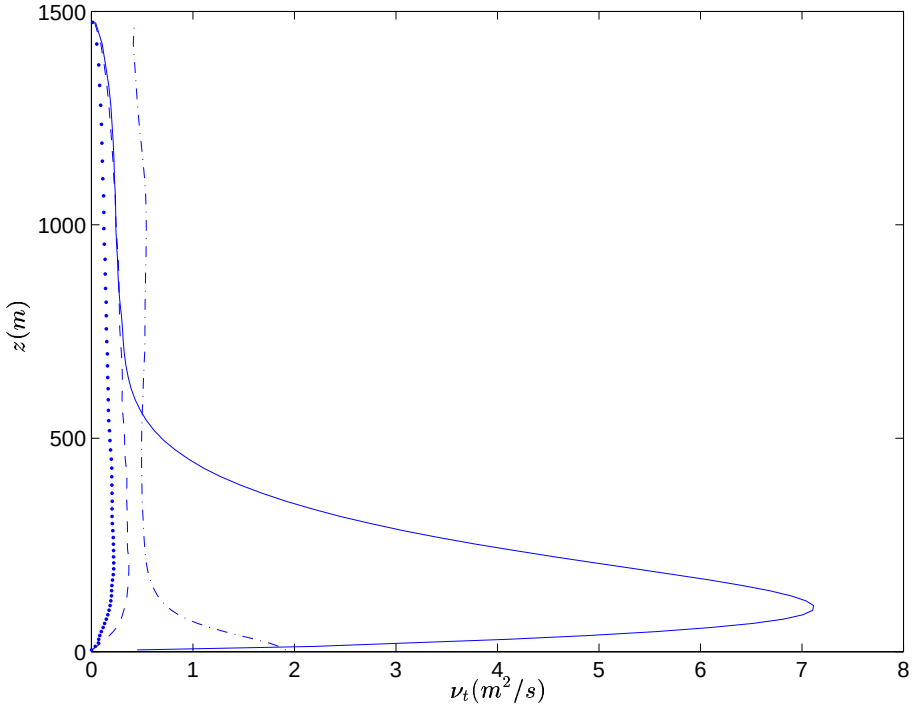

FIGURE 5. Comparison of turbulent eddy viscosity profiles. · · · : no near-surface model, ——— : hybrid RANS/LES model, — — — : canopy stress model, — · — : Mason-Thomson model

considered the near-surface models of Mason & Thomson (1992), Brown *et al.* (2001) and also suggested a hybrid RANS/LES model that blends Prandtl's mixing length model with the dynamic Smagorinsky model. We have also considered the dynamic Smagorinsky model with no near-surface model to highlight the need for surface modeling in the case of coarse numerical resolution.

Off all the near-surface models considered, the hybrid RANS/LES model shows better agreement with mean logarithmic wind profile. In the canopy stress model, it appears that surface stresses should be distributed to a larger distance from the surface to improve the predictions. The downside of adopting any of the near-surface models is that the spanwise component of the velocity vector does not vanish at the top of the computational domain. For the current numerical resolution with the hybrid RANS/LES model, the contribution from RANS modeling is effective on about the lower one fourth of the domain. A finer numerical resolution might help confine the RANS contribution very close to the surface and get better predictions at the same time.

Although comparable predictions can be obtained by either adopting the hybrid RANS/LES or the canopy stress model, the hybrid RANS/LES model has the advantage of easy implementation. In a parallel effort (Senocak *et al.* 2004), we are implementing the immersed boundary method in DHARMA. We find that it is much more convenient to implement the hybrid RANS/LES model to simulate flow over topography with the immersed boundary method because only the eddy viscosity term needs modification. However, it might not be straightforward to adopt the canopy stress model in Cartesian grid techniques for complex topography simulations.

REFERENCES

ANDREN, A., BROWN, A. R., GRAF, J., MASON, P. J., MOENG, C.-H., NIEUWSTADT, F. T. M. & SCHUMAN, U. 1994 Large-eddy simulation of a neutrally stratified boundary layer: A comparison of four computer codes. *Q. J. R. Meteorol. Soc.* **120**, 1457–1484.

BAGGETT, J. S. 1998 On the feasibility of merging LES with RANS for the near-wall region of attached turbulent flows. Annual Research Briefs, Center for Turbulence Research, NASA-Ames/Stanford Univ.

BALARAS, E., BENOCCI, C. & PIOMELLI, U. 1996 Two-layer approximate boundary conditions for large-eddy simulation. *AIAA J.* **34**, 1111–1119.

BELL, J. B. & MARCUS, D. L. 1992 A second-order projection method for variable-density flows. *J. Comp. Phys.* **101**, 334–348.

BROWN, A. R., HOBSON, J. M. & WOOD, N. 2001 Large-eddy simulation of neutral turbulent flow over rough sinusoidal ridges. *Boundary-Layer Meteorol.* **98**, 411–441.

CABOT, W. 1997 Wall models in large-eddy simulation of seperated flow. Annual Research Briefs, Center for Turbulence Research, NASA-Ames/Stanford Univ.

CABOT, W., JIMENEZ, J. & BAGGETT, J. S. 1999 On wakes and near-wall behavior in coarse large-eddy simulation of channel flow with wall models and second-order finite difference methods. Annual Research Briefs, Center for Turbulence Research, NASA-Ames/Stanford Univ.

CABOT, W. & MOIN, P. 2000 Approximate wall boundary conditions in the large-eddy simulation of high Reynolds number flow. *Flow, Turbul. Combust.* **63**, 269–291.

CHOW, F. K. & STREET, R. 2002 Modeling unresolved motions in LES of field-scale flows. In *15th Symposium on Boundary Layers and Turbulence*.

VAN DRIEST, E. R. 1956 On turbulent flow near a wall. *J. Aero. Sci.* **23**, 1007–1011.

GARRATT, J. R. 1992 *The Atmospheric Boundary Layer*. Cambridge University Press.

GERMANO, M., PIOMELLI, U., MOIN, P. & CABOT, W. H. 1991 A dynamic subgrid-scale eddy viscosity model. *Phys. Fluids* **3**, 1760–1765.

KIRKPATRICK, M. P., MANSOUR, N. N., ACKERMAN, A. S. & STEVENS, D. E. 2003 Dynamic turbulence modeling in large-eddy simulations of the cloud-topped atmospheric boundary layer. Annual Research Briefs, Center for Turbulence Research, NASA-Ames/Stanford Univ.

MASON, P. & THOMSON, D. 1992 Stochastic backscatter in large-eddy simulations of boundary layers. *J. Fluid Mech.* **242**, 51–78.

MOENG, C. H. 1984 A large-eddy simulation model for the study of planetary boundary-layer turbulence. *J. Atmos. Sci* **41**, 2052–2062.

MOENG, C. H. 1986 Large-eddy simulation of a stratus-topped boundary layer. Part-1: Structure and budgets. *J. Atmos. Sci* **43**, 2886–2900.

PANOFSKY, H. A. & DUTTON, J. A. 1984 *Atmospheric Turbulence*. John Wiley.

PRANDTL, L. 1925 Bericht uber die entstehung der turbulenz. *Z. Angew. Math. Mech.* **5**, 136–139.

SAGAUT, P. 2002 *Large Eddy Simulation for Incompressible Flows*. Springer-Verlag.

SCHUMANN, U. 1975 Subgrid-scale model for finite difference simulations of turbulent flows in plane channels and annuli. *J. Comp. Phys.* **18**, 376–404.

SENOCAK, I., ACKERMAN, A. S., STEVENS, D. E. & MANSOUR, N. N. 2004 Topogra-

phy modeling in atmospheric flows using the immersed boundary method. Annual Research Briefs, Center for Turbulence Research, NASA-Ames/Stanford Univ.

SMAGORINSKY, J. 1963 General circulation experiments with the primitive equations. I. The basic experiment. *Mon. Weather Rev.* **91**, 99–164.

STEVENS, B. & LENSCHOW, D. H. 2001 Observations, experiments, and large eddy simulation. *Bull. Amer. Meteor. Soc.* **82**, 283–294.

STEVENS, D. E., BELL, J. B., ALMGREN, A. S., BECKNER, V. E. & RENDLEMAN, C. A. 2000 Small-scale processes and entrainment in a stratocumulus marine boundary layer. *J. Atmos. Sci.* **57**, 567–581.

STEVENS, D. E. & BRETHERTON, C. S. 1996 A forward-in-time advection scheme and adaptive multilevel flow solver for nearly incompressible atmospheric flow. *J. Comp. Phys.* **129**, 284–295.

STULL, R. B. 1988 *An Introduction to Boundary Layer Meteorology*. Kluwer Academic Publishers.

SULLIVAN, P. P., MCWILLIAMS, J. C. & MOENG, C. H. 1994 A subgrid-scale model for large-eddy simulation of planetary boundary layer flows. *Boundary-Layer Meteorol.* **71**, 247–276.

TEMPLETON, J. A., WANG, M. & MOIN, P. 2002 Towards LES wall models using optimization techniques. Annual Research Briefs, Center for Turbulence Research, NASA-Ames/Stanford Univ.

WANG, M. & MOIN, P. 1992 Dynamic wall modeling for large-eddy simulation of complex turbulent flows. *Phys. Fluids* **14**, 2043–2051.

Velocity field decomposition in 3D numerical simulations of solar turbulent convection

By D. Georgobiani, N.N. Mansour, A.G. Kosovichev †, R.F. Stein ‡ AND Å. Nordlund ¶

1. Motivation and objectives

Recent achievements in helioseismic observations, in particular, ground-based GONG (Hill *et al.* 1994) and space mission SOHO/MDI (Scherrer *et al.* 1995), provide large amounts of data about the structure and dynamics of the Sun. These data impose observational constraints on numerical and analytical models of turbulent convection, differential rotation, large-scale circulation etc., therefore serving a purpose of testing and calibrating these models. In turn, these models are important for explaining the exciting helioseismic observations and predicting new effects. Therefore it is important to develop the most accurate and realistic models of solar convection and oscillations in order to obtain a clarified picture of the excitation of solar oscillations by turbulent convection and the interaction between turbulence and oscillations on the Sun. These models can be applied to other stars and provide predictions of properties of stellar oscillations, which are important for planned NASA asteroseismology space missions, or to the data from the Kepler mission (Borucki *et al.* 2003).

Realistic 3D numerical models represent a powerful tool for this investigation, because they do not suffer from simplifying assumptions and free parameters common for their analytical counterparts, yet they render the underlying physical picture of a phenomenon rather tractable. We pursue several goals while implementing numerical models. One of the aspects of our investigation is to use realistic simulations of the convective zone to better understand the interactions between mean flow fields, turbulence and acoustics.

Three-dimensional time dependent simulations of solar convection are becoming increasingly more realistic. Simulations of the shallow upper layer of the solar convection zone by Stein & Nordlund (cf Stein & Nordlund (2000) and references therein) demonstrate excellent agreement with existing analytical theories and observations. For instance, there is a remarkable correspondence between the simulated and observed profiles of weak and intermediate strength photospheric FeI and FeII lines (Asplund *et al.* 2000a, Asplund *et al.* 2000b); also, comparison of oscillation spectra in the simulated and solar data from SOHO/MDI by Georgobiani *et al.* (2004), as well as the rates of stochastic energy input to the low-degree solar modes in the simulations and GOLF observations (Roca Cortes *et al.* 1999) show a good agreement (see Stein & Nordlund (2001), Fig 7).

The goal of this paper is to develop a technique for decomposing the simulated turbulent velocity field into its potential and rotational components. According to the fundamental theorem of vector analysis, any well-behaved vector field has a unique representa-

† Hansen Experimental Physics Laboratory, Stanford University, Stanford, CA 94305, USA
‡ Department of Physics and Astronomy, Michigan State University, Lansing, MI 48824, USA
¶ Niels Bohr Institute for Astronomy, Physics and Geophysics, Juliane Maries Vej 30, DK–2100 Copenhagen, Denmark

tion, to within constant vectors, as a sum of a potential field and a solenoidal (rotational) field,

$$\vec{V} = \vec{V}_P + \vec{V}_R, \tag{1.1}$$

where

$$\vec{V}_P = \nabla\phi, \qquad \vec{V}_R = \nabla \times \vec{\psi}. \tag{1.2}$$

For these fields, the following relations hold by definition:

$$\nabla \times \vec{V}_P = 0, \qquad \nabla \cdot \vec{V}_P = \nabla \cdot \vec{V}; \qquad \nabla \cdot \vec{V}_R = 0, \qquad \nabla \times \vec{V}_R = \nabla \times \vec{V}. \tag{1.3}$$

Roughly speaking, all sources and sinks of a given field $\vec{V}$ are collected in $\vec{V}_P$, whereas all its vortices appear in $\vec{V}_R$. This formalism, also called the Helmholtz-Hodge decomposition, is widely used in computational fluid dynamics, because it helps to better visualize complex flows, to recognize their important features, to describe vector fields and study their topology; but it has never been applied before to the 3D numerical simulations of solar convection.

We use flow fields from the 3D hydrodynamic code by Stein & Nordlund for our example of separation of the mean field into the rotational and potential components (see Nordlund & Stein (1990), Stein & Nordlund (2000) and references therein).

2. Vorticity and divergence

In an attempt to decouple turbulent and acoustic components, we look at two characteristics of the mean velocity field - its vorticity and divergence - in the data obtained with the numerical simulations of Stein & Nordlund. Vorticity $|\vec{\omega}| = |\nabla \times \vec{u}|$ is concentrated primarily in strong, fast, turbulent downdrafts, formed in intergranular lanes, whereas flow divergence $d = \nabla \cdot \vec{u}$ is predominantly concentrated in smooth, slow, laminar upflows.

Recent theories, supported by observations, suggest that excitation of solar oscillations originates in the intergranular lines where turbulent motions are particularly strong. As a first step towards a separation of the acoustic signal from turbulence, we look at the temporal power spectra of simulated horizontally averaged vertical velocity u_z, divergence d and enstrophy $|\omega^2|$ signals (Fig 1). The divergence signal shows prominent resonant acoustic modes. It is very similar to the vertical velocity spectrum, but somewhat flatter at higher frequencies. Enstrophy contains mostly background stochastic component, with no resonant modes, except for the first mode peak. This suggests some nonlinear coupling between the divergence and vorticity signals at a particular frequency.

3. Velocity field decomposition

Without loss of generality, we can split the mean velocity field into a potential and rotational components:

$$u_i = \epsilon_{ijk}\psi_{k,j} + \phi_{,i} = u_i^R + u_i^P \tag{3.1}$$

We take divergence of the above, getting:

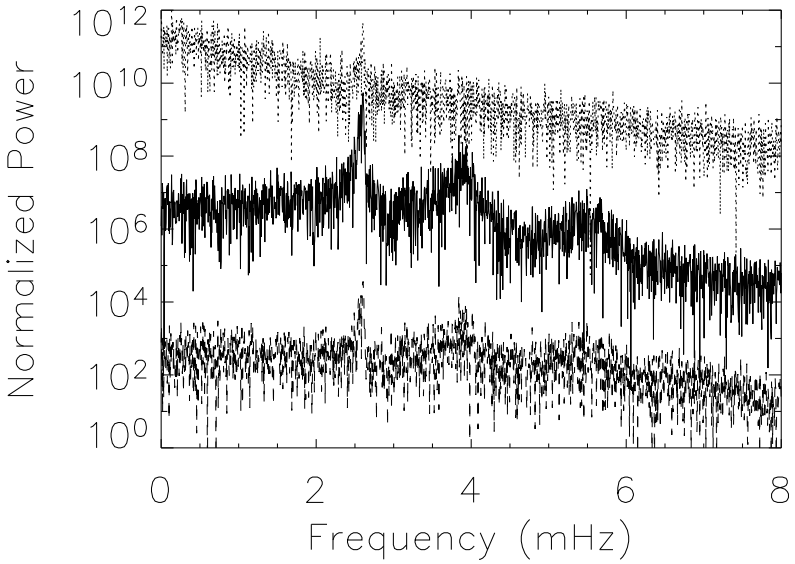

FIGURE 1. Normalized power spectra of radial modes in velocity (solid line), its divergence (dashed line) and enstrophy (dotted line), scaled arbitrarily to facilitate feature recognition. Divergence profile is similar to velocity, although it is flatter at higher frequencies. Enstrophy shows mostly the background noise, with weak first mode.

$$\phi_{,ii} = u_{i,i} = u^P_{i,i} \tag{3.2}$$

and then solve the resulting Poisson equation to obtain the potential velocity component. Then, the rotational component is calculated as a difference between the total velocity and its potential component.

We apply this decomposition to the simulated velocity field. Examples of the potential and rotational components of the flow field are shown as vertical slices through the simulation domain in Fig 2 and as horizontal slices in Fig 3. The total and the rotational velocity slices closely resemble each other visually, therefore we do not present the total velocity pictures. From this, one can conclude that the rotational velocity component is dominant, whereas the potential component is rather weak and featureless. This conclusion is reinforced by the comparison of spatial energy spectra of the three velocity components (Fig 4): the energy content is much lower in the potential velocity component, and it peaks at lower spatial wavenumber (larger characteristic spatial scale) than the vortical (or total) velocity with its dominant sharp small-scale turbulent features. We study different aspects of the velocity decomposition, for instance, temporal power spectra of different components. Our results show that the potential velocity component displays prominent acoustic modes, whereas the rotational component mostly contributes to the characteristic slope of the background noise, with no mode signal (Fig 5). In the last picture, we plot nonradial power spectra, because the horizontally averaged (radial) rotational velocity component is zero.

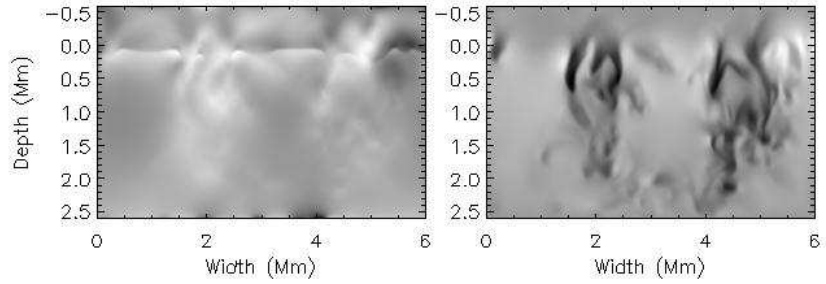

FIGURE 2. Vertical slices of the potential velocity (left panel) and the rotational velocity (right panel) at a fixed arbitrary horizontal coordinate. Potential component looks structureless, while rotational component, similarly to the total velocity, shows strong turbulent downdrafts. The magnitudes change from smallest (light) to largest (dark).

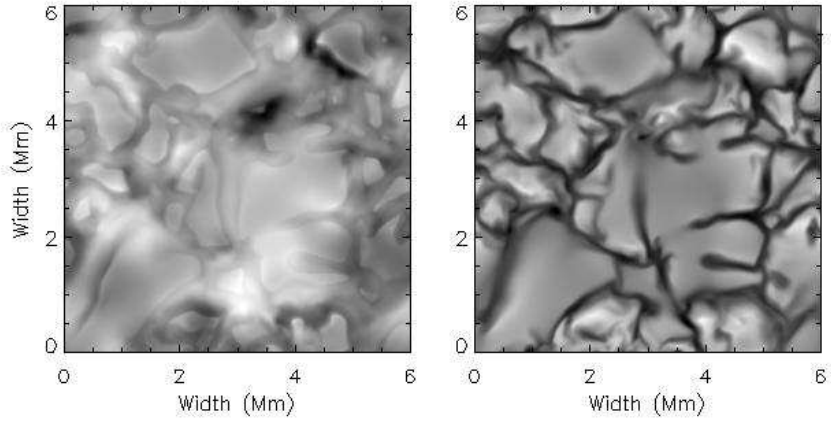

FIGURE 3. Horizontal slices of the potential velocity (left panel) and the rotational velocity (right panel) at the visible surface. There are no sharp features in the potential component, while the rotational component, like the total velocity, exhibits sharp intergranular turbulent features. Black is for largest, white is for smallest magnitudes.

4. Summary and future plans

We have simulated the turbulent velocity field of solar convection using Stein & Nordlund 3D code, and decomposed it into a potential and a rotational component. We have analyzed spatial and temporal spectra of these components. We have found that the kinetic energy content is higher in the rotational velocity component, and that the potential component can be treated as a small perturbation of the total flow field, in agreement with earlier findings (cf Nordlund & Stein 2001). The temporal power spectrum of the potential component shows distinct acoustic mode peaks, while the rotational component spectrum primarily consists of convective background noise, dominating at very low frequencies and quickly decaying at higher frequencies. This suggests that in the potential component, the power is concentrated in the acoustic resonant modes trapped in

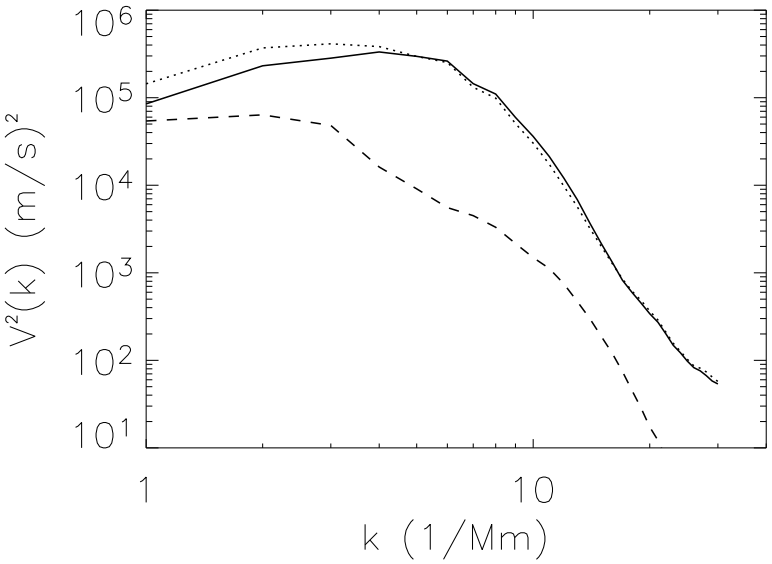

FIGURE 4. Spatial spectra of the total velocity squared (solid line) and its potential (dashed line) and rotational (dotted line) components. The energy content is much lower in the potential component, and its characteristic spatial scales are larger than for the rotational or total velocities.

the upper convection zone. We continue investigating the relationship between acoustics and turbulence in the simulated velocity fields, trying to address the problem of energy equipartition between turbulence and oscillations, and to understand the mechanism of generation of acoustic waves by stellar turbulence.

REFERENCES

ASPLUND, M., NORDLUND, Å., TRAMPEDACH, R., ALLENDE PRIETO, C. & STEIN, R. F. 2000a Line formation in solar granulation. I. Fe line shapes, shifts and asymmetries. *Astronomy & Astrophysics*, **359**, 729

ASPLUND, M., LUDWIG, H.-G., NORDLUND, Å., & STEIN, R. F. 2000b The effects of numerical resolution on hydrodynamical surface convection simulations and spectral line formation. *Astronomy & Astrophysics*, **359**, 669

BORUCKI, W. J., KOCH, D., BASRI, G., BROWN, T., CALDWELL, D., DEVORE, E., DUNHAM, E., GAUTIER, T., GEARY, J., GILLILAND, R., GOULD, A., HOWELL, S. & JENKINS, J. 2003 Kepler mission: a mission to find Earth-size planets in the habitable zone. *Proceedings of the conference on Towards other Earths: DARWIN/TPF and the search for extrasolar terrestrial planets, 22-25 April 2003, Heidelberg, Germany*

GEORGOBIANI, D., STEIN, R. F., NORDLUND, Å., KOSOVICHEV, A. G., & MANSOUR, N. N. 2004 High degree solar oscillations in 3D numerical simulations. *Proceedings of the SOHO14/GONG 2004 workshop "Helio- and asteroseismology: towards a golden future" from July 12-16 2004 at New Haven CT (USA)*

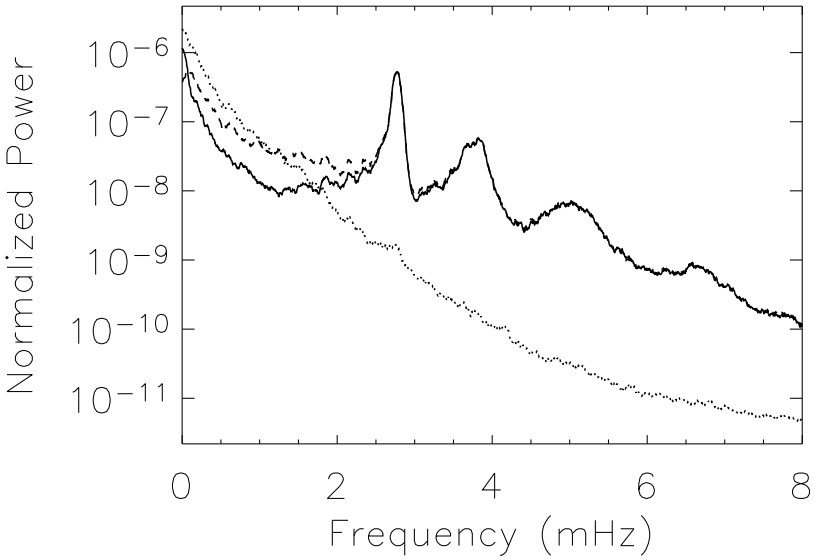

FIGURE 5. Non-radial power spectra of different velocity components. Total (solid line) and potential (dashed line) velocity show the oscillation mode peaks; they are very similar, except at low frequencies. Rotational (dotted line) velocity signal represents the background convective noise. The curves are smoothed over $\Delta\nu = 0.1$ mHz.

HILL, F., FISCHER, G., GRIER, J., LEIBACHER, J. W., JONES, H. B., JONES, P. P., KUPKE, R. & STEBBINS, R. T. 1994 The Global Oscillation Network Group site survey. 1: Data collection and analysis methods. *Solar Physics*, **152**, 321

NORDLUND, Å. & STEIN, R. F. 1990 3-D simulations of solar and stellar convection and magnetoconvection. *Computer Physics Communications*, **59**, 119

NORDLUND, Å. & STEIN, R. F. 2001 Solar oscillations and convection. I. Formalism for radial oscillations. *Astrophysical Journal*, **546**, 576

ROCA CORTES, T., MONTANES, P., PALLE, P. L., PEREZ HERNANDEZ, F., JIMENEZ, A., REGULO, C., & THE GOLF TEAM 1999 Low l solar p-mode oscillations parameters and convection. *ASP Conf. Ser. 173: Stellar structure: theory and test of convective energy transport*, 305

SCHERRER, P. H., BOGART, R. S., BUSH, R. I., HOEKSEMA, J. T., KOSOVICHEV, A. G., SCHOU, J., ROSENBERG, W., SPRINGER, L., TARBELL, T. D., TITLE, A., WOLFSON, C. J., ZAYER, I. & MDI ENGINEERING TEAM 1995 The Solar Oscillations Investigation - Michelson Doppler Imager. *Solar Physics*, **162**, 129

STEIN, R. F. & NORDLUND, Å. 2000 Realistic solar convection simulations. *Solar Physics*, **192**, 91

STEIN, R. F. & NORDLUND, Å. 2001 Solar oscillations and convection. II. Excitation of radial oscillations. *Astrophysical Journal*, **546**, 585

High degree oscillations in 3D numerical simulations of solar convection

By D. Georgobiani, R.F. Stein †, Å. Nordlund ‡, A.G. Kosovichev ¶
AND N.N. Mansour

1. Motivation and objectives

High-degree acoustic modes probe shallow solar layers, where convection drives oscillations. We study these oscillations by means of the three-dimensional hydrodynamic code of Nordlund & Stein (1990). The code simulates a small part of the solar convection zone, and is therefore suitable for studies of high degree modes. In our previous work Georgobiani *et al.* (2000), we looked at the modes with angular degree $\ell = 740$. However, these modes in the Sun are reflected at 9-10 Mm beneath the surface, but the simulated domain was too shallow to include their lower turning points. As a result, the mode frequencies did not match the observed ones, although the velocity amplitudes were quite similar.

In this work, we study modes of higher degree, $\ell = 1480$. These modes have their lower turning points around 3 Mm, and therefore their eigenfunctions fit inside the simulated box. We compare these modes with the observed oscillations of the same angular degree. We find a good match in their power spectra, except for the noise level at very low frequencies. Frequencies, amplitudes and widths of the modes match rather well. Similarity of mode line asymmetries and widths in observations and simulations suggests that mode excitation and damping mechanisms are correctly captured in the simulations.

We also compare spectra of full-disk and high-resolution solar observations, trying to establish a link between power spectral densities in observational data sets of different spatial resolution, in order to facilitate their comparison with the simulated data.

This work is organized as follows: Section 2 describes the simulation code; Section 3 presents the two sets of the SOHO/MDI data analyzed in our work; Section 4 outlines the procedure for calculating the power spectra; Section 5 is devoted to the results, followed by a discussion and a description of our future plans.

2. Numerical model

To simulate a small region of the upper solar convection zone, we use the 3D radiative–hydrodynamic (RHD) code by Stein and Nordlund (for a detailed description, see Stein & Nordlund (2000) and references therein). The code solves a complete system of hydrodynamic equations. It has a detailed radiative transfer treatment, thus properly represents both convection and radiation in the upper convection zone and the photosphere. The detailed radiative model in the code is very important for studies of solar oscillations. The computational domain is 3 Mm deep, starting from near the temperature minimum

† Department of Physics and Astronomy, Michigan State University, Lansing, MI 48824, USA
‡ Niels Bohr Institute for Astronomy, Physics and Geophysics, Juliane Maries Vej 30, DK–2100 Copenhagen, Denmark
¶ Hansen Experimental Physics Laboratory, Stanford University, Stanford, CA 94305, USA

at 0.5 Mm above the $\tau = 1$ surface, and extending to 2.5 Mm beneath it. The horizontal area of the domain is 6 Mm × 6 Mm. The horizontal resolution is 100 km, while the vertical one varies from 35 to 70 km, depending on the height (superadiabatic region is resolved better than the convective zone). The number of mesh points was 63 × 63 × 63. Three-dimensional snapshots of several physical properties (velocity, temperature, density, internal energy) are recorded every 30 seconds, and the total simulation sequence spans 72 hours of solar time.

To compare our results with SOHO/MDI observations, for each time step we extract 2D horizontal planes of the vertical velocity component at approximately 200 km above the visible surface ($\tau = 1$). This level approximately corresponds to the height of the NiI 6768 line formation, in which the observations are taken.

3. Observed velocity data

The SOHO/MDI Doppler velocity data used for comparison are simultaneous high-resolution (0.6 arcsec/pixel) and full-disk (2 arcsec/pixel) images taken on June 14 - 16, 1997. The high-resolution sub-region of 62.5 Mm × 62.5 Mm (128 × 128 pixels) was tracked with solar rotation for 2.5 days. The full-disk data spans 3 days. In both data sets, the time interval between the images is 1 minute. The high-resolution data represent a patch of the solar surface, therefore, after removing the solar rotation, we can apply the same spectral analysis as the one we use for the simulated velocity data. The full-disk data underwent spatial filtering in terms of spherical harmonic transform, and are available for different values of angular degree ℓ, from 0 to 1000, and corresponding azimuthal orders $m = -\ell, ..., \ell$. We used these data for $\ell = 740$, to compare with the high-resolution data, and also for $\ell = 370$, to see how the oscillation power might scale with angular degree.

4. Power spectra calculations

To calculate the velocity power spectrum for the simulated data, we perform spatial filtering using harmonic functions of horizontal coordinates on the 2D surfaces of vertical velocity at each time step, take Fourier transform in time and multiply by its conjugate. The horizontal spatial filtering allows us to extract modes corresponding to a given angular degree. Horizontal averaging extracts radial modes, while filtering with spatial sines and cosines of different horizontal wavenumbers gives non-radial modes. For waves with horizontal wavelength $L = 6$ Mm (the box size), the horizontal wavenumber is $k_h = 2\pi/L \simeq 1$ Mm^{-1}, and their angular degree is $\ell \simeq k_h R \simeq 740$, where R is the solar radius; for waves with $L = 3$ Mm (half the box size), $k_h \simeq 2$ Mm^{-1}, and $\ell \simeq 1480$ (for more details, see Georgobiani *et al.* (2000)). These are the modes we are especially interested in, because we expect them to be captured within the simulated domain.

In non-radial cases, we get the spectra for four spatial filters (sine and cosine in x and y direction), and then perform summation over these spectra. We remove the solar rotation trend from the high-resolution SOHO/MDI data and perform similar spectral analysis. For the full-disk data, we also remove the effect of solar differential rotation for different m by imposing frequency shifts according to the solar rotation law, and then sum over $m = 2\ell + 1$ resulting spectra. In addition, we multiply all power spectra by the relevant time duration in seconds. This arises from the definition of a temporal Fourier transform; the result represents so called power spectral density, and it takes care of

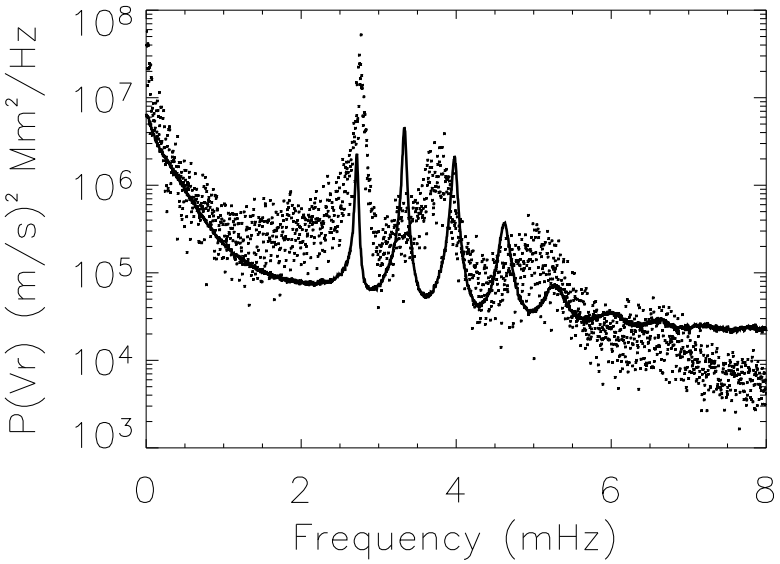

FIGURE 1. Power spectral density of vertical velocity in simulations (dots) and Doppler velocity in full disk observations (solid line) for angular degree $\ell = 740$.

different time duration and cadence between various data. We call the resulting power spectral densities, "power spectra", for brevity. The power spectra are also multiplied by an area over which the velocity measurements take place; this comes from the definition of a spatial Fourier transform. The result represents the oscillation power in this area.

5. Results

We start by reproducing the results of our earlier work (Georgobiani *et al.* (2000)). Figure 1 shows two power spectra of $\ell = 740$ modes, from simulations and the full-disk observations. One can see that the observed and simulated modes have similar amplitudes, but different mode structure, frequencies and mode widths. Also, the simulated power falls off more rapidly at high frequencies than the observed one.

Next, we compare the simulated power spectra with the high-resolution SOHO/MDI data. The results of comparison between the simulated and observed power spectra for $\ell = 740$ are presented in Fig 2, and for $\ell = 1480$ in Fig 3. Fig 2 is reminiscent of our earlier results (Fig 1). Fig 3, for $\ell = 1480$, shows remarkable similarity between simulations and observations in mode frequencies, amplitudes and widths, except for differences in the background noise level at low frequencies, away from modal structure. It is worth mentioning that the leftmost peak in all figures corresponds to the surface gravity (f) mode, while the others correspond to acoustic (p) modes. Frequencies of f-modes are independent of the depth of a resonant cavity, this is why even for $\ell = 740$ the f-mode peaks have the same frequency in simulations and observations. We sum over four individual spectra, because all of them contribute to the total power. In the full-disk data, we also need to sum over all m spectra when calculating the total power.

In Fig 4, we compare the two sets of our observational data, namely, high-resolution

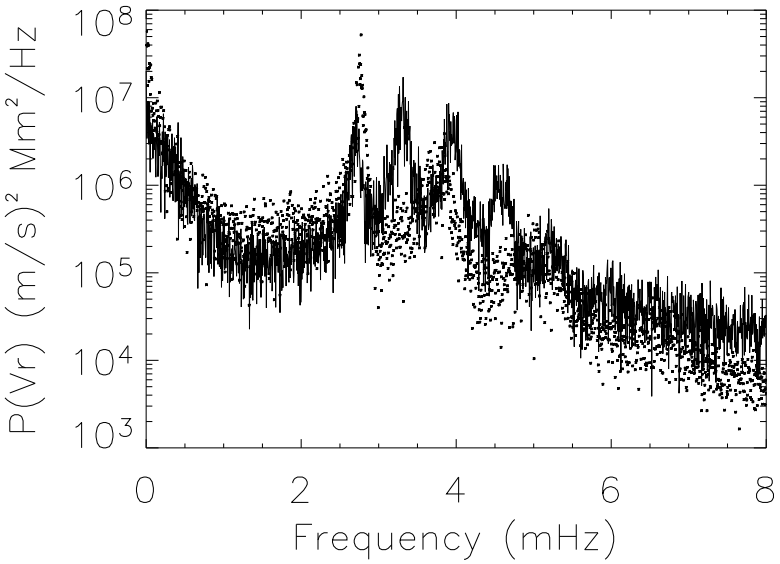

FIGURE 2. Power spectral density of vertical velocity in simulations (dots) and Doppler velocity in high-resolution observations (solid line) for angular degree $\ell = 740$. Amplitudes are similar, but frequencies and mode widths differ.

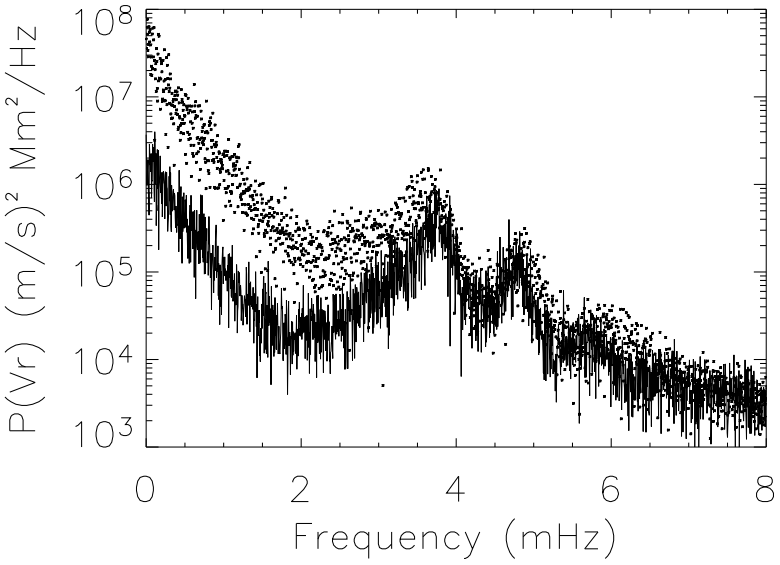

FIGURE 3. Power spectral density of vertical velocity in simulations (dots) and Doppler velocity in high-resolution observations (solid line) for angular degree $\ell = 1480$. There is a good correspondence between the two spectra, except at low frequencies.

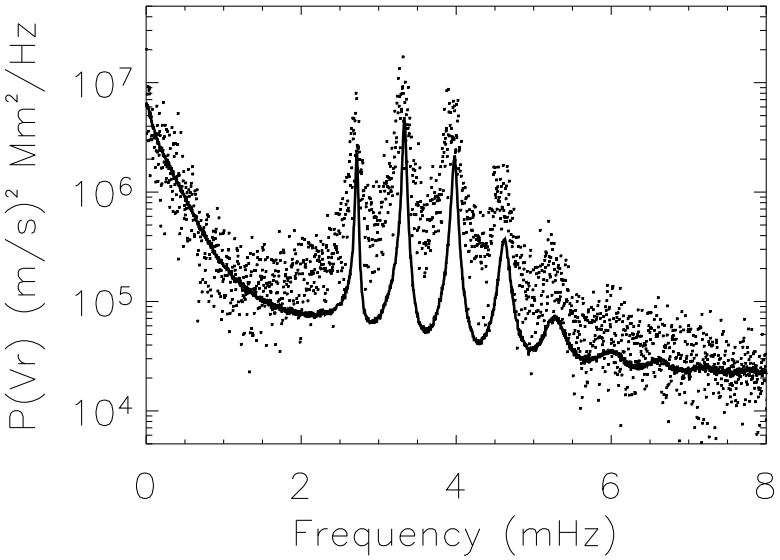

FIGURE 4. Power spectral density of Doppler velocity in the full-disk (solid line) and high-resolution (dots) observations for $\ell = 740$. Background and mode amplitudes are lower in the full-disk data, possibly because of the broad modulation of the high-resolution spectrum by leaking modes of various ℓ.

and full-disk measurements, for $\ell = 740$ (remember that we do not have $\ell = 1480$ full-disk data because of insufficient resolution of the full-disk MDI images). We perform similar comparison for $\ell = 370$ in Fig 5. The overall amplitudes of these spectra match rather well. The high-resolution spectra are much noisier than the full-disk spectra, because there are only four individual spectra to sum over, comparing to the superposition of $2\ell + 1 = 1481$ spectra in the full-disk data (cf also Fig 1). Averaging many spectra for individual m significantly decreases the noise level.

Finally, in Fig 6, we compare the two sets of full-disk spectra for $\ell = 370$ and 740. In this case, the background level became similar after the power spectra were multiplied by the inverse squared wavelength of the modes. Note that regardless of scaling, the mode amplitudes with respect to the background are somewhat smaller for larger ℓ.

6. Discussion

We find that for fully captured modes where the lower turning point is located inside the simulation domain, the simulated and observed vertical velocity power spectra are very similar, with similar amplitudes and line widths. Solar acoustic mode amplitudes are directly proportional to the excitation rate and inversely proportional to the mode damping rate. It has been shown by Stein & Nordlund (2001) that the simulated excitation rates are similar to the observed rates. The close match of the simulated and observed amplitudes, and especially mode line widths, suggests that the mode damping rates are also modeled properly by our simulation code, thus one can study the damping effects using the simulation data.

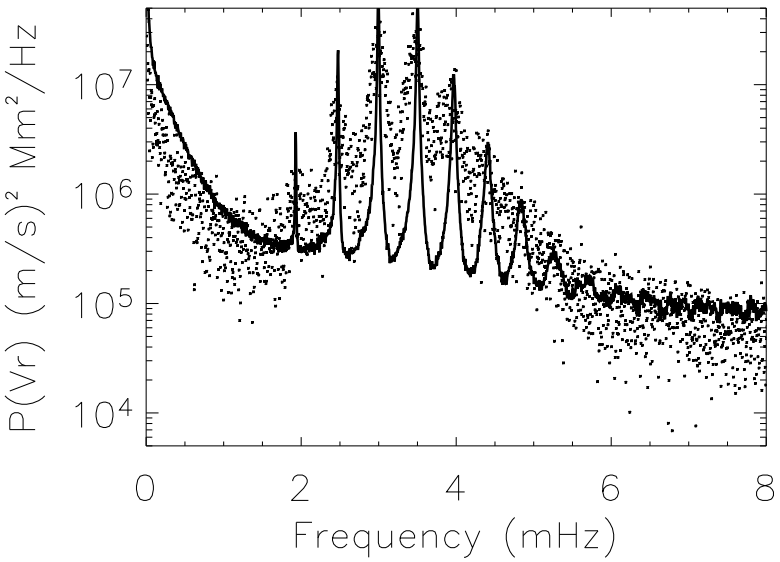

FIGURE 5. Power spectral density of Doppler velocity in the full-disk (solid line) and high-resolution (dots) observations for $\ell = 370$.

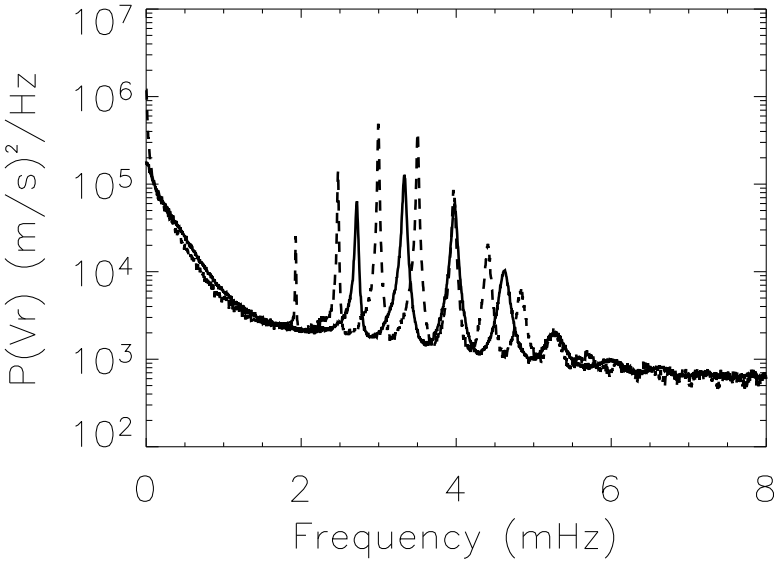

FIGURE 6. Power spectral density of Doppler velocity in the full-disk observations for $\ell = 740$ (solid line) and $\ell = 370$ (dashed line), normalized by oscillation area (6×6 and 12×12 Mm^2, respectively). Backgrounds are similar, while mode amplitudes are lower for higher ℓ.

Comparing the observed power spectra from high-resolution and full-disk data (Figs 4 and 5), we notice a broad overall peak in the high-resolution data (the mode peaks seem to be raised above the background), which is absent in the full-disk spectrum. The high-resolution spectrum calculated for a small area contains all the modes from radial to high degree, and the broad peak results from a superposition of all these modes. Apparently, the spherical transform method singles out individual ℓ modes better, although some inevitable leakage of neighboring modes is always present. In the simulation box, the horizontal boundaries are periodic, and thus the modes are far more discrete than in the patch of the real Sun.

Scaling of the power spectra of the full-disk data at different ℓ (Fig 6) with the square of the corresponding wavelength and resulting similarity between their backgrounds suggests that the background noise amplitudes (but not necessarily the mode amplitudes) of different ℓ scale with the area occupied by oscillations of a particular degree.

7. Future plans

We have compared the simulated and observed vertical velocity power spectral densities for solar oscillations of different angular degrees. We have found that there is a very good agreement between the oscillation frequencies and mode line widths when the mode radial eigenfunctions are completely contained in the simulation domain. These results, together with earlier findings about the similarity between the observed and simulated mode excitation rates, enable us to study excitation and damping mechanisms in more details. We have shown that the oscillation amplitudes in the observed and simulated data can be compared directly. In the future, similar simulations will be used to predict oscillation amplitudes and lifetimes for other stars.

Also, we have found that the power spectra for modes of different angular degree within the same data sets scale with the inverse square of their characteristic horizontal wavelength. This result is particularly prominent for the full disk solar data. It also holds for the low frequency part of the simulated power spectra, while the high-resolution power spectra do not show a clear scaling. We plan to investigate the cause of this relation between the spectra of different angular degree.

REFERENCES

GEORGOBIANI, D., KOSOVICHEV, A. G., NIGAM, R., NORDLUND, Å., & STEIN, R. F. 2000 Numerical Simulations of Oscillation Modes of the Solar Convection Zone. *Astrophysical Journal*, **530**, L139

NORDLUND, Å. & STEIN, R. F. 1990 3-D Simulations of Solar and Stellar Convection and Magnetoconvection. *Computer Physics Communications*, **59**, 119

STEIN, R. F. & NORDLUND, Å. 2000 Realistic Solar Convection Simulations. *Solar Physics*, **192**, 91

STEIN, R. F. & NORDLUND, Å. 2001 Solar Oscillations and Convection. II. Excitation of Radial Oscillations. *Astrophysical Journal*, **546**, 585

Thermal diffusivity in the SGS modeling for solar convection simulations using the ASH code

By Y.-N. Young†, M. Miesch‡ and N. N. Mansour

1. Motivation and objectives

The turbulent solar convection zone has remained one of the most challenging and important subjects in physics. Understanding the complex dynamics in the solar convection zone is crucial for gaining insight into the solar dynamo problem. Many solar observatories have generated revealing data with great details of large scale motions in the solar convection zone. For example, a strong differential rotation is observed: the angular rotation is observed to be faster at the equator than near the poles not only near the solar surface, but also deep in the convection zone. On the other hand, due to the wide range of dynamical scales of turbulence in the solar convection zone, both theory and simulation have limited success. Thus, cutting edge solar models and numerical simulations of the solar convection zone have focused more narrowly on a few key features of the solar convection zone, such as the time-averaged differential rotation. For example, Brun & Toomre (2002) report computational finding of differential rotation in an anelastic model for solar convection. A critical shortcoming in this model is that the viscous dissipation is based on application of mixing length theory to stellar dynamics with some *ad hoc* parameter tuning.

We have implemented the Smagorinsky-Lilly subgrid scale model into the ASH (anelastic spherical harmonic) code. In this report we illustrate how this subgrid scale model works in terms of recovering differential rotation in the solar convection zone. In particular we elucidate the role of thermal diffusivity in solar convection, where the molecular thermal diffusivity is much larger than the molecular viscosity. Readers are referred to (Clune *et al.* 1999) and (Miesch 1998) for a detailed description of the ASH code. This paper is organized as follows. In §2 we briefly formulate the anelastic system that describes the solar convection. We also formulate the Smagorinsky-Lilly SGS model for unstably stratified solar convection. In §3 we present some data diagnosis, such as the energy balance and angular momentum balance in the simulations. Also in §3 we illustrate by example how the thermal diffusivity can play an important role in terms of the differential rotation in the solar convection zone, and we will also provide some conclusions and future directions.

2. The anelastic equations of motions and the Smagorinsky-Lilly SGS model

2.1. *Anelastic equations*

In the solar convection zone, the depth extends over many density scale heights and thus the effects of stratification need to be captured despite the fact that acoustic timescales are much shorter than the large-scale convection timescales. An appropriate approach is

† Dept. of Mathematical Sciences, NJIT, Newark, NJ, 07102
‡ High Altitude Observatory, National Center for Atmospheric Research, Boulder, Colorado, 80301

to filter out sound waves while maintaining the density stratification, namely the anelastic approximation first proposed by Gough (1969) and later adapted to the solar convection zone by Gilman & Glatzmaier (1981). In stellar models, a fluid layer is unstable if the layer is superadiabatic. The degree of superadibaticity is quantified as (Gilman & Glatzmaier 1981)

$$\epsilon \equiv -\frac{d}{C_P}\left(\frac{\partial s}{\partial r}\right)_0, \tag{2.1}$$

where d is the depth of the convection zone, C_P the specific heat capacity at constant pressure, s the entropy, and r the radial coordinate. The entropy gradient is calculated at some fiducial level in the convection zone. In the sun, the departure from adiabaticity in the convection zone is extremely small (Christensen-Dalsgaard *et al.* 1993),

$$\epsilon \leq 10^{-4}. \tag{2.2}$$

If we assume that the velocity in the horizontal (transverse to gravity) directions is mostly driven by pressure gradients, the coupling between vertical and horizontal velocities leads to the following relationship between the convection velocity v and sound speed c_s

$$\mathcal{M} \equiv \frac{v}{c_s} \sim \sqrt{\epsilon} \ll 1, \tag{2.3}$$

where $\mathcal{M}$ is the Mach number of the flow.

The basic idea in the anelastic approximation is to expand the variables in terms of the small parameter ϵ, and collect terms of the zeroth and first orders. As is usually found in perturbation theory, the zeroth order equations describe the basic state, which remain stationary over timescales at which the first order variables vary. The fundamental equations are the compressible, stratified Navier-Stokes equations in a rotating reference frame

$$\rho\left(\frac{\partial \mathbf{v}}{\partial t} + (\mathbf{v}\cdot\nabla)\mathbf{v}\right) = -\nabla P + \rho\mathbf{g} + 2\mathbf{v}\times\Omega_0 + \nabla\cdot\mathcal{D}, \tag{2.4}$$

$$\rho\Theta\frac{\partial s}{\partial t} + \rho\Theta\mathbf{v}\cdot\nabla s = -\nabla\cdot q + 2\nu\rho\left(e_{ij}e_{ij} - \frac{1}{3}(\nabla\cdot\mathbf{v})^2\right) - \rho\mathcal{E}, \tag{2.5}$$

$$\frac{\partial \rho}{\partial t} + \nabla\cdot(\rho\mathbf{v}) = 0, \tag{2.6}$$

where s is the entropy, Θ is the temperature, and $\mathcal{E}$ is the nuclear energy generation rate. The viscous stress $\mathcal{D}$ is defined as

$$\mathcal{D} \equiv 2\rho\nu\left(e_{ij} - \frac{1}{3}(\nabla\cdot\mathbf{v})\delta_{ij}\right), \tag{2.7}$$

and q is the composite non-convective heat flux, defined as

$$q \equiv -\kappa\rho\Theta\nabla s - \kappa_r\rho C_p\nabla\Theta. \tag{2.8}$$

and the various transport coefficient such as the viscosity ν, thermal diffusion κ, and radiative thermal diffusion κ_r are assumed to be functions of the radial coordinate only.

Upon substituting the variables expanded in terms of the small parameter ϵ, at zeroth order we obtain the hydrostatic equation. Denoting the zeroth order terms with a subscript 0, the equations at the leading order are

$$\frac{\partial P_0}{\partial r} + \Lambda = -\rho_0 g, \tag{2.9}$$

$$P_0 = \mathcal{R}\rho_0\Theta_0, \tag{2.10}$$

where Λ is the radial gradient of a mean turbulent pressure

$$\Lambda \equiv \langle [\rho_0(\mathbf{v}\cdot\nabla)\mathbf{v} - \nabla\cdot\mathcal{D} - 2\rho_0(\mathbf{v}\times\Omega_0)]_r\rangle_t\,. \tag{2.11}$$

The angular brackets in Equation (2.11) denote horizontal averages, and the square brackets denote the radial component of the enclosed vector. We evaluate Λ only as we update the reference state (denoted with a subscript 0).

At the next order, we obtain the anelastic equations for compressible, stratified fluids

$$\frac{\partial \rho_0\mathbf{v}}{\partial t} + \rho_0(\mathbf{v}\cdot\nabla)\mathbf{v} = -\nabla P + \nabla\cdot\mathcal{D} + \rho\mathbf{g} + 2\rho_0(\mathbf{v}\times\Omega_0) + \Lambda\hat{r}, \tag{2.12}$$

$$\begin{aligned}\rho_0\Theta_0\frac{\partial s}{\partial t} + \rho_0\Theta_0\mathbf{v}\cdot\nabla(s_0+s) = \nabla\cdot(\kappa\rho_0\Theta_0\nabla(s_0+s) + \kappa_r\rho_0 C_p\nabla(\Theta_0+\Theta)) \\ +2\nu\rho_0\left(e_{ij}e_{ij} - \frac{1}{3}(\nabla\cdot\mathbf{v})^2\right) - \rho_0\mathcal{E},\end{aligned} \tag{2.13}$$

$$\nabla\cdot(\rho_0\mathbf{v}) = 0, \tag{2.14}$$

and

$$\frac{\rho}{\rho_0} = \frac{P}{P_0} - \frac{\Theta}{\Theta_0} = \frac{P}{\gamma P_0} - \frac{s}{C_p}. \tag{2.15}$$

We note that both the reference state and perturbation terms have been retained in Equation (2.13) because the gradient of the reference state entropy (s_0) varies in amplitude from $\mathcal{O}(\epsilon)$ in the convection zone to $\mathcal{O}(1)$ in the convectively stable region. This scaling is also true for the term involving thermal diffusion of the reference temperature ($\kappa_r\partial\Theta_0/\partial r$). We retain the term $\kappa_r\partial\Theta/\partial r$ because we wish to allow for small deviations of the radiative heat flux from spherical symmetry.

The viscosity coefficient ν is assumed to be a function of the reference density ρ_0. The functional dependence is obtained from mixing length theory, and the specific value is chosen in an *ad hoc* fashion for a given numerical resolution and combination of parameters. Our main goal in this work is to replace these "mixing length" viscosity and thermal diffusivity with those based on Smagorinsky subgrid scale model. More details will be presented in §2.2.

The reference state is crucial in the simulation of the anelastic system. In the ASH code, the reference state is updated only every few hundred steps of advancing the anelastic equations. During the update process, the following equations are solved simultaneously for the reference pressure P_0 and density ρ_0:

$$\frac{1}{C_P}\frac{ds_0}{dr} = \frac{1}{\gamma}\frac{d\ln P_0}{dr} - \frac{d\ln\rho_0}{dr}, \tag{2.16}$$

$$\frac{dP_0}{dr} = -\rho_0 g. \tag{2.17}$$

Using the reference entropy gradient (ds_0/dr) and gravity ($g(r)$) profiles from the previous time step, Equations (2.16) and (2.17) are solved for the reference pressure and density. Figure 1 is an example from one of the ASH simulations. With similar

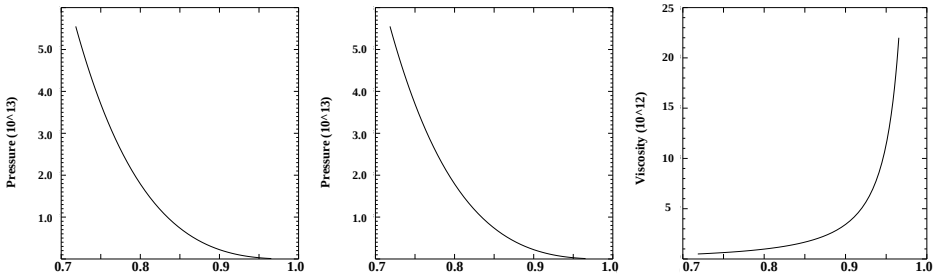

FIGURE 1. Reference state from ASH simulations, the horizontal axis is radial coordinate in units of solar radius. Panel (a): Reference pressure (dyne/cm^2) within the convection zone. Panel (b): Reference density (g/cm^3). Panel (c): the "mixing length" viscosity (cm^2/sec) as a function of r.

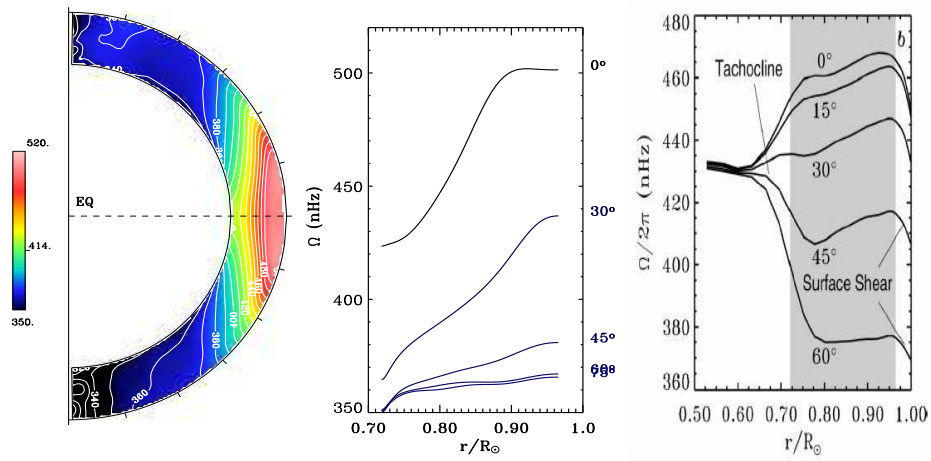

FIGURE 2. Panels (a) and (b): Differential rotation for the AB case in Brun & Toomre (2002) with different initial conditions. Panel (c) is the time-averaged rotation rates from five years of GONG data.

reference states and viscosity profiles to those illustrated in figure 1, simulations of the ASH code have successfully generated differential rotation profiles that are similar to the solar observations. An example from ASH simulations is illustrated in figure 2. The numerical resolution for figure 2 is $65 \times 128 \times 256$ in the radial, latitudinal, and azimuthal directions. The left panel is a filled contour plot of the averaged angular velocity as a function of latitude and radius, while the right panel shows the angular velocity at five latitudes as a function of radius from the bottom to the top of the convection zone. For this particular case, the viscosity is a prescribed function of radius as shown in figure 1(c), and the Prandtl number is fixed at 1/4. This corresponds to the AB case in Brun & Toomre (2002), in which the differential rotation inside the convection zone is most prominent among all the simulation data presented in Brun & Toomre (2002). Figure 2 is from simulations conducted on the NASA/Ames SGI cluster with different initial conditions. A typical differential rotation from solar helioseismic observations is shown in figure 2(c) (same as figure 1(b) in Brun & Toomre (2002)). The close similarity between observational solar differential rotation and the simulation data shows great promise that better results may be obtainable if the conveciton model is refined by building in more

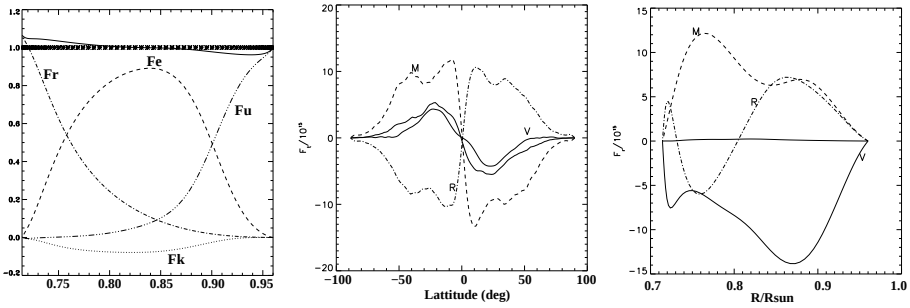

FIGURE 3. Panel (a): Energy flux scaled to the solar luminosity. Panel (b): Radial components of the momentum fluxes. Panel (c): Latitudinal components of the momentum fluxes.

physics. For example, the viscosity and thermal diffusivity may be replaced by better dynamical models. Addition of a mechanism to couple the convection zone with the tachocline below may result in better agreement between simulation and observational data. As a preliminary initiative we have undertaken is to first improve the model for viscosity using Smagorinsky-Lilly's model. Finally in figure 3 we show several energy fluxes and momentum fluxes as functions of r for the AB case:

$$\text{Fe} = \text{radial enthalpy flux} = C_p \rho v_r (T - \bar{T}), \tag{2.18}$$

$$\text{Fk} = \text{radial kinetic energy flux} = v_r K.E., \tag{2.19}$$

$$\text{Fr} = \text{radiative flux} = -\kappa_{rad} \hat{\rho} C_p \frac{d}{dr}\left[\sqrt{4\pi}\hat{T} + \left(\frac{\partial \hat{T}}{\partial \hat{S}}\hat{S} + \frac{\partial \hat{T}}{\partial \hat{P}}\hat{P}\right)\right], \tag{2.20}$$

$$\text{Fu} = \text{unresolved eddy flux} = \kappa_{00} \frac{\text{Solar luminosity}}{4\pi r^2}, \tag{2.21}$$

$$\text{R} = \hat{\rho} r \sin\theta \langle v_i' v_\phi' \rangle, \tag{2.22}$$

$$\text{M} = \hat{\rho} r \sin\theta \langle v_i \rangle \left(\langle v_\phi \rangle + \Omega_0 r \sin\theta\right) \tag{2.23}$$

$$\text{V} = \hat{\rho} r \sin\theta \left[-\nu \frac{\sin\theta}{r} \frac{\partial}{\partial r}\left(\frac{\langle v_\phi \rangle}{r}\right)\right] \text{ for panel (b), or} \tag{2.24}$$

$$\text{V} = \hat{\rho} r \sin\theta \left[-\nu \frac{\sin\theta}{r} \frac{\partial}{\partial \theta}\left(\frac{\langle v_\phi \rangle}{\sin\theta}\right)\right] \text{ for panel (c).}$$

The index i in equations 2.22 and 2.23 corresponds to the r component for panel b in figure 3, while for panel c the index i corresponds to the θ component.

2.2. *Smagorinsky-Lilly SGS model*

The principle underlying the Smagorinsky subgrid scale model is the balance of production of subgrid-scale turbulent kinetic energy and dissipation of isotropic turbulence energy at the characteristic eddy size. Let the subgrid turbulent production rate be denoted by $\mathcal{P}$, then for a given turbulent viscosity ν_T, the subgrid turbulent production rate is

$$\mathcal{P} = 2\nu_T e_{ij} e_{ij}. \tag{2.25}$$

The dissipation at scale l is $\sim q^3/l$, where q is a characteristic turbulent velocity. Finally, to find an expression for ν_T in terms of the resolved quantities, we utilize the Prandtl's assumption: $\nu_T = C_1 q l$, and upon substituting q into the dissipation rate and equating

dissipation and production rates, we obtain the Smagorinsky subgrid scale model

$$\nu_T = (C_s l)^2 \sqrt{2e_{ij}e_{ij}}, \tag{2.26}$$

where C_s is a constant in the range of $0.1 \leq C_s \leq 0.3$. Lilly (1962) later extended the Smagorinsky model to turbulence in unstably stratified convection. Due to the stratification an additional parameter, the Richardson number, appears in the expression for the eddy viscosity. The idea that led to Lilly's eddy viscosity is very similar to the above argument underlying the Smagorinsky model: buoyancy production or consumption must also be accounted for in the subgrid energy balance. Thus in the stratified case, the dissipation consists of contribution from both eddy dissipation and thermal diffusion. The Smagorinsky-Lilly eddy viscosity is simply the modified Smagorinsky model with the inclusion of stratification effect

$$\nu_T = (C_s l)^2 \sqrt{2e_{ij}e_{ij}} \left[1 - \frac{\kappa_T}{\nu_T} Ri_f\right]^{0.5}. \tag{2.27}$$

Here κ_T is the eddy thermal diffusivity, and the flux Richardson number is defined as

$$Ri_f \equiv \frac{g}{2e_{ij}e_{ij}} \frac{\partial \ln \theta}{\partial r}. \tag{2.28}$$

Alternatively, the flux Richardson number can also be defined through entropy as

$$Ri_f \equiv \frac{g}{2e_{ij}e_{ij}} \frac{\partial s_0/\partial r}{C_p}, \tag{2.29}$$

where $\partial s_0/\partial r$ is the reference entropy gradient. In spherical geometry, we choose the length scale l as

$$l \equiv \left(\frac{\Delta(r) r^2}{L_{max}(L_{max}+1)}\right)^{1/3}, \tag{2.30}$$

where $\Delta(r)$ is the radial grid spacing at location r, L_{max} is the maximum (latitudinal) angular mode index.

In the simulations we start from a stationary configuration with a negative reference entropy gradient throughout the convection zone. The boundary conditions for the velocity are stress free, which are not necessarily realistic but numerically convenient. As we are mostly interested in the differential rotation profile in the convection zone, the parameters and initial reference state are chosen to be the same as the AB case in Brun & Toomre (2002). We first obtain a turbulent convection zone using the mixing length viscosity and thermal diffusivity. As the simulation progresses, the differential rotation profile reaches a statistically stationary state. We then replace the mixing length viscosity and thermal diffusivity with the Smagorinsky-Lilly model with a prescribed constant coefficient C_s. For the following results, we present ASH simulations using the Smagorinsky-Lilly eddy viscosity to see how the differential rotation may differ from that obtained with the "mixing length" viscosity and thermal diffusivity.

3. Thermal diffusivity and differential rotation

Using the Smagoranski-Lilly SGS model with a fixed $C_s = 0.3$, an eddy Prandtl number of 0.7 and restarting from the AB case (with a differential rotation in figure 2), we find that the differential rotation to deteriorate and the spread in the angular velocity decreases to a smaller value ($\sim$ 60 nHz) as shown in figure 4. Similar results are found

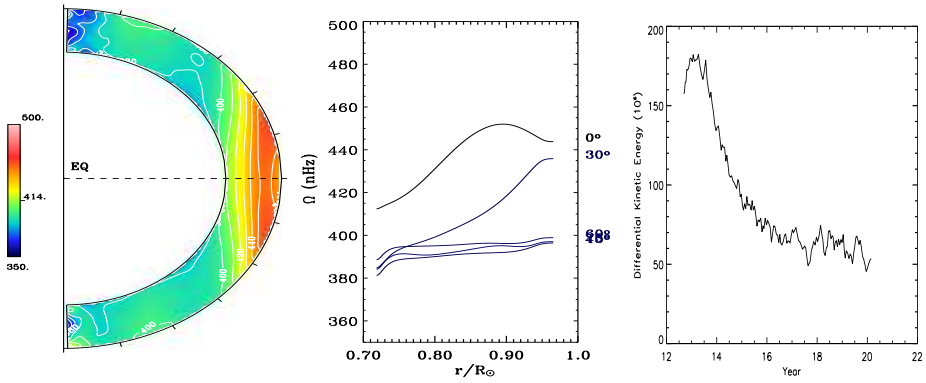

FIGURE 4. Panel (a): Differential rotation with the AB case as the initial conditions. Panel (b) is the energy associated with the differential rotation as a function of time (years).

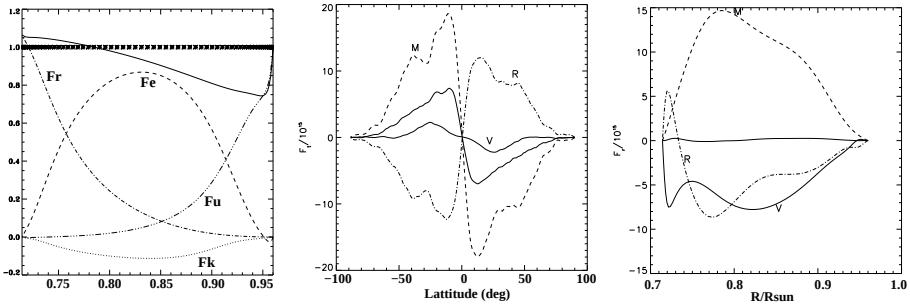

FIGURE 5. Panel (a): Energy flux scaled to the solar luminosity. Panel (b): Radial components of the momentum fluxes. Panel (c): Latitudinal components of the momentum fluxes.

as we vary C_s and the eddy Prandtl number. In figure 5 we show the fluxes for this simulation when the "statistically" steady state is reached.

We notice that the energy balance is worsened due to the decrease in the radial enthalpy flux (Fe) and the unresolved eddy flux (Fu). Based on the fact that the molecular thermal diffusivity is much larger than the molecular viscosity in the solar convection, and also the anelastic assumption that the base state evolves on the much slower time scale than the convection, we separate the thermal diffusivity from the eddy viscosity as follows: we adopt the thermal diffusivity from Brun & Toomre (2002) and use the Smagorinsky-Lilly SGS model only for the eddy viscosity. This hybrid approach may be reasonable for very small molecular Prandtl number convections. We then restart from the AB case again, and in this case the differential rotation (figure 6) does not deteriorate as much as in previous simulations where we fixed the eddy Prandtl number. Furthermore, we notice that the momentum fluxes are closer to those from the AB simulations in Brun & Toomre (2002). We further notice that the differential rotation profile from our hybrid modeling is actually quite close to the observational differential profile (panel (c) in figure 2). Thus we conclude that the thermal diffusion is a key ingredient in the anelastic modeling of solar convection, especially in terms of the differential rotation and the balances in energy and momentum fluxes.

This is encouraging for adopting the SGS modeling to extra-terrestrial turbulent convection, where the molecular Prandtl number is always much smaller than unity. Thus

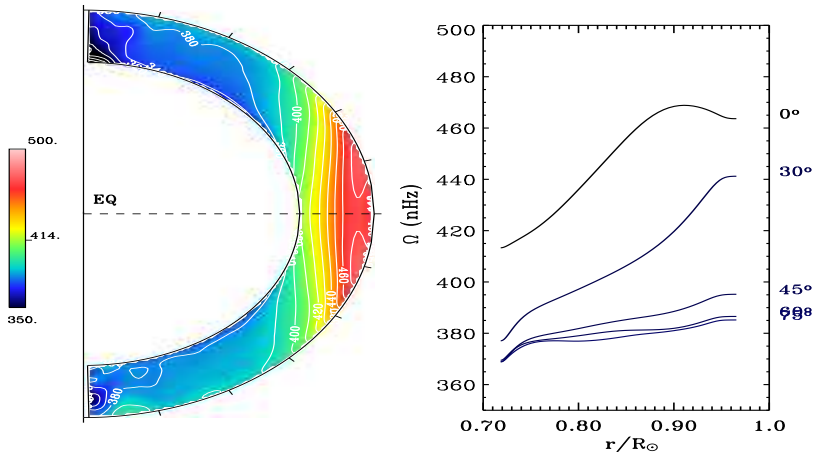

FIGURE 6. Differential rotation with the AB case as the initial conditions. The Smagorinsky-Lilly SGS is used only for the eddy viscosity, and the thermal diffusivity in Brun & Toomre (2002) is adopted here.

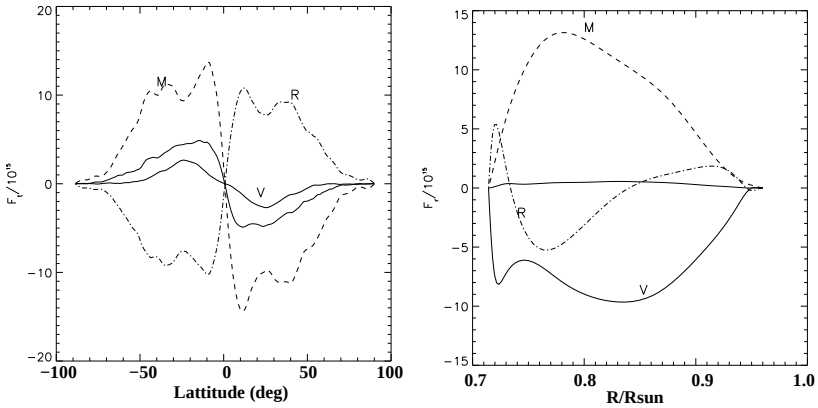

FIGURE 7. Panel (a): Radial components of the momentum fluxes. Panel (b): Latitudinal components of the momentum fluxes.

the energy balance on the micro scales may not be described by Lilly's argument where the eddy Prandtl number is assumed constant. In particular, the stratification in the solar convection may be such that the compressibility and the large thermal diffusivity conspire to give an eddy Prandtl number which depends on the radius. Thus it is possible that the dynamic procedure can give some insight to how the eddy Prandtl number adjusts itself due to stratification and large molecular thermal diffusivity.

REFERENCES

BRUN, A. S. & TOOMRE, J. 2002 Turbulent convection under the influence of rotation: sustaining a strong differential rotation. *Astrophysical Journal* **570**, 865.

CHRISTENSEN-DALSGAARD, J., PROFFITT, C. R. & THOMPSON, M. J. 1993 Effects of diffusion on solar models and their oscillation frequencies. *Astrophysical Journal* **403**, L75.

CLUNE, T. C., ELLIOTT, J. R., MIESCH, M. S. & TOOMRE, J. 1999 Computational aspects of a code to study rotating turbulent convection in spherical shells. *Parallel Computing* **25**, 361.

GILMAN, P. A. & GLATZMAIER, G. A. 1981 Compressible convection in a rotating spherical shell. i anelastic equations. *Astrophysical Journal Suppl.* **45**, 335.

GOUGH, D. O. 1969 The anelastic approximation for thermal convection. *J. Atmo. Sci.* **26**, 448.

LILLY, D. K. 1962 On the numerical simulation of buoyant convection. *Tellus* **24**, 148.

MIESCH, M. S. 1998 Turbulence and convection in stellar and interstellar environments. University of Coloardo, Boulder.

Solar convection simulations using a B-spline method

By T. Hartlep AND N. N. Mansour

1. Motivation and objectives

Convection plays a key role in energy transport and global circulation in the outer layers of the Sun, in generation of solar magnetic fields and in many phenomena associated with solar activity and variability. Observations of the solar surface reveal structures that have been classified as granules, mesogranules, and supergranules. The nomenclature reflects organization at three spatial scales ranging from about 1 Mm to 30 Mm.

Numerical simulations of the near surface region of the Sun (Stein & Nordlund 2000) capture structures on the granular scale, but have not been able to detect organization at large scales. The physical mechanism of supergranulation is presently unknown. It has been suggested that supergranulation corresponds to a large convective cells which develop due to enhanced convective instability in the HeII ionization layer. This layer lies deeper than Stein & Nordlund have investigated so far.

We know that as we go deeper from the surface of the sun, the turbulence structures become large, and the Mach number decreases. It is then advantageous to be able to change the spatial resolution in all three coordinates as a function of depth. In addition, it is numerically advantageous to use the anelastic approximation (Ogura & Phillips 1962; Gough 1969; Gilman & Glatzmaier 1981) to the compressible Navier-Stokes equations for deep domains. Using B-splines in one coordinate direction and Fourier methods in the other two coordinate directions, Kravchenko *et al.* (1996) and Loulou *et al.* (1997) have developed B-spline–spectral numerical schemes that enable changing the resolution as a function of height. Kravchenko *et al.* (1996) applied the scheme to simulate the fully developed turbulent channel flow by resolving the near-wall region and relaxing the resolution in the core region. Loulou *et al.* (1997) simulated a fully developed turbulent pipe flow. They applied the scheme to remove the centerline singularity in cylindrical coordinates.

2. Numerical method

Under this effort, a new code to simulate a rectilinear section of the solar convection zone is being implemented. As a first step, the numerical method is implemented for a simple Boussinesq fluid (Oberbeck 1879; Boussinesq 1903) and is presented in this paper for this case only. Later, once the new code is fully functional and tested, equations based on the anelastic approximation will be used.

2.1. *Basic equations*

Using the temperature difference across the fluid layer, ΔT, the layer thickness d and the thermal diffusion time d^2/κ as units of temperature, length and time, the dimensionless Boussinesq equations read:

$$\partial_t \vec{v} + (\vec{v} \cdot \nabla)\vec{v} = -\nabla\pi + Pr\nabla^2\vec{v} + RaPr\theta\vec{e}_z, \tag{2.1}$$

$$\partial_t \theta + (\vec{v} \cdot \nabla)\theta = \nabla^2 \theta + \vec{v} \cdot \vec{e}_z, \tag{2.2}$$

$$\nabla \cdot \vec{v} = 0. \tag{2.3}$$

$\vec{v}$, θ and π denote the velocity of the fluid and the deviations of the temperature and pressure from their static profiles, i.e. the temperature and pressure profiles that would be observed in the case of no motion. The equations contain two dimensionless parameters: the Prandtl number Pr and the Rayleigh number Ra, which are defined as

$$Pr = \frac{\nu}{\kappa}, \quad Ra = \frac{g\alpha \Delta T d^3}{\kappa \nu}, \tag{2.4}$$

with κ, ν, α and g being the coefficients of thermal conductivity, kinematic viscosity and thermal expansion, and the accelleration due to gravity, which points in negative z direction. The Boussinesq approximation assumes all these properties to be constant throughout the layer.

2.2. *Velocity decomposition*

A poloidal/toroidal decomposition is used for the velocity to automatically fulfill the continuity equation $\nabla \cdot \vec{v} = 0$. Even though the divergence of the velocity does not vanish in the anelatic approximation, the equations that we are ultimately going to use, such a representation can still be used. Just not for the velocity itself, but for the quantity $\rho_0 \vec{v}$, where ρ_0 denotes the reference density.

In the Boussinesq case, the representation is in the form of

$$\vec{v}(x,y,z,t) = \nabla \times [\psi(x,y,z,t)\vec{e}_z] + \nabla \times \nabla \times [\phi(x,y,z,t)\vec{e}_z] + \vec{U}(z,t). \tag{2.5}$$

In this way the poloidal and toroidal scalars ϕ and ψ are periodic in x and y, and $\vec{U}$ represents the horizontal average of the velocity, i.e

$$\vec{U}(z,t) = \left\langle \vec{v}(x,y,z,t) \right\rangle_{x,y}. \tag{2.6}$$

The z component of $\vec{U}$ must be zero to satisfy the continuity equation. $\vec{U}$ is thus a toroidal flow. However, the corresponding toroidal scalar varies linearly in x and y and is unbounded. Obviously, we require ϕ to be periodic and to remain finite in the numerical representation. Therefore $\vec{U}$ needs to be included in the decomposition of $\vec{v}$ (Schmitt & von Wahl 1992).

Equations of motion for ϕ, ψ and $\vec{U}$ can be derived by evaluating the z component of the curl of the curl of (2.1), the z component of the curl of (2.1) and the horizontal average of (2.1), respectively.

2.3. *Spectral method for the horizontal directions*

Periodic boundary conditions are used in the horizontal directions to reduce the influence of the horizontal boundaries on the flow. A natural choice is the use of Fourier modes in those directions, i.e.

$$f(x,y,z,t) = \sum_{\vec{k}} \hat{f}_{\vec{k}}(z,t) e^{-i(k_x x + k_y y)} \qquad (f = \phi, \psi, \theta), \tag{2.7}$$

with $\vec{k} = k_x \vec{e}_x + k_y \vec{e}_y$ being the horizontal wave vector. Multiplying the equations of motion with weight functions $e^{i(k'_x x + k'_y y)}$ and integrating over the entire horizontal plane then yields equations for the z and t dependent Fourier coefficients:

$$[\partial_z^2 - k^2]\Big[\partial_t - Pr[\partial_z^2 - k^2]\Big]\hat{\phi}_{\vec{k}}(z,t) = \mathcal{R}_{\hat{\phi}_{\vec{k}}}(z,t), \tag{2.8}$$

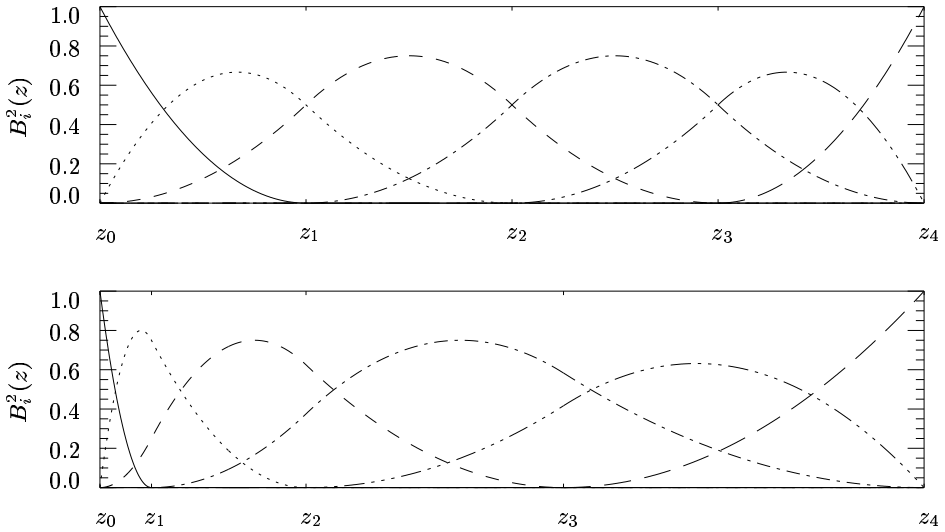

FIGURE 1. Second-order B-splines defined on sets of 5 knot point in the case of equally spaced knot points (top diagram) and non-equally spaced knot points (bottom diagram). In both cases solid, dotted, dashed, dash-dotted, dash-dot-dotted and long-dashed lines denote splines $B_1^2, \ldots, B_6^2$, respectively.

$$\Big[\partial_t - Pr[\partial_z^2 - k^2]\Big]\hat{\psi}_{\vec{k}}(z,t) = \mathcal{R}_{\hat{\psi}_{\vec{k}}}(z,t), \tag{2.9}$$

$$\Big[\partial_t - [\partial_z^2 - k^2]\Big]\hat{\theta}_{\vec{k}}(z,t) = \mathcal{R}_{\hat{\theta}_{\vec{k}}}(z,t). \tag{2.10}$$

All non-linear terms are contained in the right-hand sides $\mathcal{R}$. The equation for $\vec{U}$ is very similar:

$$[\partial_t - Pr\partial_z^2]\vec{U}(z,t) = \mathcal{R}_{\vec{U}}(z,t). \tag{2.11}$$

If fact, we can discuss the equation for $\hat{\psi}_{\vec{k}}$, $\hat{\theta}_{\vec{k}}$ and $\vec{U}$ together, since they all can be written in the form

$$[\partial_t + C_0 - C_2\partial_z^2]f(z,t) = \mathcal{R}_f(z,t) \qquad (f = \hat{\psi}_{\vec{k}}, \hat{\theta}_{\vec{k}}, \vec{U}), \tag{2.12}$$

with some parameters C_0 and C_2.

2.4. *B-spline method for the vertical direction*

Spatial discretization in the vertical direction z is done by a B-spline method (Kravchenko & Moin 1998), i.e. the unknowns, $\hat{\phi}_{\vec{k}}, \hat{\psi}_{\vec{k}}, \hat{\theta}_{\vec{k}}$ and $\vec{U}$, are expanded in terms of m-order piecewise polynomials called basis splines, or B-splines. With a given set of knot points $\{z_0, \ldots, z_N\}$ that divide the z domain into N subintervals, one can construct $N + m$ of these spline functions using the recursive expression

$$B_j^m(z) = \frac{z - z_{j-m-1}}{z_{j-1} - z_{j-m-1}} B_{j-1}^{m-1}(z) + \frac{z_j - z}{z_j - z_{j-m}} B_j^{m-1}(z) \qquad (j = 1, \ldots, N + m). \tag{2.13}$$

Here, B_j^m denotes the j-th B-spline of order m. The 0-order splines are given by

$$B_j^0(z) = \begin{cases} 1 & \text{if } z_{j-1} \leq z \leq z_j \\ 0 & \text{otherwise} \end{cases} . \tag{2.14}$$

As it turns out, m additional points at each side of the domain ($z_{-m}, \ldots, z_{-1}$ and $z_{N+1}, \ldots, z_{N+m}$) are needed in the construction of B-splines near the boundaries. These virtual points are chosen to be equal to the boundary points z_0 and z_N, i.e. $z_{-m} = \ldots = z_{-1} = z_0$ and $z_{N+m} = \ldots = z_{N+1} = z_N$.

Second-order B-spline functions for two different sets of knot points are shown in figure 1 to illustrate how these functions look like. As can be seen from the figure, B-splines have compact support and are non-negative:

$$B_j^m(z) \begin{cases} > 0 & \text{if } z_{j-m-1} < z < z_j \\ = 0 & \text{otherwise} \end{cases} , \tag{2.15}$$

and can be tuned to the specific needs at hand by the choice of knot points. In areas where small structures need to be resolve, e.g. in boundary layers, one can choose closely spaced knot points, while in areas where such high resolution is not required, the grid can be coarse to save computational costs.

Incorporating a B-spline expansion of the unknowns, i.e.

$$f(z,t) = \sum_{j=1}^{N+m} \alpha_{f,j}(t) B_j^m(z) \qquad (f = \hat{\phi}_{\vec{k}}, \hat{\psi}_{\vec{k}}, \hat{\theta}_{\vec{k}}, \vec{U}), \tag{2.16}$$

into the governing equations (2.8) and (2.12), multiplying with weight functions B_i^m and integrating over the z domain yields equations for the expansion coefficients $\alpha_{f,j}(t)$:

$$\sum_{j=1}^{N+m} \left[(\partial_t + C_0) \left(\mathcal{M}_0 \right)_i^j - C_2 \left(\mathcal{M}_2 \right)_i^j \right] \alpha_{f,j} = \int B_i^m \mathcal{R}_f dz \qquad (f = \hat{\psi}_{\vec{k}}, \hat{\theta}_{\vec{k}}, \vec{U}), \tag{2.17}$$

$$\sum_{j=1}^{N+m} \left[-(k^2 \partial_t + k^4 Pr) \left(\mathcal{M}_0 \right)_i^j + (\partial_t + 2k^2 Pr) \left(\mathcal{M}_2 \right)_i^j - Pr \left(\mathcal{M}_4 \right)_i^j \right] \alpha_{\hat{\phi}_{\vec{k}},j} = \int B_i^m \mathcal{R}_{\hat{\phi}_{\vec{k}}} dz. \tag{2.18}$$

Three matrices, $\mathcal{M}_0$, $\mathcal{M}_2$ and $\mathcal{M}_4$, occur in these equations, which contain integrals of the product of two B-splines and the product of a B-spline with a derivative of a B-spline:

$$\left(\mathcal{M}_n \right)_{i=1,\ldots,N+m}^{j=1,\ldots,N+m} = \int B_i^m \partial_z^n B_j^m dz \qquad (n = 0, 2, 4). \tag{2.19}$$

It follows from the property (2.15) that all of these matrices are of band-diagonal form. Specifically, they have only m subdiagonals and m superdiagonals which contain non-zero entries.

2.5. *Time advancement*

A mixed implicit/explicit method using a Crank-Nicolson scheme for the diffusive terms and a second-order Adams-Bashforth scheme for the advection and buoyancy terms is used for the time advancement.

In the end, one has to solve a matrix equation for each Fourier mode of each field (poloidal, toroidal, mean flow and temperature) in the form

$$\mathcal{N}_f \vec{a}_f = \vec{b}_f, \tag{2.20}$$

with $\vec{a}_f$ representing the vector of B-spline coefficients at the new time step t_{n+1}, i.e. $\vec{a}_f = (\alpha_{f,1}(t_{n+1}), \ldots, \alpha_{j,N+m}(t_{n+1}))$ (f again stands for either $\hat{\phi}_{\vec{k}}$, $\hat{\psi}_{\vec{k}}$,$\hat{\theta}_{\vec{k}}$ or $\vec{U}$), and the matrix $\mathcal{N}_f$ is composed of the previously introduced matrices $\mathcal{M}_0$, $\mathcal{M}_2$ and $\mathcal{M}_4$. $\mathcal{N}_f$ is therefore band-diagonal and a fast method for solving band-diagonal systems can be used.

2.6. *Imposing boundary conditions*

So far, no boundary conditions have been imposed in the vertical direction. Since only one B-spline, and the derivative of only two B-splines are non-zero at the boundary, it is rather easy to implement various boundary conditions. If for example one needs to prescribe the value of $f(z,t)$ at the boundary z_0, e.g. $f(z = z_0, t) = g(t)$, one simply has to set the first B-spline coefficient to that value, i.e. $\alpha_{f,1}(t) = g(t)$. The original equation for $\alpha_{f,1}$ has to be removed from the linear system (2.20), and $\alpha_{f,1}$'s contribution has to be deducted from the right hand, i.e. equation (2.20) is modified in the following way:

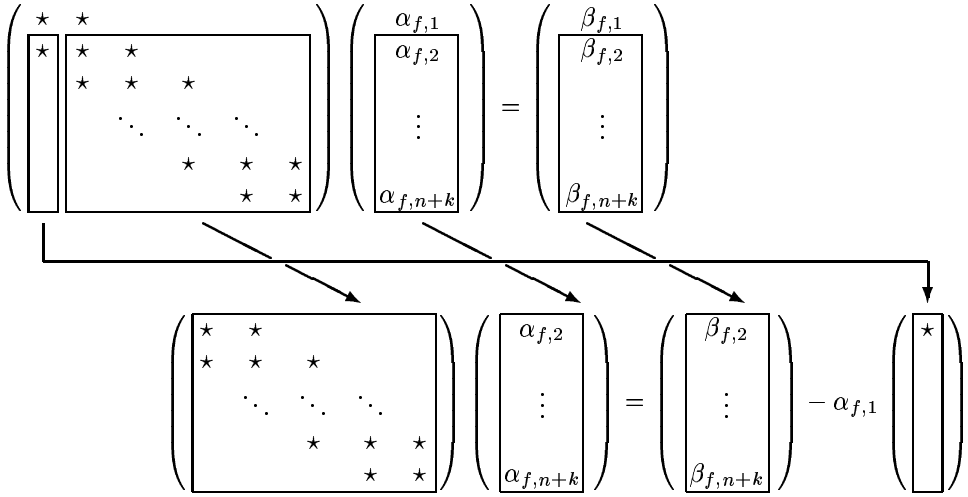

More complicated boundary conditions in which the value of the B-spline coefficients at the boundary depend on the coefficients in the interior can be implemented by directly manipulating the matrix elements of $\mathcal{N}_f$.

2.7. *Varying numerical resolution with depth*

The main advantage of such a B-spline method is the ability to vary the spatial resolution in all directions as a function of depth. As already mentioned, the choice of knot points in the construction of the B-spline functions determines the vertical resolution. Near the surface of the sun, where high spatial resolution is required, closely spaced knot points will be chosen, while the spacing can be increased in deeper parts of the convection zone. The spatial resolution in horizontal directions is determined by the number of Fourier modes that one wants to consider in the discretization:

$$f(x,y,z,t) = \sum_j \sum_{\vec{k}} \alpha_{f,j}(t) e^{-i(k_x x + k_y y)} B_j^m(z) \qquad (f = \phi_{\vec{k}}, \psi_{\vec{k}}, \theta_{\vec{k}}), \tag{2.21}$$

and this number can be changed from one spline index j to the next. Since according to (2.15) B-splines of different j overlap, the change in resolution occurs over several knot points. A consequence of the variation of horizontal resolution is, that for a given set of

wavenumbers k_x and k_y only a subset of B-splines has to be considered, namely those for which the maximum wavenumbers that we have chosen are larger or equal to k_x and k_y. The other coefficients are zero and the corresponding rows and columns in the matrix equations (2.20) can therefor be dropped to reduce the numerical cost.

3. Future work

The implementation of the presented numerical method is nearly complete and will be tested shortly for some test cases of turbulent Rayleigh-Bénrad convection. Comparisons will be done with the results obtained by Hartlep (2004) using a Chebyshev method. After that, the anelastic equations will be implemented in place of the Boussinesq equations.

The final ingredient for the solar simulations is the definition of reasonable boundary conditions. As a start, we can use rather simple conditions like the ones used by Miesch (1998) and others: stress-free, impenetrable upper und lower boundaries with constant heat flux at the bottom and constant entropy at the top of the computational domain. A refinement to these boundary conditions would be the treatment of the upper surface as a free surface, which could be realized by additionally tracking a height function $h(x, y, t)$ above the top end of the discretization (2.21).

REFERENCES

BOUSSINESQ, J. 1903 *Theorie Analytique de la Chaleur*, vol. 2. Paris: Gauthier-Villars.

GILMAN, P. & GLATZMAIER, G. A. 1981 Compressible convection in a rotating spherical shell. I. Anelastic equations. *Astrophys. J. Suppl.* **45**, 335–388.

GOUGH, D. O. 1969 The anelastic approximation for thermal convection. *J. Atmos. Sci.* **26**, 448–456.

HARTLEP, T. 2004 *Strukturbildung und Turbulenz. Eine numerische Studie zur turbulenten Rayleigh-Bénard Konvektion*. Doctoral thesis. Institute of Geophysics, University of Göttingen.

KRAVCHENKO, A. G. & MOIN, P. 1998 *B-spline methods and zonal grids for numerical simulations of turbulent flows*. Report No. TF-73, Department of Mechanical Engineering, Stanford University.

KRAVCHENKO, A. G., MOIN, P. & MOSER, R. 1996 Zonal embedded grids for numerical simulations of wall-bounded turbulent flows. *J. Comp. Phys.* **127(2)**, 412–423.

LOULOU, P., MOSER, R. D., MANSOUR, N. N. & CANTWELL, B. J. 1997 *Direct numerical simulation of incompressible pipe flow using a B-Spline Spectral Method*. Technical Memorandum 110436, NASA Ames Research Center.

MIESCH, M. S. 1998 *Turbulence and convection in stellar and interstellar enviroments*. PhD thesis. Department of Astrophysical and Planetary Sciences, University of Colorado.

OBERBECK, A. 1879 Über die Wärmeleitung der Flüssigkeiten bei Berücksichtigung der Strömungen infolge von Temperaturdifferenzen. *Ann. Phys. Chem.* **7**, 271–292.

OGURA, Y. & PHILLIPS, N. A. 1962 Scale analysis of deep and shallow convection in the atmosphere. *J. Atmos. Sci.* **19**, 173–179.

SCHMITT, B. J. & VON WAHL, W. 1992 Decomposition into poloidal fields, toroidal fields, and mean flow. *Differential and Integral Equations* **5**, 1275–1306.

STEIN, R. F. & NORDLUND, A. 2000 Realistic solar convection simulations. *Solar Phys.* **192**, 91–108.